Conference Proceedings of the Society for Experimental Mechanics Series

Hae Young Noh
Matthew Whelan
P. Scott Harvey *Editors*

Dynamics of Civil Structures, Volume 2

Proceedings of the 41st IMAC, A Conference and Exposition on Structural Dynamics 2023

SEM

Springer

Conference Proceedings of the Society for Experimental Mechanics Series

Series Editor

Kristin B. Zimmerman
Society for Experimental Mechanics, Inc.,
Bethel, CT, USA

The Conference Proceedings of the Society for Experimental Mechanics Series presents early findings and case studies from a wide range of fundamental and applied work across the broad range of fields that comprise Experimental Mechanics. Series volumes follow the principle tracks or focus topics featured in each of the Society's two annual conferences: IMAC, A Conference and Exposition on Structural Dynamics, and the Society's Annual Conference & Exposition and will address critical areas of interest to researchers and design engineers working in all areas of Structural Dynamics, Solid Mechanics and Materials Research.

Hae Young Noh • Matthew Whelan • P. Scott Harvey
Editors

Dynamics of Civil Structures, Volume 2

Proceedings of the 41st IMAC, A Conference and Exposition on Structural Dynamics 2023

Springer

Editors
Hae Young Noh
Stanford University
Stanford, CA, USA

Matthew Whelan
University of North Carolina at Charlotte
Charlotte, NC, USA

P. Scott Harvey
University of Oklahoma
Norman, OK, USA

ISSN 2191-5644 ISSN 2191-5652 (electronic)
Conference Proceedings of the Society for Experimental Mechanics Series
ISBN 978-3-031-36662-8 ISBN 978-3-031-36663-5 (eBook)
https://doi.org/10.1007/978-3-031-36663-5

© The Society for Experimental Mechanics, Inc. 2024
This work is subject to copyright. All rights are solely and exclusively licensed by the Publisher, whether the whole or part of the material is concerned, specifically the rights of translation, reprinting, reuse of illustrations, recitation, broadcasting, reproduction on microfilms or in any other physical way, and transmission or information storage and retrieval, electronic adaptation, computer software, or by similar or dissimilar methodology now known or hereafter developed.
The use of general descriptive names, registered names, trademarks, service marks, etc. in this publication does not imply, even in the absence of a specific statement, that such names are exempt from the relevant protective laws and regulations and therefore free for general use.
The publisher, the authors, and the editors are safe to assume that the advice and information in this book are believed to be true and accurate at the date of publication. Neither the publisher nor the authors or the editors give a warranty, expressed or implied, with respect to the material contained herein or for any errors or omissions that may have been made. The publisher remains neutral with regard to jurisdictional claims in published maps and institutional affiliations.

This Springer imprint is published by the registered company Springer Nature Switzerland AG
The registered company address is: Gewerbestrasse 11, 6330 Cham, Switzerland

Paper in this product is recyclable.

Preface

Dynamics of Civil Structures represents one of ten volumes of technical papers presented at the 41st IMAC, A Conference and Exposition on Structural Dynamics, organized by the Society for Experimental Mechanics, and held February 13–16, 2023. The full proceedings also include volumes on Nonlinear Structures and Systems; Dynamics of Civil Structures; Model Validation and Uncertainty Quantification; Dynamic Substructures; Special Topics in Structural Dynamics and Experimental Techniques; Computer Vision and Laser Vibrometry; Dynamic Environments Testing; Sensors and Instrumentation and Aircraft/Aerospace Testing Techniques; Topics in Modal Analysis and Parameter Identification; and Data Science in Engineering.

Each collection presents early findings from analytical, experimental, and computational investigations on an important area within Structural Dynamics. Dynamics of Civil Structures is one of these areas which cover topics of interest of several disciplines in engineering and science.

The Dynamics of Civil Structures Technical Division serves as a primary focal point within the SEM umbrella for technical activities devoted to civil structures analysis, testing, monitoring, and assessment. This volume covers a variety of topics including structural vibrations, damage identification, human-structure interaction, vibration control, model updating, modal analysis of in-service structures, innovative measurement techniques and mobile sensing, and bridge dynamics, among many other topics.

Papers cover testing and analysis of different kinds of civil engineering structures such as buildings, bridges, stadiums, dams, and others.

The organizers would like to thank the authors, presenters, session organizers, and session chairs for their participation in this track.

Stanford, CA, USA — Hae Young Noh
Charlotte, NC, USA — Matthew Whelan
Norman, OK, USA — P. Scott Harvey

Contents

Chapter 1
Forced Response Measurements on a Seven-Story Timber Building

A. Linderholt, P. Landel, and M. Johansson

Abstract Within the project Dyna-TTB, vibrational tests have been conducted on eight high-rise timber buildings, in Europe. A main objective of the project is to gain knowledge about damping in timber buildings to assist in predicting the accelerations, at the top of a building, due to wind-induced vibrations.

One of the buildings is Eken (the oak) in Mariestad in Sweden. That building is seven stories tall, thus questionable as a tall timber building, yet an interesting test object. The building structure is made up of glue laminated timber beams and columns stabilized with glulam trusses.

Forced vibration were conducted on Eken with the aim to estimate the building's dynamic properties from test data. Estimates of the eigenfrequencies, mode shapes, and their scalings are useful both in the calculations of wind-induced vibrations and to calibrate numerical models. However, the most important outcome is estimates of the modal damping values. The damping impacts the acceleration and thus the serviceability of the building, and at the same time, it is very hard to model damping. So, during the design phase, one must rely on previous test data (of which very few exist for taller timber buildings) and rule of thumbs. It is therefore important to gain knowledge about the damping for timber buildings in order to enable good designs of future and taller timber buildings.

Keywords Forced vibration · Tall timber building · Dyna-TTB · Wind induced motion · Stepped Sine excitation

1.1 Introduction

Within the project Dyna-TTB, measurements on eight high-rise timber building around Europe have been conducted [1]. The response of a structure is governed by four quantities: the mass, the damping, the stiffness, and the dynamic load. The damping is the one that is hardest to predict; reliable models are rare, and most often the damping is taken from tests or as one value of modal viscous damping taken from rule of thumbs. The dynamic wind load and the calculation of horizontal acceleration in serviceability level state has also shown to vary a lot between different standards [2]. One of the primary objectives of the Dyna-TTB project [3] is to broaden the knowledge base regarding damping in timber buildings. Such a data base is useful during the development of future, possibly even taller than the tallest today, high rise timber buildings. The seven-story building Eken, see Fig. 1.1, is one of the test objects in the project. Eken is situated in Mariestad in Sweden. The forced vibration test campaign on that building, which build up this paper, was made in the spring of 2022.

A. Linderholt (✉)
Department of Mechanical Engineering, Linnaeus University, Växjö, Sweden
e-mail: andreas.linderholt@lnu.se

P. Landel
Department of Mechanical Engineering, Linnaeus University, Växjö, Sweden

Wood Building Technology, RISE Research Institutes of Sweden, Borås, Sweden

M. Johansson
Wood Building Technology, RISE Research Institutes of Sweden, Borås, Sweden

H. Y. Noh et al. (eds.), *Dynamics of Civil Structures, Volume 2*, Conference Proceedings of the Society for Experimental Mechanics Series, https://doi.org/10.1007/978-3-031-36663-5_1

Fig. 1.1 The seven-story building Eken situated in Mariestad in Sweden

1.2 Background

The building Eken contains 31 rental apartments, and its height, width, and depth are 24, 27, and 19 m, respectively. The building was built by the company *Stenmarks Bygg*, it is owned by *Mariehus*, and it was finished in the autumn of 2019 [1]. Half of the bottom floor is made of concrete whereas the remaining storeys, including the elevator shaft, are made of timber. The load bearing system consists of glue laminated (glulam) beams and columns whereas 12 glulam trusses form the stabilizing elements, with a floor system of strengthened LVL sheets acting as a diaphragm system. The elevator shaft is made of cross laminated timber (CLT) which is vibrationally separated from the glulam structure. These building components are manufactured and assembled by the company *Moelven Töreboda*. The apartments are vibrationally isolated from each other.

1.3 Forced Vibration Measurements

Mass inertia forces were used to excite the building in forced vibration tests. For that purpose, an APS 420 shaker was used, see Fig. 1.2. Several accelerometers: PCB 393B12 and PCB 393M62, with the sensitivity 10 V/g, were used. The accelerometers were positioned at different levels on the four corners of the building, under the balconies, see Fig. 1.3. LMS Scadas data acquisition (DAQ) units, connected via fiber-optic cables, were used to control the excitation and to collect measurement data. Each DAQ was put into a plastic box for weather protection, and the boxes communicated with the accelerometers via cables.

The measurements were made as stepped sine tests spanning from 2 to 20 Hz and the excitations were made in 0°, 45°, and 90° in relation to the axis along the width of the building. To make sure that the force excites the complete building and not just the floor on which the shaker is positioned, a steel construction is used, see Fig. 1.2. The steel plate is connected to a main column of the building. Thus, the force is likely to excite the global modes of the building.

The test data were evaluated using the software LMS Test Lab. The first bending mode in the weak direction was found to have a frequency of 2.4 Hz and a relative viscous damping of 1.6%. The first torsional mode was found to have a frequency equal to 2.7 Hz and a relative viscous damping of 1.9%. In addition, the modal masses seem reliable. Thus, scaled mode shapes were also extracted from test data. An auto-MAC was calculated, and it shows that the mode shapes extracted from the test data are very close to orthogonal. The modal parameters will be used to calibrate an FE-model representing the building. However, the most important outcome is the contribution to the knowledge base regarding damping in high-rise timber buildings. Although there are variations, the damping values are roughly 2% for the modes extracted.

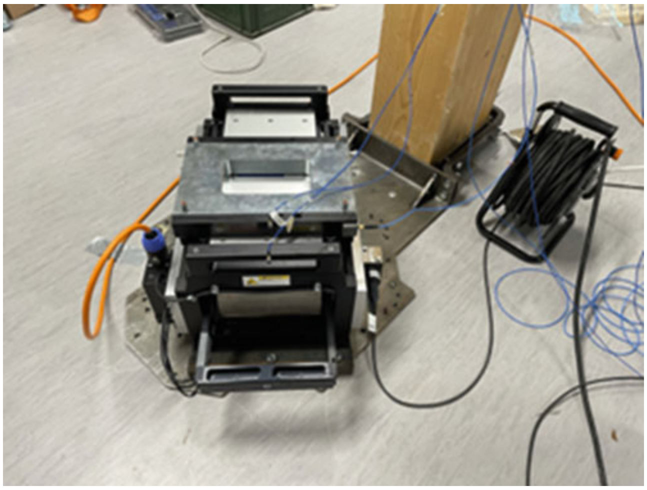

Fig. 1.2 Excitation by mass inertia, using an APS 420 shaker

Fig. 1.3 An accelerometer positioned under a balcony at one of the corners of the building

1.4 Conclusion

In this chapter, the vibrational test campaign made on the seven-story timber building Eken in Mariestad in Sweden is presented. By using mass inertia forces generated by an APS 420 shaker in combination with sensitive accelerometers, 10 mV/g, the fundamental and global eigenmodes were successfully extracted from test data even when the excitation force amplitude was low. The estimated damping values agree with estimated damping values from other test campaigns within the project Dyna-TTB. The results contribute to the knowledge base regarding damping in high-rise timber buildings and is thus useful for future design of tall timber buildings.

Acknowledgments The research leading to these results has received funding from the ForestValue Research Programme which is a transnational research, development and innovation programme jointly funded by national funding organizations within the framework of the ERA-NET Cofund "ForestValue – Innovating forest-based bioeconomy." The authors also express gratitude to the building owner Mariehus for allowing us to perform the measurements.

References

1. Abrahamsen, R., et al.: Dynamic response of tall timber buildings under service load-the DynaTTB research program. In: Papadrakakis, M., Fragiadakis, M., Papadimitriou, C. (eds.) EURODYN 2020, XI International Conference on Structural Dynamics: Proceedings, Volym II (2020) Available from: http://urn.kb.se/resolve?urn=urn:nbn:se:lnu:diva-99080
2. Landel, P., Johansson, M., Linderholt, A.: Comparative study of wind-induced accelerations in tall timber buildings according to four methods. In: World Conference on Timber Engineering 2021, WCTE 2021 (2021)
3. Dynamic Response of Tall Timber Buildings Under Service Load [Internet]. [cited 2022 Oct 23]. Available from: https://www.dynattb.com/

Chapter 2
Application of a Structural Digital Twin on a Laboratory Model for Performance Monitoring of Aging and Degradation

Lauren Thomas, Timothy Kernicky, Matthew Whelan, Youngjin Park, and Robert Cox

Abstract The application of digital twin technology offers the potential to significantly enhance the reliability and performance of structural health monitoring techniques by providing detailed information on, and measurements of, the as-built properties and performance of structures. In addition, a digital twin provides greater support for the application of probabilistic methods for prognostication and risk assessment following model updating and diagnostics provided by structural health monitoring. To date, digital twins have been predominantly applied in the advanced manufacturing space, although the increased use of modular and prefabricated construction has driven interest in the extension of digital twin technology to both civil and nuclear structures. This chapter details the implementation of a structural digital twin and investigates its influence on the performance of a Bayesian vibration-based structural health monitoring approach. In this chapter, a digital twin is developed throughout the construction of a model-scale steel-plate composite modular wall in a laboratory environment. Throughout the design, fabrication, and erection of the specimen, design calculations, numerical models, LiDAR point clouds, physical measurements of geometric features, and quality control inspection data are integrated into a digital twin framework to develop an as-built representation of the structural geometry, material properties, and condition throughout the stages of construction. The modular nature of the construction results in different effective section properties for wall modules as the early-age elastic properties of the structural concrete are developed. This time dependency of the section properties is leveraged to produce a series of datasets where structural parameters in the model evolve due to aging. Probabilistic model updating using modal parameters obtained from experimental modal analyses is used for structural identification of the as-built model. Static loading of the specimen with supplemental instrumentation is used to validate the parameter estimates. The performance of the vibration-based structural identification is evaluated both with and without the as-built information produced by the structural digital twin framework.

Keywords Digital twin · Probabilistic model updating · Vibration-based condition assessment · Structural health monitoring · LiDAR structural scanning

2.1 Introduction

A five-dimensional architecture for a complete digital twin was described by Tao et al. [1] as consisting of: (1) the physical entity, (2) the virtual model, (3) the services model, (4) data, and (5) connections. In a recent comprehensive review of digital twin research and implementations in civil engineering, Jiang et al. [2] highlighted how these five necessary components distinguish a digital twin from building information modeling (BIM) and cyber-physical systems (CPS). The basis of the digital twin is a physical system or structure and a corresponding virtual representation of the physical part that are connected by defined data streams. Necessarily, data sourced from the physical system must be connected to the virtual representation. Likewise, the virtual representation must produce meaningful data to support services, such as simulation, oversight, analytics, or asset management. In this way, a digital twin serves not only as a real-time digital repository of critical

---

L. Thomas · T. Kernicky · M. Whelan (✉) · Y. Park
Department of Civil and Environmental Engineering, University of North Carolina at Charlotte, Charlotte, NC, USA
e-mail: Lthom109@uncc.edu; tkernick@uncc.edu; mwhelan3@uncc.edu; Y.Park@uncc.edu

R. Cox
Department of Electrical and Computer Engineering, University of North Carolina at Charlotte, Charlotte, NC, USA
e-mail: rcox3@uncc.edu

H. Y. Noh et al. (eds.), *Dynamics of Civil Structures, Volume 2*, Conference Proceedings of the Society
for Experimental Mechanics Series, https://doi.org/10.1007/978-3-031-36663-5_2

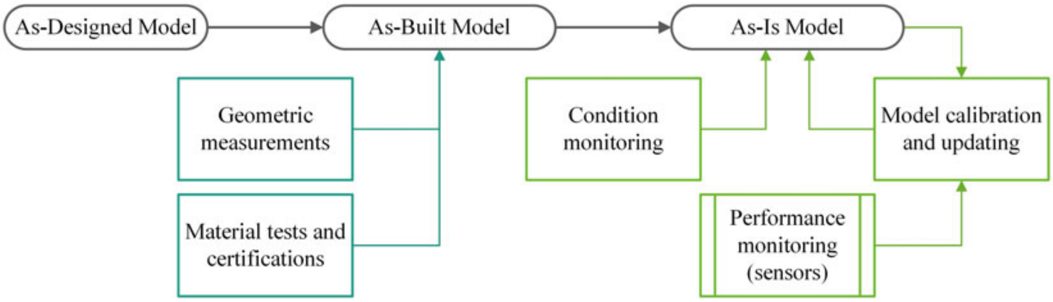

Fig. 2.1 Progression of the underlying finite-element model within the structural digital twin framework

attributes and histories of structural components and systems, but also leverages condition and performance data alongside empirical or physics-based models to produce diagnostic and prognostic capabilities.

The concept of digital twinning is broadly applicable to a variety of different application spaces, and, consequently, it encompasses a wide range of different embodiments, sensing modalities, and technological approaches for achieving and maintaining a virtual representation of a physical system. In this chapter, the objective of the digital twin is to serve as a trusted model of a physical structure reflecting and maintaining known information about the structure, while producing services capable of accurately simulating the structural performance and tracking potential changes in condition. In the current work, the digital twin framework for a laboratory structure is developed by connecting as-built geometric information as well as performance monitoring data acquired from sensors deployed on the physical structure to a virtual model of the system. A physics-based virtual model, in the form of a finite-element model, is selected to leverage physics-based model updating to calibrate the virtual model to the physical response while preserving the ability to account for uncertainties.

Figure 2.1 schematically details the progression of fidelity within the underlying finite-element model serving as the digital twin within the envisioned framework. The model originates from engineering and design of the structure and is developed using a prescribed geometry, specified material properties, and modeling assumptions informed by published guidance or practitioner experience. This original model is referred to herein as the as-designed model. During construction of the structure, material test reports and certifications as well as geometric measurements from contact methods as well as non-contact 3D laser scanning or photogrammetry techniques can be acquired and utilized within the digital twin framework to directly update the underlying finite-element model to an as-built model. In the context of this chapter, the as-built model reflects the inclusion of material or geometric information that can be directly updated within the finite-element model. However, the as-built model does not yet benefit from structural response measurements obtained from performance monitoring or nondestructive evaluation data produced by condition monitoring. Consequently, while there is a reasonable expectation that an as-built model will produce more faithful predictions of structural behavior than an original design model, the predictive fidelity of the as-built model is not yet validated against any measured response. The development and maintenance of an as-is model require condition monitoring and performance monitoring data to ensure the fidelity of the model predictions. If nondestructive evaluations from condition monitoring, such as residual thickness determinations, are available, then they can often be directly incorporated into the as-is model. However, the use of performance monitoring data, such as strain, displacement, and vibration, to update uncertain parameters in the model to improve correlation between the model predictions and the measured response requires use of either a deterministic or probabilistic model updating technique. The application of model updating can correct erroneous assumptions in the underlying finite-element model, such as material properties, section properties, and boundary condition fixity, as well as minimize the effects of idealization and discretization errors on the model predictions [3]. By maintaining the as-is model over the service life of the structure, assignments for uncertain parameters in the finite-element model can be used to assess the potential presence and severity of aging and degradation in the structure.

Despite the relatively brief history of structural digital twin implementations for civil structures, there are several related works that proposed digital twin frameworks for civil structures or infrastructure with similar sensing modalities as the present paper. In a recent work, Funari et al. propose a digital twin methodology for historic masonry structures that involves generation of a finite-element model of the structure from a 3D survey point cloud followed by subsequent manual calibration of uncertain parameters in the finite-element model to achieve improved correlation with measured modal parameters [4]. Chetan et al. presented the incremental development of a trusted digital twin model for a wind turbine blade incorporating measurements of the as-built mass distribution and performance measurements in the form of deflections recorded during static load testing and natural frequencies obtained from modal testing [5].

In this chapter, a structural digital twin is developed for a laboratory model of a modular wall, and performance monitoring of the structure is performed to demonstrate a use case scenario for aging management. In the development of the digital twin, caliper measurements and a 3D laser scanning point cloud are used to profile the actual geometry of individual structural components and the assembled structure to transform an as-designed model to an as-built model. Experimental modal parameter estimates obtained from periodic vibration testing are then used within a probabilistic model updating approach to maintain an as-is finite-element model of the structure. In the study, the digital twin was implemented through development on a commercial product lifecycle management (PLM) collaborative software platform; however, the focus of this particular paper is on the progression of a virtual model from an as-designed model to an as-built model and ultimately to an as-is model that is maintained with performance and condition monitoring data sourced from the physical structure.

2.2 Description of Laboratory Structure

A case study structure consisting of a model-scale steel-plate composite (SC) wall developed by geometric similitude at approximately 1:10 scale from a prototype design. It should be noted, however, that the model-scale wall was developed only for exploration of the digital twin architecture and not to develop insight into the SC wall behavior or limit states. Furthermore, the scaling employed does not maintain mechanical dynamic similitude. The model-scale wall was fabricated with 1.60-mm (63 mil)-thick steel faceplates and having a design section thickness of 63.5 mm (2.5 in). The wall was comprised of four modular sections with each individual SC module consisting of two faceplates tied by 1.60-mm-thick diaphragm plates inset by 6.4 mm (0.25 in) from the edges of the faceplates. The diaphragm plates were fillet welded to the faceplates by flux core arc welding with a 0.89-mm (35 mil) wire. To encourage composite action and model shear studs, 2-mm-diameter steel pins of 8.4-mm length were spot welded to the faceplates on a uniform 25-mm (1 in) grid. Figure 2.2 provides dimensional drawings and photographs for the fabricated wall modules and assembly.

Erection of the laboratory model consisted of welding the bottom SC module to a 6.4-mm (0.25 in)-thick steel base plate that was anchored to a laboratory strong floor foundation with four 35-mm (1 3/8 in)-diameter Dywidag bars. A second SC module was then butt welded to the first module. A commercial self-consolidating concrete mix with specified 28-day

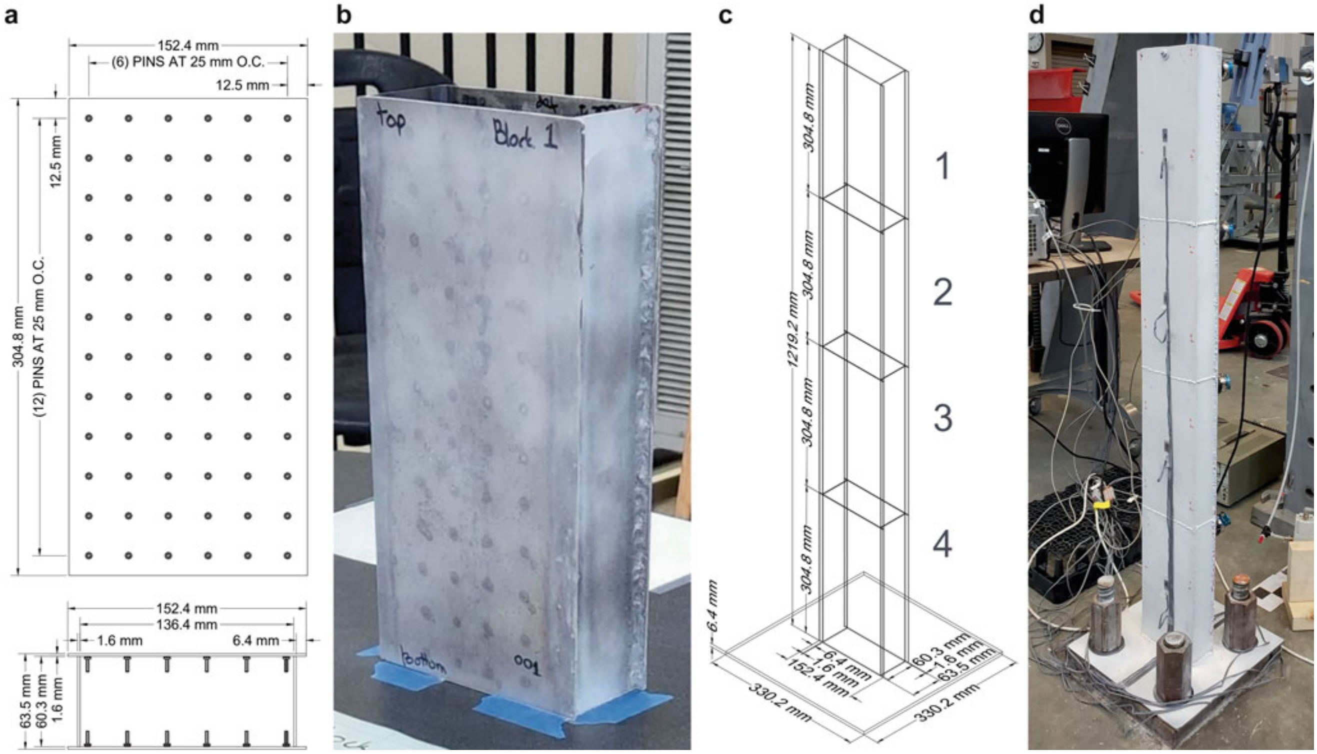

Fig. 2.2 Model-scale wall: (**a**) design dimensions of individual wall modules; (**b**) photograph of fabricated module; (**c**) design dimensions for wall assembly; (**d**) photograph of instrumented specimen

compressive strength of 44.8 MPa (6.5 ksi) was poured into the core of the two modules. Six days after pouring this concrete, the remaining two modules were welded in place and filled with self-consolidating concrete of the same mix. This erection and casting sequence was designed to produce two characteristics for the model updating experiments. First, by staggering the casting of concrete by six days, modules cast at each instance should exhibit significantly different effective stiffness during the early-age development of the section properties. Second, by simultaneously casting pairs of modules, the laboratory model should exhibit similar effective section properties for the modules cast at the same time. If the uncertain parameters in the model are identified for the modules individually, then the performance of the model updating technique and plausibility of the results can be assessed by comparing estimates for properties that should be consistent between the modules.

2.3 Development of As-designed and As-built Models

A finite-element model was initially generated for the as-designed structure using Abaqus FEA. The steel faceplates, diaphragm plates, and base plate were modeled with linear 4-sided shell elements with an aspect ratio of 1 and an edge length of approximately 13 mm. The concrete was modeled using 8-node linear hexahedral elements with an edge length of approximately 13 mm. The discretization of the model was informed by a convergence study that investigated the effect of the mesh size on the natural frequencies of the flexural and torsional modes measured in the subsequent experimental test program. Composite behavior between the steel and concrete was enforced by use of common nodes. It is acknowledged that design guidance for SC construction recommends use of a cracked section, citing the effects of shrinkage strains and partial composite action [6]. However, due to the small scale of the model structure and the extremely low strain magnitudes that the model was subject to throughout the experiment, an assumption of uncracked, fully composite behavior was assumed in the development of the finite-element model. Under this assumption, if the uncracked composite stiffness is not exhibited within the experimental program, then model updating of uncertain parameters in the finite-element model could be used to minimize the deviations between the measurements and the predictions of the analysis model. In idealizing the boundary condition, all nodes within the radius of the washers under the nuts used in securing the base plate to the laboratory strong floor foundation were restrained from translation.

Translation of the as-designed finite-element model to an as-built finite-element model involved the incorporation of geometric measurements obtained by either direct physical measurements or 3D laser scanning. A scale ruler and calipers were used to measure the average height, width, and faceplate thicknesses for the individual modules, since these dimensions could readily and reliably be measured by direct physical measurement. The variation in section thickness and the plumbness of the erected structure were obtained through processing of a dense point cloud developed with a FARO Focus^{S} 150 Plus laser scanner. The 3D scanning was conducted by sequentially positioning the laser scanner at a distance between one and two meters from each corner of the model and acquiring one 360° view preliminary scan with a resolution of 1/10 followed by two high-density scans with a resolution of 1/1. For the high-density scans, the scanning range was restricted to the extents of the model and supporting foundation. Collectively, a total of 12 scans were acquired and the FARO Technologies software, SCENE, was used to register the scans and create a 3D point cloud. Registration of the individual scans was aided by a series of checkerboard registration targets temporarily affixed to the laboratory floor. The scans were manually cleaned of stray and irrelevant points and then further cleansed using noise reduction algorithms available in the SCENE software. After cleansing the scans, the point cloud consisted of approximately 1.3 million points.

The Mathworks LiDAR Toolbox [7] was used to develop a script to perform coordinate transformations on the point cloud and extract the as-built geometry of the faceplates to update the nodal coordinates of the finite-element model. Within this post-processing of the point cloud, weld metal was removed from the point cloud geometry to avoid an artificial extrapolation of increased section thickness that would occur when the density of the cloud was resampled to the discretization of the finite-element model. To generate the geometric data for the finite-element model, a slicing technique similar to the one employed in [8] was used to profile the cross section of the faceplates at discrete elevations corresponding with the coordinates of the initial finite-element model. Polynomial functions were then fit to points within the slices to smooth the measurement data and facilitate interpolation of the faceplate profile at the location of the nodes in the finite-element model.

Figure 2.3 depicts the progression of the as-designed model to the as-built model using the geometric measurements. The as-built mesh, depicted in Fig. 2.3d, reflects the direct physical measurements of module height, width, and faceplate thicknesses as well as the out-of-plumbness and out-of-plane deformation of the individual faceplates obtained from the point cloud. Due to distortions produced during welding as well as pressure imparted from the concrete fill, the section thickness of the modules was typically several millimeters larger than the nominal 63.5-mm thickness developed at the location of the diaphragms. Table 2.1 summarizes the average measured geometric properties of the modules alongside the original design values. To provide preliminary insight into the idealization errors arising from use of the as-designed

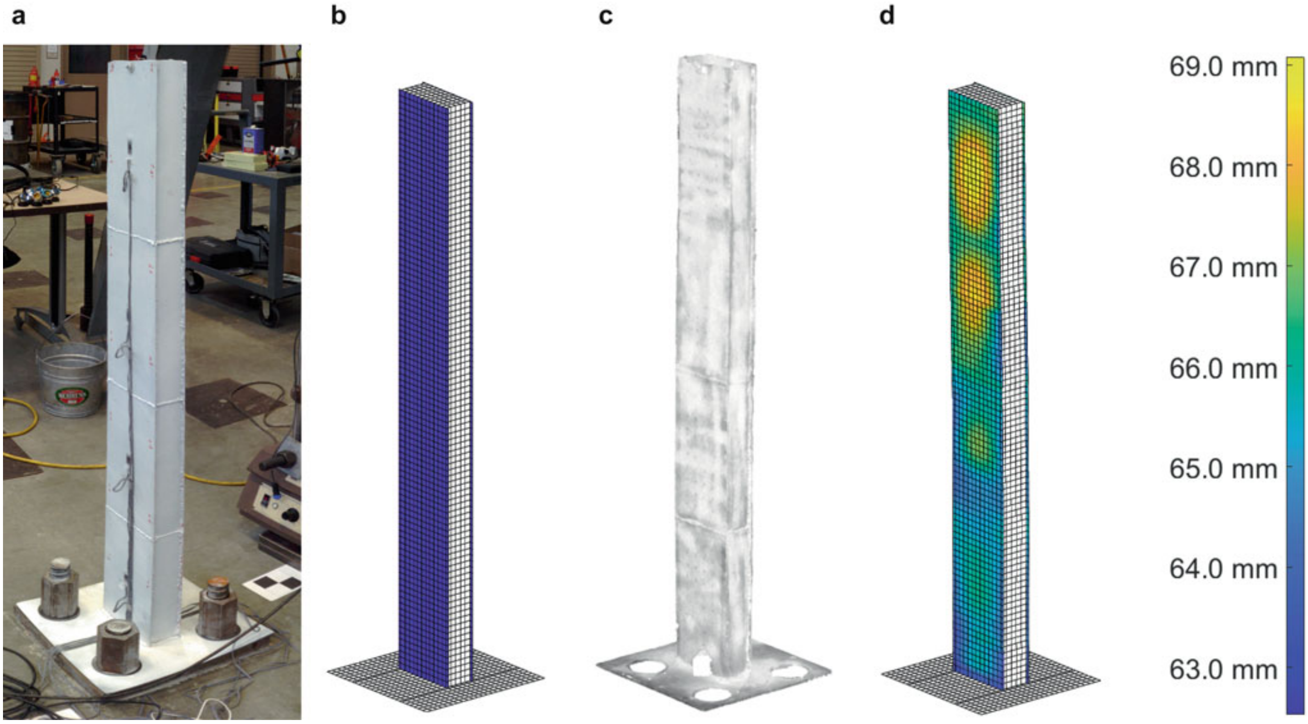

Fig. 2.3 Progression of as-designed model to as-built model: (**a**) Photograph of fabricated model; (**b**) As-designed FE mesh; (**c**) 3D laser scanning point cloud; (**d**) As-built FE mesh

Table 2.1 Averaged measured geometric properties of as-built wall modules

	Design	As-built Module 1	As-built Module 2	As-built Module 3	As-built Module 4
Faceplate 1 thickness	1.60 mm	1.63 mm	1.60 mm	1.62 mm	1.62 mm
Faceplate 2 thickness	1.60 mm	1.63 mm	1.63 mm	1.62 mm	1.62 mm
Width of faceplate	152.4 mm	153.1 mm	153.3 mm	152.9 mm	153.2 mm
Length of faceplate	304.8 mm	304.8 mm	303.4 mm	302.6 mm	304.8 mm
Section thickness	63.5 mm	67.1 mm	66.7 mm	65.5 mm	65.1 mm

Table 2.2 Effect of model geometry on natural frequencies of flexural and torsional modes

	$f_{n,1}$	$f_{n,2}$	$f_{n,3}$	$f_{n,4}$	$f_{n,5}$	$f_{n,6}$	$f_{n,7}$	$f_{n,8}$
As-designed model	17.71	159.7	402.7	483.7	966.3	1209.9	1584.2	2022.4
As-built model	17.68	167.7	411.7	512.2	1020.9	1260.1	1667.6	2096.0
Percent difference	0.1	4.9	2.2	5.7	5.5	4.1	5.1	3.6

geometry, eigenanalysis of the as-designed and as-built models was performed, and the natural frequencies of the flexural and torsional mode shapes corresponding to those measured in the experimental tests were analyzed. For brevity, renderings of the mode shapes are presented only in the subsequent section of this chapter. Table 2.2 contrasts the natural frequencies obtained with the as-designed model from those associated with the as-built model. In both models, the previously described idealized boundary condition was present, and the concrete throughout the model was assigned a dynamic elastic modulus of 38.44 GPa (5575 ksi).

2.4 Experimental Modal Analysis

In this chapter, performance monitoring for the conceptual digital twin was envisioned to encompass vibration measurements from which experimental estimates of natural frequencies and mode shapes could be obtained and monitored. To simulate this on the laboratory model, experimental modal analysis was conducted using a roving impulse hammer technique after

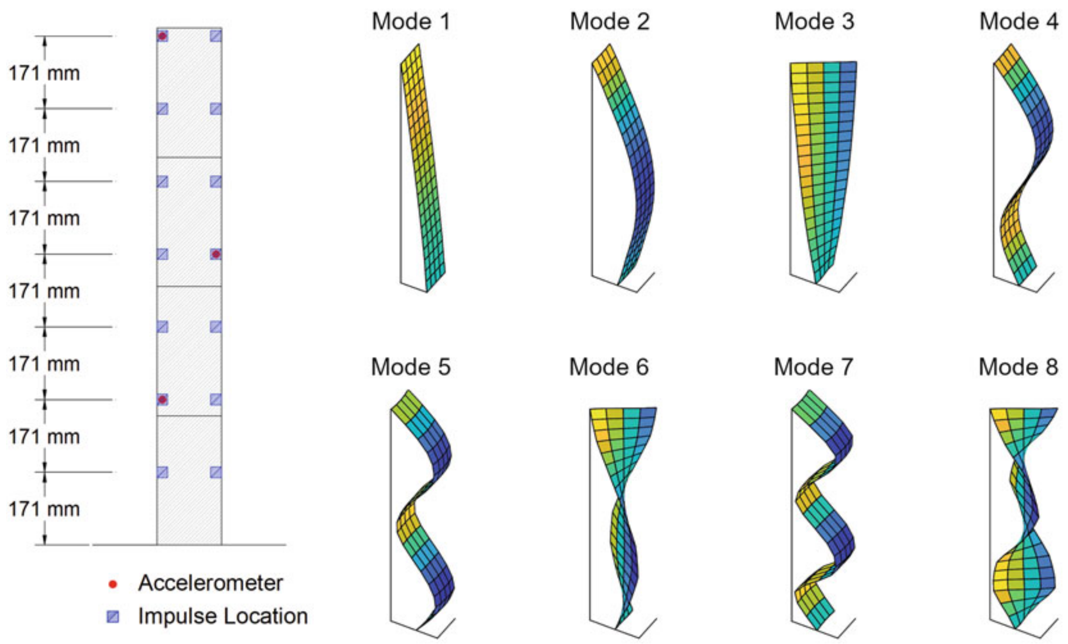

Fig. 2.4 Schematic of test setup for experimental modal analysis and renderings of representative experimental mode shape estimates

Table 2.3 Experimental natural frequency estimates

	$f_{n,1}$	$f_{n,2}$	$f_{n,3}$	$f_{n,4}$	$f_{n,5}$	$f_{n,6}$	$f_{n,7}$	$f_{n,8}$
1 day	21.5	158.9	388.6	462.3	941.1	1127.4	1487.8	1894.6
2 day	21.6	161.8	392.9	471.9	945.3	1160.6	1519.1	1932.5
3 day	21.6	162.9	394.7	475.8	951.8	1172.3	1530.4	1948.0
7 day	22.1	165.0	398.0	481.6	959.5	1190.2	1549.1	1972.6
28 day	22.4	167.4	402.8	488.0	970.2	1207.8	1569.4	1998.4

1, 2, 3, 7, and 28 days from the casting of concrete in the final two modules of the assembly. By acquiring the modal measurements during the early-age development of concrete stiffness, the resulting dataset can be used to explore the use of the digital twin to track changes to parameters in the model over time. Furthermore, while the experiment leveraged the early-age development of stiffness to drive the physical changes in the structure, it is plausible to extrapolate the application of the approach to degradation of stiffness associated with aging and deterioration mechanisms.

A PCB Piezotronics 086C03 impulse hammer with 160g hammer mass was used to apply measured impulse excitation to the structure across an array of 14 uniformly spaced locations on the front face of the wall. Three PCB Piezotronics 353B31 uniaxial accelerometers with 50 mV/g sensitivity and 1–5000 Hz frequency range were affixed to the back face of the wall to measure the out-of-plane motion. Figure 2.4 depicts the instrumentation plan for the experimental modal analysis alongside representative estimates for the mode shapes experimentally obtained during each day of testing. Modal parameter estimates were obtained for each day by application of the Eigenvalue Realization Algorithm [9] to impulse responses computed from the H1 transfer function estimator. Stabilization criteria were used to aid in distinguishing plausible modal poles from spurious poles across a range of model orders. By applying the system identification routine to experimental data obtained from multiple impulses, multiple hammer tips, and with a range of model orders, a large set of experimental estimates were obtained for each mode shape. The uncertainty reflected by the variation in the experimental modal parameter estimates is later considered in the subsequent probabilistic model updating of the as-is models by sampling directly from the full set of experimental estimates.

Table 2.3 presents the average experimentally obtained estimates for the natural frequencies corresponding to the eight mode shapes depicted in Fig. 2.4 over each day of testing. As reflected in the table, the early-age development of concrete stiffness produced a modest increase in all of the natural frequencies for the measured modes of the structure, with the most significant increases occurring in the higher order modes. On a percent error basis, the most notable discrepancy between the predicted natural frequencies of the as-built model and the measured values is for the fundamental natural frequency. The experimental estimates suggest that concrete maturity had only a mild effect on the fundamental natural frequency of the wall and the discrepancy cannot be attributed to incorrectly assumed material properties for the concrete. In this case, the discrepancy is attributed to the idealization of the boundary condition, which does not account for stiffness contributed by the contact between the base plate and the laboratory strong floor foundation. While the contact is a nonlinear phenomenon, the stiffness is approximated in the as-is model by introducing linear elastic springs oriented in the gravity direction across all nodes defining the base plate of the structure. Since the spring stiffness cannot readily be calculated, it is treated as an uncertain parameter in the model updating process.

2.5 Probabilistic Model Updating to Generate As-is Models

A Bayesian probabilistic model updating approach is used in this chapter to maintain as-is models that minimize the discrepancies between the model predictions and measurements obtained from performance monitoring, while incorporating uncertainty. Within the model updating approach, five uncertain modeling parameters were considered: the dynamic elastic modulus assigned to the concrete elements contained within each individual wall module (E_1, E_2, E_3, and E_4, where the subscript denotes the module) and the elastic spring stiffness associated with the stiffness contribution from contact at the boundary condition across the base plate (k_{spring}). An adaptive Metropolis–Hastings Markov Chain Monte Carlo method was used to sample posterior probability distribution functions using the likelihood function proposed in [10]. This likelihood function takes the form

$$J(\theta) = \sum_{r=1}^{N_m} \sum_{j=1}^{N_s} \left[\left(\frac{(1 - \hat{\omega_{r,j}}^2/\omega_r^2)^2}{\varepsilon^2} \right) + \left(\frac{\phi_r^T (I - \hat{\phi_{r,j}} \hat{\phi_{r,j}^T}) \phi_r}{\delta^2 ||\phi_r||^2} \right) \right], \tag{2.1}$$

where N_m is the number of modes included in the identification, N_s is the number of sets of modal data, $\hat{\omega_{r,j}}$ and $\hat{\phi_{r,j}}$ are the experimental natural frequency and mode shape, respectively, for the r-th mode of the j-th dataset, ω_r and ϕ_r are the corresponding natural frequency and mode shape for the model with parameter assignments θ, and ε and δ are weighting parameters that reflect the uncertainty in the experimentally measured natural frequencies and mode shapes, respectively. To reflect measurement uncertainties, a total of 25 modal datasets were used for each of the eight natural frequencies and mode shapes by randomly sampling from the larger set of experimental estimates obtained in the system identification process. For the parameters associated with the dynamic elastic modulus of concrete, the prior distribution was taken as a uniform distribution over the range from 13.8 GPa (2000 ksi) to 48.3 GPa (7000 ksi). The prior distribution for the boundary spring stiffness parameter was taken as a uniform distribution over the range from 0.18 kN/mm to 18 kN/mm, which was established through sensitivity analysis of the finite-element model. For clarity in the presented results, as-is models were developed only for 1, 3, and 28 days following the casting of the concrete in the final two modules.

Figure 2.5 presents the posterior samples obtained from a chain consisting of 5000 samples with 500 burn-in samples removed. For each individual plot, the x-axis extents are set to the range of the prior distribution. Table 2.4 presents the expected values associated with these posterior distributions. As expected, there is strong correlation between the identified E_1 and E_2 as well as E_3 and E_4, as these pairs were cast simultaneously, although in general the identified concrete modulus for the upper module in each pair is slightly lower. This may be a result of the placement or differences in initial curing due to the construction sequence. The stiffness associated with the concrete in modules 3 and 4 is initially greater than that of modules 1 and 2 because the concrete was cast six days earlier. With the exception of a modest deviation for E_1,

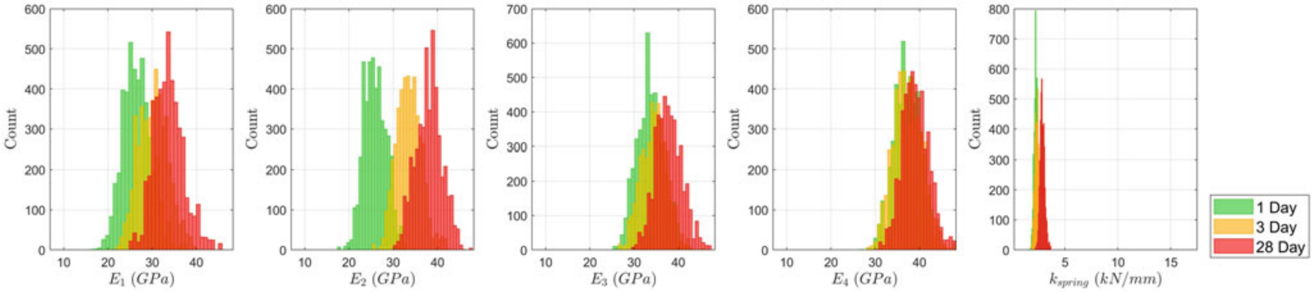

Fig. 2.5 Posterior samples of the uncertain model parameters

Table 2.4 Expected values of the posterior distributions for the as-is models

	1 day	3 day	28 day
E_1 (GPa)	26.6	30.2	33.7
E_2 (GPa)	25.9	33.6	38.1
E_3 (GPa)	33.6	34.6	37.8
E_4 (GPa)	37.2	37.4	39.0
k_{spring} (kN/mm)	2.23	2.34	2.87

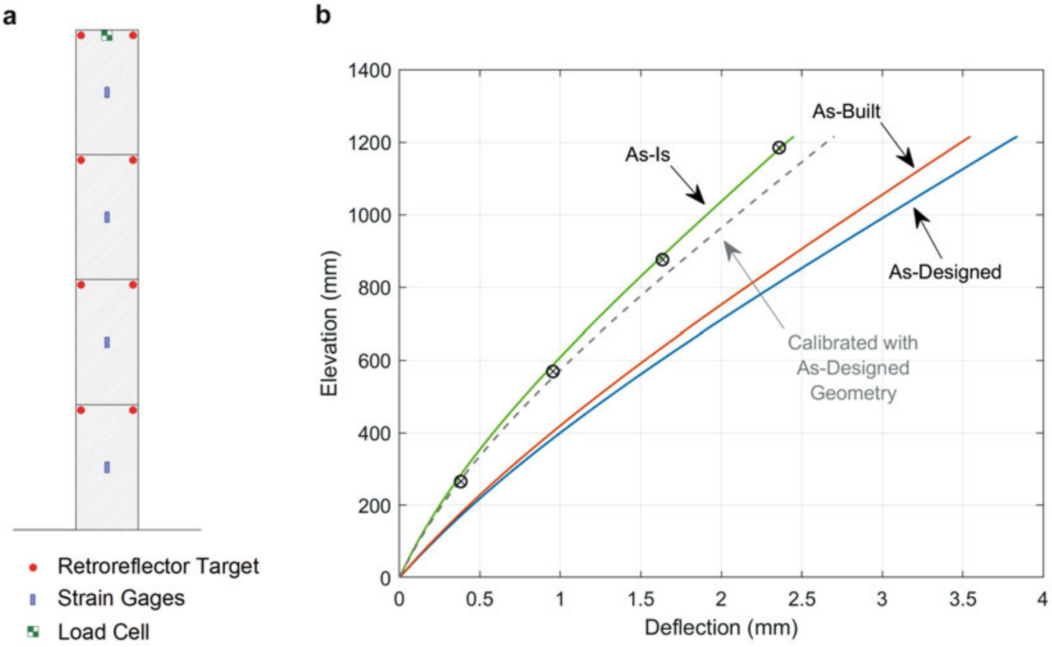

Fig. 2.6 Validation of finite element models: (**a**) Schematic of test setup for static load test; (**b**) comparison of model predictions to measured deflection under load

the expected values for the 28-day dynamic elastic moduli are in strong agreement with the 38.44 GPa estimate predicted using the ACI318 [11] relationship between modulus of elasticity, unit weight, and compressive strength and the empirical relationship between static and dynamic elastic moduli proposed by Lydon and Balendran [12]. The slightly lower identified dynamic elastic modulus for module 1 may be physically manifest due to the placement or differences in curing condition, or it may be an artifact of reduced sensitivity of the measured modal parameters to the stiffness of this uppermost module. The boundary spring stiffness is generally unchanged across the three as-is models, which is expected since the boundary condition should not have been affected by development of early-age concrete stiffness.

2.6 Validation with Static Load Test

To contrast the differences between the predictive fidelity of the as-designed, as-built, and as-is finite-element models, the deflection of the model structure under static load was compared to the prediction produced by each model. During the static load test, monotonically applied lateral load was applied at the top of the wall by means of a pneumatic actuator regulated by an electronic pressure controller. A load cell positioned between the actuator and the specimen was used to directly measure the applied force. Spherical retroreflector targets were positioned at the top corners of each module and were surveyed using an API Tracker3 laser tracker throughout the duration of the test to measure the deflection of the wall resulting from the application of the static load. Figure 2.6 presents a schematic illustration of the test setup and comparison between the measured and predicted deflection of the modular wall at 28 days following the casting of concrete into the final modules. In producing the estimates for deflected shape of the wall using the as-is model, the widely utilized empirical relationship between the dynamic and static moduli of elasticity of concrete proposed by Lydon and Balendran [12] was used to estimate the static modulus of elasticity of the concrete elements in the model using the expected values of the parameters identified through model updating of the dynamic response. For this model, the deflection is particularly sensitive to the rotational fixity imposed by the connection of the base plate, and consequently, the as-designed and as-built models both significantly overestimate the deflection of the wall since the geometric data provided to the as-built model contain no information on the boundary fixity. By calibrating the uncertain stiffness of the boundary condition as well as the uncertain modulus of the concrete in each module, the as-is model is able to achieve exceptionally strong correlation with the measured deflections.

To further illustrate the importance of incorporating the measured as-built geometry in the finite-element model, probabilistic model updating was performed using the same methodology previously described but with a finite-element mesh developed from the as-designed geometry rather than the as-built geometry. In general, the use of a mesh with the as-designed geometry produced only nominal changes in the expected value of the posterior samples for the uncertain parameters. However, the finite-element model calibrated with the as-designed geometry resulted in a greater prediction of deflection than the as-is model and the experimental measurement.

2.7 Conclusion

In this chapter, the development of as-designed, as-built, and as-is models serving as the virtual representation of a laboratory modular wall in a digital twin was presented to examine the benefits of connecting as-built geometric data and performance measurements from the physical structure to the virtual model. The case study demonstrates a potential use case scenario for structural digital twins related to aging and degradation by maintaining an as-is model through a Bayesian probabilistic model updating approach that preserves uncertainty quantification. Although modifying the geometry of the finite-element model to reflect the as-built measurements did notably affect the natural frequencies of the model, the uncertain parameters identified by updating a model with the as-designed geometry did not differ significantly from those identified by updating the model after adjusting the geometry to reflect the as-built data. However, comparison of model predictions with static load test data suggests that the predictive fidelity of the as-is model is indeed enhanced by incorporating the as-built geometry.

Acknowledgments This work was supported by the Electric Power Research Institute (EPRI) and the University of North Carolina at Charlotte Energy Production and Infrastructure Center (EPIC).

References

1. Tao, F., Zhang, M., Liu, Y., Nee, A.Y.: Digital twin driven prognostics and health management for complex equipment. Cirp Ann. **67**(1), 169–172 (2018)
2. Jiang, F., Ma, L., Broyd, T., Chen, K.: Digital twin and its implementations in the civil engineering sector. Automat. Construct. **130**, 103838 (2021)
3. Mottershead, J.E., Link, M., Friswell, M.I.: The sensitivity method in finite element model updating: a tutorial. Mech. Syst. Signal Process. **25**(7), 2275–2296 (2011)
4. Funari, M.F., Hajjat, A.E., Masciotta, M.G., Oliveira, D.V., Lourenço, P.B.: A parametric scan-to-FEM framework for the digital twin generation of historic masonry structures. Sustainability **13**(19), 11088 (2021)
5. Chetan, M., Yao, S., Griffith, D.T.: Multi-fidelity digital twin structural model for a sub-scale downwind wind turbine rotor blade. Wind Energy **24**(12), 1368–1387 (2021)
6. American Institute of Steel Construction, ANSI/AISC N690-18 Specification for Safety-Related Steel Structures for Nuclear Facilities (2018)
7. The MathWorks Inc: Lidar Toolbox. Natick, Massachusetts, United State (2022)
8. Castellazzi, G., Presti, N.L., D'Altri, A.M., de Miranda, S.: Cloud2FEM: a finite element mesh generator based on point clouds of existing/historical structures. SoftwareX **18**, 101099 (2022)
9. Juang, J.-N., Pappa, R.S.: An eigensystem realization algorithm for modal parameter identification and model reduction. J. Guidance Control Dyn. **8**(5), 620–627 (1985)
10. Vanik, M., Beck, J., Au, S.: Bayesian probabilistic approach to structural health monitoring. J. Eng. Mech. **126**(7), 738–745 (2000)
11. American Concrete Institute, Building Code Requirements for Structural Concrete (ACI 318-19): An ACI Standard (2019)
12. Lydon, F., Balendran, R.: Some observations on elastic properties of plain concrete. Cement Concrete Res. **16**(3), 314–324 (1986)

Chapter 3
Full-Scale Multi-Dataset OMA on a 368-Meter High TV and Radio Transmission Tower

L. Gaile, S. D. R. Amador, E. Lydakis, and R. Brincker

Abstract The state-of-the-art OMA algorithms have been used to identify the dynamic parameters from output-only vibration data acquired in a testing campaign carried out on a remarkable 368 m high steel structure, namely, the Riga Television and Radio transmission tower. The structure is unique both in terms of the structural system and of societal relevance since it is a historical monument and a landmark for Riga, one of the capitals of the Baltic States. Two independent acquisition systems were used to measure the vibration responses of the tower at a total of 48 DOFs along its height.

Each acquisition system is constituted of two 3D vibration sensors. One of the acquisition systems is used as a reference, and the other one is a moving system. The latter was relocated to different stories and antenna, and the former remained at the same (reference) storey throughout the test. Because the two different systems were not synchronized, advanced post-processing techniques were employed to synchronize the different datasets and subsequently identify the global modal properties of the tower.

Keywords Operational Modal Analysis · Civil engineering structures · Modal parameters · Mode shapes · Steel tower

3.1 Introduction

Today, architecturally significant buildings are becoming more and more complex from a structural point of view. This is due to the possibilities offered by the wide application of numerical analysis and simulation methods. Therefore, it is very important that the assumptions made in the design phase about boundary conditions, materials, geometric nonlinearities, etc., of the structure are consistent with the building as built.

The knowledge of modal parameters, namely the natural frequencies, damping ratios, and mode shapes from the numerical model and tested structure after its construction completion gives the opportunity to assess the correctness of the assumptions made by the structural designer. Furthermore, knowing the experimental modal parameters it is possible to use modal updating techniques [1] that significantly improve the accuracy of the numerical model compared to the actual behavior of the civil engineering structure. The designer is thus able to numerically test the structure under different loading scenarios more reliably.

A technique that allows determining those experimental modal quantities for large structures that cannot be artificially excited is Operational Modal Analysis (OMA) [2]. Unlike the Experimental Modal Analysis (EMA) [3] techniques widely used in mechanical engineering applications, this method does not measure the vibration excitation force, but assumes that the ambient vibrations (due to wind, weak seismic activities, traffic, etc.) have a very broadband excitation spectrum, approaching the characteristics of the white noise [4]. So, if the vibration responses are measured long enough, it is assured that all the modes of interest are sufficiently excited. The measurements are taken at predetermined locations so that enough response and, thereby, information of these modes are recorded.

L. Gaile (✉)
Institute of Structural Engineering, Riga Technical University, Riga, Latvia
e-mail: Liga.gaile_1@rtu.lv

S. D. R. Amador · E. Lydakis
Department of Civil and Mechanical Engineering (CONSTRUCT), Technical University of Denmark, Copenhagen, Denmark

R. Brincker
Brincker Monitoring, ApS, Copenhagen, Denmark

H. Y. Noh et al. (eds.), *Dynamics of Civil Structures, Volume 2*, Conference Proceedings of the Society
for Experimental Mechanics Series, https://doi.org/10.1007/978-3-031-36663-5_3

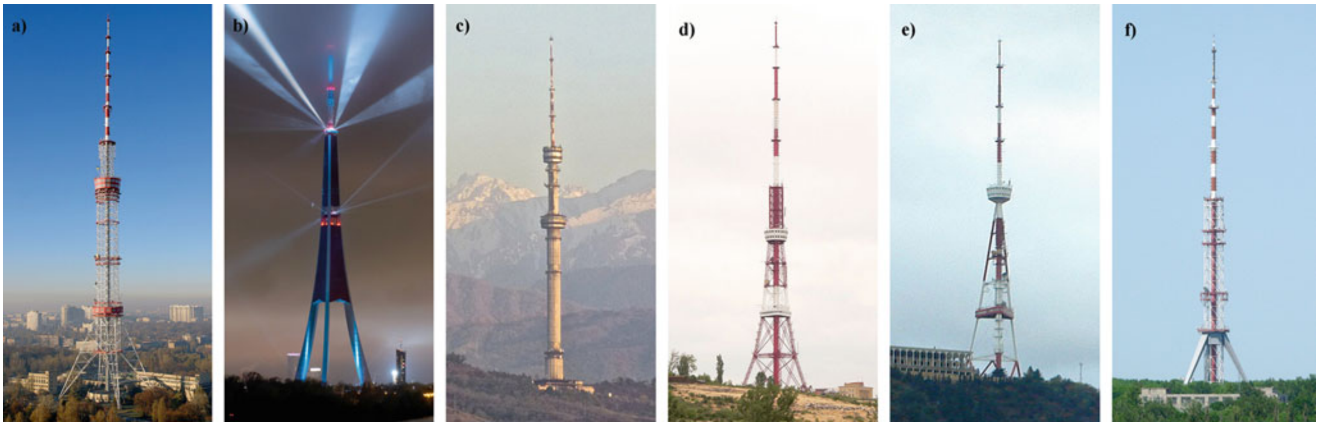

Fig. 3.1 TV-towers: (**a**) Kyiv (380 m), (**b**) Riga (368 m), (**c**) Almaty (361.7 m) [20], (**d**) Yerevan (311.7 m) [21], (**e**) Tbilisi (274.5 m) [22], (**f**) Kharkiv (240.7 m) [23]

This chapter reports the application of OMA technique to a remarkable 368 m high steel structure with distinct architecture and structural behavior presented in Fig. 3.1b. Result comparison is made with historical testing results based on peak peaking from auto spectrum density and information about phase from Fourier transform that was obtained just after the structure was built in 1989. This chapter follows the principles of the full case studies of OMA applications, e.g., [5–12] in the civil engineering field. Several technical and practical challenges were bypassed by using the data postsynchronization technique. Thus, successful application examples like this are a key factor in transferring state-of-the-art techniques to the industry.

3.2 Methodology

One of the most recent and up-to-date publications demonstrating the application of OMA technique is [8]. The 230 m high reinforced concrete building in Qatar with 53-stories above the ground and two stories below the ground is tested under ambient vibrations. Here the modal parameter estimation is done by using one of the Frequency Response Function (FRF)-based curve fitting techniques, the Rational Fractional Polynomial (RFP) curve fitting [13] implemented in the commercial software ME'scope.

In this chapter, other classical OMA identification techniques implemented in the commercial software Artemis Modal are used and the results are compared to demonstrate the readiness of the technology for the industry. These are Frequency Domain Decomposition (FDD) [14], Enhanced Frequency Domain Decomposition (EFDD) [15], and Crystal-Clear Stochastic Subspace Identification methods (CC-SSI) [16]. The first two techniques are frequency domain methods, but the third one is a time domain method.

The SSI is a time domain technique from the 1990s [17]. It is based on building a Hankel matrix $\boldsymbol{H}$ of the responses

$$\boldsymbol{H} = \begin{bmatrix} \boldsymbol{H}_1 \\ \boldsymbol{H}_2 \end{bmatrix} \tag{3.1}$$

where the upper block matrix, $\boldsymbol{H}_1$, is called "the past" and the bottom block matrix, $\boldsymbol{H}_2$, is called "the future." We can then define a projection matrix that is the expectation of the future given the past that can be calculated as a product of the matrices $\boldsymbol{H_1}$ and $\boldsymbol{H_2}$, and it can be shown that the physical properties are concentrated in this matrix and define the basis for the modal analysis.

FDD is the Frequency Domain Decomposition that is based on the singular value decomposition (SVD) of the spectral density matrix $\boldsymbol{G}(\omega)$:

$$\boldsymbol{G}(\omega) = \boldsymbol{U}(\omega)\, \boldsymbol{S}(\omega)\, \boldsymbol{V}^H(\omega) \tag{3.2}$$

where the column space matrix $\boldsymbol{U}$ is the orthogonal matrix that contains the mode shapes, and the singular values in the diagonal matrix $\boldsymbol{S}$ are related to the modal coordinates, $\boldsymbol{V}$ is an orthogonal matrix and $(_*)^H$ denotes the complex conjugate transpose (or Hermitian) of a complex matrix. More information about both methods can be found, for instance, in [4]. Both time and frequency domains carry the same information but are represented differently. Therefore, it is common practice to compare the results of both domains, i.e., identified frequencies and mode shapes using, for example, in terms of Modal Assurance Criterion (MAC) values [18].

Other differences from the study [8] are the used sensor type and test setup. The structures like TV and Radio transmission towers have very strong electromagnetic field disturbances due to powerful transmission equipment as well as low or unevenly covered GPS signals to the height of the structure itself. Therefore, in such situations, it limits the use of wireless sensors or long cables between them. In these cases, one might turn to more simple ways of obtaining a reasonable synchronization between the signals of the two independent measurement chains. One way to do this is to maximize the correlation between the signals, which basically means to secure that all autocorrelation functions have their maximum value at time lag zero.

In this case, however, we will use another way which is based on minimizing the phase between signals from the two measurement chains. Let us consider a signal $y_1(t)$ from the reference data set and the corresponding signal $y_2(t)$ from the moving data set, both measured as a function of time t. The two signals are now assumed to be dominated by the same mode shape but with a time lag T in between them, so that

$$y_2(t) = C y_1\left(t + T\right) \tag{3.3}$$

where the constant C accounts for the difference in mode shape components. We then know from the time shift property of the Fourier transform theory, that we have the Fourier transform pair

$$y_1\left(t + T\right) \leftrightarrow Y_1\left(\omega\right) e^{i\omega T} \tag{3.4}$$

which means that we have a phase of $\varphi = \omega T$ in between the two signals. Obtaining the phase of the cross-spectral density function between the two signals will give us the phase, and then we can remove the linear part to synchronize the signals.

Despite the fact that the building tested in [8] is reinforced concrete and is lower than the TV tower by 138 m, the range of modal parameters is very similar to the structure considered in this study.

3.3 Operational Modal Analysis Case Study

The TV and Radio Transmission Tower is located on the island of the river Daugava that runs through the city center of the capital of Latvia Riga. This tower is one of the tallest towers in Europe. It was built between 1979 and 1989, and its highest point reaches 368 meters. The structure is unique due to its distinct shape and societal relevance since it is a modern historical monument and a landmark of the city. It also currently provides TV and radio broadcasting for half of the country and is the most important collocation point for electronic communications service providers in the Baltics.

In the mid-1980s, it was common in the former Soviet Union territory to build tall and flexible towers usually made from steel. This type of construction can be found in Kyiv, Vilnius, Tallinn, Baku, Almaty, Tashkent, Tbilisi, Yerevan, and other cities. Figure 3.1 shows examples of those TV Towers. In [19] stressed durability issues in some of the towers' initial designs. This further justifies the need for modal parameter determination, model updating, and fatigue cycle assessment using modern technologies and methods.

Operational Modal Analysis was used to estimate the modal parameters of the 368 m high TV and Radio Transmission Tower in Riga. The three supporting columns (or legs) are composed of boxed cross sections with strengthening ribs whose dimensions vary along the height. In the plan, the tower columns (legs) are rotated by an angle of 120° with respect to each other. The dimensions of the boxed cross-section of the columns decreases from 3.816×9.860 m at -1.5 m to 1.5×1.6 m at $+217.7$ m. Above the $+82$ m height mark, the outline of the tower is a pyramid with three sides, where the tower columns are tied together with the structures of the technical floor slabs. The cladding of the pyramid is profiled metal sheets. The pyramid part has an antenna section on the top two floors. The total height of the antenna is 135 m, and it has a varying diameter from 5 m to 0.72 m. In two of the tower columns (e.g., legs #1 and #3), there are elevators that run until level $+97$ m. Inside the third column (leg 2) there is a staircase. Each of the legs is clamped supported on fields of piles.

Tower vibration measurement data was obtained by recording tower vibration responses in accelerations in ambient vibration tests carried out in the summer of 2022. Measurements were taken at predetermined locations based on the constructed initial FE model of the structure and shown in the schematic representation of the test setup in Fig. 3.2.

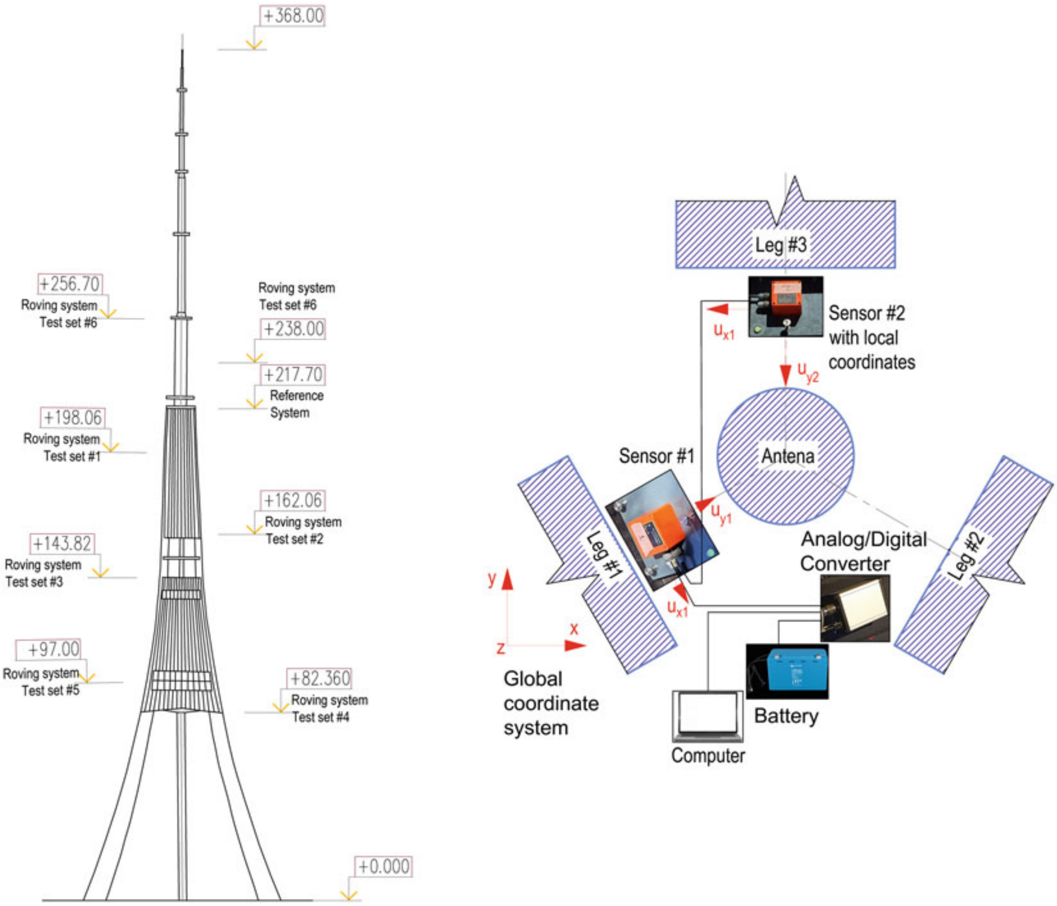

Fig. 3.2 Recorded levels of the tower and test setup example on level +217.7 m

Altogether four triaxial sensors (3D geophones) and two independent acquisition systems (two Sensenet base stations, 24 bits A/D with integrated sigma-delta principle [24]) were used to measure the vibration responses of the tower at a total of 48 DOFs along its height. One measurement system with two 3D sensors was allocated as a reference system on the level +217.70 m. Another measurement system with two triaxial sensors was used as a roving system, and six setups were conducted to accurately estimate the natural frequencies and mode shapes. The functionality test of the measurement system prior to the test was done by means of a simple collocation test whose methodology is explained in reference [4]. Despite this relatively low wind speed, the sensors used have clearly captured the dynamics of the tower.

Because the two different systems were not synchronized due to the limited possibilities of using a wireless system and long cables, post-processing techniques were employed to synchronize the different datasets and subsequently identify the global modal properties of the tower. Therefore, it was essential that ambient excitation provided mainly by wind excitation was similar on both testing days. The mean ambient temperature recorded during the test was around 20 °C on both days with wind excitation characterized by mean wind speed of around 4 m/s and gusts of 8 m/s. The synchronization results for the first reference and roving data sets are shown in Fig. 3.3. The reader should notice, that we do not want to remove the overall linear trend, but only the trend in some of the frequency bands typically in the low-frequency region where the assumption of the dominant mode can be fulfilled. Thus, for the considered case, we are obtaining an approximate flat phase in some of the frequency bands from DC to 3 Hz. Uncertainty on time synchronization is evaluated to be approximately 0.1 s. For the case shown in Fig. 3.3, the time shift was estimated to be 1.28 s.

During the test, sensors were placed in predetermined prepared locations and carefully leveled. Since the geometry of the tower varies with height and is not visible from inside of the tower, it is important to follow the vertical curved lines to determine the mode shapes, a constant distance from the inner edge of the main boxed cross section columns is used as a reference distance for the level. Thus, the local coordinate system of the sensors (see Fig. 3.2) is chosen as a basis, which is later transformed into a global coordinate system for the visualization of mode shapes.

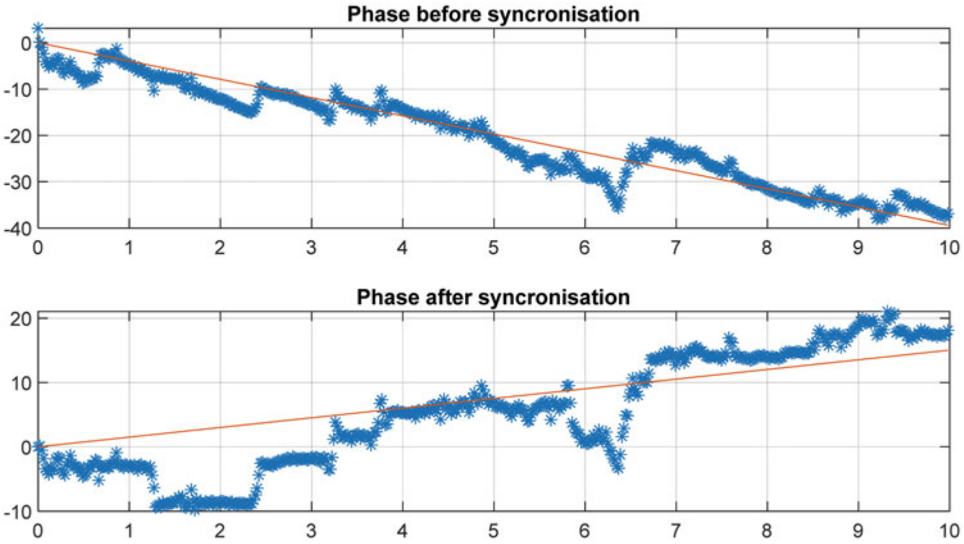

Fig. 3.3 Synchronizing the first reference data set with the first roving data set by removing the linear trend (note that for the synchronized data in the bottom plot, the overall phase change still has a trend, but the three frequency bands with approximately constant phase below 3 Hz does not)

Each of the recorded data sets with a sampling frequency of 20 Hz and a length of 90 min (following the recommendations given in reference [4]) was band passed at 0–2.5 Hz and decimated to a Nyquist frequency of 2.5 Hz. Therefore, in total each data set contains 26,624 data samples. FDD, EFDD, and SSI OMA identification methods were applied according to the methodology described in the previous section, and the Singular Value of Spectral Densities (SVD) was obtained with a chosen resolution of 2048.

In contrast, in 1989 after the tower was built, tests were carried out by recording the vibration velocities with seismometers C5C. In order to obtain the spectrum, vibrations also were recorded under wind loads but only on three levels (+332 m, +217.7 m, +161 m) at different wind speeds [25]. Duration of processed time series only from 1 min to 6.8 min. Therefore, with the testing methods used at the time, it was impossible to obtain the experimental mode shapes for large civil structures. Only estimation of frequencies and damping were done. That idea about actual mode shapes came from theoretical calculations and model wind tunnel tests.

3.4 Results

Compared to the frequency identification methods used for the initial testing of the tower in 1989, the Operational Modal Analysis is the Multiple Input Multiple Output (MIMO) technique. Therefore, all the identification algorithms used in this chapter were able to estimate closely spaced and repeated modes. An example of obtained SVD plot for the tower is demonstrated in Fig. 3.4.

Even more, now it was possible to detect that one of the frequencies previously considered as the structural mode seems to be harmonic possibly due to the movement of the elevator up and down during the dynamic testing. SVD plot shows that at considered bandwidth at least 13 singular values are well separated from the noise floor. As expected from the FEM calculations, at each of the SVD peaks of bending modes there are two closely spaced mode shapes due to the geometry of the tower. This is typical for various forms of towers with two or more horizontal axis of symmetry [26]. Nevertheless, three closely spaced torsional mode shapes at 0.82 Hz were identified, which were not predicted in the FE model.

A comparison in terms of natural frequencies between the results obtained from the modal testing campaign carried out in the summer 2022 and those from modal testing realized in 1989 is summarized in Table 3.1, and mode shapes are presented in Fig. 3.5. As the vibration responses were measured at only two of the three legs at each level, the movement of the third leg was obtained for visualization purposes by writing “slave” equations.

Direct comparison of frequency values in Table 3.1 between tests should be made with caution due to the nature of different ambient and operational conditions (EOV). It is well known that, for example, the alone temperature can modify the natural frequencies of the structure considerably [27–29]. In the future, long-term monitoring of the tower modal parameters

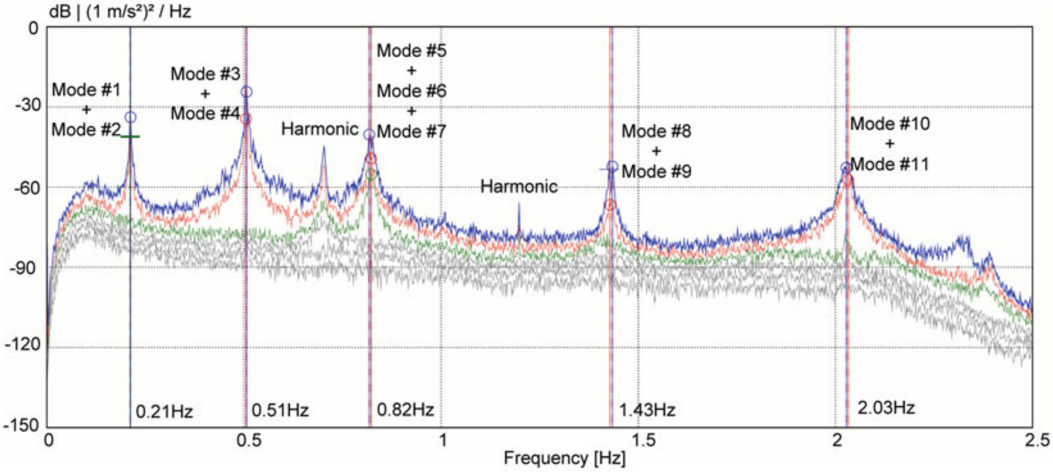

Fig. 3.4 Plots of the singular values of spectral densities (SVD)

Table 3.1 Experimentally determined frequencies of the Riga TV Tower

Mode #	Ambient vibration testing in the year 1989		Ambient vibration testing in the year 2022	
	Frequency, Hz	Conclusion about mode shape	Frequency, Hz	Mode description
1	0.212	Bending mode	0.215	Complex repeated bending mode shapes with a more pronounced movement of the antenna part
2	–	–	0.215	Complex repeated bending mode shapes with more pronounced movement on the damper level around +198 m. Highest energy input in the SVD graph
3	0.517	Bending mode	0.508	
4	–	–	0.508	Appears to be a harmonic induced by narrow band external loading with a more pronounced movement of the level around +97 m
–	0.708	Bending mode	0.703	
–	–	–	0.703	Complex global repeated torsional mode with more pronounced torsional movement in levels around +150 m mark
5	0.830	Possibly torsion mode	0.820	
6	–	–	0.820	Cantilever global torsional mode (highly complex)
7	–	–	0.820	Complex global repeated torsional mode with more pronounced torsional movement in levels around +90 m mark
8	1.464	Bending mode	1.426	Triple curvature repeated real bending mode with waves evenly distributed along tower height except for antenna where deformation is more pronounced
9	–	–	1.426	Triple curvature complex repeated bending modes with more pronounced movement around +150 m mark
10	–	–	2.031	
11	–	–	2.031	

would be valuable to consider. Nevertheless, Table 3.1 clearly shows the advancement of OMA methods. The accuracy of the information about modal parameters is considerably higher now.

Despite the successful determination of frequencies and mode shapes, the correct determination of the damping coefficient from a short OMA test program remains a challenge. A report of testing in 1989 gives the logarithmic decrement for the fundamental frequency between 0.063 and 0.093. The data obtained at level +332 m were processed. This corresponds to a damping coefficient from 1% to 1.5%. But now we identified that most of the mode shapes have a degree of high complexity. This suggests that the energy dissipation mechanisms are not uniformly distributed along the height of the structure, being the prismatic part of the tower dissipates more energy than the top part. This seems logical, as both the tower supports up to +82 m and the antenna part above +217 m consists of continuously welded elements. The prismatic part, on the other hand, has many different joints and details that dissipate energy more (cladding, different layers of materials, bolted joints, etc.).

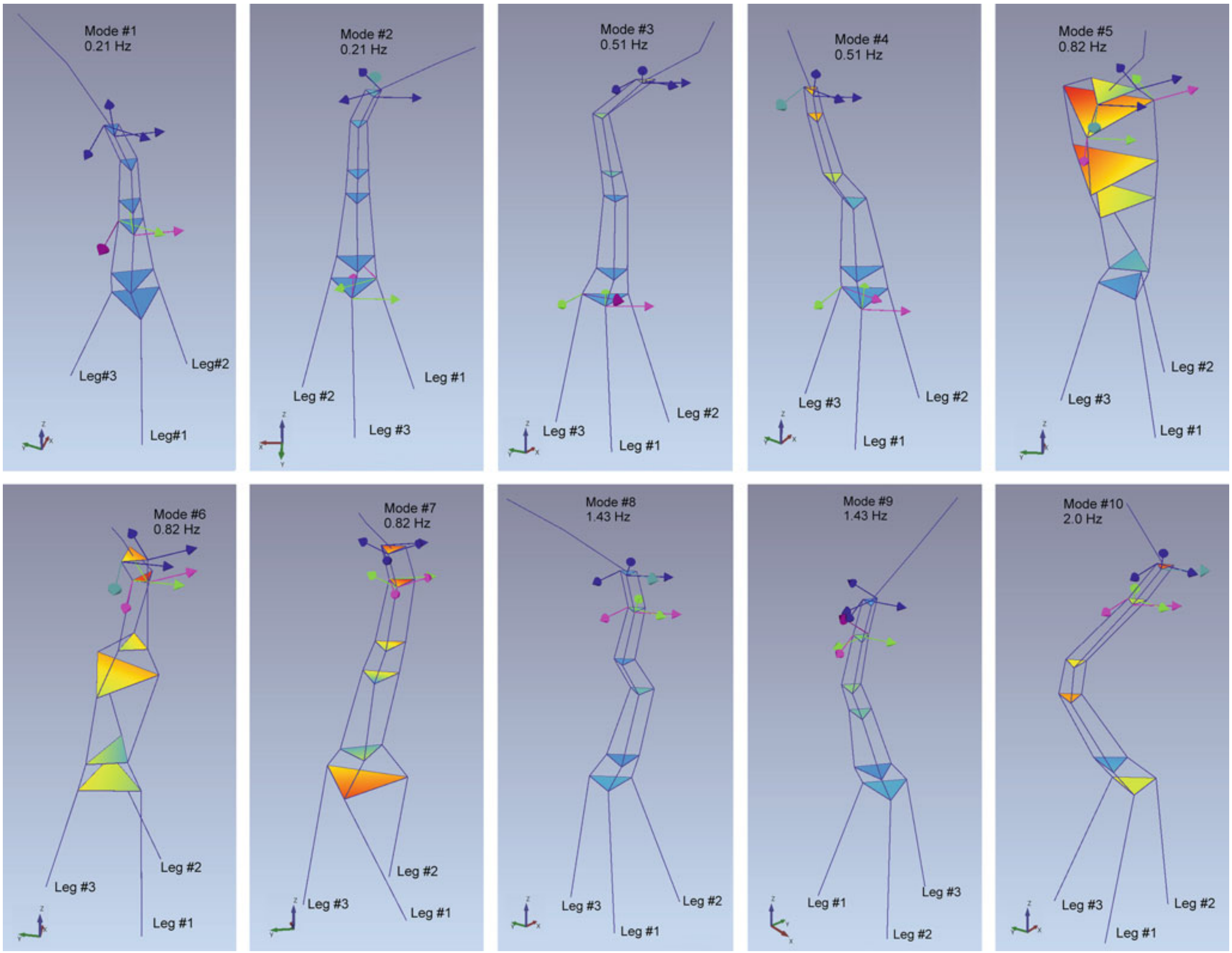

Fig. 3.5 Identified first ten mode shapes from ambient vibration data by commercial software Artemis

Table 3.2 MAC value between identified mode shapes

Mode #	MAC value		Mode #	MAC value	
	FDD/EFDD	FDD/SSI	FDD/EFDD	FDD/SSI	
1	0.74	0.45	6	1	0.10
2	0.98	0.75	7	1	0.10
3	0.91	–	8	0.923	0.76
4	1	0.41	9	0.99	0.84
5	1	0.52	10	0.99	0.63

Also, aerodynamic damping properties could vary for those three distinct parts considerably. Therefore, identified damping ratios with the commercial software Artemis have high scatter and do not seem to reflect reality.

MAC values between results of different identification algorithms are summarized in Table 3.2. It is known that a system with closely spaced eigenvalues is perturbed and the associated mode shapes are mainly rotating in their initial subspace [30]. This explains low MAC values in Table 3.2 when comparing modes shapes one-by-one obtained with different identification algorithms. The solution is to use the mode shape projections obtained through the transformation matrix for the calculations of MAC values. The proof of the existence of an approximate transformation matrix between two corresponding mode shape clusters is given in [31]. Furthermore, the low MAC value observed for modes #6 and #7, as well as the absence of these exact mode shapes in the FEM model, indicates that at frequency 0.82Hz, there might actually be two bending modes and only one torsional mode shape that have not been accurately identified using the chosen identification algorithms.

3.5 Conclusion

This chapter explores the practical application of modal parameter identification techniques with a time lag of more than 30 years for one of the tallest self-supporting structures in Europe, namely, the 368-meter High TV and Radio Transmission Tower in Riga. This highlights the development of Operational Modal Analysis techniques by comparing the amount and quality of information extracted from ambient vibration test data. This chapter also adds to the full case studies of OMA applications in the civil engineering field under challenging conditions, when the use of long cables or wireless systems is limited. The post-processing time series data synchronization technique based on minimizing the phase between signals from the two measurement chains produced excellent results for frequency estimation and was reasonable for mode shape determination. It is found that although frequencies and mode shapes can be reliably identified with different algorithms from the ambient vibration data, it is still a challenge to identify damping ratios when closely spaced and repeated complex mode shapes are present. The next activities will include the development of a more detailed FEM model and the application of model updating procedures to this case study.

Acknowledgments The raw data for the publication courtesy of 100% Latvia state-owned company "Latvijas Valsts radio un televīzijas centrs" (LVRTC). The authors especially would like to thank the technicians – high climbers of LVRTC Normunds Patmalnieks and Eduards Putilins for their valuable support and assistance in the dynamic testing of the structure and Julija Batalauska for excellent organizational help. The technicians Klaus Myndal and Ian Rasmussen of the Civil and Mechanical Engineering Department (CONSTRUCT) at the Technical University of Denmark (DTU) for their assistance in the preparation and testing of the measurement system used in the multi-dataset vibration test of the Riga TV and Radio Transmission Tower.

This work has been supported by the European Regional Development Fund within the Activity 1.1.1.2 "Post-doctoral Research Aid" of the Specific Aid Objective 1.1.1 "To increase the research and innovative capacity of scientific institutions of Latvia and the ability to attract external financing, investing in human resources and infrastructure" of the Operational Programme "Growth and Employment" (No.1.1.1.2/VIAA/3/19/393).

References

1. Zahid, F.B., Ong, Z.C., Khoo, S.Y.: A review of operational modal analysis techniques for in-service modal identification. J. Braz. Soc. Mech. Sci. Eng. **42**(8) (2020). https://doi.org/10.1007/S40430-020-02470-8
2. Zhang, L., Brincker, R.: An overview of operational modal analysis: Major development and issues. In: Proceedings of the 1st International Operational Modal Analysis Conference, IOMAC 2005 (2005)
3. Cunha, Á., Caetano, E.: Experimental modal analysis of civil engineering structures. Clin. Microbiol. Infect. **12**(SUPPL. 3), 12–24 (2006). https://doi.org/10.1111/J.1469-0691.2006.01393.X
4. Brincker, R., Ventura, C.E.: Introduction to operational modal analysis. In: Introduction to Operational Modal Analysis, pp. 1–360. John Wiley & Sons (2015). https://doi.org/10.1002/9781118535141
5. Gara, F., Arezzo, D., Nicoletti, V., Carbonari, S.: Monitoring the modal properties of an RC school building during the 2016 Central Italy Seismic Swarm. J. Struct. Eng. **147**(7), 05021002 (2021). https://doi.org/10.1061/(ASCE)ST.1943-541X.0003025
6. Ramos, L.F., Marques, L., Lourenço, P.B., de Roeck, G., Campos-Costa, A., Roque, J.: Monitoring historical masonry structures with operational modal analysis: Two case studies. Mech. Syst. Signal Process. **24**(5), 1291–1305 (2010). https://doi.org/10.1016/J.YMSSP.2010.01.011
7. Regni, M., Arezzo, D., Carbonari, S., Gara, F., Zonta, D.: Effect of environmental conditions on the modal response of a 10-story reinforced concrete tower. Shock. Vib. **2018**, 9476146 (2018). https://doi.org/10.1155/2018/9476146
8. Avci, O., Alkhamis, K., Abdeljaber, O., Alsharo, A., Hussein, M.: Operational modal analysis and finite element model updating of a 230 m tall tower. Structures. **37**, 154–167 (2022). https://doi.org/10.1016/J.ISTRUC.2021.12.078
9. Savnik, N.J., Katsanos, E.I., Amador, S.D.R., Ventura, C.E., Brincker, R.: Influence of diaphragm modelling on the dynamic performance of a reinforced concrete high-rise building. In: Proceedings of ISMA 2018 – International Conference on Noise and Vibration Engineering and USD 2018 – International Conference on Uncertainty in Structural Dynamics (2018)
10. Gargaro, D., Rainieri, C., Fabbrocino, G.: Structural and seismic monitoring of the 'cardarelli' Hospital in Campobasso. Procedia Eng. (2017). https://doi.org/10.1016/j.proeng.2017.09.244
11. Reynolds, T., Harris, R., Chang, W.S., Bregulla, J., Bawcombe, J.: Ambient vibration tests of a cross-laminated timber building. Proc. Inst. Civ. Eng. Constr. Mater. (2015). https://doi.org/10.1680/coma.14.00047
12. Pecorelli, M.L., Ceravolo, R., Epicoco, R.: An automatic modal identification procedure for the permanent dynamic monitoring of the Sanctuary of Vicoforte. Int. J. Archit. Heritage. (2018). https://doi.org/10.1080/15583058.2018.1554725
13. Omar, O., Tounsi, N., Ng, E.G., Elbestawi, M.A.: An optimized rational fraction polynomial approach for modal parameters estimation from FRF measurements. J. Mech. Sci. Technol. **24**(3), 831–842 (2010). https://doi.org/10.1007/S12206-010-0123-Z
14. Brincker, R., Zhang, L., Andersen, P.: Modal identification of output-only systems using frequency domain decomposition. Smart Mater. Struct. **10**(3), 441 (2001). https://doi.org/10.1088/0964-1726/10/3/303
15. Magalhães, F., Cunha, Á., Caetano, E., Brincker, R.: Damping estimation using free decays and ambient vibration tests. Mech. Syst. Signal Process. **24**(5), 1274–1290 (2010). https://doi.org/10.1016/J.YMSSP.2009.02.011
16. Goursat, M., Döhler, M., Mevel, L., Andersen, P.: Crystal clear SSI for operational modal analysis of aerospace vehicles. Conf. Proc. Soc. Exp. Mech. Ser. **3**(PART 2), 1421–1430 (2011). https://doi.org/10.1007/978-1-4419-9834-7_125/COVER

17. van Overschee, P., de Moor, B.: Subspace Identification for Linear Systems. Springer US, Boston (1996). https://doi.org/10.1007/978-1-4613-0465-4
18. Ewins, D.J.: Model validation: Correlation for updating. Sadhana. **25**(3), 221–234 (2000). https://doi.org/10.1007/BF02703541
19. Mikitarenko, M.A., Perelmuter, A.V.: Safe fatigue life of steel towers under the action of wind vibrations. J. Wind Eng. Ind. Aerodyn. **74–76**, 1091–1100 (1998). https://doi.org/10.1016/S0167-6105(98)00100-7
20. Grau, M.: "Almaty Tower," Wikimedia Foundation, Oct. 09, 2012. https://en.wikipedia.org/wiki/Almaty_Tower#/media/File:TV-Turm_Almaty_-_3.jpg (Accessed 13 Oct 2022)
21. Yakovlev, S.: "Yerevan TV Tower," Wikimedia Foundation, July 03, 2006. https://en.wikipedia.org/wiki/Yerevan_TV_Tower#/media/File:Yerevan_TV_tower.jpg (Accessed 13 Oct 2022)
22. Kober, "Tbilisi TV Broadcasting Tower," Wikimedia Foundation, Jan 01, 2007. https://en.wikipedia.org/wiki/Tbilisi_TV_Broadcasting_Tower#/media/File:Mt_Mtats'minda,_Tbilisi,_Georgia_(view_from_Metekhi_cliff).JPG (Accessed 13 Oct 2022)
23. Aceˆ eVg, "Kharkiv TV Tower," Wikimedia Foundation, May 22, 2007. https://en.wikipedia.org/wiki/File:Kharkov_TV_tower.jpg (Accessed 13 Oct 2022)
24. Fundamental Principles Behind the Sigma-Delta ADC Topology: Part 1 | Analog Devices. https://www.analog.com/en/technical-articles/behind-the-sigma-delta-adc-topology.html (Accessed 16 Sept 2022)
25. Рижская радиотелевизионная башня. Экспериментальное определение параметров колебаний башни от ветрового воздействия. ОНИС 549, Днепропетровск (1989)
26. Au, S.K., Brownjohn, J.M.W., Li, B., Raby, A.: Understanding and managing identification uncertainty of close modes in operational modal analysis. Mech. Syst. Signal Process. **147**, 107018 (2021). https://doi.org/10.1016/J.YMSSP.2020.107018
27. Kita, A., Cavalagli, N., Ubertini, F.: Temperature effects on static and dynamic behavior of Consoli Palace in Gubbio, Italy. Mech. Syst. Signal Process. (2019). https://doi.org/10.1016/j.ymssp.2018.10.021
28. Yuen, K.V., Kuok, S.C.: Ambient interference in long-term monitoring of buildings. Eng. Struct. (2010). https://doi.org/10.1016/j.engstruct.2010.04.012
29. Cornwell, P., Farrar, C.R., Doebling, S.W., Sohn, H.: Environmental variability of modal properties. Exp. Tech. **23**(6), 45–48 (1999). https://doi.org/10.1111/J.1747-1567.1999.TB01320.X
30. García-Fernández, N., Pelayo, F., Aenlle, M.: Examples of model correlation with closely spaced modes. In: 9th International Operational Modal Analysis Conference, pp. 35–45 (2022)
31. Brincker, R., Lopez-Aenlle, M.: Mode shape sensitivity of two closely spaced eigenvalues. J. Sound Vib. **334**, 377–387 (2015). https://doi.org/10.1016/J.JSV.2014.08.015

Chapter 4
Acceleration Evaluation of a High-Speed Railway PC Box Girder Bridge with Slab Track

Haruki Yotsui, Kodai Matsuoka, and Kiyoyuki Kaito

Abstract The resonance of railway bridges that occurs under high-speed trains passage is an important academic and practical issue. The bridge design code in Europe (Eurocode) sets an upper limit of 5 m/s^2 on the bridge deck acceleration for a slab type track. However, the performance of high-speed railway bridges regarding train-induced deck acceleration specified in Eurocode has not been sufficiently verified. In this study, a slab track type PC box girder bridge in Japanese high-speed railway is targeted, and multipoint acceleration measurement is conducted. Based on the measurement results, the global and deck local modal characteristics are identified with ERA method, and the maximum deck acceleration is evaluated. As a result, the maximum deck acceleration of the bridge is much lower than the Eurocode limit value of 5 m/s^2 even under the resonance condition. Unlike previous reports for European composite box girder bridges, the main deck vibration modes of the bridge are over 40 Hz, thus the deck local vibration did not affect the evaluation of deck acceleration.

Keywords Railway · Resonance · Eurocode · Deck · Modal analysis

4.1 Introduction

The resonance of railway bridges is an important practical and academic issue for high-speed railways in Japan, and many studies have been conducted and various standards have been developed [1, 2]. Resonance phenomena in high-speed trains are caused by the proximity of the excitation frequency due to the regular axle arrangement of the passing train to the natural frequency of the bridge, which increases the dynamic response when the train passes [1]. In particular, for high-speed trains traveling at speeds exceeding 200 km/h, the period of train excitation exceeds 2 Hz and is close to the natural frequency of the bridge's first-order deflection mode, so the occurrence of resonance tends to be unavoidable [2]. When resonance occurs, the vibration of the bridge increases, which may affect the ride quality [3]. In addition, there have been reports of damage to the overhead contact line systems via vibration of poles built on the bridge [4]. Based on these facts, the design system in Japan has been shifted from the one that does not allow the occurrence of resonance to the one that allows the occurrence of resonance itself but ensures safety and usability [2].

In Europe, resonance phenomena in high-speed railway bridges are one of the major issues, and many studies and standards have been developed, just as in Japan. On the other hand, unlike in Japan, upper limits for deck acceleration during train passage are set in Eurocode [5] as a standard for resonance of high-speed railway bridges. This standard is in consideration of the stability of ballasted track, which is frequently used in European high-speed railways [6]. Upper limits are also set for slab track to prevent excessive vibration that could cause uplift of bearings [6]. However, girder acceleration has customarily been used to evaluate deck acceleration [7]. On the other hand, it has been pointed out that the effect of deck local vibration may not be negligible [8]. However, no tests or surveys were conducted when the standard values were set, and there are few examples of subsequent verification by actual measurements. Therefore, it can be said that the validity

---

H. Yotsui (✉) · K. Kaito
Department of Global Architecture, Graduate School of Engineering, Osaka University, Suita-City, Osaka, Japan
e-mail: h.yotsui@civil.eng.osaka-u.ac.jp

K. Matsuoka
Data Analytics in Information and Communication Technology Division, Railway Technical Research Institute, Kokubunji-City, Tokyo, Japan

H. Y. Noh et al. (eds.), *Dynamics of Civil Structures, Volume 2*, Conference Proceedings of the Society for Experimental Mechanics Series, https://doi.org/10.1007/978-3-031-36663-5_4

and effectiveness of the standards have not been sufficiently verified [9]. Based on the above issues, in this study, multipoint acceleration measurements are performed on a PC box girder bridge with a slab track of a high-speed railway in Japan during train passage, and the acceleration response is evaluated based on the criterion of deck acceleration in Eurocode. By identifying the vibration modes of the deck, the effect of deck local vibration to modal characteristics during train passage is empirically analyzed.

4.2 Methods

In this study, bridges with relatively large amplitude due to resonance during train passage were targeted. Figure 4.1 and Table 4.1 show the diagram and specifications of the target bridge. The bridge is a PC one-box girder bridge for high-speed railways. It is a standard PC box girder bridge with a span length of 48.6 m and a girder height of 2.8 m. Transverse girders and diaphragms are installed at the midspan and at $L_b/4$ and $3L_b/4$. As a result, the 5.2 m wide deck is assumed to behave as a single panel with supported areas approximately every 12 m. The natural frequency calculated from the cross section in Fig. 4.1b is 2.1 Hz without considering the stiffness of nonstructural members such as the track. Assuming resonance with the excitation period per car of a moving train (25 m), the resonance speed can be calculated as 2.1 [Hz] × 25 [m] × 3.6 = 190 [km/h]. However, since the stiffness of the nonstructural members is not taken into account [10], the actual natural frequency and resonance speed can be considered higher than the calculated values. As shown in Fig. 4.1b, a total of 23 accelerometers, 17 (D1–D17) and 6 (G1–G6), were installed on the top and bottom surfaces of the box girder, respectively, to determine the vibration characteristics of the deck members and entire girder. Accelerometers on the underside of the girder were installed near the cross-structure in order to grasp the behavior of the entire girder. As a deck, one panel on the right side of the midspan shown in Fig. 4.1b was focused, and an array of accelerometers was placed. A total of 24 trains, including both inbound and outbound trains, passed through the target bridge. Two types of trains were included: 6-cars trains and 8-cars, with speeds ranging from 220 to 240 km/h. The obtained acceleration response during train passage was decimated to 200 Hz and used for the following two analyses. First, the free vibration after the train passage was cut out for 5 s, and the vibration modes of the girder and deck were identified by applying the Eigensystem Realization Algorithm (ERA) method [11], in

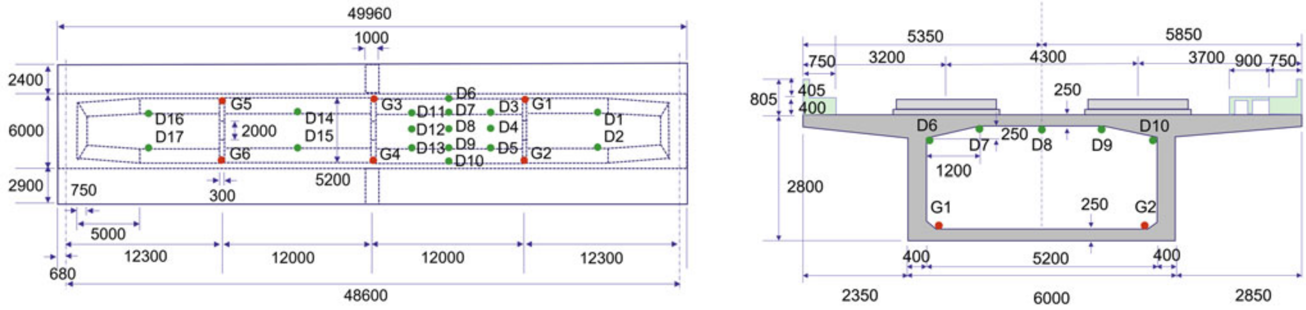

(a) Plan view (a) Cross-sectional view

Fig. 4.1 Target bridge and measurement setup. (**a**) Plan view. (**b**) Cross-sectional view

Table 4.1 Specifications of the target bridge

Contents	Type/Values
Bridge type	Double-track PC box girder (1-box)
Span length L_b [m]	48.6
Bridge length [m]	50.0
Girder height [m]	2.8
Girder width [m]	6.0
Track type	Slab track
Calculated natural frequency[a] [Hz]	2.1
Calculated resonance speed [km/h]	190

[a] Calculated according to Fig. 4.1b (Stiffness of track and ancillary structures are not considered)

which the degrees of freedom were set to 50. Second, in order to analyze the excursion vibration during train passage, a waveform processed by a 30 Hz low-pass filter (LPF) corresponding to the European deck acceleration standard (30 Hz LPF acceleration) was calculated.

4.3 Measured Acceleration Responses

Figure 4.2 shows the measured acceleration responses of girder acceleration G3 and deck acceleration D11 at the midspan. In this example, an eight-car train passed through the bridge at 235 km/h in outbound direction. This figure shows the 30 Hz LPF acceleration calculated according to Eurocode along with the acceleration decimated at 200 Hz. The amplitudes of both the girder acceleration G3 and the deck acceleration D11 increase as the train passes, and it can be confirmed that they are in the resonance condition where the free vibration waveform remains after the train passage. Specifically, given that the vibration amplified during train passage is eight waves corresponding to the number of cars, it can be confirmed that it is a first order resonance between the length of the cars and the vibration mode of the bridge.

First, the maximum values of each acceleration response were focused. The maximum value of the 30 Hz LPF acceleration corresponding to the Eurocode standard value is much less than 1 m/s^2. Therefore, even if the bridge is under the resonance condition, it does not reach the Eurocode standard value of 5 m/s^2 for the deck acceleration of the slab track. The maximum acceleration is about 1 m/s^2 even in the acceleration response up to 200 Hz, which is about 1/5 or less than the standard value of the deck acceleration in Eurocode.

Next, we focus on the difference between the 200 Hz LPF and the 30 Hz LPF. At both measurement points, the 30 Hz LPF showed only periodic vibrations and almost no high-frequency vibration components. As described below, this resonance is caused by the length of the train car and the first-order mode of the overall bending of the bridge. In light of this result, in this bridge, the vibration below 30 Hz is mainly composed of the overall bending mode, and the influence of the deck vibration mode is assumed to be small. Note that this trend differs from past results for composite girders [8]. In fact, comparing the maximum 30 Hz LPF acceleration values of the girder acceleration G3 and the deck acceleration D11, the deck acceleration D11 has a smaller value, which is considered to have a greater influence of the local vibration mode of the deck. However, the maximum value of the deck acceleration is higher in the 200 Hz LPF acceleration response, suggesting that the effect of the local vibration mode of the deck is greater in the region above 30 Hz in this bridge.

Figure 4.3 shows the Fourier spectra of the acceleration response of girder acceleration G3 and deck acceleration D11 shown in Fig. 4.2. Note that the spectra include the excitation properties of a running train [12], since the spectra include the acceleration response while the train is passing. As seen in the acceleration response, there is only a prominent peak around 2.5 Hz below 30 Hz shown as A. Peak A corresponds to the vibration component whose resonance was confirmed in Fig. 4.2. On the other hand, several peaks, including the three peaks indicated by B to D, can be observed in the region above 30 Hz.

Focusing on peak A, both the girder acceleration G3 and the deck acceleration D11 have the same spectral amplitude, and thus are considered to be the global mode in which they vibrate simultaneously. On the other hand, peaks B to D have larger spectral amplitudes for the deck acceleration D11 than for the girder acceleration G3. Therefore, it is highly likely that these modes are local vibration modes in which the vibration of the deck dominates. In the target bridge, such a peak due to the local vibration mode cannot be observed below 30 Hz. Therefore, as mentioned in the discussion of Fig. 4.2, the 30 Hz LPF acceleration in the bridge is mainly composed of the global mode. Although the spectral amplitudes of the peaks varied from one measurement point to another, the peak frequencies were generally similar for all measurement points and train cases.

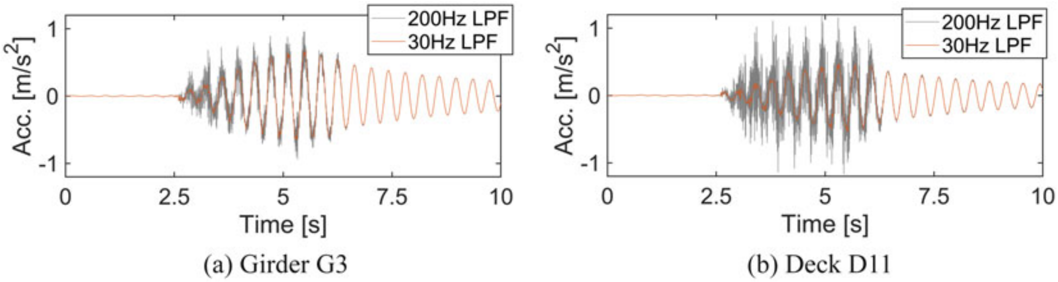

Fig. 4.2 Example of acceleration responses (outbound train, 235 km/h). (**a**) Girder G3. (**b**) Deck D11

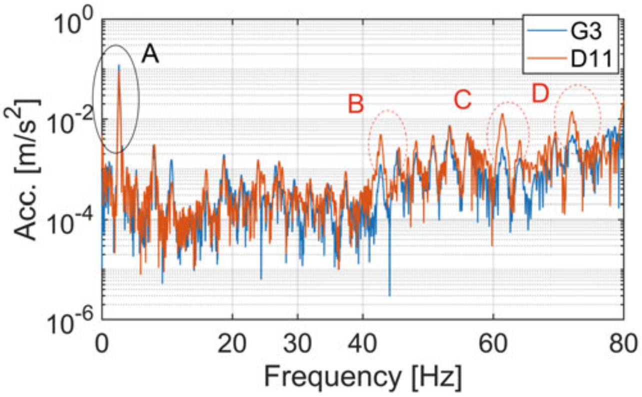

Fig. 4.3 Example of acceleration spectrum (outbound train, 235 km/h)

Table 4.2 Identified natural frequencies of global vibration modes

Global modes	Ave. [Hz]	CV [%]
First bending	2.58	0.6
First torsional	7.88	1.4
Second bending	9.25	1.0

Table 4.3 Identified modal damping ratios of global vibration mode

Global modes	Ave. [%]	CV [%]
First bending	1.57	30.0
First torsional	2.29	59.6
Second bending	2.63	27.1

In order to obtain a more detailed understanding of the vibration properties of the bridge at these peaks, mode identification was performed by regarding the residual waveform after the train passed as free vibration.

4.4 Identification Results

Tables 4.2 and 4.3 show the natural frequencies and mode damping ratios of the global vibration modes obtained by the ERA method, and Fig. 4.4 shows the vibration mode shapes. The mean values and coefficients of variation (CV) for all global vibration modes are calculated based on the results obtained for at least 6 of the 24 cases of residual waveforms after the train passed (first order bending: 24 cases, first order torsion: 16 cases, second order bending: 6 cases). The coefficient of variation is calculated by dividing the standard deviation by the mean value and is expressed as a percentage. In addition to the girder measurement points, the vibration mode shapes are shown together with the values of the deck acceleration measurement points except for D4, D6, D8, D10, and D12.

As global modes, first-order bending, first-order torsion, and second-order bending modes were identified with natural frequencies of 2.58 Hz, 7.88 Hz, and 9.25 Hz, respectively. The vibration mode shapes of each identified mode shown in Fig. 4.4 can be confirmed to have the same vibration mode shapes as listed in Tables 4.2 and 4.3. The coefficients of variation of the natural frequencies for each train running case are less than 1%. This result indicates that the natural frequencies can be identified with high accuracy.

The mode damping ratios are in the range of 1.5 ~ 3%. The coefficient of variation of the mode damping ratio is approximately 30–60%. In general, it is reported that there are cases where the variation exceeds 100%. However, the use of relatively clear free vibration waveforms for mode identification is considered to have reduced the variability of the identified modal damping ratios in this study. The mode damping ratio of the first-order bending mode was about 1.6%, which is lower than the 2% used in the design. However, because the residual waveforms after the train passed were used here, the additional damping effect [13] caused by the dynamic interaction between the running vehicle and the bridge was not taken into account. Therefore, the modal damping ratio during train passage is considered to be about 0.5–1% higher than the identified value. Further details on additional damping are beyond the scope of this study and can be found in Ref. [13].

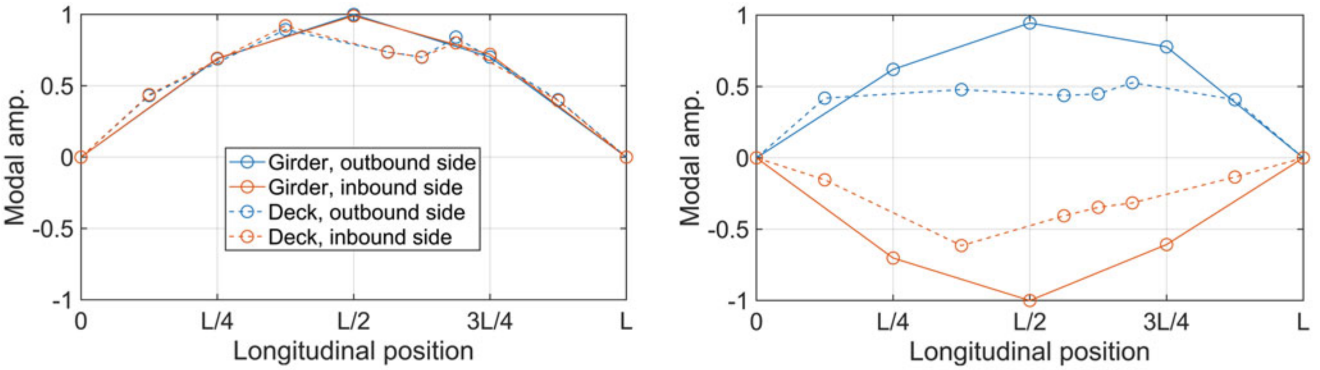

(a) First bending (2.58Hz)

(b) First torsional (7.88Hz)

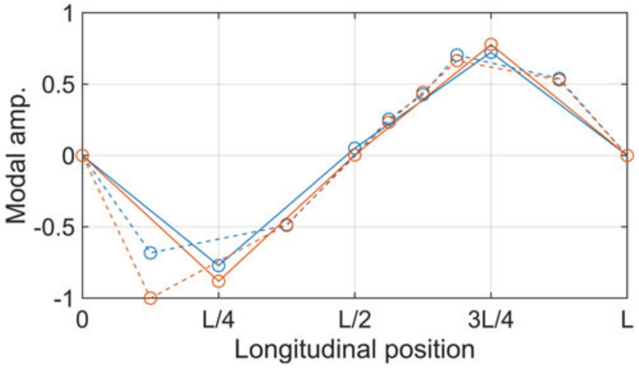

(c) Second bending (9.25Hz)

Fig. 4.4 Identified mode shapes of global vibration modes. (**a**) First bending (2.58 Hz). (**b**) First torsional (7.88 Hz). (**c**) Second bending (9.25 Hz)

Table 4.4 Identified natural frequencies of local deck vibration modes

Local modes (Longitudinal × Transverse)	Ave. [Hz]	CV [%]
1 × 1 A	23.9	–
1 × 2 (Coupled with other parts)	41.4	2.8
1 × 1 B	52.7	4.8
2 × 1 B	60.3	3.1

We focus on the vibration mode shapes shown in Fig. 4.4. In the first-order mode of global bending, which is the major component below 30 Hz and where resonance occurs, the girder and deck accelerations have approximately the same modal amplitude at many locations. However, the mode amplitude of the deck tends to be smaller than that of the girder in the section between the midspan (L/2) and 3 L/4. Therefore, for the target bridge of this study (PC box girder bridge for high-speed railway), the vibration of the deck does not significantly affect the evaluation of deck acceleration up to 30 Hz, and there is no problem in evaluating the acceleration by girder acceleration. Note that this trend differs from the results of a previous study on composite box girder bridges [8], which pointed out the importance of considering the effect of deck in the evaluation of deck acceleration up to 30 Hz.

Tables 4.4 and 4.5 show the natural frequencies and mode damping ratios of the local vibration modes obtained by the ERA method, and Fig. 4.5 shows the identified vibration mode shapes. The contour plot in Fig. 4.5 was created by spline interpolation based on the mode amplitudes at 11 points from D3 to D13, assuming that the mode amplitude at the transverse structure position is 0. The first order local modes exist in a small spectral amplitude region of 23 Hz and could be identified in only one case in the identification analysis for each train case. Therefore, coefficients of variation could not be calculated. However, since it is the most basic vibration modes of the deck, it is listed in Tables 4.4, 4.5, and Fig. 4.5.

Except for the first-order local modes, second-order modes in the longitudinal direction or transverse direction were identified up to about 60 Hz. The natural frequencies of these second-order modes correspond to the peaks indicated as B

Table 4.5 Identified modal damping ratios of local deck vibration modes

Local modes	Ave. [%]	CV [%]
1 × 1 A	1.4	–
1 × 2 (Coupled with other parts)	1.5	32.4
1 × 1 B	0.3	75.2
2 × 1 B	0.3	71.8

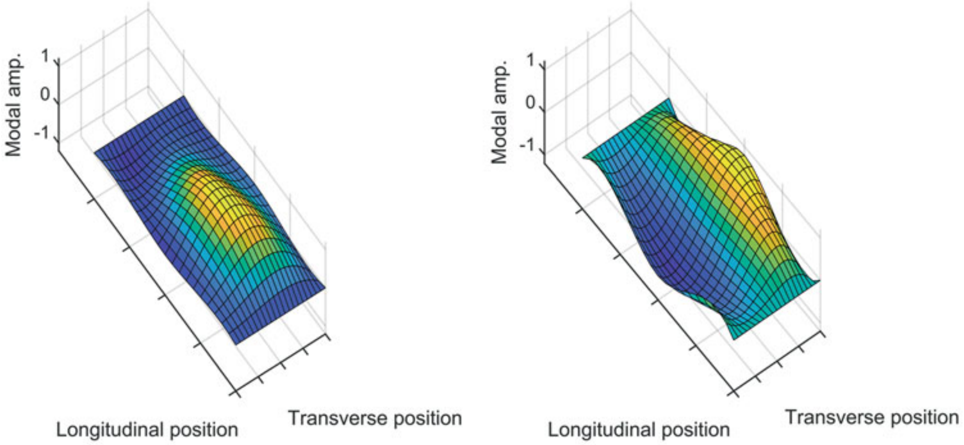

(a) 1×1 A (23.9Hz)

(b) 1×2 (41.4Hz)

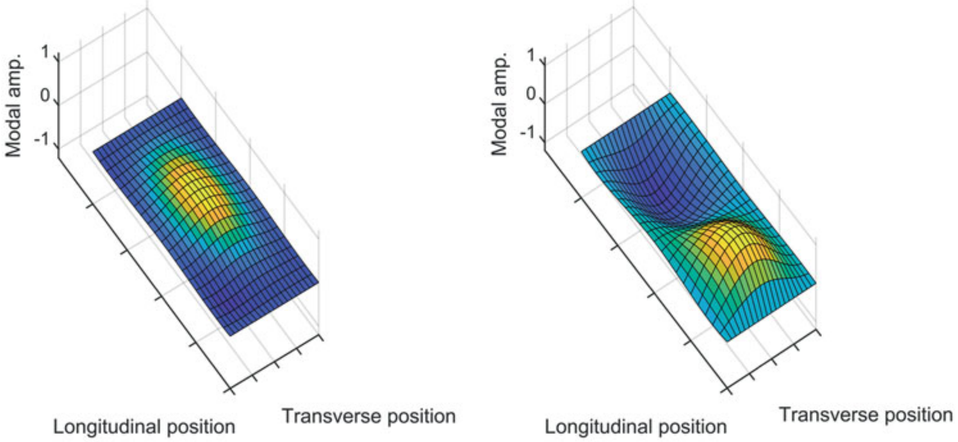

(c) 1×1 B (52.7Hz)

(d) 2×1 B (60.3Hz)

Fig. 4.5 Identified mode shapes of local deck vibration modes. (**a**) 1 × 1 A (23.9 Hz) (**b**) 1 × 2 (41.4 Hz) (**c**) 1 × 1 B (52.7 Hz) (**d**) 2 × 1 B (60.3 Hz)

and C in the spectrum of a passing train shown in Fig. 4.3. By confirming the mode order from Fig. 4.5, there were two first-order modes (mode A and mode B) in the longitudinal direction at 23.9 Hz and 52.7 Hz, respectively, among the identified vibration modes. As shown in Fig. 4.6, this is considered to be caused by the difference in the coupling properties with the adjacent deck panels (same phase or opposite phase mode). The same phase mode is considered to have a higher natural frequency because of the rotational restraint at the deck boundary, which is closer to the peripheral fixed support condition.

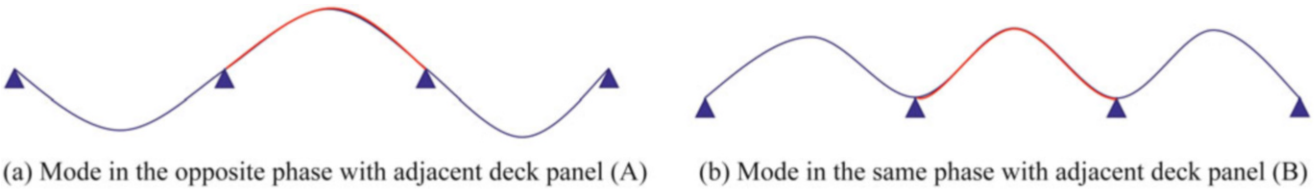

Fig. 4.6 Conceptual figures regarding the difference in coupled properties. (**a**) Mode in the opposite phase with adjacent deck panel (Mode A) (**b**) Mode in the same phase with adjacent deck panel (Mode B)

The 41.4 Hz vibration mode appears to be a 1 × 2 mode of the deck, but since the mode amplitude at the web position is also large, it is considered to be excited by the coupling of a higher order global torsional mode and the vibration mode of the overhanging slab. Above 70 Hz, several modes which are similar to second-order or third-order vibration mode shapes were observed in the longitudinal direction. However, since the shapes of these modes changed with train speed, it is highly likely that they are pseudo-modes affected by the excitation force properties.

Table 4.5 shows that the modal damping ratios of the deck local vibration modes tend to be smaller than those of the global vibration mode, with average values below 1%, although some coefficients of variation exceed 50% and are somewhat unreliable. This trend is consistent with the characteristics of higher order vibration modes reported in previous studies [14]. Therefore, when the natural frequency of the local vibration mode of the deck that forms the dominant component when a train passes by is less than 30 Hz (e.g., the case in reference [8]), the dominant vibration of the deck with a small mode damping ratio is likely to affect the evaluation of the deck acceleration and should be kept in mind. However, since the dominant vibration modes of the deck members were above 50 Hz for the target bridge in this study, it can be said that only the global vibration modes need to be considered for the evaluation of deck acceleration.

4.5 Conclusion

In this study, the acceleration of girders and deck members of a PC one-box girder bridge, which is a standard type of high-speed railway in Japan, during train passage was measured to evaluate the deck acceleration specified in Eurocode. Moreover, the effect of deck local vibration modes on the value of deck acceleration was investigated. The obtained results are as follows.

1. Accelerometers were arrayed on the girders and deck of a 50 m-long PC one-box girder bridge to measure the acceleration response during train passage. The maximum acceleration up to 30 Hz was less than 1 m/s^2 for both girders and deck, even at resonance in the global first-order bending mode, well below the Eurocode standard value of 5 m/s^2.
2. The global and deck local vibration modes were identified from the residual waveforms after the train passed by using the ERA method. The results showed that the natural frequency of the global first-order bending mode of the target bridge is about 2.5 Hz, and that resonance occurs at a train speed of 235 km/h. Since most deck vibration modes are above 40 Hz, the vibration of deck has no effect on the acceleration evaluation below 30 Hz.
3. Unlike the composite girders with ballasted track reported in the previous study, the vibration modes of the deck do not affect the acceleration evaluation up to 30 Hz, and it was found that the deck acceleration specified in Eurocode may be evaluated only by the lower-order global modes.

On the other hand, there are some issues to be addressed in the future. First, as mentioned in the main text, it is necessary to clarify the range where the deck vibration modes do not contribute to the evaluation of deck acceleration up to 30 Hz for standard Japanese high-speed railway decks. Depending on the results of this study, the method of considering deck acceleration in Eurocode (i.e., whether only the global behavior or the behavior of the deck is required) may change significantly.

Next, this study indicates that the maximum deck acceleration of the bridge can be represented only by the lower-order global vibration modes, but this point needs to be verified using actual numerical simulations. In addition, a method to account for the relatively large uncertainty of the measured maximum acceleration in the numerical simulation needs to be separately considered.

Acknowledgments This work was supported by JSPS KAKENHI Grant Number 22H01579.

References

1. Matsuura, A.: A study of dynamic behavior of bridge girder for high speed railway. Proc. Jpn. Soc. Civ. Eng. **256**, 35–47 (1976) (In Japanese)
2. Sogabe, M., Matsumoto, N., Fujino, Y., Wakui, H., Kanamori, M., Miyamoto, M.: Dynamic response and design of continuous concrete railway bridges in resonance area. J. Jpn. Soc. Civ. Eng. **724**, 83–102 (2003) (In Japanese)
3. Matsuoka, K., Tokunaga, M., Kaito, K.: Bayesian estimation of instantaneous frequency reduction on cracked concrete railway bridges under high-speed train passage. Mech. Syst. Signal Process. **161**(107944) (2021)
4. Matsuoka, K., Tsunemoto, M., Tokunaga, M.: Dynamic behaviour of railway poles built on bridges under train passage in high-speed railways and a simple evaluation method. Eng. Struct. **257**(114099) (2022)
5. CEN E. 1: Actions on structures-Part 2: Traffic loads on bridges. EN. **2**(6), 2003 (1991)
6. ERRI D214 Committee: Rail bridges for speeds higher than 200 km/h. Research Report of the European Rail Research Institute. (1999)
7. Martínez-Rodrigo, M.D., Lavado, J., Museros, P.: Dynamic performance of existing high-speed railway bridges under resonant conditions retrofitted with fluid viscous dampers. Eng. Struct. **32**(3), 808–828 (2010)
8. Matsuoka, K., Collina, A., Somaschini, C., Sogabe, M.: Influence of local deck vibrations on the evaluation of the maximum acceleration of a steel-concrete composite bridge for a high-speed railway. Eng. Struct. **200**(109736) (2019)
9. Arvidsson, T., Andersson, A., Karoumi, R.: Train running safety on non-ballasted bridges. Int. J. Rail Transp. **7**(1), 1–22 (2019)
10. Tokunaga, M., Ikeda, M.: Evaluation method of vibration characteristics of main structure of railway bridge considering non-structural members. J. Jpn. Soc. Civ. Eng. Ser. A1. **76**(3), 580–596 (2020) (In Japanese)
11. Juang, J.N., Pappa, R.S.: An eigensystem realization algorithm for modal parameter identification and model reduction. J. Guid. Control. Dyn. **8**(5), 620–627 (1985)
12. Miyashita, T., Ishii, H., Fujino, Y., Shoji, T., Seki, M.: Understanding of high-speed-train induced local vibration of a railway steel bridge using laser measurement and its effect by train speed. J. Jpn. Soc. Civ. Eng. A. **63**(2), 277–296 (2007) (In Japanese)
13. Matsuoka, K., Kaito, K., Sogabe, M.: Bayesian time–frequency analysis of the vehicle–bridge dynamic interaction effect on simple-supported resonant railway bridges. Mech. Syst. Signal Process. **135**(106373) (2020)
14. Matsuoka, K., Kaito, K., Watanabe, T., Sogabe, M.: Identification of dynamic properties of open-deck viaducts under passing train loads and consideration on high speed train. J. Appl. Mech. **13**, 997–1008 (2010) (In Japanese)

Chapter 5
Examining Methods for Modeling Road Surface Roughness Effects in Vehicle–Bridge Interaction Models via Physical Testing

Omar Abuodeh, William Locke, Laura Redmond, Rakesh Vulchi Sreenivasulu, and Matthias Schmid

Abstract Numerically simulating vehicle–bridge interaction (VBI) models within finite-element models (FEMs) has been a topic of interest over the last two decades. Its applications have been well-established in the structural health monitoring community for extracting the dynamic properties of bridges using instrumented vehicles. Often times, analytically generated surface profiles adopted from renowned standards such as the ISO-8608 are used to simulate road surface conditions and approach a more realistic model. However, previous analytical studies have indicated that current methodologies for modeling the effect of road surface roughness on the vehicle response tend to exaggerate the dynamic response of a vehicle and overshadow bridge frequencies in the vehicle response. To alleviate this issue, several studies have recommended relatively low-amplification roughness factors (G_d) or have used a moving average filter (MAF) to de-noise analytically generated surface profiles prior to prescribing it into the FEM, but to the authors' knowledge no experimental investigation has been conducted to validate these recommendations. In this chapter, a full-scale road test is conducted using a passenger vehicle instrumented with accelerometers. A vehicle model is developed using the bicycle concept to approximate the dynamic response of the tested vehicle while including road surface roughness effects. The results are then compared to observe whether the vehicle model contains higher acceleration amplitude values than those of the experiment while using ISO-8608's G_d factors for the appropriate road class observed in the test. It is concluded that low G_d factors, which are commonly used in VBI studies, seem to underestimate the surface roughness effects and thus produce an unrealistic VBI model. Moreover, the use of higher G_d factors without the implementation of a MAF tends to significantly exaggerate the vehicle's response. The implementation of a MAF was successful in attenuating high frequency noise while also reducing the acceleration amplitude of the vehicle, but the G_d value still needed to be relatively low to represent the data from the road testing. Finally, the study concludes with recommendations on how to improve the current approach for modeling road surface roughness in VBI problems and suggestions for future work.

For feedback and support, please see the https://github.com/omarabuodeh1994/surface_roughness.git. No promises are made in terms of timely help from the author.

Keywords Vehicle–bridge interaction model · Surface roughness · Model verification · Finite element · State-space representation

---

O. Abuodeh (✉)
Glenn Department of Civil Engineering, Clemson University, Clemson, SC, USA
e-mail: oabuode@g.clemson.edu

W. Locke
Exponent, Atlanta, GA, USA
e-mail: wrlocke@g.clemson.edu

L. Redmond
Glenn Department of Civil Engineering, Clemson University, Clemson, SC, USA

Department of Mechanical Engineering, Clemson University, Clemson, SC, USA
e-mail: lmredmo@clemson.edu

R. V. Sreenivasulu · M. Schmid
Department of Automotive Engineering, Clemson University, Greenville, SC, USA
e-mail: rvulchi@g.clemson.edu; schmidm@clemson.edu

H. Y. Noh et al. (eds.), *Dynamics of Civil Structures, Volume 2*, Conference Proceedings of the Society
for Experimental Mechanics Series, https://doi.org/10.1007/978-3-031-36663-5_5

5.1 Introduction

Many studies have demonstrated that the acceleration response of instrumented vehicles crossing a bridge enables the efficient extraction of bridge modal properties [1–3]. It is regarded as a spatially capable, practical, and economically beneficial structural health monitoring (SHM) technique in the maintenance of bridges [4]. The concept is based on treating the vehicle as a moving sprung mass that acts as both an exciter and a receiver [5]. Several numerical studies were conducted to simulate vehicle–bridge interaction (VBI) using finite-element models (FEM) to investigate its feasibility in extracting the natural frequencies [6–8], mode shapes [9–11], and damping ratios [12, 13] of bridges using vehicle signals. However, the effects of road surface roughness pollute the vehicle signals with spurious frequencies and increase the amplitudes of the vehicle frequencies, making it difficult for the researcher/engineer to discern the bridge frequencies [14]. Therefore, multiple techniques were proposed to minimize surface roughness effects while also maintaining bridge information in the signal [14–16]. These studies are mainly numerical and employ VBI modeling via FEMs where the effects of surface roughness are simulated by passing a vehicle over an artificially generated road surface profile using the International Organization of Standardization (ISO)-8608 [17]. The application of road roughness effects is conducted by prescribing concentrated forces acting on the axle or sprung mass [14, 18]. It has been widely accepted in the literature that this methodology overestimates the effects of road surface roughness as the contact patch between the tire and road is represented as a single point and thus all spatial frequencies affect the forces on the analytical unsprung mass [14].

The artificially generated road profiles, as per ISO-8608 [17], are categorized into eight road classes distinguished by letters from A–H, where Road Class A corresponds to a road with the lowest roughness and Road Class H corresponds to a road with the highest roughness. Yang and Chang [14] stated that the amplitude roughness factors to generate these road classes are too large to be compatible with the road roughness in the field. They tackle this issue by proposing to take amplitude roughness factor (G_d) to equal 0.001×10^{-6} m^3 for Road Class A and the square root of the geometric mean of the amplitude roughness factor for the rest of the road classes provided by ISO-8608 [17]. In another paper by Yang et al. [19], the authors employed a moving average filter (MAF) that uses a moving window to average the local elevation points where the window simulates the tire's contact patch with the road. This helps attenuate acceleration amplitudes corresponding to high spatial frequency road surface effects [20]. To the authors' knowledge, these are the only two techniques proposed for generating road roughness elevation profiles that do not over-exaggerate the vehicle response, and neither have been explicitly compared to results from vehicle testing.

The aim of this chapter is to first calibrate a vehicle model to represent a vehicle that has undergone road testing, simulate different road roughness effects by varying the G_d factors based on the ISO-8608 [17] road classes, and finally compare the acceleration response of the front and rear axles to those measured during the test. The authors will investigate the effect of varying these G_d factors and apply a MAF to the surface profile prior to prescribing it into the vehicle model. This chapter is organized into the following sections: Theoretical Background describes the techniques used to process the acceleration measurements taken during the road test; Model Description describes the vehicle model and how its dynamic response is simulated; Model Calibration overviews the steps carried out to calibrate the vehicle model to represent the physical vehicle in the road test; Comparison of Vehicle Simulations with Varying G_d Factors to Experimental Data compares the acceleration response generated by the FEMs to those measured during the test; and Conclusion summarizes the findings of the study and provides suggestions for future research to improve representation of road surface roughness effects in VBI models.

5.2 Theoretical Background

In this chapter, a FEM that employs the bicycle concept was constructed using state-space representation to simulate the dynamic response of a vehicle driving over a road with stochastic surface roughness. This model was tuned with acceleration measurements taken by a 2012 Buick Regal four door sedan that was driven across a patch of road along the US 221 in Greenwood Country, SC. These measurements were analyzed using signal processing and operational modal analysis (OMA) techniques to extract approximate natural frequencies corresponding to a bicycle model's four mode shapes: namely, body bounce, body pitch, front axle bounce, and rear axle bounce. The specific OMA techniques used in this chapter are: variational mode decomposition (VMD) and frequency-domain decomposition (FDD). Both techniques were employed using Python [21] where the `vmd()` [22] was used to execute VMD and both `PyOMA.FDDsvp()` and `PyOMA.FDDmodEX()` [23] were used to execute FDD.

5.2.1 *Variational Mode Decomposition*

A signal processing technique called variational mode decomposition (VMD) was used to decompose the acceleration response of the vehicle after the road test. It is a mathematically driven algorithm for delicately decomposing signals into several bandwidth-limited modes [24]. An extensive and detailed overview of VMD with its derivations can be viewed in the following works [19, 22, 24]. Generally, VMD requires input parameters such as the number of modes (K), quadratic penalty factor (α), and Lagrangian update parameter (τ). The number of modes selected determines how many times the algorithm decomposes the signal, the quadratic penalty factor controls the bandwidth size for capturing the correct center frequency of the particular mode, and the Lagrangian update parameter is used to control the Lagrangian multiplier to help reconstruct modes with more decompositions. In this chapter, τ is taken as zero to reduce noise levels [24], while the values of K and α will be discussed in Model Calibration.

5.2.2 *Frequency-Domain Decomposition*

A well-established OMA technique called frequency-domain decomposition (FDD) was also used to estimate modal parameters (e.g., natural frequencies and mode shapes) using input/output data of an n-degree-of-freedom (DOF) system stochastic process [23]. This is imperative for calibrating the vehicle model to the properties of the physical vehicle using the road test data. A detailed overview of FDD and its derivations can be viewed in [25]. Generally, the FDD method takes the cross power spectral density (PSD) of signals measured from multiple sensors and performs a singular value decomposition (SVD) using `PyOMA.FDDsvp()` [23]. Afterward, both the singular values and vectors were used to estimate the mode shapes of the signals using `PyOMA.FDDmodEX()` based on a user-given frequencies, typically, the frequencies that are within close proximity of high amplitudes in the singular values.

5.3 Model Description

As previously mentioned, the vehicle was modeled using the bicycle model concept, which is shown in Fig. 5.1. It has four DOFs, where u_v, θ_v, u_{wF}, and u_{wR} are the sprung vertical bounce, sprung pitch, front unsprung vertical bounce, and rear unsprung vertical bounce, respectively. The vehicle model's mass properties M_v, I_v, M_F, and M_R are the sprung mass in kg, sprung mass moment of inertia in kg-m^2, front unsprung mass in kg, and rear unsprung mass in kg, respectively; its suspension's stiffness/damping properties K_{FS}, K_{RS}, C_{FS}, and C_{RS} are the front stiffness in N/m, rear stiffness in N/m, front damping in N-s/m, and rear damping, respectively; lastly, its tire stiffness properties K_{FT} and K_{RT} are the front stiffness in N/m and rear stiffness in N/m, respectively. The road surface roughness ($r(x)$) was also numerically generated as per ISO-8608 and will be discussed later in this section [17].

The dynamic response of the four-DOF vehicle model was simulated by writing its equations of motion in state-space representation, as shown in Eq. 5.1, where $x(t)$, $u(t)$, and $y(t)$ are the state vector, input matrix, and output vector, respectively; $\boldsymbol{A}$, $\boldsymbol{B}$, $\boldsymbol{C}$, and $\boldsymbol{D}$ are the state, input, output, and direct transmission matrices, respectively; and $(\dot{\ })$ and $(\ddot{\ })$ are the

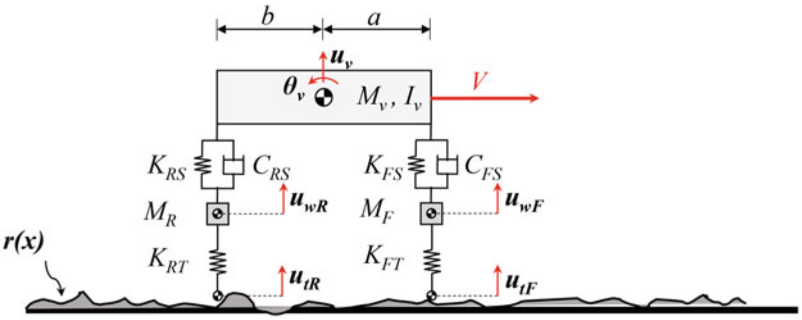

Fig. 5.1 Vehicle and bridge models in VBI system

derivatives with respect to time. State-space modeling was conducted using Python [21] where the `control.ss()` [26] was used to create the state-space linear time-invariant model. Typically, accelerometers mounted on the axles during road tests are minimally influenced by high frequency noise resulting from the vehicle's body [27]. Therefore, the output vector from the model consists only of the acceleration response of the front and rear axles and is compared to the acceleration response of the axles in the physical test.

$$\begin{aligned} \dot{x}(t) &= \boldsymbol{A} \cdot x(t) + \boldsymbol{B} \cdot u(t) \\ y(t) &= \boldsymbol{C} \cdot x(t) + \boldsymbol{D} \cdot u(t), \end{aligned} \tag{5.1}$$

where

$$\begin{aligned} x(t) &= \left[u_v(t)\ \theta_v(t)\ u_{wF}(t)\ u_{wR}(t)\ \dot{u}_v(t)\ \dot{\theta}_v(t)\ \dot{u}_{wF}(t)\ \dot{u}_{wR}(t)\right]^T \\ y(t) &= \left[\ddot{u}_{wF}(t)\ \ddot{u}_{wR}(t)\right]^T \\ u(t) &= \left[\frac{K_{FT} r(x_{FT})}{M_F}\ \ \frac{K_{RT} r(x_{RT})}{M_R}\right] \end{aligned}$$

$$\boldsymbol{A} = \begin{bmatrix} 0 & 0 & 0 & 0 & 1 & 0 & 0 & 0 \\ 0 & 0 & 0 & 0 & 0 & 1 & 0 & 0 \\ 0 & 0 & 0 & 0 & 0 & 0 & 1 & 0 \\ 0 & 0 & 0 & 0 & 0 & 0 & 0 & 1 \\ -\left(\frac{K_{FS}+K_{RS}}{M_v}\right) & \frac{K_{RS}b-K_{FS}a}{M_v} & \frac{K_{FS}}{M_v} & \frac{K_{RS}}{M_v} & -\frac{(C_{FS}+C_{RS})}{M_v} & \frac{C_{RS}b-C_{FS}a}{M_v} & \frac{C_{FS}}{M_v} & \frac{C_{RS}}{M_v} \\ \frac{K_{RS}b-K_{FS}a}{I_v} & -\left(\frac{K_{FS}a^2+K_{RS}b^2}{I_v}\right) & \frac{K_{FS}a}{I_v} & -\frac{K_{RS}b}{I_v} & \frac{C_{RS}b-C_{FS}a}{I_v} & -\left(\frac{C_{FS}a^2+C_{RS}b^2}{I_v}\right) & \frac{C_{FS}a}{I_v} & -\frac{C_{RS}b}{I_v} \\ \frac{K_{FS}}{M_F} & \frac{K_{FS}a}{M_F} & -\left(\frac{K_{FS}+K_{FT}}{M_F}\right) & 0 & \frac{C_{FS}}{M_F} & \frac{C_{FS}a}{M_F} & -\left(\frac{C_{FS}}{M_F}\right) & 0 \\ \frac{K_{RS}}{M_R} & -\frac{K_{RS}b}{M_R} & 0 & -\left(\frac{K_{RS}+K_{RT}}{M_R}\right) & \frac{C_{RS}}{M_R} & -\frac{C_{RS}b}{M_R} & 0 & -\left(\frac{C_{RS}}{M_R}\right) \end{bmatrix}$$

$$\boldsymbol{B} = \begin{bmatrix} 0 & 0 \\ 0 & 0 \\ 0 & 0 \\ 0 & 0 \\ 0 & 0 \\ 0 & 0 \\ 1 & 0 \\ 0 & 1 \end{bmatrix}; \quad \boldsymbol{C} = \begin{bmatrix} \frac{K_{FS}}{M_F} & \frac{K_{FS}a}{M_F} & -\left(\frac{K_{FS}+K_{FT}}{M_F}\right) & 0 & \frac{C_{FS}}{M_F} & \frac{C_{FS}a}{M_F} & -\left(\frac{C_{FS}}{M_F}\right) & 0 \\ \frac{K_{RS}}{M_R} & -\frac{K_{RS}b}{M_R} & 0 & -\left(\frac{K_{RS}+K_{RT}}{M_R}\right) & \frac{C_{RS}}{M_R} & -\frac{C_{RS}b}{M_R} & 0 & -\left(\frac{C_{RS}}{M_R}\right) \end{bmatrix}; \quad \boldsymbol{D} = \begin{bmatrix} 1 & 0 \\ 0 & 1 \end{bmatrix}.$$

Moreover, the input matrix ($u(t)$) to this system is a time-varying matrix equal to the product of both the road surface elevation ($r(x)$) and tire stiffness properties of the affected tire divided by the mass of the affected body. These inputs were applied to the front and rear axles, similar to previously published VBI works [14, 18]. As previously mentioned, analytically generating the surface profile of a patch of road is typically carried out by the following the ISO-8608 standards [17]. In this chapter, the road surface profile was computed using the PSD functions defined by ISO-8608 [17]. Equation 5.2 describes how the surface profile is generated where $G_d(n)$ is the PSD function for the surface profile, n is the spatial frequency per meter ranging from 1 to 100 cycles/m at an increment of Δ_n, w is a constant equal to 2, n_0 is 0.1 cycle/m, Δ_n is the spatial frequency increment (0.04 cycles/m), and $G_d(n_0)$ is the amplitude roughness factor based on road roughness class (A–H). The `control.matlab.lsim()` [26] was used to input the vector $u(t)$ into the state-space model and perform vehicle simulation over a patch of road.

$$r(x) = \sum d_i \cos\left(n_{s,i} x + \theta_i\right), \tag{5.2}$$

where

$$d = \sqrt{2G_d(n)\Delta_n}; \quad G_d = G_d(n_0)\left(\frac{n}{n_0}\right)^{-w}.$$

Some researchers implement a moving average filter (MAF) to the elevation points of the surface profile before passing it into the dynamic system. This aids in simulating the behavior of a vehicle's tire contact patch and its ability to attenuate high frequencies resulting from the high spatial frequencies of the road surface roughness profile [28]. The MAF works by sweeping a constant length window across a signal and taking the mean value of the local points within the window. Equation 5.3 shows the MAF where i and M are the vector index and length of window. In this chapter, the length of the window used in the MAF was the tire contact patch's length, which was taken as 10 inches (25.4 cm) according to [29].

$$y[i] = \frac{1}{M}\sum_{j=0}^{M-1} x[i+j]. \tag{5.3}$$

5.4 Model Calibration

In this chapter, the bicycle model concept was used to simulate the dynamic response of the vehicle. This was carried out by computing the mass, center of mass (CM), stiffness of suspension/tire, and damping magnitudes of the vehicle, followed by transforming these quantities into equivalent forms that could be used to construct the bicycle model. The mass, CM, and suspension stiffness values were computed using measurements taken from the static test, which will be explained in the next subsection. The tire stiffness and damping were calibrated from data in the road test, described in Road Test. The tire stiffness values were approximated by iteratively selecting tire stiffness values until the vehicle model's unsprung natural frequencies matched with the natural frequencies of the physical vehicle. The physical vehicle frequencies were obtained by post-processing the measured road test acceleration data using VMD and FDD. Finally, the damping values were selected to match the initial transient acceleration response recorded from the axle when the vehicle passes over a speed bump during the road test. It is worth mentioning that since the Buick vehicle was simulated using the bicycle model concept, the roll mode was not required and, therefore, the vehicle was segmented longitudinally where the authors have taken the readings from only the right side of the vehicle (i.e., passenger's side, front right, and rear right sensors).

5.4.1 Static Test

The mass of a 2012 Buick Regal four door sedan was measured using the SW777 Scale System [30] where the vehicle was parked on four pads. Each pad measures the mass of the vehicle from the tires where the summation of these four measured quantities yields the vehicle's mass ($M_{v,total}$). This is depicted in Fig. 5.2 where M_{FL}, M_{FR}, M_{RL}, and M_{RR} are the mass values measured on the SW777 system's scale pads corresponding to the front left, front right, rear left, and rear right wheels, respectively; and t_{wb}, l_{wb}, x_{cm}, and y_{cm} are the wheel base width, wheel base length, CM measured laterally from the rear left wheel, and CM measured longitudinally from the rear wheels, respectively. In this chapter, the quantities M_{FL}, M_{FR}, M_{RL}, M_{RR}, t_{wb}, and l_{wb} were measured three times, and their resulting averages were 501.5 kg, 482.5 kg, 333.0 kg, 324.0 kg, 1.6 m, and 2.74 m, respectively. Equations 5.4 and 5.5 were then be used to compute the Buick's CM locations: $x_{cm} = 0.814$ m and $y_{cm} = 1.64$ m.

$$x_{cm} = \frac{(M_{FR} + M_{RR})\, t_{wb}}{M_{v,total}} \tag{5.4}$$

$$y_{cm} = \frac{(M_{FL} + M_{FR})\, l_{wb}}{M_{v,total}}. \tag{5.5}$$

The suspension stiffness values were obtained by applying concentrated forces using sandbags and measuring the added weight using the SW777 scale pads [30], while also measuring the body's displacement from equilibrium using Kistler HF series laser height sensors [31]. This instrumentation setup is depicted in Fig. 5.3, where the laser sensors were mounted to

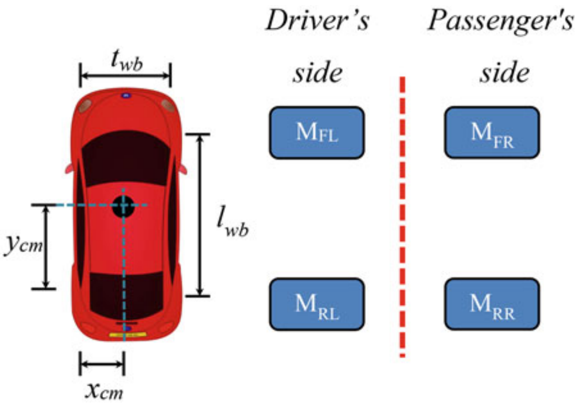

Fig. 5.2 Vehicle top-view schematic and location of SW777 scale pads

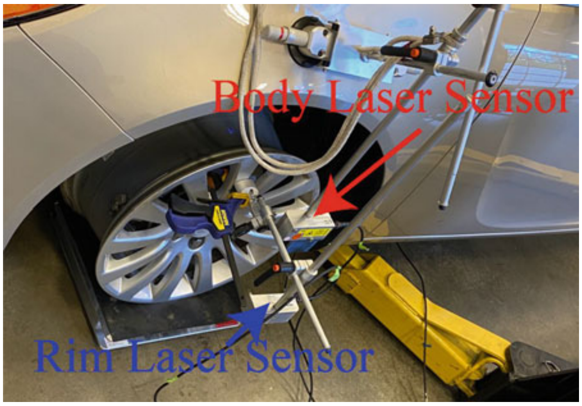

Fig. 5.3 Buick vehicle ride height sensor instrumentation from the driver's side

Table 5.1 Measured vehicle corner forces and displacements of Buick vehicle

	F (N)				Measured displacement (mm)	
Loading pattern	FR[a]	FL[a]	RR[a]	RL[a]	Right	Left
Right focused	−39.24	196.2	−652.37	−495.41	−13.1	−10.2
Left focused	225.63	−78.48	−495.41	−657.3	−9.2	−13.25
Distributed	122.625	88.29	−588.6	−622.9	−12.2	−12.7
Right focused	−323.73	−171.68	−44.145	44.145	−7.3	−5.1
Left focused	−171.68	−318.83	53.955	−53.955	−4.9	−6.7
Distributed	−260	−230.5	−14.72	14.72	−6.2	−5.3

[a] *FR* front right, *FL* front left, *RR* rear right, *RL* rear left

the body of the vehicle and rim. In this test, two types of load cases were implemented, namely, a concentrated load case and a distributed load case. The concentrated load case was created by stacking sandbags on one corner of the vehicle, and the distributed load case was created by distributing the sandbags laterally over one axle. These forces were applied separately between the rear and front sides while also the measuring the Buick's vertical displacements at the corners of loaded side (front or rear corners). To minimize additional displacements resulting from the tire's stiffness, the tires were completely removed where the Buick's tire rims rest on the scale pad. However, the authors continued to measure the displacement of the rim by mounting laser height sensors to monitor any change in displacement from the rim. Since the rear of the vehicle permitted more sandbags to be loaded in the trunk, the rear and front were loaded with 100 and 50 kg of sandbags, respectively. Table 5.1 shows the added forces and displacement magnitudes corresponding to the location and load case of the test, where F is the difference in weight between the vehicle before and after loading (i.e., force acting on the vehicle). It is worth mentioning that minimal displacement was observed laser sensors mounted on the rim.

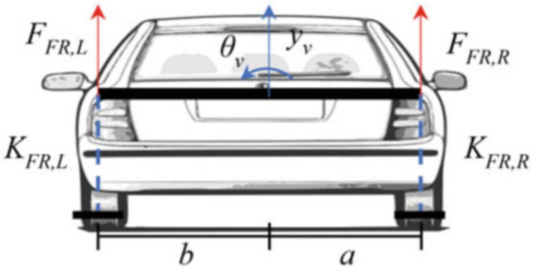

Fig. 5.4 Front/rear views of vehicle with the bicycle model concept in the lateral direction

5.4.2 *Suspension Properties*

The suspension stiffness values of the Buick vehicle were computed statically by writing the force–displacement relationship and taking the moment around the length of the vehicle in the lateral direction, as shown in Fig. 5.4. To begin the calibration process, the authors initially assumed that the vertical and rotational DOFs between the front and rear sides were independent of each other. A schematic of how the authors modeled this is shown in Fig. 5.4, where $K_{FR,L}$ and $K_{KR,R}$ are the left and right suspension stiffness magnitudes in the front/rear side of the vehicle, respectively; and $F_{FR,L}$ and $F_{FR,R}$ are the left and right concentrated forces acting on the front/rear side of the vehicle, respectively, which can be found in Table 5.1. Therefore, the force–displacement and moment–rotation equations in both the front and rear sides can be written in matrix form as shown in Eq. 5.6. Afterward, assuming rigid body motion between the right and left sides, the vertical bounce and rotational roll of the vehicle can be approximated by using Eqs. 5.7 and 5.8, where y_{RS} and y_{LS} are the displacements measured by the laser sensors attached to the body of the vehicle in the right and left sides, respectively. The authors used the displacement measurements of the distributed loading case since it simulated two dominant modes: vertical bounce and pitch, which are the mode shapes exhibited by the bicycle vehicle model. As a result, the suspension stiffness values were initially calculated as: K_{FL} = 43,497.2, K_{FR} = 41,929.8, K_{RL} = 49,050, and K_{RR} = 48,245.9 N/m.

$$\begin{bmatrix} y_v + a\theta_v & y_v - b\theta_v \\ ay_v + a^2\theta_v & -by_{FS} + b^2\theta_v \end{bmatrix} \cdot \begin{bmatrix} K_{RS} \\ K_{LS} \end{bmatrix} = \begin{bmatrix} F_R + F_L \\ F_R a - F_L b \end{bmatrix} \tag{5.6}$$

$$\theta_v = \frac{y_{RS} - y_{LS}}{t_{wb}} \tag{5.7}$$

$$y_v = \theta_v \cdot x_{cm} + y_{LS}. \tag{5.8}$$

Next, a 3D FE model of the vehicle was constructed using the commercial FE software Abaqus [32] to determine if the initial assumption of independence between the front and rear suspension was sufficient to capture the vehicle's behavior in the static test. The vehicle body was modeled by using rigid linear quadrilateral elements with 4 nodes. The suspension stiffness was modeled using vertical spring elements, and the applied forces resulting from adding sandbags were modeled by prescribing concentrated forces on all four corners of the vehicle body. All load cases taken from Table 5.1 were simulated using the initial values of suspension stiffness calculated in the previous section. The vehicle displacements from the model were compared to those measured in the physical test as shown in Table 5.2. Generally, the FE model's results show good agreement with the measurements taken during the static test except for the front right focused and left focused loadings, where the computed errors are 12.57 and 10.81%.

5.4.3 *Mass Properties*

As mentioned in the first paragraph of this section, only the right side of the vehicle was modeled, and therefore, the total mass used hereafter is the total mass on the right side of the vehicle ($M_{v,tot,r} = M_{FR} + M_{RR}$). Since the bicycle model concept was used to simulate the dynamic response of the Buick vehicle, the $M_{v,tot,r}$ was transformed into sprung and unsprung mass values, as shown in Fig. 5.1. This was carried out by using Eqs. 5.9 and 5.10, where $i_{m,f}$ and $i_{m,r}$ are coefficients that depend on the location of the axle ($i_{m,f}$ = 0.12 and $i_{m,r}$ = 0.13 [33]), and M_{FR} and M_{RR} are the total vehicle masses measured on

Table 5.2 Computed vehicle displacements using Abaqus compared to those measured during the static test

		F (N)				Measured displacement (mm)		Computed displacement (mm)		Percentage error	
Location	Loading pattern	FR	FL	RR	RL	Right	Left	Right	Left	Right	Left
Rear	Right focused	−39.24	196.2	−652.37	−495.41	−13.1	−10.2	−13.999	−9.63076	−6.86%	5.58%
Rear	Left focused	225.63	−78.48	−495.41	−657.3	−9.2	−13.25	−9.3133	−14.3401	−1.23%	−8.23%
Rear	Distributed	122.625	88.29	−588.6	−622.9	−12.2	−12.7	−12.107	−12.79	0.76%	−0.71%
Front	Right focused	−323.73	−171.68	−44.145	44.145	−7.3	−5.1	−7.1897	−4.45888	1.51%	12.57%
Front	Left focused	−171.68	−318.83	53.955	−53.955	−4.9	−6.7	−4.3703	−7.06404	10.81%	−5.43%
Front	Distributed	−260	−230.5	−14.72	14.72	−6.2	−5.3	−6.1205	−5.37668	1.28%	−1.45%

the scale pads. After computing the front and rear unsprung masses, the sprung mass was calculated by taking the difference between the total mass of the right side of the vehicle and the total unsprung masses. The location of the body's CM was computed from the rear axle (b) by taking the difference between the mass recorded on the front right scale pad (M_{FR}) and the front unsprung mass (M_F), multiplying it by the wheel base length (l_{wb}), and dividing by the sprung mass (M_v). Finally, the mass moment of inertia of the sprung mass (I_v) was calculated using Eq. 5.11. As a result, the sprung mass, mass moment of inertia, and front and rear unsprung masses are 681.7 kg, 1263.74 kg· m^2, 45.4 kg, and 39.4 kg, respectively, and the CM locations from the front and rear unsprung masses are 1.218 and 1.522 m, respectively.

$$M_F = \frac{i_{m,f} M_{FR}}{1 + i_{m,f}} \tag{5.9}$$

$$M_R = \frac{i_{m,r} M_{RR}}{1 + i_{m,r}} \tag{5.10}$$

$$I_v = (M_{FR} - M_F)a^2 + (M_{RR} - M_R)b^2. \tag{5.11}$$

5.4.4 *Road Test*

A road test was conducted on a patch of road before crossing over Hard Labor Creek (HLC) bridge along US 221 in Greenwood County, SC. A total of three vehicle passes were conducted during this road test. The Buick vehicle was instrumented with MECALC accelerometers that were mounted on the axles and body near all four wheels. The frequency range, sensitivity, sample rate, and mounting method used for the accelerometers were 1–7000 Hz, 20 ± 5 mV/g, 2048 Hz, and cement resin, respectively. In addition, a speed bump trigger was used to inform the driver when the vehicle was 30.5 m away from the HLC bridge. In this chapter, the vehicle signals measured at the axles in the front and rear right corners of the Buick vehicle were taken as data to post-process and were divided into two signals: transient and steady-state signals. The transient signal was obtained by extracting the time history from the time when the vehicle crosses the speed bump to 0.5 seconds later. This signal is mainly composed of acceleration resulting from the speed bump such that the damping effects of the vehicle were captured and used to calibrate damping of the vehicle model to match its acceleration response with that of the transient signal from the road test. The steady-state signal was obtained by extracting the acceleration response from 1 second after the vehicle passes the speed bump to 1 second before it enters the bridge. The steady-state signal contains the acceleration response resulting mainly from the surface roughness effects. This signal was used to approximate the front and rear axles' unsprung natural frequencies using VMD and FDD.

5.4.5 *Tire Stiffness Properties*

Obtaining the tire stiffness properties requires a more sophisticated approach where both VMD and FDD were employed to post-process acceleration readings taken during the road test. The aim of using these algorithms was to obtain approximate natural frequencies and mode shapes of the front and rear axles, separately. Prior to implementing VMD and FDD, the acceleration readings taken from the front and rear axles in the passenger's side were pre-processed by implementing downsampling, low-pass, and high-pass filters to remove excessive noise. First, the acceleration readings were downsampled by a factor of four, which decreased the sampling rate from 2048 to 512 Hz. Afterward, the acceleration readings were filtered using the Butterworth filter [34] where low-pass and high-pass filters were implemented with cut-off frequencies at 50 and 0.5 Hz, respectively, using a filter order of eight.

The signals were then passed into the VMD algorithm to decompose the measured acceleration signals. Since the bicycle model has four natural frequencies corresponding to four mode shapes, four mode decompositions were implemented. A quadratic penalty factor of 1500, which was a reasonable value according to [24, 35], was used. Afterward, the PSD of each mode with its corresponding frequency vector was computed using Welch's algorithm [36]. In the Welch's algorithm, the sampling frequency and frequency resolution used were 512 and 0.2 Hz, respectively, while also employing a moving Hann window with a 66% overlap. The first two vehicle natural frequencies correspond to the vehicle body bounce and pitch mode shapes, while the last two natural frequencies correspond to the front and rear axle bounce mode shapes. However, due to significant mode mixing in the signal, closely spaced modes could cause VMD to classify more than one natural frequency

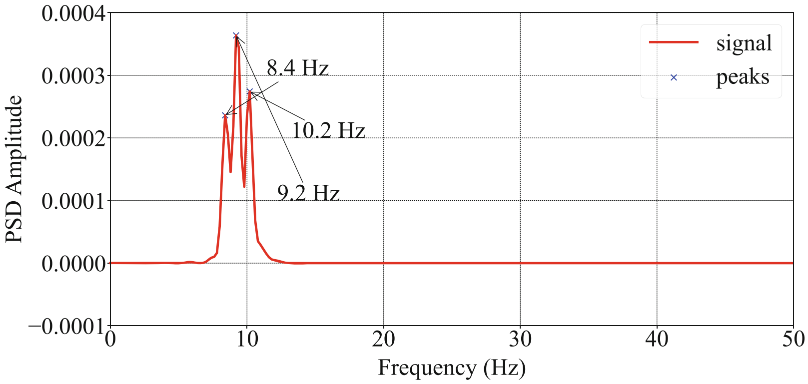

Fig. 5.5 PSD plot of fourth mode for front axle during first vehicle pass

Table 5.3 Frequencies picked from the decompositions

	Sprung passenger side frequencies picked			Unsprung passenger side frequencies picked		
Sensor location	Pass #1	Pass #2	Pass #3	Pass #1	Pass #2	Pass #3
Front	[1.6,2.8]	[2.2,3.4]	2.2	[8.4,9.2,10.2]	[7.2,8.4,9.4]	[8.8,9.6]
Rear	2	2.2	[1.4,2.4]	[9.4,10.2]	[9.2,10.6]	[8.2,9,10]

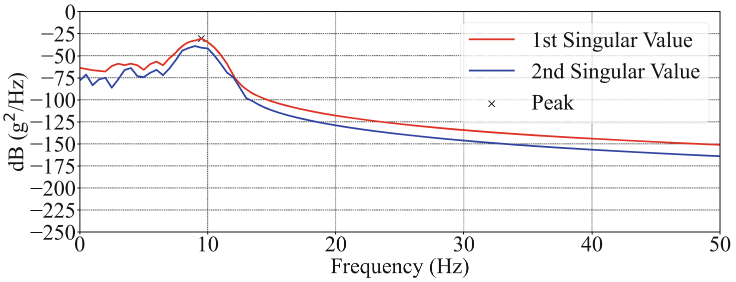

Fig. 5.6 PSD plot of fourth mode for front axle during first vehicle pass

in a mode with a particular central frequency. Therefore, the authors used the PSD plots of the second and last modes to extract the four natural frequencies corresponding to the aforementioned mode shapes. In addition, the authors also have prior knowledge from [27] that the natural frequencies of the sprung and unsprung masses fall within the ranges of 1–2 Hz and 8–15 Hz, respectively. It is worth mentioning that these picked frequencies were used as initial values to be passed into the FDD functions, which is discussed in the next paragraph. SciPy's `find_peaks()` [34] was then employed to locate the local peaks of the PSD amplitudes with its corresponding frequencies. Figure 5.5 shows the PSD plot of the fourth mode extracted from the front axle's acceleration reading during the first vehicle pass. This step was repeated for all vehicle passes using the acceleration readings taken from the passenger's side on the front and rear sides of the Buick's body and axles, where the extracted peak frequencies are shown in Table 5.3. It can be observed that the sprung mass natural frequencies are within 1.5–3 Hz, while the unsprung natural frequencies are within 8–11 Hz, which are ranges that roughly agree with the values published in the literature [27, 37].

As previously mentioned, the picked frequencies were used as initial inputs to compute the approximate mode shapes using `PyOMA.FDDsvp()` and `PyOMA.FDDmodEX()` [23]. This was carried out by separately passing the body's and axles' measured accelerations to return the singular values and vectors of the estimated cross PSD between the front and rear sides using `PyOMA.FDDsvp()`. Figure 5.6 shows the singular values for the accelerations measured at the front and rear axles in Pass #1. Afterward, the estimated singular values and vectors along with the initially picked frequencies in Table 5.3 were passed into `PyOMA.FDDmodEX()`. The mode shapes were generated in the form of a vector with a size that is dependent on the number of sensors used. Each mode shape corresponds to the frequency passed into `PyOMA.FDDmodEX()` in which the authors started with the initial frequencies in Table 5.3 and slightly varied the frequencies until the approximate four mode shapes that are exhibited by a bicycle model were observed. Table 5.4 shows the mode shape in the form of a vector where the first and second elements are the front and rear sides, respectively, while also showing the frequency for that particular mode in the adjacent column. For example, in Pass #1 the passenger sprung

Table 5.4 Mode shapes for picked frequencies using FDD

Passenger sprung modal properties					Passenger unsprung modal properties			
Pass #	Bounce mode	f_{bounce} (Hz)	Pitch mode	f_{pitch} (Hz)	Front bounce mode	$f_{f,bounce}$ (Hz)	Rear bounce mode	$f_{r,bounce}$ (Hz)
Pass #1	[1,0.95]	1.5	[1,−0.477]	2	[1,0.67]	8.4	[0.418,1]	10.2
Pass #2	[1,0.841]	1.5	[1,−0.956]	2	[1,−0.0285]	9	[−0.205,1]	10.5
Pass #3	[1,−0.44]	1.5	[1,−0.44]	2	[0.12,1]	9	[0.0188,1]	9.6

mass shows a clear bounce mode because the first and second elements are equal/close to one. The frequencies estimated using `PyOMA.FDDmodEX()` can then be used to obtain approximate tire stiffness properties.

A vehicle model with the previously computed mass properties and suspension system was modeled with an arbitrary tire stiffness value. An eigenvalue analysis of this vehicle model was then executed in which the tire stiffness values were varied until computed frequencies approximately converged with the frequencies outlined in Table 5.4. As a result, the tire stiffness values for the front and rear axles are both 110,000 N/m. An eigenvalue analysis of the vehicle with the updated tire stiffness was carried out, and the natural frequencies corresponding to the body bounce, body pitch, front axle bounce, and rear axle bounce are 1.42, 1.66, 9.25, and 10.1 Hz, respectively. These computed frequencies generally agree with those computed from the measured accelerations shown in Table 5.4.

5.4.6 Damping Properties

By combining all the dynamic properties computed in this section, an undamped vehicle model was obtained. The suspension system's damping was then approximated by matching the acceleration response of the vehicle model to the transient portion of the signal, which was 0.5 seconds long. The sudden impulse load caused by the speed bump was simulated by measuring the dimensions of the speed bump and applying it as a series of concentrated forces following its shape, and equal to the product of both the measured elevations and tire stiffness for the affected tire divided by its mass. In this chapter, the speed bump profile roughly resembled that of a trapezoid where its total length and elevation are 9.2 inches (23.4 cm) and 1.625 inches (4.13 cm), respectively. Afterward, two vectors containing the elevation at which the vehicle passes over the speed bump were created and used as the input matrix ($u(t)$). This was carried out by using `control.matlab.lsim()` where the damping values in the front and rear suspensions were iteratively varied until the acceleration response of both the front and rear axles match those recorded during the speed bump impulse. As a result, the damping values for the front and rear suspensions are 2200 and 1000 Ns/m, respectively, where Fig. 5.7 shows the acceleration response and its fast Fourier transformation for both the FEM and road test. It can be observed that the FEM generally shows good agreement with that of the experiment. A summary of the dynamic properties of the calibrated vehicle model is shown in Table 5.5.

5.5 Comparison of Vehicle Simulations with Varying G_d Factors to Experimental Data

The calibrated vehicle model was used to simulate the road test by subjecting the model to concentrated forces resulting from an analytically generated road surface profile, as per the ISO-8608 standard [17]. A road class of A was assumed since the road was recently paved. The acceleration responses of both the front and rear axles in the models were compared to those of the Buick vehicle from the passenger side during the road test. According to [14], the ISO-8608 standard's amplification roughness factors that affect the amplitude of the generated road profile were considered too large to be compatible with the road profile found in the field. Therefore, they recommended reducing these factors to prevent amplifying the vehicle signal with road roughness features. In this chapter, three distinct road surface profiles were generated based on amplification roughness factors, where values of 0.001×10^{-6}, 2×10^{-6}, and $16\times 10^{-6}\,\mathrm{m}^3$ were used. The first value was used because it was suggested as a reasonable amplification roughness factor to describe minimal roughness (road class A) by Yang et al. [14], and the last value is the geometric mean of the amplification roughness factor for Road Class A provided by ISO-8608 [17]. The second value was selected because it showed the closest agreement to the acceleration response measured in the road test. Since the road surface profile generated is stochastic, the vehicle simulations are run five times where the mean acceleration is taken for the front and rear axles, separately, and compared to those measured in the road test. Figure 5.8 shows the vertical acceleration response of the FEM and road test for both the front and rear axles. It can be observed that the vehicle model passing over a road profile with a G_d of $2\times 10^{-6}\,\mathrm{m}^3$ showed the closest agreement with those measured

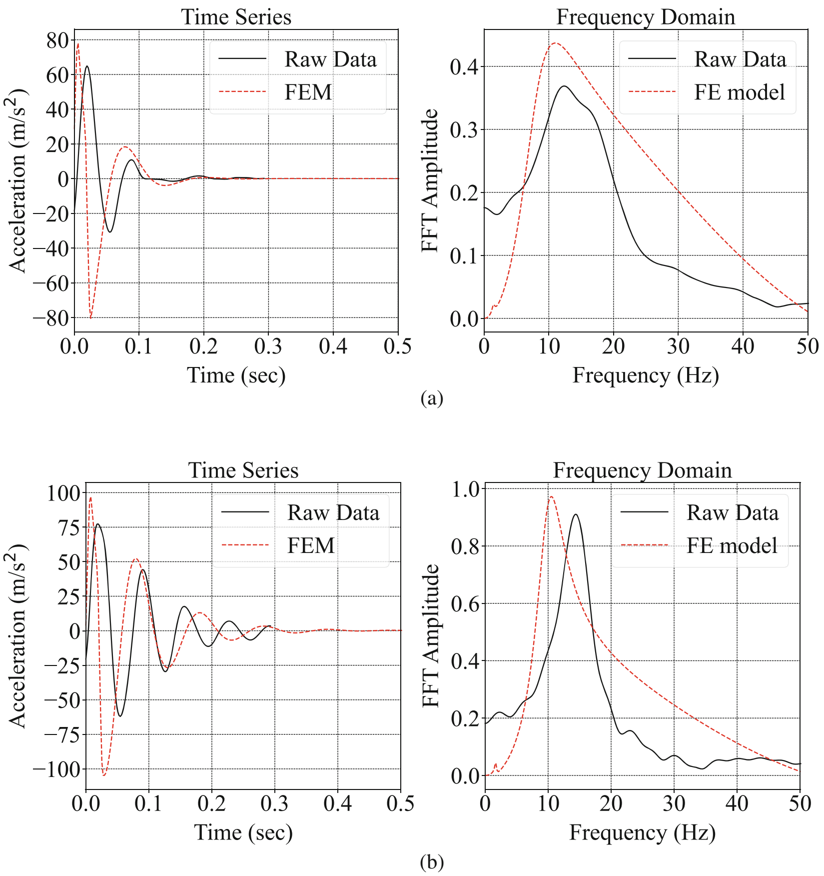

(a)

(b)

Fig. 5.7 Measured and computed vehicle response when excited by speed bump. (**a**) Front axle. (**b**) Rear axle

Table 5.5 Dynamic properties used in the half-car model

M_v (kg)	I_v (kg· m^2)	a (m)	b (m)	Location	$K_{F,RS}$ (N/m)	$C_{F,RT}$ (N/m)	$K_{F,RT}$ (sN/m)	$M_{F,R}$ (kg)
681.7	1263.74	1.218	1.522	Front	41,929.8	2200	110,000	45.4
				Rear	48,245.9	1000	110,000	39.4

in the road test. On the other hand, G_d values of $0.001\times\ 10^{-6}$ and $16\times\ 10^{-6}\,\mathrm{m}^3$ showed significantly lower and higher acceleration responses than those measured in the road test, respectively. Interestingly, these G_d factors are still within the lower half of the values that can be generated for the most ideal road profile; Road Class A.

Some researchers implemented a MAF to the elevation profile of the road prior to prescribing it into the FEM to account for the fact that the contact between the tire and road is a contact patch rather than a single point [19, 28]. Therefore, a MAF was also used to investigate its effects in minimizing the over-amplification observed in Fig. 5.8. Figure 5.9 shows the vertical acceleration response of the FEM and road test for both the front and rear axles after using the MAF. It can be observed that the vehicle passing over a road profile with a G_d of $2\times\ 10^{-6}\,\mathrm{m}^3$ demonstrated lower acceleration response amplitudes than those measured in the road test. Similar to Fig. 5.8, the vehicle model that passes over road profiles with G_d values of $0.001\times\ 10^{-6}$ and $16\times\ 10^{-6}\,\mathrm{m}^3$ showed significantly lower and higher acceleration responses than those measured in the road test, respectively. Examining both Figs. 5.8 and 5.9, the MAF was successful in reducing the acceleration amplitudes; however, the reduction may still not be significant enough since the highest G_d factor used in this chapter is still the geometric mean for Road Class A.

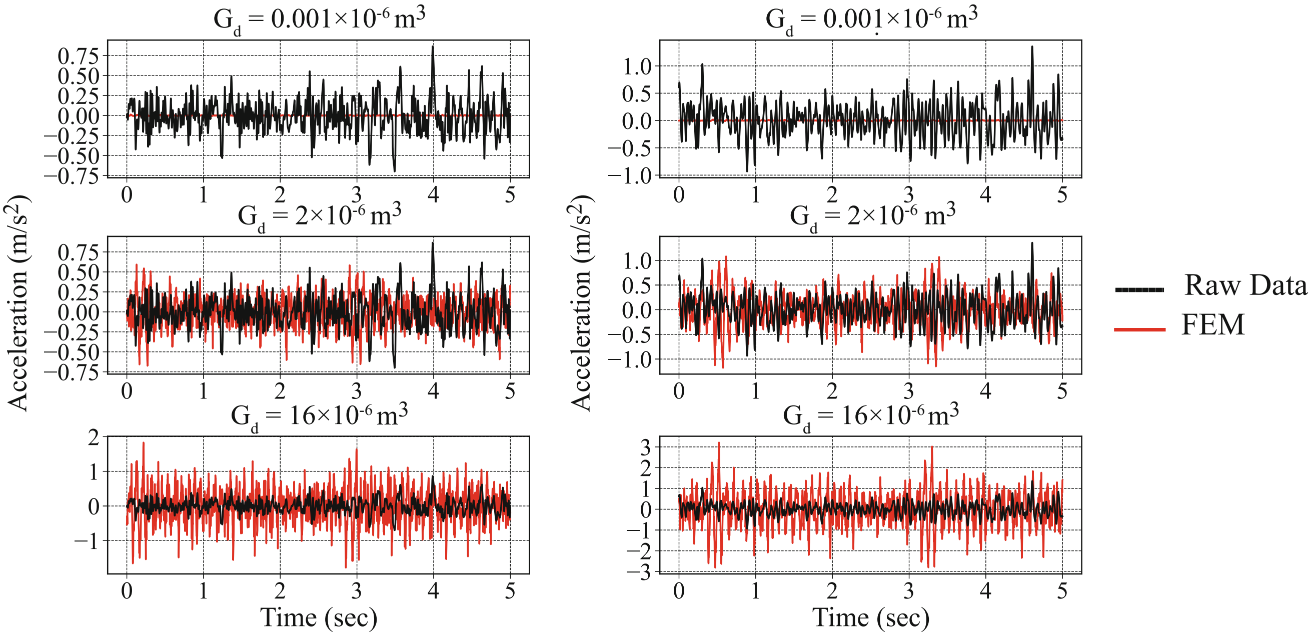

(a) (b)

Fig. 5.8 Vehicle and bridge models in VBI system. (**a**) Front axle. (**b**) Rear axle

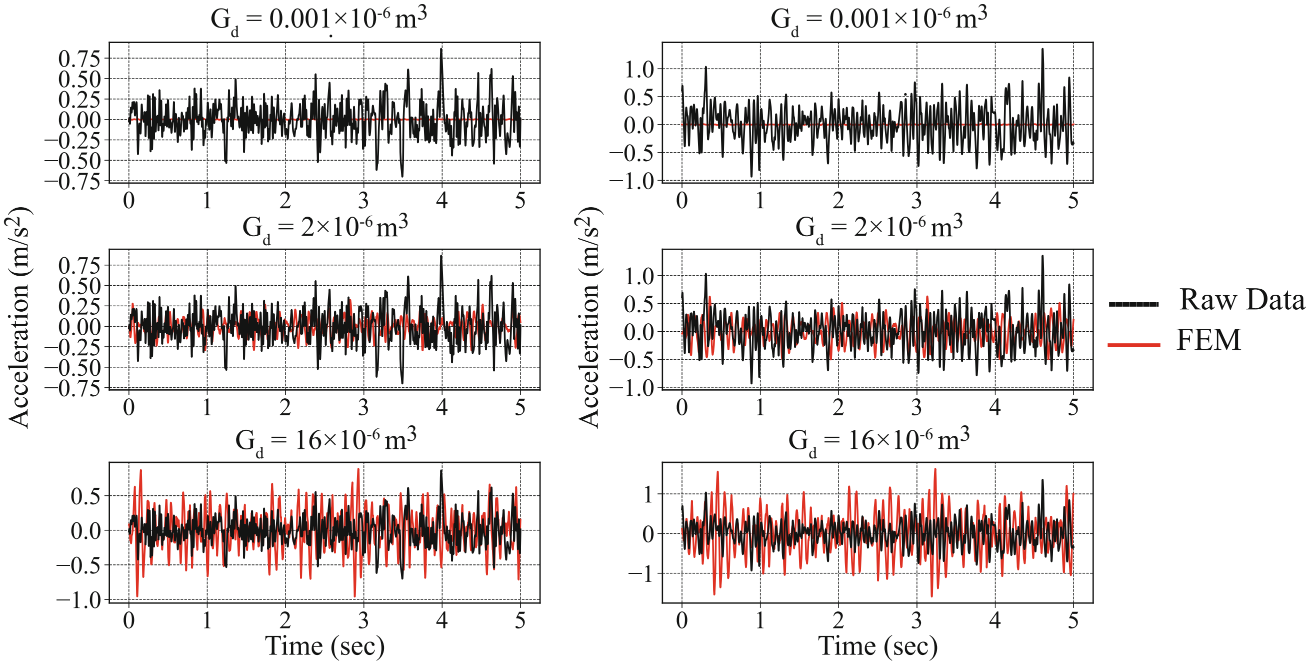

(a) (b)

Fig. 5.9 Vehicle and bridge models in VBI system. (**a**) Front axle. (**b**) Rear axle

5.6 Conclusion

Constructing realistic and accurate vehicle models is imperative for researchers in the SHM community who investigate the use of acceleration data taken from passing vehicles to perform system identification (SI) within the scope of bridge health monitoring. Typical problems that researchers and engineers attempt to overcome in numerical studies are the spurious frequency content or amplified acceleration amplitudes corresponding to the vehicle's natural frequencies, which both result from surface roughness effects. However, most of these numerical studies implement surface roughness profiles where their model's acceleration response is exaggerated compared to what an actual vehicle exhibits, hindering the effectiveness of any proposed technique. In this chapter, a calibrated vehicle FEM with varying amplification roughness factors (G_d) and the optional use of MAF were executed where the acceleration response of both axles was compared to those measured in the physical road test. The following conclusions can be drawn from this chapter:

- A G_d value of $0.001\times 10^{-6}\,\text{m}^3$, which was a commonly used amplification roughness factor in VBI studies, seems to underestimate road roughness effects and thus does not represent a realistic condition even for the recently paved road such as the one used for this test.
- G_d roughness coefficients greater than $2\times 10^{-6}\,\text{m}^3$, without the use of a moving average filter (MAF), tend to exaggerate the vehicle model's acceleration response, for a recently paved road, when compared to that measured during the road test.
- The use of a MAF is successful in attenuating high frequency noise while also reducing the acceleration amplitude of the vehicle when driving over a road.
- The combination of using low G_d coefficients with MAF may be a reasonable way of overcoming the exaggerated vehicle response resulting from road roughness effects.

The present work can be further expanded to include physical vehicle testing that explicitly measures road surface profiles and forces within the wheel hub to provide recommended amplification roughness factors or alternative methods for modeling road surface roughness within VBI models.

References

1. Yang, Y.B., Chang, K.C.: Extracting the bridge frequencies indirectly from a passing vehicle: parametric study. Eng. Struct. **31**(10), 2448–2459 (2009)
2. Shi, Z., Uddin, N.: Extracting multiple bridge frequencies from test vehicle - a theoretical study. J. Sound Vibrat. **490**, 115735 (2021)
3. Yang, Y.B., Lin, C.W.: Vehicle-bridge interaction dynamics and potential applications. J. Sound Vibrat. **284**(1), 205–226 (2005)
4. Malekjafarian, A., McGetrick, P.J., OBrien, E.J.: A review of indirect bridge monitoring using passing vehicles. Shock Vibrat. **2015**, 1–16 (2015)
5. Yang, Y.-B., Lin, C.W., Yau, J.D.: Extracting bridge frequencies from the dynamic response of a passing vehicle. J. Sound Vibrat. **272**(3–5), 471–493 (2004)
6. Yang, Y.B., Xiong, F., Wang, Z.L., Xu, H.: Extraction of bridge frequencies inclusive of the higher modes by the esmd using the contact-point response. Int. J. Struct. Stabil. Dyn. **20**(04), 2050045 (2020)
7. Shi, Z., Uddin, N.: Theoretical vehicle bridge interaction model for bridges with non-simply supported boundary conditions. Eng. Struct. **232**, 111839 (2021)
8. Nagayama, T., Reksowardojo, A.P., Su, D., Mizutani, T.: Bridge natural frequency estimation by extracting the common vibration component from the responses of two vehicles. Eng. Struct. **150**, 821–829 (2017)
9. Malekjafarian, A., OBrien, E.J.: On the use of a passing vehicle for the estimation of bridge mode shapes. J. Sound Vibrat. **397**, 77–91 (2017)
10. Jian, X., Xia, Y., Sun, L.: An indirect method for bridge mode shapes identification based on wavelet analysis. Struct. Control Health Monitor. **27**(12), e2630 (2020)
11. He, W.-Y., He, J., Ren, W.-X.: Damage localization of beam structures using mode shape extracted from moving vehicle response. Measurement **121**, 276–285 (2018)
12. Yang, Y.B., Shi, K., Wang, Z.L., Xu, H., Zhang, B., Wu, Y.T.: Using a single-DOF test vehicle to simultaneously retrieve the first few frequencies and damping ratios of the bridge. Int. J. Struct. Stabil. Dyn. **21**(08), 2150108 (2021)
13. Yang, Y.B., Zhang, B., Chen, Y., Qian, Y., Wu, Y.: Bridge damping identification by vehicle scanning method. Eng. Struct. **183**, 637–645 (2019)
14. Yang, Y.B., Li, Y.C., Chang, K.C.: Effect of road surface roughness on the response of a moving vehicle for identification of bridge frequencies. Int. Multiscale Mech. **5**(4), 347–368 (2012)
15. Eshkevari, S.S., Matarazzo, T.J., Pakzad, S.N.: Bridge modal identification using acceleration measurements within moving vehicles. Mech. Syst. Signal Process. **141**, 106733 (2020)
16. Keenahan, J., OBrien, E.J., McGetrick, P.J., Gonzalez, A.: The use of a dynamic truck–trailer drive-by system to monitor bridge damping. Struct. Health Monitor. **13**(2), 143–157 (2014)
17. ISO-8608. Mechanical Vibration, Road Surface Profiles, Reporting of Measured Data. ISO (2016)
18. Abuodeh, O., Redmond, L.: A framework for developing efficient vehicle-bridge interaction models within a commercial finite element software. In: Dynamics of Civil Structures, vol. 2, pp. 67–73. Springer International Publishing, Berlin (2023)
19. Yang, Y.B., Xu, H., Mo, X.Q., Wang, Z.L., Wu, Y.T.: An effective procedure for extracting the first few bridge frequencies from a test vehicle. Acta Mechanica **232**(3), 1227–1251 (2021)
20. Zhang, L., Zhao, H., OBrien, E. J., Shao, X., Tan, C.: The influence of vehicle–tire contact force area on vehicle–bridge dynamic interaction. Canadian J. Civil Eng. **43**(8), 769–772 (2016)

21. Van Rossum, G., Drake, F.L.: Python 3 Reference Manual. CreateSpace, Scotts Valley (2009)
22. Carvalho, V.R., Moraes, M.F.D., Braga, A.P., Mendes, E.M.A.M.: Evaluating five different adaptive decomposition methods for EEG signal seizure detection and classification. Biomed. Signal Process. Control **62**, 102073 (2020)
23. Pasca, D.P., Aloisio, A., Rosso, M.M., Sotiropoulos, S.: PyOMA and PyOMA_GUI: A Python module and software for operational modal analysis. SoftwareX **20**, 101216 (2022)
24. Dragomiretskiy, K., Zosso, D.: Variational mode decomposition. IEEE Trans. Signal Process. **62**(3), 531–544 (2014)
25. Brincker, R., Zhang, L., Andersen, P.: Modal identification of output-only systems using frequency domain decomposition. Smart Mat. Struct. **10**(3), 441–445 (2001)
26. Control systems library for Python. http://github.com/python-control/python-control (2017)
27. Heißing, B., Ersoy, M.: Chassis Handbook Fundamentals, Driving Dynamics, Components, Mechatronics, Perspectives. Vieweg+Teubner Verlag, Berlin (2011)
28. Xu, H., Huang, C.C., Wang, Z.L., Shi, K., Wu, Y.T., Yang, Y.B.: Damped test vehicle for scanning bridge frequencies: theory, simulation and experiment. J. Sound Vibrat. **506**, 116155 (2021)
29. AASHTO LRFD Bridge Design Specifications. American Association of State Highway and Transportation Officials (2017)
30. Sw777rfx wireless professional scale system.
31. HF sensors: Optical laser height-sensors.
32. Smith, M.: ABAQUS/Standard User's Manual, Version 6.14. Dassault Systèmes Simulia Corp, United States (2020)
33. Jornsen, R.: The Automotive Chassis. Arnold, London (1998)
34. Virtanen, P., Gommers, R., Oliphant, T.E., Haberland, M., Reddy, T., Cournapeau, D., Burovski, E., Peterson, P., Weckesser, W., Bright, J., van der Walt, S.J., Brett, M., Wilson, J., Jarrod Millman, K., Mayorov, N., Nelson, A.R.J., Jones, E., Kern, R., Larson, E., Carey, C.J., Polat, İ., Feng, Y., Moore, E.W., VanderPlas, J., Laxalde, D., Perktold, J., Cimrman, R., Henriksen, I., Quintero, E.A., Harris, C.R., Archibald, A.M., Ribeiro, A.H., Pedregosa, F., van Mulbregt, P.: SciPy 1.0 Contributors. SciPy 1.0: fundamental algorithms for scientific computing in Python. Nat. Methods **17**, 261–272 (2020)
35. Wang, Z., He, G., Du, W., Zhou, J., Han, X., Wang, J., He, H., Guo, X., Wang, J., Kou, Y.: Application of parameter optimized variational mode decomposition method in fault diagnosis of gearbox. IEEE Access **7**, 44871–44882 (2019)
36. Welch, P.: The use of fast Fourier transform for the estimation of power spectra: a method based on time averaging over short, modified periodograms. IEEE Trans. Audio Electroacoust. **15**(2), 70–73 (1967)
37. Garcia-Pozuelo, D., Gauchia, A., Olmeda, E., Diaz, V.: Bump modeling and vehicle vertical dynamics prediction. Adv. Mech. Eng. **6**, 736576 (2014)

Chapter 6
A Very Efficient Method to Estimate Statistics in the Spectral Domain: Application to the Aero- and Hydro-Elastic Responses of a Floating Bridge

M. Geuzaine, J. Heremans, Ole Øiseth, and V. Denoël

Abstract This chapter presents a very efficient method to perform the spectral analysis of structures subjected to both wind and wave loadings at second order. It hinges on a framework called the Multiple Timescale Spectral Analysis, which generalizes the Background/Resonant decomposition. It offers therefore a quick way to estimate the variances and the covariances of modal responses, with a small but controllable discrepancy. This method also helps to better understand the behavior of the structure at stake as it shows how the statistics of the modal responses are distributed between the background, the resonant and the inertial regimes.

Keywords Variance · Correlation · Multiple timescale spectral analysis · Aeroelasticity · Hydroelasticity

6.1 Introduction

To cross wide and deep straits, long-span bridges usually rest on floating supports, but traditional analysis methods struggle to evaluate their extreme responses in a reasonable amount of time because the timescales associated with their free oscillations are most often quite different from those of the loading processes.

In time domain, for instance, these extreme values rely on the statistical treatment of response signals which thus need to be simulated long enough to capture the slow dynamics of the surge motions and the wind loads, but with a sufficiently short time step to see the fast variations in the heave and pitch motions, as well as in the wave loads [1]. Moreover, fluid-structure interactions typically result in frequency-dependent mass, stiffness, and damping matrices which are difficult to handle, unless in the frequency domain [2].

Yet, even there, the computational demand remains high because the extreme values are then based on the variances of the responses which are obtained by integrating their power spectral densities, but these integrands usually feature sharp peaks due to the separation of timescales mentioned above. Their numerical integration hence requires using many points, at which intensive tasks are also to be performed [3]. Alternatively, acknowledging the existence of sharp peaks in these integrands historically allowed to formalize the Multiple Timescale Spectral Analysis method and to derive analytical formulas for their integrals which helped to drastically reduce the number of heavy operations to be executed [4].

Since they were able to deal with the slow loading of the buffeting winds only [5, 6], they have recently been developed to consider the fast loading of the waves as well, for which the lower modes respond in their inertial regime, and the higher modes respond in their background regime as all modes before, while a matching between these two limit cases is ensured for the intermediate modes [7]. They have then been extended to cope with the frequency-dependency of the properties and the nonclassicality of the damping which come from the aero- and hydro-elastic effects [8].

These expressions are used in the proposed communication, and the results obtained for the responses of an actual floating pontoon bridge to wind and wave loads are compared to the outcomes given by the numerical integration of the power spectral densities. They are shown to be quite accurate and to provide a clear understanding of how the structure behaves. Overall, and more importantly, the computational time is also divided by 100 when using these formulas instead of integrating the power spectral densities in a numerical way [8].

M. Geuzaine (✉) · J. Heremans · V. Denoël
Structural and Stochastic Dynamics, University of Liège, Liege, Belgium

O. Øiseth
Structural Engineering Department, NTNU Trondheim, Trondheim, Norway

H. Y. Noh et al. (eds.), *Dynamics of Civil Structures, Volume 2*, Conference Proceedings of the Society for Experimental Mechanics Series, https://doi.org/10.1007/978-3-031-36663-5_6

6.2 Background

The dynamics of a linear structure with N degrees-of-freedom subjected to aero- and hydro-elastic forces is governed by a set of N second order differential equations, whose side-by-side Fourier transforms is given by

$$\left[-\omega^2\boldsymbol{M}\left(\omega\right)+i\omega\boldsymbol{C}\left(\omega\right)+\boldsymbol{K}\left(\omega\right)\right]\boldsymbol{x}\left(\omega\right)=\boldsymbol{f}\left(\omega\right)$$

where i is the imaginary unit, ω is the circular frequency, $\boldsymbol{x}(\omega)$ and $\boldsymbol{f}(\omega)$ are two $N \times 1$ vectors containing the frequency-domain representations of the structural displacements in every degree-of-freedom and the undisturbed loads acting on each of them, respectively. The three remaining $N \times N$ matrices – $\boldsymbol{M}(\omega)$, $\boldsymbol{C}(\omega)$, and $\boldsymbol{K}(\omega)$ – correspond to the sum of the structural, the aero- and the hydro-dynamic stiffness, damping, and mass matrices. Being related to fluid-structure interactions, they are typically based on experimental or numerical side studies and established as functions of the frequency.

The static analysis of the structure is usually performed beforehand to define a reference position for each degree-of-freedom. Hence, the fluctuating parts of the loading processes are supposed to be zero-mean. As they are deemed to be stationary as well, they are known to be completely described, in a probabilistic sense, by their power spectral densities. Once computed as in [3], they are gathered in the matrix $\boldsymbol{S_f}(\omega)$ which is then multiplied by the matrix of frequency response functions, $\boldsymbol{H_x}(\omega)$, to yield a similar matrix for the power spectral densities of the responses, $\boldsymbol{S_x}(\omega)$. Overall, it reads as follows:

$$\boldsymbol{S_x}\left(\omega\right)=\boldsymbol{H_x}\left(\omega\right)\boldsymbol{S_f}\left(\omega\right)\boldsymbol{H}_{\boldsymbol{x}}^{\dagger}\left(\omega\right)\qquad\text{where}\qquad\boldsymbol{H_x}\left(\omega\right)=\left[-\omega^2\boldsymbol{M}\left(\omega\right)+\mathrm{i}\omega\boldsymbol{C}\left(\omega\right)+\boldsymbol{K}\left(\omega\right)\right]^{-1}$$

and the superscript $(.)^{\dagger}$ stands for the conjugate transpose operation.

Given that the behavior of the structure is considered as being linear, the responses subsequently inherit the zero-mean Gaussian nature of the forces. Their probabilistic properties are therefore fully defined on the sole basis of their power spectral densities as well. In particular, the variances of the structural responses and their time derivatives correspond to the diagonal elements of the following matrices:

$$\boldsymbol{\Sigma_x}=\int_{-\infty}^{+\infty}\boldsymbol{S_x}\left(\omega\right)\mathrm{d}\omega\qquad\text{and}\qquad\boldsymbol{\Sigma_{\dot{x}}}=\int_{-\infty}^{+\infty}\omega^2\boldsymbol{S_x}\left(\omega\right)\mathrm{d}\omega$$

where the overhead dot indicates differentiation with respect to time.

These quantities are essential from a design perspective, but their determination requires to invert a matrix which can possibly be very large to compute $\boldsymbol{H_x}(\omega)$. This is a very demanding operation which additionally needs to be repeated at each integration point. On top of that, a lot of them are necessary to provide accurate results due to the existence of sharp peaks in the spectra to integrate. To avoid such problems, the structural responses are most often defined by using a limited number of modal responses. Globally, this approach also intends to decouple the equations of motion, so that they can be solved independently of one another without requiring any costly matrix inversion.

This last step is however not as trivial as it seems, for two main reasons. First, the hydrodynamic damping is in general not classical. This means that the matrix of transfer functions can only be diagonalized by using a modal state formulation of the governing equations. But second, this is only valid if the frequency-dependency of the constitutive matrices is negligible. Otherwise, as long as it remains somewhat limited, the matrix of transfer functions expressed in the modal state space is still diagonally dominant even though it is not exactly diagonal anymore. In this event, it can be expanded in series on the basis that its off-diagonal entries are small in front of the diagonal ones, to virtually decouple the set of governing equations as in [9].

Nevertheless, it is still necessary to project the power spectral densities of the loading processes into the modal state basis at all the numerous points of integration. This is actually in such circumstances that it becomes interesting to use the Multiple Timescale Spectral Analysis. Indeed, once in a decoupled setting, this method allows to reduce the number of times such a heavy operation needs to be performed by relying on semi-analytical approximate expressions for the main components of the integrals at stake.

6.3 Novelties

The Multiple Timescale Spectral Analysis has just recently been extended to handle the specificities associated with the consideration of the interactions between the fluids (air + water) and the structure: the nonclassicality of the aero- and

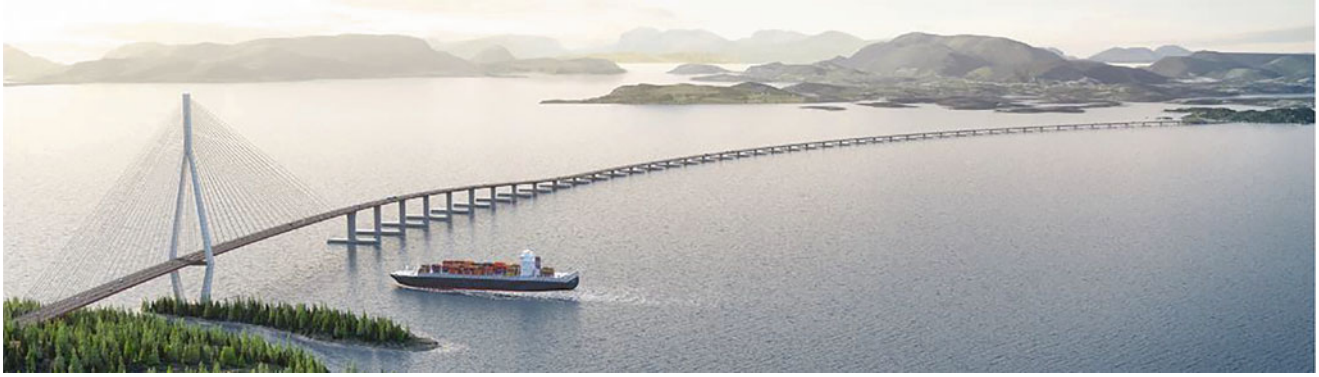

Fig. 6.1 Artistic illustration of the Bjørnafjorden Bridge. (Courtesy of the Norwegian Public Road Administration)

hydro-dynamic damping, the frequency dependent nature of the constitutive matrices, and the possibility that some modal state responses are excited at much higher frequencies than their natural one. For interested readers, details about the resulting decomposition of the modal state variances and covariances into a resonant and a loading component, which covers the background, the inertial and the intermediate regimes all at once, can be found in [8]. Meanwhile, in the proposed communication, these formulas will be used for the very first time to tackle the aero- and hydro-elastic analysis of an actual floating pontoon bridge called the Bjørnafjorden Bridge (see Fig. 6.1).

6.4 Conclusions

In all cases treated so far, this one included, the Multiple Timescale Spectral Analysis has shown remarkable accuracy in estimating the statistics of the response. This is because the method relies on clear assumptions of timescales separation and parameter smallness, which can be very simply assessed. It thus provides simple analytical solutions to capture the essential features of the response. In this paper, it has been applied to analyze the aero- and hydro-elastic responses of multi degree-of-freedom structures. Although it is currently restricted to the second-order statistics only, supplementary efforts are now being done to apply the same notions to higher-order statistics, such as the skewness and the kurtosis coefficients. These quantities are indeed necessary to account for the non-Gaussianities and the nonlinearities related to both the external excitations and the structural oscillations.

Acknowledgments The first author received a FRIA grant from the Belgian Fund for Scientific Research (F.R.S.-FNRS) which is therefore gratefully thanked. The support of two grants from the Rotary and the Walloon-Brussels Federation is also acknowledged. They have been awarded to the first author for conducting a research stay at the Norwegian University of Science and Technology.

References

1. Xu, Y., Øiseth, O., Moan, T.: Time domain simulations of wind- and wave-induced load effects on a three-span suspension bridge with two floating pylons. Mar. Struct. **58**(November 2017), 434–452 (2018)
2. Watanabe, E., Utsunomiya, T., Wang, C.M.: Hydroelastic analysis of pontoon-type VLFS: A literature survey. Eng. Struct. **26**(2), 245–256 (2004)
3. Giske, F.-I.G., Leira, B.J., Øiseth, O.: Efficient computation of cross-spectral densities in the stochastic modelling of waves and wave loads. Appl. Ocean Res. **62**, 70–88 (2017)
4. Denoël, V.: Multiple timescale spectral analysis. Probabilistic Eng. Mech. **39**, 69–86 (2015)
5. Heremans, J., Mayou, A., Denoël, V.: Background/Resonant decomposition of the stochastic torsional flutter response of an aeroelastic oscillator under buffeting loads. J. Wind Eng. Ind. Aerodyn. **208**(July), 104423 (2021)
6. Denoël, V., Carassale, L.: Response of an oscillator to a random quadratic velocity-feedback loading. J. Wind Eng. Ind. Aerodyn. **147**, 330–344 (2015)
7. Geuzaine, M., Fenerci, A., Øiseth, O., Denoël, V.: Multiple timescale spectral analysis of floating structures subjected to hydrodynamic loads, Forthcoming, J. Eng. Mech. https://doi.org/10.1061/jenmdt/emeng-6654
8. Geuzaine, M.: Multiple Timescale Spectral Analysis of Wave-Loaded Floating Structures, no. April, 2022.
9. Canor, T., Blaise, N., Denoël, V.: Efficient uncoupled stochastic analysis with non-proportional damping. J. Sound Vib. **331**(24), 5283–5291 (2012)

Chapter 7
System Identification of a Steel Arch Bridge Using Ambient Vibration Tests, Video-Motion Analysis Technique, and Modal Response Analysis

Mehrtash Motamedi and Carlos E. Ventura

Abstract This chapter describes how the modal properties of bridges can be identified by ambient vibration tests and modal analysis. For this purpose, a typical steel arch highway bridge in the Province of British Columbia, Canada, was selected and subjected to a series of ambient vibration measurements. Modal response analysis was then performed to identify the dynamic properties of the structure, including predominant natural frequencies and the corresponding mode shapes to support seismic assessment and upgrading of the bridge. The bridge was constructed in 1960 and consists of a 72.3 m long single span. The superstructure consists of three tied arches, with a steel ladder deck system comprised of transverse floor beams (located at the arch hanger points) and longitudinal stringers, supporting a cast-in-place concrete deck.

The ambient vibration testing method was implemented using sophisticated methods of modal analysis. Vibration tests were conducted at the bridge in order to determine the dynamic modal properties (modal frequencies and mode shapes) of the bridge. The testing program consisted of static tests, speed test, and ambient vibration tests including multiple measurement setups. Tromino® velocity/acceleration wireless sensors were used for these measurements which were placed on predetermined locations. The computer program ARTeMIS was used to perform the system identification of the structure. The software allows to develop a 3D model of the structure and test points; the resulting mode shapes are displayed using this geometry. Two different techniques were used for modal identification: Enhanced Frequency Domain Decomposition (EFDD), and Stochastic Subspace Identification (SSI). These two modal identification techniques were used to cross-validate the results. The joint analysis of the signals measured in various strategic points of the structure made it possible to identify the modal configurations and the corresponding natural frequencies.

As result, a total of 11 modes were identified in the 0–20 Hz range. Modal frequencies, modal damping, and mode shape were identified for each of the 11 modes. The modes associated with torsional response of the deck showed that the bridge supports are flexible. Video-motion analysis of videos obtained during the load tests were also used to estimate the vertical deformation of the arch near its center. The results were consistent with those obtained from a topographical survey during the load tests.

Keywords Ambient vibration · System identification · Modal response · Bridge · Video motion analysis

7.1 Introduction

A targeted load rating evaluation of the arches of a bridge was planned in the province of British Columbia, Canada. The purpose of the assessment was to determine whether the bridge arches have sufficient capacity to support highway live loading and, if required, quantify the extent of strengthening works required to increase the capacity of the bridge. A series of ambient vibration test (AVT) were conducted at this bridge in order to determine the modal frequencies and the mode shapes of the bridge. Prior to the AVTs, a site visit to the bridge was conducted to determine the location of the measurements and develop a test plan. The test plan included ambient vibration measurements on the bridge deck, abutments, and approaches, as well as deck vibration measurements during the planned static load tests. A series of vibration tests were then carried out using acceleration and velocity sensors on the bridge. The main purpose of the AVTs was to determine the fundamental frequency and corresponding mode shape of the bridge. This information would help calibrate the computer model being

---

M. Motamedi (✉) · C. E. Ventura
Department of Civil Engineering, University of British Columbia, Vancouver, BC, Canada
e-mail: mmotamedi@civil.ubc.ca

H. Y. Noh et al. (eds.), *Dynamics of Civil Structures, Volume 2*, Conference Proceedings of the Society
for Experimental Mechanics Series, https://doi.org/10.1007/978-3-031-36663-5_7

used for the load assessment evaluation of the bridge. A secondary purpose was to determine deflections of the center the arch of the bridge due to static load tests using video motion analysis techniques.

7.2 Description of the Bridge

The selected bridge for this study was constructed in 1960 and consists of a 72.3 m long single span. The superstructure consists of three tied arches, with a steel ladder deck system comprised of transverse floor beams (located at the arch hanger points) and longitudinal stringers, supporting a cast-in-place concrete deck. Since construction, the bridge has received several minor renewal treatments, including a concrete overlay, seismic retrofit and, most recently, localized structural repairs and recoating [1]. Figure 7.1 shows a satellite view of the bridge and the view of the bridge from west side. Figure 7.2 presents plan, elevation, and cross section views of the bridge.

(a) (b)

Fig. 7.1 (**a**) Satellite view of the bridge (Google Map), (**b**) View of the bridge (looking east)

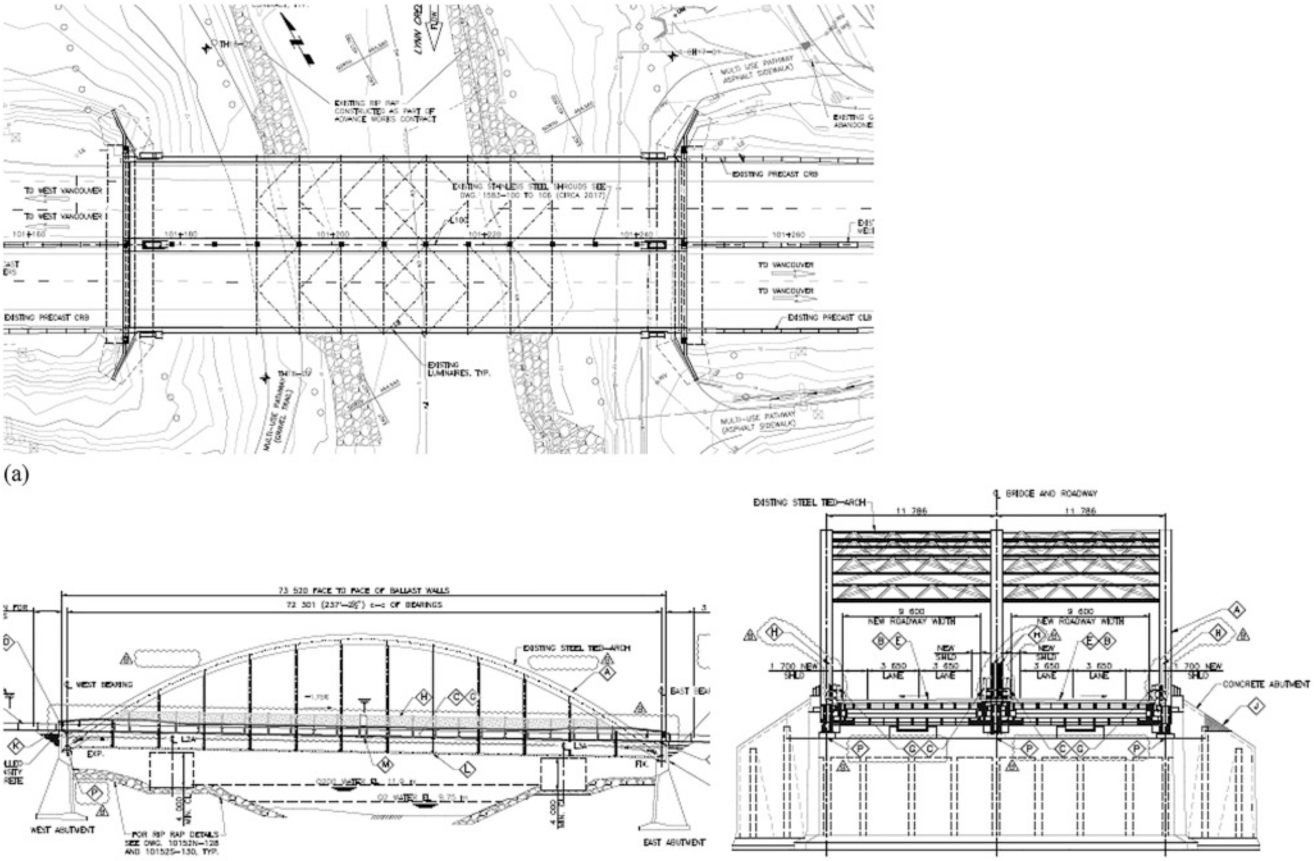

(a)

(b)

(c)

Fig. 7.2 Sectional views of the bridge: (**a**) plan view; (**b**) south elevation; and (**c**) cross-section of the bridge [1]

7.3 Description of Ambient Vibration Tests

Vibration Tests (VTs) were conducted at the bridge in order to determine the dynamic modal properties (modal frequencies and mode shapes) of the bridge. The testing program consisted of static tests, speed test, and ambient vibration tests, including 16 measurement setups, as described below. Tromino® velocity/acceleration sensors were used to carry out these VTs. The collected records were time synchronized with a radio antenna and amplifier in each sensor. This allowed the synchronization of the recordings both within each measurement setup and between setups. The Tromino sensors are suitable for high-resolution ambient vibration tests as they are fully portable, wireless, compact, and light instruments. Each sensor is equipped with two sets of three orthogonal high-resolution electrodynamics sensors (high gain and low gain velocity meter) and one set of three orthogonal digital accelerometers with a frequency range of 0.1 to 300 Hz. For these tests the high-gain velocity data was used for the modal identification process [2].

7.4 Static Tests

The static tests consisted of several synchronized vibration measurements of the deck of the bridge when it was subjected to weight of two trucks: Truck 1: half-loaded (20,800 Kg); and Truck 2: fully loaded (27,400 Kg). The trucks were located in different predetermined locations with various arrangements on the deck and stopped for 16 min. The vibration of the deck was then measured in each arrangement using 9 Tromino sensors. The static tests consisted of six measurement setups each 16 min duration. Table 7.1 describes the test setups performed with their unique trucks pattern. The frequency of the recordings at each setup was 128 samples per second (sps), and the total recording duration for each setup was 16 min. This testing approach allows to capture the most important vibration modes up to a frequency of about 64 Hz. The longitudinal component (or north component) of each sensor was oriented parallel to the longitudinal axis of the deck.

Figure 7.3 shows the layout of the sensors located on the deck in static tests. Figure 7.4 illustrates the location of the sensors and trucks' position on the deck in all test setups.

Table 7.1 Static tests information

Setup #	No. of sensors in use	Truck 1 (half-loaded) position	Truck 2 (fully loaded) position
Setup 1	9	Position #1	Not used
Setup 2	9	Position #2	Not used
Setup 3	9	Not used	Position #1
Setup 4	9	Not used	Position #2
Setup 5	9	Position #4	Position #3
Setup 6	9	Position #6	Position #5

Truck position numbers are shown in Fig. 7.3

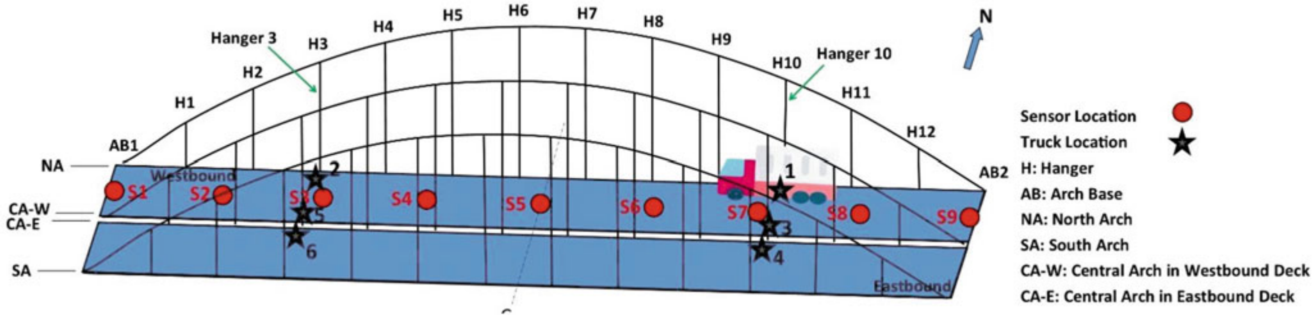

Fig. 7.3 Sensors' layout at top of the deck for static tests (The truck is shown schematically in the position #1)

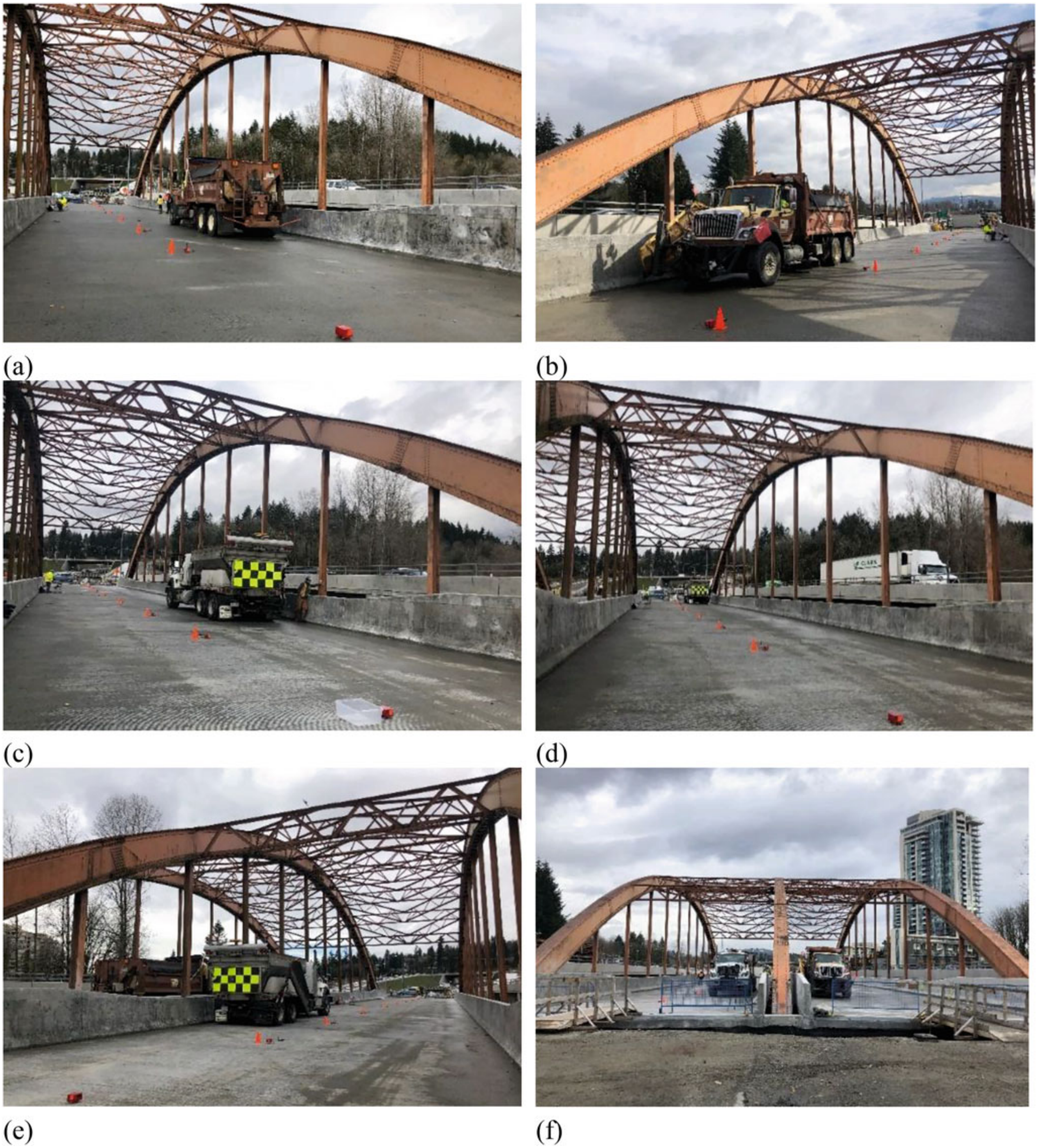

Fig. 7.4 Location of sensors and trucks' position on the deck in static tests: (**a**) half-loaded truck at Hanger #10 (Setup 1); (**b**) half-loaded truck at Hanger #3 (Setup 2); (**c**) fully loaded truck at Hanger #10 (Setup 3); (**d**) fully loaded truck at Hanger #3 (Setup 4); (**e**) two trucks at Hanger #10 (Setup 5); and (**f**) two trucks at Hanger #3 (Setup 6)

7.5 Speed Test

The speed test consisted of a synchronized measurement of decks vibration with 12 min duration while the Truck 2 (fully loaded with sand) was traveling along the westbound deck at about 40 km/h forward and 10 km/h backward for seven passes. Table 7.2 presents the speed test details. Figure 7.5 shows the weight and geometry of the trucks' axles used for the static and speed tests. Figures 7.6 and 7.7 illustrate the sensors' layout for the speed test and the location of sensors on top of the decks, respectively.

A total of nine sensors were used in this test setup. The frequency of the recordings was 128 samples per second (sps), and the total recording duration was 12 min.

Table 7.2 Speed tests' information

Setup #	No. of sensors in use	Truck 1 (half-loaded) position	Truck 2 (fully loaded) position
Setup 1	9	Not used	Drown in back and forth at center point of westbound deck

Fig. 7.5 Weight and geometry of the trucks' axles used for the static and speed tests [1]

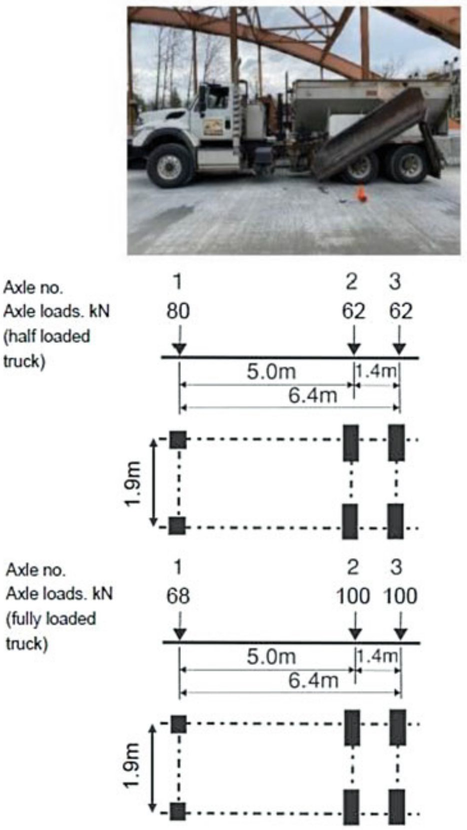

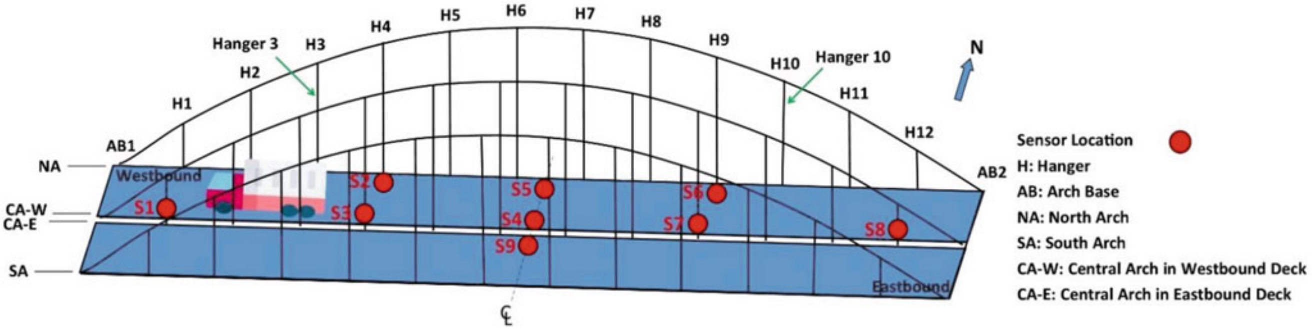

Fig. 7.6 Sensors' layout on top of the deck for speed test (The truck is shown schematically while crossing the bridge)

(a) (b)

Fig. 7.7 Location of sensors in speed test: (**a**) fully loaded truck prior to testing and (**b**) fully loaded truck while crossing the bridge

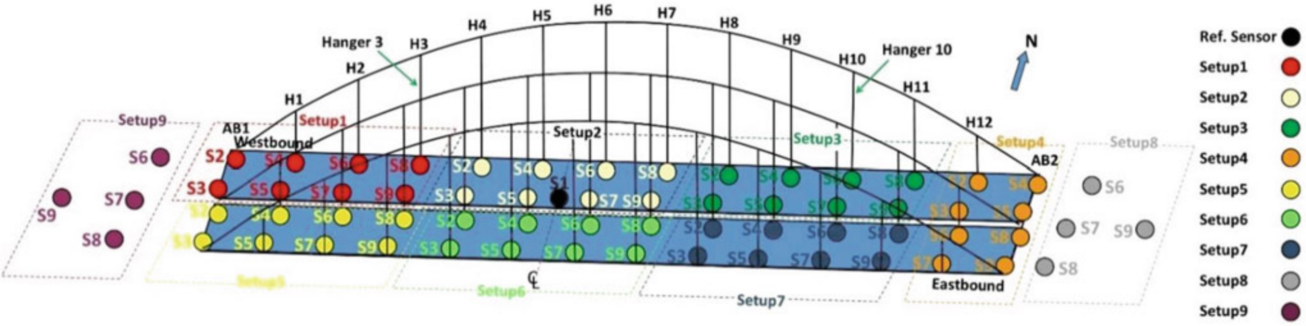

Fig. 7.8 Sensors' layout on top of the deck and embankments for ambient vibration tests (Sensors located on the abutments are not shown – Refer to Fig. 7.10 to see the sensors in Setups 8 and 9)

(a) (b)

Fig. 7.9 Location of sensors on the deck in ambient vibration tests: (**a**) Setup 1 and (**b**) Setup 3

7.6 Ambient Vibration Tests

Ambient vibration tests consisted of nine measurement setups each including 9 sensors. Figure 7.8 shows the layout of the measurement setups and sensor locations. One stationary reference sensor (S1) was used for all setups and located at the center line of the bridge. Setups 1 to 7 were performed on the decks while Setups 8 and 9 were conducted on the bridge abutments and the embankments. Figure 7.9 shows the view of the deck during Setup 1 and 3 of the AVTs. Figure 7.10 shows the Sensors' layout on the abutments and embankments. Location of the sensors in Setup 8 and 9 can be seen in Fig. 7.11. The frequency of the recordings at each setup was 128 samples per second (sps), and the total recording duration for each setup was 26 min. This testing approach allows to capture the most important vibration modes up to a frequency of about 64 Hz. The longitudinal component (or north component) of each sensor was oriented parallel to longitudinal direction of the bridge.

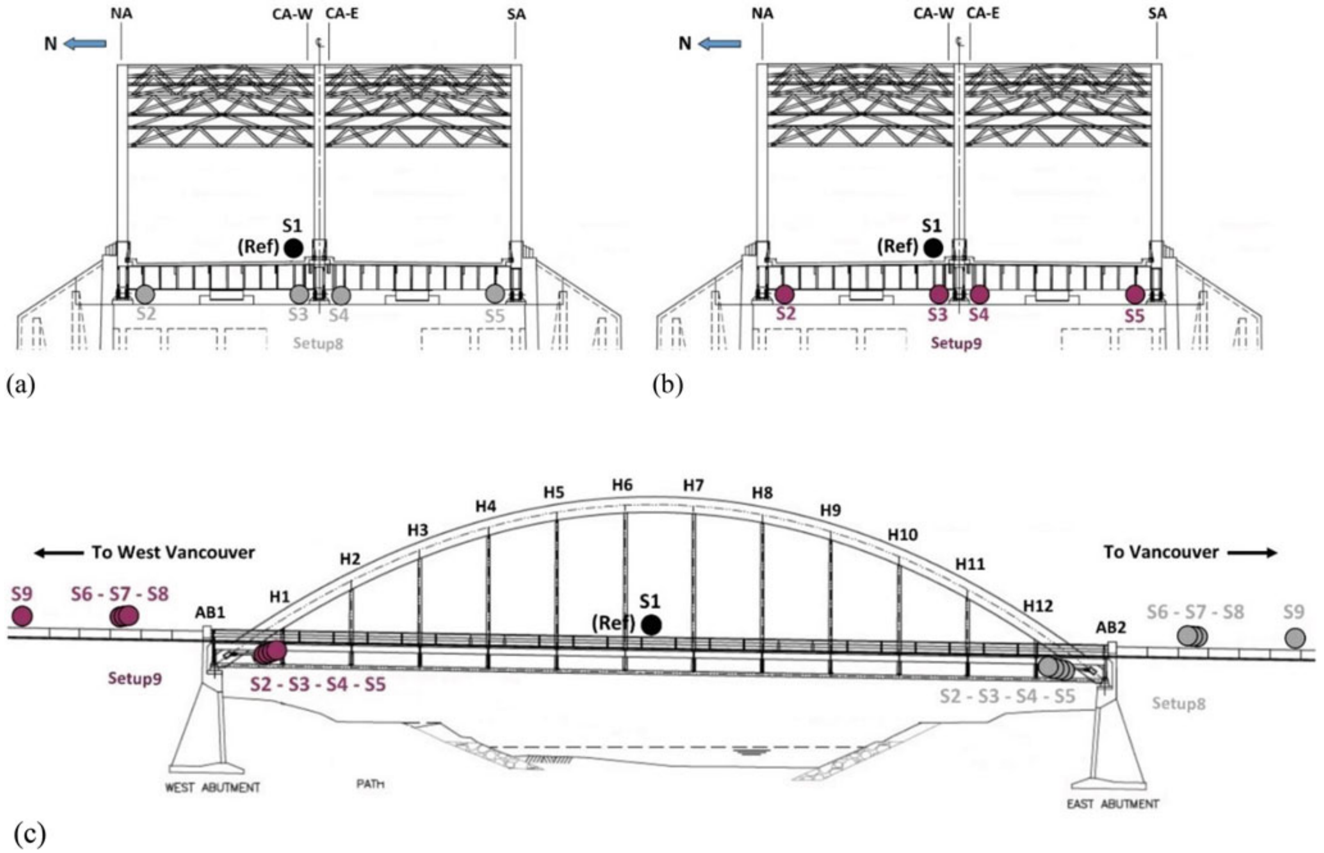

(a) (b) (c)

Fig. 7.10 Sensors' layout on the abutments and embankments: (**a**) Setup 8 at east side of the bridge (the sensors located on the embankments are not shown); (**b**) Setup 9 at west side of the bridge (the sensors located on the embankments are not shown); (**c**) Setups 8 and 9 shown in longitudinal section of the bridge

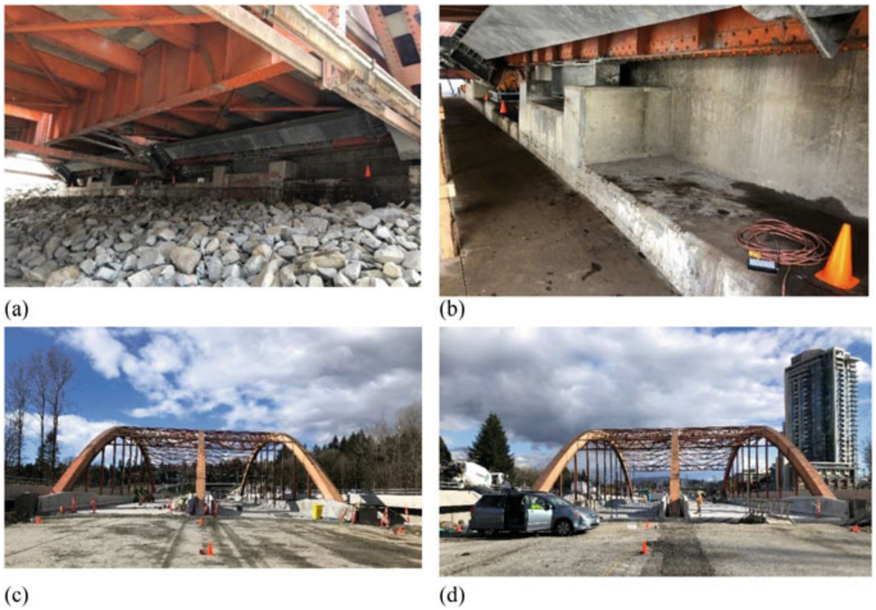

(a) (b) (c) (d)

Fig. 7.11 Location of sensors on the bridge abutments and embankments: (**a**) sensors on abutment at east side (Setup 8); (**b**) sensors on abutment at west side (Setup 9); (**c**) sensors on embankment at east side (Setup 8); and (**d**) sensors on embankment at west side (Setup 9)

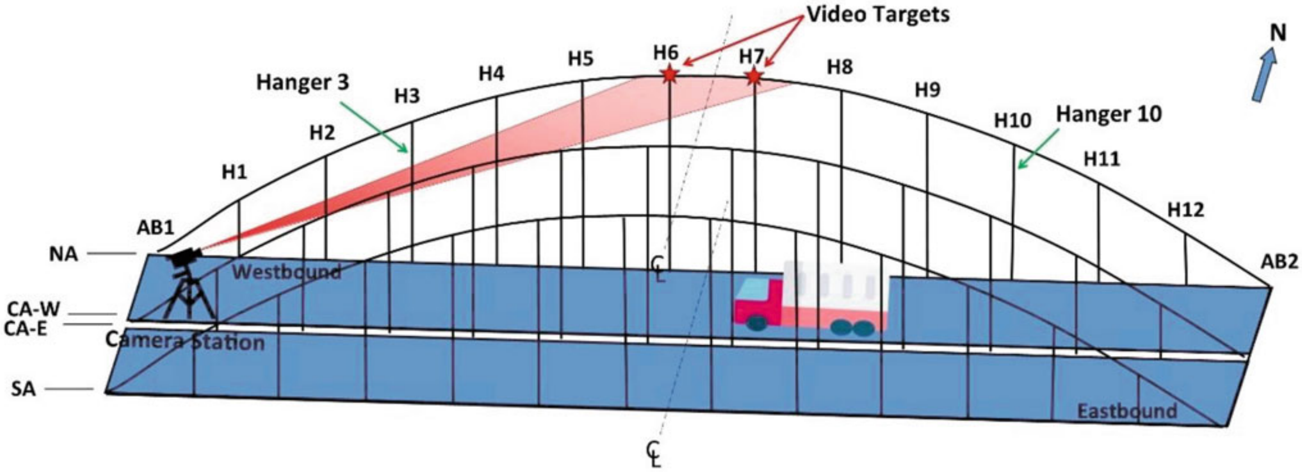

Fig. 7.12 Location of video camera on the deck for measuring the vertical movements of the arches

A high-resolution video camera (Sony Handycam) was used to determine vertical displacements of Hanger 6 and 7 in the middle of the bridge (North Arch) during static and speed tests. Video-motion analysis techniques (using ProAnalyst software) were employed for this purpose. Each video was divided to several frames, and the software captured any movements of the selected points for each frame. Figure 7.12 shows the location of the camera, and the video targets at the top of the North Arch (at the location of Hangers 6 and 7).

7.7 Methodology and Data Processing

The computer program ARTeMIS version 4 [3] was used to perform the modal identification of the bridge. The software allows the user to develop a 3D model of the structure and test points; the resulting mode shapes are displayed using this geometry. Two different, complementary techniques are usually used for modal identification [4]: the Enhanced Frequency Domain Decomposition (EFDD) and the Stochastic Subspace Identification (SSI). These two modal identification techniques are used to cross-validate the results. The joint analysis of the signals measured in various strategic points of the structure makes it possible to identify the modal configurations and the corresponding natural frequencies.

The EFDD technique is an enhanced frequency domain method, and the procedure consists of decomposing the system output into a set of systems of a specific degree of freedom, which are independent for each mode. The singular values are estimated from the spectral density of the specific degree of freedom system, and the configuration of the modes is estimated from the singular vectors by selecting the highest peaks of the responses.

The SSI technique is a time domain method which consists of adjusting a parametric model to the time series recorded by the sensors. SSI method takes a matrix of the time history data and performs a series of geometric manipulations, which results in a set of mathematical models that represent the system that produces the data; the analysis provides modes based on those models. The advantage of the SSI is more accurate modal estimations, especially in the lower frequencies when the data is properly decimated. The disadvantage is that the SSI method takes a considerable amount of time for analysis and is not easily applied to broadband data. In contrast, the FDD method is very quick and allows for the user to pick modes anywhere in the frequency range of interest [5].

Ambient vibration data recorded on and off the bridge contains both noise and the response of the bridge under ambient vibrations. The noise component of the recorded data is mainly due to mechanical imperfections in the sensors, instrument noise, installation, and other aspects in the sensor such as digitalization. The noise components of the vibration data, by its nature, usually appear as a random phenomenon in the data; however, the response of the bridge is not random but consistent at certain frequencies due to resonance effects of the bridge to environmental excitations. Removing the noise components from the data is generally achieved by using signal processing tools such as decimation, filtering, and data averaging.

The data collected at all measurement locations on the bridge was processed and analyzed with ARTeMIS Modal. A 3D model (for animation purposes only) of the bridge was created using the structural geometry provided by the owner [1]. The model includes the discretized locations of 73 measurement points as seen in Fig. 7.13. The blue arrows represent the

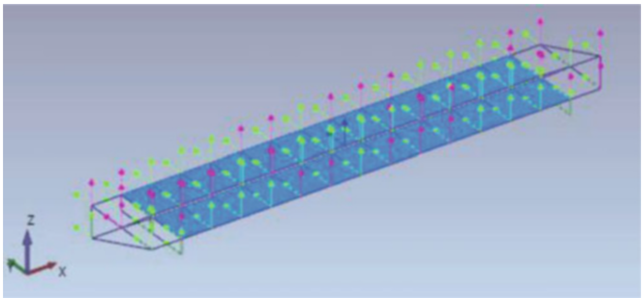

Fig. 7.13 3D ARTeMIS model showing the locations of the measurement points on the bridge

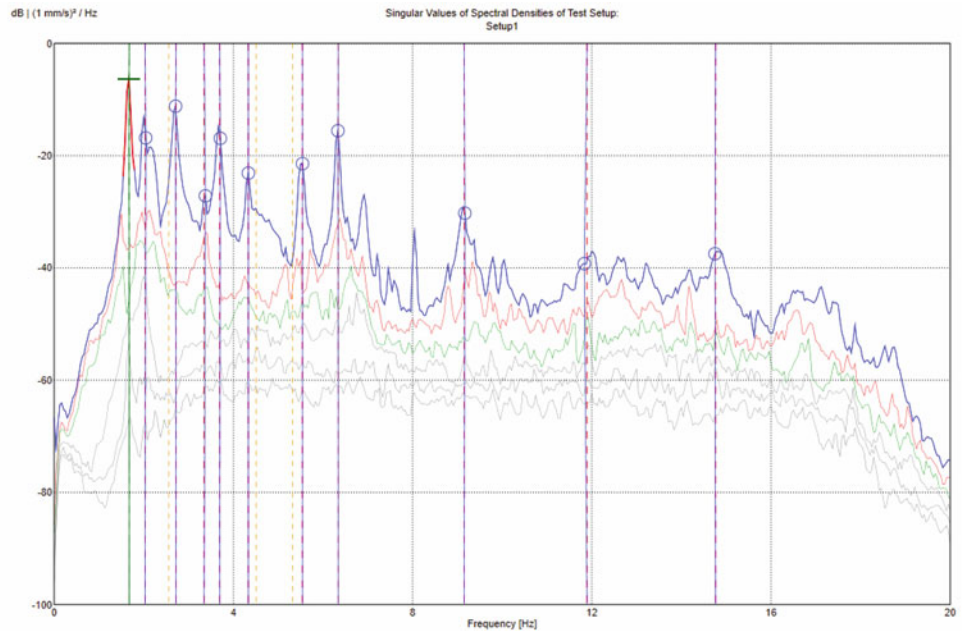

Fig. 7.14 Singular values of spectral densities of all test setups in the frequency range of 0 to 20 Hz using EFDD

location and orientation of the reference sensor for setups 1 to 9, while the green and pink arrows represent the location and orientation of the roving sensors. The estimation of the mode shapes requires that all the readings from each setup are fully synchronized. This is a critical step that will ensure a reliable estimation of each mode shape.

7.8 Test Results

The results of the analysis using the Enhanced Frequency Domain Decomposition method (EFDD) are shown in Fig. 7.14. This figure shows a plot of the spectral density of the peak singular values of all the data from setups 1 to 9 as a function of frequency. The peak values in this plot can be associated to dominant frequencies in the datasets, and some of these correspond to modal frequencies. The results of the analysis of the data using the SSI method can be used to determine with greater certainty the most dominant frequencies in the dataset. Figure 7.15 shows the Stabilization Diagram of all the data from setup 1 as an illustrative example of this verification process. The vertical red dotted lines indicate the frequencies at which the modal frequencies are stable and can be associated to natural modes of the structure. By combining the results from both methods, it is possible to determine what of the peaks in Fig. 7.14 are associated to modal frequencies of the bridge [3].

Based on this analysis, the predominant frequency (the first natural frequency) of the structure is estimated to be 1. 68 Hz, and it corresponds to the fundamental mode of the bridge in the vertical direction. The second modal frequency is at 2.03 Hz, and it corresponds to torsional mode of the deck. A total of 11 modal frequencies in the 0 to 20 Hz range were identified

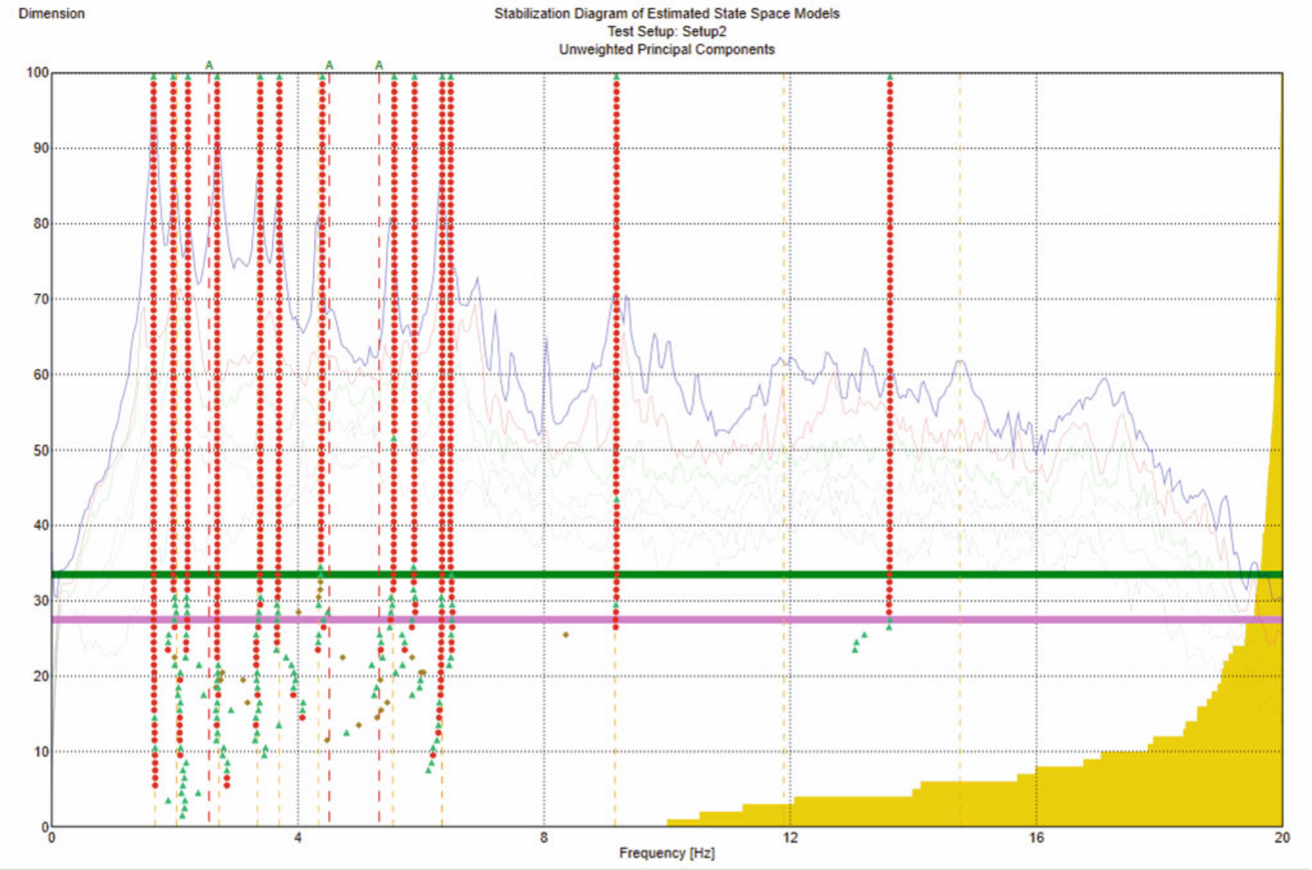

Fig. 7.15 Stabilization diagram of estimated state space models from all the data in setup 2. This plot is for the unweighted principal components (UPC)- merged test setups in the frequency range of 0 to 20 Hz

Table 7.3 Modal frequencies and damping obtained from modal analysis estimated by EFDD method (Hz)

Mode no.	Frequency (Hz)	Damping (%)
1	1.677	1.7
2	2.031	1.7
3	2.719	1.3
4	3.346	0.9
5	3.695	1.1
6	4.333	0.0
7	5.542	0.0
8	6.341	0.5
9	9.153	0.9
10	11.895	0.9
11	14.763	0.6

with confidence. The identified modal frequencies and associated damping values are presented in Table 7.3. The presented modal frequencies from the vibration data are those for which the confidence on the results is high from both the EFDD and SSI-UPC methods. The associated mode shapes are presented in Fig. 7.16.

The mode shapes associated with torsional modes of the deck clearly show that the supports of the bridge also move. This fact should be taken into consideration for the calibration of the computer model of the bridge. Different modal identification techniques were used to identify the modes of the bridge. The results were cross-validated in terms of frequencies and mode shapes.

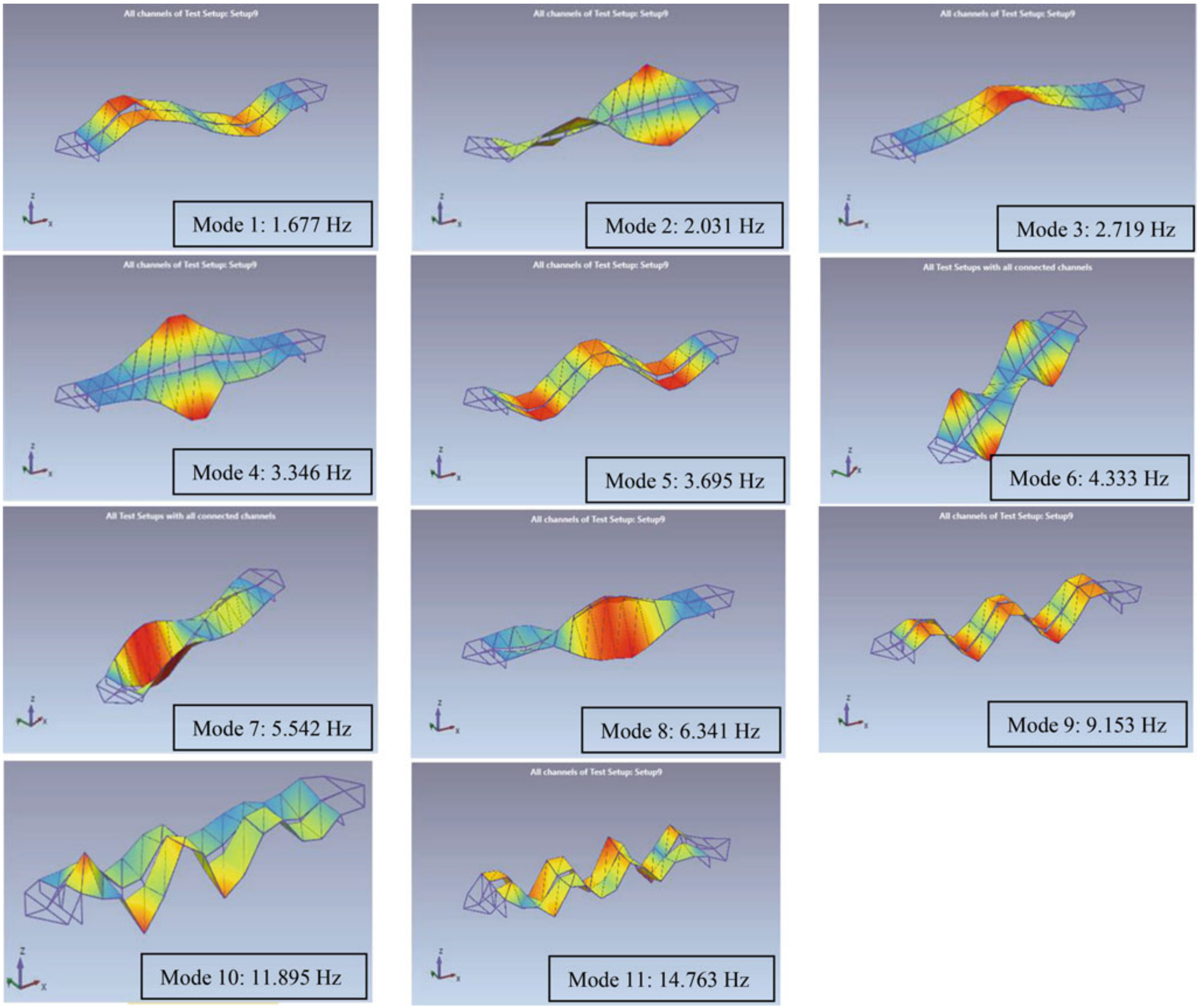

Fig. 7.16 Identified mode shapes of the bridge

7.9 Comparison of Ambient Vibration Test, Load Tests, and Speed Tests Results

In order to identify the variability of the estimated modal frequencies caused by the presence of the trucks used for the static and speed tests, the modal frequencies and damping were estimated using the data from each load test using the same procedures described above. Table 7.4 presents a comparison of the estimated frequencies for the 11 modes identified from the ambient vibration data with those from the load tests.

From the results presented in this table, it can be seen that the additional mass provided by the trucks results in a lowering of the estimated frequency values. This is expected as the added mass will cause a reduction of the frequencies.

7.10 Conclusion

Ambient vibration tests of a bridge in British Columbia, Canada, were conducted. The main objectives of these vibration tests were: (1) to determine the vibration characteristics of the bridge and (2) to perform a modal analysis using the vibration data in order to determine the predominant natural frequency and the corresponding mode shapes of the bridge. The testing program consisted of static tests, speed test, and ambient vibration tests including 16 measurement setups. The results from

Table 7.4 Comparison of modal frequencies identified from ambient-speed and static load tests

Mode no.	Ambient test (Hz)	Speed test (Hz)	Static test 1 (Hz)	Static test 2 (Hz)	Static test 3 (Hz)	Static test 4 (Hz)	Static test 5 (Hz)	Static test 6 (Hz)
1	1.677	1.583	1.642	1.681	1.628	1.650	1.565	1.610
2	2.031	1.966	2.137	2.023	1.970	1.982	2.010	2.006
3	2.719	2.150	2.656	2.595	2.142	2.748	2.162	2.771
4	3.346	2.669	3.050	3.121	3.298	3.443	3.418	3.408
5	3.695	3.510	3.559	3.604	3.660	3.765	4.473	3.675
6	4.333	4.283	4.574	4.573	4.565	4.449	5.483	4.373
7	5.542	5.487	5.537	5.330	5.491	NI	6.195	5.523
8	6.341	6.268	6.886	6.843	6.396	6.325	6.518	6.372
9	9.153	9.042	9.305	9.340	9.262	9.784	9.421	9.146
10	11.895	12.971	12.241	12.376	12.426	12.591	12.320	12.585
11	14.763	14.631	NI	14.810	14.797	14.781	14.672	14.781

the modal analyses indicated that the fundamental frequency of the bridge in the vertical direction 1.677 Hz. The first torsional mode of the deck is at 2.031 Hz. A total of 11 modes were identified in the 0 to 20 Hz range. Modal frequencies, modal damping and mode shape were identified for each of the 11 modes. The modes associated with torsional response of the deck showed that the bride supports are flexible. Video-motion analysis of videos obtained during the load tests were used to estimate the vertical deformation of the arch near its center. The results were consistent with those obtained from a topographical survey during the load tests.

Acknowledgments This chapter has been extracted from a report prepared by VC Structural Dynamics Ltd. for Miller Capilano Maintenance Corporation and McElhanney Consulting Services Ltd. for the purpose of determining the modal properties of the Lynn Creek Bridge in North Vancouver, BC, as part of a load rating evaluation of the bridge. This collaboration is acknowledged.

References

1. McElhanney. 01583 Lynn Creek Bridge TransCanada Highway 1 Live Load Rating Report, McElhanney Consulting Services Executive Summary, March 2018
2. Micromed: Tromino: Portable Ultra-Light Acquisition System for Seismic Noise and Vibration- User's Manual. Macromed, Italy (2012)
3. Structural Vibration Solutions, A/S, ARTeMIS Modal Software, Version 4, Copyright 1998–2014
4. Brincker, R., Ventura, C.E.: Introduction to Operational Modal Analysis, 1st edn. John Wiley & Sons, United Kingdom (2015)
5. Peeters, B.: System Identification and Damage Detection in Civil Engineering, Ph.D. Thesis, Katholieke University of Leuven, Belgium (2000)

Chapter 8
Structure-Agnostic Gait Cycle Segmentation for In-Home Gait Health Monitoring Through Footstep-Induced Structural Vibrations

Yiwen Dong and Hae Young Noh

Abstract This chapter aims to characterize the structural vibrations induced by footsteps to segment a sequence of gait patterns into critical gait phases (including stance phase and swing phase) for in-home gait health monitoring across various floor structures. Gait cycle segmentation is an essential step in quantitative gait assessments for early diagnosis and progressive tracking of neuroskeletal and neuromuscular disorders. Especially, in-home monitoring of peoples' gait health is beneficial for low-income families and those who have limited access to medical services. Existing studies have adopted cameras, wearable devices, and force plates/pressure mats to segment gait cycles, but they have operational requirements such as direct line-of-sight, carrying devices, and dense deployment, which are not practical for continuous monitoring at an individual's home. In this chapter, we develop a gait cycle segmentation framework through footstep-induced structural vibrations. The primary research challenges are the complex interplay of the: (1) gait phases and (2) structural properties with the vibration signals. First, gait involves a continuous sequence of multiple types of motions, making it challenging to separate them. Second, people's living spaces have distinct types of floor structures, leading to difficulty of adapting our framework to multiple structure types. To address the first challenge, we leverage the main insight that human motions at the onset of each gait phase (e.g., heel strike and toe-off) involve unique types of excitation force (e.g., impulsive vs. friction forces). These forces incur peaks at distinct frequency ranges in the responses of the structure. Therefore, we separate gait phases by analyzing the structural responses over various frequency ranges. Second, to make our framework structure-agnostic, we formulate the structural influence on the vibration signals and extract structure-dependent features to represent such influence. Overall, our framework first identifies the structure-dependent dominant frequency ranges for each structure through a time–frequency-domain analysis and extracts vibration signals within these frequency ranges. It then detects time-domain peaks within each structure-dependent frequency range to identify the onset of gait phases. We evaluate our method on two different structures in a real-world setting and achieved consistent results with only a 5% average error in detecting various gait phases.

Keywords Temporal gait parameter · Structural vibration · Time–frequency segmentation · In-home gait analysis · Scalability

8.1 Introduction

Structural vibrations induced by human footsteps contain important information about their gait health [1–7], which is critical for early diagnosis and progressive tracking of neurodegenerative and neuromuscular disorders, affecting every 1 in 6 people today [8–11]. In-home monitoring of peoples' gait health is especially beneficial for low-income families and those with limited access to medical services, saving travel costs for in-person visits in specialized clinics [12–14]. A person's walking pattern typically consists of a series of repetitive steps and stride cycles (i.e., gait cycles), which are the fundamental units to be examined during gait analysis. Segmenting a gait cycle into critical phases is essential in quantitative gait health assessments to detect and track gait disorders [15]. Existing studies have adopted various sensing systems, including cameras, wearable devices, and force plates/pressure mats to segment gait cycles [16–19]. However, they have operational requirements such as direct line-of-sight, carrying devices, and dense deployment, which are not practical for continuous monitoring at an individual's home.

Y. Dong (✉) · H. Y. Noh
Department of Civil and Environmental Engineering, Stanford University, California, CA, USA
e-mail: ywdong@stanford.edu; noh@stanford.edu

H. Y. Noh et al. (eds.), *Dynamics of Civil Structures, Volume 2*, Conference Proceedings of the Society
for Experimental Mechanics Series, https://doi.org/10.1007/978-3-031-36663-5_8

In this chapter, we develop a gait cycle segmentation framework that aims to segment gait cycles into critical gait phases (i.e., stance phase and swing phase) through footstep-induced structural vibrations for in-home gait health monitoring. Our approach is low-cost, wide-ranged, and only requires vibration sensors that are sparsely mounted on the floor [1, 20, 21], which is suitable for in-home usage. The main research challenges in developing this framework are the complex interplay between the: (1) gait phases and (2) structural properties with the vibration signals. First, decomposing gait cycle data into gait phases is challenging because human gait involves a continuous sequence of multiple types of motions inducing subtle floor vibrations. Second, it is difficult to adapt our framework to multiple people's homes because people's living spaces typically have distinct structural properties, resulting in unique floor vibration responses to human footsteps.

To overcome these challenges, we investigate frequency-domain characteristics of the gait phase and the structural influences on footstep-induced structural vibration. To characterize the structural vibrations with respect to various types of gait motions, we leverage the insight that the gait events (i.e., heel strike and toe-off) at the onset of each gait phase impose unique types of excitation forces (e.g., impulsive vs. friction forces) to the floor. For example, the impulsive forces typically generate surface waves (e.g., lamb wave), whereas the friction forces typically generate slip-pulse body waves (e.g., shear wave) [22–24]. These forces incur peaks at distinct frequency ranges in the responses of the structure. Therefore, by analyzing the frequency responses of the floor vibration signals, we capture these gait events to separate gait phases. To overcome the structure difference challenge, we formulate the structural influence on the vibration signals and identify structure-dependent features to make our framework structure-agnostic. In summary, when a new gait cycle is detected on this structure, our framework first identifies the structure-dependent dominant frequency ranges for each structure through a time–frequency-domain analysis. Then, it extracts the vibration signals within these dominant frequency ranges. After that, it detects time-domain peaks within each structure-dependent frequency range to identify the onset of gait phases, which allows gait cycle segmentation. We evaluate our method on two different structures in a real-world setting and achieved consistent results (with only a 5% average error) in detecting gait events and segmenting gait phases.

8.2 Physical Insights of Footstep-Induced Structural Vibration Across Different Structures

In this section, we introduce and discuss the physical insights behind footstep-induced structural vibrations across different structures from both analytical and empirical perspectives. Specifically, we: (1) characterize footstep-induced structural vibration in view of gait phases and (2) formulate the structural influence on footstep-induced structural vibration.

The overall physical intuition of using footstep-induced structural vibrations for gait health monitoring is described as follows: when a person is walking on a structure, each footstep exerts forces on the floor that generates structural vibrations containing the person's gait information. Such information includes the duration of gait phases, the location of each footstep, the left and right foot contact forces with the floor, and so on [1, 4, 25]. By analyzing these vibrations, we estimate the gait parameters and detect gait disorders, enabling structures to provide quantitative scales and references for clinical decision-making.

8.2.1 Characterizing Footstep-Induced Structural Vibration in View of Gait Phases

In this subsection, we characterize the footstep-induced structural vibration with respect to different gait events and phases in order to detect the gait events for gait cycle segmentation. Figure 8.1 illustrates how different frequency ranges in the floor vibration signals correspond to the gait events and phases.

There are various gait events and phases within a gait cycle. Existing literature suggests a gait cycle is defined as the duration between a foot strike and the subsequent foot strike of the same foot [15, 26]. A typical gait cycle consists of two primary phases: the stance phase and the swing phase. The stance phase is the time that the foot contacts the ground; the swing phase consists of the time that the foot is swinging in the air. The stance and swing phases can be separated by gait events because the onset of the stance phase is a heel strike and the onset of the swing phase is a toe-off. Within these two phases, other gait phases, such as loading response, mid/terminal swing, are also defined and studied in clinical practices [26, 27]. In this chapter, we focus on the stance and swing time because they are the fundamental metrics for gait health assessments.

From the structural vibration perspective, a gait cycle consists of two consecutive footstep impulses from the left and right foot (see the vibration signal in Fig. 8.1). This is because, after the first footstep impulse occurs, the toe-off of this foot occurs after the person alters the support foot to another, resulting in the second impulse. As described in Fig. 8.1, we

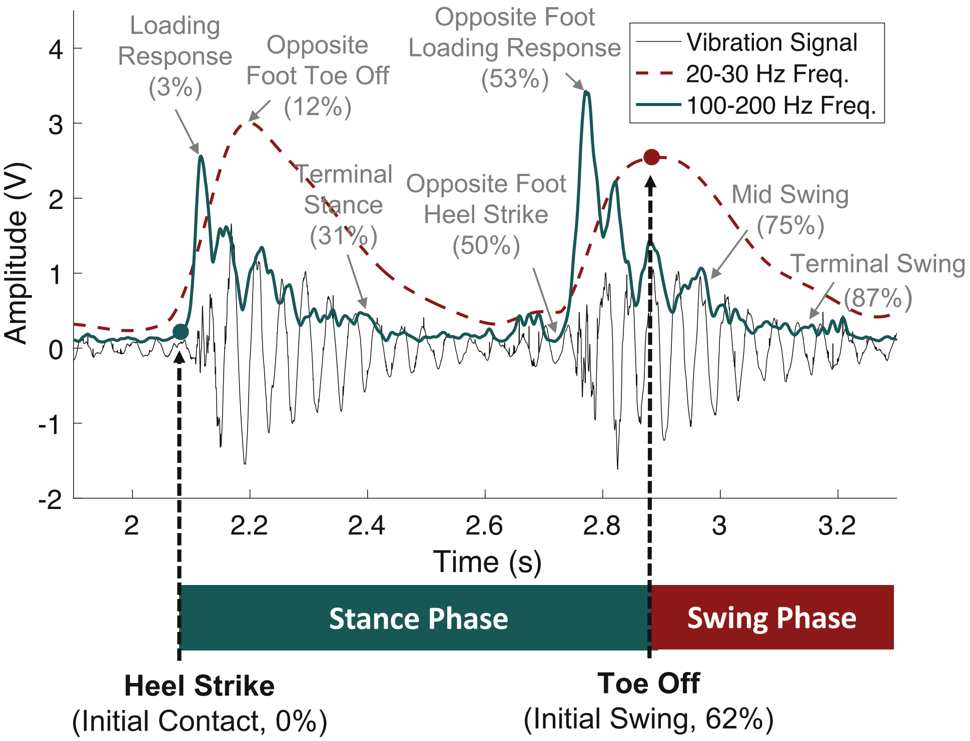

Fig. 8.1 A representation of gait phases with respect to footstep-induced structural vibration signals: the heel strike and toe-off divide the gait cycle into stance and swing phases. The heel strike occurs at the valley right before the high-frequency peak, while toe-off occurs at the peaks of the low-frequency range

observed that the gait events occur at special points in their dominant frequency ranges. Specifically, the heel strike excites a higher frequency in vibration signals than the toe-off, which occurs at the valley right before the high-frequency peak; the toe-off occurs at the peaks of the low-frequency range. This aligns with our intuition that the heel strike force resembles an impulse that leads to a significant increase in floor vibrations, whereas the toe-off occurs when the gradual friction force reaches the maximum.

8.2.2 *Formulating the Structural Influence on Footstep-Induced Structural Vibration*

In this section, we derive the structural dynamics of footstep-induced floor vibrations based on linear time-invariant (LTI) system formulation to understand the influence of the structure on footstep-induced floor vibrations. Existing models to represent the structural responses under footstep forces using LTI systems are not formulated in terms of the dynamic properties of the structure, such as the mass, stiffness, mode shapes, and frequency response function [28–30]. This limits the ability to develop structure-agnostic approaches or validate them analytically.

To begin with, we focus on a simplified scenario when a single pedestrian is walking along a simply supported beam with consistent footstep force [31, 32]. As described in Fig. 8.2, a footstep force $F_l(t)$ is applied at location l, and the sensor is mounted at location x to collect the structural vibrations $u_x(t)$ at the vertical direction.

Based on the LTI system formulation [33], the Fourier transform of the structural response $u_x(t)$ is related to the Fourier transform of its input footstep force $F_l(t)$ as below:

$$\mathscr{F}u_x(t) = H(l,x)\mathscr{F}F_l(t), \quad \text{where} \quad H(l,x) = \begin{bmatrix} h_1(l,x) & & & \\ & h_2(l,x) & & \\ & & \ddots & \\ & & & h_N(l,x) \end{bmatrix}, \tag{8.1}$$

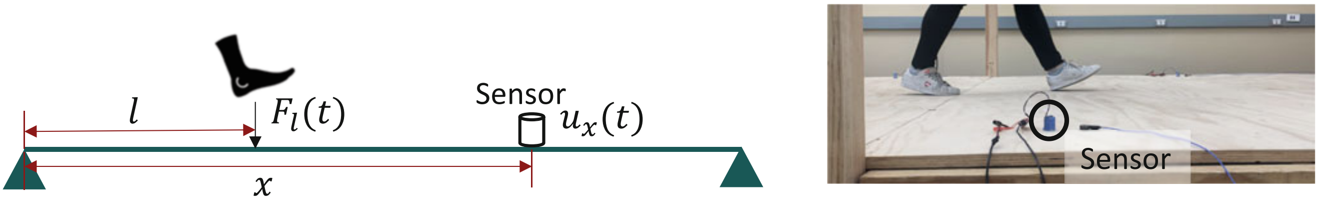

Fig. 8.2 A 2D model of a pedestrian walking on a simply supported beam, simplified from the real-life photo on the right

where H is a diagonal matrix with each row h_j representing the frequency response function (FRF) at a given frequency bin (i.e., mode) j, where N is the number of frequency bins after the Fourier transform.

From the perspective of the structural dynamics, we establish the relationship between the gait force $F_l(t)$ and vertical displacement $u_x(t)$ through the principle of modal decomposition—this multi-degree of freedom (MDOF) system can be represented as the superposition of multiple single-degree of freedom (SDOF) systems [34]:

$$m_j^* \ddot{q}_j(t) + c_j^* \dot{q}_j(t) + k_j^* q_j(t) = \phi_j F_l(t) \tag{8.2}$$

$$u_x(t) = \sum_{j=1}^{N} \phi_{jx} q_j(t), \tag{8.3}$$

where m_j^*, c_j^*, and k_j^* represent the mass, damping, and stiffness for the jth mode. $q_j(t)$ is the jth modal coordinates in the vertical direction, and ϕ_j is the normalized mode shape vector for that mode.

To **formulate the dynamic responses of the structure under footstep forces as a LTI system**, we derive H by taking the Fourier transform of Eqs. (8.2) and (8.3) at both sides:

$$\mathscr{F} u_x(t) = \sum_{j=1}^{N} \phi_{jx} \mathscr{F} q_j(t) \tag{8.4}$$

$$\mathscr{F} q_j(t) = FRF_j^*(\omega_j) \phi_{jl} \mathscr{F} F_l(t), \tag{8.5}$$

where $FRF_j^*(\omega)$ is the FRF of the jth SDOF system after modal decomposition; ϕ_{jl} denotes the jth mode shape vector at footstep location l, whereas ϕ_{jx} denotes the jth mode shape vector at sensor location x. To this end, the influence of the structure is encoded in matrix H from Eq. (8.1) as below:

$$h_j(j, x) = \phi_{jx} FRF_j^*(\omega_j) \phi_{jl}. \tag{8.6}$$

In this equation, ϕ_{jx} and ϕ_{jl} are constants for a given structure, and $FRF_j^*(\omega_j)$ has large values only when ω_j is close to the modal frequency. Therefore, the dominant frequencies observed in the structural response spectrum $\mathscr{F} u_x(t)$ indicate the footstep force spectrum $\mathscr{F} F_l(t)$ is amplified around the modal frequencies.

To this end, we develop a method based on time–frequency segmentation through wavelet transform to preserve the information of both the frequency spectrum and the time-domain gait phases. Figure 8.3 shows the wavelet coefficient plot of a person's footstep on wooden and concrete structures. While the footsteps for the left and right figures are from the same person wearing the same pair of shoes, the dominant frequencies in the wavelet spectra from wood and concrete structures are significantly different for heel strike and toe-off. This observation can be interpreted based on Eqs. (8.1) and (8.6): assuming the same person has a consistent footstep force pattern, the spectrum of the footstep force appears to be amplified around the modal frequencies of each structure. Since the modal frequencies of the wooden and concrete structures are different due to their discrepancies in mass, stiffness, and damping ratio, the same footstep force results in different dominant frequencies at both heel strike and toe-off.

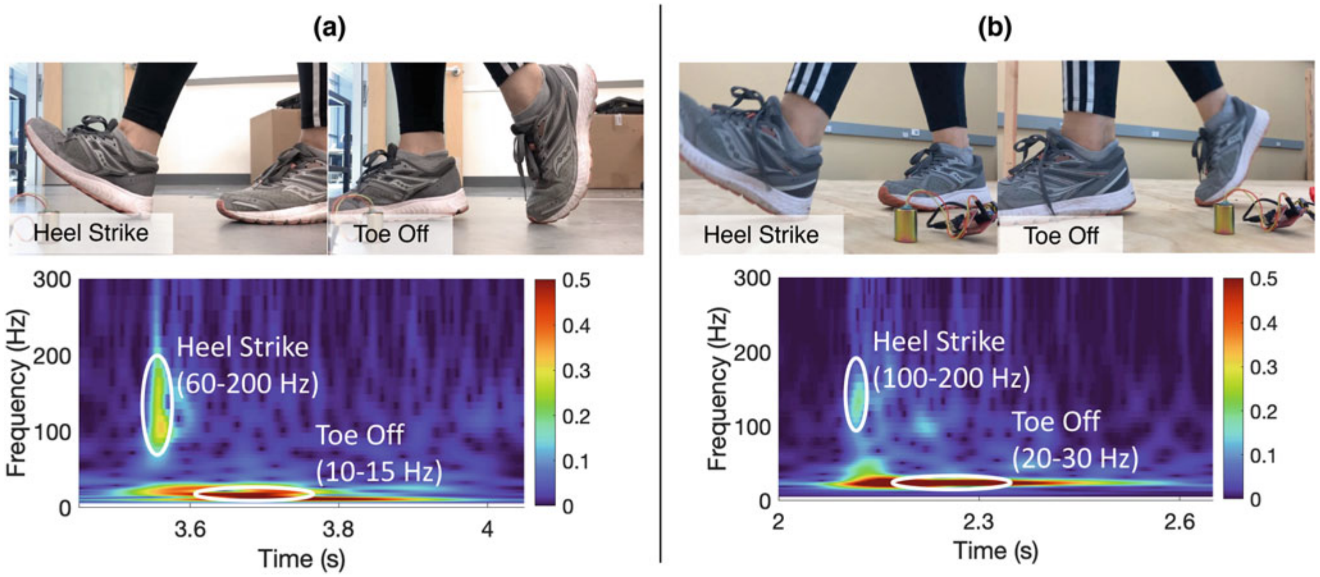

Fig. 8.3 Structural vibrations induced by a person walking on two structures: (**a**) concrete structure and (**b**) wooden structure. The heel strike and toe-off events are captured in **different dominant frequency ranges** by the wavelet coefficient map. The heel strike has a dominant frequency range of 60–200 Hz and 100–200 Hz for concrete and wooden structures, respectively. The toe-off has a dominant frequency range of 10–15 Hz and 20–30 Hz for concrete and wooden structures, respectively

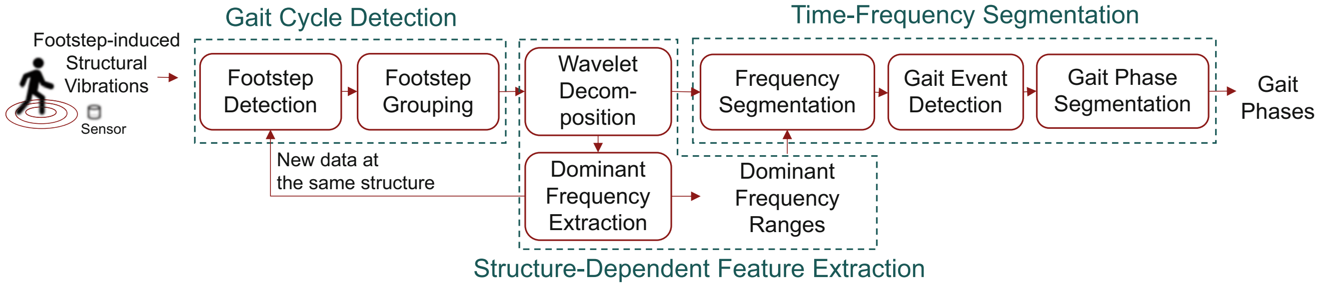

Fig. 8.4 An overview of our gait cycle segmentation framework

8.3 Structure-Agnostic Gait Cycle Segmentation Framework

Our framework consists of three stages: (1) gait cycle detection, (2) structure-dependent feature extraction, and 3) time–frequency segmentation of gait phases. The main idea of this framework is that we first extract the dynamic properties of each structure (i.e., the dominant frequency ranges) and then use those properties to update the gait cycle segmentation model during testing. The framework is illustrated in Fig. 8.4.

8.3.1 Gait Cycle Detection

In the first stage, we detect the gait cycle by first detecting individual footsteps and then grouping each pair of consecutive left and right footsteps as a gait cycle. Individual footsteps are detected through an anomaly detection algorithm, which detects structural vibration signals that exceed three standard deviations of the normal ambient vibration amplitudes as footsteps. Then, every two consecutive footstep impulses are grouped as a gait cycle.

8.3.2 Structure-Dependent Feature Extraction

For each new structure, we extract the structure-dependent features from the vibration signals to represent the structural influence. As discussed in Sect. 8.2.2, the structure-dependent features are the dominant frequency ranges during various gait phases. As is shown in Fig. 8.3, while the response spectra from two structures share similar trends under the gait force, the main difference is the dominant frequency ranges where heel strike and toe-off occur. To this end, we conduct a time–frequency analysis through wavelet transform to extract these structure-dependent features that are the dominant frequency ranges for heel strike and toe-off.

8.3.3 Time–Frequency Segmentation of Gait Phases

In the third stage, we segment the gait cycle into the stance phase and swing phase by detecting heel strike and toe-off within their structure-dependent dominant frequency ranges. First, we compute the sum of wavelet coefficients over frequency within the extracted structure-dependent dominant frequency ranges, resulting in two time series for heel strike and toe-off, respectively. Then, we conduct peak-picking among the resultant wavelet coefficient time series to detect the time for heel strike and toe-off. This is because, based on our observation in Sect. 8.2.1, the heel strike leads to a peak in the high frequency range due to its impulsive force and the toe-off occurs at the peak in the low frequency range. Next, we adjust the heel strike time to find the initial heel contact time (i.e., onset of stance phase) by detecting when the vibration signal amplitude starts increasing before reaching the peak. Finally, the gait cycle is segmented based on the heel strike and toe-off time to compute the duration of stance and swing phases.

8.4 Evaluation

We evaluate our framework through a real-world experiment on two different structures: (1) a wood-framed platform and (2) a concrete floor on the second floor of a campus building. In this section, we first introduce the experiment setup and then discuss the evaluation results.

8.4.1 Experiment Setup

The primary sensing devices include four SM-24 geophone sensors mounted on both structures to collect vertical vibration responses of the floors with 25,600 Hz sampling frequency (see Fig. 8.5a). The signals from the sensors are first amplified by 100–500× during the preliminary testing to improve the signal-to-noise ratio while minimizing clipping. The layout of the sensors on both structures is shown in Fig. 8.5c and d. A Vicon Lock Lab system is connected to the vibration sensors to acquire, synchronize, and convert the analog signal into the digital signal.

The ground truths are collected using Vicon Motion Capture System with a frame rate of 100 fps (see Fig. 8.5b). During the experiment, 16 markers are attached to each subject's lower limbers, and eight infrared cameras capture the moving trajectories of these markers as the subjects walk across the floor. The moving trajectories of these markers are reconstructed, smoothed, and interpolated by Vicon built-in algorithms. Gait events of each gait cycle are identified manually by observing the heel contact with the floor and toe-off from the floor. Temporal parameters estimated from these gait events are then extracted as labels.

A total of 80 walking trials with 628 footsteps from two participants are collected during the experiment. Each participant is advised to walk across the wooden and concrete structure using their natural gait. All experiments are conducted following the approved IRB (No.: IRB-55372).

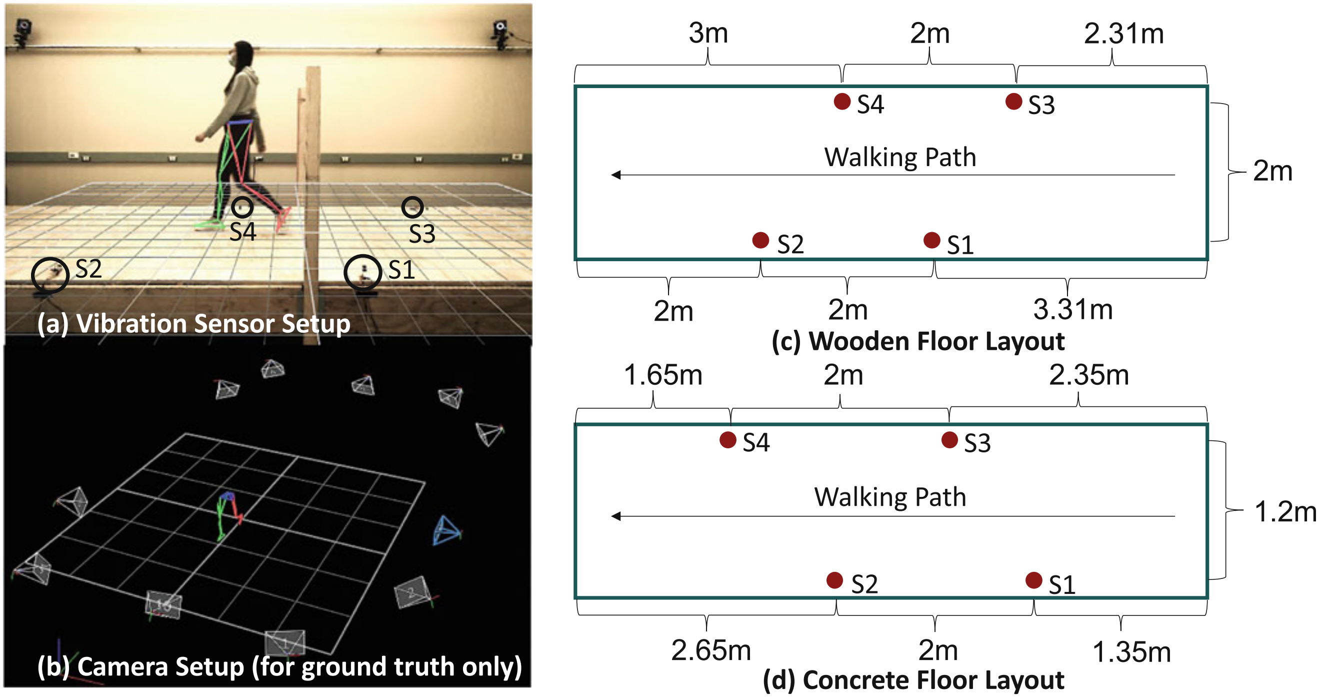

Fig. 8.5 Experiment setup for structure-agnostic gait cycle segmentation evaluation: (**a**) geophone setup for footstep-induced structural vibration sensing, (**b**) camera setup for ground truth collection, (**c**) wooden floor layout of sensors and walking path, (**d**) concrete floor layout of sensors and walking path

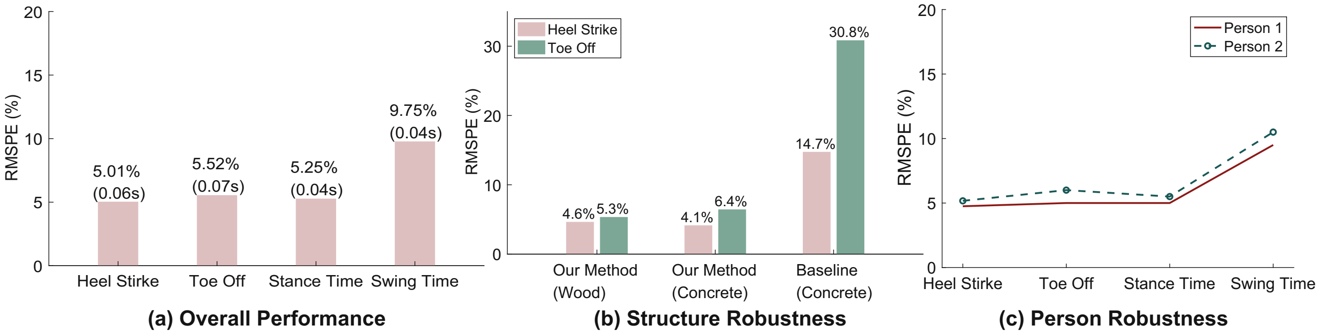

Fig. 8.6 Evaluation results for structure-agnostic gait cycle segmentation evaluation: (**a**) overall performance on temporal gait parameter estimation, (**b**) robustness to structure types, (**c**) robustness to people

8.4.2 *Results and Discussions*

Overall, our method achieves an average root mean squared percentage error (RMSPE) of 5% (0.060s) and 5.5% (0.066s) for heel strike and toe-off time estimation, and 5.25% (0.042s) and 9.7% (0.039s) for stance phase and swing phase duration prediction, respectively (see Fig. 8.6a). The RMSPE is computed by dividing the root mean squared error (in seconds) by the average duration of gait cycles or gait phases. The average gait cycle duration is 1.2s, and the average stance and swing phase duration are 0.75s and 0.45s, respectively. The slightly larger error in swing time estimation is due to the shorter duration of the swing phase. In addition, we notice that an average error in manually labeling the ground truth is about 0.02 s (2 frames) when we conducted repeated labeling by multiple people.

Robustness to Structure Types

We evaluate the robustness of the approach by comparing its performance over two structures and a baseline model that assumes the concrete structure's dominant frequency ranges are the same as the wooden structure. As shown in Fig. 8.6b, the error rates are consistent across the wooden and concrete structures, indicating it is structure-agnostic. In addition, a significant error is observed in the baseline where the structure-dependent dominant frequency ranges are not adapted to the new structure (i.e., the concrete floor), especially in toe-off time estimation. This is because the toe-off force is typically non-impulsive and gradual and often excites the structure in a low-frequency range with a small bandwidth (e.g., 10–20 Hz on concrete vs. 20–30 Hz on wood), so that the error in the dominant frequency range detection leads to large errors in toe-off detection.

Robustness to People We examine the sensitivity of our approach across people by comparing the errors between the two subjects. Results in Fig. 8.6c show that the errors for both people are consistent (the difference is less than 2%). However, person 2 has a slightly larger error than person 1 because person 1 has 17% higher signal energy in their footstep-induced floor vibration signals than person 2, resulting in better SNR for gait event detection. In addition, our observations during the experiment show that the differences may also result from their distinct body configurations and shoe types. For example, person 2 is shorter and of lighter weight and wears a pair of softer shoes than person 1, leading to a smoother peak at the toe-off that lowers the detection precision in time. For future work, we will explore the effect of individual differences among people.

8.5 Future Work

For future work, we will continue exploring in-home gait health monitoring through footstep-induced structural vibrations in these three aspects:

Fine-Grained Gait Cycle Segmentation In addition to the stance and swing phases, there are many sub-phases within a gait cycle, including weight acceptance, mid-stance, terminal stance, terminal swing, etc. Estimating the time of each phase not only allows fine-grained anomaly detection on gait patterns, but also enables progression assessments during the foot and ground contact to evaluate its smoothness and completeness. This additional information will be an important reference for detecting various gait disorders in clinical practices.

Multiple Gait Parameters Estimation While this chapter focuses on temporal gait parameter estimation, other gait parameters, such as spatial parameters and force balance indicators, are also crucial for gait health monitoring. Our prior works have investigated these topics but are limited to one structure [4, 5, 20]. Therefore, we plan to develop structure-agnostic models that can estimate multiple gait parameters at the same time.

Multi-Modal Fusion Gait disorders can lead to multiple distinct symptoms that can be captured through various types of sensing modalities. While structural vibration contains mainly kinetic gait information, other modalities such as cameras and wearables capture kinematic information. The combination of both types of information is complementary for a more robust in-home gait analysis. To this end, we will develop a sensor fusion framework that leverages the advantages of multiple modalities to improve the accuracy of structural vibration-based gait health monitoring.

8.6 Conclusions

In this chapter, we develop a structure-agnostic gait cycle segmentation framework that detects stance and swing phases in gait cycles using footstep-induced structural vibrations for in-home gait health monitoring. The primary research challenges are the complex interplay of the gait phases and structural properties with the vibration signals, resulting in difficulties separating gait phases and limited generalizability to different types of structures. To overcome the challenges, we characterize the structural responses over various frequency ranges and formulate the structural influence to extract the structure-dependent dominant frequency ranges for structure-agnostic time–frequency segmentation of gait cycles. Our method was evaluated on two real-world structures and achieved a 5% average error in detecting various gait events and phases.

Acknowledgments This work was funded by the U.S. National Science Foundation (under grant number NSF-CMMI-2026699).

References

1. Davis, B.T., Bryant, B.I., Fritz, S.L., Handlery, R., Flach, A., Hirth, V.A.: Measuring gait parameters from structural vibrations. Measurement **195**, 111076 (2022)
2. Kessler, E., Sriram Malladi, V.V.N., Tarazaga, P.A.: Vibration-based gait analysis via instrumented buildings. Int. J. Distrib. Sensor Netw. **15**(10), 1550147719881608 (2019)
3. Dong, Y., Fagert, J., Zhang, P., Noh, H.Y.: Stranger detection and occupant identification using structural vibrations. In: European Workshop on Structural Health Monitoring, pp. 905–914. Springer, Berlin (2023)
4. Fagert, J., Mirshekari, M., Pan, S., Zhang, P., Noh, H.Y.: Characterizing left-right gait balance using footstep-induced structural vibrations. In: Sensors and Smart Structures Technologies for Civil, Mechanical, and Aerospace Systems 2017, vol. 10168, pp. 357–365. SPIE, France (2017)
5. Dong, Y., Zou, J.J., Liu, J., Fagert, J., Mirshekari, M., Lowes, L., Iammarino, M., Zhang, P., Noh, H.Y.: MD-Vibe: Physics-informed analysis of patient-induced structural vibration data for monitoring gait health in individuals with muscular dystrophy. In: Adjunct Proceedings of the 2020 ACM International Joint Conference on Pervasive and Ubiquitous Computing and Proceedings of the 2020 ACM International Symposium on Wearable Computers, pp. 525–531 (2020)
6. Pan, S., Berges, M., Rodakowski, J., Zhang, P., Noh, H.Y.: Fine-grained recognition of activities of daily living through structural vibration and electrical sensing. In: Proceedings of the 6th ACM International Conference on Systems for Energy-Efficient Buildings, Cities, and Transportation, BuildSys '19, pp. 149–158, New York, NY. Association for Computing Machinery, New York (2019)
7. Fagert, J., Bonde, A., Srinidhi, S., Hamilton, S., Zhang, P., Noh, H.Y.: Clean vibes: hand washing monitoring using structural vibration sensing. ACM Trans. Comput. Healthcare **3**(3), 1–25 (2022)
8. Emery, A.E.H.: Population frequencies of inherited neuromuscular diseases–a world survey. Neuromuscul. Dis. **1**(1), 19–29 (1991)
9. Mehta, K.M., Yeo, G.W.: Systematic review of dementia prevalence and incidence in United States race/ethnic populations. Alzheimer's Dementia **13**(1), 72–83 (2017)
10. Brown, R.C., Lockwood, A.H., Sonawane, B.R.: Neurodegenerative diseases: an overview of environmental risk factors. Environ. Health Perspect. **113**(9), 1250–1256 (2005)
11. Cicirelli, G., Impedovo, D., Dentamaro, V., Marani, R., Pirlo, G., D'Orazio, T.R.: Human gait analysis in neurodegenerative diseases: a review. IEEE J. Biomed. Health Informat. **26**(1), 229–242 (2021)
12. Finkelstein, S.M., Speedie, S.M., Potthoff, S.: Home telehealth improves clinical outcomes at lower cost for home healthcare. Telemed. J. e-Health **12**(2), 128–136 (2006)
13. Naylor, K.B., Tootoo, J., Yakusheva, O., Shipman, S.A., Bynum, J.P., Davis, M.A.: Geographic variation in spatial accessibility of US healthcare providers. PLOS One **14**(4), e0215016 (2019)
14. Andrews, J.G., Davis, M.F., Meaney, F.J.: Correlates of care for young men with Duchenne and Becker muscular dystrophy. Muscle Nerve **49**(1), 21–25 (2014)
15. Whittle, M.W.: Gait Analysis: An Introduction. Butterworth-Heinemann, Oxford (2014)
16. Stone, E.E., Skubic, M.: Capturing habitual, in-home gait parameter trends using an inexpensive depth camera. In: 2012 Annual International Conference of the IEEE Engineering in Medicine and Biology Society, pp. 5106–5109. IEEE, Piscataway (2012)
17. De Rossi, S.M., Crea, S., Donati, M., Reberšek, P., Novak, D., Vitiello, N., Lenzi, T., Podobnik, J., Munih, M., Carrozza, M.C.: Gait segmentation using bipedal foot pressure patterns. In: 2012 4th IEEE RAS & EMBS International Conference on Biomedical Robotics and Biomechatronics (BioRob), pp. 361–366. IEEE, Piscataway (2012)
18. Mohammed, S., Same, A., Oukhellou, L., Kong, K., Huo, W., Amirat, Y.: Recognition of gait cycle phases using wearable sensors. Robot. Auton. Syst. **75**, 50–59 (2016)
19. Agostini, V., Balestra, G., Knaflitz, M.: Segmentation and classification of gait cycles. IEEE Trans. Neural Syst. Rehabil. Eng. **22**(5), 946–952 (2013)
20. Dong, Y., Liu, J., Noh, H.Y.: GaitVibe+: Enhancing structural vibration-based footstep localization using temporary cameras for in-home gait analysis. In: Proceedings of the 4th ACM Workshop on Continual and Multimodal Learning for Internet of Things (CML-IOT), New York, NY. Association for Computing Machinery, New York (2022)
21. Fagert, J., Mirshekari, M., Pan, S., Zhang, P., Noh, H.Y.: Structural property guided gait parameter estimation using footstep-induced floor vibrations. In: Dynamics of Civil Structures, vol. 2, pp. 191–194. Springer, Berlin (2020)
22. Pan, S., Ramirez, C.G., Mirshekari, M., Fagert, J., Chung, A.J., Hu, C.C., Shen, J.P., Noh, H.Y., Zhang, P.: SurfaceVibe: Vibration-based tap & swipe tracking on ubiquitous surfaces. In: 2017 16th ACM/IEEE International Conference on Information Processing in Sensor Networks (IPSN), pp. 197–208 (2017)
23. Persson, B.N.J.: Sliding Friction: Physical Principles and Applications. Springer Science & Business Media, Berlin (2013)
24. Whittle, M.W.: Generation and attenuation of transient impulsive forces beneath the foot: a review. Gait Posture **10**(3), 264–275 (1999)
25. Hahm, K.S., Anthony, B.W.: In-home health monitoring using floor-based gait tracking. Int. Things **19**, 100541 (2022)
26. Kharb, A., Saini, V., Jain, Y.K., Dhiman, S.: A review of gait cycle and its parameters. IJCEM Int. J. Comput. Eng. Manag. **13**, 78–83 (2011)
27. Tugui, R.D., Antonescu, D.: Cerebral palsy gait, clinical importance. Maedica **8**(4), 388 (2013)
28. Mirshekari, M., Fagert, J., Pan, S., Zhang, P., Noh, H.Y.: Step-level occupant detection across different structures through footstep-induced floor vibration using model transfer. J. Eng. Mech. **146**(3), 04019137 (2020)
29. Zhang, Y., Zhizhang, H., Susu, X., Pan, S.: AutoQual: task-oriented structural vibration sensing quality assessment leveraging co-located mobile sensing context. CCF Trans. Pervasive Comput. Interact. **3**(4), 378–396 (2021)
30. Dong, Y., Zhu, J., Noh, H.Y.: Re-vibe: Vibration-based indoor person re-identification through cross-structure optimal transport. In: Proceedings of the 1st ACM Workshop on the Future of Work, Workplaces, and Smart Buildings (FoWSB'22), New York, NY. Association for Computing Machinery, New York (2022)
31. Caprani, Colin C., Ahmadi, Ehsan: Formulation of human-structure interaction system models for vertical vibration. Journal of Sound and Vibration **377**, 346–367 (2016)

32. Racic, V., Pavic, A., Brownjohn, J.M.W.: Experimental identification and analytical modelling of human walking forces: literature review. J. Sound Vibrat. **326**(1–2), 1–49 (2009)
33. Oppenheim, A.V., Buck, J., Daniel, M., Willsky, A.S., Nawab, S.H., Singer, A.: Signals & Systems. Pearson Educación, London (1997)
34. Chopra, A.K.: Dynamics of Structures. Pearson Education India, Noida (2007)

Chapter 9
Feasibility of Using Accelerometers to Detect Human Footsteps for Cadence Estimation on Health Sciences

Jean M. Franco, Yohanna MejiaCruz, Juan M. Caicedo, and Zhaoshuo Jiang

Abstract In recent years, tracking gait parameters of older adults in a non-intrusive way is attacking a lot of attention in the community due to their close correlation with health status. This chapter attempts to investigate the feasibility of using seismic accelerometers to detect human footsteps from floor vibration measurements for cadence estimation. Algorithms building upon high energy peaks in the time-domain acceleration signals were proposed to estimate cadence, and the proposed technique is called the peak acceleration for cadence estimations (PACE). A specialized cadence filter was also developed and implemented to improve the overall cadence estimation from three-step instant cadence estimations. To validate the proposed algorithms, a hallway with four accelerometers placed behind a wall was used as a testbed to measure the structural response generated by the footsteps. A subject walking at three different paces with wireless APDM sensors, the gold standard in health science to measure gait parameters, was used to generate ground-truth data for validation. The results showed that proposed algorithms successfully detect human footsteps with a high degree of accuracy and that the estimated cadence was highly correlated with the cadence measured by the APDM sensors. The specialized filter was able to clean out highly unlikely instant-cadence estimations that substantially improved the overall cadence estimation.

Keywords Floor vibrations · Cadence · Accelerometers

9.1 Introduction

In recent years, tracking gait parameters of older adults in a non-intrusive way is attacking a lot of attention in the community due to their close correlation with health status. This chapter attempts to investigate the feasibility of using seismic accelerometers to detect human footsteps from floor vibration measurements for cadence estimation. Algorithms building upon high energy peaks in the time-domain acceleration signals were proposed to estimate cadence, and the proposed technique is called the peak acceleration for cadence estimations (PACE). A specialized cadence filter was also developed and implemented to improve the overall cadence estimation from three-step instant cadence estimations. To validate the proposed algorithms, a hallway with four accelerometers placed behind a wall was used as a testbed to measure the structural response generated by the footsteps. A subject walking at three different paces with wireless APDM sensors, the gold standard in health science to measure gait parameters, was used to generate ground-truth data for validation. The results showed that proposed algorithms successfully detect human footsteps with a high degree of accuracy and that the estimated cadence was highly correlated with the cadence measured by the APDM sensors. The specialized filter was able to clean out highly unlikely instant-cadence estimations that substantially improved the overall cadence estimation.

J. M. Franco (✉) · Y. MejiaCruz · J. M. Caicedo
Department of Civil and Environmental Engineering, University of South Carolina, Columbia, SC, USA
e-mail: francolj@email.sc.edu; mejiacru@email.sc.edu; caicedo@cec.sc.edu

Z. Jiang
School of Engineering, San Francisco State University, San Francisco, CA, USA
e-mail: zsjiang@sfsu.edu

H. Y. Noh et al. (eds.), *Dynamics of Civil Structures, Volume 2*, Conference Proceedings of the Society for Experimental Mechanics Series, https://doi.org/10.1007/978-3-031-36663-5_9

9.2 Background

The use of footstep-induced floor vibrations (FVs) is one of the approaches that have received more attention in recent years to extract and monitor gait parameters[1]. Floor vibrations induced by footsteps are caused by the short-duration impact forces of the foot strike. Given the differences during the striking of the floor, the walking pattern of a person@ is unique. Techniques using this uniqueness have been developed to separate and identify individuals [2–5]. Gait parameters such as walking speed, stride length, cadence, balance, and others have also been extracted from vibration signals and used as statistics to evaluate and monitor changes in the subject's health status [6].

9.3 Analysis

Cadence provides useful information for the health status of a person and can serve as the basis for calculating other gait parameters, such as walking speed, when the step length is known. The proposed technique uses previously classified clean-gait floor vibrations and combines the information of multiple sensors to extract peaks and calculate cadence using a shifting moving window and a proposed median filter. Cadence (γ) can be calculated as the total amount of steps (S) divided by the change in time. A moving window is incorporated to analyze the data. The moving window, created for a specified number of steps, is moved across the acceleration record until all the step events have been analyzed. In each window, an instant estimation of cadence is extracted (Eq. 9.1), where N is the total of estimations available from the moving window, and α is the desired number of steps to use in the fixed moving window and can be determined by considering that a gait cycle is completed when the same foot touches the floor twice. After sorting the instant-cadence estimations and performing a difference around the median value, a threshold is determined and applied to remove outliers. The mean value of the remaining estimations is used as the final parameter estimation. Four PCB 393B31 seismic accelerometers were placed with equal spacing next to a hallway and used to record acceleration data (Fig. 9.1) to validate the proposed approach. The data were acquired using a NI-9234 vibration input module and a NI-9162 CompactDAQ Chassis with a sampling frequency of 1706.67 Hz.

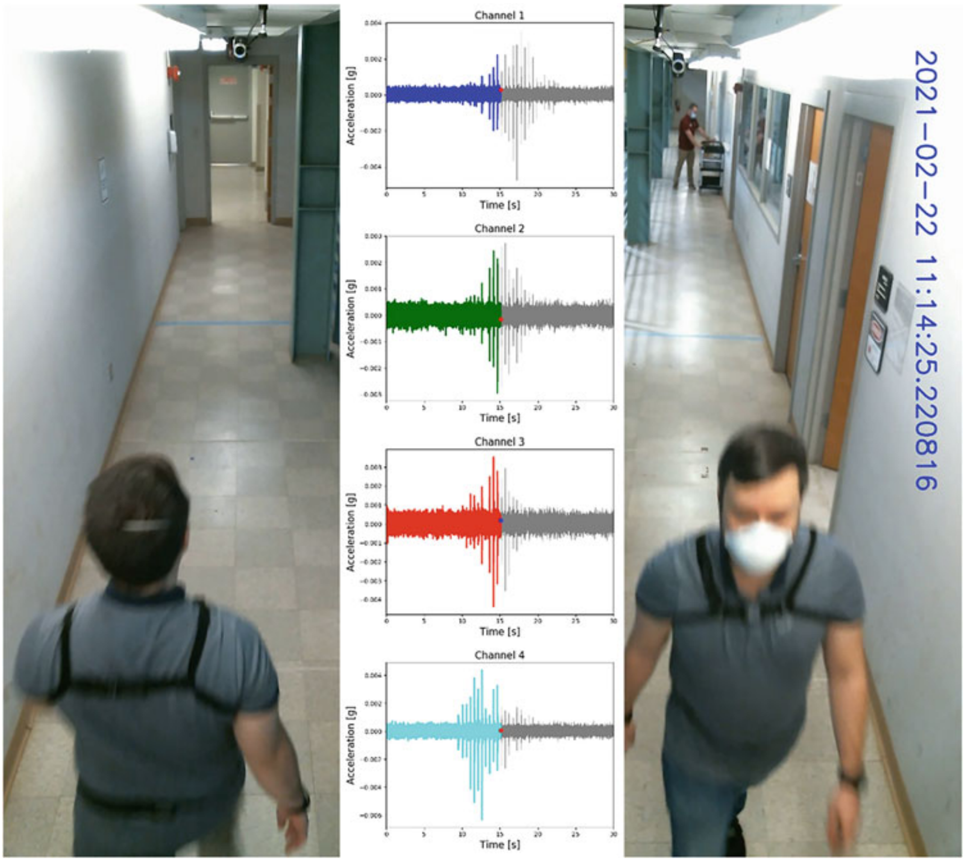

Fig. 9.1 Experimental setup

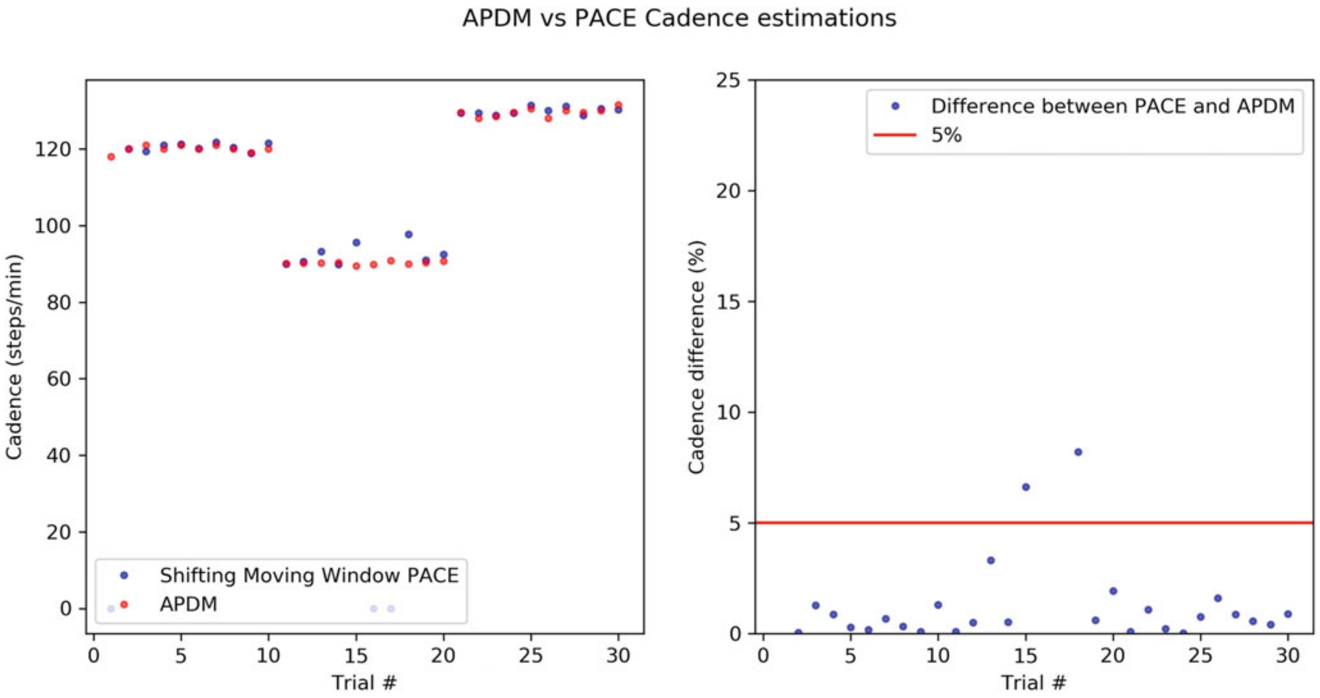

Fig. 9.2 Cadence estimations

$$\gamma = \frac{1}{N}\sum_{i=0}^{N}\frac{\alpha S}{t_{i+\alpha}-t_i}. \tag{9.1}$$

To further test the gait estimation of the PACE, thirty trials of the same individual walking along the hallway were recorded to validate the cadence estimation from AGE. During these experiments, the subject wore six OPAL-APDM wireless body-mounted inertial sensors as the golden standard in practice to estimate gait parameters. The individual was instructed to walk using a metronome at three different cadence speeds, namely, 90, 120, and 130 steps/minute, as presented in Fig. 9.2. The estimation results from OPAL-APDM were on par with those obtained from the PACE algorithm.

Acknowledgments Research reported in this publication was supported by National Institute on Aging of the National Institute of Health under award number: R01AG067395.

References

1. MejiaCruz, Y., Franco, J., Hainline, G., Fritz, S., Jiang, Z., Caicedo, J.M., Davis, B., Hirth, V.: Walking speed measurement technology: a review. Current Geriat. Rep. **10**, 1–10 (2021)
2. Pan, S., Wang, N., Qian, Y., Velibeyoglu, I., Noh, H.Y., Zhang, P.: Indoor person identification through footstep induced structural vibration. In: Proceedings of the 16th International Workshop on Mobile Computing Systems and Applications, pp. 81–86 (2015)
3. Kessler, E., Malladi, V.V.S., Tarazaga, P.A.: Vibration-based gait analysis via instrumented buildings. Int. J. Distrib. Sensor Netw. **15**(10), 1550147719881608 (2019)
4. Ekimov, A., Sabatier, J.M.: Vibration and sound signatures of human footsteps in buildings. J. Acoust. Soc. Amer. **118**(3), 2021–768 (2006)
5. Pan, S., Yu, T., Mirshekari, M., Fagert, J., Bonde, A., Mengshoel, O.J., Noh, H.Y., Zhang, P.: Footprintid: indoor pedestrian identification through ambient structural vibration sensing. Proc. ACM Interact. Mob. Wearable Ubiquitous Technol. **1**(3), 1–31 (2017)
6. Fagert, J., Mirshekari, M., Pan, S., Zhang, P., Noh, H.Y.: Characterizing left-right gait balance using footstep-induced structural vibrations. In: Sensors and Smart Structures Technologies for Civil, Mechanical, and Aerospace Systems 2017, vol. 10168, p. 1016819. International Society for Optics and Photonics, Bellingham (2017)

Chapter 10
Assessment of a Vision-Based Technique to Estimate the Synchronization of Jumping Crowds in Civil Structures

S. Turrisi, E. Zappa, and A. Cigada

Abstract Vibration serviceability criteria for civil structures follow a three-step framework, namely the excitation source, the path and the receiver. The first step, which is also the focus of this study, deals with the characterization of human-induced loads. However, the design models reported in the current guidance and codes are very often overly conservative and cannot adequately represent the real nature of crowd excitation. In this work, we present a computer vision technique, based on the use of Digital Image Correlation (DIC), as a solution to this problem. In addition to a cheap and an easy to install set up, the system can provide a comprehensive assessment of the coordinate motion induced by occupying crowds of various sizes. To demonstrate the efficacy of the proposed method, the measured DIC data are compared to those coming from the accelerometers installed on multiple subjects while performing jumping activities on a real grandstand. Then, the vision-based approach is used to study and to quantify the level of synchronization among the individuals for a range of songs and metronome beats. Results demonstrate that the DIC technique achieves similar performance as the inertial sensors but overcomes some practical limitations related to these traditional systems.

Keywords Vibration serviceability · Crowd loading · Synchronization · Digital image correlation · Civil structures

10.1 Introduction

Advancements in materials and construction technologies have made modern grandstands increasingly slender and lighter, with low natural frequencies that typically fall in the frequency range of dance-like group activities [1]. When the frequencies of such activities approach or coincide with one of the natural frequencies of the structure, resonant phenomena may induce severe vibration responses that are critical for both structural and public safety. This phenomenon becomes even more accentuated when the music beat or an external stimulus help the individuals to reach a well-synchronized motion. Related to this, in the last decades we are witnessing numerous examples of grandstands that cracked or collapsed under the synchronized action of the audience [2]. Therefore, the prediction of coordinated dynamic loads due to crowd activities is becoming a crucial aspect for the design and the assessment of grandstands structures [3]. Although several experimental and theoretical studies of individual jumping loads actually exist [4, 5], the availability of reliable crowd load models is still an open issue. This is mainly due to the fact that one has to consider the stochastic nature of the people motion, other than additional difficulties in the experiments due to the intrusiveness and the high costs of the setup [6].

This paper proposes a non-contact optical method, based on the use of Digital Image Correlation (DIC) [7], that is able to directly measure the synchronization level of jumping crowds on a real grandstand. First, the measurement accuracy of the technique has been assessed by comparing the estimated accelerations with those from standard reference sensors in case of three different individuals. Then, the overall crowd loading is computed for a group of 183 volunteers while jumping to different songs and metronome beats. Starting from this, two indicators are introduced to quantify both people synchronization and load intensity. The main aim of the study is thus to provide important indications about the real behaviour of dynamic crowd activities, that can be used for vibration serviceability problems.

S. Turrisi (✉) · E. Zappa · A. Cigada
Department of Mechanical Engineering, Politecnico di Milano, Milan, IT, Italy
e-mail: simone.turrisi@polimi.it

H. Y. Noh et al. (eds.), *Dynamics of Civil Structures, Volume 2*, Conference Proceedings of the Society for Experimental Mechanics Series, https://doi.org/10.1007/978-3-031-36663-5_10

10.2 Experimental Activity at the G. Meazza Stadium

This section describes the experimental activities held at the Giuseppe Meazza stadium in Milan. A jumping crowd made of 183 volunteers was positioned on a grandstand of the second ring, then it was asked to jump following the beat of both pop/rock songs and metronome beats. The jumping motion generated by the individuals were recorded using an off-the-shelf reflex camera (Canon EOS 750D), having an image resolution of 1920 × 1080 px^2 and a sampling frequency of 25 frame per second. The experimental setup adopted for the activities is illustrated in Fig. 10.1. To have a reference measure for the individual and crowd motion, volunteers recorded the acceleration time histories of the jumping activities through the app Pyphox©, which has been installed on their smartphones and make use of the embedded accelerometer. The app was set to have a common sampling frequency of 50 Hz for all the accelerometers.

The main characteristics of the tests analysed in the following sections are resumed in Table 10.1. ‘Popularity’, ‘Energy’, and ‘Danceability’ are song-related parameters [8] and indicate the average score retrieved from a questionnaire given to the participants. The scores have been scaled so that they assume a value between 0 and 1. The tests were designed to cover a range of jumping frequencies (f_{beat}) between 2 and 3 Hz, which were judged as comfortable jumping paces by the participants. Also other experimental studies [9, 10] found that these frequencies were those where people tend to synchronize better.

To let the volunteers jump in the most natural way, they were not informed in advance about the song played. To maximize the performance of the audience, instead, each test lasted no more than 40 seconds and a short break was granted between a test and the next one.

After the experimental campaign, the acquired movies have been processed by the DIC algorithm to compute the jumping forces of the crowd, following the same procedure proposed in [11]. First, the vertical relative displacement of each subset associated to the crowd region (ds_{ij}) is calculated. To obtain a faithful reconstruction of the crowd displacements, all the subsets associated to non-moving areas have been discarded from the analysis. A fraction of the total mass was assigned to the remaining n_m subsets ($m_s = m_c/n_m$). As the elapsed time between two consecutive images (dt) is known, it was possible to retrieve the acceleration time history of each subset from its relative displacement through numerical differentiation, i.e. $a_{ij}(t) = d^2 s_{ij}(t)/dt^2$. At this point, the force of each subset can be easily obtained by multiplying the acceleration time history by the mass, then adding the gravity contribution g, i.e. $F_{ij}(t) = m_s a_{ij}(t) + m_s g$. Finally, the crowd force is calculated as the sum of the contributions of each subset, $F_c(t) = \sum_{i=1}^{n_m} F_{ij}(t)$.

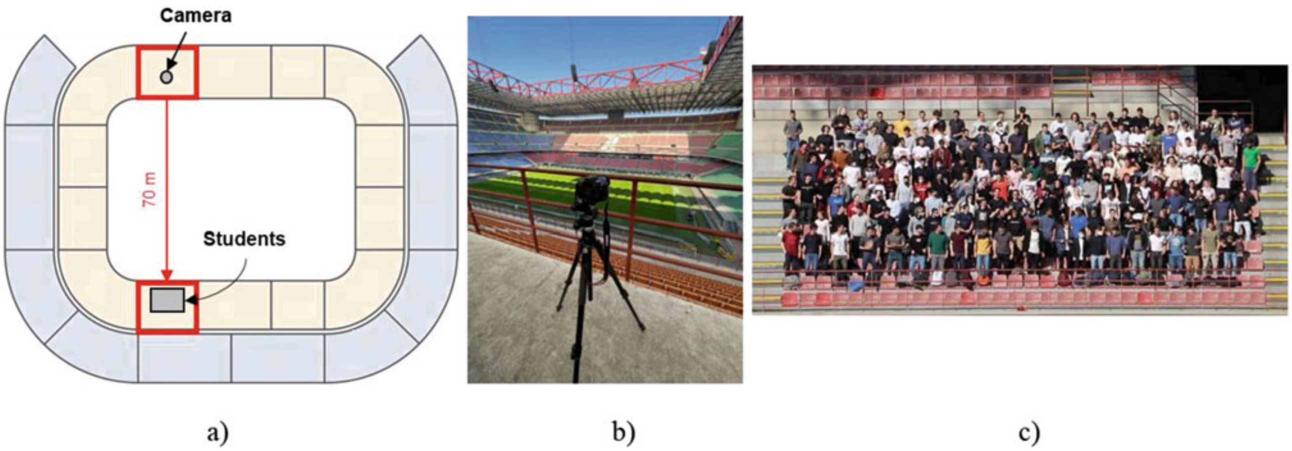

Fig. 10.1 (**a**) Experimental setup for the tests at the G. Meazza stadium, (**b**) camera position, (**c**) volunteers’ position on tested grandstand

Table 10.1 Test protocol for the experimental activities

Test ID	Song name/metronome	f_{beat} [Hz]	Popularity (P)	Energy (E)	Danceability (D)
T1	Metronome (120 bpm)	2.00	–	–	–
T2	Metronome (160 bpm)	2.67	–	–	–
T3	Born in the USA (Bruce Springsteen)	2.06	0.75	0.95	0.40
T4	Freed from desire (Gala)	2.15	0.76	0.86	0.70
T5	Sarà perché ti amo (Ricchi e Poveri)	2.17	0.54	0.68	0.83
T6	Thunderstruck (AC/DC)	2.23	0.84	0.89	0.50

A conversion factor of 14.7 mm/px, a subset size of 15 px and a step size of 5 px are used to run DIC for all the tests. According to [12], these values fall in an optimal range which allows to minimize the measurement uncertainty of DIC when applied to estimate human motion.

10.3 Comparison Between Accelerometers and Digital Image Correlation Data

This section investigates the possibility to use DIC to obtain reliable non-contact force estimations in a real-world structure. To do that, DIC measurements were compared with those obtained through standard reference sensors, i.e. the smartphone accelerometers attached to the body of the volunteers. As demonstrated in a previous laboratory test study [13], indeed, there was a high correspondence between the force estimated by means of the DIC data estimated on the upper body region and the force estimated relying on the inertial sensor mounted on the trunk.

The jumping loads of three volunteers following the rhythm of the metronome beat (T1) have been analysed. Their positions have been randomly picked from the area occupied by the crowd. The use of individual time series instead of the one of the whole crowd in the comparison arose from the fact that only some accelerometers records were properly acquired by the volunteers to obtain meaningful information. Figure 10.2 shows a frame extracted from the recorded movie during T1, where the pixels regions used to compute the average motion of each individual using DIC were highlighted with a yellow bounding box.

Camera and accelerometers signals came from two different sources, with no shared trigger. To synchronize the signals, their cross-correlation R_{xy} was calculated. As the cross-correlation is the maximum at a lag equal to the signals delay, this allowed either to synchronize the signals or to obtain a direct measure of their similarity. Figure 10.3 compares the estimated and measured accelerations, after synchronization. For all the cases, there was a good match in terms of general morphology in the time domain, also testified by a cross-correlation always higher than 80%. Figure 10.4, instead, illustrates the comparison of the above signals, but expressed in terms of amplitude of the spectrum. The beat frequency and its higher order harmonics which characterize the jumping activity are clearly visible. First of all, it is possible to observe how ‘P70’ and ‘P113’ jumped at a frequency slightly higher than the metronome beat (2 Hz), while ‘P116’ was well-synchronized. The measured and the estimated signals show a high correspondence also in the frequency domain. To assess the performance of the proposed method in the investigated frequency range, the peak discrepancy D_1 has been introduced and defined as in Eq. (10.1):

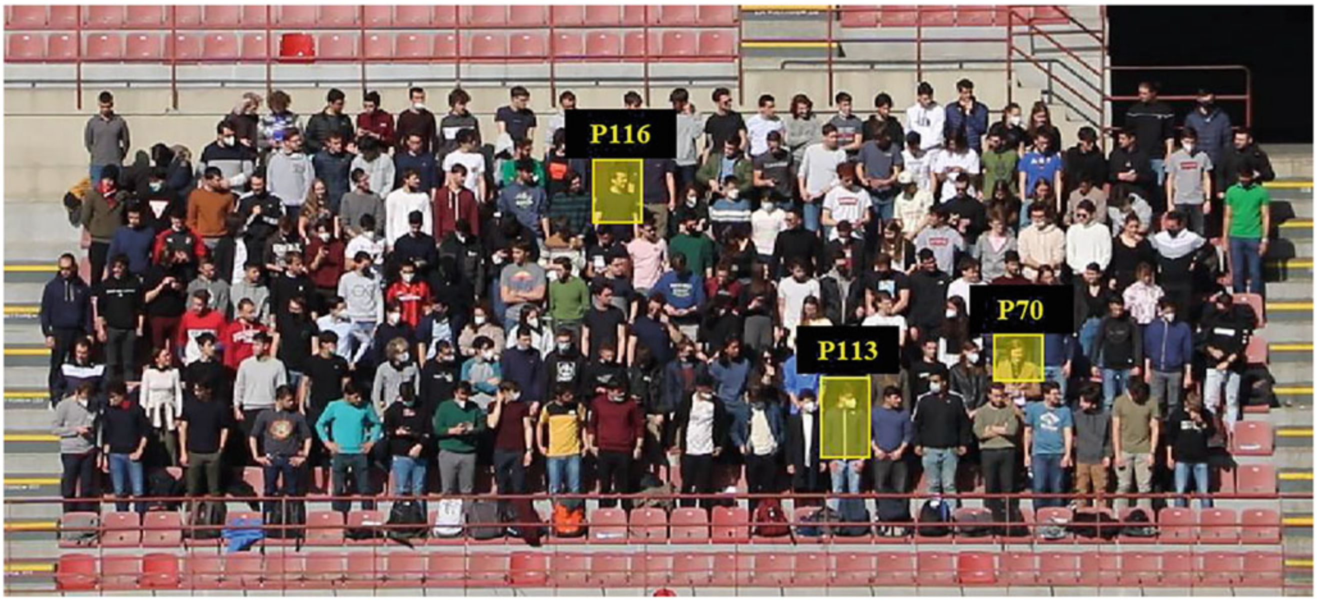

Fig. 10.2 Bounding regions used to estimate the forces of the tested individuals (‘P70’, ‘P113’, ‘P116’) with DIC for T1

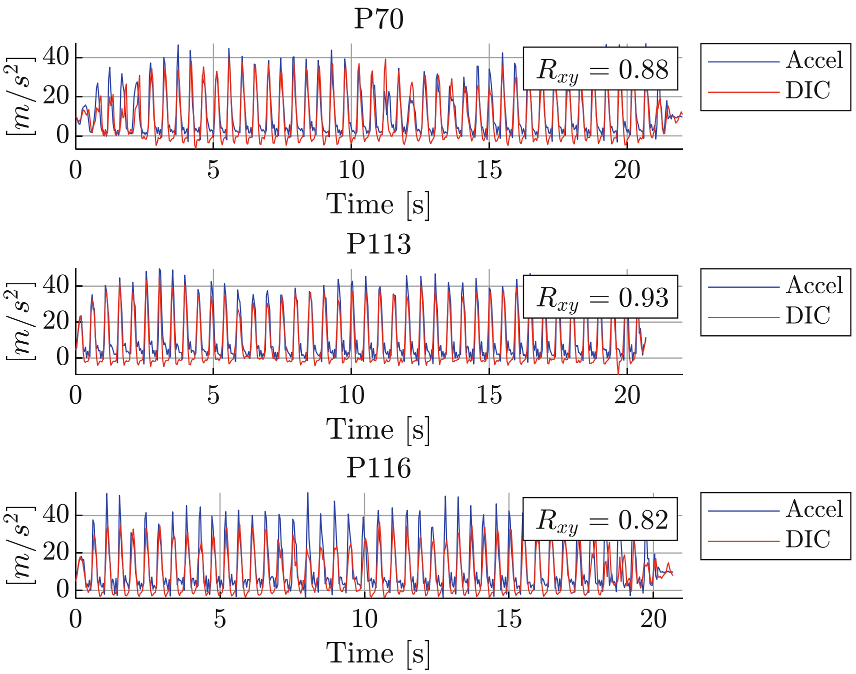

Fig. 10.3 Comparison in time domain between the measured (blue) and estimated (red) vertical accelerations for the three analysed people in T1

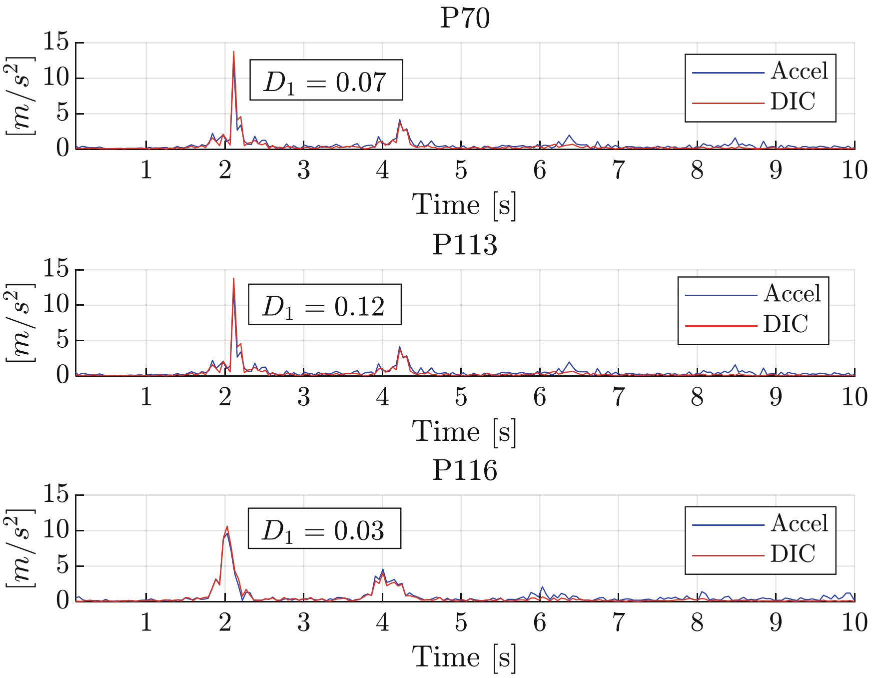

Fig. 10.4 Comparison between the measured (blue) and estimated (red) acceleration spectra for the three analysed people in T1

$$D_1 = \frac{A_1^{\text{est}} - A_1^{\text{meas}}}{A_1^{\text{meas}}} \tag{10.1}$$

where A_1 indicates the spectrum amplitude of the first harmonic component. The choice to evaluate the peak discrepancy only for the first harmonic came from the fact that the dynamic loading due to the crowd jumping almost contains the first harmonic only [8]. The low values obtained for D_1 is another proof of the good measurement accuracy of the DIC technique.

10.4 Estimation of Crowd Synchronization and Dynamic Loading

The ability of the DIC technique to measure the synchronization level among jumping individuals is investigated here. To estimate the synchronization level within the group for each test, the correlation coefficient (ρ) was calculated between the acceleration time histories of each subset. After that, the root-mean-square (RMS) of the correlation matrix was taken as indicator of the group synchronization for each test, referred to as *SL* in the remainder of this paper. The dynamic load factor (*DLF*) has been also calculated from the power spectral density (PSD) of the estimated crowd force signal, according to their state-of-the-art definition [8] and for a frequency range around the first harmonic (f_1). It represents another important parameter to quantify the severity of human-induced loading on civil structures. We introduced also a new parameter, namely song involvement coefficient (SIC), which has been calculated from the song-related parameters of Table 10.1 as SIC $= \sqrt{P^2 + E^2 + D^2}$ and indicates an average measure of the people involvement for that song.

Figure 10.5 summarizes the results of the above coefficients as a function of the beat frequency. The low values of group synchronization for all the tests (SL $\leq$ 0.30) highlighted the low ability of the participants to properly coordinate among themselves at any jumping rate. Moreover, there was no particular evidence that people followed the metronome rhythm better with respect to the music one. On the contrary, it would seem that the level of correlation achieved by people depends on how much they enjoy a specific song. These observations can be further confirmed by the two plots of Fig. 10.6, which demonstrate that the SF has a marked linear relationship with both the *DLF* and the SIC.

Figure 10.7 provides as illustrative example the estimated force signal of the crowd (normalized with respect to the mass) together with its PSD representation, for T4 and T5, respectively. These signals were obtained according to the procedure explained in Sect. 10.2. By summing up the time series of all the subset regions associated to the jumping crowd, the technique intrinsically accounted for the lack of synchronization among the individuals. In agreement to what anticipated before, from the plot of the PSD one can observe also how the contribution of the first harmonic is predominant, the second harmonic is barely noticeable, while the higher order harmonics have disappeared. Finally, the low involvement of the song played during T5 towards the participants (lowest SIC) resulted in a less severe input excitation. The opposite is true for T4.

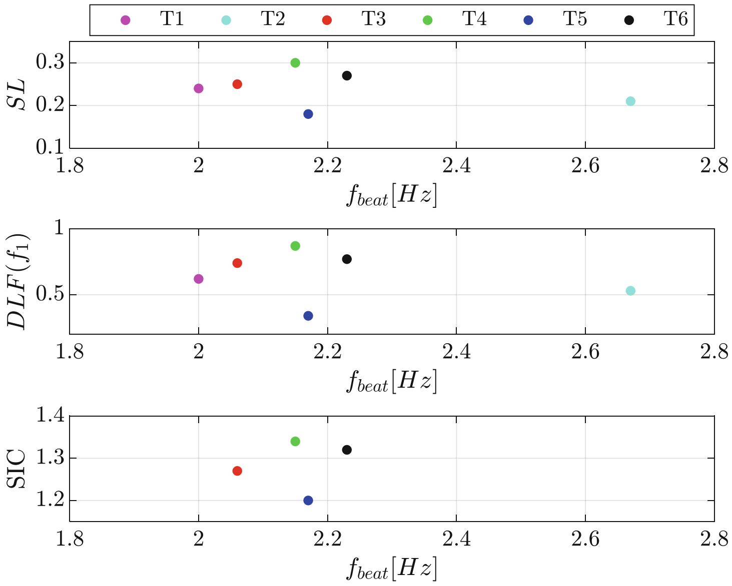

Fig. 10.5 Synchronization level (*SL*) and dynamic load factor (*DLF*) and song involvement coefficient (SIC) as a function of the analysed jumping frequencies

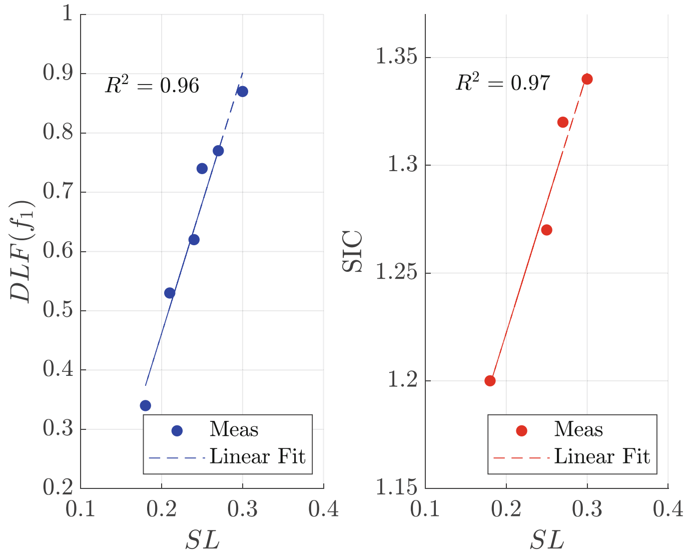

Fig. 10.6 Plot of *DLF(f1)* and SIC as a function of the synchronization level (*SL*), together with their linear regression line

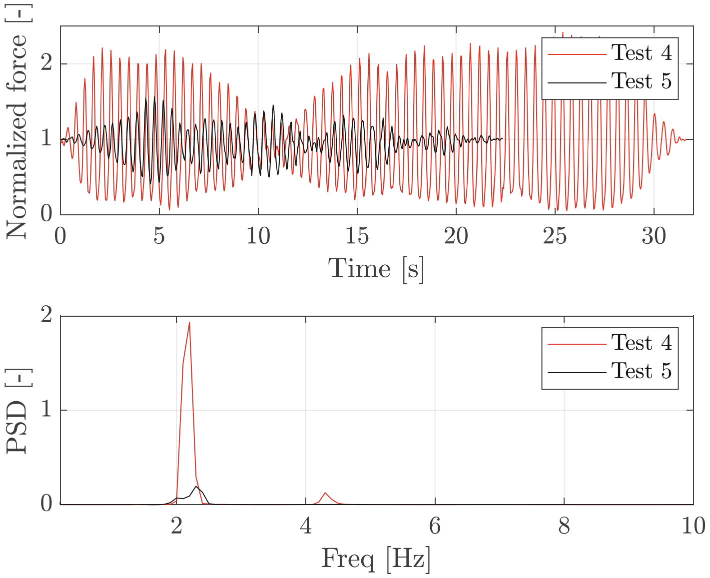

Fig. 10.7 Normalized crowd force time signal and its PSD representation for T4 and T5

10.5 Conclusions

This study deals with the application of a vision-based approach to estimate the crowd induced loading on civil structures. The technique has been validated in a realistic scenario like the G. Meazza stadium in Milan, where a group of 183 volunteers was asked to jump on a grandstand following the beat of both metronome and popular songs. The acquired movies have been processed with digital image correlation (DIC) to extract the people displacement, acceleration, and forces by summing up the contribution of the subset regions associated to the moving crowd. The measurement accuracy of the technique has been first assessed by comparing the DIC estimates with the accelerations measured by embedded smartphone sensors attached to the body of the jumping volunteers. A high correspondence between the two signals was found both in terms of general morphology and characteristics of the main harmonic components. Starting from the crowd forces extracted from the analysed tests, authors introduced two parameters to measure the level of people coordination and the severity of the induced-loads, referred to as synchronization level (*SL*) and dynamic load factor (*DLF*), respectively. As values obtained for these two parameters strongly reflected the actual behaviour of the crowd, they can be effectively used in the design and in the assessment of grandstand structures. Other tests will follow, aimed at improving the statistical relevance of the findings emerged from this paper.

Acknowledgements The work presented in this paper was partially supported by the PRIN grant 2017 – Lifelong optimized structural assessment and proactive maintenance with pervasive sensing techniques, sponsored by the Italian Ministry of University and Research (MIUR). Moreover, the authors want to thank all the test subjects for their contribution in the experimental activities.

References

1. Catbas, F.N., Celik, O., Avci, O., Abdeljaber, O., Gul, M., Do, N.T.: Sensing and monitoring for stadium structures: A review of recent advances and a forward look. Front. Built Environ. **3**(August), 1–18 (2017). https://doi.org/10.3389/fbuil.2017.00038
2. de Brito, V.L., Pimentel, R.L.: Cases of Collapse of Demountable Grandstands. J. Perform. Constr. Facil. **23**(3), 151–159 (2009). https://doi.org/10.1061/(ASCE)CF.1943-5509.0000006
3. IStructE Joint Working Group: Dynamic Performance Requirements for Permanent Grandstands Subject to Crowd Action. IStructE Ltd (2008)
4. Harrison, R.E., Yao, S., Wright, J.R., Pavic, A., Reynolds, P.: Human jumping and bobbing forces on flexible structures: Effect of structural properties. J. Eng. Mech. **134**(8), 663–675 (2008). https://doi.org/10.1061/(ASCE)0733-9399(2008)134:8(663)
5. Alexander, N.A., Macdonald, J.H.G., Champneys, A.R.: Numerical investigation of a simple model of human jumping on an oscillating structure. Procedia Eng. **199**(December), 2844–2849 (2017). https://doi.org/10.1016/j.proeng.2017.09.550
6. Fangliang, J., Wu, D.: A random crowd load model for human-induced vibration analysis. In: 2011 International Conference on Electric Technology and Civil Engineering (ICETCE), pp. 4751–4754. IEEE (April 2011). https://doi.org/10.1109/ICETCE.2011.5776407
7. Schreier, H., Orteu, J.-J., Sutton, M.A.: Image Correlation for Shape, Motion and Deformation Measurements. Springer US, Boston, MA (2009)
8. Parkhouse, J.G., Ewins, D.J.: Crowd-induced rhythmic loading. Proc. Inst. Civ. Eng. Struct. Build. **159**(5), 247–259 (2006). https://doi.org/10.1680/stbu.2006.159.5.247
9. Comer, A., Blakeborough, A., Williams, M.S.: Grandstand Simulator for Dynamic Human-Structure Interaction Experiments. Exp. Mech. **50**(6), 825–834 (2010). https://doi.org/10.1007/s11340-010-9334-6
10. Georgiou, L., Racic, V., Brownjohn, J.M.W., Elliot, M.T.: Coordination of Groups Jumping to Popular Music Beats, pp. 283–288. Springer International Publishing (2015)
11. Turrisi, S., Zappa, E., Cigada, A.: Experimental validation of a vision-based technique to estimate the crowd loading on stadium grandstands. IEEE Open J. Instrum. Meas. **1**, 1–12 (2022). https://doi.org/10.1109/OJIM.2022.3175255
12. Turrisi, S., Zappa, E., Cigada, A., Vivanco, M.R., Avin, N.C.: Effect of image acquisition and processing parameters on the estimation of crowd-induced dynamic loading on stadium grandstands. IEEE Instrum. Meas. Technol. Conf. (2021). https://doi.org/10.1109/I2MTC50364.2021.9460021
13. Mazzoleni, P., Zappa, E.: Vision-based estimation of vertical dynamic loading induced by jumping and bobbing crowds on civil structures. Mech. Syst. Signal Process. **33**, 1–12 (2012). https://doi.org/10.1016/j.ymssp.2012.06.009

Chapter 11
Human-Structural Dynamics Interfaces Using Augmented Reality

Fernando Moreu and Elijah Wyckoff

Abstract This chapter summarizes the work investigating the capability of interfacing human control of vibrations with a new interface between vibrations and humans. The area of interest is structural dynamics, especially in experimentation and structural health monitoring (SHM) methods. The researchers developed a new interface to enable that the inspector maintain awareness of test structures while observing sensor data and inputting control on real time. Sensor data does not collect other contextual information of critical value to the operator during the experiment, therefore the human needs to observe the experiment in person to better assess the actual behavior of the structure as well as to identify the quality of the test. The researchers developed a new augmented reality (AR) interface in the laboratory that can also be utilized in the field that shares the information of dynamics with the operators on real time and further investigated the effect of this interface in the controlling abilities of humans with and without this interface. The results include time domain and frequency domain comparisons, as well as future laboratory applications including sensor deployment and augmented robotic control.

Keywords Dynamics · Augmented reality · Human control · Sensor

11.1 Introduction

When monitoring structural responses, humans rely on their own senses to understand and evaluate the perceived response. Sensor networks are deployed to the structure to inform the human on data that they cannot collect with their senses alone. This introduces the main challenge of overcoming distraction. Monitoring data, controlling actuators and devices, interacting with robots, and monitoring structures divide the experimenter's attention. A review of AR technology found that humans receive between most information through vision [1]. According to that same study, the amount of information humans can receive and process is limited by their mental capacity, thus AR can help reduce the cognitive load. For example, AR has been applied to robot teleoperation to reduce gaze distraction by augmenting live video feed from the robot [2]. Instead of constricting the user's focus to one task, this example of AR allows the user to focus on information from the robot as well as control. The work demonstrated in this chapter uses AR technology in a head-mounted device (Microsoft Hololens 2) to consolidate information to reduce the human's cognitive load. The methodology of generating a new communication pipeline between sensors and humans and robots and humans is presented.

11.2 Results

Data visualization can be useful for research in detecting outliers, recognizing trends, etc., and in turn data visuals are important to understand results. Specific factors in visualization have been considered that have an effect on subjects' ability to understand and remember data and results. For example, color [3] and embellished visuals [4] have been proven to

---

F. Moreu (✉)
Department of Civil, Construction, and Environmental Engineering, University of New Mexico, Albuquerque, NM, USA
e-mail: fmoreu@unm.edu

E. Wyckoff
Department of Structural Engineering, University of California San Diego, La Jolla, CA, USA
e-mail: ewyckoff@ucsd.edu

H. Y. Noh et al. (eds.), *Dynamics of Civil Structures, Volume 2*, Conference Proceedings of the Society
for Experimental Mechanics Series, https://doi.org/10.1007/978-3-031-36663-5_11

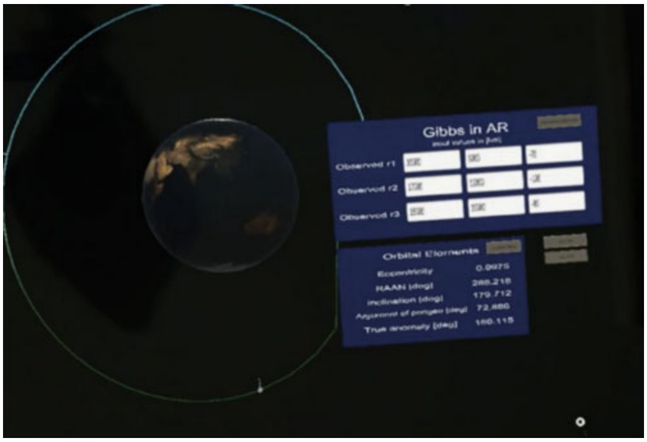

Eccentricity 0.0975
RAAN (deg) 288.218
Inclination (deg) 179.712
Argument of perigee (deg) 72.480
True anomaly (deg) 180.115

Fig. 11.1 AR application to plot satellite orbit

Fig. 11.2 Connection between an AR interface between human and robot

significantly increase a person's memory of the results or numbers communicated through visuals. As stated previously, one of AR's primary functions is visualization. Immersive technology in education is rapidly growing in application, and AR is an example of technology that is being increasingly applied to education to help students learn with positive results. This research applies AR to dynamics interfaces to help experimenters draw conclusions and make informed decisions. The first example of this is applied to satellite attitude. Shown in Fig. 11.1 is an application developed to plot Gibbs Method of orbit estimation to demonstrate satellite dynamics in orbit. This visualization tool is developed as a preliminary result.

This framework is applied to laboratory experimentation for feedback and control. Robots give an automation advantage through endurance and durability which can be coupled with human intuition and perception. Visualizing control components improves human cognition while allowing the human to observe the nearby environment, including the robot. Preliminary results are intended to establish communication between a 7DOF robot arm and an AR device, shown in Fig. 11.2. The robot runs pick-and-place commands based on the user's control.

From the established connection an advanced application is developed for modern robots. An application is developed to plot sensor data in the experimenter's view to give a full understanding of robot motion and the external environment. Communication between human and robot is established through a MySQL database read from the robot control application, where data is sent from the Hololens to the database. This interface is shown in Fig. 11.3.

11.3 Conclusion

This work considers the importance of a human-centered framework where SHM experimenters prefer to be present to make decisions rather than rely solely on artificial intelligence or other algorithms. The research solves a challenge with HCI where the experimenter faces gaze distraction when trying to monitor data and dynamic events. AR provides additional information via a head-mounted device, which allows the experimenter to continue to operate and observe the physical space without

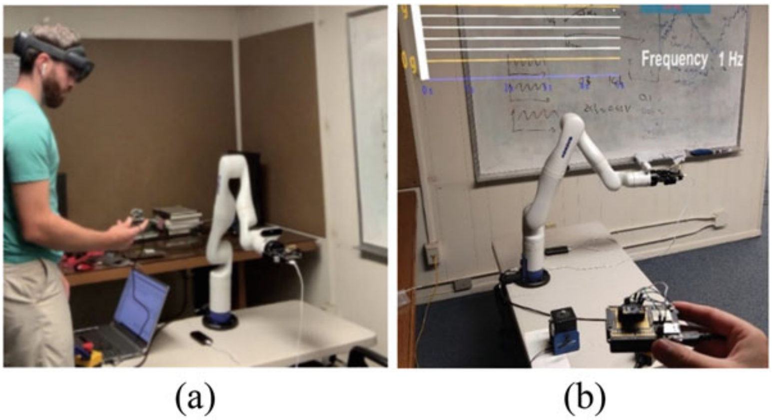

Fig. 11.3 (**a**) The user observes sensor data and the robot; (**b**) the AR interface plots sensor data and allows the user to set a frequency for robot movement

impedance. Visualization and control are considered as two primary areas of AR development. Preliminary results develop an application for better visualization of satellite dynamics in 3D space. The resultant applications provide AR users with a high level of understanding of sensor data and the environment, resulting in better informed decisions.

Acknowledgments The authors thank the support from the New Mexico Space Grant Consortium, Air Force Research Laboratory, New Mexico Consortium, the Federal Railroad Administration, the National Academy of Sciences, and the Department of Energy through a project in collaboration with Florida International University. We would like to thank the UNM Center for Advanced Research Computing, supported in part by the National Science Foundation, for providing the laboratory and testing resources used in this work.

References

1. Porter, M.E., Heppelmann, J.E.: A Manager's guide to augmented reality. Harvard Business Review, pp. 46–57. (2017). https://hbr.org/
2. Hedayati, H., Walker, M., Szafir, D.: Improving collocated robot teleoperation with augmented reality. In: Proceedings of the 2018 ACM/IEEE International Conference on Human-Robot Interaction. (2018). https://doi.org/10.1145/3171221.3171251
3. Kim, J.-I., Humphreys, G.W.: The interactive effects of colors on visual attention and working memory: in case of images of tourist attractions. Atten. Percept. Psychophys. **72**(6), 1533–1555 (2010). https://doi.org/10.3758/app.72.6.1533
4. Bateman, S., Mandryk, R.L., Gutwin, C., Genest, A., McDine, D., Brooks, C.: Useful junk? The effects of visual embellishment on comprehension and memorability of charts. In: Proceedings of the 28th International Conference on Human Factors in Computing Systems – CHI'10. (2010). https://doi.org/10.1145/1753326.1753716

Chapter 12
The Effects of an Extended Sensitivity Analysis of Sensor Configurations for Bridge Damage Detection Using Experimental Data

Gabriel A. del Pozo, Bjørn T. Svendsen, and Ole Øiseth

Abstract The damage detection capabilities of sensor setups are essential for any structural health monitoring (SHM) system. In this chapter, the performance of different subsets of sensor configurations selected from a set of 40 accelerometers is evaluated using metrics such as misclassification rate, false positive (FP), and false negative (FN) indications of damage. The subsets of sensor configurations are based on experimental data from a benchmark study that involved capturing the dynamic behavior of a full-scale steel bridge in undamaged and damaged conditions of the bridge. Several iterations with new subsets of decreasing size are generated by the elimination of random sensors. These subsets are then tested using Mahalanobis squared distance (MSD) as the novelty detection algorithm. Additionally, a manual selection of subsets is evaluated, where the sensors located farthest from the damages are eliminated. The results highlight the advantages of a dense sensor network and indicate a complex mechanism behind the damage detection capabilities of sensor networks with a clear trend of inverse proportionality between the sensor set size and FN indications of damage.

Keywords Structural health monitoring · Damage detection · Sensitivity analysis · Unsupervised learning · Sensor placement

12.1 Introduction

Structures close to reaching their design service life, such as a significant proportion of European bridges [1], require careful and continuous supervision to ensure safe usage. In the case of steel and composite steel-concrete bridges, one of the most common damage types is located in or below the bridge deck and is caused by fatigue [2, 3]. Human on-site inspection of this damage type can be complex because of visual obstructions and therefore be subject to human error. SHM can complement traditional periodic inspections of bridges by utilizing continuously measured data from the structure [4]. Vibration-based SHM utilizes time series, of the dynamic response of the structure, that are acquired using accelerometers or strain gauges. This data is used to calibrate finite element (FE) models or to construct statistical models, for model-based and data-based SHM, respectively.

The data-based SHM approach makes use of machine learning algorithms and statistical inference methods to identify damage by contrasting new data with a baseline statistical model [5]. This approach includes supervised learning and unsupervised learning, where labeled data of the damaged condition is available in the first one. In contrast, unsupervised learning relies exclusively on data from the undamaged condition. Labeled data for the damaged condition is seldom available when dealing with bridges and civil structures. Therefore, novelty detection algorithms in unsupervised learning are primarily used for bridges under operation. This has increased interest in applying the data-based SHM approach [6, 7].

This chapter is an extension of a sensitivity analysis based on unsupervised learning for bridge damage detection performed by Svendsen et al. [8]. In that work, a data-based SHM approach was applied using supervised and unsupervised machine learning algorithms on experimental data from the Hell Bridge Test Arena (HBTA). The HBTA is a steel riveted truss bridge that was moved to a test site after several years of operation and now serves as a full-scale damage detection test structure. Data was obtained through an extensive experimental study where the HBTA was subjected to dynamic excitation under different structural state conditions. The bridge was excited using a modal vibration shaker, and two groups of accelerometers captured the dynamic response of the structure. The first group consisted of 18 tri-axial accelerometers

---

G. A. del Pozo (✉) · B. T. Svendsen · O. Øiseth
Department of Structural Engineering, Norwegian University of Science and Technology, Trondheim, Norway
e-mail: gabriel.a.d.p.alarcon@ntnu.no

H. Y. Noh et al. (eds.), *Dynamics of Civil Structures, Volume 2*, Conference Proceedings of the Society for Experimental Mechanics Series, https://doi.org/10.1007/978-3-031-36663-5_12

located along the vertical walls of the bridge. The second group consisted of a large set of 40 single-axis accelerometers. Autoregressive (AR) coefficients [9], generated from the time series of the second group of accelerometers, were selected as damage-sensitive features. The AR coefficients for the complete set of 40 accelerometers comprise the entire dataset. The AR coefficients were given as input into the Mahalanobis squared distance (MSD) algorithm to identify damage when the algorithm was tested on data obtained from the damaged states. The damage detection capabilities of this classifier were evaluated using false positive (FP) indications of damage, false negative (FN) indications of damage, and total misclassification rate as performance metrics. These metrics were established and compared in the sensitivity analysis for subsets with fewer sensors.

The outline of the chapter is as follows. First, a description of the experimental study with details of the structural system, imposed damage, sensor network, and a description of the damage detection algorithm is provided. The following two sections describe the sensitivity analysis procedure and present the corresponding results. Finally, the results are discussed, and conclusions are presented.

12.2 Experimental Study and Feature Extraction

The HBTA, shown in Fig. 12.1, is an open-deck steel railway truss bridge. The bridge consists of two vertical walls, a deck, and lateral bracing located below the deck. After more than 100 years of operation, the bridge was moved to a test facility in Hell, Norway. The length of the bridge is 35 m, and the width of the bridge is 4.5 m. The bridge serves as a full-scale experimental test bridge for damage detection and SHM [10].

The structural system, shown in Fig. 12.2a, is composed of stringers a–d, with cross beams between them with labeled 1′–10′. The sleepers are supported by floor beams, identified with labels 1–11. These floor beams are connected to the vertical walls labeled A and B. The lateral bracing of the structure is connected to the lower chords of these walls.

An extensive experimental campaign has been carried out in the HBTA. The structure was excited by a modal vibration shaker in both damaged and undamaged conditions. The modal vibration shaker was configured to provide white noise as load, while the bridge response was recorded using 40 single-axis accelerometers (Dytran 3055D3) located below the bridge deck. The accelerometers were distributed along and across the bridge deck, as shown in Fig. 12.2a.

Table 12.1 describes the different damaged and undamaged conditions in which the structure was excited while recording its response. Figure 12.2b and c indicate the location of the eight damage states. These damage states were imposed on different connections and were introduced by temporally removing all the bolts of these connections. Four different damage types were selected: stringer-to-floor beam connections (DS 1 and 2), stringer cross beams (DS 3 and 4), lateral bracing connections (DS 5–7), and connections between floor beams and main load-carrying members (DS 8). The two undamaged states considered the baseline condition correspond to the undamaged condition, i.e., before any damage is imposed and after repairing the damage. Eighty sets of acceleration time series were obtained for each state condition adding up to 800 instances. Additional documentation of the data acquisition system, signal processing, and experimental conditions is available in [11].

AR parameters are selected to characterize the acceleration time series as damage-sensitive features such as done in previous studies [12, 13]. An AR model utilizes past data points of a time series to obtain the present data point. The quantity of past data points used by the model is the order of the model. The p-order autoregressive model ($AR(p)$) for a given time series is defined as [9]

Fig. 12.1 The Hell Bridge Test Arena

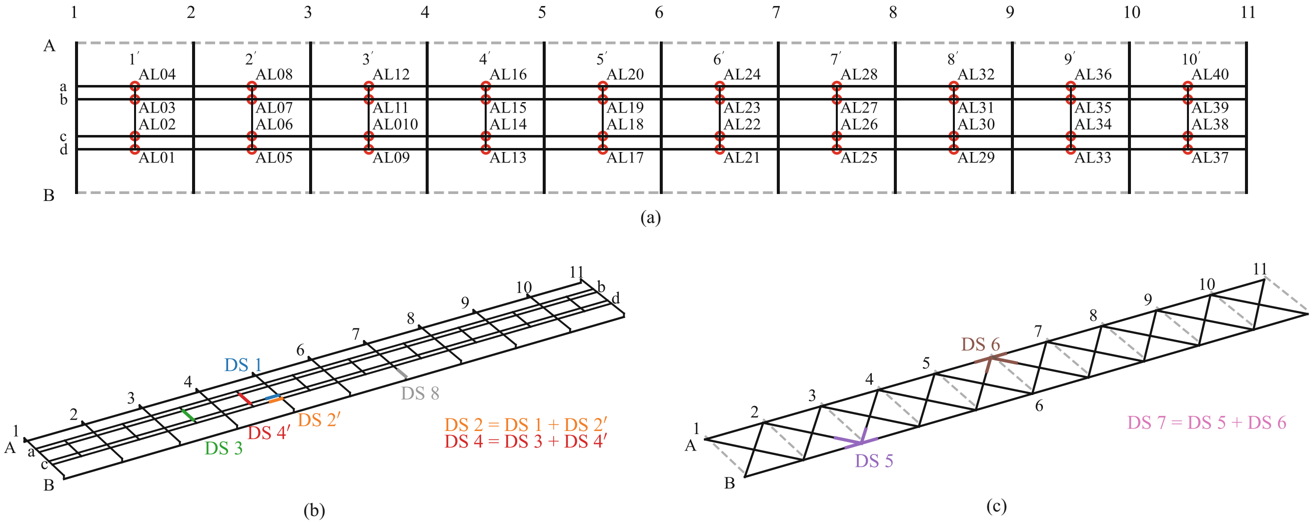

Fig. 12.2 Overview of the experimental conditions. (**a**) Location and numbering of accelerometers on the bridge deck. (**b**) Damage locations on bridge deck. (**c**) Damage locations on the lateral bracing

Table 12.1 Overview of the states of the structure during the experiment

Label	State condition	Type	Description
UDS 1	Undamaged	Baseline condition	Before all damage state conditions
UDS 2	Undamaged	Baseline condition	After all damage state conditions
DS 1	Damaged	Stringer-to-floor beam connection	Single connection damaged
DS 2	Damaged	Stringer-to-floor beam connection	Multiple connections damaged
DS 3	Damaged	Stringer cross beam	Main part of single cross beam removed
DS 4	Damaged	Stringer cross beam	Main parts of multiple cross beams removed
DS 5	Damaged	Lateral bracing connection	Single connection damaged
DS 6	Damaged	Lateral bracing connection	Single connection damaged
DS 7	Damaged	Lateral bracing connection	Multiple connections damaged
DS 8	Damaged	Connection between floor beam and main load-carrying member	Single connection damaged

$$y_t = \sum_{j=1}^{p} \phi_j y_{t-j} + \varepsilon_t$$

where y_t and y_{t-j} are the data points at indexes t and $t-j$, ϕ_j is the autoregressive parameter j, and ε_t corresponds to the residual of the model at index t. An AR(5) model is selected and each accelerometer time series is characterized by five coefficients. This leads to 200 features per instance. The complete set of AR coefficients becomes a matrix with 800 rows and 200 columns, where each row corresponds to a specific structural state and each column to an AR coefficient for a specific sensor. This matrix is divided for training and testing, and the MSD algorithm is applied to obtain damage indices (DIs). These DIs are the numerical values of the MSD, which indicate the distance between point z_i and the mean $\overline{x}$ of a sample distribution, given by:

$$DI_i = (z_i - \overline{x})\, C^{-1} (z_i - \overline{x})^T$$

where C is the covariance matrix. C and $\overline{x}$ are obtained from the training matrix.

The approach to define the threshold, which separates damaged behavior from baseline behavior for a 99% confidence, is based on Monte Carlo simulations according to Worden et al. [14].

12.3 Sensitivity Analysis

Figure 12.3 presents the adopted methodology for the sensitivity analysis, which is based on the iterative generation of subsets via the elimination of one random sensor at a time. This analysis requires the definition of the number of iterations. An iteration starts with the complete set of 40 sensors and reduces to 1 sensor. This is achieved through 39 eliminations, each of a randomly chosen sensor. After each elimination, the columns of the AR coefficient matrix corresponding to the eliminated sensor are deleted, and the classifier is applied to this new feature matrix.

The sensitivity analysis process starts with loading the complete set of AR coefficients, an 800 × 200 matrix. The iteration loop is started; within this loop, a nested random elimination loop is used to apply the MSD classifier to each new feature matrix. The results of this classifier are evaluated by FP indications of damage, FN indications of damage, and total misclassification rate for each elimination. These metrics and the sensor labels for each elimination are saved before starting a new iteration. After a desired number of iterations are completed, all the accumulated results of FP indications of damage, FN indications of damage, and total misclassification rate for different subset sizes are collected and compared. In addition to the procedure shown in Fig. 12.3, one manual iteration was performed where the subset selection was based on its proximity to the damage locations. This analysis allows observing the influence of the number of sensors on the performance metrics. Additionally, the results present a range of values that these metrics yield for different subsets with an equal number of sensors.

12.4 Results

The performance metrics of different subsets of sensor configurations selected from a full set of 40 accelerometers are presented in this section. Figure 12.4 shows the relationship between the number of sensors and FP indications of damage, FN indications of damage, and total misclassification rate. The figures include a shaded range of results for different numbers of iterations. The lower bounds of this range, plotted with dash-dotted lines, correspond to best performance metrics whereas the upper bounds, plotted with dashed lines, correspond to worst performance metrics. The results obtained from the manual selection of sensors, which lie between the bounds as expected, are included with continuous red lines.

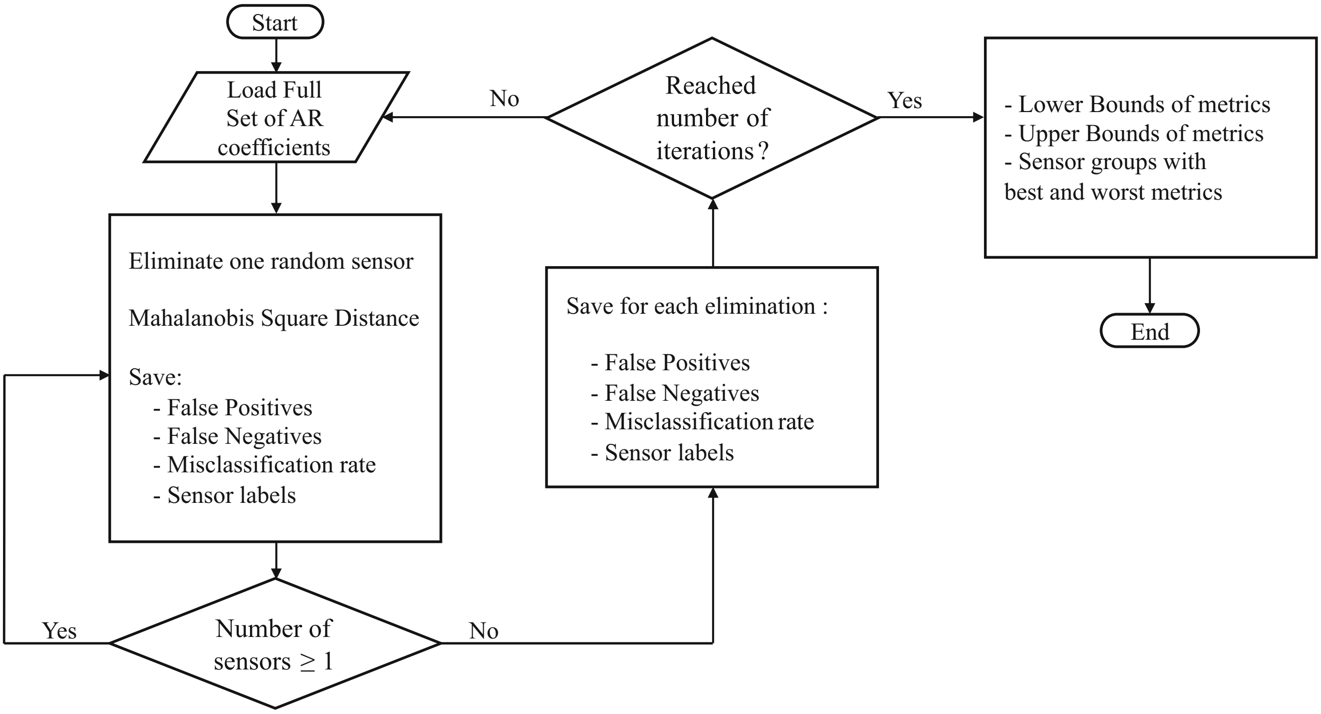

Fig. 12.3 Sensitivity analysis flowchart

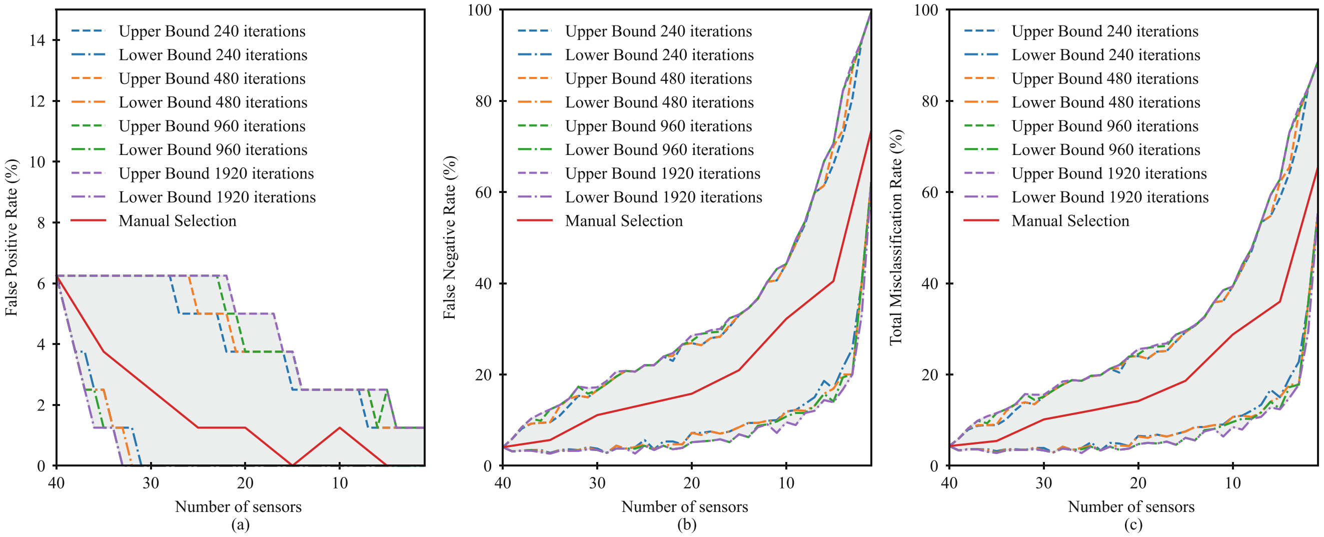

Fig. 12.4 Performance metrics for different subset sizes. (**a**) FP rate. (**b**) FN rate (**c**) total misclassification rate

Table 12.2 Damage detection metrics of lower, upper, and manual selection subsets for different number of sensors

Number of sensors	Error					
	FP rate		FN rate		Misclassification rate	
	Lower bound	Upper bound	Lower bound	Upper bound	Lower bound	Upper bound
40[a]	6.3%		4.1%		4.3%	
35	1.3%	6.3%	3.8%	9.7%	3.8%	9.3%
30	0.0%	6.3%	3.4%	17.2%	3.3%	15.6%
25	0.0%	6.3%	4.4%	22.0%	4.2%	19.7%
20	0.0%	5.0%	5.2%	28.6%	4.7%	25.6%
15	0.0%	3.8%	6.9%	33.1%	6.1%	29.6%
10	0.0%	2.5%	9.5%	44.2%	8.5%	39.3%
5	0.0%	2.5%	13.9%	70.6%	12.4%	62.8%

[a] A single FP rate, FN rate, and misclassification rate are obtained for 40 sensors since it is the complete set

The results from Fig. 12.4 are summarized in Table 12.2, where the lower and upper bounds of FP indications of damage, FN indications of damage, and total misclassification rate for different number of sensors after 1920 iterations are presented.

The DIs and ROC curves for the best and worst-performing subsets with 30, 20, and 10 sensors are shown in Fig. 12.5. The DI plots show the numerical values of the MSD for different structural states and display the statistical threshold with dashed horizontal black lines. Receiver operating characteristic (ROC) curves, which are obtained by varying the threshold value, show the relationship between true positive rate (TPR) and false positive rate (FPR).

Figure 12.6 shows the best 25-sensor configuration and compares the DIs and ROC curves of this subset with the complete set of 40 sensors.

12.5 Discussion

The results of the sensitivity analysis show convergence in the lower and upper bounds of the metrics as the number of iterations increases. This convergence establishes the confidence intervals shown as the shaded areas in Fig. 12.4. Increasing FN indications of damage and decreasing FP indications of damage are observed as the number of sensors is reduced. Furthermore, the total misclassification rates increase as fewer sensors are used. Thus, indicating the advantage of a dense sensor network.

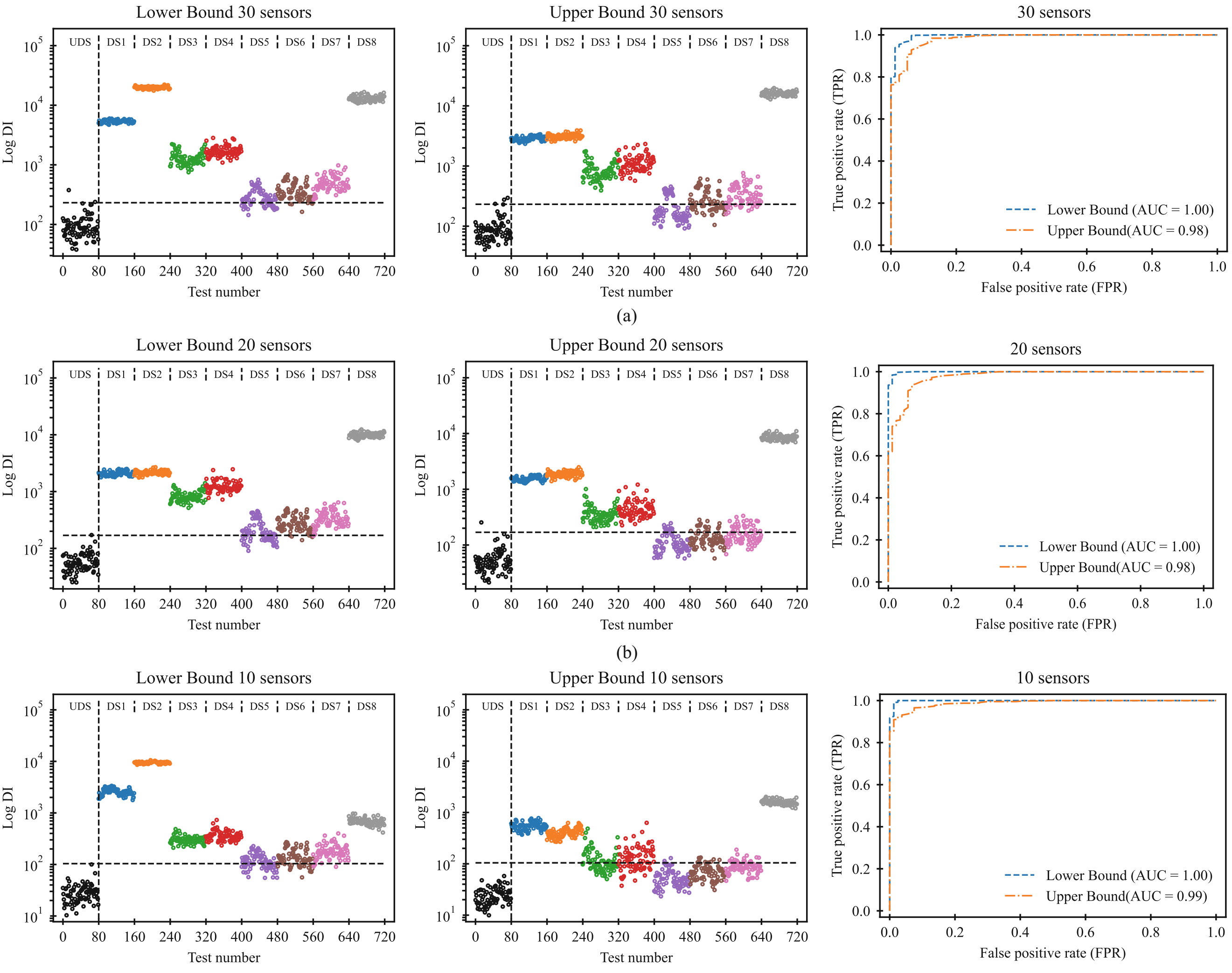

(a)

(b)

(c)

Fig. 12.5 Damage indices (DIs) by MSD and corresponding ROC curves for lower and upper bounds. (**a**) 30 sensors. (**b**) 20 sensors. (**c**) 10 sensors

Concerning the total misclassification rate, the lower bound of the confidence interval indicates that similar results as for the full set of sensors can be obtained with smaller subsets of specific sensor configurations. However, as shown by the manual iteration, the selection of these subsets is not straightforward and is not solely related to their sensors being close to the damage. Furthermore, the upper bound steep increase, as fewer sensors are considered, shows the risk of substantial information loss when trying to limit the number of sensors. The similar trend between the total misclassification rate and FN indications of damage could be due to the number of instances corresponding to the damaged states compared to the undamaged state. As shown in the DI plots, 640 out of 720 tests involve obtaining the MSD of AR coefficients for the damaged state of the bridge.

The DIs plots in Fig. 12.5 show that DIs below the confidence threshold, FN indications of damage, are characteristic of upper bound sensor subsets. These FN indications of damage correspond to DS 5–7 for sensor sets with 20 and 30 sensors. The worst performing subset of 10 sensors yields FN indications of damage from DS 3–4 in addition to DS 5–7. The intuitive reasoning that single-axis sensors measuring vertical acceleration are not very suitable for detecting damage types that influence a change in the horizontal displacement of the bridge, such as DS 5–7, is confirmed. The ROC curves of the lower bound subsets in Fig. 12.5 are all very similar whereas the ROC curves of the upper bound subsets show an unexpected enhancement as fewer sensors are used. The DIs of the undamaged state tend to be closer between them as the subset number of sensors is reduced. This proportionality between the number of sensors and the scattering of the DIs of the undamaged state could partially explain the lower bound sensor ROC curves change as the subset size is diminished. Therefore, when

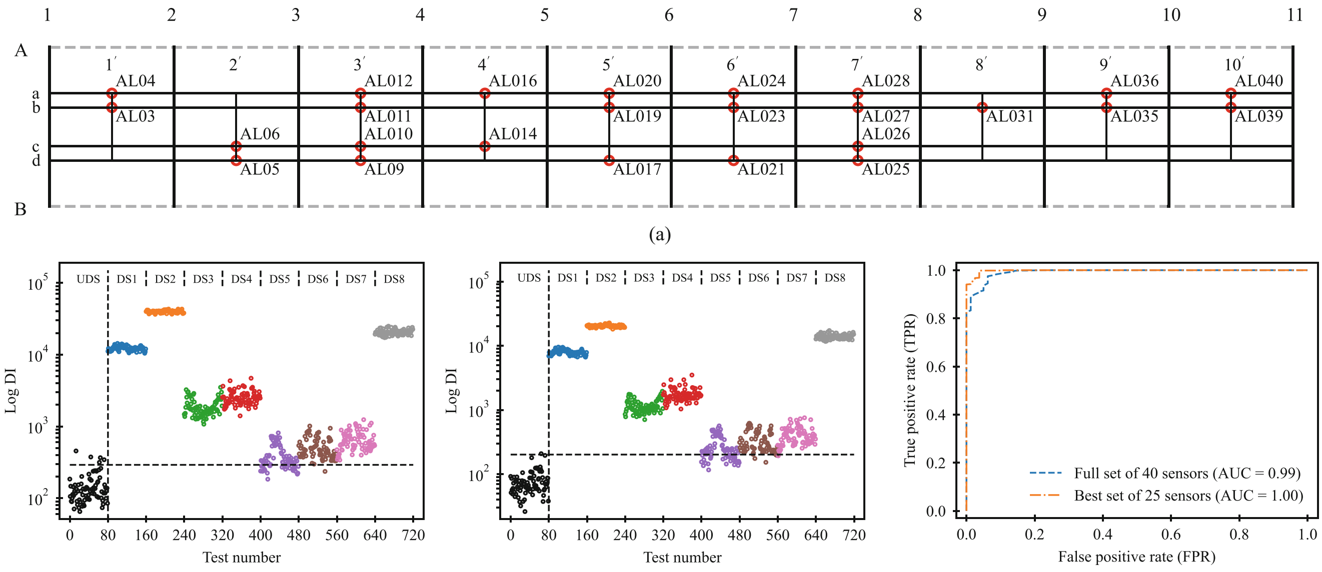

(a)

(b)

(c)

(d)

Fig. 12.6 Comparison between full set and best 25 sensors subset. (**a**) Best 25 sensors configuration, (**b**) damage Indices by MSD for the full set of 40 sensors, (**c**) damage Indices by MSD for the best subset of 25 sensors. (**d**) Corresponding ROC curves

considering the effects of reducing sensors, the performance metrics, such as the total misclassification rate, provide much clearer results in this study than the ROC curves.

The best subset of 25 sensors and the full set yield similar damage detection metrics. Likewise, the DIs and ROC curves in Fig. 12.6 show the same capacity to differentiate damage types and structural states. This observation implies that for a particular structural system, in addition to given damage types and locations, a specific combination of sensors from all possible sensor locations carries the most significant portion of the information required to detect these damage types. One of the main challenges in selecting this specific sensor configuration lies in the uncertainty of the damage locations and types. This sensitivity analysis does not introduce this variability since damage types, locations, and severities are known and constant.

12.6 Conclusion

This chapter aims to understand the effects of the selection of subsets of sensor configurations on the damage detection capabilities of a classifier based on AR coefficients. This was done by utilizing data from an extensive experimental study and extending the sensitivity analysis performed in a previous study. The results of the work highlight the advantages of a dense sensor network and indicate a complex mechanism behind the damage detection capabilities of sensor networks which involves (1) the structural system, (2) changes in the system imposed by location and type of damage, (3) location of sensors, and (4) number of sensors.

Acknowledgments The authors would like to acknowledge the Norwegian Railway Directorate for funding the project.

References

1. Olofsson, I., et al.: Assessment of European railway bridges for future traffic demands and longer lives – EC project ‘Sustainable Bridges’. Struct. Infrastruct. Eng. **1**(2), 93–100 (2005). https://doi.org/10.1080/15732470412331289396
2. Haghani, R., Al-Emrani, M., Heshmati, M.: Fatigue-prone details in steel bridges. Buildings. **2**(4), 456–476 (2012). https://doi.org/10.3390/buildings2040456
3. Skoglund, O.: Understanding distortion induced fatigue. KTH, Stockholm (2021)
4. Wenzel, H.: Health Monitoring of Bridges. Wiley, Vienna (2009)

5. Farrar, C.R., Worden, K.: Structural Health Monitoring: A Machine Learning Perspective. John Wiley & Sons (2012)
6. Maes, K., Van Meerbeeck, L., Reynders, E., Lombaert, G.: Validation of vibration-based structural health monitoring on retrofitted railway bridge KW51. Mech. Syst. Signal Process. **165**(September 2021), 108380 (2022). https://doi.org/10.1016/j.ymssp.2021.108380
7. Avci, O., Abdeljaber, O., Kiranyaz, S., Hussein, M., Gabbouj, M., Inman, D.J.: A review of vibration-based damage detection in civil structures: From traditional methods to Machine Learning and Deep Learning applications. Mech. Syst. Signal Process. **147**, 107077 (2021). https://doi.org/10.1016/j.ymssp.2020.107077
8. Svendsen, B.T., Frøseth, G.T., Øiseth, O., Rønnquist, A.: A data-based structural health monitoring approach for damage detection in steel bridges using experimental data. J. Civ. Struct. Heal. Monit. **12**(1), 101–115 (2022). https://doi.org/10.1007/s13349-021-00530-8
9. Box, G., Jenkins, G., Reinsel, G.C.: Time Series Analysis: Forecasting and Control. John Wiley & Sons, Hoboken (2008)
10. Svendsen, B.T., Øiseth, O., Frøseth, G.T., Rønnquist, A.: A hybrid structural health monitoring approach for damage detection in steel bridges under simulated environmental conditions using numerical and experimental data. Struct. Health Monit. **22**(1), 540–561 (2023). https://doi.org/10.1177/14759217221098998
11. Svendsen, B.T., Petersen, Ø.W., Frøseth, G.T., Rønnquist, A.: Improved finite element model updating of a full-scale steel bridge using sensitivity analysis. Struct. Infrastruct. Eng. **19**(3), 315–331 (2022). https://doi.org/10.1080/15732479.2021.1944227
12. Figueiredo, E., Figueiras, J., Park, G., Farrar, C.R., Worden, K.: Influence of the autoregressive model order on damage detection. Comput. Civ. Infrastruct. Eng. **26**(3), 225–238 (2011). https://doi.org/10.1111/j.1467-8667.2010.00685.x
13. Azim, M.R., Gül, M.: Damage detection of steel girder railway bridges utilizing operational vibration response. Struct. Control. Health Monit. **26**(11), 1–15 (2019). https://doi.org/10.1002/stc.2447
14. Worden, K., Manson, G., Fieller, N.R.J.: Damage detection using outlier analysis. J. Sound Vib. **229**(3), 647–667 (2000). https://doi.org/10.1006/jsvi.1999.2514

Chapter 13

Localization of Structural Damage Based on First Passage Times for a Pre-stressed Steel Strip

K. Theunissen, E. Verstraelen, J.-C. Golinval, and V. Denoël

Abstract First passage time (FPT) maps and histograms of FPT are known to be capable of detecting slight deliberately operated structural changes in a steel strip. In this chapter, the question of the localization of the damage is tackled. It is studied by comparing the predictions of a 2-D updated finite-element model and the observed experimental results. We numerically simulated various damage scenarios by modifying the damage location until a good match of FPT histograms was found with the experimental investigations of virtually damaged structures. The detection and localization process was proven to be successful, and we attribute it to the large sensitivity of the FPT maps and histograms to slight changes in the model.

Keywords Health monitoring · Detection change · Ageing · Finite-element updating · Damage localization

13.1 Introduction

In structural health monitoring, damage can be localized by directly using modal parameters such as eigenfrequencies [1] and mode shapes obtained from experimental data [2] or by comparing those parameters to modal parameters that come from a numerical model [3]. In our case, we used the concept of first passage time (FPT) and their histograms in order to detect and to localize damage. The concept of FPT map was first introduced in [4, 5] and applied to an experimental model of a tower crane in a wind tunnel in [6]. In this chapter, the studied structure is a steel strip whose damage has been deliberately materialized by placing a small cubic magnet on the structure. In a previous work of the authors [7], it has been shown that FPT maps and histograms can be used to detect damage. The question tackled here is to localize it. To this aim, a numerical model has been updated and is used to compare numerical and experimental results until a good agreement is observed on FPT maps and histograms.

K. Theunissen (✉)
Structural & Stochastic Dynamics, University of Liège, Liège, Belgium

F.R.S.-FNRS, National Fund for Scientific Research, Bruxelles, Belgium
e-mail: kevin.theunissen@uliege.be

E. Verstraelen
V2i S.A., Angleur, Belgium
e-mail: e.verstraelen@v2i.be

J.-C. Golinval
Department of Aerospace & Mechanics, University of Liège, Liège, Belgium
e-mail: JC.Golinval@uliege.be

V. Denoël
Structural & Stochastic Dynamics, University of Liège, Liège, Belgium
e-mail: v.denoel@uliege.be

H. Y. Noh et al. (eds.), *Dynamics of Civil Structures, Volume 2*, Conference Proceedings of the Society
for Experimental Mechanics Series, https://doi.org/10.1007/978-3-031-36663-5_13

13.2 Modal Identification and Numerical Model

The experimental setup is made of a steel strip, a horizontal shaker (TV 50009), and a polytech laser transducer as shown in Fig. 13.1a and is the same as in [8]. The modal identification has been achieved by using a white band-limited noise in the range [3; 200] Hz. The first six bending modes have been identified as in [8]. Then, the numerical model has been updated until a good match was observed for the eigenfrequencies and the mode shapes. The updated parameters of the model include the rotational constraints at supports, Young's modulus, and geometrical and mechanical modeling of the shaker and impedance head. The Bayesian model updating was performed with the Metropolis–Hastings algorithm that returns credible intervals for the model parameters.

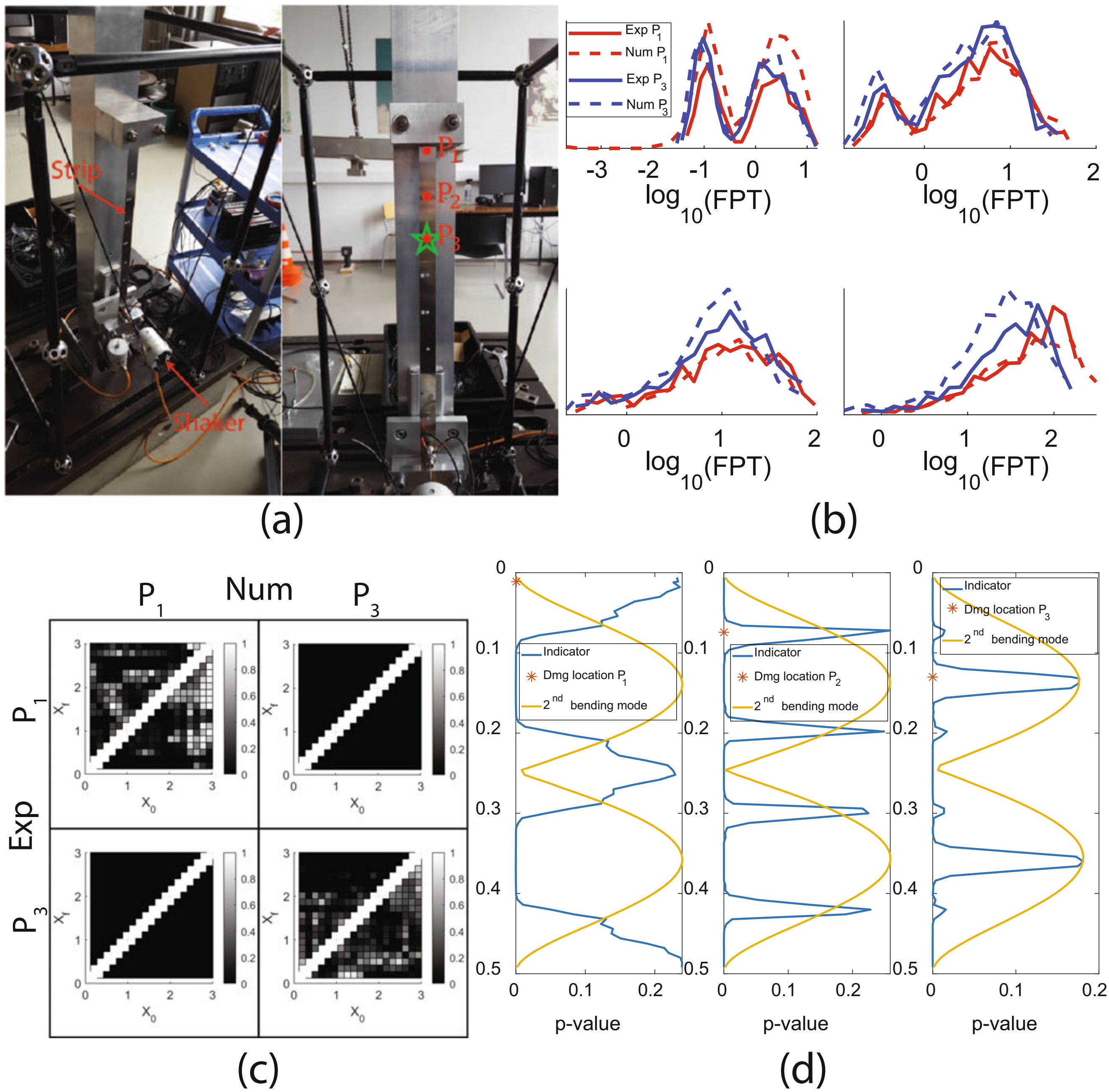

Fig. 13.1 (**a**) Experimental setup, (**b**) histograms of FPT at four different locations on the FPT map, (**c**) p-values from Kolmogorov–Smirnov test when the magnet is at P_1 and P_3, and (**d**) localization of the damage based on the average of p-values as an indicator for each magnet location

13.3 Damage Localization

In order to simulate damage on the steel strip, a small cubic magnet has been placed at three different locations called P_1, P_2, and P_3 as shown in Fig. 13.1a. The structure has been excited by a white band-limited noise whose frequency content is in the range of the second bending mode. The structure velocity has been measured by a laser at location P_3 represented as the green star in Fig. 13.1a. Then, the response of the numerical model has been computed by placing the magnet at each of the 85 nodes of the FE model. FPT histograms are derived from the experimental and numerical data. In Fig. 13.1b, four histograms of the FPT at four different locations on the FPT map are represented; each of them is given in the configuration where the magnet is at location P_1 or P_3. Good agreement can be observed for the same magnet location. In order to compare those histograms, the Kolmogorov–Smirnov test has been used, and for each combination of histograms, a p-value can be obtained. In Fig. 13.1c, four p-value maps are therefore shown, combining two numerical histograms and two experimental ones. It can be observed that greater p-values are located inside the map when the magnet is at the same location, while p-values are closer to zero when this is not the case. This gives us great confidence in using p-values as an indicator for damage location. With this in mind, we used the average p-value of the whole maps as an indicator of the likeliness of similarity in damage scenarios between the actual experimentally observed damage and the numerically simulated ones. In Fig. 13.1d, this similarity indicator is represented for three different experimental tests where the damage was localized at points P_1, P_2, and P_3, respectively. The use of the average p-value on the maps provides very satisfactory results. Indeed, when the magnet is close to the support (damage is difficult to detect), the proposed method concludes that the most probable positions of the damage are close to the supports or to the mid-span. In other words, by placing the magnet close to the supports or in the middle of the beam, the average p-value is very similar since the histograms of FPTs on the maps are very similar. When the magnet is at locations P_2 and P_3, the idea is more or less the same. For P_2, four different locations are identified, which results from the symmetry of the second bending mode. For P_3, the magnet is located on the maximum value of the second bending mode, and therefore, two locations are identified.

13.4 Conclusion

P-values from FPT histograms show good results for damage localization. In order to improve the results, two different bending modes could be used to reduce the number of identified regions as potential damage location such as the second and third bending modes.

Acknowledgment K. Theunissen has been supported by the Belgian Fund for Scientific Research.

References

1. Kraemer, P., Friedmann, H., Ebert, C., Mahowald, J., Wölfel, B.: Experimental validation of stochastic subspace algorithms for structural health monitoring of offshore wind turbine towers and foundations. In: Proceedings of the 8th European Workshop on Structural Health Monitoring, Bilbao, Spain (2016)
2. Roy, K., Ray-Chaudhuri, S.: Fundamental mode shape and its derivatives in structural damage localization. J. Sound Vibr. **332**(21), 5584–5593 (2013)
3. Markogiannaki, O., Arailopoulos, A., Giagopoulos, D., Papadimitriou, C.: Vibration-based damage localization and quantification framework of large-scale truss structures. Struct. Health Monitor. **22**(2), 1376–1398 (2023)
4. Vanvinckenroye, H., Denoël, V.: Average first-passage time of a quasi-Hamiltonian Mathieu oscillator with parametric and forcing excitations. J. Sound Vibrat. **406**, 328–345 (2017)
5. Vanvinckenroye, H., Denoël, V.: Second-order moment of the first passage time of a quasi-Hamiltonian oscillator with stochastic parametric and forcing excitations. J. Sound Vibrat. **427**, 178–187 (2018)
6. Vanvinckenroye, H., Andrianne, T., Denoël, V.: First passage time as an analysis tool in experimental wind engineering. J. Wind Eng. Ind. Aerodyn. **177**, 366–375 (2018)
7. Theunissen, K., Verstraelen, E., Golinval, J.-C., Denoël, V.: "Influence of structural damages on first passage time maps. In: ISMA-USD Noise and Vibration Engineering Conference 2022 (2022)
8. Delhez, E., Vanvinckenroye, H., Golinval, J.-C., Denoël, V.: Numerical and experimental study of first passage time of a steel strip subjected to forced and parametric excitations. In: ISMA-USD Noise and Vibration Engineering Conference 2018 (2018)

Chapter 14
Experimental Vibration Analysis on the Rykkjem Ferry Dock During Ferry Berthing

Bartosz Siedziako, Aksel Fenerci, and Torodd Skjerve Nord

Abstract This chapter presents results from measurements on the Rykkjem ferry dock in Møre and Romsdal county in Norway. The study was conducted as a part of a bigger project that aims to examine the resilience of critical coastal infrastructure when exposed to extreme events. The work presented herein includes a qualitative assessment of recorded time series and describes results from the modal analysis. It is further discussed how long-term monitoring of the existing ferry docks can improve understanding of underlying dynamics, ferry-induced loads and ongoing deterioration processes for ferry dock bridges and as a result of that, improve design safety and the economic aspects when it comes to maintaining this critical part of infrastructure.

Keywords Ferry Quay · Monitoring · Modal analysis · Ferry Dock Bridge · Experimental vibration analysis

14.1 Introduction

Ferry docks together with bridges are part of the critical infrastructure that makes it possible to establish connections between two destination points separated by a large body of water. For coastal nations with the majority of the population living by the sea, ferries and bridges are an indispensable part of almost any travel. One of such nations is Norway with its famous landscapes that often present a serious challenge when it comes to planning, building, and maintaining infrastructure. Although, the Norwegian government launched in recent years the Ferry-free coastal route project [1] with a goal of replacing many of the most important ferry connections with bridges, it is unlikely that it is going to be realized in its original form. Despite the recent advances in bridge engineering and new bridge concepts [2–4], not all ferry connections can be replaced and therefore, they will continue to serve as critical connections in Norway that provide efficient means of transportation for local communities and industries. In addition, the importance of those structures can be considered to increase with time as the number of vehicles transported by the ferries has doubled in recent [5] decades – see Fig. 14.1.

Møre and Romsdal, where the research was conducted, is a county that contributes the most to the numbers shown in the Fig. 14.1 [5]. The county has a population of 265.000, an area of 14.300 km^2, and over 50 ferry docks in active use that needs to be regularly inspected and maintained. Some of them are part of the E39 road – the main economical artery in Norway. It is therefore difficult to overestimate the importance of ferry docks from both local and global perspectives. A potential failure or closure of one ferry dock can lead to substantial economic losses and massive delays, as one has to often drive far inland along the Norwegian fjords, or put a strain on smaller, surrounding road systems that were designed to accommodate traffic expected on the national highway.

In recent years, the attention of scholars in Norway was put on various aspects of ferry operation rather than coastal infrastructure enabling safe docking. Several researchers have tried to provide input on issues related to ferry placement and waiting times [6–8], examine the effect of electrification of ferries in Norway [9], and improve autonomous operations [10–12]. However, little to no research has been made to improve understanding of underlying dynamics, loading conditions, and deterioration processes that ferry docks undergo, despite that recent study have shown that they are prone to frequent and severe damages [13]. When taking into account that many of the ferry docks approach their design life [14] of 50 years (Fig. 14.2), it becomes crucial to understand how those structures perform. From Fig. 14.2, it can also be deduced that many

---

B. Siedziako (✉) · A. Fenerci · T. S. Nord
Department of Ocean Operations and Civil Engineering, Faculty of Engineering, University of Norwegian Science and Technology,Ålesund, Norway
e-mail: bartosz.siedziako@ntnu.no

H. Y. Noh et al. (eds.), *Dynamics of Civil Structures, Volume 2*, Conference Proceedings of the Society
for Experimental Mechanics Series, https://doi.org/10.1007/978-3-031-36663-5_14

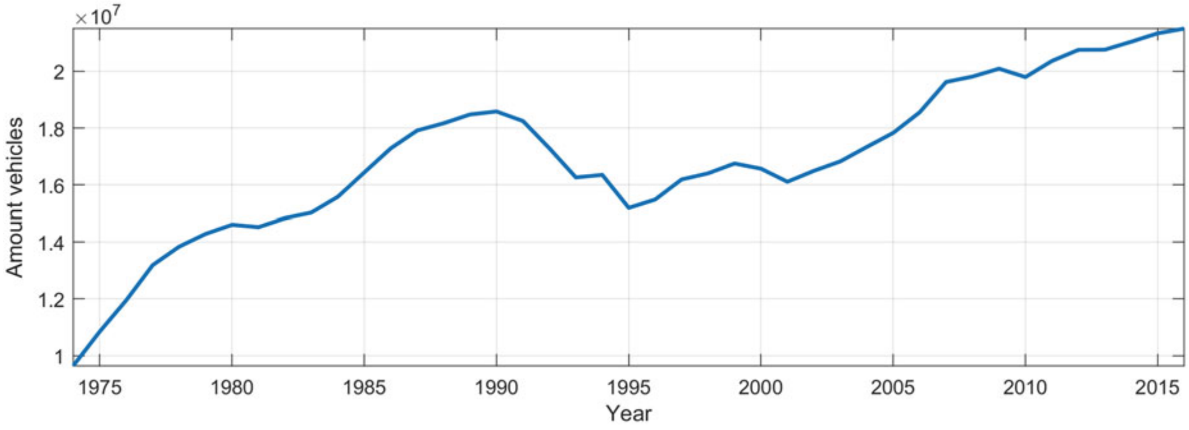

Fig. 14.1 Historical development in ferry traffic in Norway between 1974 and 2016

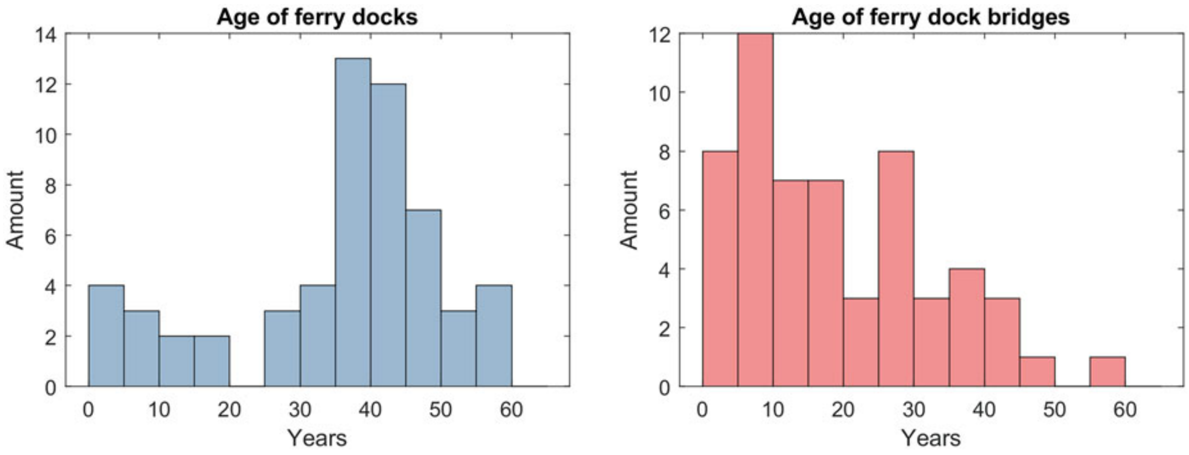

Fig. 14.2 Age statistics for actively used vehicle-carrying ferry docks in Møre and Romsdal county

of the ferry dock bridges, that are drivable platform connecting ferry and quay, needed replacement before they reach their design life. It is another reason of urgency to investigate those structures.

This chapter presents lessons learned from measurements on the Rykkjem ferry dock and provides insight into potential benefits coming from long-term monitoring of such structures. Firstly, a description of the monitoring system and analysis of time series will be given. Secondly the results from modal analysis will be presented. Obtained results indicate that measurements taken at the site can be helpful in evaluation of two design loads that are caused by a ferry, namely impact load and forced rotation at the bridge front [15]. Further it has been shown that the modal analysis can be used to examine ferry bridge dynamics and changes in the structural behavior caused by ferry docking.

14.2 Case Study: Rykkjem Ferry Dock

Rykkjem ferry dock was selected for this study. This selection is based on the fact it will be a subject of retrofitting to accommodate a new charging tower for electric ferries as the authors and local authorities want to investigate how mounting of such a colossal object will affect the dynamic behavior of the ferry dock in the future. Moreover, it should be emphasized that the dynamics of a traditional ferry quay is also unknown and is time variant under operation. The location of the Rykkjem ferry dock is displayed in Fig. 14.3. The ferry dock is a part of the road 670 that links Rykkjem and Kvanne through Stangvik fjord with an annual average daily traffic of 440, and it has been in operation for over 26 years.

The Rykkjem ferry dock consists of the 18 m long and 7 m wide ferry dock bridge with four conical fenders placed below the deck and behind main longitudinal beams, two lifting towers and a side support quay with vertical fenders. Those sub-elements are showed in Fig. 14.4. It should be noted that in this study we limit our analysis to the ferry dock bridge only.

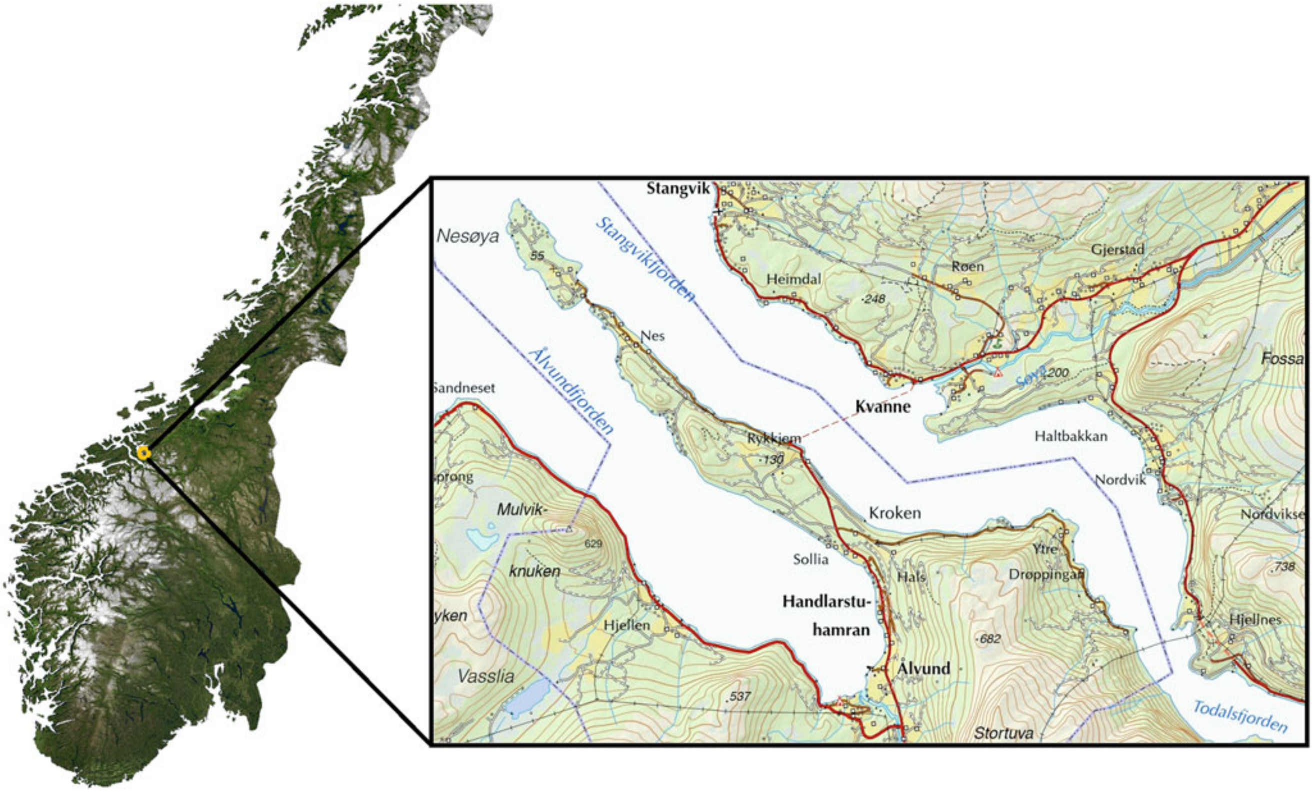

Fig. 14.3 Location of ferry connection between Rykkjem and Kvanne ferry docks

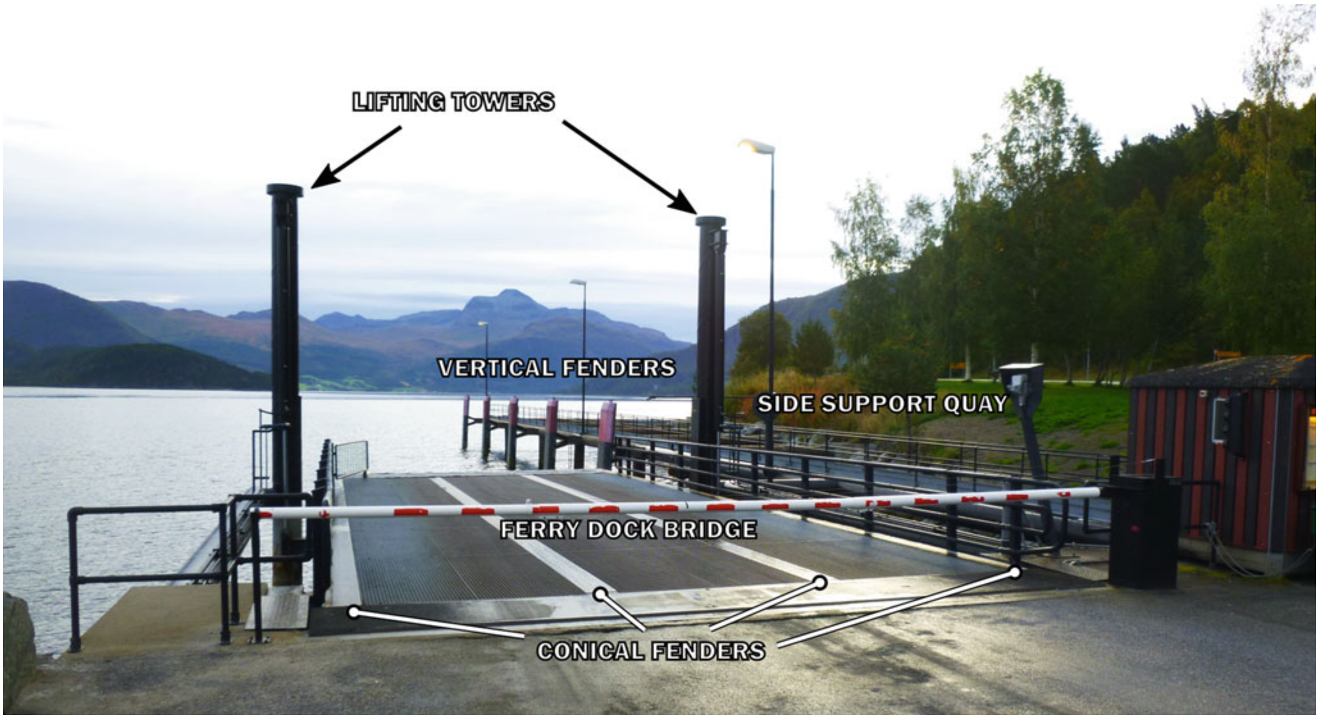

Fig. 14.4 Picture of Rykkjem ferry quay with its main substructures. (Picture from Brutus [14], Statens Vegvesen)

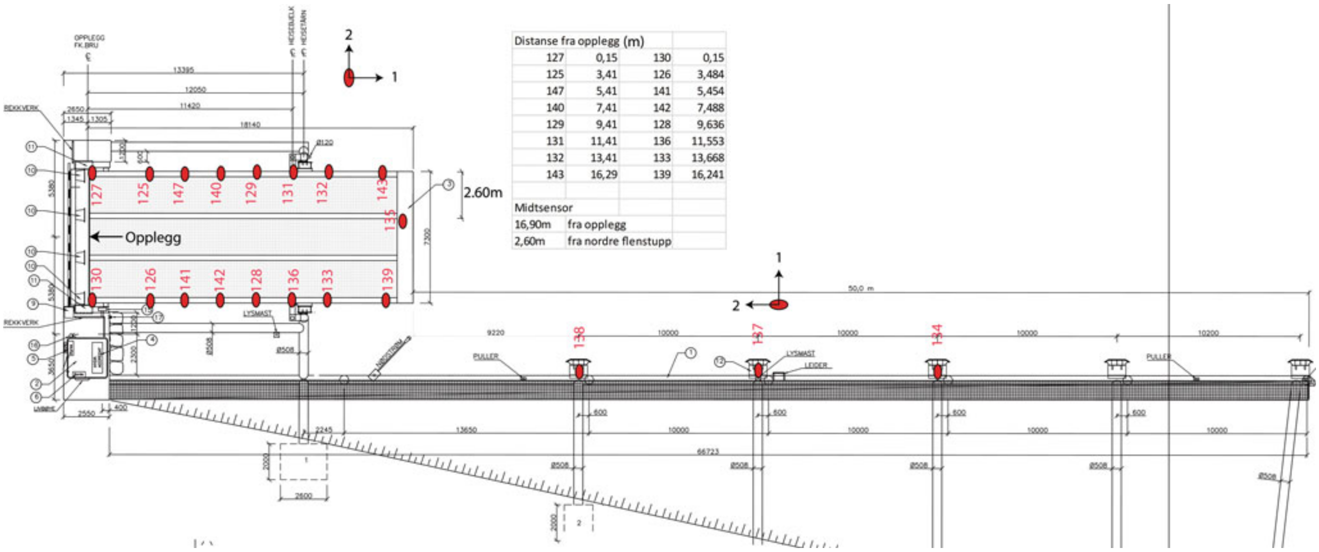

Distanse fra opplegg (m)			
127	0,15	130	0,15
125	3,41	126	3,484
147	5,41	141	5,454
140	7,41	142	7,488
129	9,41	128	9,636
131	11,41	136	11,553
132	13,41	133	13,668
143	16,29	139	16,241
Midtsensor			
16,90m	fra opplegg		
2,60m	fra nordre flenstupp		

Fig. 14.5 Sensor placement at the Rykkjem ferry dock

Measurements at the ferry dock location were taken on February 28, 2022. The acquisition system used in this study was designed to be flexible and allow for fast deployment such that sensor could be installed without disrupting the ferry schedule. Measurements were taken with a use of 20 G-Link-200 3-axis accelerometers with waterproof enclosure from Parker LORD MircoStrain that wirelessly transmit data to WSDA-2000 gateway that can communicate with a laptop via ethernet or USB cable. Sampling frequency was set to 128 Hz, while accelerometer's range was set to lowest possible ±2 g in order to improve noise density that is defined by the supplier as 25 $\mu g/\sqrt{Hz}$ [16]. The sensors were placed directly on the Rykkjem ferry dock bridge using magnets causing no conflict with the operation of the ferry. As the main focus of this study was the ferry dock bridge, 17 sensors were placed there, while the remaining 3 were installed on the side support quay. Location of the installed sensors is shown in the Fig. 14.5.

14.3 Analysis of Time Series

Norwegian standard N400 [15] instructs that the following loads induced by the ferry should be considered in the design of the ferry dock bridges in Norway:

- Impact load
- Longitudinal pressure
- Forced deformations

The two latter ones should be considered to occur simultaneously with the traffic loads, while the impact load appears separately during berthing operation (vessel sway motion) according to N400. Longitudinal pressure is defined as the force along the bridge deck center line induced by the vessel pushing towards or away from the land (vessel sway and yaw motions), while forced deformations correspond to a rotation of the front of the ferry deck bridge that is in contact with a ferry. Those rotations arise from the fact that a ferry is not able to keep itself perfectly aligned with the horizontal plane as it is affected by wind and waves when attached to the ferry dock bridge, and it will transfer its own tilt to a ferry deck bridge (vessel roll motion).

The ability to determine above mentioned loads under real-life conditions is crucial for a proper estimation of fatigue service life, tracking deterioration process and finally, as a result of that, a cost-effective planning of inspections and maintenance schedule. If ferry-induced and traffic loads can be estimated accurately from measurements, then long-term monitoring will provide valuable data that can be used to validate the design approach and recommendations in N400. In this study, we try to examine whether such loads can be identified using measured acceleration time series. A recorded time series from one of the sensors during berthing operation and loading/unloading of vehicles is displayed in the Fig. 14.6.

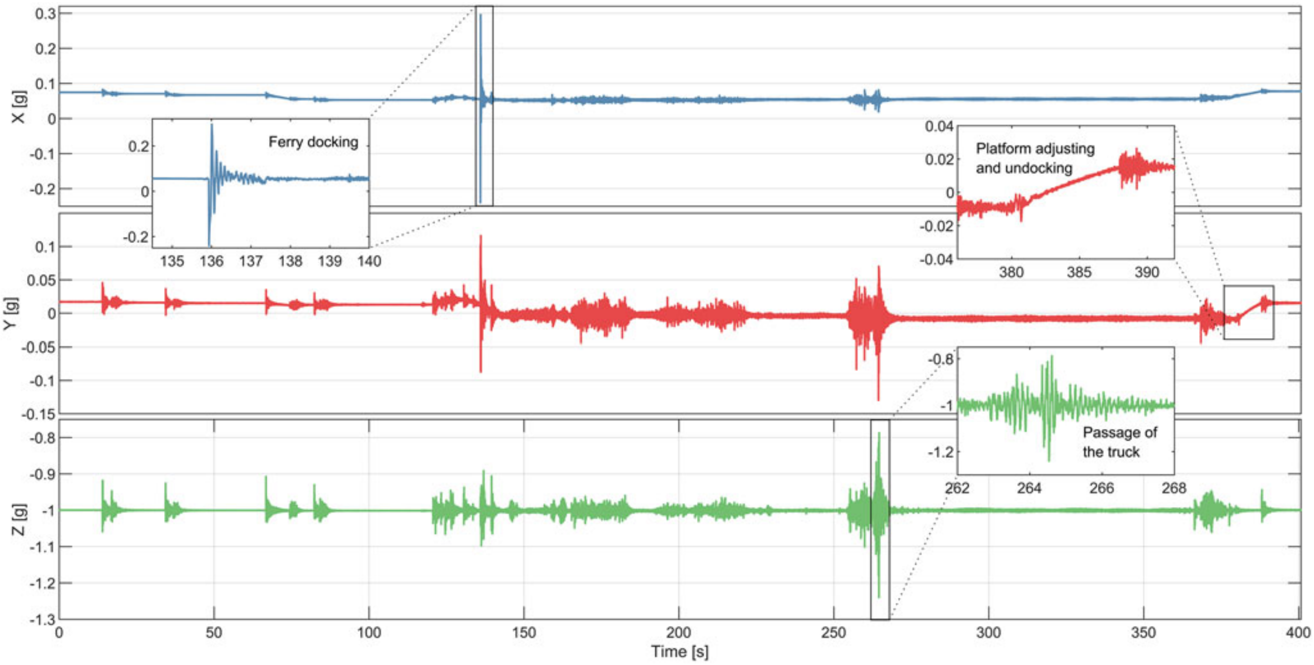

Fig. 14.6 Data overview of berthing event from the sensor 129, including unloading and loading of vehicles. Symbols *X*, *Y*, and *Z* refer to longitudinal transverse and vertical directions

It can be seen that measurements make it possible to detect and investigate the most important events such as ferry docking, passage of a heavy truck, and adjusting the position of the bridge deck bridge after undocking operation. Those events have been marked in Fig. 14.6 separately. The first 120 s of recordings are primarily affected by the lifting towers, followed by the ferry impact. Despite the subjectively gentle berthing event, the impact induced serious accelerations in *X* and *Y* directions that clearly stand out from the rest of time series. Therefore data gathered from recordings looks promising when it comes to identification of impact force by means of for instance Kalman filters [17] that have been successfully used to estimate forces from various sources such as ice [18], wind [19], or wave [20] actions on real structures. Time series in vertical – *Z* direction on the other hand, can be used to evaluate the weight of vehicles entering and exiting a ferry with a use of weight-in-motion technique that is popular for bridge structures [21]. However, it should be emphasized that both of the mentioned methods require understanding of the underlying dynamics of the ferry dock bridge namely the information about eigenmodes and eigenfrequencies. Those can be obtained from the finite element analysis or modal analysis.

As for the loads responsible for causing forced deformations, they can be measured by examining how gravitational pull is distributed among accelerations measured in local *X*, *Y*, and *Z* directions for each sensor. Herein, it was done by firstly applying low-pass filter with a cut off frequency of 0.1 Hz and later using Eqs. (14.1–14.3) based on trigonometry [22, 23]:

$$\theta = \tan^{-1}\left(\frac{X}{\sqrt{Y^2 + Z^2}}\right) \tag{14.1}$$

$$\psi = \tan^{-1}\left(\frac{Y}{\sqrt{X^2 + Z^2}}\right) \tag{14.2}$$

$$\phi = \tan^{-1}\left(\frac{\sqrt{X^2 + Y^2}}{Z}\right) \tag{14.3}$$

Here θ is the angle between horizontal plane and the x-axis (along the ferry deck bridge) of the accelerometer, ψ is the angle between horizontal plane and the y-axis (across the ferry deck bridge) of the accelerometer, and ϕ is the angle between the gravity vector and the z-axis – see Fig. 14.7 for ferry bridge dock displacements associated with θ and ψ angles.

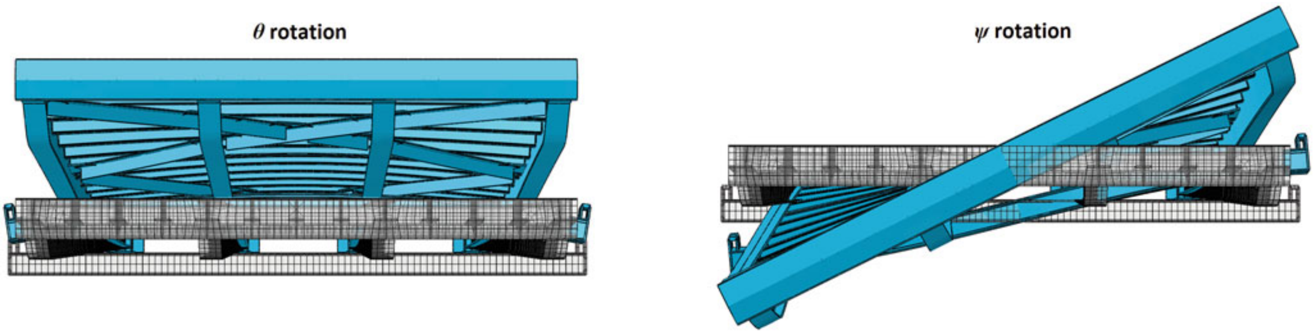

Fig. 14.7 Displacements of the ferry bridge deck associated with θ and ψ rotations

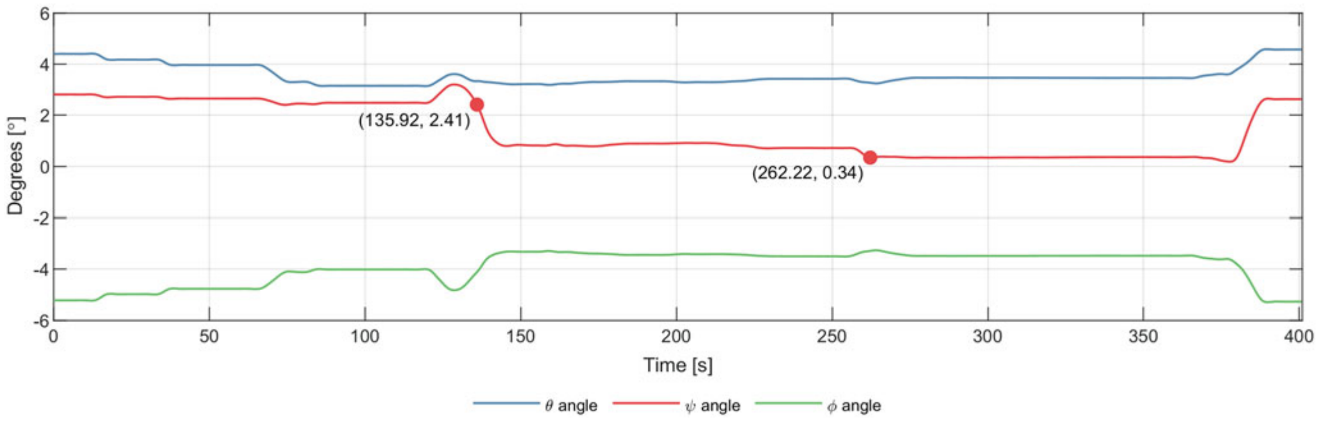

Fig. 14.8 Inclination angles for the sensor 143 placed at the edge of the ferry dock bridge. Markers indicate events of ferry docking and passage of the large truck

When the ferry bridge deck is lying perfectly flat then should X, $Y = 0$ g, $Z = 1$ g and $\theta,\psi,\phi = 0^{\circ}$. Figure 14.8 shows all three angles calculated based on Eqs. (14.1–14.3) for the sensor 143 that was placed at the front edge of the Rykkjem ferry dock bridge (cf. Fig. 14.5).

Two different events have been marked in the figure: ferry docking and passage of a large truck. It can be clearly seen that both events forced permanent torsional tilt on the deck. The value of maximal rotation at the end of the bridge deck can be estimated as 2.41–0.34° = 2.07° that is significantly lower than the design value of 5° [15]. In addition, it is also possible to detect small vertical adjustments (θ angle) made by ferry technicians prior and after the docking operation.

14.4 Modal Analysis

It is not difficult to assume ferry dock bridges to be generally low-complexity structures with their simple geometry. However, in addition to being exposed to complex loading conditions, harsh environment, and having uncertain boundary conditions, they operate also in two different states: (1) free state – when being disconnected from a ferry, and (2) working mode – when attached to a ferry. This fact adds a layer of complexity to their design and analysis as it makes it more difficult to predict stress levels that ferry dock bridges would frequently experience. In this chapter we try to examine, whether modal analysis based on measurements conducted on-site can be used to shed a light on dynamic behavior of the Rykkjem ferry dock bridge in different operational states.

A spectrogram (Fig. 14.9) of the first singular value of all acceleration channels in vertical directions shows clearly a difference in dynamic response of the Rykkjem ferry dock bridge after docking operation. Several new vibration frequencies appear in the spectrogram of about 160 s at the time of the ferry impact. Especially a 30 Hz frequency is visible all the time when the ferry dock bridge was in working state, and it is likely that this frequency should be associated with 1800 rpm engine noise.

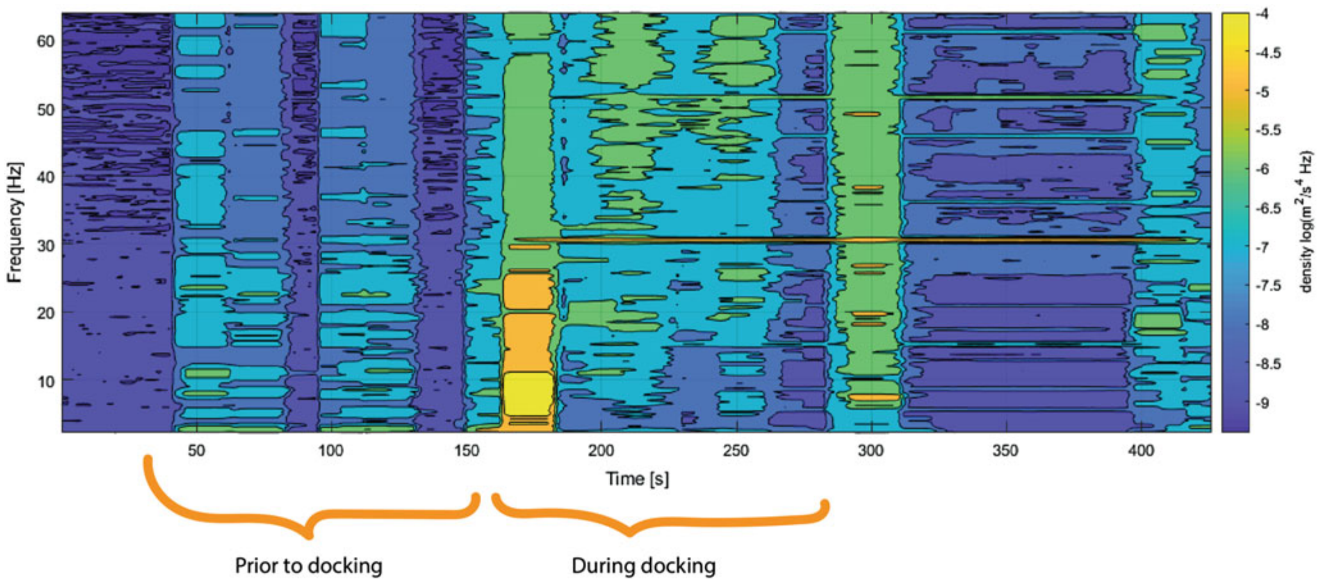

Fig. 14.9 Spectrogram of first singular value of all acceleration channels in vertical direction

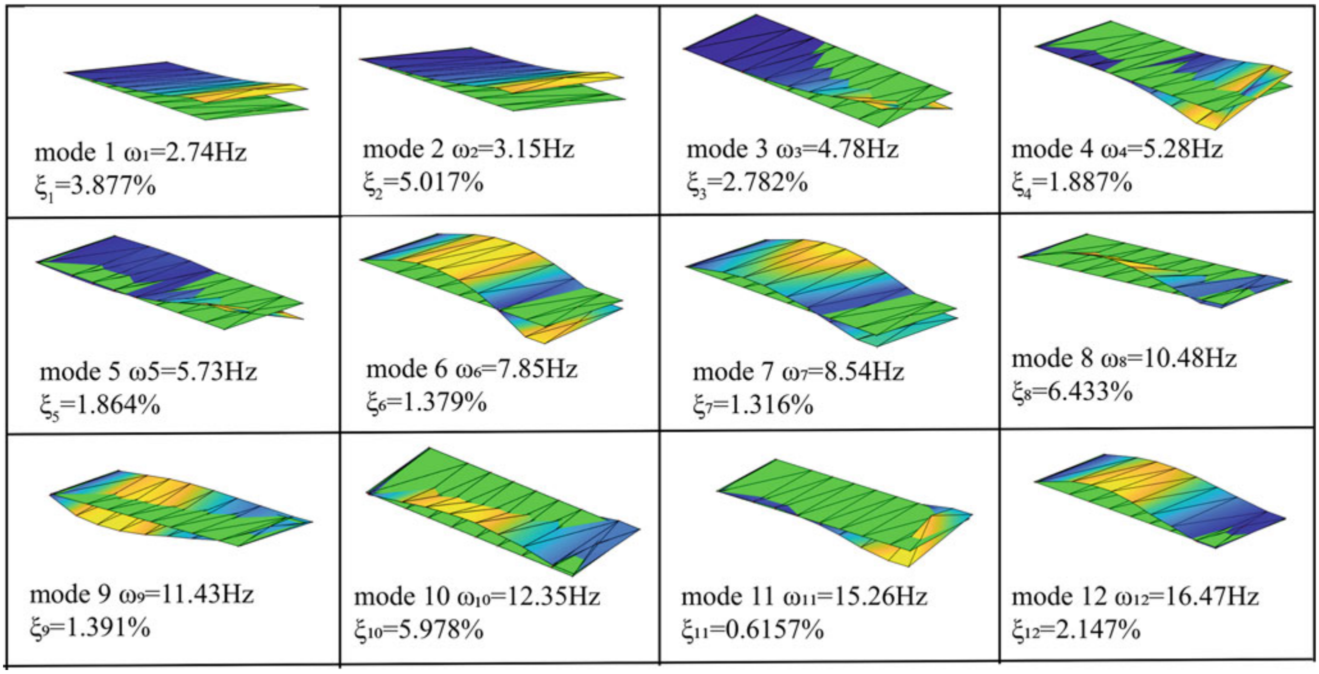

Fig. 14.10 Mode shapes, damping, and eigenfrequencies prior to docking (free state)

In order to perform the modal analysis, the full recording of data was split into two: prior and during berthing as showed in in Fig. 14.9. The data was then high-passed filtered with a cut-off frequency of 0.5 Hz. Data from 17 sensors were used to perform modal analysis with the use of covariance-driven stochastic subspace identification algorithm [24, 25]. The number of blockrows was set to 100, and the number of blocks for the covariance of the subspace matrix was set to 20. Modes presented in Figs. 14.10 and 14.11 were later manually selected from stabilization diagrams. It should be noted that some modes were difficult to distinguish as their mode shape was very similar.

There exists a great similarity between the first two modes in free and working inactive states for the Rykkjem ferry dock bridge. However, the next modes are expectedly different. In free state the torsion modes between 4.7 and 5.8 Hz are not present anymore when ferry is docking, and instead the second bending mode is excited. A possible explanation to the

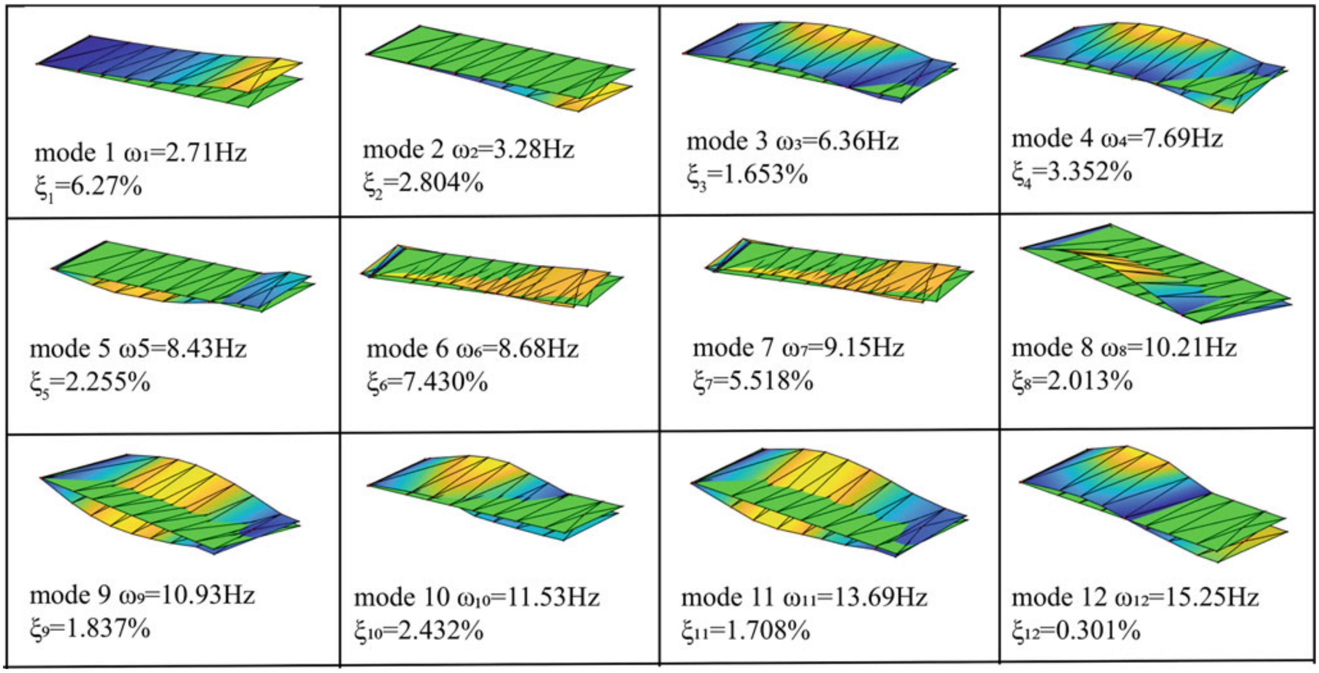

Fig. 14.11 Mode shapes, damping, and eigenfrequencies during docking (working state)

absence of torsion modes is the fact that the ferry provides vertical support when docking, so that it becomes difficult to excite the torsion modes.

Modes 6 and 7 found in working state are primarily axial modes, presumably excited by the first ferry impact on the ferry dock bridge. These modes are likely to be governed by the properties of the conical fenders placed behind the 4 main longitudinal beams. This also finds confirmation in high damping values in those modes as the main task of fenders is to the energy in axial direction. While modes 6 and 7 presented in Fig. 14.10 can be used to examine the condition of the conical fenders or perhaps even stresses they undergo when in working state, bending and torsional modes presented in Fig. 14.11 can provide insight into amount of support in vertical direction provided by the lifting towers with a help of a finite element model updating technique and even detect possible malfunction of the towers.

14.5 Conclusion

In this study, preliminary results from measurements conducted at the Rykkjem ferry dock have been presented. The goal was to investigate, whether and to what extent monitoring of a ferry dock bridge can improve understanding of underlying dynamics of these structures, resulting in safer design and more economical asset management. It has been showed that structural monitoring can be an essential tool to facilitate this process.

Firstly, presented results clearly show that there is significant difference in dynamic behavior depending on operational state the structure is in. In free state, when the ferry dock bridge is functioning as a separate structure detached from the ferry, torsional modes become much more prominent, while when in working state, bending and longitudinal contribute more to the overall dynamic response. Identified vibration modes, natural frequencies, and damping ratios have a potential to be used for finite element model updating in order to estimate uncertain parameters such as amount of stiffness provided by the hydraulic lifting towers or condition of the rubber in conical fenders responsible for taking the energy of impact. Long-term monitoring of those properties could potentially help in more accurate degradation modelling and early damage detection.

Secondly, it has been showed that acquisition system is able to deliver good quality data as it is easy to understand from the time-series what is happening at the ferry dock bridge: from height adjustment made by technician and ferry impact to passage of vehicles and undocking. Accelerations measured at the moment of impact clearly stand out, and in the further study the authors aim to utilize recordings together with results from the modal analysis to estimate impact load using force identification techniques. Therefore, long-term monitoring has a potential to shed the light and validate design approach when it comes to the ferry-induced loads.

Finally, data gathered from accelerometers can also be used to assess forced deformations appearing during docking that are also a part of the current design practice. It has been showed that inclination along the main ferry bridge deck axis and horizontal plane as well as tilt in transverse direction can be evaluated by considering mean value of *X*, *Y*, and *Z* accelerations.

Acknowledgments The study was conducted with support from the Research Council of Norway through the Norwegian Regional Research fund in Møre og Romsdal county (SHMBru project 331578). This research was conducted with financial support from the Møre og Romsdal fylke. The authors gratefully acknowledge this support the support from Møre og Romsdal County during planning and execution of instrumentation and measurements.

References

1. Dunham, K.K.: Coastal highway route E39 – extreme crossings. Transp. Res. Procedia. **14**(2352), 494–498 (2016)
2. Xu, Y., Øiseth, O., Moan, T., Naess, A.: Prediction of long-term extreme load effects due to wave and wind actions for cable-supported bridges with floating pylons. Eng. Struct. **172**, 321–333 (2018)
3. Minoretti, A., Xiang, X., Eidem, M., Wang, J., Dunham, K.: Design analysis and validation of the submerged floating tube bridge over the Bjørnefjord BT. In: Proceedings of the 14th International Conference on Vibration Problems, pp. 757–770 (2021)
4. Andersen, M.S., Johansson, J., Brandt, A., Hansen, S.O.: Aerodynamic stability of long span suspension bridges with low torsional natural frequencies. Eng. Struct. **120**, 82–91 (2016)
5. Vegvesen, S.: Hånbok V620 – Ferjestatistikk 2016, 2018. [Online]. Available: http://www.vegvesen.no/Fag/Trafikk/Trafikkdata/Ferjestatistikk
6. Høyem, H., Odeck, J.: Assessing the socially optimal capacity at a selection of Norwegian car ferry crossings. Case Stud. Transp. Policy. **10**(1), 41–56 (2022)
7. Nørstebø, V.S., Johansen, U.: Optimal transportation of logs and location of quay facilities in coastal regions of Norway. For. Policy Econ. **26**, 71–81 (2013)
8. Andersen, S.N., Tørset, T.: Waiting time for ferry services: Empirical evidence from Norway. Case Stud. Transp. Policy. **7**(3), 667–676 (2019)
9. Sæther, S.R., Moe, E.: A green maritime shift: Lessons from the electrification of ferries in Norway. Energy Res. Soc. Sci. **81**(August), 102282 (2021)
10. Veitch, E., et al.: From captain to button-presser: operators' perspectives on navigating highly automated ferries. J. Phys. Conf. Ser. **2311**(1), 012028 (2022)
11. Thyri, E.H., Breivik, M., Lekkas, A.M.: A path-velocity decomposition approach to collision avoidance for autonomous passenger ferries in confined waters. IFAC-PapersOnLine. **53**(2), 14628–14635 (2020)
12. Aurlien, A., Breivik, M., Eriksen, B.O.H.: Multivariate modeling and adaptive control of autonomous ferries. IFAC-PapersOnLine. **54**(16), 395–401 (2021)
13. Najdorf, E.: Tilstandsovervåkning av ferjekaier, bachelor thesis. Norwegian University of Technology (2022)
14. Vegvesen, S.: Brutus – management system for bridges, ferry quays and other load-bearing structures in Norway. https://brutus.atlas.vegvesen.no/
15. Vegvesen, S.: Håndbok N400 Bruprosjektering. Vegdirektoratet, Oslo (2015)
16. Parker Hannifin MicroStrain Sensing, MicroStrain Sensing Product Datasheet, 3DM-CV5-IMU, (2020). [Online]. Available: https://www.microstrain.com/sites/default/files/g-link-200_datasheet_8400-0102_rev_h.pdf
17. Lourens, E., Reynders, E., De Roeck, G., Degrande, G., Lombaert, G.: An augmented Kalman filter for force identification in structural dynamics. Mech. Syst. Signal Process. **27**(1), 446–460 (2012)
18. Nord, T.S., Oiseth, O., Lourens, E.M.: Ice force identification on the Nordströmsgrund lighthouse. Comput. Struct. **169**, 24–39 (2016)
19. Petersen, W., Øiseth, O., Lourens, E.: Wind load estimation and virtual sensing in long-span suspension bridges using physics-informed Gaussian process latent force models. Mech. Syst. Signal Process. **170**(October 2021), 108742 (2022)
20. Fallais, D.J.M., Voormeeren, S., Lourens, E.: Vibration-based identification of hydrodynamic loads and system parameters for offshore wind turbine support structures. Energy Procedia. **94**(September), 191–198 (2016)
21. Cantero, D.: Moving point load approximation from bridge response signals and its application to bridge Weigh-in-Motion. Eng. Struct. **233**, 111931 (2021)
22. Zhu, J., Wang, W., Huang, S., Ding, W.: An improved calibration technique for mems accelerometer-based inclinometers. Sensors (Switzerland). **20**(2) (2020)
23. Fisher, C.: Using an accelerometer for inclination sensing, AN-1057, Appl. note, Analog Devices, pp. 1–8, 2010, [Online]. Available: http://healthcare.analog.com/static/imported-files/application_notes/AN-1057.pdf
24. Döhler, M., Mevel, L.: Efficient multi-order uncertainty computation for stochastic subspace identification. Mech. Syst. Signal Process. **38**(2), 346–366 (2013)
25. Reynders, E., Pintelon, R., De Roeck, G.: Uncertainty bounds on modal parameters obtained from stochastic subspace identification. Mech. Syst. Signal Process. **22**(4), 948–969 (2008)

Chapter 15
Application of Impact-Driven Vibrations to Estimate Axial Stress in Continuous Welded Rails

Alireza Enshaeian, Matthew Belding, and Piervincenzo Rizzo

Abstract Track segments welded together form a continuous welded rail (CWR). Although CWRs are widely used, they are prone to buckling in warm seasons. To prevent rail buckles, accurate estimates of the axial stress and rail neutral temperature (i.e., the temperature at which the axial stress is zero) are needed. This study proposes a noninvasive method to determine the axial load in CWRs using numeric models and field test data. A general finite element model under varying boundary conditions and axial stresses was formulated. The model was then validated experimentally by testing a real track in the field. During the experiment, the rail was subjected to the impact of an instrumented hammer, and the triggered vibrations were recorded with conventional accelerometers. These vibration frequencies were compared with numerical predictions to estimate the neutral temperature of the rail using a machine learning algorithm. The estimates showed good agreement with the measurements conducted by a third independent party that used a very cumbersome approach based on strain gages.

Keywords Continuous Welded Rails · Finite Element Method · Accelerometers · Impact Hammer · Rail Neutral Temperature

15.1 Introduction

In continuous welded rails (CWR), track segments are connected by welded joints. As a result, CWRs require less maintenance, provide smoother rides to the passengers, increase the life cycle of the tracks, and can be traveled at higher speeds compared to mechanically-jointed rails. However, CWR are prone to buckling during the warm seasons when high temperatures induce large compressive loads in the rails. These buckling events may lead to train derailments. Rail buckling and derailments can be prevented if accurate estimates of the axial stress and rail neutral temperature (i.e., the temperature at which the axial stress is zero) are available. To mitigate such thermal effects, CWR are pretensioned during installation such that the rail neutral temperature (RNT) is within the range of 32–43 °C. The pretension force cannot be higher to avoid fractures during the cold seasons.

The axial stress σ_{R} and the neutral temperature T_{N} are linked by the following equation:

$$T_{\mathrm{N}} = T_{\mathrm{R}} - \frac{\sigma_{\mathrm{R}}}{E\alpha} \tag{15.1}$$

where σ_{R} is considered positive when the rail is in compression. Here E and α are the Young's modulus and the coefficient of thermal expansion of the steel, respectively. The longitudinal stress σ_{R} at any temperature T_{R} can be attained by field measurements and then infer T_{N} using Eq. (15.1).

There are many nondestructive evaluation (NDE) methods that aim to measure axial stress or RNT in situ. They are based on static [1] or dynamic [2] principles and may rely on electromagnetism [3], ultrasounds [4], or acoustics [5], just to mention a few. The beam-column bending theory is the foundation of VERSE®, acronym of Vertical Rail Stressing Equipment [1].

A. Enshaeian (✉) · P. Rizzo
Laboratory for Nondestructive Evaluation and Structural Health Monitoring Studies, Department of Civil and Environmental Engineering, University of Pittsburgh, Pittsburgh, PA, USA
e-mail: ale69@pitt.edu

M. Belding
Department of Electrical and Computer Engineering, University of Pittsburgh, Pittsburgh, PA, USA

H. Y. Noh et al. (eds.), *Dynamics of Civil Structures, Volume 2*, Conference Proceedings of the Society for Experimental Mechanics Series, https://doi.org/10.1007/978-3-031-36663-5_15

This static method links the axial load acting on the rail to the vertical force required to lift, by a certain amount, the same rail that must be unanchored from the fasteners for about 30 m. Another commercial system consists of strain gages welded to the web of the rail of interest [6]. An electromagnetic-based approach measures the magnetic Barkhausen noise associated with the rail's magnetic permeability, which increases with the increase in tensile stress and vice versa [3]. The ultrasonic birefringence method uses linearly polarized shear waves propagating along two perpendicular directions. The difference in the time-of-flight of these two beams depends upon the stress and the residual stress within the material [7].

In this study, the results of a novel approach to measure axial stress in CWR based on structural dynamics, finite element analysis (FEA), and data processing are presented. The method relies on the fact that the characteristics of flexural modes (frequency and mode shapes) of the rail depend upon the longitudinal stress at any given rail geometry and boundary conditions. The idea behind the study is that the FEA provides a comprehensive set of data that frames the interdependency among stress, modal characteristics, and boundary conditions. The dataset is then used to train a machine learning (ML) algorithm to learn such interdependency, to quantify the axial stress using field data presented in the form of frequencies of vibration. During the experiment, the rail was subjected to the impacts of an instrumented hammer, and the triggered vibrations were recorded with an array of accelerometers. In this study, the experimental frequencies were extracted via power spectral density (PSD) functions and then fed into the developed ML algorithm in order to estimate the neutral temperature of the rail.

15.2 Measurements and Results

The field test was conducted at Transportation Technology Center (TTC), in Pueblo, Colorado, on a 5° curved RE 141 rail sitting on concrete ties. An array of tri-axial accelerometers was bonded to the railhead. The accelerometers were triggered via an instrumental hammer. Two thermocouples were attached to the rail, one on the head and one on the web. The rail location was also equipped with strain gages, and temperature measurement devices operated independently by TTC.

For illustrative purposes Fig. 15.1a shows a time series associated with the lateral vibration measured by one of the accelerometers. The corresponding power spectral density is presented in Fig. 15.1b along with the spectrum of the vertical acceleration. Several peaks are visible around 150 Hz, 220 Hz, 350 Hz, 490, 500, and 530 Hz.

The extracted peaks from the PSDs and the rail temperature showed an inverse correlation, i.e., the frequencies decrease as the rail temperature increased. On the other hand, a FEM corresponding to the tested rail was generated and then analyzed. The numerical results showed the same inverse correlation. In addition, the FEM was used to generate a synthetic database in which the interdependency between the rail resonant frequencies, axial stress and boundary conditions were presented. Using this synthetic database, an ML algorithm was trained. The input features associated with this MLA were resonant frequencies, and rail temperature and the predictions were made for the axial stress and boundary conditions.

The predicted RNTs by the MLA are presented in Fig. 15.2, where they are overlapped to the estimation of the neutral temperature provided independently by TTC.

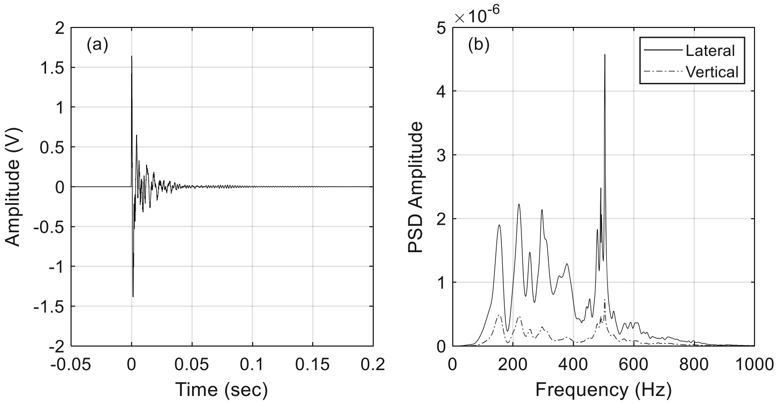

Fig. 15.1 (**a**) Typical time-series associated with the lateral displacement and recorded by the accelerometers on the rail (**b**) Corresponding power spectral density overlapped to the PSD of the vertical direction

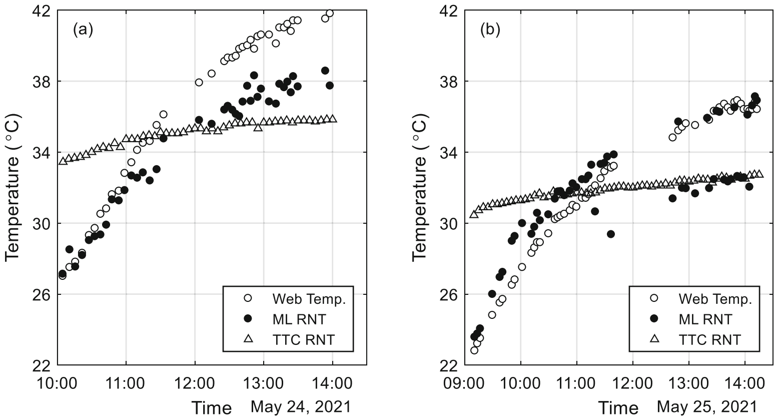

Fig. 15.2 ML predictions based on the database obtained with the finite element analysis. The value of the predicted neutral temperature is overlapped to the independent estimation provided by TTC. (**a**) Results relative to day 1; (**b**) results relative to day 2 of test at TTC

Figure 15.2 shows that the algorithm performs well when the rail was in compression but is heavily biased by the temperature of the rail otherwise. The bias originates from a difference in distributions between the FEM training dataset and the empirical test set. Finally, Fig. 15.2 confirms that the RNT is a function of the rail temperature, which has daily fluctuations.

15.3 Conclusion

This chapter proposes a vibration-based approach supported by artificial intelligence and finite element modeling to provide noninvasive estimates of the neutral temperature of continuous welded rails. This approach consists of monitoring rail vibrations and the extraction of the associated modal characteristics to evaluate the axial stress using a machine learning algorithm trained with synthetic finite element data. The feasibility of this technique was proven in the field at a testing facility in Colorado.

Acknowledgments The authors would like to acknowledge the sponsorship and support of the Federal Railroad Administration's Office of Research, Development and Technology. The authors acknowledge the logistic support provided by TTC during the planning and execution of the field test.

References

1. PANDROL: VERSE® technical information pack. https://railway-news.com/wp-content/uploads/2020/02/VERSE-Technical-Information-Pack.pdf. Accessed 20 Feb 2022
2. Enshaeian, A., Luan, L., Belding, M., Sun, H., Rizzo, P.: A contactless approach to monitor rail vibrations. Exp. Mech. **61**(4), 705–718 (2021). https://doi.org/10.1007/s11340-021-00691-z
3. Kelleher, J., Prime, M.B., Buttle, D., Mummery, P.M., Webster, P.J., Shackleton, J., Withers, P.J.: The measurement of residual stress in railway rails by diffraction and other methods. J. Neutron Res. **11**(4), 187–193 (2003)
4. Nucera, C., Lanza di Scalea, F.: Nondestructive measurement of neutral temperature in continuous welded rails by nonlinear ultrasonic guided waves. J. Acoust. Soc. Am. **136**(5), 2561–2574 (2014)
5. Bagheri, A., Rizzo, P., Al-Nazer, L.: A numerical study on the optimization of a granular medium to infer the axial stress in slender structures. Mech. Adv. Mater. Struct. **23**(10), 1131–1143 (2016)
6. Wang, P., Xie, K., Shao, L., Yan, L., Xu, J., Chen, R.: Longitudinal force measurement in continuous welded rail with bi-directional FBG strain sensors. Smart Mater. Struct. **25**, 015019 (2016)
7. Hurlebaus, S.: Determination of longitudinal stress in rails. Safety IDEA Project 15, Transportation Research Board (2011)

Chapter 16
Towards Risk-Informed PBSHM: Populations as Hierarchical Systems

A. J. Hughes, P. Gardner, and K. Worden

Abstract The prospect of informed and optimal decision-making regarding the operation and maintenance (O&M) of structures provides impetus to the development of structural health monitoring (SHM) systems. A probabilistic risk-based framework for decision-making has already been proposed. The framework comprises four key submodels: the utility model, the failure-modes model, the statistical classifier, and the transition model. The cost model consists of utility functions that specify the costs of actions and structural failures. The failure-modes model defines the failure modes of a structure as combinations of component and substructure failures via fault trees. The statistical classifier and transition model are models that predict the current and future health-states of a structure, respectively. Within the data-driven statistical pattern recognition (SPR) approach to SHM, these predictive models are determined using machine learning techniques. However, in order to learn these models, measured data from the structure of interest are required. Unfortunately, these data are seldom available across the range of environmental and operational conditions necessary to ensure good generalisation of the model.

Recently, technologies have been developed that overcome this challenge, by extending SHM to *populations* of structures, such that valuable knowledge may be transferred between instances of structures that are sufficiently similar. This new approach is termed population-based structural heath monitoring (PBSHM).

The current paper presents a formal representation of populations of structures, such that risk-based decision processes may be specified within them. The population-based representation is an extension to the hierarchical representation of a structure used within the probabilistic risk-based decision framework to define fault trees. The result is a series, consisting of systems of systems ranging from the individual component level up to an inventory of heterogeneous populations. The current paper considers an inventory of wind farms as a motivating example and highlights the inferences and decisions that can be made within the hierarchical representation.

Keywords Population-based structural health monitoring · Risk · Decision-making · Value of information

16.1 Introduction

Structural health monitoring (SHM) is a technology that aims to detect damage within mechanical, civil, and aerospace structures and infrastructure [1]. By inferring information about the health of a structure from discriminative features extracted from data acquired throughout a monitoring campaign, these systems can facilitate informed predictions relating to one or more of the following problems regarding the health of a structure, as summarised in Rytter's hierarchy [2]:

- The presence of damage in a structure (detection)
- The location of damage within a structure (localisation)
- The type of damage present in a structure (classification)
- The extent of damage in a structure (severity)
- The remaining safe/useful life of a structure (prognosis)

By informing predictions with data from a monitoring system, one can also inform decision-making regarding the operation and maintenance of structures, and this can yield benefits such as improved safety, reduced operation costs, and operational lifetime extension.

A. J. Hughes (✉) · P. Gardner · K. Worden
Dynamics Research Group, Department of Mechanical Engineering, University of Sheffield, Sheffield, UK
e-mail: ajhughes2@sheffield.ac.uk; p.gardner@sheffield.ac.uk; k.worden@sheffield.ac.uk

H. Y. Noh et al. (eds.), *Dynamics of Civil Structures, Volume 2*, Conference Proceedings of the Society for Experimental Mechanics Series, https://doi.org/10.1007/978-3-031-36663-5_16

Recent works have explicitly framed structural health monitoring in the context of decision-making [3–5]. The approach to decision-making for SHM presented in [5] adopts a probabilistic risk-based perspective. In this approach, probability distributions over structural health states are inferred from data via statistical classifiers. The distributions are then forecast via a transition model and mapped to probabilities of failure for specific failure modes of interest via Bayesian network representations of fault trees. Optimal decisions are found by maximising the expected utility when considering both the risk of structural failure and the cost of maintenance actions. Several submodels have been identified as elements that are required to sufficiently define SHM decision processes; these submodels include statistical classifiers for inferring health-states and health-state transition models. In order to achieve robust decision-making, these submodels require labelled data for learning and/or validation.

A critical challenge associated with the development of SHM systems is the scarcity of the data necessary for the learning and validation of models. Prior to the implementation of a monitoring system, there is often a lack of comprehensive labelled data across the health-states of interest for a given structure as obtaining data corresponding to damage states tends to be prohibitively expensive or otherwise infeasible. One approach to circumvent this issue in the development of classification models is to utilise online active learning algorithms to preferentially obtain labelled data via structural inspections after a monitoring system is installed [6–8]. In [9], a methodology for determining a transition model using qualitative data from historical inspections is demonstrated.

Population-based structural health monitoring (PBSHM) provides a holistic framework for overcoming data scarcity in the development of predictive models for SHM [10–13]. The core principal of PBSHM is that predictions about individual structures can be improved with the use of information transferred from other similar structures.

The current paper aims to further the core principal of PBSHM, such that *decisions* about the operation of both individual structures and populations of structures can be improved via the transfer of information. This is achieved by extending the hierarchical representation of structures, used to develop fault trees in the risk-based approach to decision-making for traditional SHM, to hierarchical representations of populations of structures. Throughout the current paper, an inventory of offshore wind farms is referenced as a motivating example.

The layout of the current paper is as follows. Background theory is provided for both PBSHM and risk-based SHM in Sects. 16.2 and 16.3, respectively. Subsequently, a hierarchical representation of individual structures is presented in Sect. 16.4. This representation is extended to populations of structures in Sect. 16.5. Inferences and decisions within the population hierarchy are defined and discussed in Sect. 16.6. Finally, conclusions are provided in Sect. 16.7.

16.2 Population-Based SHM

The foundations of PBSHM have been presented in a series of journal papers, each detailing the fundamental concepts of the approach: homogeneous populations [10], heterogeneous populations [11], mapping and transfer [12], and the geometric spaces in which structures exist [13]. By adopting a population-based approach to SHM, such that knowledge and information can be transferred between similar structures, there is the potential for improved diagnostic and prognostic capabilities [14].

In the most general sense, a population can be considered to simply be a set of structures. Given the broad nature of this definition, in order to achieve useful transfer of knowledge and information between structures, it is discerning to consider specific classes of populations based upon the similarity of the constitutive structures. Thus, the notions of homogeneous and heterogeneous populations are introduced in [10–12].

16.2.1 Homogeneous and Heterogeneous Populations

Within a population, structures may share common characteristics such as geometries, topologies, materials, and boundary conditions. Consider a population of wind turbines in an offshore wind farm, and suppose these turbines are of the same model: developed to the same ISO standards and possessing common components, materials, aerodynamic design, and so on. Qualitatively, these structures can be regarded as nominally identical. Populations comprised exclusively of nominally identical structures are termed *homogeneous populations*. Specific instances of structures in a homogeneous population can be considered to be perturbations of a population *form* [10]. For further discussions on population forms, the reader is directed to [10]. Other examples of homogeneous populations include a fleet of Airbus A380s, an array of small modular nuclear reactors, and the Global Positioning System (GPS) satellite constellation.

Variation between structures in homogeneous populations may arise because of factors such as environmental conditions and manufacturing defects. Returning to the example of an offshore wind farm, one could imagine that two turbines at differing locations in the farm may experience different geotechnical conditions—perhaps as a result of varying geological composition in the seabed. Variability in such conditions could affect the boundary conditions of the monopile turbine towers and therefore modify the behaviours and data exhibited by these otherwise nominally identical structures.

In essence, *heterogeneous* populations form the complement of the set of homogeneous populations [14]; that is, heterogeneous populations are not exclusively comprised of structures that are nominally identical. Heterogeneous populations represent more general sets of structures and allow for differing designs, large variability in boundary conditions, and even multiple types of structure. While there may be stark differences between individual structures in a heterogeneous population, there may nonetheless be similarities that can be exploited to achieve useful knowledge and information transfer.

Consider again the offshore wind farm example, and suppose that the population is comprised of wind turbines each with three blades. Suppose also that the operating company manages an additional wind farm in a distinct location, comprised of four-blade turbines. Useful inferences could be achieved by considering these wind farms as two homogeneous populations; however, further insights could also be gained by considering them as a single heterogeneous population. For example, similarities may be present in the tower design between both types of wind turbines; hence, by considering a larger population from which to make observations, improved predictive models can be developed for this specific substructure. Other types of heterogeneous populations that may be useful to consider include inventories of aircraft comprised of a variety of models and multiple suspension bridges with differing designs (e.g., single-span, multi-span).

Thus far, similarities between structures have been described somewhat qualitatively; however, to better indicate where information transfer may work, it is useful to quantify this similarity.

16.2.2 Similarity Between Structures

Graph theory provides a rigorous and rich framework for representing and comparing discrete structured objects and has proved to be an invaluable modelling tool in fields such as chemistry and proteomics.

In [11], the notion of the irreducible element (IE) model for structures is introduced as a representation of structures with relatively low-dimension when compared to alternatives such as finite element or CAD models. The IE representation involves abstracting a structure into discrete elements having geometrical and material information (e.g., beams, plates, shells) and relationships (e.g., joints) so as to sufficiently capture the nature of a structure. Here, the "nature" one wishes to capture pertains to health monitoring problems associated with a structure.

Once an IE representation of a structure has been obtained, the information can be encoded into an attributed graph (AG). Whereas the purpose of the IE model is to present key characteristics of a structure in a human-readable format, the purpose of the AG is to embed a structure space, so as to facilitate the efficient pair-wise comparison of structures. With structures embedded into a metric space via AGs, one can utilise graph-matching algorithms to find common subgraphs between sets of structures. These subgraphs indicate substructures that are common within sets of structures and can be used to inform where transfer may be applicable. Furthermore, measures of closeness within the space of AGs (or common subgraphs) can be used to quantify similarity; in [11], the Jaccard index is used, and in [15], a variety of graph kernels are demonstrated.

In summary, structures can be mapped into a graphical domain to facilitate comparison, identify common substructures, and quantify similarity. By conducting this similarity assessment for structures within a population, one can determine where it is likely that information and knowledge can be successfully transferred between individual structures.

16.2.3 Mapping and Transfer

As mentioned previously, the primary benefit in taking a population-based approach to SHM is gaining the ability to transfer knowledge and information between sufficiently similar individual structures, thereby overcoming issues associated with data scarcity.

The sharing of knowledge and information between individual structures can be achieved via a number of methodologies. One manner in which this can be achieved is by having a statistical representation of the aforementioned population form, as demonstrated in [10]. Another approach, presented in [16], shares datasets in joint hierarchical statistical models of a population. Methodologies founded upon *transfer learning* have also been successfully demonstrated [12]. The principal of transfer learning is closely aligned with the goals of PBSHM, specifically, a branch of transfer learning known as *domain* *adaptation*. In domain adaptation, datasets are adapted in a manner that allows a model constructed for a *source* domain to generalise to a *target* domain.

For knowledge/information transfer to be successful, it is imperative that these source and target domains are comparable. This constraint can be adhered to by employing the similarity assessment outlined in the previous section.

Thus far, PBSHM has been considered with respect to predictions and inferences. Before incorporating decisions into the PBSHM framework, background on the risk-based approach to decision-making for traditional SHM is provided.

16.3 Probabilistic Risk-Based SHM

The probabilistic risk-based approach to SHM is founded on the notion that monitoring systems should be designed and developed with consideration for the specific decision-support applications motivating their implementation.

In the SHM paradigm detailed in [1], monitoring campaigns begin with a process termed *operational evaluation*. This stage in the development of an SHM system is concerned with specifying the context for an SHM system, dealing with aspects such as the safety/economic justification and the environmental and operational conditions. In [5], it is proposed that the decision-making processes associated with an SHM campaign should be considered from the outset of a monitoring campaign as part of the operational evaluation.

To begin defining the decision processes that one may wish to inform with a monitoring system, one must identify a set of failure modes or conditions for a structure that one may wish to prevent, in addition to a set of actions that can be executed to aid in the mitigation of failures. Furthermore, as part of the economic justification of a monitoring system, costs or utilities must be assigned to these failures and actions. The prediction of specific failure events and the informed selection of optimal mitigating actions should provide the basis for the development of monitoring systems guiding, choices for aspects of the monitoring system such as: sensors and their placement on the structure; data processing; and the discriminative features and models used to classify structural health states.

Once a monitoring system developed with respect to decision-making is implemented, optimal strategies can be found by maximising expected utility with consideration for the risk of failure and the cost of mitigating actions. This can be achieved by representing the decision processes as a probabilistic graphical model (PGM). The following two subsections provide background on PGMs and the modelling of SHM decision processes as PGMs, respectively.

16.3.1 Probabilistic Graphical Models

Probabilistic graphical models (PGMs) are graphical representations of factorisations of joint probability distributions and are a powerful tool for reasoning and decision-making under uncertainty. For this reason, they are apt for representing and solving decision problems in the context of SHM, where there is uncertainty in the health states of structures. While there exist multiple forms of probabilistic graphical model, the key types utilised for representing SHM decision processes are Bayesian networks (BNs) and influence diagrams (IDs) [17].

Bayesian networks are directed acyclic graphs (DAGs) comprised of nodes and edges. Nodes represent random variables, and edges connecting nodes represent conditional dependencies between variables. In the case where the random variables in a BN are discrete, the model is defined by a set of conditional probability tables (CPTs). For continuous random variables, the model is defined by a set of conditional probability density functions (CPDFs).

Figure 16.1 shows a simple Bayesian network comprised of three random variables X, Y, and Z. Y is conditionally dependent on X and is said to be a *child* of X, while X is said to be a *parent* of Y. Z is conditionally dependent on Y and can be said to be a child of Y and a *descendant* of X, while X is said to be an *ancestor* of Z. The factorisation described by the Bayesian network shown in Fig. 16.1 is given by $P(X, Y, Z) = P(X) \cdot P(Y|X) \cdot P(Z|Y)$. Given observations on a subset of nodes in a BN, inference algorithms can be applied to compute posterior distributions over the remaining unobserved variables. Observations of random variables are denoted in a BN via grey shading of the corresponding nodes, as is demonstrated for X in Fig. 16.1.

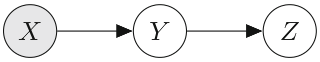

Fig. 16.1 An example Bayesian network

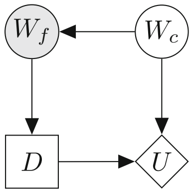

Fig. 16.2 An example influence diagram representing the decision of whether to go outside or stay in under uncertainty in the future weather condition given an observed forecast

Bayesian networks may be adapted into influence diagrams to model decision problems. This augmentation involves the introduction of two additional types of nodes, as shown in Fig. 16.2: decision nodes, denoted as squares, and utility nodes, denoted as rhombi. For influence diagrams, edges connecting random variables to utility nodes denote that the utility function is dependent on the states of the random variables. Similarly, edges connecting decisions nodes to utility nodes denote that the utility function is dependent on the decided actions. Edges from decision nodes to random variable nodes indicate that the random variables are conditionally dependent on the decided actions. Edges from random variable or decision nodes to other decision nodes do not imply a functional dependence but rather order, i.e., that the observations/decisions must be made prior to the next decision being made.

To gain further understanding of IDs, one can consider Fig. 16.2. Figure 16.2 shows the ID for a simple binary decision; stay home and watch TV or go out for a walk, i.e., $\text{dom}(D) = \{\text{TV}, \text{ walk}\}$. Here, the agent tasked with making the decision has access to a weather forecast W_f that is conditionally dependent on the future weather condition W_c. The weather forecast and future condition share the same possible states $\text{dom}(W_f) = \text{dom}(W_c) = \{\text{bad}, \text{ good}\}$. The utility achieved U is then dependent on both the future weather condition and the decided action. For example, one might expect high utility gain if the agent decides to go for a walk and the weather condition is good.

In general, a policy δ is a mapping from all possible observations to possible actions. The problem of inference in influence diagrams is to determine an optimal strategy $\boldsymbol{\Delta}^* = \{\delta_1^*, \ldots, \delta_n^*\}$ given a set of observations on random variables, where δ_i^* is the ith decision to be made in a strategy $\boldsymbol{\Delta}^*$ that yields the *maximum expected utility* (MEU). For further details on the computation of the MEU for influence diagrams, the reader is directed to [18]. Defined as a product of probability and utility, the expected utility can be considered as a quantity corresponding to risk.

16.3.2 Decision Framework

A probabilistic graphical model for a general SHM decision problem across a single time-slice is shown in Fig. 16.3. Here, a maintenance decision d is shown for a simple fictitious structure $\boldsymbol{S}$, comprised of two substructures $\boldsymbol{s}_1$ and $\boldsymbol{s}_2$, each of which are comprised of two components: $c_{1,2}$ and $c_{3,4}$, respectively.

The overall decision process model shown in Fig. 16.3 is based upon a combination of three submodels: a statistical classifier, a failure-mode model, and a transition model.

The failure condition of the structure $F_{\boldsymbol{S}}$ is represented as a random variable within the PGM. This failure condition $F_{\boldsymbol{S}}$ can be expressed as a failure mode of the global structure that can be specified by a fault tree: a combination of local failures at a component, joint, and substructure level related by Boolean logic gates. In order to fit into the PGM framework, fault trees must be mapped into Bayesian networks. Fortunately, there is a well-established mapping for this presented in [19, 20]. Essentially, components, joints, and substructures receive random variables in the PGM corresponding to their respective local health states. The conditional probability tables defining the relationship between these random variables correspond to the Boolean truth tables for each of the logic gates in the fault tree defining the failure mode $F_{\boldsymbol{S}}$.

Figure 16.3 considers a failure mode dependent on two substructures $\boldsymbol{s}_{1-2}$, which in turn are each dependent on two components $c_{1,2}$ and $c_{3,4}$. For the decision process shown in Fig. 16.3, component health states are denoted by hc_{1-4}, and substructure health states are denoted by $hs_{1,2}$. An advantage of considering specific failure modes and their representations as fault trees is that doing so yields the health states that must be targeted by the monitoring system; the local health states of the components can be summarised in a global health-state vector. For the example shown in Fig. 16.3, this health-state vector is given by $\boldsymbol{H} = \{hc_1, hc_2, hc_3, hc_4\}$. In essence, the purpose of this failure model is to map from a distribution over the global health states to a probability of structural failure. Finally, the failure states associated with the variable $F_{\boldsymbol{S}}$ are given utilities via the function represented by the node U_F. As it is necessary to consider the future risk of failure in the decision process, this failure-mode model and utility function are repeated for each time-step.

As previously mentioned, a random variable denoted $\boldsymbol{H}_t$ is used to represent the latent global health state of the structure at time t. Within the decision process, the function of the statistical classifier is to provide a posterior probability distribution

Fig. 16.3 An influence diagram representing a partially observable Markov decision process over one time-slice for determining the utility-optimal maintenance strategy for a simple structure comprised of four components. The fault-tree failure-mode model for time $t + 1$ has been represented as the node F'_{t+1} for compactness

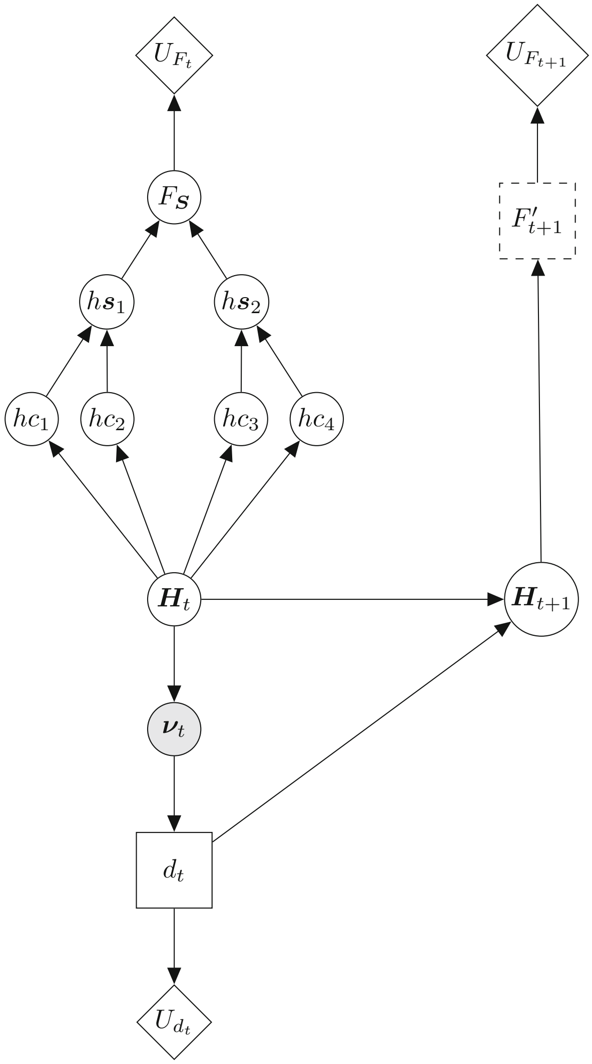

over the latent health state $\boldsymbol{H}_t$, inferred via observations on a set of discriminative features $\boldsymbol{\nu}_t$. This probability distribution over health-states may be obtained via a generative model $P(\boldsymbol{\nu}|\boldsymbol{H})$ as shown in Fig. 16.3 or obtained more directly via a discriminative classifier that yields $P(\boldsymbol{H}|\boldsymbol{\nu})$. Here, the use of a probabilistic classifier is vital to ensure decisions made are robust to uncertainty in the health state of the structure.

Finally, a transition model is used to forecast the future health states, given the current health state and a decided action, i.e., $P(\boldsymbol{H}_{t+1}|\boldsymbol{H}_t, d_t)$. The transition model considers the degradation of the structure under the various operational and environmental conditions a structure may experience, while accounting for uncertainties in each.

By employing decision-process models such as the one presented here, one can obtain optimal strategies regarding the operation and maintenance of individual structures by maximising the expected utility.

16.4 Structures as Hierarchies

A key assumption implicit in the development of the fault-tree failure models within the risk-based SHM decision framework is that structures can be represented as a hierarchy, or, in other terms, as a system of systems of systems. As it is outside the scope of the current paper, a comprehensive and consistent notation for referencing specific elements of a structure is not established here. Rather, the constituent levels and elements within the hierarchical representation are presented, in addition to the process by which one arrives at them.

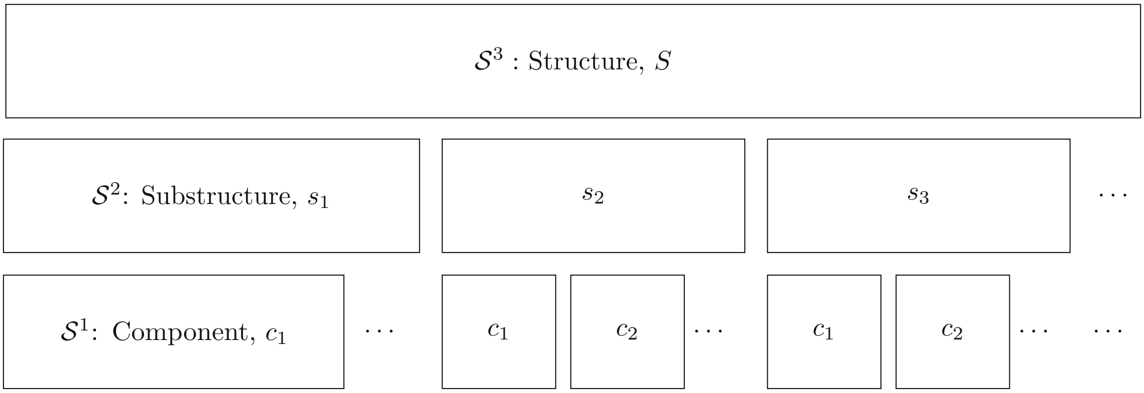

Fig. 16.4 A structure as systems of systems

Consider a structure of interest S. To obtain a hierarchical representation for S, one must first decompose S into a discrete number of constituent elements, which are referred to as *substructures*. Substructures are considered to be entities that may, in principle, be assembled remotely or available for independent testing prior to incorporation into the full-scale structure. Within the hierarchical representation, some substructures may be further decomposed up until the stage at which it would no longer be meaningful or useful to do so. Substructures at this stage are referred to as *components*. As such, components are considered to be substructures that cannot (or need not) be decomposed further; these are the smallest element of a structure one might reasonably monitor. A notable sub-class of component is the *joint*. Joints are considered to be the physical mechanisms by which substructures are joined together.

A diagram illustrating the hierarchical representation of a structure is shown in Fig. 16.4. The levels in the hierarchy that specifies the system of systems of systems shown are denoted as $\mathcal{S}^1$, $\mathcal{S}^2$, and $\mathcal{S}^3$—corresponding to the component, substructure, and structure levels, respectively. Within each level of the hierarchy, elements can be listed.

Returning to the example of a wind farm, it would be perfectly reasonable to consider a single turbine as an individual structure, representing the $\mathcal{S}^3$ level in a hierarchy. In the $\mathcal{S}^2$ level, one may consider substructures such as the drive train, blades, or tower. Finally, in the $\mathcal{S}^1$ level, one may have components such as the gearbox or bearings comprising the drive train, or the web and shells comprising the blades.

The hierarchical representation of structures facilitates the specification of the decision process that motivates the development and implementation of SHM technologies. This facilitation is achieved by decomposing structures into constituent substructures and components that can then be used to define failure modes of the structure. Given a finite set of failure modes of interest, one can then specify critical components, and therefore health states, to be targeted by a monitoring system.

16.5 Populations of Structures as Hierarchies

A natural method for incorporating decision-making into PBSHM is to extend the hierarchical representation of structures to hierarchical representations of populations. The number of levels required in a hierarchy is of course dependent on context. However, it is deemed that an additional three levels provide sufficient generality for most PBSHM applications, and indeed the discussions in the current paper.

The additional levels necessary to extend the hierarchical representation to populations of structures can be summarised as follows:

- $\mathcal{S}^4$—Type/Model Inventory: This level of the hierarchy corresponds to the lowest population level and represents an organisational grouping in which all individual structures in the population are of the same type/model and can be considered to be nominally identical. Thus, populations at this level in the hierarchy are homogeneous.
- $\mathcal{S}^5$—Group Inventory: This next population level corresponds to a set of $\mathcal{S}^4$ inventories for which it is necessary or convenient to consider as a group for operational reasons such as asset management. As a group inventory may be formed of disparate type/model inventories, in general, group inventories are heterogeneous populations.
- $\mathcal{S}^6$—Inventory: This level of the hierarchy corresponds to the total set of structural assets operated or owned by an organisation or company. Again, this level will generally represent a heterogeneous population.

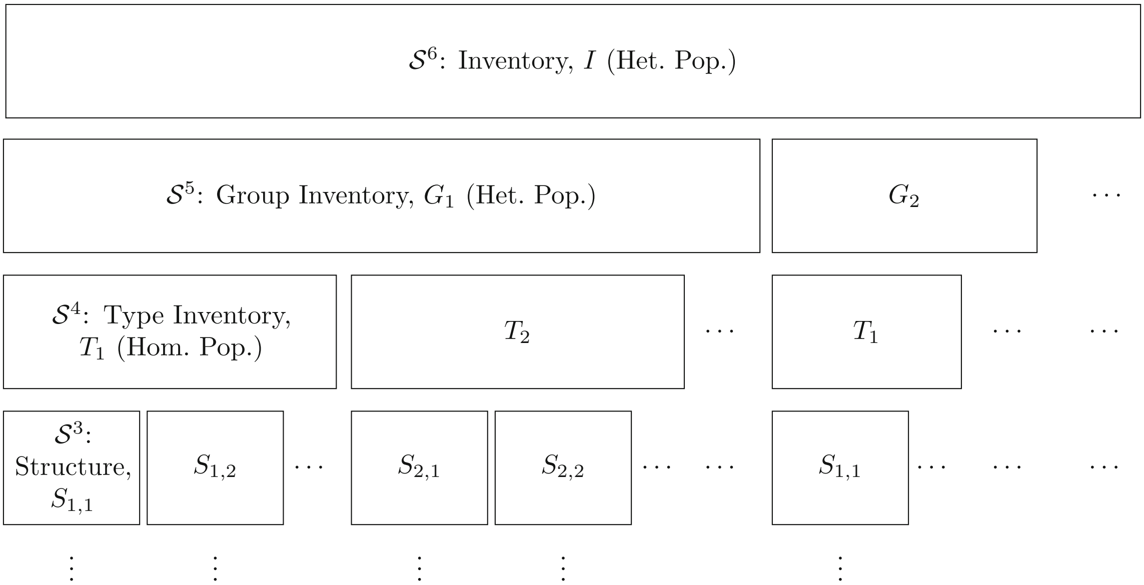

Fig. 16.5 An inventory as a system of systems of systems of systems

Figure 16.5 depicts the continuation of the hierarchical representation from $\mathcal{S}^3$ to $\mathcal{S}^6$. In Fig. 16.5, an inventory I is considered as a system of systems of systems of systems. Once again, a list can be formed of the constituent elements for each level in the hierarchy.

To further elucidate this extension of the hierarchy, once again, consider the example of an organisation operating offshore wind farms. As previously indicated, a wind farm comprised exclusively of turbines of a single type or model can form a homogeneous population; this corresponds to $\mathcal{S}^4$ in the hierarchy. In the case that the organisation is responsible for multiple wind farms, or a single farm with a mixture of turbine types, one may wish to organise these type/model inventories into group inventories. For example, these group inventories may be formed from type inventories according to the geographical jurisdiction of sub-divisions within the organisation, or even formed from a collection of type inventories that are overseen by a single maintenance crew. Should these populations each be comprised of a different model of wind turbine, the group inventories formed would be heterogeneous populations and correspond to $\mathcal{S}^5$ in the hierarchy. Alternatively, if all the wind farms consist of a single type of turbine, $\mathcal{S}^4$ and $\mathcal{S}^5$ can be merged and the group inventories are instead homogeneous populations. Finally, the group inventories owned by the wind farm organisation can be aggregated as an inventory in the $\mathcal{S}^6$ level of the hierarchy. This level would represent the organisation's total structural assets and could amount to, for example, multiple wind farms spread across the globe, maritime vessels, and aircraft that may be used for inspection, maintenance, or other operational activities.

As is the case for traditional SHM, the hierarchical representation of structures and populations of structures can help facilitate decision-making for PBSHM in several ways. These decision processes are discussed further in the following section.

16.6 Risk-Informed PBSHM

Numerous decisions must be made throughout the life cycle of a PBSHM system. Most obvious are the operation and maintenance decisions an organisation may have to make, following the installation of a monitoring system, such as inspections and repairs. Equally important, however, are the decisions that must be made prior to implementation such as those made in the operational evaluation stage of PBSHM.

16.6.1 Operational Evaluation

One significant way in which adopting a hierarchical risk-based approach to PBSHM facilitates decision-making occurs very early on, in the operational evaluation stage. By considering specific failure modes and constructing fault trees for individual structures, one can decide the key elements of a structure that should be modelled in IEs and AGs. In other words, the specification of failure modes as combinations of component and substructure failures can be used to inform the granularity at which IEs and AGs are constructed. A further benefit of the population-based approach is that, as structures are considered nominally identical, large proportions of the fault trees may be mapped across a homogeneous population, with the exception of perhaps environment-specific failure modes.

The extension of the hierarchy to represent populations of structures via the inclusion of levels $\mathcal{S}^4$ to $\mathcal{S}^6$ prompts one to consider how failures may be defined at the population level. One possible way to approach the failure of a population would be to consider the critical missions for the operating organisation. Depending on the nature of the organisation—whether they are non-commercial or commercial—these missions may be related to performance measures such as availability and/or profitability. Consider the wind farm example. Suppose that the operating organisation is required to supply energy from the wind farm to an electrical grid while maintaining a total population availability of 99%. This population can then be considered to have failed if the population structural availability falls below 99%. This population failure may be specified then by extending the fault tree, defining the population failures as a combination of individual failures. In addition, the organisation may wish to specify a failure condition based upon profitability, perhaps based upon a performance criterion related to a moving-average of the total power output. Again, this failure could be represented as a combination of individual structure failures and environmental conditions. This distinct failure mode is likely to be highly correlated with the availability failure mode; fortunately, the probabilistic graphical models employed in the risk-based approach can account for these "common-cause" failures. This approach to defining population failures can be applied at any of the population levels within the hierarchical representation by considering combinations of failures in the levels below.

Defining failures at the population level within the hierarchy allows one to assign costs during the operational evaluation stage. Following on from this, population-scale actions can also be defined.

16.6.2 Inferences and Decisions

A fundamental process of decision-making for PBSHM is reasoning under uncertainty. This is typically achieved via inferences. Within the hierarchical framework for PBSHM, different types of inferences can be defined:

- I-inference: This type of inference corresponds to those usually made in traditional SHM and occur within the individual structure levels $\mathcal{S}^3$ to $\mathcal{S}^1$. An example of an I-inference is the process of determining a probability distribution over the health states of an individual structure using data acquired from that structure.
- L-inference: This type of inference occurs between levels in the hierarchical representation of structures. These may also be types of I-inference, for example, determining the probability of failure for a (sub)structure given local component health states. Other L-inferences may include those relating to the validation and verification of predictive models (V&V). For example, one may be able to validate a predictive model for a structure at the $\mathcal{S}^3$ level with data measured from substructures or components at the $\mathcal{S}^2$ and $\mathcal{S}^1$ levels, respectively.
- P-inference: This type of inference occurs across populations. If the inference is across a type inventory in $\mathcal{S}^4$, i.e., a homogeneous population, they can be denoted as HomP-inferences. These inferences across populations may utilise technologies such as forms [10]. An example of a HomP-inference is inferring the health state of a member in a population using data aggregated across all members in the population. On the other hand, if a P-inference is between populations containing different types of structure, such as within a group inventory in $\mathcal{S}^5$, then the inferences can be referred to as HetP-inferences. HetP-inferences may involve using transfer learning techniques such as domain adaptation [12]. An example of a HetP-inference is transferring the degradation (transition) model for a blade from a population of four-blade wind turbines to a population of three-blade wind turbines.

These inferences within the hierarchical representation of populations facilitate reasoning under uncertainty using PBSHM systems; this can naturally be extended to decision-making under uncertainty, by considering the following types of decisions:

- I-decision: This type of decision is made at the individual structure levels in the hierarchy, $\mathcal{S}^1$ to $\mathcal{S}^3$. Again, this type of decision corresponds to decisions one may make with a traditional SHM system. An example of an I-decision is selecting a maintenance strategy for an individual structure, substructure, or component for repair. Unlike in traditional SHM, in the risk-informed PBSHM approach, I-decisions can be informed by I-, L-, and P-inferences alike.
- L-decision: The actions selected via this type of decision operate between levels of the hierarchical representation. As with L-inferences, these decisions may pertain to the V&V of predictive models. For example, deciding whether can

one proceed with using a structural model validated on substructures. Another example of this type of decision relates to resource allocation. Suppose one has a limited budget to carry out some structural testing to acquire data for mode updating. Under these circumstances, one should aim to decide on a set of tests, and the levels at which these tests are carried out, such that the largest improvement in model performance is obtained for the given budget.

- P-decision: This type of decision is made at the population levels in the hierarchy, S^4 to S^6. These actions may pertain to resource management. For example, one may decide to send a team of engineers to perform inspections on a type inventory based on the probability of failure for a population rather than the probability of failure of an individual structure. Scheduling inspections in this manner could save both time and expenditure. Again, these decisions may be informed via I-, L-, and P-inferences.

To summarise, the hierarchical representation of populations of structures facilitates both making inferences and making decisions for PBSHM, by allowing for the definition of specific types of inferences and decisions.

16.6.3 Value of Information Transfer

Value of information (VoI) is a concept in decision theory defined to be the amount of money/resource a decision-maker should be willing to pay in order to gain access to information prior to making a decision. The concept of VoI has seen some application to traditional SHM in recent works [7, 21].

Extending the risk-based approach to decision-making from traditional SHM to PBSHM opens up the possibility of value of information transfer, i.e., the price a decision-maker should be willing to pay in order to gain information via transfer, prior to making a decision. This value arises as a result of change in maximum expected utility that can be achieved should a change in optimal policy occur as a result of the additional information made available via transfer. This notion of value of information transfer yields the thought-provoking implication that, in some contexts, it may be an optimal decision to allow a (sub)structure to fail, since the data obtained throughout the failure process may improve the management of the other individuals in a population.

16.7 Conclusions

To conclude, PBSHM provides a general framework for overcoming issues of data scarcity associated with developing predictive models for detecting and forecasting damage within structures. This advantage is achieved via technologies that allow for the transfer of information between individual structures within a population. Adopting a probabilistic risk-based approach to SHM allows inferences made about the health-states of individual structures to inform operation and maintenance decisions via the use of hierarchical representations of structures and fault trees. The current paper extends this hierarchical representation of structures to representations of populations, such that decision process can be defined over populations. Other advantages can be gained by adopting a risk-based approach to PBSHM; for example, the identification of critical components and substructures can be used to inform the development of irreducible element models and the associated attributed graphs.

Acknowledgments The authors would like to gratefully acknowledge the support of the UK Engineering and Physical Sciences Research Council (EPSRC) via grant references EP/W005816/1 and EP/R006768/1. For the purpose of open access, the authors have applied a Creative Commons Attribution (CC BY) licence to any Author Accepted Manuscript version arising. KW would also like to acknowledge support via the EPSRC Established Career Fellowship EP/R003625/1.

References

1. Farrar, C.R., Worden, K.: Structural Health Monitoring: A Machine Learning Perspective. Wiley, Hoboken (2013)
2. Rytter, A.: Vibration Based Inspection of Civil Engineering Structures. Ph.D. Thesis, Aalborg University (1993)
3. Schöbi, R., Chatzi, E.N.: Maintenance planning using continuous-state partially observable Markov decision processes and non-linear action models processes and non-linear action models. Struct. Infrastruct. Eng. **12**(8), 977–994 (2016)
4. Vega, M.A., Todd, M.D.: A variational Bayesian neural network for structural health monitoring and cost-informed decision-making in miter gates. Struct. Health Monit. 21, 1475921720904543 (2020)

5. Hughes, A.J., Barthorpe, R.J., Dervilis, N., Farrar, C.R., Worden, K.: A probabilistic risk-based decision framework for structural health monitoring. Mech. Syst. Signal Process. **150**, 107339 (2021)
6. Bull, L.A., Rogers, T.J., Wickramarachchi, C., Cross, E.J., Worden, K., Dervilis, N.: Probabilistic active learning: an online framework for structural health monitoring. Mech. Syst. Signal Process. **134**, 106294 (2019)
7. Hughes, A.J., Bull, L.A., Gardner, P., Barthorpe, R.J., Dervilis, N., Worden, K.: On risk-based active learning for structural health monitoring. Mech. Syst. Signal Process. **167**, 108569 (2022)
8. Hughes, A.J., Bull, L.A., Gardner, P., Dervilis, N., Worden, K.: On robust risk-based active-learning algorithms for enhanced decision support. Mech. Syst. Signal Process. **181**, 109502 (2022)
9. Vega, M.A., Hu, Z., Todd, M.D.: Optimal maintenance decisions for deteriorating quoin blocks in miter gates subject to uncertainty in the condition rating protocol. Reliabil. Eng. Syst. Safety **204**, 107147 (2020)
10. Bull, L.A., Gardner, P., Gosliga, J., Rogers, T.J., Dervilis, N., Cross, E.J., Papatheou, E., Maguire, A.E., Campos, C., Worden, K.: Foundations of population-based SHM, part I: homogeneous populations and forms. Mech. Syst. Signal Process. **148**, 107141 (2021)
11. Gosliga, J., Gardner, P.A., Bull, L.A., Dervilis, N., Worden, K.: Foundations of population-based SHM, part II: heterogeneous populations - graphs, networks, and communities. Mech. Syst. Signal Process. **148**, 107144 (2021)
12. Gardner, P., Bull, L.A., Gosliga, J., Dervilis, N., Worden, K.: Foundations of population-based SHM, part III: heterogeneous populations - mapping and transfer. Mech. Syst. Signal Process. **148**, 107142 (2021)
13. Tsialiamanis, G., Mylonas, C., Chatzi, E., Dervilis, N., Wagg, D.J., Worden, K.: Foundations of population-based SHM, part IV: the geometry of spaces of structures and their feature spaces. Mech. Syst. Signal Process. **157**, 107692 (2021)
14. Worden, K., Bull, L.A., Gardner, P., Gosliga, J., Rogers, T.J., Cross, E.J., Papatheou, E., Lin, W., Dervilis, N.: A brief introduction to recent developments in population-based structural health monitoring. Front. Built Environ. **6**, 146 (2020)
15. Wickramarachchi, C.T., Gosliga, J., Cross, E.J., Worden, K.: On the use of graph kernels for assessing similarity of structures in population-based structural health monitoring. In: Proceedings of the Thirteenth International Workshop on Structural Health Monitoring (2022)
16. Dhada, M., Girolami, M., Parlikad, A.K.: Anomaly detection in a fleet of industrial assets with hierarchical statistical modeling. Data-Centric Eng. **1**, e21 (2020)
17. Sucar, L.E.: Probabilistic Graphical Models: Principles and Applications. Springer, London (2015)
18. Kjaerulff, U.B., Madsen, A.L.: Bayesian Networks and Influence Diagrams: A Guide to Construction and Analysis. Springer, New York (2008)
19. Bobbio, A., Portinale, L., Minichino, M., Ciancamerla, E.: Improving the analysis of dependable systems by mapping fault trees into Bayesian networks. Reliabil. Eng. Syst. Safety **71**(3), 249–260 (2001)
20. Mahadevan, S., Zhang, R., Smith, N.: Bayesian networks for system reliability reassessment. Struct. Safety **23**(3), 231–251 (2001)
21. Kamariotis, A., Chatzi, E., Straub, D.: Value of information from vibration-based structural health monitoring extracted via Bayesian model updating. Mech. Syst. Signal Process. **166**, 108465 (2022)

Chapter 17
On the Influence of Corrosion Levels in the Dynamic Behavior of Pretensioned Concrete Structural Elements

M. Brambilla, P. Chiariotti, A. Cigada, P. Darò, F. Di Carlo, P. Isabella, and A. Meda

Abstract Corrosion of internal reinforcements represents a serious issue in prestressed concrete structures, as it progressively decreases the load bearing capacity of components, hence contributing to reduce the service life of the whole structure and potentially inducing unexpected and uncontrolled cracking phenomena. A proper assessment of the health status of a structural element is the key priority of any Structural Health Monitoring (SHM) system. As SHM systems are finally getting the credits they deserve, given their relevance in keeping structures monitored and hence in contributing to people life safety, the focus has shifted towards the development of automated approaches to promptly detect incipient damages potentially jeopardizing the structural integrity of the target system.

Within this context, this chapter, which describes a part of a wider research program targeted to the development of robust strategies for SHM of civil structures, aims at discussing a preliminary study carried out to identify the potential correlation between corrosion levels in pretensioned concrete elements and their dynamic behavior. Several pretensioned concrete beams of the same geometry (cross section 200 × 300 mm; total length 3700 mm) have been subjected to an artificial corrosion process that was induced through electrolytic cells by dipping the beams within a 3% saline solution, up to half of the height of the cross section. Four-point bending tests were performed up to failure. Dynamic impact tests were also performed to identify any eventual variation in terms of dynamic behavior of the beams. The chapter shows that increased corrosion induces wider changes in the dynamic behavior of the structural elements.

Keywords Pretensioned concrete beams · Corrosion · Structural alterations · Modal testing · Dynamic behavior

17.1 Introduction

Potential consequences of corrosion of internal reinforcements of prestressed reinforced concrete (PC) beams can be extremely serious, as witnessed by recent cases worldwide, in which severe damages can lead to unexpected structural crisis. The combined effect of corrosion-induced sectional reductions and wires rupture failures can be fatal for the structural safety. Despite the need to deepen the knowledge of the influence of corrosion on the behavior of PC elements, not many research documents are available in literature. Experimental tests have been performed on rectangular-shaped [1] and T-shaped [2] PC beams in four-point bending, varying the corrosion level. The results of cyclic loading tests on T-shaped corroded PC beams are discussed in [3]. The fatigue behavior of pretensioned partially prestressed concrete beams with corroded prestressing wires or rebars is studied in [4]. Posttensioned concrete beams with corroded strands were tested in bending by [5]. Studies regarding the possible relationship between the prestressed concrete cracking induced by strand corrosion and the corrosion itself can be found in [6, 7]. An investigation on the coupled effect of sustained load and corrosion on the long-term behavior of PC beams has been done in [8]. Finally, experimental tests on PC beams [9–10] and actual bridge PC beams [11–13] subjected to natural corrosion are also available.

M. Brambilla · P. Chiariotti (✉) · A. Cigada
Department of Mechanical Engineering, Politecnico di Milano, Milan, Italy
e-mail: paolo.chiariotti@polimi.it

P. Darò
Sacertis Ingengeria S.r.l., Torino, Italy

F. Di Carlo · P. Isabella · A. Meda
Department of Civil Engineering and Computer Science Engineering, Università degli Studi di Roma "Tor Vergata", Rome, Italy

H. Y. Noh et al. (eds.), *Dynamics of Civil Structures, Volume 2*, Conference Proceedings of the Society
for Experimental Mechanics Series, https://doi.org/10.1007/978-3-031-36663-5_17

Modal testing of prestressed reinforced concrete beams already proved to be an effective technique for damage detection, as demonstrated for example by the work of Ren and De Roeck [14] in case of increasing cracking. The importance of experimental testing is of high relevance especially when these are targeted to validate and update numerical models, with the aim to investigate the presence of eventual damages [15, 16]. As for the identification of damages caused by corrosive environments, great effort has been made to combine chemical causes and structural consequences in numerical models, as done by Ožbolt et al. [17]. Nevertheless, it is important to underline the complexity of this phenomenon when addressing composite materials like concrete. Therefore, practical examples are still demanded to study such a complex phenomenon. The use of dynamic response to evaluate structural alteration in case of corrosion is still of great interest in the field of Structural Health Monitoring (SHM) [18].

This chapter aims at investigating whether the corrosion levels in prestressed beams are somehow correlated to their dynamic behavior. The chapter is organized in this way: the experimental campaign is described at first, focusing on the samples preparation and the approach used to induce corrosion phenomena; results are then presented in terms of static and dynamic data; the last section draws the main conclusions of the work.

17.2 Experimental Campaign

Five PC beams were cast and then tested under four-point bending at the Laboratory of the University of Rome "Tor Vergata," within the framework of an Italian PRIN project, for the evaluation of the flexural response of corroded reinforced concrete and PC beams [19]. The specimens feature a 200 × 300 mm rectangular cross section and a total length of 3700 mm. The longitudinal reinforcement is made of three ½-inch seven wires strands, two placed at the bottom of the section and one at the top, and four Ø10 mm ordinary rebars. Ø8 mm bars are adopted for the stirrups, with a spacing of 100 mm and 200 mm in the outer (1450 mm) and inner (800 mm) zones of the beams, respectively. The concrete cover is equal to 20 mm. Figure 17.1 shows the geometry and reinforcement details of the specimens.

Concrete with a mean compressive strength equal to 52.6 MPa – value measured on 100 mm side cubes – has been used, while the ordinary rebars are characterized by yielding and ultimate strengths equal to 510 MPa and 630 MPa, respectively. The initial wire prestressing stress is equal to 1300 MPa, corresponding to about 70% of the ultimate strength equal to 1860 MPa. One beam was kept uncorroded (PC-UC) for reference, while four specimens were subjected to accelerated corrosion, with different corrosion levels. The artificial corrosion has been provided with an accelerated process through electrolytic cells, by dipping the beams within a 3% saline solution, up to half of the height of the cross section. Only the two bottom longitudinal ½-inch strands have been connected to the positive pole of the power supply (anode), while the cathodes have been realized with Ø10 mm steel bars soaked in the saline solution. A current intensity equal to 0.5 A for each strand has been applied, in agreement with the values suggested in [20], while the ordinary rebars and the stirrups have been epoxy coated to avoid corrosion. The duration of the artificial corrosion process has been properly defined for each specimen, to obtain the desired corrosion level. For further details see [21]. The setup for the accelerated corrosion process is shown in Fig. 17.2.

At the end of the corrosion process, the beam specimens have been further tested by carrying out an Experimental Modal Analysis (EMA) measurement, specifically targeted to investigate how a diffuse accelerated degradation process affects the dynamic behavior of each beam.

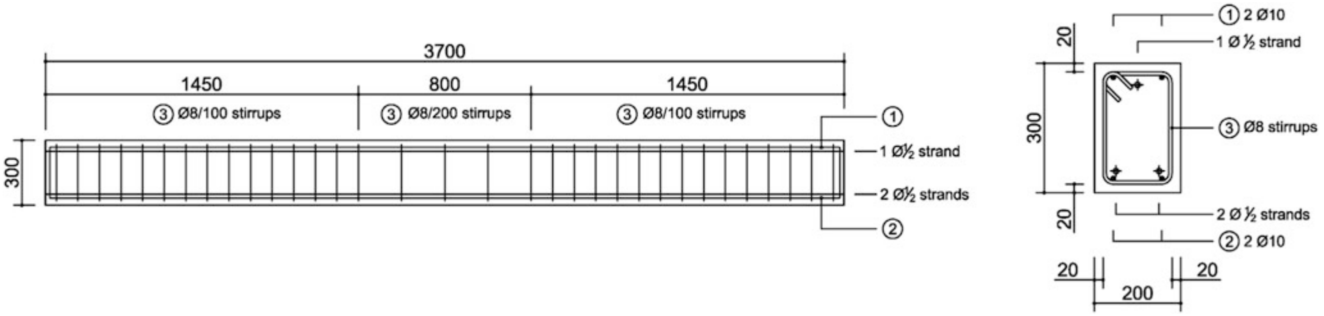

Fig. 17.1 Geometry and reinforcement details of the PC beam

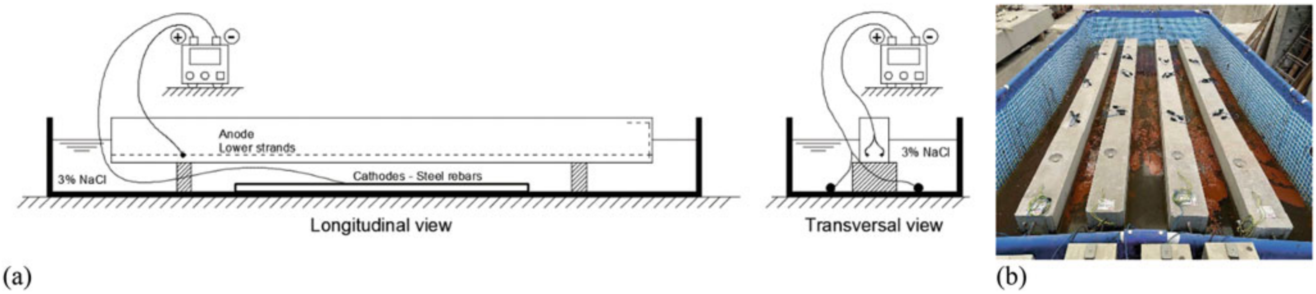

Fig. 17.2 (**a**) Experimental setup for the accelerated corrosion process. (**b**) Detail of the PC beams dipped within the saline solution

Table 17.1 Nominal corrosion severity expressed as percentage mass loss for the considered specimens

N	Beam	Mass loss %
1	PC-UC	–
2	PC-C1	1.6
3	PC-C2	9.03
4	PC-C3	19.15
5	PC-C4	27.48

Four specimens of prestressed concrete (PC) are of interest, as they have been tested for increasing nominal corrosion (C) severity: PC-C1, PC-C2, PC-C3, and PC-C4. The correspondent nominal corrosion levels, expressed as percentage mass loss, are reported in Table 17.1. The nominal corrosion level has been evaluated after the tests by cleaning [22] and weighing the strands extracted from each specimen. In addition, for reference, the uncorroded beam, PC-UC, is also reported in the table, to provide a full list of all the available tests.

Two remarks are worth of mention to justify the adopted procedure:

(i) Time constraint of the experimental campaign allowed for only one dynamic test per specimen. Corroded beams have been tested right after being pulled out from the pool and before starting the four-points bending test; therefore, PC-UC served as healthy reference condition.
(ii) As basic assumption, the five original beams are considered as nominally identical in terms of design and material properties.

The dynamic testing experimental campaign has been divided in two consecutive steps. A preliminary test has been carried out to appreciate fluctuations in the dynamic response of two beams, namely PC-UC (uncorroded) and PC-C4 (medium/high level of corrosion), due to corrosion. To isolate the eventual dynamic variations related to the corrosion level from other variables potentially able to change the beam dynamics, the two beams were tested in free-free conditions, i.e., by hanging the beams to a bridge crane. In the second part of the testing campaign, for safety issues, all the five specimens have been tested in simply-supported configuration (Fig. 17.3). In this latter series, each beam was tested through impact testing in roving accelerometer mode. Six measurement points have been set on each beam, as reported in Fig. 17.3a. Node number 2 was identified as driving point. A two-channels, synchronous acquisition module has been used for the task: one channel always dedicated to the input force in node 2, while the other dedicated to the acquisition of one output acceleration response at a time. Data were recorded for 1 s and sampled at 8 kHz.

17.3 Experimental Results

A four-point bending test has been carried out on the five specimens, according to the test setup shown in Fig. 17.4. The vertical load is applied through two hydraulic 300 kN jacks and measured with a load transducer. The contrast frame, made with steel beams, is anchored to the laboratory strong floor by means of two pretensioned high strength rebars. The two supports were realized with two rotating cylinders. The span of the beams during the test was equal to 2700 mm, while the shear length was 900 mm, corresponding to one third of the total span length. Five potentiometer transducers have been used to measure the vertical displacements at the midspan (P1), under the point load (P2 and P3) and at the support point (P4 and P5). A square 50 mm grid was plotted on the lateral surfaces to facilitate the cracks detection and measures. Furthermore, the specimens were also instrumented with ceramic stress sensor for the measurement of compressive stress, placed inside

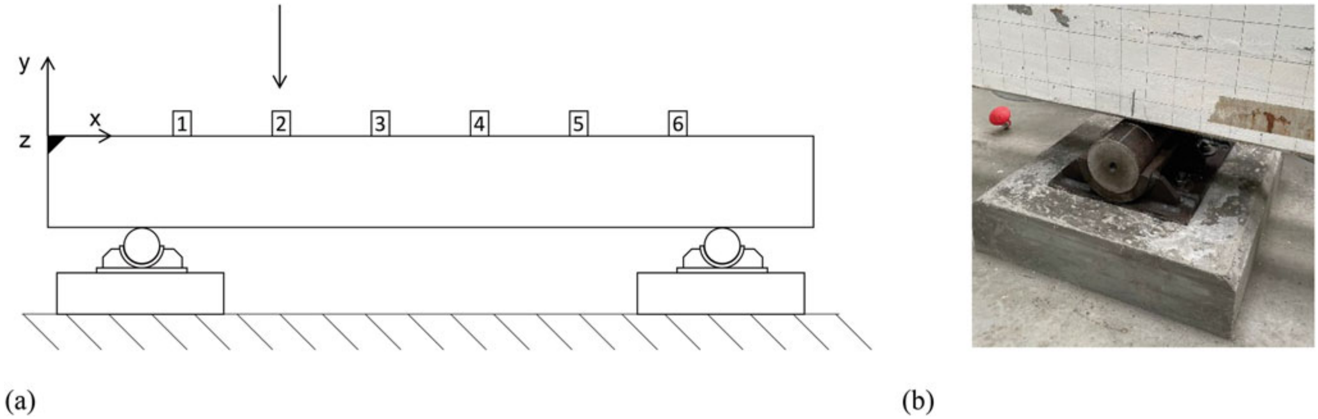

Fig. 17.3 (**a**) Experimental setup for PC specimens. A roving accelerometer configuration has been used, for driving point in 2. (**b**) Detail of the final pin

the beam, before casting. In particular, three cross sections have been instrumented, each one with two stress sensors, one located at the top and another at the bottom (Fig. 17.4b).

The experimental results of the analyzed specimens are summarized in Fig. 17.5, in terms of Load-Midspan deflection. In all the tests, indeed, the displacement measured at the midspan by the potentiometer P1 has been corrected for the support settlement (even if almost negligible), measured by the potentiometers P4 and P5.

Dynamic tests were performed before the static tests. Nevertheless, results are presented after the static analysis results to have a clearer picture of the correlation between the corrosion levels and the dynamic behavior of the beams.

As already mentioned, a preliminary test was carried out to compare, in free-free conditions, the healthy beam, PC-UC, with the most corroded specimens, PC-C4. Figure 17.6 shows the two amplitude FRFs estimated at the driving point location. The two curves show similar dynamic behavior, as the resonance frequencies associated with the first three bending modes are located around 90 Hz, 230 Hz, and 440 Hz, respectively. The small resonance detected on PC-UC at 270 Hz might be a torsional mode likely due to nonperfect alignment of the measurement nodes with beam midspan, while peaks at low frequencies are the rigid modes of the free-free system. Focusing on bending modes, the largest drop on structural resonances due to the corrosion phenomena is evident in the high frequency range. Despite testing in free-free condition makes it possible to avoid any disturbance related to the compliance of the supports, safety constraints mainly related to the test duration, imposed to test the five beams in simply supported conditions. Nevertheless, the magnification effect identified in the high-frequency range suggests focusing the analysis on the third bending mode of the beams, which occurs above 400 Hz.

Indeed, if focusing on this frequency range for the results of the dynamic tests carried out on the entire set of specimens, which have been dynamically tested in pinned-pinned conditions, a down-shift of the third bending mode resonant frequency seems to occur with increased corrosion level (Fig. 17.7 – sum FRFs of the beams tested).

This is more evident if looking at Table 17.2, which reports the differential percentage on the third mode resonant frequency for the four corroded beams with respect to the uncorroded one (PC-UC). The higher the percentage mass loss, the wider the frequency range percentage.

Indeed, this behavior suggests a decrease in the stiffness of the beams, the more important the higher the corrosion level characterizing each beam. To better understand and justify this behavior, the corroded beams have been further analyzed to verify both the distribution of corrosion on the strands and the effective stress characterizing each beam.

Once cracked, the lower left-hand and right-hand strands of each beam were extracted from concrete, and the inner 3 meters span was divided into three slices of 1 meter length: T1, T2, T3. Each slice was then visually inspected in 10 different sections (10 cm span) along its longitudinal axis, and the state of corrosion was classified based on two parameters:

- Number of visible corroded wires out of the seven wires constituting a single strand.
- Severity of the corrosion process based on visual inspection (low, medium, and high tags).

The purpose of this additional check is to appreciate how corrosion distributes along the beam strands, as it has a direct impact on the prestress of each specimen and hence the static and dynamic responses of each beam. Figure 17.8 reports the results of this analysis. PC-C3 and PC-C4 show the highest strand cross-section size reduction. The highest mass loss of PC-C4, however, suggests the presence of a distributed corrosion phenomenon rather than a localized one. Contrarily, PC-C3 shows more severe corrosion on specific locations. This localized corrosion might justify the lower bearing capacity

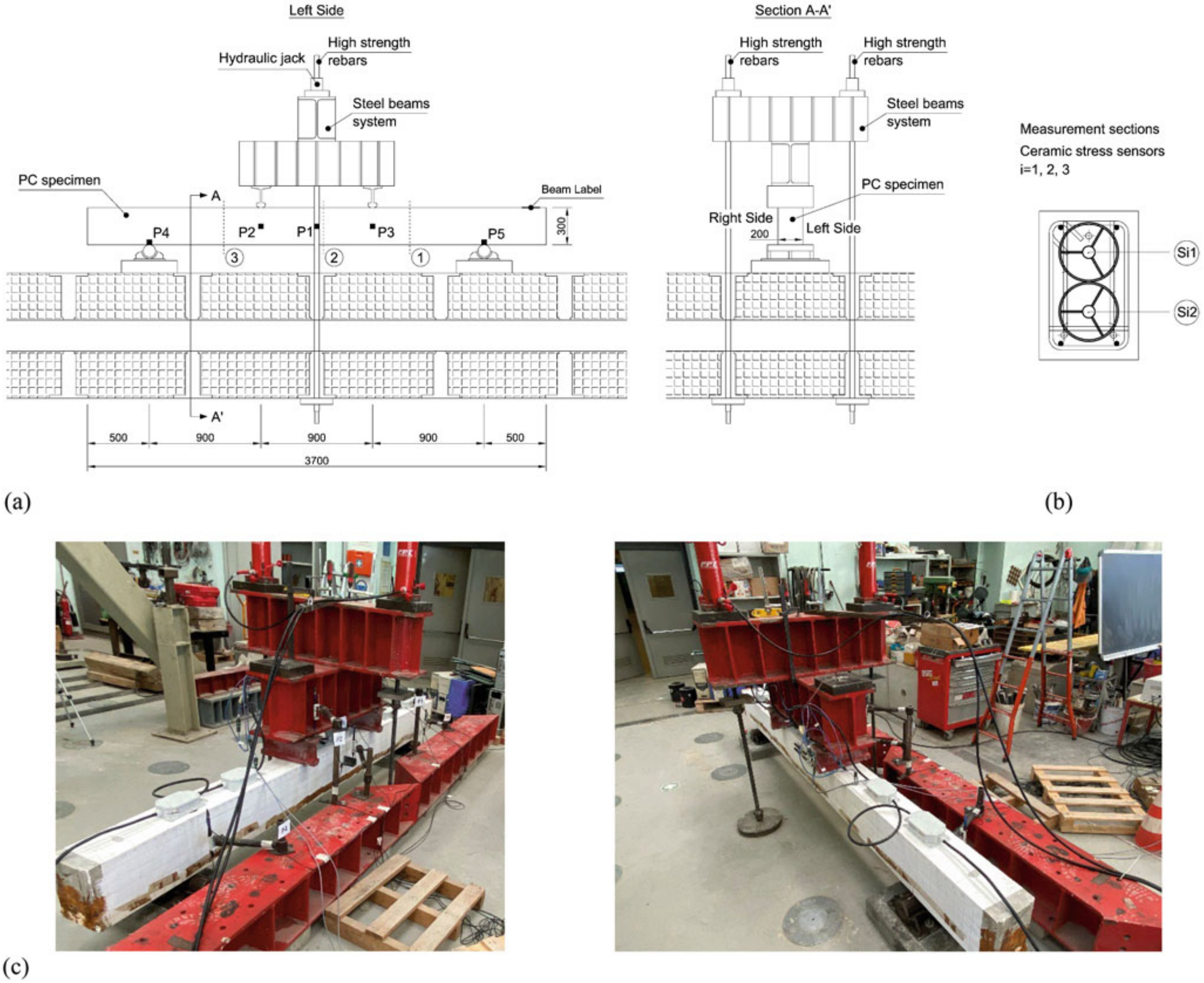

Fig. 17.4 (**a**) Test setup. (**b**) Detail of the location of the ceramic stress sensors. (**c**) Views of the experimental test setup

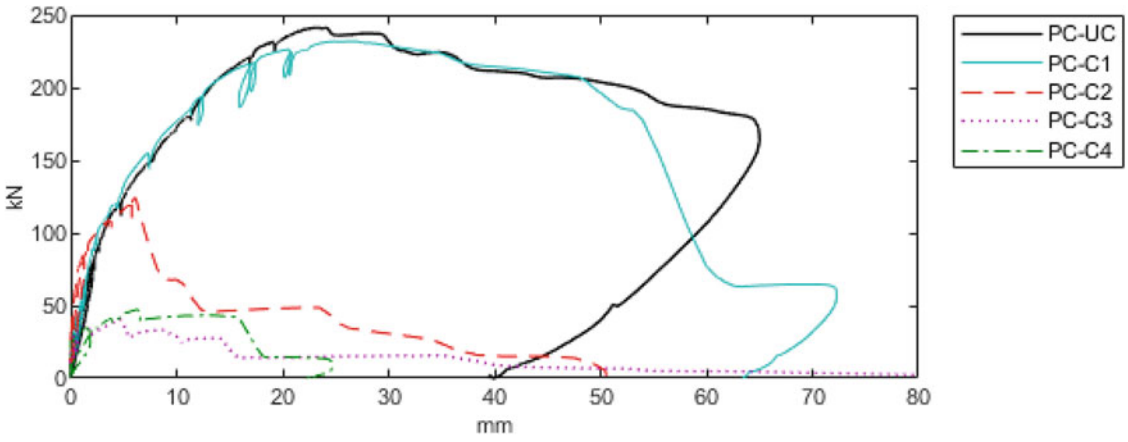

Fig. 17.5 Load-Midspan deflection curves

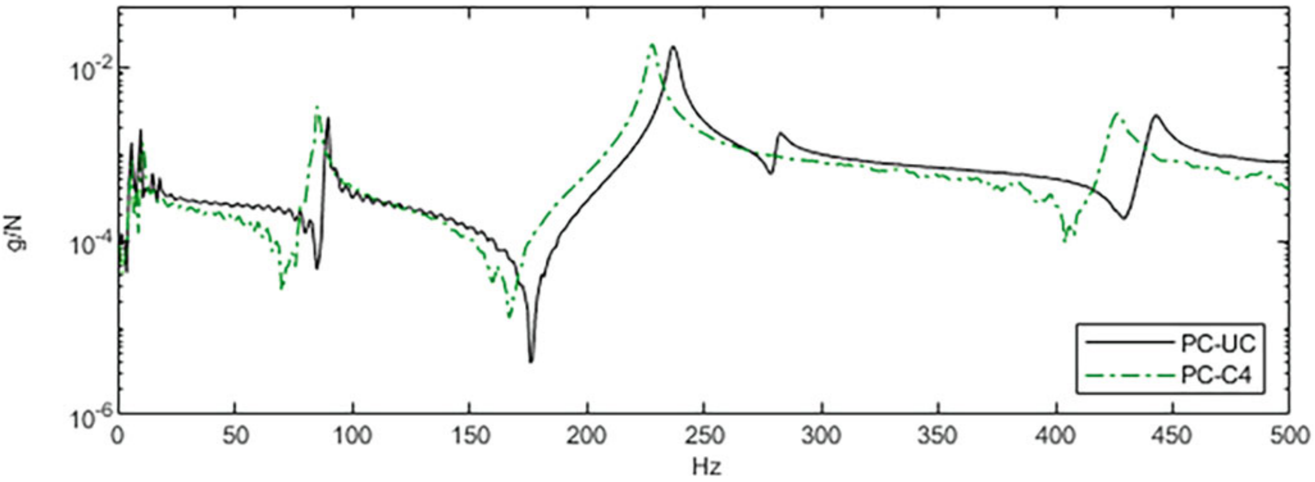

Fig. 17.6 Frequency response functions at driving point for the uncorroded specimen PC-UC and the most corroded specimen PC-C4 according to nominal mass loss of Table 17.1. Beams are tested in free-free configuration

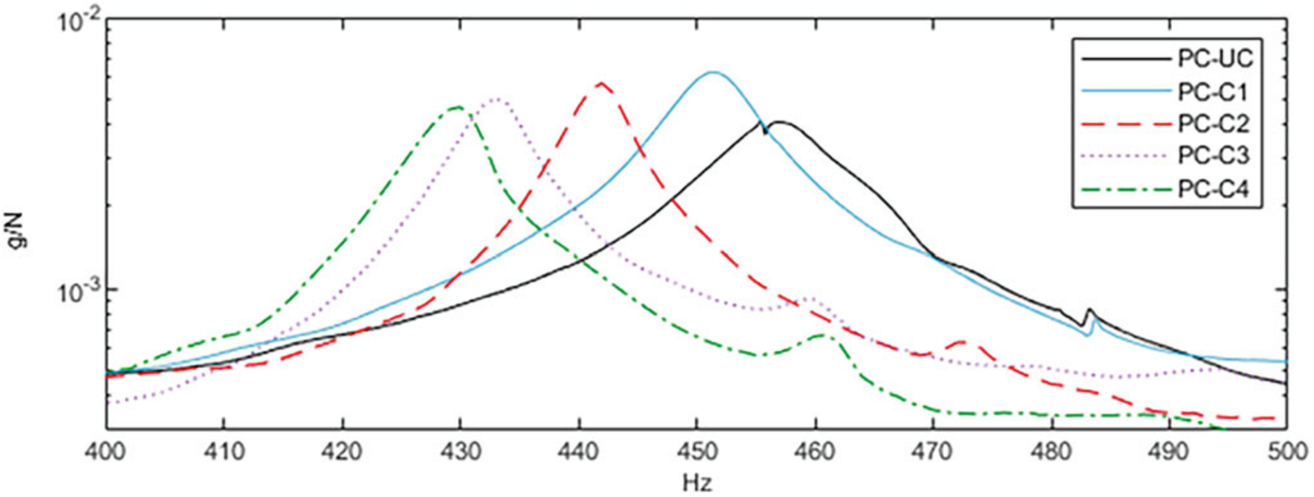

Fig. 17.7 Resonances at third bending mode in terms of amplitudes of the sum of the FRFs of the six nodal points for each specimen. Beams are tested in pinned-pinned configuration (Fig. 17.3)

Table 17.2 Resonant frequency differential percentage with respect to PC-UC for the four corroded beams – third bending mode

N	Beam	Mass loss %	Δ Resonant frequency %
1	PC-UC	–	–
2	PC-C1	1.6	−1.1
3	PC-C2	9.03	−3.2
4	PC-C3	19.15	−5.1
5	PC-C4	27.48	−6.0

of PC-C3 with respect to PC-C4. As for PC-C1 and PC-C2, neither localized nor distributed corrosion-induced damages worth of mention are to be reported.

The former results are further supported by the data recorded by the stress sensors embedded in the beams (Fig. 17.4b) and reported in Fig. 17.9. For each PC beam, the values of the compressive stress measured in the three instrumented sections (dashed vertical lines), after the artificial corrosion process and before the execution of the four-point bending test, are reported. For each section, data for both intrados and extrados locations of the sensors are provided.

Despite some sensors malfunctioning, which prevented to have all data available for all the beams at both extrados and intrados, it appears quite clear that an increase in the corrosion level induces a reduction on the stress magnitude at the intrados. This is particularly evident for the PC-C4 beam, which embeds the highest corrosion level (highest mass-loss level).

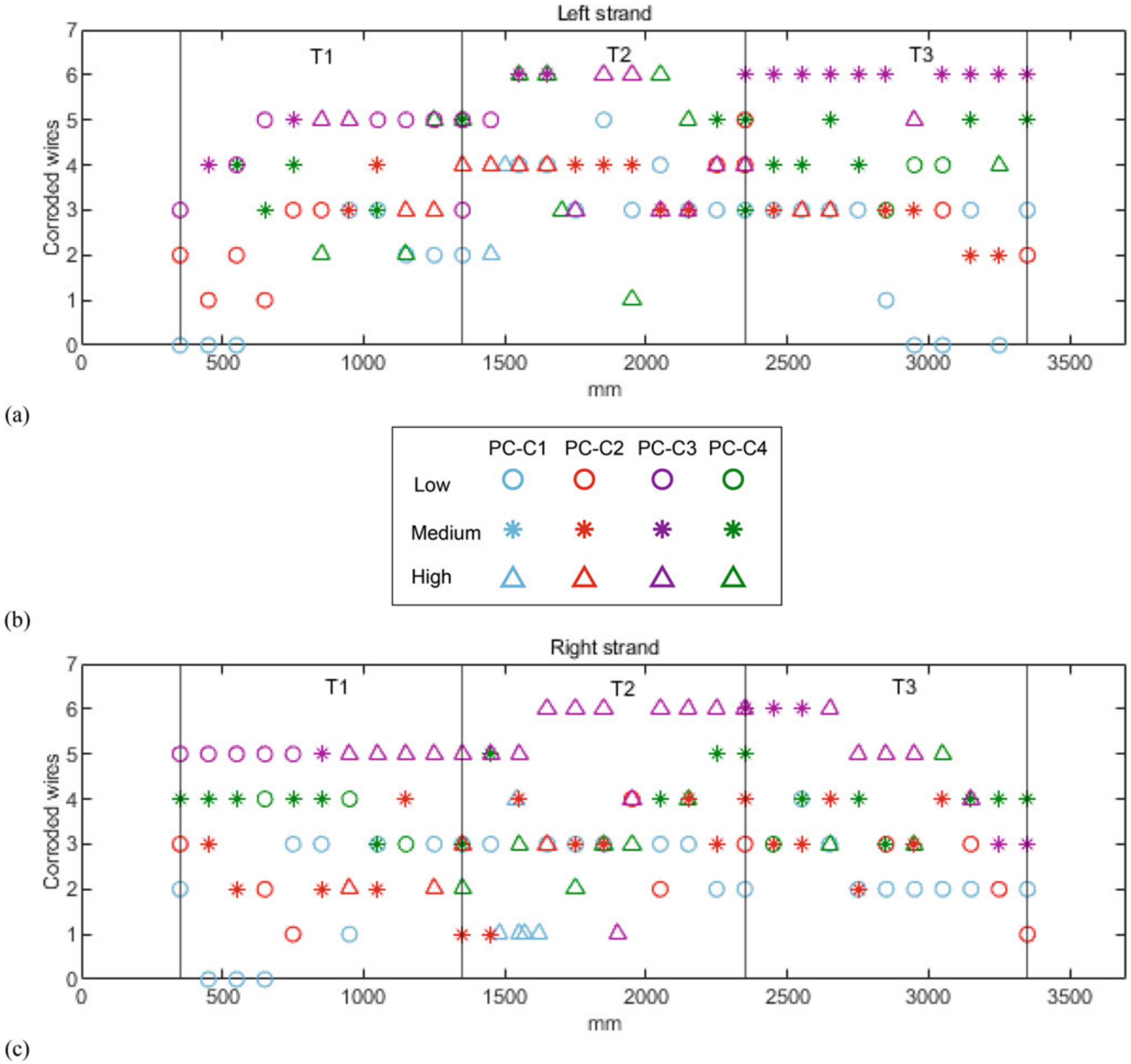

Fig. 17.8 Morphology of the corrosion along beam axis, divided in the three slices T1, T2, T3. On the abscissa axis, the beam axis. On the ordinate axis, the number of corroded wires in that section of the strand. A strand is composed of seven wires. (**a**) Left strand of the corroded beam specimens. (**b**) Legend table for the three tag-levels of corrosion severity: low, medium, high. (**c**) Right strand of the corroded beam specimens

17.4 Conclusion

Corrosion is one of the main problems affecting the durability of concrete and, hence, the health status of the structures. Understanding the effects of different corrosion levels on static and dynamic behaviors of the structure is then of key importance. This chapter demonstrated, in a multitest approach, that higher corrosion levels might induce stress reduction in prestressed concrete beams. Lower residual stress values, in turns, cause stiffness reductions that downshifts the resonant frequency of the target beams with respect to the uncorroded reference. It is interesting to highlight, however, that diffused corrosion seems to impact more on the dynamic behavior of the structure, while localized corrosion has higher impact on the static load generating the first cracks.

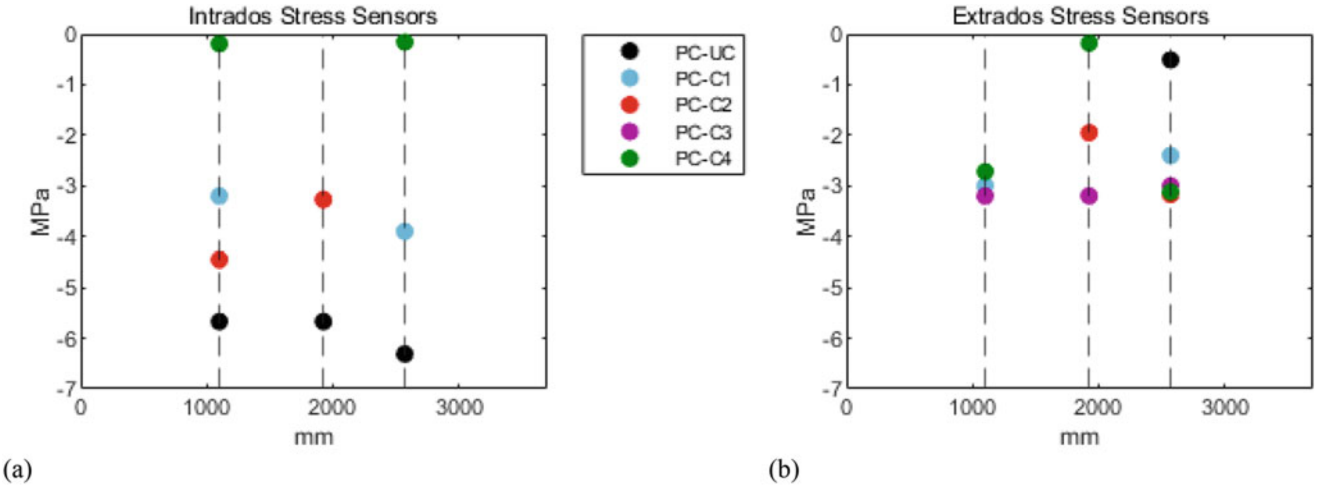

Fig. 17.9 Stress-data from the stress sensors embedded in the beams as in Fig. 17.4b. (**a**) Intrados and (**b**) extrados stress-data. On the abscissa, the beam axis

The analysis presented is indeed preliminary and quite far from the possibility of generating general valid for all prestressed concrete structures. On this purpose, authors are carrying out further tests targeted to increase the analysis dataset and the general validation.

Acknowledgments The research presented in this chapter is supported by the PRIN 2017 grant, from the Italian Ministry of University and Research, within the project "Life-long optimized structural assessment and proactive maintenance with pervasive sensing techniques."

References

1. Rinaldi, Z., Imperatore, S., Valente, C.: Experimental evaluation of the flexural behavior of corroded P/C beams. Constr. Build. Mater. **24**(11), 2267–2278 (2010). https://doi.org/10.1016/j.conbuildmat.2010.04.029
2. Menoufy, A.E., Soudki, K.: Flexural behavior of corroded pretensioned girders repaired with CFRP sheets. PCI J. **59**(2), 129–143 (2014)
3. ElBatanouny, M.K., Nanni, A., Ziehl, P.H., Matta, F.: Condition Assessment of prestressed Concrete Beams Using Cyclic and Monotonic Load Tests. ACI Struct. J. **112**(1), 81–90 (2015). https://doi.org/10.14359/51687181
4. Zhang, W., Liu, X., Gu, X.: Fatigue behavior of corroded prestressed concrete beams. Constr. Build. Mater. **106**, 198–208 (2016). https://doi.org/10.1016/j.conbuildmat.2015.12.119
5. Zhang, X., Wang, L., Zhang, J., Ma, Y., Liu, Y.: Flexural behavior of bonded post-tensioned concrete beams under strand corrosion. Nucl. Eng. Des. **313**, 414–424 (2017). https://doi.org/10.1016/j.nucengdes.2017.01.004
6. Dai, L., Wang, L., Zhang, J., Zhang, X.: A global model for corrosion-induced cracking in prestressed concrete structures. Eng. Fail. Anal. **62**, 263–275 (2016). https://doi.org/10.1016/j.engfailanal.2016.01.013
7. Dai, L., Bian, H., Wang, L., Potier-Ferry, M., Zhang, J.: Prestress Loss diagnostics in pretensioned concrete structures with corrosive cracking. J. Struct. Eng. **146**(3), 04020013 (2020). https://doi.org/10.1061/(ASCE)ST.1943-541X.0002554
8. Yang, J., Guo, T., Li, A.: Experimental investigation on long-term behavior of prestressed concrete beams under coupled effect of sustained load and corrosion. Adv. Struct. Eng. **23**(12), 2587–2596 (2020). https://doi.org/10.1177/1369433220919
9. Mircea, D., Ioani, A., Filip, M., Pepenar, I.: Long-term durability of reinforced and prestressed elements in aggressive environments. Dent. Mater. J. **91**(2), 135–140 (1994)
10. Belletti, B., Rodríguez, J., Andrade, C., Franceschini, L., Sánchez Montero, J., Vecchi, F.: Experimental tests on shear capacity of naturally corroded prestressed beams. Struct. Concr. **21**(5), 1777–1793 (2020). https://doi.org/10.1002/suco.202000205
11. Pape, T.M., Melchers, R.E.: The effects of corrosion on 45-year-old prestressed concrete bridge beams. Struct. Infrastruct. Eng. **7**(1–2), 101–108 (2011). https://doi.org/10.1080/15732471003588411
12. Rogers, R., Wotherspoon, L., Scott, A.N., Ingham, J.M.: Residual strength assessment and destructive testing of decommissioned concrete bridge beams with corroded pretensioned reinforcement. PCI J. **57**(3), 100–118 (2012). https://doi.org/10.15554/pcij.06012012.100.118
13. Rogers, R.: Assessing pre-tensioned reinforcement corrosion within the New Zealand concrete bridge stock, Doctoral Dissertation, Department of Civil and Environmental Engineering, University of Auckland, August 2016
14. Ren, W.-X., de Roeck, G.: Structural damage identification using modal data. II: Test verification. J. Struct. Eng. **128**(1), 96–104 (2002). https://doi.org/10.1061/(ASCE)0733-9445(2002)128:1(96)
15. Ren, W.-X., de Roeck, G.: Structural damage identification using modal data. I: Simulation verification. J. Struct. Eng. **128**(1), 87–95 (2002). https://doi.org/10.1061/(ASCE)0733-9445(2002)128:1(87)

16. Teughels, A., de Roeck, G.: Damage detection and parameter identification by finite element model updating. Rev. Eur. Génie Civ. **9**, 109 (2005)
17. Ožbolt, J., Oršanić, F., Balabanić, G.: Modelling processes related to corrosion of reinforcement in concrete: coupled 3D finite element model. Struct. Infrastruct. Eng. **13**(1), 135–146 (2017). https://doi.org/10.1080/15732479.2016.1198400
18. Farrar, C.R., Worden, K.: An introduction to structural health monitoring. Philos. Trans. R. Soc. A Math. Phys. Eng. Sci. **365**(1851), 303–315 (2007). https://doi.org/10.1098/rsta.2006.1928
19. Di Carlo, F., Meda, A., Rinaldi, Z.: Structural performance of corroded R.C. beams. Eng. Struct. **274**, 115117 (2023)
20. El Maaddawy, T.A., Soudki, K.A.: Effectiveness of impressed current technique to simulate corrosion of steel reinforcement in concrete. J. Mater. Civ. Eng. **15**(1), 41–47 (2003). https://doi.org/10.1061/(ASCE)0899-1561(2003)15:1(41)
21. Di Carlo, F., Isabella, P., Rinaldi, Z., Meda, A.: Structural performance of corroded prestressed concrete beams. In: NBSC 2022. The New Boundaries of Structural Concrete 2022, Lecce, Italy (8–9 September 2022)
22. ASTM G1–90: Practise for Preparing, Cleaning and Evaluating Corrosion Test Specimens. ASTM International, West Conshohocken (2002)

Chapter 18
Force Identification and Response Prediction of an Offshore Platform Using Admittance Function and Incomplete Response Measurements

Amirali Sadeqi, Luigi Caglio, Henrik Stang, Jørgen S. Nielsen, Ulf T. Tygesen, and Evangelos Katsanos

Abstract In several existing structures and infrastructure systems, the loads and responses are hard to be accurately measured especially when the structural systems are partly or wholly inaccessible or located in harsh conditions (e.g., offshore structures). The chapter proposes a frequency-domain technique to estimate the force and response of vibrating structures using limited response signals. The frequency response function of a structure can be reconstructed either based on an updated finite element model's properties or identified modal parameters by a data-driven approach. Next, the components of the frequency response function corresponding to a few degrees of freedom, whose response measurements are available, can be selected to create the admittance function and, consequently, to estimate the applied loads and predict the response of any degree of freedom. The technique is implemented on the finite element model of an offshore platform exposed to wave loads. The estimated wave loads and response of the submerged elements indicate the proposed technique's competence in simplicity and efficiency compared with other methods.

Keywords Force Identification · Response Estimation · Offshore Jacket · Output-only Data · Sparse Data · Frequency Response Function · Admittance Function

18.1 Introduction

Obstacles associated with measuring loads that induce vibrations in large-scale structures have triggered the development of output-only (i.e., response-based) approaches for modal analysis, system identification as well as structural health monitoring (SHM), and damage detection. However, knowing the loads a structure experiences on a long-term basis is essential for optimized structural design and modification, fatigue analysis, and eventually, life-cycle management. Such a need can be addressed through inverse problem techniques. Measuring large-scale structures' response in all degrees of freedom (DOF) constitutes an additional challenge, especially when the sensor installation and data acquisition are cumbersome. However, the accuracy of several damage localization techniques depends on the mode shape resolution that, in turn, requires the response of, at least, numerous, DOFs to be measured. The latter has extensively been studied through optimization and finite element (FE) model updating problems [1–5].

Both measuring and monitoring offshore supporting structures are associated with the challenges introduced above. Braced jackets, designed to carry platforms and rigs, are operating under harsh conditions since excessive wave loads, hard to be measured, may jeopardize the integrity of those remote structures. Furthermore, they are partly submerged where the response measurements are inaccessible or highly noisy. One of the common approaches for joint input-state estimation is Kalman Filter based on sparse output-only measurements, namely, the Augmented Kalman Filter (AKF) for linear systems and its Extended (EKF) and Unscented (UKF) versions for the nonlinear ones. However, these recursive algorithms involve high computations and runtime especially when applied to high-dimensional digital twins of existing structures with continuous and online SHM plans. Despite the capabilities of these statistical methods for force and state

---

A. Sadeqi (✉) · L. Caglio · H. Stang · E. Katsanos
Department of Civil and Mechanical Engineering, Technical University of Denmark, Lyngby, Denmark
e-mail: amisa@dtu.dk

J. S. Nielsen
TotalEnergies EP Danmark A/S, Esbjerg, Denmark

U. T. Tygesen
Rambøll Group, Global Division-Jackets, Esbjerg, Denmark

H. Y. Noh et al. (eds.), *Dynamics of Civil Structures, Volume 2*, Conference Proceedings of the Society for Experimental Mechanics Series, https://doi.org/10.1007/978-3-031-36663-5_18

estimation, they are sensitive to the applied load type and distribution and suffer from uncertainties related to the initial state prediction. Moreover, the associated process-measurement noise covariance parameters need, most of the time, separate tuning [6–8].

The frequency response function (FRF) has some interesting properties containing the system characteristics that render it unique for each linear system, updatable in terms of dynamic and modal properties, as well as independent from the input (load) and output (response) measurements but adjustable with respect to the input-output locations. One of the FRF's advantages is making an explicit relation between the system output (i.e., measured responses) and the applied input (i.e., loads). Many applications can be studied using FRF-based methods for linear and nonlinear system identification, force identification, as well as damage detection (e.g., [9–12]). This study proposes a classical frequency-domain technique for force identification and response prediction using only incomplete response measurements. The idea introduced herein is to obtain the FRF of an updated model and the admittance function, i.e., the inversion of partial FRF components concerning the available response signals. The admittance function and response signals are then applied to estimate the loads in the frequency domain. Finally, the response in any DOF can be achieved using the FRF and estimated loads. The technique is easy to adopt and implement with a low computation burden and it is applied to the FE model of a real-world offshore platform. Furthermore, the efficiency and accuracy of the technique are studied and compared to an AKF-based algorithm.

18.2 Problem Description

The offshore structure studied herein is an offshore platform in the North Sea, operated by TotalEnergies. The photo of the structure is displayed in Fig. 18.1a.

It consists of a symmetric jacket structure with steel tubular members and braces carrying a large refinery station at the top. A major part of the jacket is submerged and may experience excessive load due to abnormal waves bringing difficulties for sensor installation and data acquisition. Hence, the responses measured only from the out-of-water sensors will be used to facilitate the load identification and response prediction for both nonsubmerged and submerged structural members respectively. The final goal is to achieve the full-set measurements of the jacket's element as a reference in the undamaged state for the subsequent steps (e.g., SHM, modal analysis, fatigue analysis, and damage detection) of a structural integrity management task. The conditions describe an inverse problem based on incomplete or sparse output-only measurements. The solution could normally be a model-based (non-data-driven) identification procedure that requires an FE model of the asset to be built and updated. A simplified 3D FE model of the platform has been simulated in OpenSees and presented in Fig. 18.1b. The jacket framing has been created by tubular elastic beam elements with six DOF at each node. The diameter of members varies from 500 to 1700 mm, and the thickness varies from 20 to 50 mm. The deck framing above the jacket is created using HEB/IPE elastic beam elements with various section properties and the topside framing is simulated using rigid tubular elements. The total weight of the topside station including the building, machinery, and appurtenance is about 8000 tons and simulated through several lumped masses as highlighted in Fig. 18.1b, at the edges of each floor. The total number of DOFs of the current FE model created by the possible minimum nodes is more than 3100. A conventional solution for the problem described above, is a model-based Kalman Filter input-state estimation process. However, for the mentioned number of DOFs, the process is time-consuming in a continuous SHM scheme. In the present chapter a classical FRF-admittance-based approach is used which is more robust and efficient for the linear regime, meaning no so extreme wave loads.

18.2.1 Methodology

Let x be the output or response vector of a q degrees of freedom (DOF) system under m input forces as shown in Fig. 18.2 (left).

The governing equation of motion in the frequency domain can be stated as

$$X_i(\omega) = \sum_{j=1}^{m} H_{ij}(\omega) F_j(\omega), \quad 1 \le i \le l \tag{18.1}$$

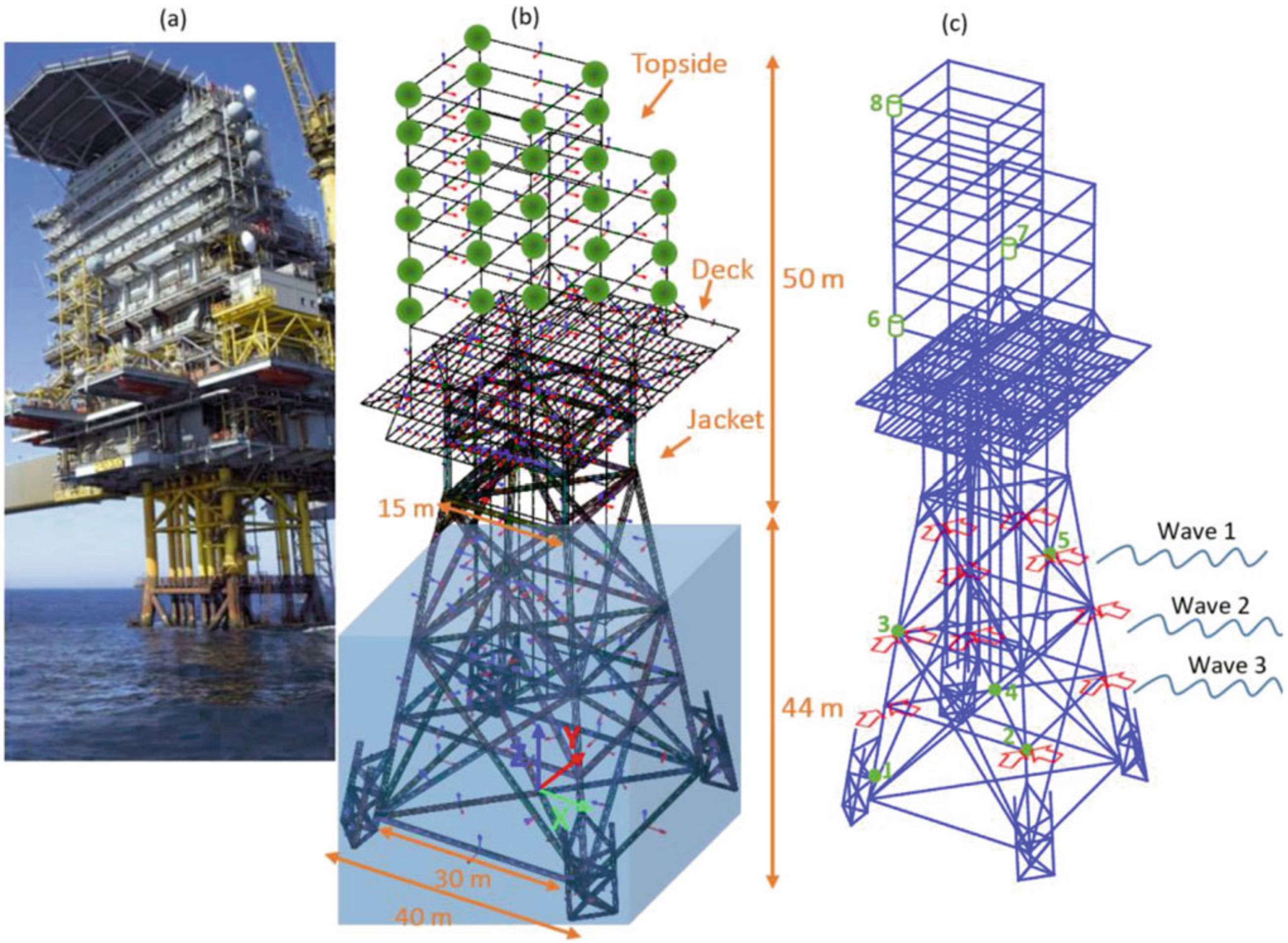

Fig. 18.1 (**a**) Photo of the accommodation platform in North Sea, (**b**) FE model with approximate dimensions, (**c**) Wave loads and sensors' location at three typical nodes (6 to 8), and five typical under water nodes (1 to 5) for response estimation testing

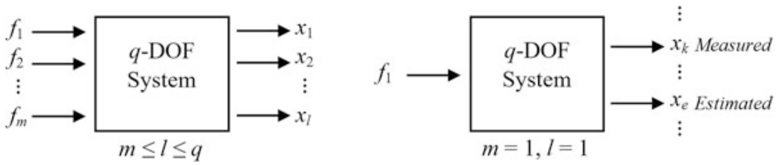

Fig. 18.2 General view of a q-DOF system under m inputs and l outputs (left); and case with one input (right)

where F and X are the force and response vectors. Moreover, H_i is a row vector of the FRF being invariant for linear systems and can be expressed as

$$\begin{gathered} H(\omega) = C(j\omega I - A)^{-1}B, \\ A = \begin{bmatrix} [0]_{q\times q} & [\mathrm{I}]_{q\times q} \\ -\left[M^{-1}K\right]_{q\times q} & \left[-M^{-1}D\right]_{q\times q} \end{bmatrix}, B = \begin{bmatrix} [0]_{q\times m} \\ \left[M^{-1}\eta\right]_{q\times m} \end{bmatrix}, C = [\mathrm{I}]_{l\times 2q} \end{gathered} \tag{18.2}$$

where I is the identity matrix of dimension $2q$ or less when indicated beside the bracket. Additionally, M, K, and D are the mass, stiffness, and damping matrices of dimension q, respectively. Also, $\eta = \alpha I_{q\times m}$ and α is a scalar value of zero at DOFs with no input and one elsewhere. A simplified formula for the calculation of the FRF can be formed using the modal properties:

$$H_0(\omega) = \sum_{i=1}^{q} \frac{\phi_i \phi_i^T}{\phi_i^T M_{ii} \phi_i \left(\omega_i^2 - \omega^2 + 2j\omega_i \zeta_i \omega\right)} \tag{18.3}$$

where ω_i and ζ_i are the *i*th natural angular frequency and damping ratio respectively, (i.e., scalar) and ϕ_i is the *i*th mode shape (column vector of dimension q). The final FRF, H, can be obtained by selecting l rows and m columns of H_0 that correspond to the measured response and the applied force. Rewriting Eq. (18.1) in terms of the force results in

$$F_j(\omega) = \sum_{i=1}^{l} G_{ji}(\omega) X_i(\omega), 1 \leq j \leq l \tag{18.4}$$

where G is the admittance function as

$$G(\omega) = B^{\dagger}(j\omega I - A) C^{\dagger} \tag{18.5}$$

where '†' indicates the pseudo-inverse of a matrix. Once a state-space model of the structure is available (either identified or simulated-updated), the H and G are known and independent of the force type and amplitude. Following Eq. (18.1) to obtain an arbitrary response X_i, the concerning FRF columns must be multiplied by the applied forces as

$$X_i(\omega) = \underbrace{\left[H_{i1}(\omega)\, H_{i2}(\omega) \ldots H_{im}(\omega)\right]}_{G_i^{-1}(\omega)} \begin{bmatrix} F_1(\omega) \\ \vdots \\ F_m(\omega) \end{bmatrix} \tag{18.6}$$

Contrarily, based on Eq. (18.4), to inversely obtain any of the applied forces, the admittance function needs to be multiplied only by one response signal e.g., $G_i(\omega)X_i(\omega)$, that is the advantage of the proposed admittance-based method since G_i is determined as the pseudo-inverse of a few relevant components of H, not the full matrix or Eq. (18.5). To better understand, one could consider a simple case, as illustrated by Fig. 18.2 (right), with only one force, f_1, and two arbitrary response signals; one given (measured) and the other desired (to estimate). The admittance and FFT of the response x_k can be used to obtain the force from the following expression:

$$F_1(\omega) = G_{1k}(\omega) X_k(\omega) = H_{k1}^{-1}(\omega) X_k(\omega) \tag{18.7}$$

Then, the desired response x_e can be obtained after taking inverse FFT of the following:

$$X_e(\omega) = H_{e1}(\omega) F_1(\omega) \tag{18.8}$$

It must be noted that, unlike H and G, the FFT of the measured response, X_k, is mirrored, and needs to be adjusted before being multiplied by G. If the FRF is calculated according to Eq. (18.2), the estimated force F_1 and response X_e, can be switched to the time-domain (f_1 and x_e) after removing the right half band of the data and taking the inverse FFT to cope with the truncation. Hence, the reconstructed signals will contain half samples of the original ones unless the response signals applied to the process are up-sampled beforehand. On the other hand, if Eq. (18.3) is used to calculate the FRF, the full-length signal estimates will be achieved. Either way, it is inferred from Eqs. (18.7) and (18.8), that only one arbitrary response signal x_k is sufficient to estimate one applied force. In general, for G being a full-row-rank matrix, the number of applied response signals or DOFs in Eq. (18.4) must be equal or more than the number of forces applied to the system. The latter matters in real-world and large-scale structures, where the number of all DOFs is significantly more than the DOFs imposed to the external load, especially when the response of all DOFs is not measurable.

Given that the relation between the displacement and acceleration response signals is $\ddot{X}_i(\omega) = -\omega^2 X_i(\omega)$, the force signal can also be obtained from the acceleration measurements as

$$F_j(\omega) = \frac{1}{\omega^2} \sum_{i=1}^{l} G_{ji}(\omega) \ddot{X}_i(\omega), 1 \leq j \leq l \tag{18.9}$$

In the presence of high-level noise in the acceleration data, the time history f_j obtained from the inverse FFT of F_j might be distorted and one may need to pre-apply smoothing filters and detrending schemes.

18.3 Analysis

The transient dynamic analysis is performed in OpenSees by applying three independent wave loads. Two sensing scenarios are considered for the force-response estimation process using response-only data measured by three and 34 sensors, respectively. Figure 18.1c depicts the wave load positions (each wave force applied to four nodes in two directions) and typical locations of three sensors (first scenario) at the topside frame, i.e., nodes 6 to 8. In the scenario with 34 sensors (second scenario), the response of the jacket's head (above wave 1) is also considered in the force-response estimation process. In both scenarios, the sensor nodes are typically chosen above the sea level. The first scenario is a theoretical case with minimum response signals to be included in the estimation process (i.e., as many as the number of independent applied loads). However, including more sensors, as in the second scenario, improves the estimation in practical cases with noise. The transient analysis is conducted with a time step equal to 0.1 s, and the displacement (and acceleration) responses are recorded in both x and y directions for 300 s. Also, the FRF and admittance are calculated with a sampling frequency of 10 Hz, hence, $\omega = 20\pi[1, \ldots, 3000]/3000$. The objective is to estimate the three wave loads as well as the displacement (and acceleration) at five nodes, 1 to 5, on the submerged part of the platform.

18.4 Results

Since the applied wave loads at each elevation are identical along the x and y directions and the geometry of the structure is, to some extent, symmetric, the results from the estimation process are presented for only one direction. Figure 18.3 plots the admittance function in the x-direction corresponding to the three wave loads in Fig. 18.1c) and the first sensing scenario that includes three response signals measured by sensors at nodes 6, 7, and 8. For the first scenario, the admittance function can be obtained as follows:

$$G(\omega) = \begin{bmatrix} H_{11}(\omega) & H_{12}(\omega) & H_{13}(\omega) \\ H_{21}(\omega) & H_{22}(\omega) & H_{23}(\omega) \\ H_{31}(\omega) & H_{32}(\omega) & H_{33}(\omega) \end{bmatrix}^{\dagger} \tag{18.10}$$

In Eq. (18.10), each term $H_{ij}(\omega) \in \mathbb{C}^{6 \times 1}$ is a column vector (selected from full H in Eq. (18.2)), with six elements corresponding to six DOFs of each FE model node pointed from 6 to 8, hence,$G(\omega) \in \mathbb{C}^{3 \times 18}$. For instance,$G_{21}(\omega)$in Fig. 18.3 represents the admittance function of node 6, in the x direction under wave 2. Likewise, for the second scenario with 34 sensors, G can be calculated so that the rows are extended as $G(\omega) \in \mathbb{C}^{3 \times 204}$. Note that if the applied wave loads to each node in the x and y directions were different, the columns must also have been extended as $G(\omega) \in \mathbb{C}^{6 \times 18}$ and$G(\omega) \in \mathbb{C}^{6 \times 204}$. After calculating G, estimating both the wave loads and the corresponding response is made feasible.

Particularly, Fig. 18.4 displays the applied wave loads and estimated ones, using only displacement measurements in two scenarios (i.e., three and 34 sensors). The estimates have been obtained by substituting $G(\omega) \in \mathbb{C}^{3 \times 18}$ (for the first scenario) and $G(\omega) \in \mathbb{C}^{3 \times 204}$ (for the second scenario) into to Eq. (18.4). After taking the inverse FFT of the lower sideband of F, a smoothing filter was applied in the time domain only to compare with the exact wave loads, not for the following response estimation. It must be noted that the load estimates based on three sensor data with noise are disordered and not displayed herein. The normalized mean square errors (NMSE) for the estimates in the noiseless scenario with three sensors are less than 5% indicating the accuracy of the technique with the least number of sensors. On the other hand, the estimation of the lower amplitude waves, such as wave 3, is more affected by the noise that increases the NMSE up to 30%. Nevertheless, as shown in Fig. 18.5, the response estimates at the selected nodes are overlaid with the exact ones with NMSE less than 1% for both scenarios, where the noise effect is more observable in lower amplitude signals (e.g., nodes 1 and 2). The estimates have been obtained by applying the above-mentioned F to Eq. (18.6) and taking the inverse FFT of X with no smoothing or detrending process.

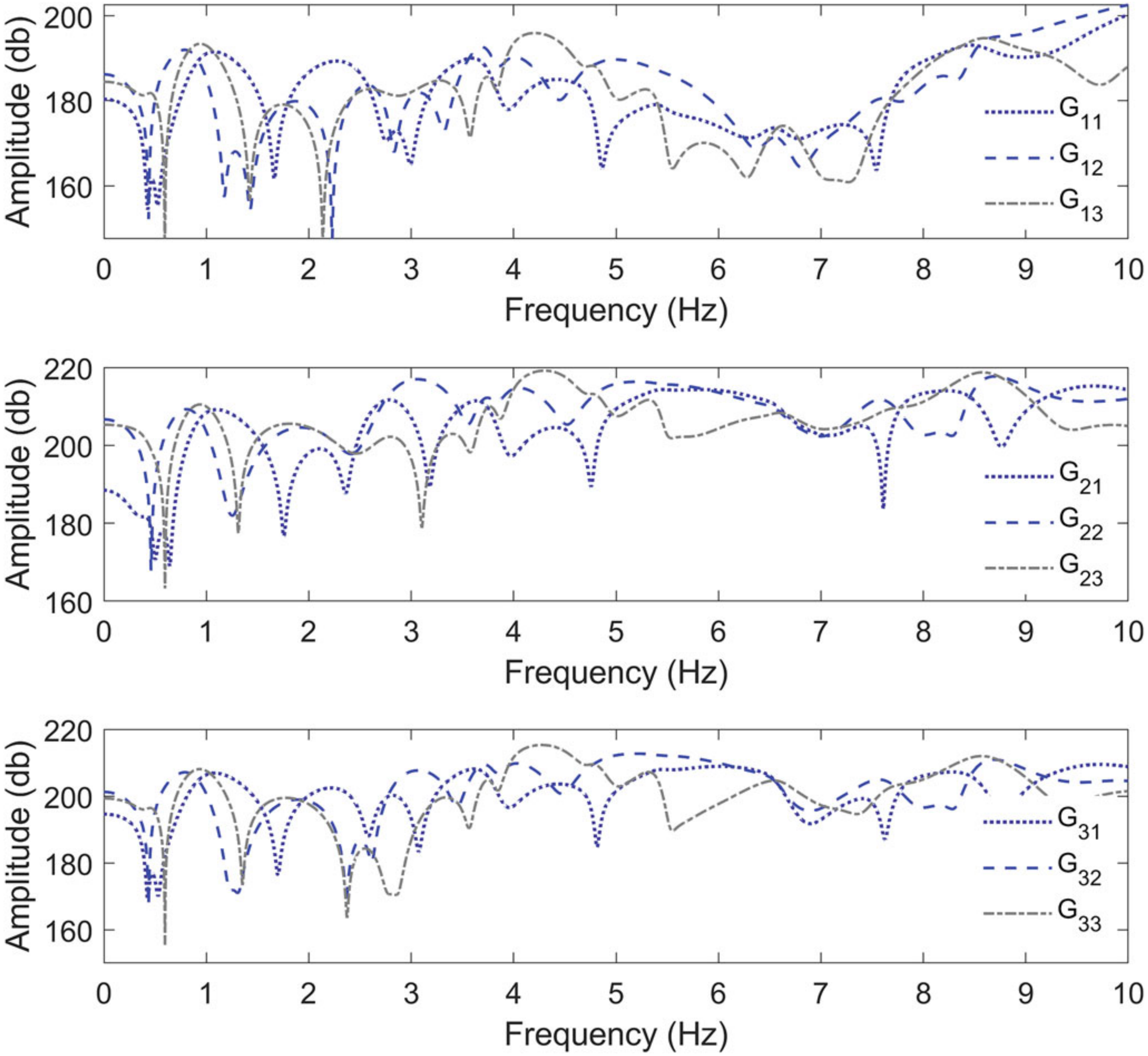

Fig. 18.3 Admittance function corresponding to the three measured response signals by sensors at nodes 6, 7, and 8 (scenario I) and three independent wave loads 1 to 3

Figures 18.6 and 18.7 depict the estimation results based on only the acceleration measurements in two scenarios. The estimates in Fig. 18.6 have been obtained by substituting Eq. (18.10) into Eq. (18.9), taking the inverse FFT of *F* and detrending the signals. Again, the estimates in the noiseless scenario appropriately fit the exact wave loads with NMSE lower than 6% whereas the noise significantly distorts the low amplitude wave estimates and induces a strong trend. Furthermore, in contrast to the displacement data, the zoomed box at typical node 3 in Fig. 18.7 demonstrates that the acceleration measurements are scattered and require a higher sampling rate than 10 Hz.

The response estimates are also compared with those obtained from Augmented Kalman Filter (AKF). Regarding the current number of DOFs, AKF is a time-consuming process. Therefore, the comparison is made in the modal coordinates. Figure 18.8 illustrates the first five natural frequencies and mode shapes of the FE model. Figure 18.9 typically exhibits the displacement of node 3, estimated based on different number of modes by: (a, b) the proposed admittance function by utilizing Eq. (18.3) in Eq. (18.6) and using only displacement data, and (c, d) AKF algorithm using displacement, velocity,

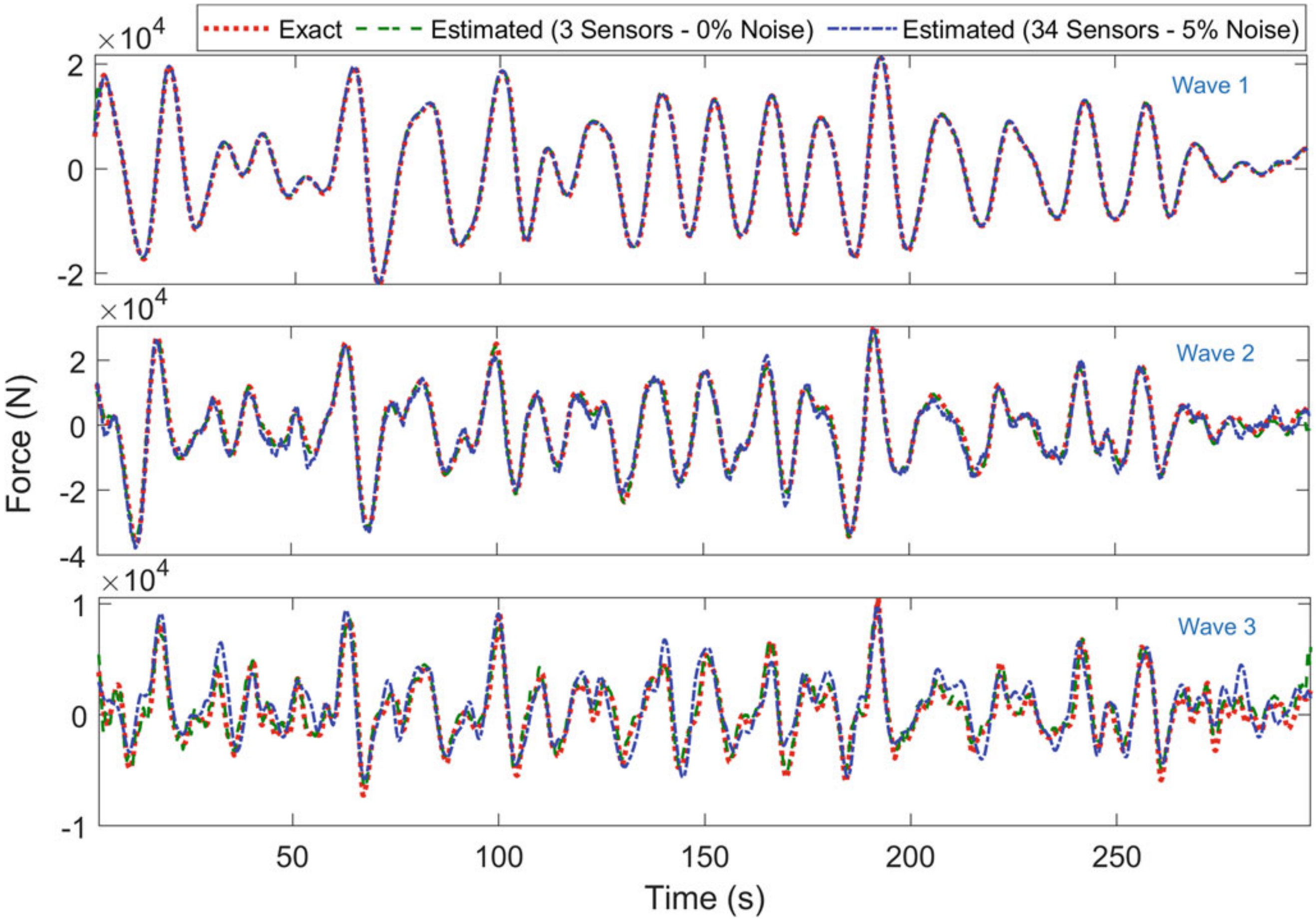

Fig. 18.4 Exact wave load time-histories vs estimates based on 3 and 34 displacement signals

and acceleration data. It is seen that considering a few modes and the least sensors, the proposed technique leads to an acceptable estimation. On the other hand, AKF appropriately works for enough modes, but the estimates using lower than 10 modes are out of order and not presented.

18.5 Conclusion

In this study, a simple frequency-domain technique has been proposed for force identification and response prediction. The idea relies on the uniqueness of the FRF concerning the real structure's digital twins. The applied loads are associated with limited response signals in the frequency domain through the admittance function which is achievable from the inverse of a few relevant components of the frequency response function. The technique was implemented on the FE model of a real-world offshore platform that is partly submerged, and the response of the underwater elements, as well as the wave loads cannot be measured. Hence, the response signals at the platform's topside are utilized in the proposed technique to estimate the wave loads and predict the response of the underwater members. Since the position of the sensors and sampling rate are constant, the frequency response and admittance function can be calculated only once and saved, and later called, updated, dimensionally adjusted, and used for new test conditions and loads. For comparison, an Augmented Kalman Filter algorithm was also performed in the modal coordinates. The algorithm follows the Gaussian process assumptions and requires forming a set of displacement, velocity, and acceleration measurements at a time in the state-space representation and predicting the initial set at each step to tune the process/measurement noise covariance matrices and update that set. In contrast, the proposed technique does not require any assumptions for the force type and statistical distribution, it applies to either measurement type while there is no convergence issue, and the estimates are not biased due to prediction uncertainties. Especially, when

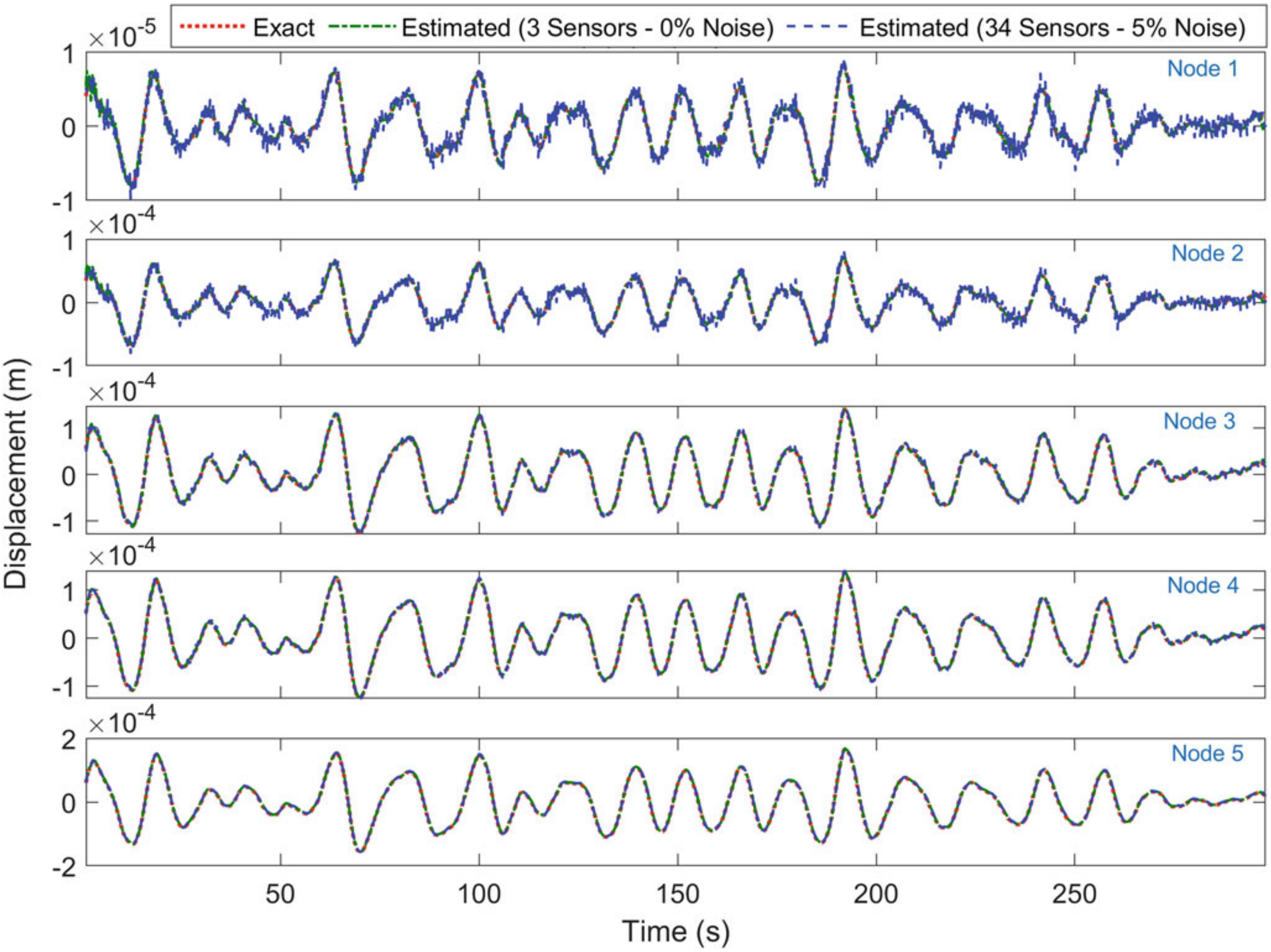

Fig. 18.5 Exact displacement time-histories vs estimates based on 3 and 34 displacement signals

using displacement data, the technique is more robust and efficient than common Kalman Filter algorithms. However, the quality of the estimates generally depends on the number of sensors and resolution of the measurements (length, sampling rate, and noise). In particular, the estimates obtained based on noisy acceleration data are distorted and need additional treatment by detrending or smoothing filters.

Acknowledgments The authors would like to acknowledge the Innovation Foundation of Denmark (IFD), which has funded this study via the financial support of the Grand Solutions Project titled "Innovative Structural Health Monitoring and Risk Informed Structural Integrity Management" (InnoSHM) (0175-00028B), and also contribution of Jesper Tychsen from TotalEnergies EP Danmark A/S and Gediminas Bulatovas from Rambøll Group A/S.

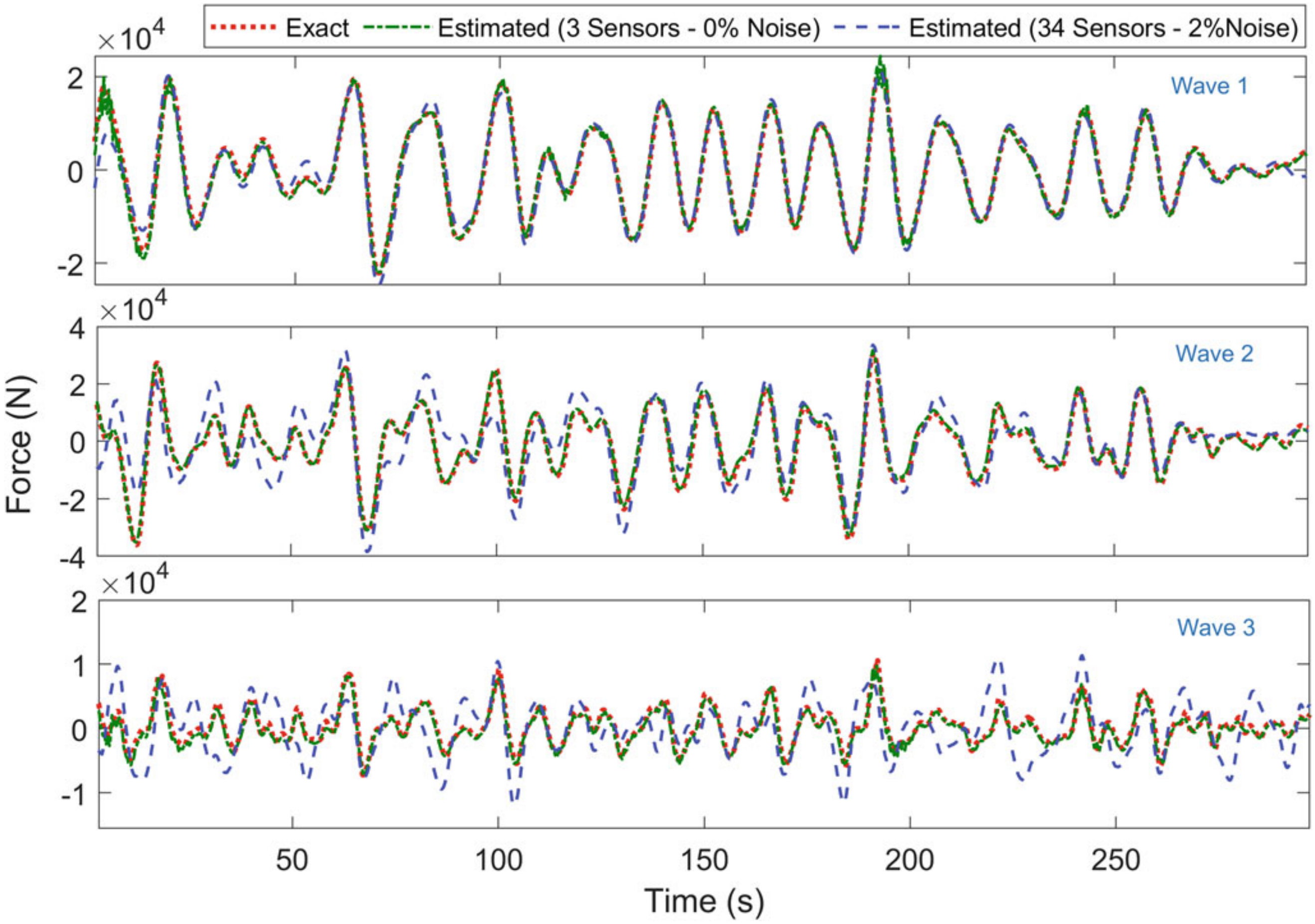

Fig. 18.6 Exact wave load time-histories vs estimated ones based on 3 and 34 acceleration signals

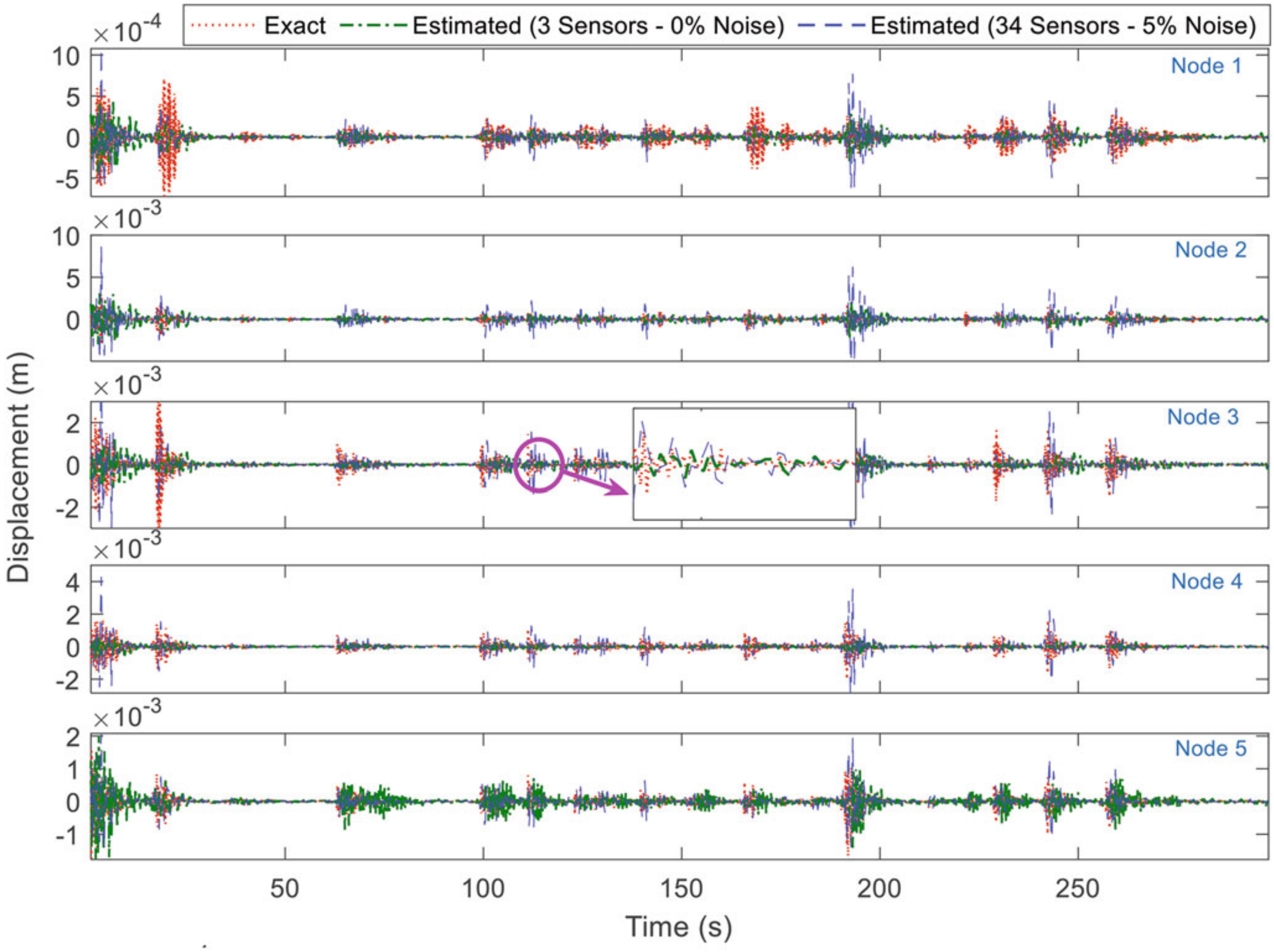

Fig. 18.7 Exact acceleration time-histories vs estimates based on 3 and 34 acceleration signals

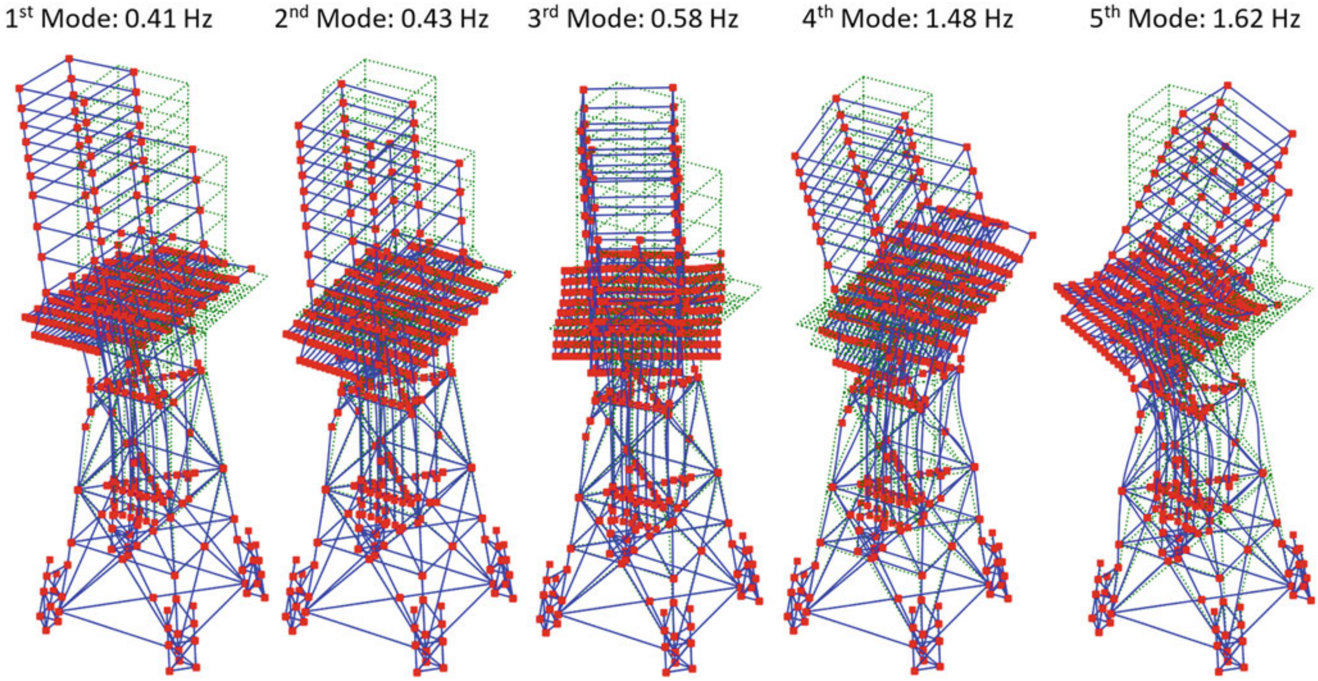

Fig. 18.8 The first five mode shapes of the structure

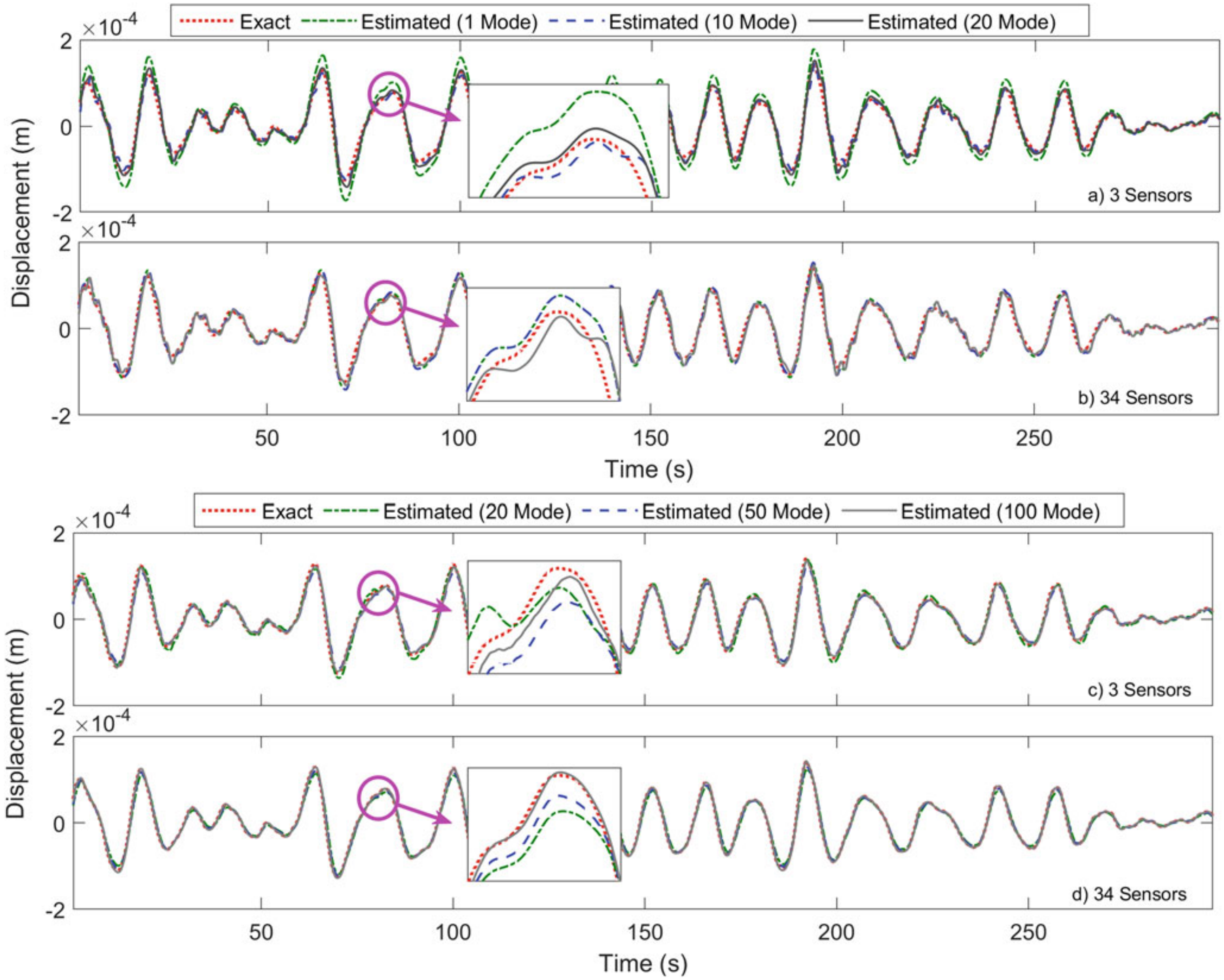

Fig. 18.9 Exact displacement time-histories vs estimates via admittance function (a and b) and Kalman Filter (c and d) based on modal model for different number modes adjusted to 3 and 34 sensors locations

References

1. Carvalho, J., Datta, B.N., Gupta, A., Lagadapati, M.: A direct method for model updating with incomplete measured data and without spurious modes. Mech. Syst. Signal Process. **21**(7), 2715–2731 (2007)
2. Das, A., Debnath, N.: A Bayesian model updating with incomplete complex modal data. Mech. Syst. Signal Process. **136**, 106524 (2020)
3. Marano, G.C., Quaranta, G., Monti, G.: Modified genetic algorithm for the dynamic identification of structural systems using incomplete measurements. Comput. Aided Civ. Inf. Eng. **26**(2), 92–110 (2011)
4. Uhl, T.: The inverse identification problem and its technical application. Arch. Appl. Mech. **77**(5), 325 (2007). https://doi.org/10.1007/s00419-006-0086-9
5. Gallet, A., et al.: Structural engineering from an inverse problems perspective. Proc. R. Soc. A: Math. Phys. Eng. Sci. **478**(2257) (2022). https://doi.org/10.1098/rspa.2021.0526
6. Branlard, E., Giardina, D., Brown, C.S.D.: Augmented Kalman filter with a reduced mechanical model to estimate tower loads on a land-based wind turbine: a step towards digital-Twin simulations. Wind Energy Sci. **5**(3), 1155 (2020). https://doi.org/10.5194/wes-5-1155-2020
7. Khodarahmi, M., Maihami, V.: A Review on Kalman Filter Models. Arch. Comput. Meth. Eng. **30**, 727 (2022). https://doi.org/10.1007/s11831-022-09815-7
8. Wang, P., Tian, X., Peng, T., Luo, Y.: A review of the state-of-the-art developments in the field monitoring of offshore structures. Ocean Eng. **147**, 148 (2018). https://doi.org/10.1016/j.oceaneng.2017.10.014
9. Lang, Z.-Q., et al.: Transmissibility of non-linear output frequency response functions with application in detection and location of damage in MDOF structural systems. Int. J. Non Linear Mech. **46**(6), 841–853 (2011)
10. Lee, U., Shin, J.: A frequency response function-based structural damage identification method. Comput. Struct. **80**(2), 117 (2002). https://doi.org/10.1016/S0045-7949(01)00170-5
11. Guillaume, P., Parloo, E., Verboven, P., de Sitter, G.: An inverse method for the identification of localized excitation sources. In: Proceedings of SPIE - The International Society for Optical Engineering, vol. 4753 II, (2002)
12. Fabro, J., Vogl, G.W., Qu, Y.: Run-time cutting force estimation based on learned nonlinear frequency response function. J. Manuf. Sci. Eng. **144**(9) (2022). https://doi.org/10.1115/1.4054157

Chapter 19
Calculating Structure Similarity via a Graph Neural Network in Population-Based Structural Health Monitoring: Part II

Daniel S. Brennan, Timothy J. Rogers, Elizabeth J. Cross, and Keith Worden

Abstract Population-based Structural Health Monitoring (PBSHM) aims to gain additional insights on the health of a structure when using data available across a population of similar structures, as compared to the insight available when using only data from a single structure. Before knowledge can be transferred across structures, the similarity between structures (or substructures) within the population must be established. The first paper in this series explored the use of Graph Neural Networks (GNNs), to compute similarity measures via an Irreducible Element (IE) model representation of structures stored within the PBSHM database. While the work explored so far uses a pure topological matching to determine the similarity, this chapter builds upon the aforementioned research and explores the viability of matching using the recently introduced Canonical Form (CF).

Keywords Population-based Structural Health Monitoring · Graph Neural Network · Irreducible Element Model

19.1 Introduction

Population-based Structural Health Monitoring (PBSHM) [1–3] expands upon the "classical" process of Structural Health Monitoring (SHM) [4], by monitoring multiple structures of different types (*the population*). The goal of PBSHM is that by monitoring multiple structures, additional insights into a given structure's health are available in comparison to the knowledge available when using only the single structure data. To achieve the goals of PBSHM, there are two themes that need to be addressed: finding which structures (*or components of the structure*) are similar [2] and transferring learnt knowledge across the population [3].

To achieve the goal of determining whether structures are similar, a common basis for describing structures is required; Irreducible Element (IE) models are the aforementioned vehicle for this description within PBSHM. The recent introduction of the PBSHM database [5] has enabled a unified format for storage of PBSHM data. This development has led to the generation of an IE Model Schema [6], which expands upon the notation and terminology introduced by Gosliga et al. [2], to provide a rich language for embedding structural knowledge within an IE model.

The first paper in this series [7] addressed the inherent issues of author ambiguity—each author will have differing requirements for their IE model—by introducing the idea of a Canonical Form (CF), an IE model that has been reduced down via the CF reduction rules to remove any author-introduced ambiguity. The CF of an IE model is the very essence of that model, which can be used for structural comparison within the PBSHM database. A Graph Matching Network [8] was also introduced as a possible viable avenue for the comparison of IE models within the PBSHM framework.

This chapter summarizes the work conducted in Part I of this series in the background section and then expands upon these foundations laid by, exploring the novel idea of using the CF representations as a matching layer in-between the IE models in the Graph Matching Network section.

D. S. Brennan (✉) · T. J. Rogers · E. J. Cross · K. Worden
Dynamics Research Group, Department of Mechanical Engineering, University of Sheffield, Sheffield, UK
e-mail: d.s.brennan@sheffield.ac.uk; tim.rogers@sheffield.ac.uk; e.j.cross@sheffield.ac.uk; k.worden@sheffield.ac.uk

H. Y. Noh et al. (eds.), *Dynamics of Civil Structures, Volume 2*, Conference Proceedings of the Society
for Experimental Mechanics Series, https://doi.org/10.1007/978-3-031-36663-5_19

19.2 Background

The inherent issue when trying to perform comparisons against multiple IE models is trying to distinguish between differences that are present because of variance in the underlying structure that the model is representing and differences that are present because of the differing goals of the authors who generated the model. If one was to take the example used within this first paper in this series [7], a simplified two-span bridge in the middle of a valley (see Fig. 19.1), there are multiple different variations of the IE model that could be submitted into the PBSHM framework for comparison within the network. The right deck may be separated into multiple different elements for a myriad of reasons: damage localisation within the model, geometrical differences, material properties, etc. The relationship between the decks and the column could be stated to be from the left deck to the column, from the right deck to the column, or from both decks to the column.

The *Canonical Form* (CF) preserves all the structural knowledge and engineering decisions embedded within the IE model but provides a common form for use within the PBSHM framework for determining the structural similarity within the network. A non-canonical form version of an IE model would be provided by the author and stored within the PBSHM database, and a CF version of the IE model generated any time the similarity of a model is to be determined.

The generation of a CF is achieved by applying a set of reduction rules against the IE model (*the canonical form reduction rules*). These rules outline how and why a specific pattern can be removed or simplified from within the IE without impairing the key structural knowledge of the system. As an IE model has an associated Attributed Graph (AG) representation, these rules can often be seen as removing any unrequired loops from within the graph. There are currently three canonical form reduction rules; every boundary relationship must be to a unique ground, perfect–joint–joint (PJJ) relationships can be reduced to a single perfect–joint relationship, and multiple perfect relationships can be reduced to a single perfect relationship. For the interested reader, these rules, and how and why they can be used, are described in detail in the first paper in this series [7]. Figure 19.2 depicts the transformation from a non-canonical form IE model into a canonical form IE model using the canonical form reduction rules.

As aforementioned, an IE model has an associated AG representation, where each node corresponds to an element and each edge corresponds to a relationship. This facilitates using graph theory for similarity matching as outlined by Gosliga et al. [2]. Part I in this series explored the viability of using a Graph Matching Network [8] to determine the similarity of structures within the network. Graph Matching Networks are a recent development within the Graph Neural Network [9] community, which generate a similarity score via a cross-graph attention-based mechanism.

The GMN can be trained in two distinct ways: the first option is to provide the algorithm with pairs of labelled graphs (G_1, G_2) whereupon the label $t \epsilon \{-1, 1\}$ represents if the graphs within the pair are to be considered similar $t = 1$ or dissimilar $t = -1$. The second option is to provide the algorithm with triplets of graphs (G_1, G_2, G_3), where G_1 and G_2 are similar, but G_1 and G_3 are dissimilar. To gain a full understanding into the inner workings of the GMN, interested readers are encouraged to read Li et al. [8]. While the precursory work in this series has established the viability of a GMN to determine the similarity of IE models, the dataset was trained using only the topological knowledge within the simulated-bridge IE model dataset. This chapter expands upon the aforementioned argument by considering if a GMN could instead be trained using the synthetic bridge dataset in conjunction with a new CF dataset.

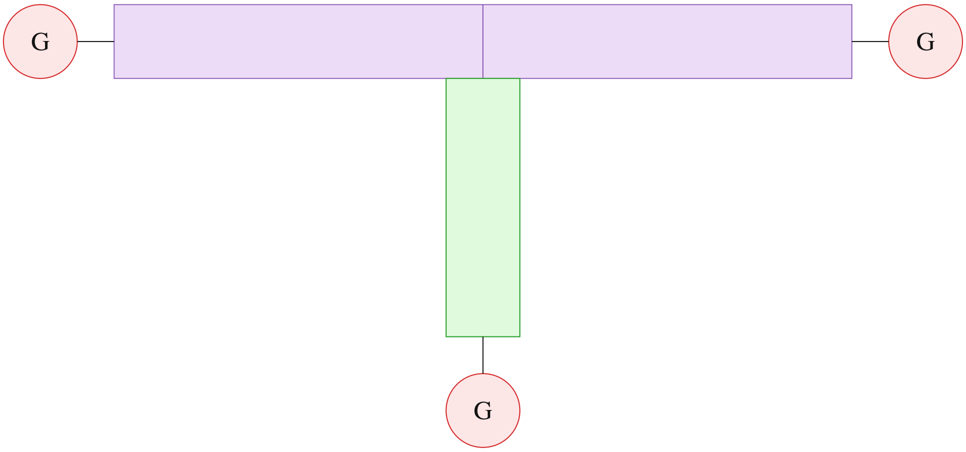

Fig. 19.1 A simplified two-span bridge with two deck elements and one column element. The model interacts with the ground at the left and right of the deck, as well as at the bottom of the column

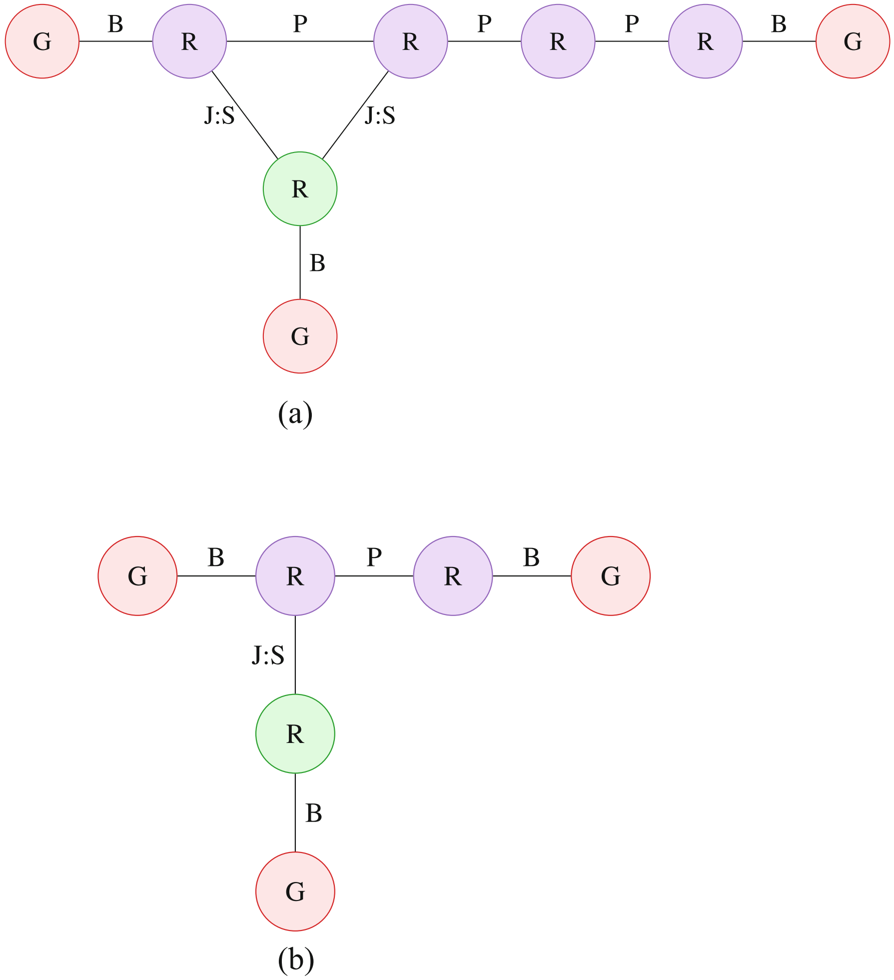

Fig. 19.2 The IE model reduction that could be generated from the two-span bridge as depicted in Fig. 19.1. Ground elements are represented by a G in the centre of the node, and regular elements are represented by a R in the center of the node. Boundary relationships are represented by a B on the edge, perfect relationships are represented by a P on the edge, and static joint relationships are represented by a J:S on the edge. (**a**) A possible IE model representation of the two-span bridge depicted in Fig. 19.1 that can be reduced to its CF using the PJJ and perfect relationship reduction rules. (**b**) A CF representation of the IE model in (**a**)

19.3 Graph Matching Network

In the previous work in this series, the GMN was trained using the pairs method (G_1, G_2), outlined in the background section of this chapter. The GMN was trained using the "learning-slab-bridge-500-span-1-9-column-1-1-node-1-3" dataset from the IE model learning data repository found at https://github.com/dsbrennan/ie-model-learning-data. The pairs were constructed by determining the number of spans N for both G_1 and G_2, if the number of spans N matched, the label $t = 1$ was provided, and if not, the label $t = -1$. This method provided positive results for the initial viability study; however, when one envisions how the GMN would operate within the context of the network, it is apparent that there would be scalability issues in the PBSHM framework.

To understand the similarity of a new structure injected into the network, a similarity score—or dissimilarity—must be computed against every existing IE model within the network. While this is of little consequence when exploring the viability of an algorithm with a simulated toy dataset, it becomes of great consequence when considering real-world data. A simplified toy example will have numbers of elements in the order of 10, whereas a real-world example may have elements in the order of 100s or even 1000s, depending upon how specific the author is of the structure.

If one instead takes inspiration from a fundamental hypothesis in Neural Networks, could a reduction layer be placed in front of the IE models within the network and comparisons be computed against this reduced layer? This chapter proposes that the recently introduced Canonical Form (CF) is used for this such purpose. Using the foundation that an IE model can

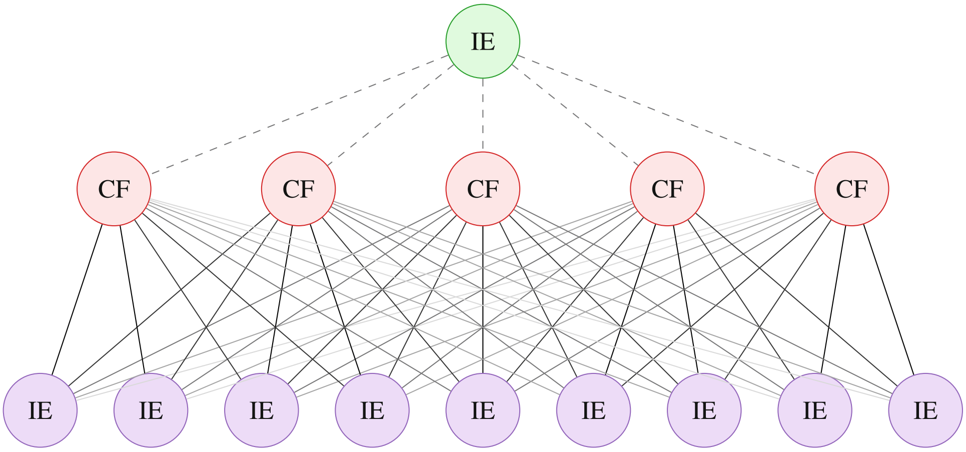

Fig. 19.3 The outline of the proposed process of adding a new IE model into the network of IE models. The green IE node represents the IE model being added into the network. The purple IE nodes represent the existing IE model within the network, and the red CF node represents the proposed CF IE model layer which all IE models have been compared against

be reduced down to a CF version without losing any of the engineering knowledge required for comparing the similarity of structures, a library of CF IE models is established, which hold the essence of a structure, i.e., a CF exists for a two-span beam-and-slab bridge, another for a three-span beam-and-slab bridge, another for a wind turbine, etc. On the injection of a new IE model into the network, the similarity would be calculated against the layer of CF representations. As each IE model within the network would already have been given their similarity score against the same CF layer when they were introduced into the network, one could postulate that IE models that had similar similarity scores to the same CF were a population within the network. See Fig. 19.3 for a diagram of this process.

To determine if this hypothesis is well-founded, the GMN is trained using two distinct datasets. The first dataset is a simplified synthetic beam bridge dataset that should contain all the variations which a CF attempts to remove: perfect–joint–joint relationships and multiple perfect relationships that can be seen as a single relationship. The second dataset is a reduced dataset containing only one CF IE model for each corresponding number-of-span simplified beam bridge: a CF IE model for a two-span bridge, a CF IE model for a three-span bridge, etc. In the interests of simplicity, these datasets from this time forth are called *non-canonical form graphs* $NCFG$ and *canonical form graphs* CFG, respectively.

Training of the GMN is thus conducted by the pair method described earlier in this chapter; however, the graphs within the pair are no longer from the same dataset. The pairs are constructed using one non-canonical form graph and one canonical form graph per pair $(NCFG, CFG)$, where the label provided is $t = 1$ providing the number of spans in $NCFG$ matches the number-of-spans in CFG; otherwise, $t = -1$.

As one can see from the included distance heatmap in Fig. 19.4b, the GMN when using the non-canonical form and canonical form graphs still clearly identifies graphs with the same number-of-spans with the lowest distance. The distance metric increases the further away within the number-of-spans neighbourhood, the non-canonical and canonical graphs are. In comparison to the original results (see Fig. 19.4a), one can see that the non-canonical and canonical graph results are within the same region as the original non-canonical graph only results, with only minor variations.

Currently, the results have been generated using a pure topological approach within the GMN. No attributes within the AG have been embedded into the GMN; however, the embedding of both node and edge features are facilitated within the GMN. Embedding element and relationship attributes within the algorithms used to determine the similarity of structures is a fundamental requirement for the algorithm adaptation into the PBSHM framework. The PBSHM framework needs to be able to determine the differences between a three-element two-span bridge and a three-element plane; element and relationship attributes are the primary vehicle for embedding the knowledge required to determine these structural differences.

Figure 19.4c shows the results of how the distance metric changes when the element and relationship types—regular, ground, boundary, perfect, connection, static joint, or dynamic joint—are embedded as node and edge features, respectively. As one can see, the results still conform to the non-canonical form graph and the canonical form graph having a small distance metric when the spans are the same. Again, the metric increases the further the number away within the span neighborhood the comparison is. The results do also indicate that embedding the node and edge features into the GMN provides a greater distinction between each level of distance away from the same spans.

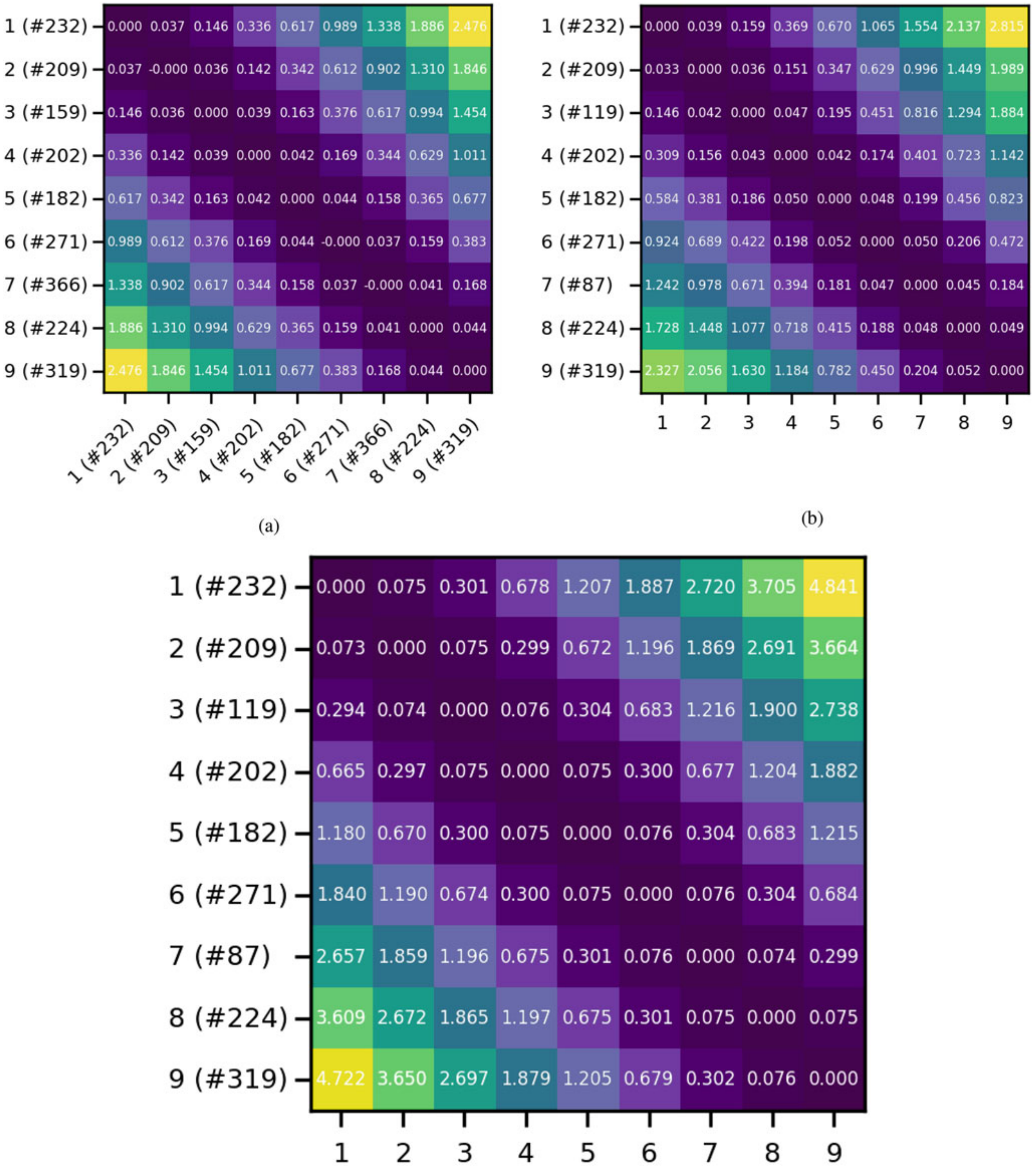

(a)

	1 (#232)	2 (#209)	3 (#159)	4 (#202)	5 (#182)	6 (#271)	7 (#366)	8 (#224)	9 (#319)
1 (#232)	0.000	0.037	0.146	0.336	0.617	0.989	1.338	1.886	2.476
2 (#209)	0.037	-0.000	0.036	0.142	0.342	0.612	0.902	1.310	1.846
3 (#159)	0.146	0.036	0.000	0.039	0.163	0.376	0.617	0.994	1.454
4 (#202)	0.336	0.142	0.039	0.000	0.042	0.169	0.344	0.629	1.011
5 (#182)	0.617	0.342	0.163	0.042	0.000	0.044	0.158	0.365	0.677
6 (#271)	0.989	0.612	0.376	0.169	0.044	-0.000	0.037	0.159	0.383
7 (#366)	1.338	0.902	0.617	0.344	0.158	0.037	-0.000	0.041	0.168
8 (#224)	1.886	1.310	0.994	0.629	0.365	0.159	0.041	0.000	0.044
9 (#319)	2.476	1.846	1.454	1.011	0.677	0.383	0.168	0.044	0.000

(b)

	1	2	3	4	5	6	7	8	9
1 (#232)	0.000	0.039	0.159	0.369	0.670	1.065	1.554	2.137	2.815
2 (#209)	0.033	0.000	0.036	0.151	0.347	0.629	0.996	1.449	1.989
3 (#119)	0.146	0.042	0.000	0.047	0.195	0.451	0.816	1.294	1.884
4 (#202)	0.309	0.156	0.043	0.000	0.042	0.174	0.401	0.723	1.142
5 (#182)	0.584	0.381	0.186	0.050	0.000	0.048	0.199	0.456	0.823
6 (#271)	0.924	0.689	0.422	0.198	0.052	0.000	0.050	0.206	0.472
7 (#87)	1.242	0.978	0.671	0.394	0.181	0.047	0.000	0.045	0.184
8 (#224)	1.728	1.448	1.077	0.718	0.415	0.188	0.048	0.000	0.049
9 (#319)	2.327	2.056	1.630	1.184	0.782	0.450	0.204	0.052	0.000

(c)

	1	2	3	4	5	6	7	8	9
1 (#232)	0.000	0.075	0.301	0.678	1.207	1.887	2.720	3.705	4.841
2 (#209)	0.073	0.000	0.075	0.299	0.672	1.196	1.869	2.691	3.664
3 (#119)	0.294	0.074	0.000	0.076	0.304	0.683	1.216	1.900	2.738
4 (#202)	0.665	0.297	0.075	0.000	0.075	0.300	0.677	1.204	1.882
5 (#182)	1.180	0.670	0.300	0.075	0.000	0.076	0.304	0.683	1.215
6 (#271)	1.840	1.190	0.674	0.300	0.075	0.000	0.076	0.304	0.684
7 (#87)	2.657	1.859	1.196	0.675	0.301	0.076	0.000	0.074	0.299
8 (#224)	3.609	2.672	1.865	1.197	0.675	0.301	0.075	0.000	0.075
9 (#319)	4.722	3.650	2.697	1.879	1.205	0.679	0.302	0.076	0.000

Fig. 19.4 The GMN results using different datasets and different matching criteria. (**a**) The original GMN results when using only the non-canonical form graphs, learning from themselves. Only the topology is considered as part of the matching process. (**b**) The GMN results when using the non-canonical form graphs and the canonical form graphs for learning. Only the topology is considered as part of the matching process. (**c**) The GMN results when using the non-canonical form graphs and the canonical form graphs for learning. Not only is the topology used as part of the matching process, but the element and relationship types are embedded as features to be used during the matching process.

While the results shown in Fig. 19.4 have only included the first non-canonical graph in each span within the test dataset, the full heatmaps generated are available in the Appendices. The first result shows the topological matching while using both the non-canonical form and canonical form graphs. The second result shows the topological and type attributes embedded as features results, using both the non-canonical form and canonical form graphs. These results can also be downloaded in the original formats from https://github.com/dsbrennan/imac-2023-gmn/tree/main/results. It should be noted that the metric values displayed within the heatmaps have been multiplied by 1000 to facilitate visualisation.

As one can see from the full heatmaps, a new pattern can be seen; the non-canonical form graphs with the same span have near identical results for the similarity of each canonical form graph within the heat map, i.e., all the two-span non-canonical graphs have a near identical result when comparing them to the three-span bridges. This pattern suggests that a clustering algorithm would be successful in defining new populations within the network using the non-canonical form and canonical form methods described in this chapter.

The datasets used within this chapter are available via https://github.com/dsbrennan/ie-model-learning-data. The non-canonical form graphs are the “learning-slab-bridge-500-span-1-9-column-1-1-node-1-3” dataset, and the canonical form graphs are the “learning-slab-bridge-canonical-form-span-1-9-column-1-1” dataset. The code used to generate these results is available from https://github.com/dsbrennan/imac-2023-gmn, which is a derivative of the code published by Li et al. [8].

19.4 Conclusion

In conclusion, this chapter has proposed a novel approach for the generation of similarity—or dissimilarity—metrics within PBSHM by using the Canonical Form as a reduction layer within the network of IE models. The viability of using non-canonical form and canonical form graphs for the subject of comparisons has been shown with a simulated test set; however, there is still further research that needs to be conducted in this area.

Future research needs to be conducted on potential clustering algorithms that can use metrics generated from the node and edge feature version of the GMN and generate populations of IE models from within the network of IT models. Further investigations are required into comparisons with other types of structures and determining if the results hold when different structure types are injected into the network.

Acknowledgments The authors of this chapter gratefully acknowledge the support of the UK Engineering and Physical Sciences Research Council (EPSRC) via grant references EP/W005816/1 and EP/S001565/1. For the purpose of open access, the authors have applied a Creative Commons Attribution (CC BY) licence to any Author Accepted Manuscript version arising.

Appendices

Topological vs. attributed topological Graph Matching Network learning from non-canonical form and canonical form graphs (Fig. 19.5).

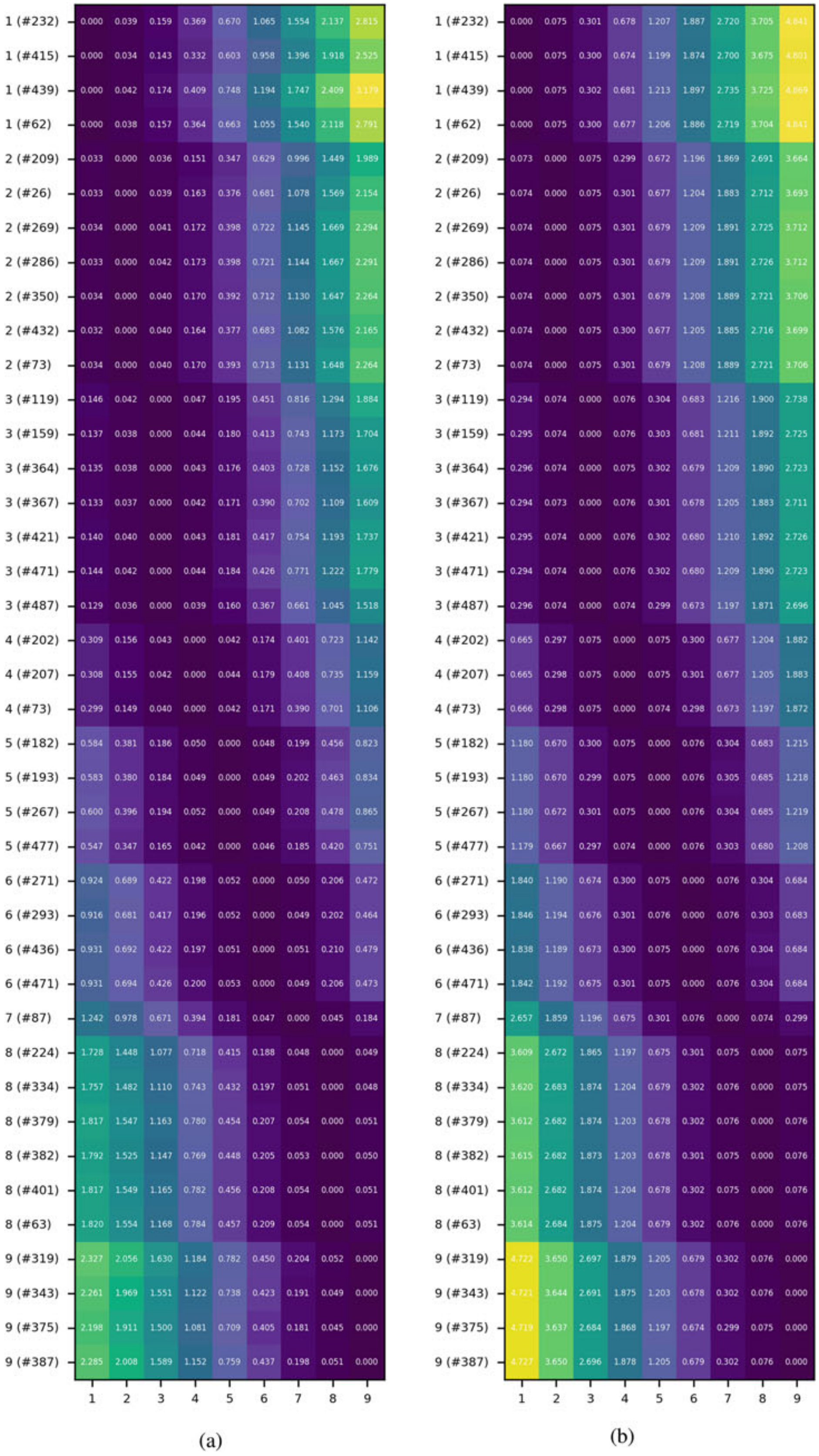

(a)

	1	2	3	4	5	6	7	8	9
1 (#232)	0.000	0.039	0.159	0.369	0.670	1.065	1.554	2.137	2.815
1 (#415)	0.000	0.034	0.143	0.332	0.603	0.958	1.396	1.918	2.525
1 (#439)	0.000	0.042	0.174	0.409	0.748	1.194	1.747	2.409	3.179
1 (#62)	0.000	0.038	0.157	0.364	0.663	1.055	1.540	2.118	2.791
2 (#209)	0.033	0.000	0.036	0.151	0.347	0.629	0.996	1.449	1.989
2 (#26)	0.033	0.000	0.039	0.163	0.376	0.681	1.078	1.569	2.154
2 (#269)	0.034	0.000	0.041	0.172	0.398	0.722	1.145	1.669	2.294
2 (#286)	0.033	0.000	0.042	0.173	0.398	0.721	1.144	1.667	2.291
2 (#350)	0.034	0.000	0.040	0.170	0.392	0.712	1.130	1.647	2.264
2 (#432)	0.032	0.000	0.040	0.164	0.377	0.683	1.082	1.576	2.165
2 (#73)	0.034	0.000	0.040	0.170	0.393	0.713	1.131	1.648	2.264
3 (#119)	0.146	0.042	0.000	0.047	0.195	0.451	0.816	1.294	1.884
3 (#159)	0.137	0.038	0.000	0.044	0.180	0.413	0.743	1.173	1.704
3 (#364)	0.135	0.038	0.000	0.043	0.176	0.403	0.728	1.152	1.676
3 (#367)	0.133	0.037	0.000	0.042	0.171	0.390	0.702	1.109	1.609
3 (#421)	0.140	0.040	0.000	0.043	0.181	0.417	0.754	1.193	1.737
3 (#471)	0.144	0.042	0.000	0.044	0.184	0.426	0.771	1.222	1.779
3 (#487)	0.129	0.036	0.000	0.039	0.160	0.367	0.661	1.045	1.518
4 (#202)	0.309	0.156	0.043	0.000	0.042	0.174	0.401	0.723	1.142
4 (#207)	0.308	0.155	0.042	0.000	0.044	0.179	0.408	0.735	1.159
4 (#73)	0.299	0.149	0.040	0.000	0.042	0.171	0.390	0.701	1.106
5 (#182)	0.584	0.381	0.186	0.050	0.000	0.048	0.199	0.456	0.823
5 (#193)	0.583	0.380	0.184	0.049	0.000	0.049	0.202	0.463	0.834
5 (#267)	0.600	0.396	0.194	0.052	0.000	0.049	0.208	0.478	0.865
5 (#477)	0.547	0.347	0.165	0.042	0.000	0.046	0.185	0.420	0.751
6 (#271)	0.924	0.689	0.422	0.198	0.052	0.000	0.050	0.206	0.472
6 (#293)	0.916	0.681	0.417	0.196	0.052	0.000	0.049	0.202	0.464
6 (#436)	0.931	0.692	0.422	0.197	0.051	0.000	0.051	0.210	0.479
6 (#471)	0.931	0.694	0.426	0.200	0.053	0.000	0.049	0.206	0.473
7 (#87)	1.242	0.978	0.671	0.394	0.181	0.047	0.000	0.045	0.184
8 (#224)	1.728	1.448	1.077	0.718	0.415	0.188	0.048	0.000	0.049
8 (#334)	1.757	1.482	1.110	0.743	0.432	0.197	0.051	0.000	0.048
8 (#379)	1.817	1.547	1.163	0.780	0.454	0.207	0.054	0.000	0.051
8 (#382)	1.792	1.525	1.147	0.769	0.448	0.205	0.053	0.000	0.050
8 (#401)	1.817	1.549	1.165	0.782	0.456	0.208	0.054	0.000	0.051
8 (#63)	1.820	1.554	1.168	0.784	0.457	0.209	0.054	0.000	0.051
9 (#319)	2.327	2.056	1.630	1.184	0.782	0.450	0.204	0.052	0.000
9 (#343)	2.261	1.969	1.551	1.122	0.738	0.423	0.191	0.049	0.000
9 (#375)	2.198	1.911	1.500	1.081	0.709	0.405	0.181	0.045	0.000
9 (#387)	2.285	2.008	1.589	1.152	0.759	0.437	0.198	0.051	0.000

(b)

	1	2	3	4	5	6	7	8	9
1 (#232)	0.000	0.075	0.301	0.678	1.207	1.887	2.720	3.705	4.841
1 (#415)	0.000	0.075	0.300	0.674	1.199	1.874	2.700	3.675	4.801
1 (#439)	0.000	0.075	0.302	0.681	1.213	1.897	2.735	3.725	4.869
1 (#62)	0.000	0.075	0.300	0.677	1.206	1.886	2.719	3.704	4.841
2 (#209)	0.073	0.000	0.075	0.299	0.672	1.196	1.869	2.691	3.664
2 (#26)	0.074	0.000	0.075	0.301	0.677	1.204	1.883	2.712	3.693
2 (#269)	0.074	0.000	0.075	0.301	0.679	1.209	1.891	2.725	3.712
2 (#286)	0.074	0.000	0.075	0.301	0.679	1.209	1.891	2.726	3.712
2 (#350)	0.074	0.000	0.075	0.301	0.679	1.208	1.889	2.721	3.706
2 (#432)	0.074	0.000	0.075	0.300	0.677	1.205	1.885	2.716	3.699
2 (#73)	0.074	0.000	0.075	0.301	0.679	1.208	1.889	2.721	3.706
3 (#119)	0.294	0.074	0.000	0.076	0.304	0.683	1.216	1.900	2.738
3 (#159)	0.295	0.074	0.000	0.076	0.303	0.681	1.211	1.892	2.725
3 (#364)	0.296	0.074	0.000	0.075	0.302	0.679	1.209	1.890	2.723
3 (#367)	0.294	0.073	0.000	0.076	0.301	0.678	1.205	1.883	2.711
3 (#421)	0.295	0.074	0.000	0.076	0.302	0.680	1.210	1.892	2.726
3 (#471)	0.294	0.074	0.000	0.076	0.302	0.680	1.209	1.890	2.723
3 (#487)	0.296	0.074	0.000	0.074	0.299	0.673	1.197	1.871	2.696
4 (#202)	0.665	0.297	0.075	0.000	0.075	0.300	0.677	1.204	1.882
4 (#207)	0.665	0.298	0.075	0.000	0.075	0.301	0.677	1.205	1.883
4 (#73)	0.666	0.298	0.075	0.000	0.074	0.298	0.673	1.197	1.872
5 (#182)	1.180	0.670	0.300	0.075	0.000	0.076	0.304	0.683	1.215
5 (#193)	1.180	0.670	0.299	0.075	0.000	0.076	0.305	0.685	1.218
5 (#267)	1.180	0.672	0.301	0.075	0.000	0.076	0.304	0.685	1.219
5 (#477)	1.179	0.667	0.297	0.074	0.000	0.076	0.303	0.680	1.208
6 (#271)	1.840	1.190	0.674	0.300	0.075	0.000	0.076	0.304	0.684
6 (#293)	1.846	1.194	0.676	0.301	0.076	0.000	0.076	0.303	0.683
6 (#436)	1.838	1.189	0.673	0.300	0.075	0.000	0.076	0.304	0.684
6 (#471)	1.842	1.192	0.675	0.301	0.075	0.000	0.076	0.304	0.684
7 (#87)	2.657	1.859	1.196	0.675	0.301	0.076	0.000	0.074	0.299
8 (#224)	3.609	2.672	1.865	1.197	0.675	0.301	0.075	0.000	0.075
8 (#334)	3.620	2.683	1.874	1.204	0.679	0.302	0.076	0.000	0.075
8 (#379)	3.612	2.682	1.874	1.203	0.678	0.302	0.076	0.000	0.076
8 (#382)	3.615	2.682	1.873	1.203	0.678	0.301	0.075	0.000	0.076
8 (#401)	3.612	2.682	1.874	1.204	0.678	0.302	0.075	0.000	0.076
8 (#63)	3.614	2.684	1.875	1.204	0.679	0.302	0.076	0.000	0.076
9 (#319)	4.722	3.650	2.697	1.879	1.205	0.679	0.302	0.076	0.000
9 (#343)	4.721	3.644	2.691	1.875	1.203	0.678	0.302	0.076	0.000
9 (#375)	4.719	3.637	2.684	1.868	1.197	0.674	0.299	0.075	0.000
9 (#387)	4.727	3.650	2.696	1.878	1.205	0.679	0.302	0.076	0.000

Fig. 19.5 (**a**) The GMN result when using topology alone as the source for matching against the non-canonical form graphs to the canonical form graphs. (**b**) The GMN result when using topology and embedding the element and relationship types as features for matching against the non-canonical form graphs to the canonical form graphs

References

1. Bull, L.A., Gardner, P.A., Gosliga, J., Rogers, T.J., Dervilis, N., Cross, E.J., Papatheou, E., Maguire, A.E., Campos, C., Worden, K.: Foundations of population-based SHM, Part I: homogeneous populations and forms. Mech. Sys. Signal Process. **148**, 107141 (2021)
2. Gosliga, J., Gardner, P.A., Bull, L.A., Dervilis, N., Worden, K.: Foundations of population-based SHM, Part II: heterogeneous populations - graphs, networks, and communities. Mech. Syst. Signal Process. **148**, 107144 (2021)
3. Gardner, P., Bull, L.A., Gosliga, J., Dervilis, N., Worden, K.: Foundations of population-based SHM, Part III: heterogeneous populations - mapping and transfer. Mech. Syst. Signal Process. **149**, 107142 (2021)
4. Farrar, C.R., Worden, K.: An introduction to structural health monitoring. Philosoph. Trans. R. Soc. A Math. Phys. Eng. Sci. **365**(1851), 303–315 (2007)
5. Brennan, D.S., Wickramarachchi, C.T., Cross, E.J., Worden, K.: Implementation of an organic database structure for population-based structural health monitoring. In: Grimmelsman, K. (ed.) Dynamics of Civil Structures. Series Title: Conference Proceedings of the Society for Experimental Mechanics Series, vol. 2, pp. 23–41. Springer International Publishing, Cham (2022)
6. Brennan, D.S., Gosliga, J., Cross, E.J., Worden, K.: On implementing an irreducible element model schema for population-based structural health monitoring. Structural Health Monitoring, p. 11 (2021)
7. Brennan, D.S., Rogers, T.J., Cross, E.J., Worden, K.: On quantifying the similarity of structures via a Graph Neural Network for population-based structural health monitoring. Conference: ISMA2022. p. 9
8. Li, Y., Gu, C., Dullien, T., Vinyals, O., Kohli, P.: Graph matching networks for learning the similarity of graph structured objects (2019). arXiv:1904.12787 [cs, stat]. arXiv: 1904.12787
9. Bacciu, D., Errica, F., Micheli, A., Podda, M.: A gentle introduction to deep learning for graphs. Neur. Netw. **129**, 203–221 (2020). arXiv: 1912.12693

Chapter 20
Three-Dimensional Structural Displacement Estimation Using a Low-Cost Sensing System Combining a Consumer-Grade Camera and an Accelerometer

Zhanxiong Ma, Jaemook Choi, and Hoon Sohn

Abstract The monitoring of structural displacements is crucial because displacements can reveal critical information about the health of civil structures. Despite this, accurate measurements of structural displacements remain a difficult task. The fusion of a vision camera and an accelerometer has previously been explored to estimate structural displacements, but only in-plane displacements can be estimated. This chapter describes a three-dimensional structural displacement estimation method that fuses measurements from a consumer-grade camera and a triaxial accelerometer mounted on a target structure. An accelerometer-aided computer vision algorithm and an adaptive multirate Kalman filter are integrated to efficiently estimate high-sampling three-dimensional displacements from low-sampling vision measurements and high-sampling acceleration measurements. All parameters associated with the computer vision algorithm are automatically calibrated without any prior knowledge or ad-hoc thresholding. Experimental validation of the proposed method is performed on a four-story building model under varying excitations. Displacements were accurately estimated with a root mean square error of less than 2 mm.

Keywords Structural displacement · Low-cost sensing system · Consumer-grade camera · Accelerometer · Data fusion

20.1 Introduction

Displacement is essential for monitoring the health condition of structures. In practice, displacement is commonly estimated from acceleration measurements by double integration. However, the double integration process could amplify the acceleration measurement noise, thereby causing a huge low-frequency drift in the estimated displacement. Though such a drift could be eliminated by high-pass filtering [1], the important low-frequency structural displacement will be eliminated as well. Attempts have been made to fuse accelerometers with other types of sensors that measure or estimate displacement for improved displacement estimation. For example, displacements have been estimated by fusing an accelerometer with either Global Positioning System (GPS) [2], strain sensors [3], inclinometers [4], or millimeter wave radar [5]. Note that such fusions allow for both high- and low-frequency displacement estimation with a high sampling rate.

Vision cameras have been studied for over a decade for structural displacement measurement, and the authors have also tried to fuse a vision camera with an accelerometer [6, 7]. Such fusion allows for improved displacement estimation accuracy and computational efficiency. However, these studies focus on in-plane displacement estimation only. In this study, we extend our previous method to estimate both in-plane and out-of-plane (i.e., three-dimensional) displacements using a consumer-grade camera and a triaxial accelerometer. An accelerometer-aided computer vision algorithm and an adaptive multi-rate Kalman filter are integrated to efficiently estimate high-sampling displacements from low-sampling vision measurements and high-sampling acceleration measurements. All parameters associated with the accelerometer-aided computer vision algorithm are automatically calibrated without any prior knowledge or ad-hoc thresholding. The remainder of this chapter is organized as follows. Section 20.2 illustrates the overall flowchart of the proposed method. The experimental validation of the proposed method on a four-story building model is presented in Sect. 20.3. The concluding remarks are provided in Sect. 20.4.

Z. Ma (✉) · J. Choi · H. Sohn
Department of Civil and Environmental Engineering, Korea Advanced Institute of Science and Technology, Daejeon, Republic of Korea
e-mail: mazhanxiong@kaist.ac.kr

H. Y. Noh et al. (eds.), *Dynamics of Civil Structures, Volume 2*, Conference Proceedings of the Society
for Experimental Mechanics Series, https://doi.org/10.1007/978-3-031-36663-5_20

20.2 Methodology

Figure 20.1 shows an overview of the proposed displacement estimation method. A triaxial accelerometer and a vision camera are placed on a target structure where displacement is to be estimated. The accelerometer measures the structural acceleration in three directions with a high-sampling rate, while the vision camera tracks a fixed target from the surrounding of the target structure with a low sampling rate. An accelerometer-aided computer vision algorithm is first used to estimate the three-dimensional structural displacement based on vision measurements. The estimated vision-based displacements are then fused with accelerometer measurements using an adaptive multirate Kalman filter, to obtain final displacements with a higher sampling rate and better accuracy than vision-based displacements. Note that a calibration process is performed automatically to estimate scale factors for unit conversions and to select active pixels with a region of interest (ROI). More details on the automated initial calibration, accelerometer-aided computer vision algorithm, and adaptive multirate Kalman filter could be found in Ma et al. [7].

20.3 Experimental Validation

Figure 20.2a demonstrates the overall configuration of the laboratory test on a four-story shear building structure. The experiment was performed inside the KAIST campus, and a window of an actual building, approximately 20 m apart, was

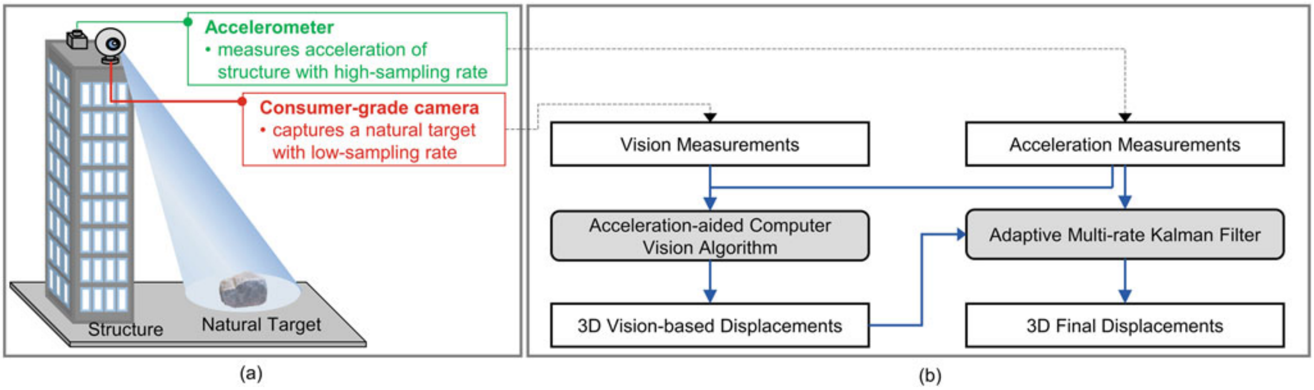

Fig. 20.1 Overview of the proposed displacement estimation method: (**a**) sensor setup and (**b**) overall flowchart

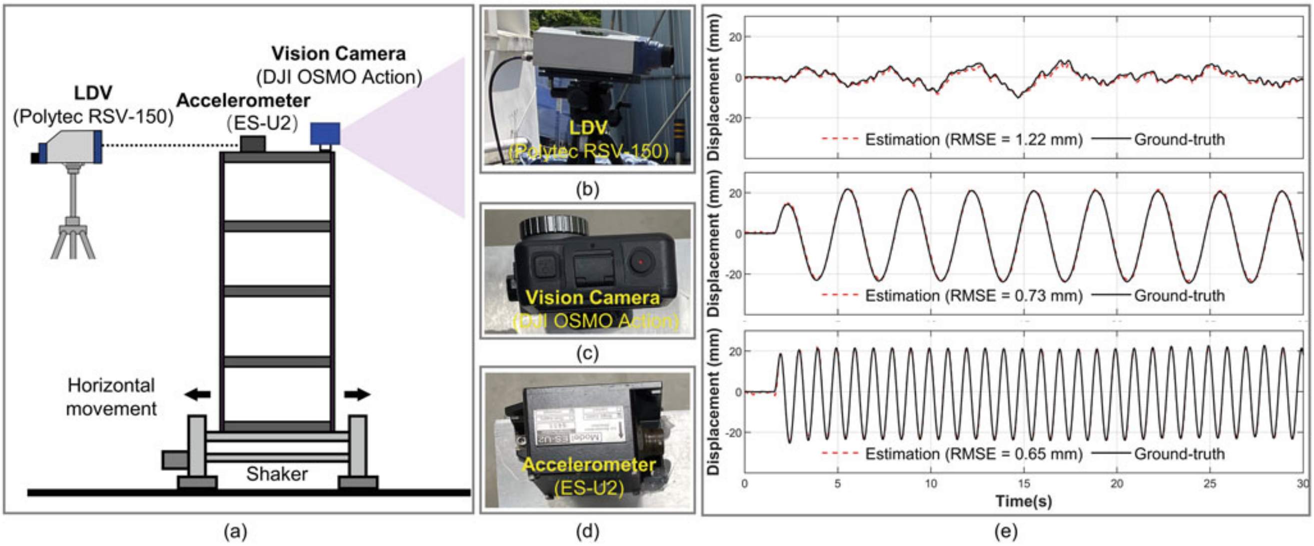

Fig. 20.2 (**a**) overall configuration of the laboratory test on a four-story shear building structure, (**b**)~(**d**) a laser Doppler vibrometer (LDV), vision camera, and accelerometer used in this test, and (**e**) displacement estimated by the proposed method using the vision camera and the accelerometer compared to the ground-true displacements measured by the LDV under three different excitations

used as a natural target. The shaking table moved the shear building structure in a horizontal direction to generate out-of-plane vibration of the structure relative to the natural target. Note that the authors have previously verified in-plane displacement estimation using a vision camera and accelerometer [6, 7], and then this test focuses on out-of-plane displacement estimation only. The displacement at the top of the shear building structure was measured using a laser Doppler vibrometer (LDV) and estimated using an accelerometer and a vision camera installed at the same location. Note that here the LDV was used for ground truth displacement measurement, which is necessary for evaluating the estimation performance of the proposed method. Figure 20.2b shows the Polytech RSV-150 LDV used in this study, and the LDV can measure displacement with a resolution of fewer than 1 μm. Figure 20.2c shows the DJI OSMO Action vision camera used in this study. The camera has a 1/2.3 inch CMOS sensor and an f/2.8 lens with a field of view of 145°. It can be used to record videos with 4K resolution (3840 pixels by 2160 pixels) at a frame per second (FPS) up to 60 Hz. Figure 20.2d shows the EpiSensor ES-U2 accelerometer used in this study, which is a force-balance type uniaxial accelerometer. The accelerometer has an extremely low self-noise with a 155 dB dynamic range and a wide frequency response of up to 200 Hz. In this study, accelerometer and LDV measurements were discretized at 100 Hz using a National Instrument USB-6366 data acquisition device, while the vision measurement was recorded at 4K resolution with an FPS of 10 Hz. Three different excitation signals were inputted to the horizontal shaker in this test. Figure 20.2e compares displacements estimated by the proposed method and measured by the LDV. In all three cases, the estimated displacements have good agreement with the ground-truth displacements measured by the LDV. The root means square error (RMSE) of the estimated displacements were calculated to quantitatively evaluate the estimation performance of the proposed method. Less than 2 mm RMSE indicates that the proposed method can accurately estimate out-of-plane displacement.

20.4 Conclusion

This study proposed a three-dimensional displacement estimation method through the fusion of a collocated vision camera and an accelerometer on a target structure. To validate the performance of the proposed displacement estimation method, a laboratory test was conducted on a four-story building structure, and out-of-plane displacements were estimated under three different excitations. The results indicate that the proposed method was able to estimate displacement accurately with an RMSE of less than 2 mm. However, displacements were estimated only in a single direction, and more experiments are required for validating the proposed method for displacement estimation in all three directions. In addition, efforts are currently being made to develop a structural displacement sensor module by integrating a vision camera, accelerometer, and microcontroller.

Acknowledgements This study was supported by the National Research Foundation of Korea (NRF) grant funded by the Korean Government (MSIT) (No. 2017R1A5A1014883).

References

1. Lee, H.S., Hong, Y.H., Park, H.W.: Design of an FIR filter for the displacement reconstruction using measured acceleration in low-frequency dominant structures. Int. J. Numer. Methods Eng. **82**(4), 403–434 (2010)
2. Moschas, F., Stiros, S.: Measurement of the dynamic displacements and of the modal frequencies of a short-span pedestrian bridge using GPS and an accelerometer. Eng. Struct. **33**(1), 10–17 (2011)
3. Ma, Z., Chung, J., Liu, P., Sohn, H.: Bridge displacement estimation by fusing accelerometer and strain gauge measurements. Struct. Control. Health Monit. **28**(6), e2733 (2021)
4. Moreu, F., Li, J., Jo, H., Kim, R.E., Scola, S., Spencer Jr., B.F., LaFave, J.M.: Reference-free displacements for condition assessment of timber railroad bridges. J. Bridg. Eng. **21**(2), 04015052 (2016)
5. Ma, Z., Choi, J., Yang, L., Sohn, H.: Structural displacement estimation using accelerometer and FMCW millimeter wave radar. Mech. Syst. Signal Process. **182**, 109582 (2023)
6. Ma, Z., Choi, J., Sohn, H.: Real-time structural displacement estimation by fusing asynchronous acceleration and computer vision measurements. Comput. Aided Civ. Inf. Eng. **37**(6), 688–703 (2022)
7. Ma, Z., Choi, J., Liu, P., Sohn, H.: Structural displacement estimation by fusing vision camera and accelerometer using hybrid computer vision algorithm and adaptive multi-rate Kalman filter. Autom. Constr. **140**, 104338 (2022)

Chapter 21
Condition Assessment of Cylindrical Structures Using Helical Guided Ultrasonic Waves

Stylianos Livadiotis and Salvatore Salamone

Abstract This work is concerned with the acoustic emission of helical guided waves generated during corrosion in cylindrical steel structures. The energy that is emitted during the corrosion progress in the steel is collected by means of acoustic emission hits and a correlation is established between the amplitude of these hits and the corrosion through a *b*-value analysis. The methodology was validated through an accelerated corrosion experiment, and a linear relationship between the *b*-value and the corrosion evolution was observed.

Keywords Helical Guided Waves · Acoustic Emission · Corrosion · Pipes · Structural Health Monitoring

21.1 Introduction

Large-diameter steel pipes are used predominantly for the transmission and distribution of oil and gas around the world. The structural integrity of these pipes is often compromised by corrosion that develops in both the inner and outer surfaces and has many different forms like uniform, pitting, and crevice. A typical result of corrosion is local wall-thinning of the pipe which can potentially lead to catastrophic failures. Traditional approaches to quantify corrosion in pipes exist although for most cases they are heavily dependent on the inspector's knowledge and expertise, are costly, and are extremely time-consuming. In the context of Acoustic Emission (AE), previous studies have proposed various methods for evaluating the state of corrosion in cylindrical structures like pipes, tanks, and vessels [1]. These methods rely on collecting the aggregate of the AE activity to infer the structural condition of the structure. In this work, the focus is set on utilizing helically propagating Lamb waves, also known as Helical Guided Waves (HGW), originating from potentially damaged areas of the pipe [2]. An advantage of using the HGW relies on the possibility of capturing with a single sensor multiple orders of the same event that propagated around the pipe circumference as illustrated in Fig. 21.1. Using this approach, it is possible to correlate typical AE features like Energy, Peak Frequency, and Amplitude with the structural condition of the pipe. Specifically, the traditional *b*-value analysis was used to study the correlation of these features to the corrosion process [3, 4].

21.2 Experiment

To validate the proposed methodology, an accelerated corrosion experiment was conducted on a 10-in diameter, 5-ft long steel pipe. The test involved the installation of a rectangular tank of dimensions 0.2 m × 0.1 m sustaining salt-water solution on the external of the pipe. Direct current (DC) was supplied to the system in 5-hour cycles to accelerate the corrosion process, and AE activity was monitored through a network of 6 Physical Acoustics sensors (R15a). The experiment was concluded after 35 cycles at which point the pipe experienced 100% thickness loss. For every cycle, the thickness loss was approximately 0.3 mm which correlates well with the theoretical prediction derived from Faraday's law of electrolysis. To allow as many helical orders to propagate to the sensors, the Hit-Lockout Time (HLT) of the data acquisition system was set to allow as much energy from a single event to be recorded as a single AE hit.

S. Livadiotis (✉) · S. Salamone
Smart Structures Research Group (SSRG), Department of Civil, Architectural and Environmental Engineering – University of Texas at Austin, Austin, TX, USA
e-mail: slivadiotis@utexas.edu; salamone@utexas.edu

H. Y. Noh et al. (eds.), *Dynamics of Civil Structures, Volume 2*, Conference Proceedings of the Society for Experimental Mechanics Series, https://doi.org/10.1007/978-3-031-36663-5_21

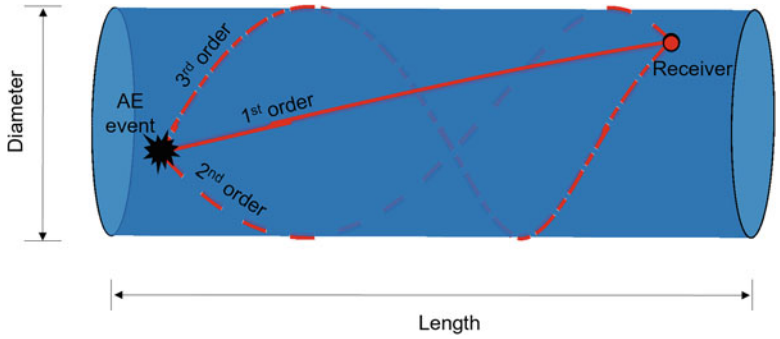

Fig. 21.1 Demonstration of multiple orders of helically propagating Lamb modes from an acoustic source

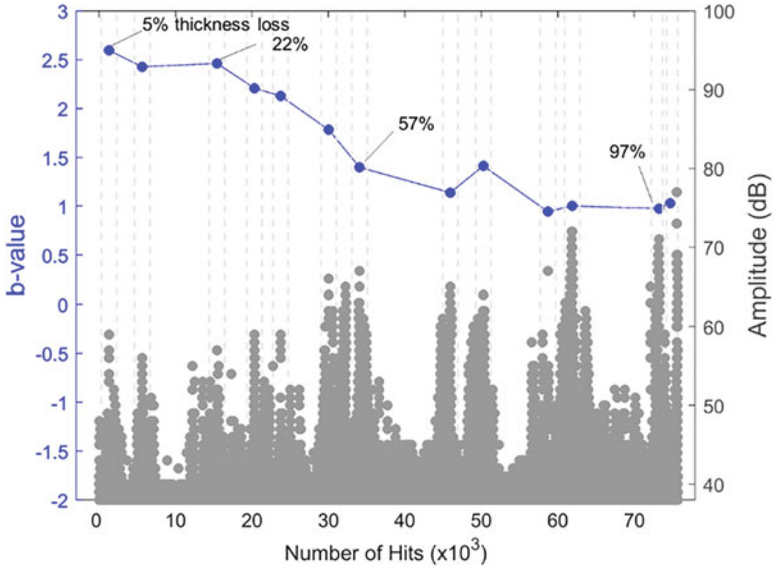

Fig. 21.2 The calculated *b*-value for different stages of corrosion

21.3 Analysis

Figure 21.2 illustrates the main findings of this work. Using the cumulative frequency-amplitude distribution of the recorded AE activity from a single AE sensor, it was possible to estimate the *b*-value for different instances of the corrosion process. As expected, the amplitude of the AE hits increased as the corrosion penetrated deeper into the pipe wall. In terms of the *b*-value, at the early stages of the experiment, it is observed to have values greater than 2 but eventually approaches 1 as corrosion becomes more severe. Overall, the *b*-value experiences an almost linear relationship with the pipe-wall thickness loss which suggests that it can be effectively used to qualitatively assess the remaining structural capacity of a pipe undergoing corrosion degradation.

Figure 21.3 presents linear fitted lines of the *b*-values derived from the AE hits of the six sensors individually, as well as the AE hits combined from all sensors. Overall, a similarity in the slope of these lines is observed which suggests that the use of the *b*-value as a predictor of the corrosion evolution is uniform between the sensors. In addition, these lines form an envelope of values ranging between 1.5 and 3 that can be potentially used as a characteristic of the specific corrosion type in the structure.

Fig. 21.3 Linear fit of *b*-values for all sensors individually and combined

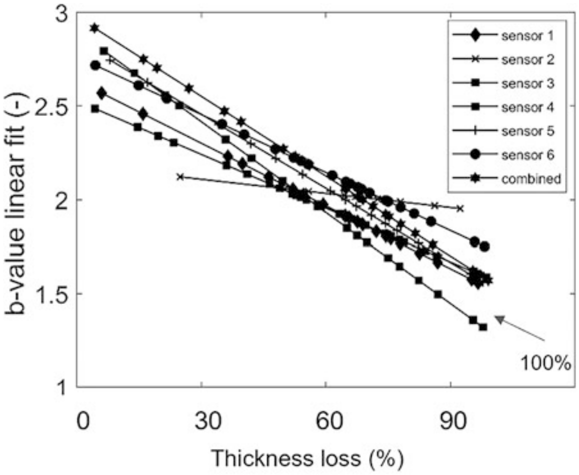

21.4 Conclusions

In this work, it was demonstrated that the helical guided wave acoustic emission can be successfully utilized to qualitatively monitor the corrosion evolution in steel pipes. Future work should address other concerns like the influence of internal pressure and the bordering of fluid on the amplitude and energy of the helical guided waves.

Acknowledgements The authors would like to acknowledge the support from the United States Department of Transportation (USDOT), Pipeline and Hazardous Materials Safety Administration (PHMSA) under the Competitive Academic Agreement Program (CAAP) (#693JK31850004CAAP).

References

1. Kwon, J.R., Lyu, G.J., Lee, T.H., Kim, J.Y.: Acoustic emission testing of repaired storage tank. Int. J. Press. Vessel. Pip. **78**(5), 373–378 (2001)
2. Livadiotis, S., Ebrahimkhanlou, A., Salamone, S.: An algebraic reconstruction imaging approach for corrosion damage monitoring of pipelines. Smart Mater. Struct. **28**(5), 055036 (2019)
3. Rao, M.V.M.S., Prasanna Lakshmi, K.J.: Analysis of b-value and improved b-value of acoustic emissions accompanying rock fracture. Curr. Sci. **89**(9), 1577–1582 (2005)
4. Colombo, I.S., Main, I.G., Forde, M.C.: Assessing damage of reinforced concrete beam using ‘ b -value’ analysis of acoustic emission signals. J. Mater. Civ. Eng. **15**(3), 280–286 (2003)

Chapter 22

A Supervised Deep Learning Method to Classify Structural Damage of a Bridge Deck Mock-Up

Burak Duran, Dominic Emory, Saeed Eftekhar Azam, and Daniel G. Linzell

Abstract Structural damage detection and prediction under various type of demands has been a significant area of research over the past few decades. Applications of machine (ML) and deep learning (DL) to this topic have provided essential insight into damage detection and prediction in many engineering disciplines, including structural health monitoring (SHM). This study mainly focuses on implementation of DL-based algorithms to help identify and classify imposed structural damage to a full-scale bridge deck mock-up whose structural response was monitored under varying loading conditions and damage levels. Strain time-history data, which represents a healthy, undamaged, state and three incremental damage states, was collected from the field experiments. Supervised ML was used to construct a dedicated two-dimensional (2D) convolutional neural network (CNN), which can extract and classify features, using sensor readings as input "images." The proposed 2D-CNN model utilized four fully connected, dense layers with pooling operations integrated after each layer. Rectified linear unit (ReLU) and SoftMax activation functions were used in the hidden and last output layers, respectively. The experimental data was split into training, testing, and validation sets. Damage labels and corresponding images were initially known for the training dataset. The constructed CNN model was trained, and damage location and a high prediction accuracy were obtained for training, validation, and testing datasets.

Keywords Damage detection · deep learning · health monitoring

22.1 Introduction

Performance assessment of the civil infrastructure is vital to serviceability and to determine and mitigate any possible severe structural damages from occurring. A visual inspection during a site visit is a conventional way to identify structure deterioration and damage, which can be time-consuming, impractical, constrained by technical limitations, and somewhat subjective. An automated way of structural condition assessment would provide a reliable, quick, and quantitative way to identify damage and its severity. Vibration-based structural health monitoring (SHM) is a robust tool for putting this concept into practice. Vibration-based SHM determines structural health states by tracking condition and collecting data using sensors placed on the structure and processing results, using various techniques and algorithms. In the last two decades, more effort has been dedicated to the development of sensor technologies and integration of data science into SHM for long-term monitoring schemes [1, 2]. Accordingly, data-driven SHM models have proven to be practical and viable alternatives to visual inspections, with various studies completed that attempt to detect structural damage using convolutional neural networks (CNNs) [3–6].

This study delves into structural damage identification of a full-scale bridge deck mock-up using supervised DL. To that end, strain time-history data, which was gathered from a number of locations on the mock-up at various controlled damage states and subject to variable moving loading conditions, was used as an input image after being converted into grayscale images. It is believed that this data represents a real-life situation owing to the size of the mock-up and loading conditions and

---

B. Duran (✉) · D. Emory · S. E. Azam
Department of Civil and Environmental Engineering, University of New Hampshire, Durham, NH, USA
e-mail: burak.duran@unh.edu

D. G. Linzell
Department of Civil and Environmental Engineering, University of Nebraska-Lincoln, Lincoln, NE, USA

H. Y. Noh et al. (eds.), *Dynamics of Civil Structures, Volume 2*, Conference Proceedings of the Society for Experimental Mechanics Series, https://doi.org/10.1007/978-3-031-36663-5_22

damage states it was subjected to. A two-dimensional (2D) CNN was developed using the strain-based images and achieved a higher level testing accuracy. The robustness of the network was further tested using Gaussian white noise-contaminated images. The studied framework allowed for identification of damage conditions not visible to the naked eye.

22.2 Methodology

Within the scope of this study, strain time-history data, which was obtained from an experimental work conducted in [7], was used as an input image for construction of 2D CNN. Collected data from different locations on the mock-up (Fig. 22.1) was first processed using low pass filtering and normalization steps to bring the data on a common and smaller scale to achieve a better computational effort. Numerical input data, represented by snapshot matrices, was converted into images for the purpose of using them in a 2D CNN. An architectural configuration was then set up to initialize the network, and hyperparameter tuning was performed to find the best architecture and parameters. Robustness of the proposed network was then examined using originally generated images and images contaminated with 15% Gaussian white noise within the range of maximum and minimum variation of strain.

22.3 Data Characteristics and Preparation

More information on the experimental study (Fig. 22.1) can be found elsewhere [7]. The mock-up was tested under moving loads provided by a pick-up truck of constant weight at variable speeds and a dump truck at a constant speed and variable weight. Four scenarios were studied: the healthy or undamaged case (UN or 0); a crash-induced case (D1 or 1) where a truck impacted the mock-up concrete barrier at midspan; a case where the specimen was subjected to controlled damage to the

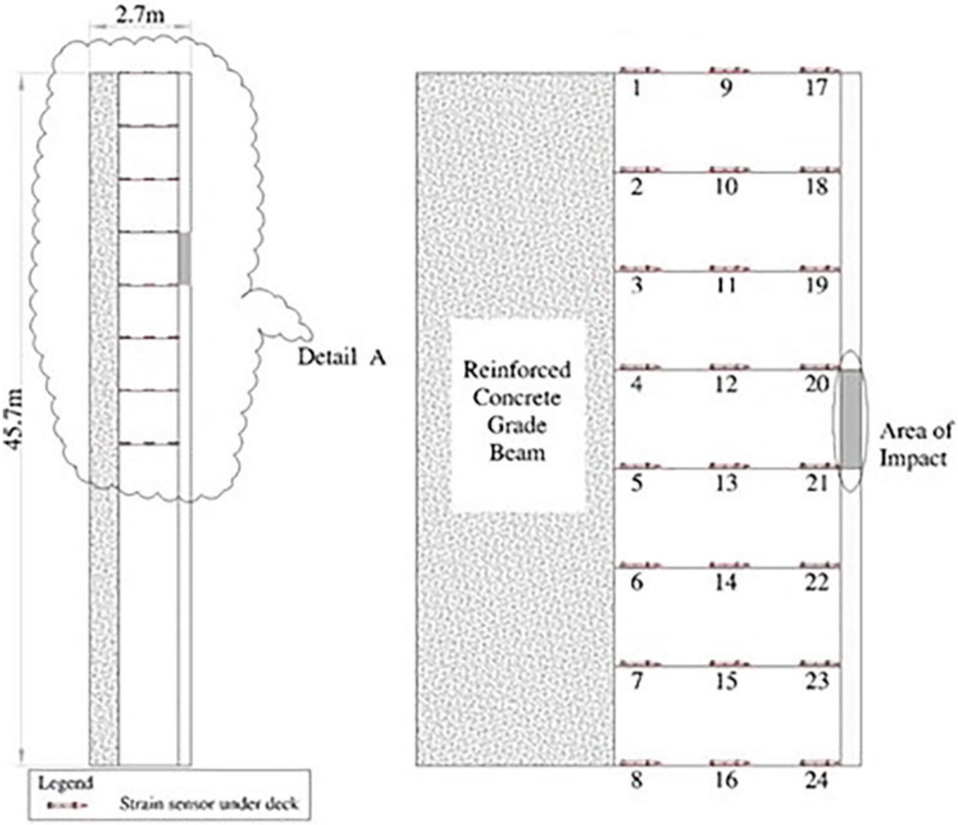

Fig. 22.1 Mock-up plan view (left), Detail A (right) with strain sensors shown (REF)

barrier (D2 or 2) by applying an entire vertical sawcut at midspan; and a case where the sawcut extended through the slab width (D3 or 3). D1 is a frequently occurring case for in-service bridges and sometimes resulting damage not visible to the naked eye. During the experiments, strain time-history data was collected at a frequency of 100 Hz from a total of 24 sensors located at different points on the mock-up during each vehicle's pass.

CNNs are an effective method of image processing. Since original data records were one-dimensional, they were converted into two-dimensional grayscale images to utilize higher classification and modeling efficiency of CNNs. After the data was filtered and normalized (Fig. 22.2), it ranged from 0 and 1, where 0 represented the maximum negative strain and 1 the maximum positive strain. Intensity so that original data features could be represented using an image, and so a 2D CNN can learn and use these features to improve performance of prediction model [8]. Input images are all 1000 × 24 × 1 in size, with 1000 being their height, 24 their width (i.e., the total number of sensors), and 1 representing the number of channels. In this study, a total of 321 images were used within the purpose of CNN implementation.

22.4 Deep Neural Network (DNN)

DNN is a branch of ML artificial intelligence (AI), which is inspired from a biological structure and functionality of a brain to assist machines with intelligence. There is a sequential and layered organization of neurons as shown in Fig. 22.3. Those neurons (or nodes) convey a signal to others based on their received input, and each node computes an activation function. The connection between the nodes has a weight, and it is updated by an iterative procedure after random initialization. CNNs are the most popular DNN implementation, which adapted to several structural damage detection works [5]. The input to the designed DL approach is an image, and the network is comprised of several building blocks, using convolutional (CONV), pooling (POOL), and layers followed by fully connected (FC) layers.

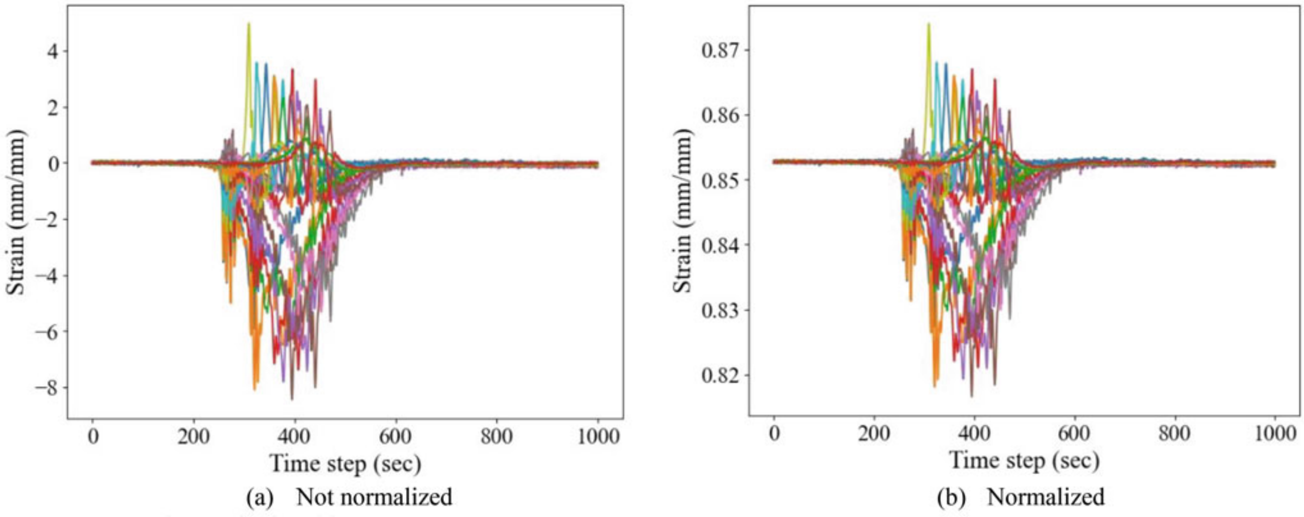

(a) Not normalized
(b) Normalized

Fig. 22.2 Representative strain time-history. (**a**) Not normalized. (**b**) Normalized

Fig. 22.3 DNN with two hidden layers

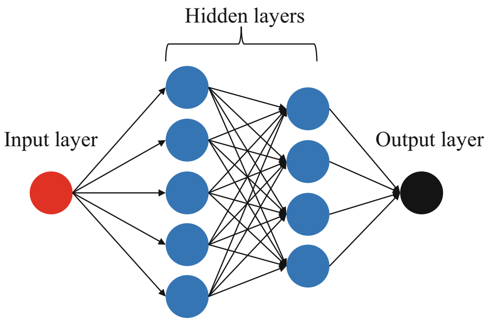

22.5 Convolutional Neural Network (CNN) and Its Implementation

CNNs are DL-based schemes that extract features more efficiently than conventional ML methods [9]. The network can be generated in several ways by sequentially combining convolutional (CONV), pooling (POOL), and fully-connected (FC) layers. Representative CNN input images are shown in Fig. 22.4. Hyperparameter tuning was performed to develop the best damage detection framework architecture for DL-based SHM. Thus, different combinations of the network were implemented using varying parameters, including the: number of CONV layers [1–4]; number of FC layers [1–3], type of POOL operation (maximum or average); learning rate [10^{-2}–10^{-4}]; number of epochs [100, 150, 200, 250, 300]; filter size [(3 × 3), (5 × 5)]; and number of filters [4, 8, 16, 32, 64, 128].

It was concluded that the proposed 2D CNN architecture (Fig. 22.5) featuring four convolutional layers, two pooling layers, three FC layers, and a dense SoftMax (Eq. (22.1)) output layer at the end with a total number of 200 epochs yielded satisfactory prediction accuracy. In Eq. (22.1), the z takes in the values from the neurons of the output layer, and the exponential function does a nonlinear operation. Any class *i* of the input is estimated by the selection of the maximum probability of this function. In the CNN configuration, the number of filters were chosen to be 16, 32, 64, and 128 with a rectified linear unit (ReLU) activation function, and fully connected layers had 128 nodes before the output layer. Lastly, the kernel size was (3 × 3) and with maximum pooling. During the training process, the Adam optimization method [10] was employed with a learning rate of 10^{-3}, and the sparse categorical cross entropy loss function (Eq. (22.2)) was selected as a cost function.

$$\mathrm{softmax}\left(z_i\right) = \frac{\exp\left(z_i\right)}{\sum_j \exp\left(z_j\right)} \tag{22.1}$$

$$J(w) = -\frac{1}{N}\sum_{i=1}^{N} y_i \log\left(\hat{y}_i\right) \tag{22.2}$$

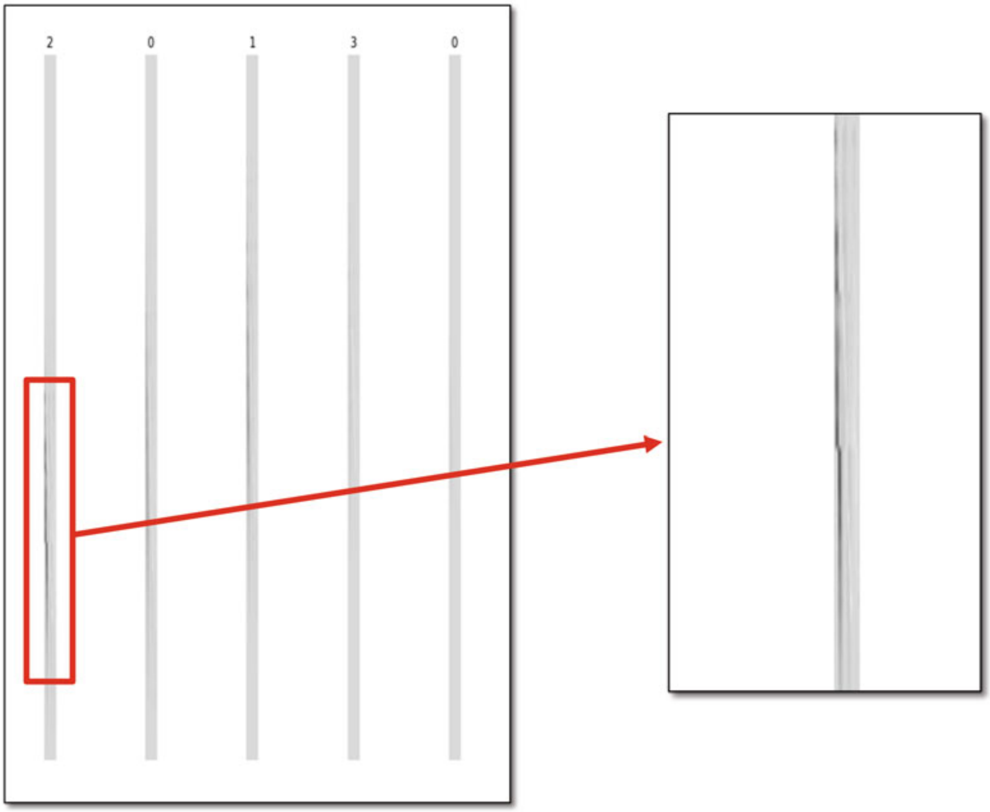

(a) Set of damage labels and images

(b) Zoomed view, D2

Fig. 22.4 CNN input image examples. (**a**) Set of damage labels and images. (**b**) Zoomed view, D2

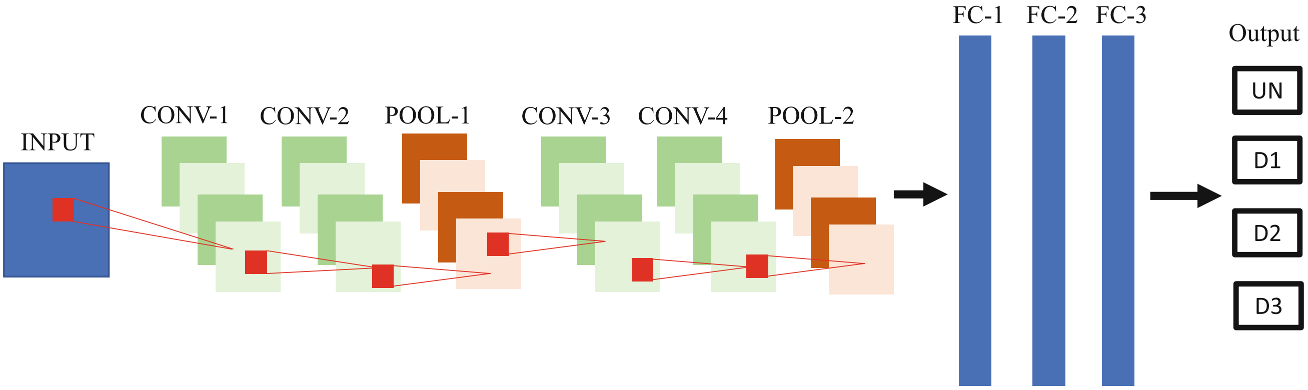

Fig. 22.5 Proposed CNN architecture

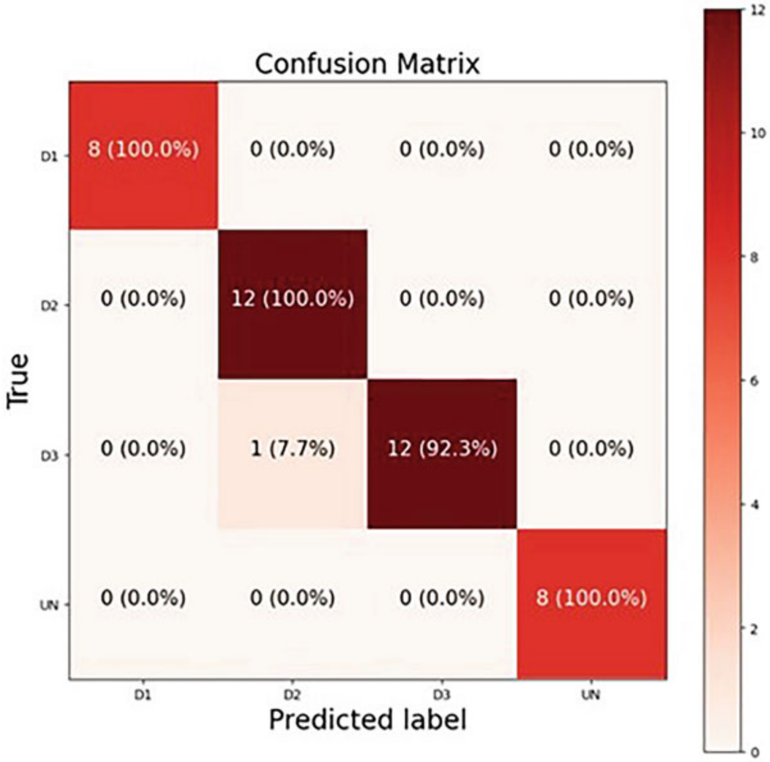

Fig. 22.6 Confusion matrix

22.6 Results

The trained network was tested on images different from the training dataset. As illustrated in Fig. 22.6, there is only one, misclassified, off-diagonal member in the confusion matrix, and the proposed network achieved 98% testing accuracy while the training and validation accuracies are 100%. To test out the robustness of the network, 15% Gaussian white noise was added to test image dataset, and then the network was retested, with 93% testing accuracy being obtained. Those results indicate that the proposed damage identification framework performed well for the data that was examined.

22.7 Conclusion

This study introduces a framework to identify structural damage based on measured structural response based on DL-based scheme. In this regard, strain-time history data was gathered from testing a full-scale bridge deck mock-up subjected to a variety of damage states and moving loading conditions. Sensor data was converted to an image data set that was used as input into a developed 2D CNN. Results showed that the proposed framework and architecture has the ability of achieving 98% testing accuracy. The constructed CNN was also tested on image data sets contaminated with 15% Gaussian white noise. The model attained a similar level accuracy. Furthermore, the first damage level (D1), which is typically the invisible case in the field, was successfully identified through the model. Overall, data-driven based SHM framework with the implementation of CNN is established to function well in the damage detection of the full-scale specimen using strain time-history data.

Acknowledgements The authors would like to acknowledge support provided by NSF Award #1762034 BD Spokes: MEDIUM: MIDWEST: Smart Big Data Pipeline for Aging Rural Bridge Transportation Infrastructure (SMARTI). The authors also gratefully acknowledge the assistance, access, computing resources, data, and expertise provided by the University of Nebraska's Holland Computing Center and Midwest Roadside Safety Facility and from Bridge Diagnostics Inc. in association with this project. The authors would also like to acknowledge assistance from Peter Hilsabeck in conducting the tests.

References

1. Entezami, A., Sarmadi, H., Behkamal, B., Mariani, S.: Big data analytics and structural health monitoring: a statistical pattern recognition-based approach. Sensors. **20**(8), Article 8 (2020). https://doi.org/10.3390/s20082328S
2. Azimi, M., Eslamlou, A., Pekcan, G.: Data-driven structural health monitoring and damage detection through deep learning: state-of-the-art review. Sensors. **20**(10), 2778 (2020). https://doi.org/10.3390/s20102778S
3. Gulgec, N.S., Takáč, M., Pakzad, S.N.: Structural damage detection using convolutional neural networks. In: Barthorpe, R., Platz, R., Lopez, I., Moaveni, B., Papadimitriou, C. (eds.) Model Validation and Uncertainty Quantification, vol. 3, pp. 331–337. Springer International Publishing (2017). https://doi.org/10.1007/978-3-319-54858-6_33
4. Khodabandehlou, H., Pekcan, G., Fadali, M.S.: Vibration-based structural condition assessment using convolution neural networks. Struct. Control. Health Monit. **26**(2), e2308 (2019). https://doi.org/10.1002/stc.2308
5. Feng, C., Zhang, H., Wang, S., Li, Y., Wang, H., Yan, F.: Structural damage detection using deep convolutional neural network and transfer learning. KSCE J. Civ. Eng. **23**(10), 4493–4502 (2019). https://doi.org/10.1007/s12205-019-0437-z
6. Teng, Z., Teng, S., Zhang, J., Chen, G., Cui, F.: Structural damage detection based on real-time vibration signal and convolutional neural network. Appl. Sci. **10**(14), Article 14 (2020). https://doi.org/10.3390/app10144720
7. Akintunde, E., Eftekhar Azam, S., Rageh, A., Linzell, D.G.: Unsupervised machine learning for robust bridge damage detection: full-scale experimental validation. Eng. Struct. **249**, 113250 (2021). https://doi.org/10.1016/j.engstruct.2021.113250
8. Zhu, Y., Brettin, T., Xia, F., Partin, A., Shukla, M., Yoo, H., Evrard, Y.A., Doroshow, J.H., Stevens, R.L.: Converting tabular data into images for deep learning with convolutional neural networks. Sci. Rep. **11**(1), Article 1 (2021). https://doi.org/10.1038/s41598-021-90923-y
9. Alzubaidi, L., Zhang, J., Humaidi, A.J., Al-Dujaili, A., Duan, Y., Al-Shamma, O., Santamaría, J., Fadhel, M.A., Al-Amidie, M., Farhan, L.: Review of deep learning: concepts, CNN architectures, challenges, applications, future directions. J. Big Data. **8**(1), 53 (2021). https://doi.org/10.1186/s40537-021-00444-8
10. Kingma, D.P., Ba, J.: Adam: a method for stochastic optimization. *arXiv preprint arXiv:1412.6980* (2014)

Chapter 23

Eigenfrequency-Based Feature for Automatic Detection of Real Damage in Tie-Rods Under Uncontrolled Environmental Conditions

F. Lucà, S. Manzoni, and A. Cigada

Abstract Data-driven approaches to damage detection are very common in the field of structural health monitoring (SHM) due to the possibility to be adopted without the need for a model of the monitored structure. These approaches rely only on the information contained in data acquired by sensors, which must be extracted through the adoption of appropriate damage features, i.e., synthetic indexes highly correlated to the structural state. In an unsupervised learning perspective, i.e., when data referring to damage are not available prior to the monitoring, the damage is detected when the damage feature shows a significant variation with respect to a reference set, containing data referring to the initial healthy condition. A critical aspect for unsupervised learning data-driven approaches is related to the fact that, usually, changes of damage features due to environmental and operational variations (EOVs) can be greater than those caused by damage. Many approaches are proposed in the literature to tackle this problem, most of which are validated on simplified cases, under controlled laboratory conditions and where, often, the effect of the damage is only simulated, resulting in a difficult translation to real applications.

In this work, attention is paid to the development of an automatic damage detection strategy for axially loaded beam-like structures, that can be used without the supervision of an expert and that allows for identifying a real state of damage, under the effects of an uncontrolled environment. More in detail, the case study of tie-rods (i.e., tensioned metallic beams used to balance lateral forces of arches and walls of civil structures) is addressed. In previous work, the authors showed that when multiple vibration modes are considered together, patterns of modal parameters associated with damage are different from those due to the effects of EOVs, allowing for defining effective damage features. In this chapter, the strategy is further developed, with a focus on the automatization of the strategy for real applications. This means not only dealing with EOVs, but also developing a successful automatic data cleansing strategy, to automatically detect and discard corrupted results obtained when the operational modal analysis algorithms fail due to unfavorable operating conditions. The validity of the proposed framework is demonstrated on real long-term monitoring data and in presence of real corrosion damage, which is a rare case-study in the field of SHM.

Keywords Structural health monitoring · Operational modal analysis · Unsupervised learning damage detection · Real damage

23.1 Introduction

Vibration-based damage detection is among the most adopted strategies for structural health monitoring (SHM) of civil structures [1, 2]. Damage is indeed a change in structural properties (i.e., mass, stiffness, and damping) that results in a change in modal parameters [3, 4]. For this reason, the dynamic response carries useful damage-related information. When real structures under operating conditions are considered, unsupervised learning approaches are the most suitable choice, since damage-related data are not available, prior to the starting of the monitoring [5]. Unsupervised learning algorithms detect damage when a statistically significant difference is assessed between current data and a reference database (baseline). When vibration-based damage features are adopted, unsupervised learning approaches are limited by the effects of environmental and operational variations (EOVs) [6]. Changes of dynamic properties associated with EOVs are often greater than those due to damage at an early stage, thus they must be properly accounted for.

F. Lucà (✉) · S. Manzoni · A. Cigada
Politecnico di Milano-Department of Mechanical Engineering, Milan, Italy
e-mail: francescantonio.luca@polimi.it

H. Y. Noh et al. (eds.), *Dynamics of Civil Structures, Volume 2*, Conference Proceedings of the Society
for Experimental Mechanics Series, https://doi.org/10.1007/978-3-031-36663-5_23

In this context, this chapter shows a challenging case study in the field of vibration-based unsupervised learning damage detection by dealing with axially-loaded beam-like structures. Slender beams naturally undergo significant vibration levels during normal operational conditions, making the adoption of automatic modal identification algorithms convenient. However, the presence of an axial load which changes according to many physical factors (e.g., temperature or loading conditions) can easily mask the effects of damage, as proved in a previous work [7]. However, when modal parameters of multiple vibration modes are considered together to define a multivariate damage feature, a separation of the effects is possible and damage detection algorithms can be successfully adopted [8].

In order to make the strategy totally automatic, a point of great importance that is often overlooked is that related to the quality of the data used to apply the algorithms. In fact, automatic identification of modal parameters can sometimes be unsuccessful, due to nonideal operational conditions. As it will be shown in the following, removing these wrong identifications from the analysis is a key factor in order to spot early signs of damage in monitoring data. In this chapter, details will be provided on an automatic data cleansing algorithm that allowed a successful adoption of unsupervised learning outlier detection to identify real damage under the effects of uncontrolled EOVs.

The chapter is organized as it follows: the case study is described in Sect. 23.2. The data cleansing algorithm is explained in Sect. 23.3, while its effects on damage detection performances are presented in Sect. 23.4. Finally, conclusions are drawn in Sect. 23.5.

23.2 The Case Study

The data that will be discussed in the following come from an experimental set-up located in the laboratory of Mechanical Deparment of Politecnico di Milano (Fig. 23.1), where a series of nominally identical tie-rods are monitored over time for research purposes (e.g., [8–10]). The length of the tie-rods is equal to 4 m, with a cross-section equal to 15×25 mm^2. Each tie-rod is equipped with general purpose piezoelectric accelerometers (PCB, model 603C01) with a sensitivity of 10.2 mV/(m/s^2) and a full scale of ±490 m/s^2. The choice for industrial accelerometers was made to consider sensor performances which are similar to those that can be found in real applications. Furthermore, the room temperature is measured by a thermocouple and the axial load of each tie-rod is monitored with strain gauges composing a full Wheatstone bridge. Data are acquired at a sampling frequency of 512 Hz by NI9234 modules with anti-aliasing filter on board.

Although being in a laboratory, the environment is characterized by uncontrolled temperature conditions, with temperature that reaches values close to 30 °C at summer and close to 5 °C at winter, with daily excursions in the order of 3–10 °C.

Fig. 23.1 The experimental set-up in the laboratory of Mechanical Department of Politecnico di Milano

Regarding the operational environment, many activities take place close to the monitored tie-rods, e.g., human activities or functioning machineries.

The data that will be discussed in the following are related to approximately 15 months of monitoring, and they include data related to real damage, obtained through a chemical attack on one of the tie-rods. The attack caused general corrosion (i.e., a loss of material that caused a section height reduction) at a distance equal to 5/8 of the free length from one fixed end. The adopted damage feature and the data cleansing algorithm developed to in presence of EOVs are introduced in the next section.

23.3 Analysis

The damage feature adopted in this work is a vector containing the eigenfrequencies of the bending modes in the vertical plane:

$$\underline{f} = \{f_1, f_2, \ldots, f_M\}^{\mathrm{T}} \tag{23.1}$$

where M is the number of considered vibration modes and the superscript "T" means the transpose. The working conditions allowed for a sufficiently stable identification of the vibration modes below 150 Hz. The eigenfrequencies can be generally identified with operational modal analysis approaches (e.g., [11–13]), that can be effectively adopted on slender structures which undergo significant vibration levels. The results presented in this chapter come from data acquired by a single sensor which is located at a 1/10 of the free length of the tie-rod from one fixed end. Using a single sensor, the adopted identification technique is the best-fitting approach [14], which uses the power spectrum of the response as input and allows for the identification of the eigenfrequency values. However, what will be discussed in the following is valid despite the adopted identification technique.

As an example, the trends of three eigenfrequencies are presented, for a period of 2 weeks in Fig. 23.2. Subscripts are used to indicate the order of the eigenfrequencies and f_1, f_2, and f_3 are the eigenfrequencies associated to the third, fourth, and fifth bending vibration modes in the vertical plane, respectively. The automatically identified eigenfrequencies are represented by black points, joint by a black-solid line. As it is possible to see, the eigenfrequencies show daily trends, associated with temperature daily cycles. Furthermore, it is possible to see some peaks (e.g., f_1 in day March 14th). This kind of behavior is associated with a wrong eigenfrequency identification that can be due to a bad signal to noise ratio or the lack of excitation of the considered vibration mode. Another abnormal behavior is that observed in period March 5th to March 10th, on eigenfrequencies f_2 and f_3. In this case, while f_1 shows daily cycles, many identifications are at the same value for both f_2 and f_3, showing a flat trend. This latter case can be associated with the presence of a monoharmonic excitation close to resonance. In such a situation, the best fitting algorithm can converge to a wrong solution, since the response to a harmonic input is mistaken for the dynamic amplification due to the resonance, when only the power spectrum obtained with a single sensor is considered. When modal identification is carried out automatically during long-term monitoring, the presence of such corrupted data can represent an issue for damage detection, as it will be shown in Sect. 23.4.

An automatic data cleansing algorithm made by two steps was developed to allow for spotting and removing the corrupted data without any human supervision. At the first step, the R^2 coefficients evaluated between the analytical power spectrum of a single-degree-of-freedom linear time invariant mechanical system, and the experimental power spectrum is used to assess the quality of the modal identification, considering one vibration mode at a time. If even a single eigenfrequency identification is associated with a R^2 below a user defined threshold, the entire feature vector is removed. As an example, by adopting a threshold of 0.9, the observations marked with a blue circle in Fig. 23.2 are removed.

In the second step, all the eigenfrequencies are considered together. The linear relationship between squared pairs of eigenfrequencies of an axially-loaded beam (see, e.g., [15, 16]) is exploited. The trend in time of the m-th squared eigenfrequency is indicated by the symbol $\underline{s}_{\mathrm{m}}$. The scatter plots of the lowest squared eigenfrequency (i.e., $\underline{s}_{1}$) and each of the others are reported in Fig. 23.3a, b.

As it is possible to observe, the majority of the observations are scattered around a linear trend. In addition, there are few observations that deviate from the majority of the others. By assuming the hypothesis that in a short-term window the eigenfrequency variations are only due to axial load variations and not by damage, these observations are clearly associated to corrupted data. It must be considered that the presence of these out-of-scale values can introduce errors in the estimate of the coefficients of the linear regression. For this reason, a preselection of data is carried out, by adopting the Hampel Identifier [17], which is a variation of the three-sigma rule of statistics that is robust against outliers [18]. Data that are less

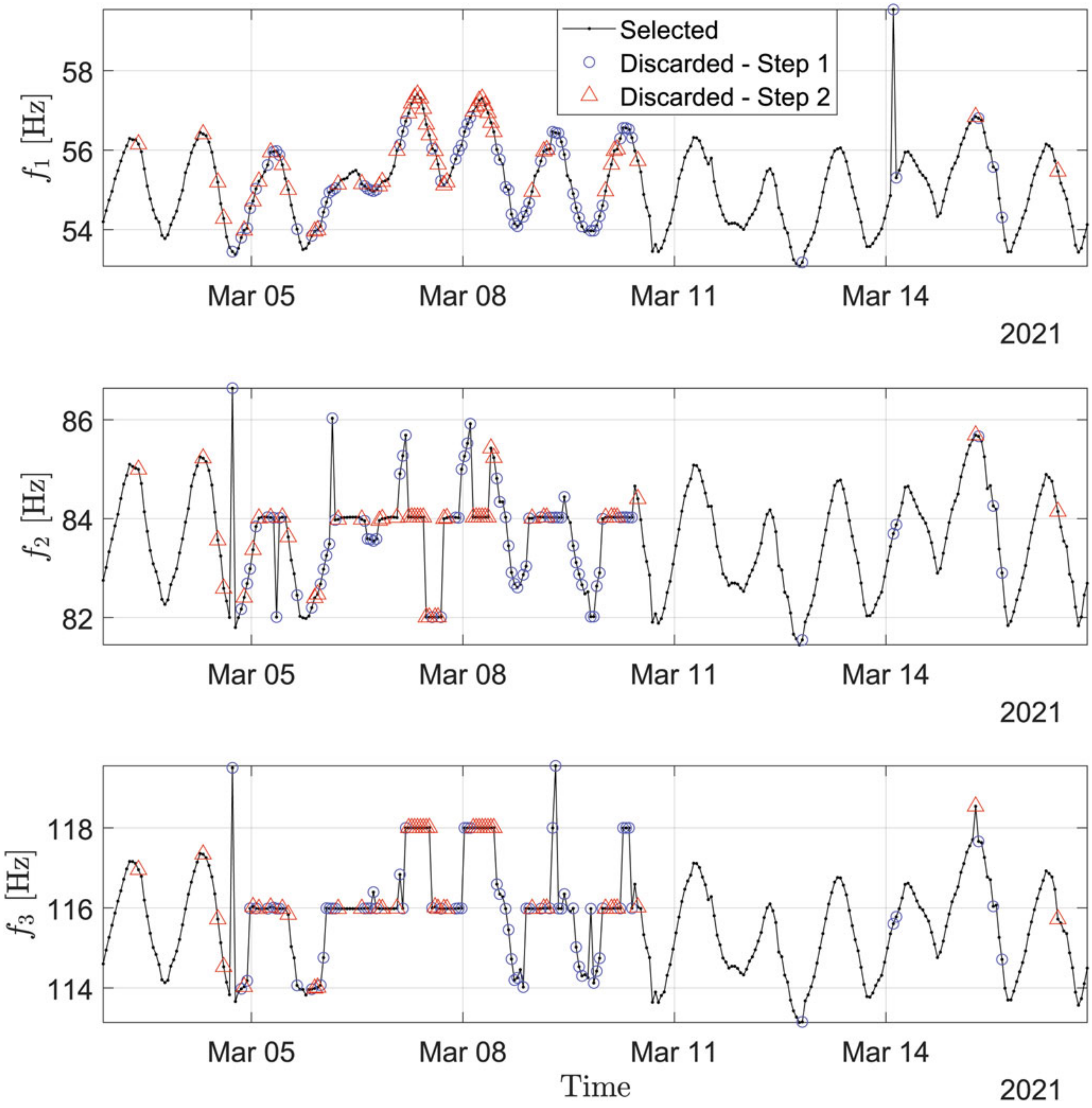

Fig. 23.2 Time-trends of three eigenfrequencies. Black points indicate all the automatically identified eigenfrequency values, blue circles and red triangles indicate the observations discarded by step 1 and 2 of the data cleansing algorithm, respectively

than 1 scaled median absolute deviation (MAD) [19] distant from the local mean over a moving window of 72 h are selected. The selected observations are indicated by the symbol $\underline{\hat{s}}_{\mathrm{m}}$ for the vibration mode number m, and they are represented with red-filled circles in Figs. 23.3c, d. A number $M - 1$ of couples are defined, composed by $\underline{\hat{s}}_{1}$ and $\underline{\hat{s}}_{\mathrm{j}}$, with $1 < j \leq M$, and the coefficients of the linear regression $\hat{a}_{1j}$ and $\hat{b}_{1j}$ (the hat symbol is to indicate that the coefficients are estimated considering the selected observations $\underline{\hat{s}}_{\mathrm{m}}$ only) can be estimated through least squares solution of the linear problem:

$$\underline{\hat{s}}_{\mathrm{j}} = \hat{a}_{1j} \cdot \underline{\hat{s}}_{1} + \hat{b}_{1j} \cdot \underline{1} \tag{23.2}$$

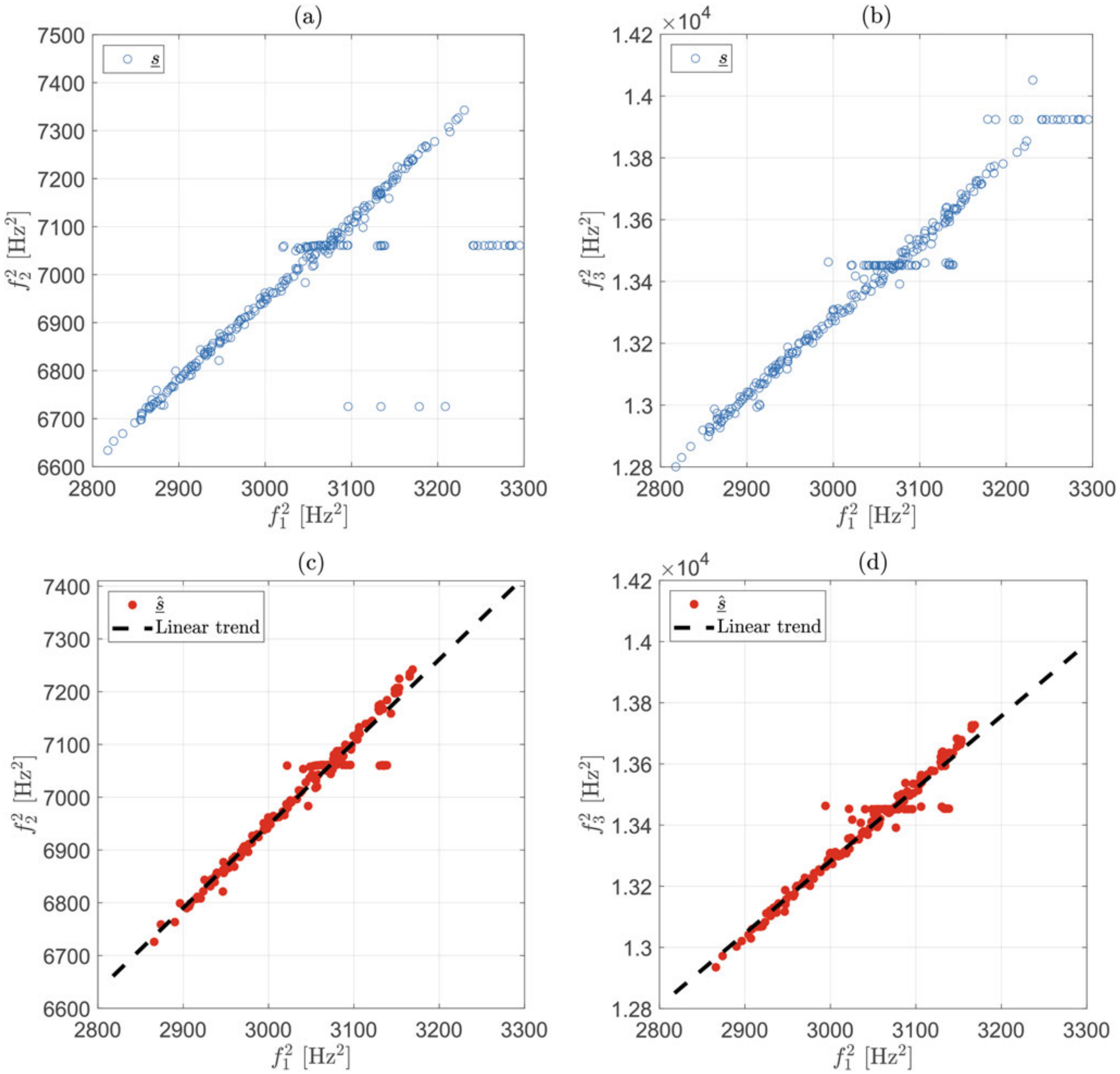

Fig. 23.3 Scatter plots of the squared eigenfrequencies. Figures (**a**) and (**b**) show all the observations available before step 2 of the data cleansing algorithm. Figures (**c**) and (**d**) show only the observations used to estimate the coefficients of the linear trend reported with black-dashed line

where $\underline{1}$ is a column vector with all elements equal to 1.

Once the coefficients are identified considering only the points of Fig. 23.3c, d, all the observations (i.e., all the points in Fig. 23.3a, b) are again considered to finally detect the ones that must be discarded and, for this purpose, the residuals of the linear regression are estimated, according to the following expression:

$$\varepsilon_{1j} = \underline{s}_{\mathrm{j}} - \hat{a}_{1j} \cdot \underline{s}_{1} - \hat{b}_{1j} \cdot \underline{1} \tag{23.3}$$

The discarding procedure is that of Fig. 23.4, where the Hampel filter is again used (this check can be done on a broader window, e.g., of length equal to 14 days). The horizontal black-dashed lines indicate the range of ±2 scaled MAD around

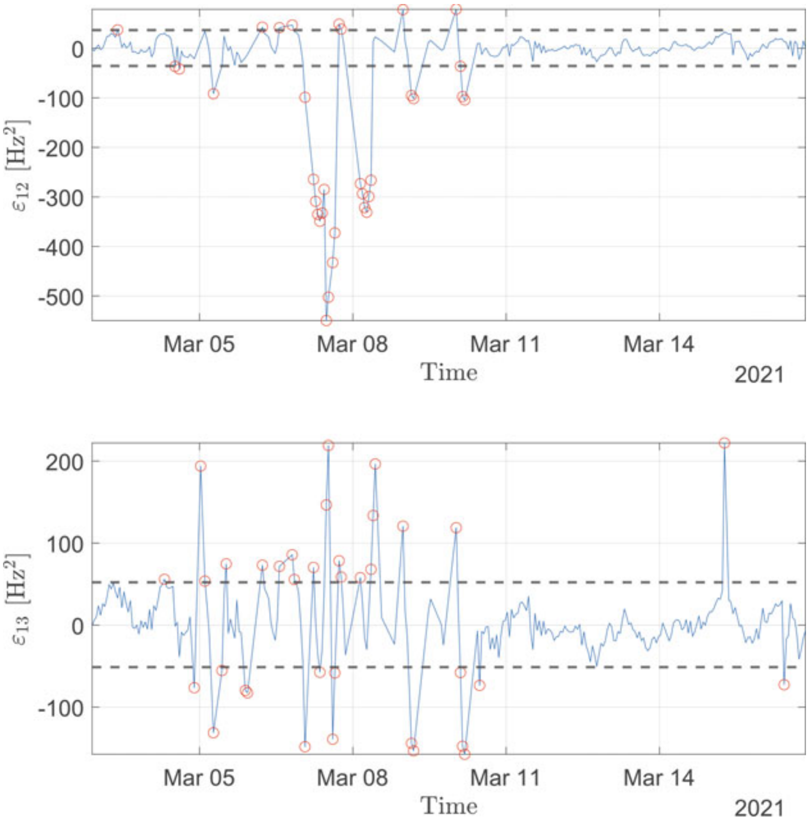

Fig. 23.4 Residuals of the linear regression. Red circles indicate the observations that are considered outliers and that are removed by step 2 of the data cleansing algorithm

the median of each of the two residuals ε_{12} and ε_{13}: observations which are not inside the range are discarded (red circles in Fig. 23.4).

The second step is able to detect and discard the observations indicated with red triangles in Fig. 23.2. As it is possible to see, the data cleansing algorithm cancels out a considerable amount of wrong identifications, while not intervening on normal data. Having explained this preliminary step, its effects on the damage detection stage are shown in the next section.

23.4 Results

The long-term data related to the eigenfrequencies associated to the third, fourth, and fifth vibration modes of one tie-rod are now considered. By using the Mahalanobis squared distance, one of the most adopted multivariate metrics in outlier detection [20], a damage index DI is defined, according to the next expression:

$$\mathrm{DI} = \left(\underline{f}^{\text{new}} - \mu^{\text{base}}\right)^{\mathrm{T}} \left([\Sigma]^{\text{base}}\right)^{-1} \left(\underline{f}^{\text{new}} - \mu^{\text{base}}\right) \tag{23.4}$$

where $\underline{s}_k \underline{f}^{\text{new}}$ is a new observation of the damage feature, μ^{base} and $[\Sigma]^{\text{base}}$ are vector mean and covariance matrix of the matrix $[f]^{\text{base}}$, which is a matrix containing multiple observations of the damage feature $\underline{f}$, when the structure is in a healthy condition. The index DI is a scalar quantity that can be checked against a threshold, here defined according to the procedure reported in [20], based on a Monte Carlo method.

In Fig. 23.5, data indicated with black crosses are those used to build a baseline set. Blue circles are the validation data, i.e., observations associated with a healthy condition but not included in the baseline matrix. Finally, red triangles are used to

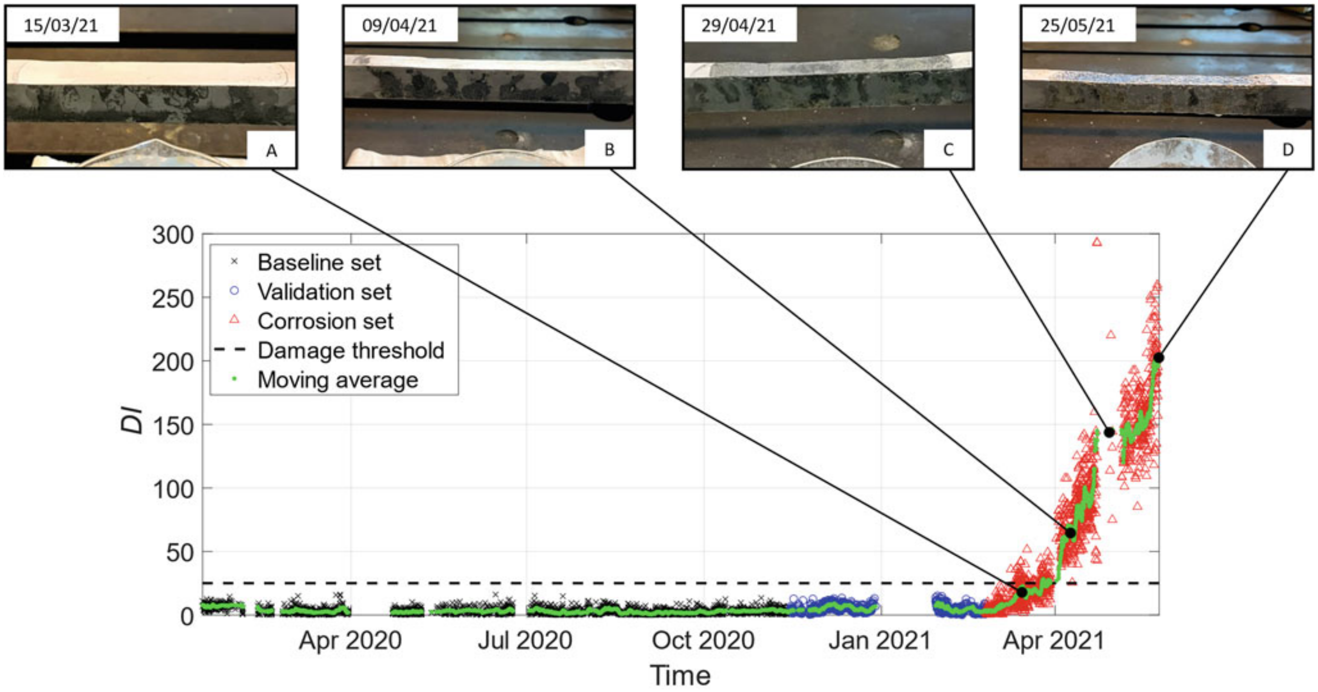

Fig. 23.5 Damage detection in presence of real damage. Black crosses are used for the baseline set, blue circles are used for the validation set, and red triangles are used for damage-related data. The horizontal black-dashed line represents the damage detection threshold. Green points are used to show a moving averaged trend obtained with a window of duration equal to one day, shifted every hour. Pictures of different stages of the corrosion are reported on top

present data associated with an ongoing damaging process (four different pictures related to different stages of the corrosion are also reported, named A, B, C, and D on top of Fig. 23.5).

The obtained results indicate that it is possible to detect real damage. Furthermore, no false alarms are produced on the validation set (i.e., blue circles are below the damage detection threshold). It is worth noticing that if condition B is considered, when damage is still barely detectable through a visual inspection, the damage index is clearly above the damage detection threshold, also considering the dispersion associated with the results.

The receiver operating characteristic (ROC) curve is shown in Fig. 23.6. This graphical tool resumes the performances of a binary classifier by reporting how the true positive and false positive rates change by variating the damage detection threshold. The performances of DI are plotted with a black-solid line, and they are very close to that of a perfect classifier (green-dashed trend that goes from the origin with coordinates (0,0) to the top left corner (0,1) and from (0,1) to the top right corner (1,1)).

The importance of the automatic algorithm presented in the previous section can be assessed by comparing the results obtained with or without the data cleansing stage (this latter case is reported with a black-dotted line). As it is possible to see, if no data cleansing is adopted, the performances of *DI* are even worse than those of a random classifier, which are represented by the red-dashed diagonal from (0,0) to (1,1).

23.5 Conclusion

The quality of data is a crucial issue when automatic monitoring is carried out. This chapter proposed a two-step automatic data cleansing algorithm that allowed to successfully adopt a simple and cost-effective damage detection strategy under the effects of uncontrolled environmental and operational conditions. The damage associated with a real deteriorative process was spotted when the effects were barely visible through a visual inspection, showing the great potential for real scenarios.

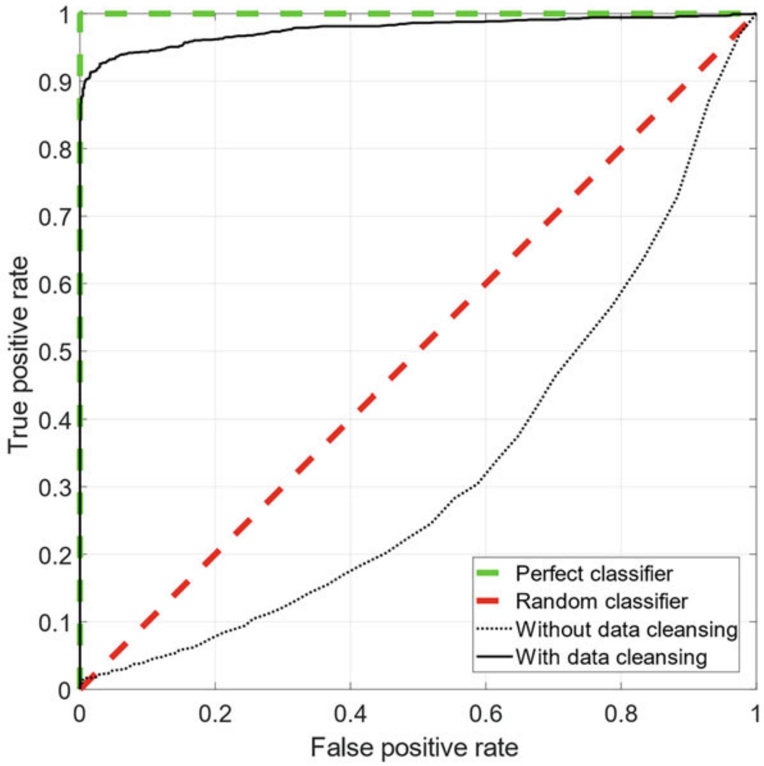

Fig. 23.6 Receiver operating characteristic curve. Comparison between with (black-solid line) and without data cleansing (black-dotted line). Red-dashed and green-dashed lines indicate the curves of a perfect classifier and a random classifier, respectively

References

1. Hou, R., Xia, Y.: Review on the new development of vibration-based damage identification for civil engineering structures: 2010–2019. J. Sound Vib. [Internet]. **491**, 115741 (2021). Available from: https://doi.org/10.1016/j.jsv.2020.115741. Elsevier Ltd.
2. Fan, W., Qiao, P.: Vibration-based damage identification methods: a review and comparative study. Struct. Health Monit. **10**, 83–111 (2011)
3. Doebling, S.W., Farrar, C.R., Prime, M.B.: A summary review of vibration-based damage identification methods. Shock Vib. Dig. **30**, 91–105 (1998)
4. Das, S., Saha, P., Patro, S.K.: Vibration-based damage detection techniques used for health monitoring of structures: a review. J. Civ. Struct. Heal. Monit. **6**, 477–507 (2016). Springer Berlin Heidelberg
5. Farrar, C.R., Worden, K.: Structural health monitoring: a machine learning perspective. Struct. Health Monit. A Mach. Learn. Perspect. (2012) John Wiley and Sons
6. Sohn, H.: Effects of environmental and operational variability on structural health monitoring. Philos. Trans. R. Soc. A Math. Phys. Eng. Sci. **365**, 539–560 (2007)
7. Lucà, F., Manzoni, S., Cigada, A., Frate, L.: A vibration-based approach for health monitoring of tie-rods under uncertain environmental conditions. Mech. Syst. Signal Process. **167**, 108547 (2022). Academic Press
8. Lucà, F., Manzoni, S., Cigada, A.: Data driven damage detection strategy under uncontrolled environment. Lect. Notes Civ. Eng. **254 LNCE**, 764–773 (2023)
9. Lucà, F., Manzoni, S., Cigada, A., Barella, S., Gruttadauria, A., Cerutti, F.: Automatic detection of real damage in operating tie-rods. Sensors. **22**, 1370 (2022)
10. Lucà, F., Manzoni, S., Cigada, A.: Vibration-based damage feature for long-term structural health monitoring under realistic environmental and operational variability. Struct Integr. **21**, 289–307 (2022)
11. Rainieri, C., Fabbrocino, G.: Development and validation of an automated operational modal analysis algorithm for vibration-based monitoring and tensile load estimation. Mech. Syst. Signal Process. [Internet]. **60**, 512–534 (2015). Available from: https://doi.org/10.1016/j.ymssp.2015.01.019. Elsevier
12. Brincker, R., Ventura, C.E.: Introduction to Operational Modal Analysis. Introd. to Oper. Modal Anal. Wiley (2015) Chichester, United Kingdom
13. Reynders, E., Houbrechts, J., De Roeck, G.: Fully automated (operational) modal analysis. Mech. Syst. Signal Process. [Internet]. **29**, 228–250 (2012). Available from: https://doi.org/10.1016/j.ymssp.2012.01.007. Elsevier
14. Ewins, D.J.: Modal Testing: Theory, Practice and Application (2001). John Wiley & Sons, Hoboken, NJ, USA
15. Valle, J., Fernández, D., Madrenas, J.: Closed-form equation for natural frequencies of beams under full range of axial loads modeled with a spring-mass system. Int. J. Mech. Sci. [Internet]. **153–154**, 380–390 (2019) Available from: https://doi.org/10.1016/j.ijmecsci.2019.02.014. Elsevier Ltd.

16. Galef, A.E.: Bending frequencies of compressed beams. J. Acoust. Soc. Am. **44**, 643–643 (1968)
17. Liu, H., Shah, S., Jiang, W.: On-line outlier detection and data cleaning. Comput. Chem. Eng. **28**, 1635–1647 (2004)
18. Hampel, F.R.: A general qualitative definition of robustness. Ann. Math. Stat. **42**, 1887–1896 (1971)
19. Hampel, F.R.: The influence curve and its role in robust estimation. J. Am. Stat. Assoc. **69**, 383 (1974)
20. Worden, K., Manson, G., Fieller, N.R.J.: Damage detection using outlier analysis. J. Sound Vib. **229**, 647–667 (2000)

Chapter 24
A New Cloud-Based Software for Automated SHM of Civil Structures

Rune Brincker, Sandro Amador, and Emmanouil Lydakis

Abstract The principle of the cloud-based Flamenco software is that the operating vibration response data is uploaded by the owner of the structure, then the modal parameters are automatically extracted, and the results are visualized by the owners on a web browser (like Google Chrome, Firefox, etc.). The software consists of a cloud-based web application with front-end and back-end data, meaning that the clients will always have access to its latest version, regardless of the operating system installed on their computers. Since it is essential for the owner of the structure to nondisclose his operational data and the extracted information, only the owner has access to these data. In this chapter, the principles for implementing the OMA extraction features are outlined, and how to check the operating data for sensor errors and how to remove influence from time-varying operating conditions are also explained. The software is illustrated on a simple case, where operating data from a wind-loaded structure is analyzed.

Keywords Automated OMA · Cloud based · Sensor errors · Condensation · Operating conditions

24.1 Introduction

Here, we will give a brief introduction on both classical OMA and to Structural Health Monitoring (SHM) as they are the broad scientific areas and then give a short review of some important papers about automated OMA.

24.1.1 OMA Overview

OMA is the technology of obtaining modal information from the operating responses. That is, we perform no test, we just put sensors on the structures as it is operating, and we use these data to obtain the modal properties of the structures.

OMA is today a well-established technology, and therefore it is easy to give the reader the right advice, that is, he should take a look at the two reference textbooks that have been published few years ago, that is, Rainieri and Fabbrocino from 2014 [1] and Brincker and Ventura from 2015 [2]. The reader should also get themselves acquainted with the broad literature and the many applications published in the IOMAC proceedings from 2005 up until now [3].

24.1.2 SHM Overview

The Wikipedia definition of SHM is as follows:

> SHM involves the observation and analysis of a system over time using periodically sampled response measurements to monitor changes to the material and geometric properties of engineering structures such as bridges and buildings.

R. Brincker (✉)
Brincker Monitoring ApS, Copenhagen, Denmark
e-mail: rune@brincker-monitoring.com

S. Amador · E. Lydakis
Department of Civil and Mechanical Engineering, Technical University of Denmark, Lyngby, Denmark

H. Y. Noh et al. (eds.), *Dynamics of Civil Structures, Volume 2*, Conference Proceedings of the Society for Experimental Mechanics Series, https://doi.org/10.1007/978-3-031-36663-5_24

Therefore, it involves sensors and sensor systems, data acquisition and storage, feature extraction, data compression, and statistical model estimation. Historically, bridges, wind turbines and to some extent offshore structures have been in focus.

In general, in SHM, the focus on modal parameters is small. In most SHM applications, signals from specific locations are being used, mainly just to describe the operating responses in the observation points.

Our reference to the reader here is the famous paper by Farrar and Worden, 2007 [4].

24.1.3 Auto OMA Overview

In this chapter, however, we will focus on one of the most important problems that this whole SHM technology is suffering from – the very limited use of the SHM data. The tradition is that data go down in large data repositories and is then taken out for further analysis if and when there might be a reason for doing so. As a result, a lot of the information in the SHM data is never used.

One of the main reasons why the OMA has been developed is actually due to the potential of using the OMA as a main source of information in SHM applications (see for instance Rainieri 2009 [6]). The development of the OMA in this direction has been going on over the last decade, and we shall here mention a few important contributions.

In Brincker 2007 [5], the principles of the well-known frequency domain decomposition (FDD) are used to describe where in the frequency band we have physical information, and which peaks that should be discarded because they are not modal peaks but harmonics. The paper focuses on theoretical considerations, and no real data is being used. A similar approach is used in Rainieri 2009 [6], where the auto OMA is also based on the FDD, and the technique is illustrated on SHM data from the engineering main building at University of Naples, where the first three modes are automatically identified over a period of 10 days. No information about the success rate is reported.

In Tcherniak et al. 2011 [7], 3000 data sets from a wind turbine were studied, but only a smaller amount was analyzed using an automated approach based on the SSI OMA algorithm. A clustering technique was used to pick physical modes. The paper confirms the ability of OMA to provide modal parameters of the entire wind turbine structure under real operational loads, but no information is given about the success rate of the applied automated OMA.

In Reynders et al. 2012 [8], the work aims at a general interpretation tool for stabilization diagrams that work for EMA, OMA, and OMAX. The paper has a good review of earlier approaches to auto OMA, especially to clustering techniques using stabilization diagrams. The automated OMA is illustrated on the Z24 bridge case, but only 14 data sets were analyzed. The paper reports that automated and manual identification ended up with similar results.

In Devriendt et al. 2014 [9], the Polymax and the SSI OMA techniques were used to analyze data continuously collected for 2 weeks resulting in 2016 data sets of 10 min duration while the wind turbine was idling or parked. It was concluded that the operating data was too far from being a result of white and stationary input. Data was measurement in four tower locations and SCADA data like rotor rotational speed, rotor pitch angle, nacelle yaw angle, and wind speed was included in the analysis. No success or failure rate was reported, but high success rate was defined as being more than 80%. The methodology has been able to successfully identify the closely spaced fore-aft and side-side modes of the tower, even when the frequencies cross each other.

In Lorenzo et al. 2014 [10], simulation data from a reference operating wind turbine was used to investigate the Polymax OMA identification using response data from both tower and blades. It was concluded that a straightforward application of the OMA technique is only possible if the turbine is in parked conditions with the brake engaged. If the blades are rotating, several preprocessing steps are needed in order to apply the conventional OMA technique. No automated identification was reported.

In Neu et al. 2017 [11], a data-driven SSI-based OMA technique and a clustering technique were used to distinguish between physical modes and noise modes on 1000 data sets from only 2 sensors. Stabilization diagram with subsequent clustering was used to find the physical modes. The experimental case was a wind tunnel test where a glass fiber–reinforced polymer plate (500 mm × 90 mm × 4 mm) was subjected to different flow conditions. It is reported that the four lowest modes were successfully identified from nearly every dataset, but no success rate was reported.

In Juul et al. 2018 [12], a short introduction is given to an automated time-domain polyreference OMA technique using a sliding filter on simulated data. Two different methods were used to find the physical modes in the sliding filter stabilization diagram, and it was concluded that the so-called Shortest Path Algorithm (SPA) had the highest success rate. No success rates were reported.

24.2 Software Solution

In an OMA based SHM solution, priorities are on other things than when we are doing OMA on a limited amount of data, where we have to get maximum information out of the limited data so we spend time on minimizing both random and bias errors.

In the SHM solution, we have enormous amounts of data, so that reducing random errors might not be essential, and bias errors are not that important either, because we are not so concerned about hitting the right frequency but more concerned about changes over time.

Further, man power must be reduced to a minimum, otherwise we will remain in the unlucky situation that we have been until now, where only a microscopic part of the total amount of monitoring data is being used.

What is really important is robustness, so for each and every data set that arrives for identification, the probability of failure to detect the natural frequency of any mode is minimal. This means that all algorithms must be robust to a degree that has not been seen before, because if there has been a storm, it would be unacceptable that nearly all identifications of data sets during the storm failed due to the unexpected environmental conditions.

Furthermore, let us say that we do SHM for earth quake damages, then it would be unacceptable that, because the power supply failed to work, the server that had the software installed also lost power and failed to work during the earth quake. If we want a system that always works, we have to install the solution in the Cloud. This is the safest place for both data and software.

That might be a challenge for some users that they have to send their data up in the Cloud – somewhere outside of their well-protected territory. This problem can only be solved by securing a strong nondisclosure policy about all user data.

Let us in the following section try to explain how the Flamenco software has been planned to deal with the above-mentioned challenges.

24.2.1 Typical OMA

Let us illustrate how the so-called poly reference technique has been planned for implementation in both time domain and frequency domain. For more information, see Brincker and Ventura [2].

Using an AR model based identification approach first step is to find the AR matrices in the homogenous free decay part of an ARMA model

$$\mathbf{y}(n) - \mathbf{A}_1\mathbf{y}(n-1) - \mathbf{A}_2\mathbf{y}(n-2) - \cdots - \mathbf{A}_{na}\mathbf{y}(n-\mathrm{na}) = 0 \tag{24.1}$$

given the free decay $\mathbf{y}(n)$ in discrete time with np number of samples. To estimate the AR matrices we form a block Hankel matrix with block rows

$$\mathbf{H}_1 = \begin{bmatrix} \mathbf{y}(1) & \mathbf{y}(2) & \cdots & \mathbf{y}(\mathrm{np}-\mathrm{na}) \\ \mathbf{y}(2) & \mathbf{y}(3) & & \mathbf{y}(\mathrm{np}-(\mathrm{na}-1)) \\ \vdots & \vdots & \ddots & \vdots \\ \mathbf{y}(\mathrm{na}) & \mathbf{y}(\mathrm{na}+1) & & \mathbf{y}(\mathrm{np}-1) \end{bmatrix} \tag{24.2}$$

and one block Hankel matrix with only a single block row

$$\mathbf{H}_2 = \begin{bmatrix} \mathbf{y}(\mathrm{na}+1) & \mathbf{y}(\mathrm{na}+2) & \cdots & \mathbf{y}(\mathrm{np}) \end{bmatrix} \tag{24.3}$$

Eq. (24.1) can then for all the possible values of be formulated as

$$\mathbf{A}\mathbf{H}_1 = \mathbf{H}_2 \tag{24.4}$$

where $\mathbf{A}$ is a side-by-side collection of the AR matrices, and the solution is then found by regression

$$\hat{\mathbf{A}} = \mathbf{H}_2\mathbf{H}_1^{+} \tag{24.5}$$

where $\mathbf{H}_1^{+}$ is the pseudo inverse of $\mathbf{H}_1$.

In time domain, we can exclude the initial conditions and only deal with the free response after the structure has been excited like we are doing in a free response formulation like Eq. (24.1). In the frequency domain, every point depends on the whole time domain, so going to the frequency domain we have somehow to include the impulse that created the free decay in the time domain. Thus, we have to add a right-hand side to Eq. (24.1). Using the Z-transform and adding the simplest possible right hand side to Eq. (24.2), we end up with the following equation:

$$\left(\mathbf{I}-\sum_{n=1}^{\mathrm{na}}\mathbf{A}_n e^{-inw(k)}\right)\mathbf{Y}\left(f(k)\right)=\mathbf{Y}_0 \tag{24.6}$$

Where $\mathbf{Y}_0$ is a constant matrix added to represent the right-hand side of Eq. (24.1), $w(k)$ is the dimensionless frequency from zero to π, and $\mathbf{Y}(f(k))$ is the frequency domain free decay where $f(k)$ goes from DC to Nyquist or defines a smaller band. It is a normal practice to use the so-called half spectral density as a free decay in the frequency domain, so imagining this, we can rewrite Eq. (24.6) by using an alternative definition of the AR matrices, and we obtain exactly the same equation like Eq. (24.4).

If the response has nc number of channels, thus the response vector is nc × 1, then the problem is over determined as long as np – na > na × nc, however since there is always some noise present, the procedure will only work satisfactory if the problem is well over determined, thus we must require that np – na ≫ na × nc.

For both the time and the frequency domain formulations, the modal parameters are found by forming the well-known companion matrix and the modal model has in this case eigenvalues corresponding to modes. The number of modes to be determined can be adjusted by adjusting the frequency band.

24.2.2 Condensation and Expansion

The smallest AR model one can use is based on one single AR matrix. This provides us with nc/2 modes, which might be useful in many cases. However, if a large channel count is being used, we might end up with too many noise modes that might cause troubles in finding the physical modes. In such a case, we might reduce the channel count. For this purpose, condensation can be used.

If our random response $\mathbf{y}(t)$ has the covariance matrix $\mathbf{C}$, then we perform the SVD that for the symmetric and real matrix has the form

$$\mathbf{C}=\mathbf{USU}^{\mathrm{T}} \tag{24.7}$$

And we then simply take the most principal vectors by reducing the number of columns in the matrix $\mathbf{U}$ to obtain to $\mathbf{U}_{\mathrm{r}}$ so that the condensed responses are, see Olsen et al. [13].

$$\mathbf{z}(t)=\mathbf{U}_{\mathrm{r}}^{\mathrm{T}}\mathbf{y}(t) \tag{24.8}$$

If on the other hand we have very low channel counts, then we can of course increase the number of AR matrices in the model, but we can also add in more channels to expand the number of measurements. This can be done by stacking the random response $\mathbf{y}(t)$ with its differentiated or integrated signals or stacking the sampled signal of one or more time-shifted responses.

As mentioned above, the most important is to assure robustness. Thus, the aim of condensation and expansion (of channels and model order) is to find the optimum number of modes in the model so that the number of noise modes optimize both accuracy and robustness.

24.2.3 Modal Participation

Normally we would be happy to obtain the classical modal parameters like mode shapes, natural frequencies, and damping ratios. However, if we want to judge what noise modes are and what physical modes are, it is useful to obtain the modal participation vector. It is also useful to have the modal participation vector for plotting how well our modal model fits the empirical spectral densities.

In Brincker et al. [14], it is shown that if the random response has the covariance matrix **C**, and the real valued mode shape matrix is **B**, then the real valued modal participation matrix **Γ** can be estimated as

$$\hat{\mathbf{\Gamma}} = \frac{1}{4\pi}\mathbf{C}\mathbf{B}^{+\mathrm{T}} \tag{24.9}$$

where $\mathbf{B}^{+T}$ is the transpose of the pseudo inverse of the mode shape matrix. The length of each modal participation vector defines a scalar measure of the modal participation for each mode.

24.2.4 Sensor Fault Detection

In a real measurement system, sensors will sooner or later fail to work as assumed. So, without sensor fault detection, we do not have a chance to make OMA based SHM work reliably. Here we are lucky to be able to make use of the most central equation in dynamics, the equation that defines the modal coordinates

$$\mathbf{y}(t) = \mathbf{B}\mathbf{q}(t) \tag{24.10}$$

The idea is now to estimate the modal coordinates from the measured responses

$$\hat{\mathbf{q}}(t) = \mathbf{B}^{+}\mathbf{y}(t) \tag{24.11}$$

to form the synthesized response

$$\hat{\mathbf{y}}(t) = \mathbf{B}\hat{\mathbf{q}}(t) \tag{24.12}$$

If we have a failing sensor, we will see a large deviation between the measured and synthesized signal for that sensor, so that the faulty sensor can be excluded from the OMA.

24.2.5 Operating Conditions

Operating conditions like temperature, power production for a wind turbine, or traffic for a bridge have a major influence on the modal parameters. In order to see if the structure has changed, we need to remove the main part of this influence.

We could of course measure the temperature, measure the power production of the wind turbine, or the traffic on the bridge and try to establish the model for how the natural frequencies depend on the environmental conditions.

But we might not have this information available, or even though we have it available, it might be difficult to use, simply because a temperature reading is very dependent upon where we measure it. Again, luckily enough, we have tools available to deal with this without any information about the environment. We will use the idea of the OMA once again.

Now we will consider a vector $\mathbf{u}(t)$ of natural frequencies as a function of time. In a certain time interval T, we will have a mean value $\mathbf{u}_0$ that is considered to represent the physics and a noise contribution $\mathbf{e}(t)$ from the changes of the environment that we like to model. We then need to model the zero-mean signal

$$\mathbf{e}(t) = \mathbf{u}(t) - \mathbf{u}_0 \tag{24.13}$$

as a random response just like doing any other OMA. We need to follow good practice once again, like looking for a low number of modes in a limited frequency band to obtain the solution like in Eq. (24.12) where we model the signal, and we can then can obtain the synthesized random response where the influence from environmental conditions is removed:

$$\hat{\mathbf{u}}(t) = \mathbf{B}\hat{\mathbf{q}}(t) - \mathbf{B}_{\mathrm{e}}\hat{\mathbf{q}}_{\mathrm{e}}(t) + \mathbf{u}_0 \tag{24.14}$$

Here $\mathbf{B}_{\mathrm{e}}$ and $\mathbf{q}_{\mathrm{e}}(t)$ are mode shapes and modal coordinates of the signal $\mathbf{e}(t)$.

24.3 SHM Case

The considered case is data from a monitoring campaign with a wind loaded wooden mast with a steel topside. The vibration response is acquired by a measurement system with four 3D sensors placed at strategic locations on the topside so that the rigid body motions of the top side can be determined. In the present case, we are demonstrating auto OMA on the first 500 data sets of the first week of the monitoring campaign where no damage was introduced.

The case is further described in Lydakis et al. 2023, [15], where a longer period is considered and damage is introduced and identified from the change of the modal parameters.

The mast structure is shown to the left of Fig. 24.1, and the five natural frequencies over time are shown to the right of Fig. 24.1. In Fig. 24.2 is shown the typical validation plot for the user to check that the identified modes fit the empirical spectral density. In this case, we can see that the fits are good. The identified modal parameters for the same plot are given in Table 24.1.

In all 500 data sets, all five modes were all identified well. The success rate was 100%.

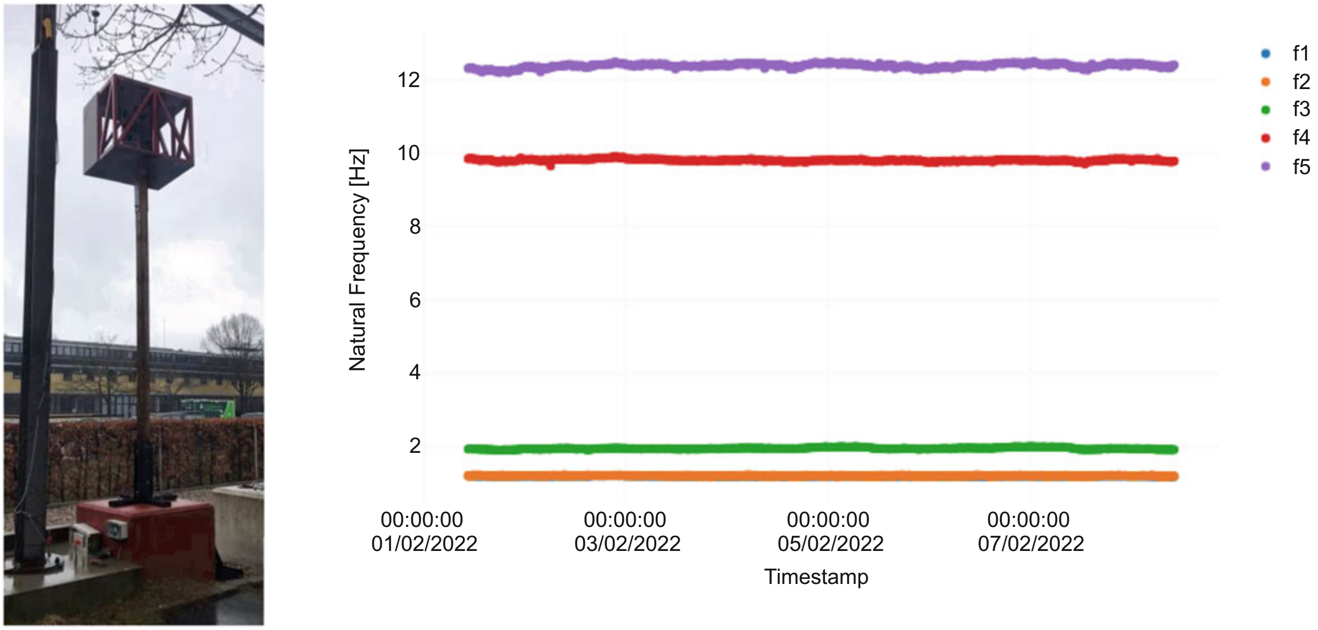

Fig. 24.1 Left: The wind-loaded mast. Right: Results of auto OMA of the first 500 data sets showing first 5 natural frequencies of the structure. Bottom line includes the first two closely spaced modes. No damage introduced

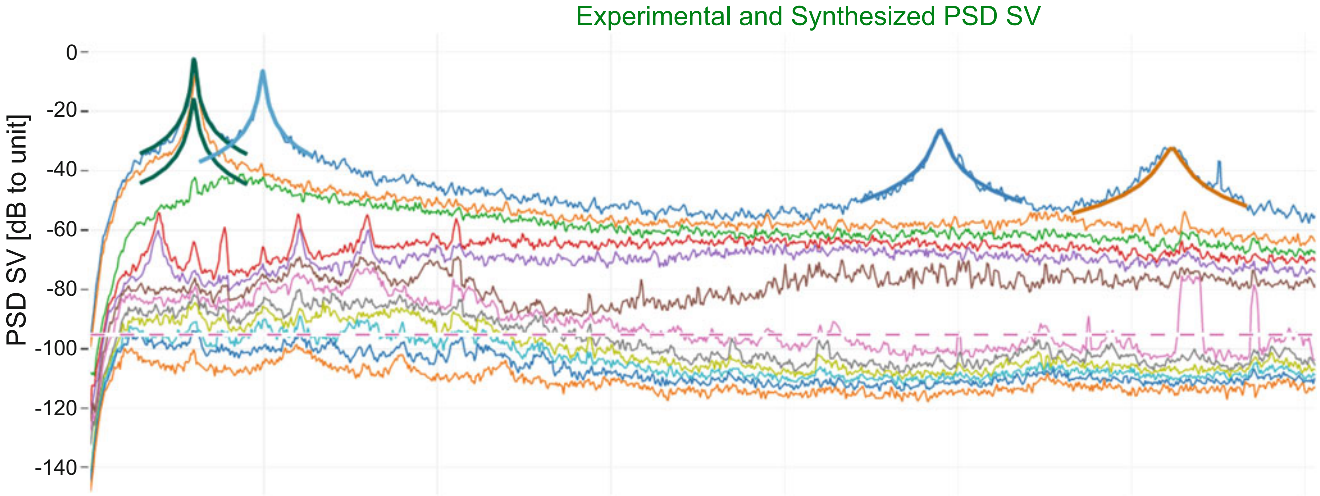

Fig. 24.2 The users validation plot for a random middle data set of the 500 uploaded data sets. Frequency band from DC to 14 Hz

Table 24.1 Modal parameters for the 5 modes of random data set shown in Fig. 24.2

Mode	Natural frequency [Hz]	Damping ratio [%]	Type of mode
1	1.188	1.829	First bending FA
2	1.194	1.098	First bending SS
3	1.984	1.013	Torsion
4	9.794	0.606	Second bending FA
5	12.465	0,744	Second bending SS

Mode shapes much like a wind turbine because the dominating mass is at the top, and the direction with the dominant moment of inertia defines fore-aft (FA) movement, and the perpendicular side-side (SS) movement

24.4 Conclusion

A cloud-based SHM software solution has been presented, and the basic principles of implementing well-known identification technique into the software solution have been explained.

The solution has been tested on 500 data sets from a monitoring campaign with a wind-loaded wooden mast, and in all 500 data sets, all 5 modes were successfully identified.

Acknowledgement The authors appreciate the investment by Innovation Fund Denmark (IFD) in the project InnoSHM: Innovative Structural Health Monitoring and Risk Informed Structural Integrity Management.

References

1. Rainieri, C., Fabbrocino, G.: Operational Modal Analysis of Civil Engineering Structures. Springer (2014)
2. Brincker and Ventura: Introduction to Operational Modal Analysis. John Wiley & Sons, Ltd (2015)
3. IOMAC proceedings, 2005 to 2019: https://www.iomac.info/
4. Farrar, C.R., Worden, K.: An introduction to structural health monitoring. Phil. Trans. R. Soc. A. **365**, published 15 February 2007, 303 (2007)
5. Brincker, R., Andersen, P., Jacobsen, N.J.: Automated frequency domain decomposition for operational modal analysis. In: Conference Proceedings of IMAC-XXIV (2007)
6. Rainieri, C., Fabbrocino, G., Cosenza, E.: Fully automated OMA: an opportunity for smart SHM systems. In: Proceedings of the IMAC-XXVII, February 9–12, 2009, Orlando, Florida, USA (2009)
7. Tcherniak, D., Chauhan, S., Basurko, J., Salgado, O., Carcangiu, C.E., Rossetti, M.: Application of OMA to operational wind turbine. In: Proccedings of IOMAC'11 – 4th International Operational Modal Analysis Conference (2011)
8. Reynders, E., Houbrechts, J., De Roeck, G.: Fully automated (operational) modal analysis. Mech. Syst. Signal Process. **29**, 228–250 (2012)
9. Devriendt, C., Magalhaes, F., Weijtjens, W., De Sitter, G., Cunha, A., Guillaume, P.: Structural health monitoring of offshore wind turbines using automated operational modal analysis. Struct. Health Monit. **13**(6), 644–659 (2014)
10. Di Lorenzo, E., Manzato, S., Peeters, B., Marulo, F.: Modal parameter estimation for operational wind turbines. In: Proceedings of 7th European Workshop on Structural Health Monitoring, July 8–11, 2014. La Cité, Nantes, France (2014)
11. Neu, E., Janser, F., Khatibi, A.A., Orifici, A.C.: Fully automated operational modal analysis using multi-stage clustering. Mech. Syst. Signal Process. **84**, 308–323 (2017)
12. Juul, M., Olsen, P., Balling, O., Amador, S., Brincker, R.: Comparison of two (geometric) algorithms for auto OMA. In: Proceedings of the 36th IMAC conference (2018)
13. Juul, P.O.M., Brincker, R.: Condensation of the correlation functions in modal testing. MSSP. **118**, 377–387 (2019)
14. Brincker, R., Amador, S.D.R., Juul, M., Lopez-Aenelle, M.: Modal participation estimated from the response correlation matrix. Shock. Vib. **2019**, 9347075 (2019)
15. Lydakis, E., Amador, S.D.R., Koss, H., Brincker, R.: Vibration-based damage detection of a monopile specimen using output-only environmental models. In: Proceedings of the IMAC Conference 2023, Austin, Texas, Feb (2023)

Chapter 25
Practical Application of Active Mass Damping for Floors in a Commercial Building

Paul Reynolds, Michael J. Wesolowsky, Emma J. Hudson, Aleksandar Pavic, and Sami Rahman

Abstract There is a clear need for floor vibration control technology that is high performance, easy to install, commercially competitive, sustainable and reliable over the long term. This technology can be used to retrofit existing structures that are exhibiting vibration problems and also to increase the efficiency and reduce embodied carbon of new-build floor structures. Active mass damping of floors in office, commercial, healthcare, laboratories, residential and other types of buildings has been the subject of a great deal of academic research over the years. This work has focused on the development of control algorithms and performance studies using off-the-shelf accelerometers, control systems and shakers. The newly developed CALM®FLOOR active mass damper (AMD) system integrates all of these components into a single unit, which is easy to install and is able to deliver active control forces to massively enhance damping in floor structures.

This chapter describes a program of analysis and testing applied to a building floor structure subject to pedestrian excitation both without and with the presence of the AMD system in operation. It was found that the AMDs were capable of significantly reducing floor responses by around 75% for this fairly typical composite steel-concrete floor system supporting an open-plan office. Deployment of AMDs throughout the building would clearly have the potential to significantly improve the performance of the whole of the environment, with very minimal disruption given the very small size of the AMDs compared with other more significant interventions such as tuned mass dampers or structural modifications.

Keywords Active Vibration Control · Active Mass Damper · Pedestrian Excitation · Vibration Serviceability

25.1 Introduction

Over the last 60 years, the vibration serviceability of building floors has been an increasing challenge for structural engineers and building owners and operators. Designing for satisfactory vibration performance increases required section sizes (and hence material costs and embodied carbon), and when vibration problems are experienced in service, the options for remediation are extremely limited and are usually very expensive, disruptive and often ineffective. An additional challenge is refurbishment and change of use of existing buildings, where changes in layouts of nonstructural elements or required vibration response criteria (e.g. change of use from offices to labs) may require additional vibration control measures to provide satisfactory vibration performance for the intended new occupants.

There is a clear need for floor vibration control technology that is high performance, easy to install, commercially competitive, sustainable and reliable over the long term. This technology can be used to retrofit existing structures that are exhibiting vibration problems and also to increase the efficiency of new-build floor structures. The latter objective in particular is of great importance as we seek to decarbonize the built environment and achieve ambitions for carbon Net Zero by 2050.

With this in mind, active mass damping of floors in office, commercial, healthcare, laboratories, residential and other types of buildings has been the subject of a great deal of academic research over the years. This work has focused on the development of control algorithms and performance studies using off-the-shelf accelerometers, control systems and shakers.

P. Reynolds (✉) · E. J. Hudson · A. Pavic
FSD Active Limited, Colyton, UK
e-mail: p.reynolds@fsdactive.com

M. J. Wesolowsky · S. Rahman
Thornton Tomasetti, Mississauga, ON, Canada

H. Y. Noh et al. (eds.), *Dynamics of Civil Structures, Volume 2*, Conference Proceedings of the Society for Experimental Mechanics Series, https://doi.org/10.1007/978-3-031-36663-5_25

The newly-developed CALM®FLOOR active mass damper (AMD) system integrates all of these components into a single unit which is easy to install and is able to deliver active control forces to massively enhance damping in floor structures.

This chapter describes a program of analysis and full-scale testing applied to a building floor structure subject to pedestrian excitation both without and with the presence of the AMD system in operation. The performance of the system is evaluated, and conclusions are drawn with respect to the effectiveness of the technology for this building and its implications for future design and sustainability of new buildings.

25.2 Implementation of Active Mass Dampers

Active mass dampers are mechatronics devices that in principle contain the following components:

- A sensor to detect structural motion
- A controller to process the motion signal to generate a force signal
- An actuator to generate a control force
- An inertial mass to which the force is applied, typically suspended using a spring suspension system for vertically generated control forces

In a great deal of prior academic research work, active mass damping has been implemented using shaker systems (such as the APS Dynamics Electro-SEIS shakers) coupled with off-the-shelf accelerometers and control systems implemented on easily-programmable hardware, e.g. by National Instruments. Whilst these systems have delivered excellent performance and have served as excellent proof-of-concept demonstrators of AMD technology, they are not deployable as a commercially viable and practically implementable permanent solution for vibration control in buildings.

CALM®FLOOR has been developed by FSD Active Limited in the UK as the world's first mass produced AMD solution that is intended to be permanently deployed for vibration control of vertical floor vibrations in buildings. It is a self-contained enclosure of dimensions 630 × 386 × 125 mm with total mass of only 67 kg (Fig. 25.1). Its development has been particularly focused on office and commercial buildings, but it is also suitable for many other buildings, such as concourses of assembly buildings, healthcare settings, general purpose laboratories and residential.

25.3 Analysis of Test Structure

The test structure is a multi-story office building in the Northeastern United States. It is of steel frame construction with composite steel-concrete slabs. The areas of the floor slabs most sensitive to pedestrian excitation have a square column grid of 30′ × 30′ (9.14 × 9.14 m) with primary beams W18x86 supporting secondary beams W16x26 at 10′ (3.05 m) centres, in turn supporting a 6″ (152 mm) deep composite slab. The structure supports an open-plan office area with few partitions primarily in the core areas (around light green areas in the floor plan shown in Fig. 25.2).

Fig. 25.1 CALM®FLOOR active mass damper

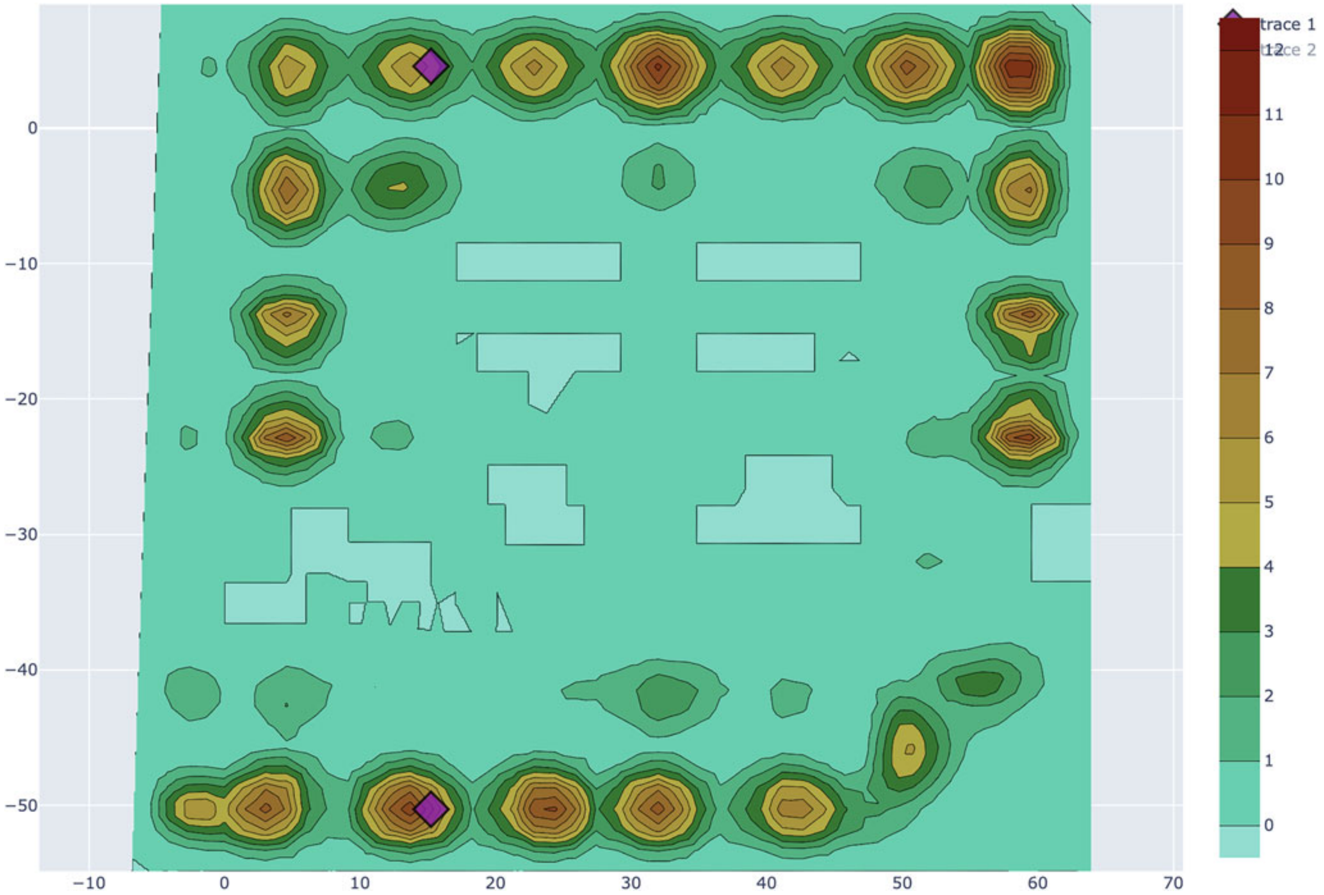

Fig. 25.2 Contour plot of predicted responses due to pedestrian excitation calculated using low frequency approach

A finite element model of one of the floors in the building was created using the SAP2000 FE software. The first 50 modes of vibration (covering frequency range from 5.5 to 9.5 Hz) were extracted and exported in ASCII format into in-house Python code. This is proprietary software written by FSD Active Limited for calculation of response to pedestrian excitation using the low frequency floor model given in the Concrete Centre CCIP-016 vibration design guidance [1] with an assumption of 2% modal damping for all modes. The contour plot of responses from this analysis is shown in Fig. 25.2. Note that the responses are given in terms of R factors, where an R factor of 1 corresponds with a baseline acceleration of 0.005 m/s^2 RMS. W_b frequency weighting [2] was used as appropriate for office environments.

Two locations on the structure had been chosen for experimental implementation of active vibration control, which were typical locations at which excessive vibrations had been observed by the building occupants. These points are indicated by the purple diamonds in Fig. 25.2 – hereafter referred to as TP01 (top) and TP02 (bottom). Note that these were slightly offset from the maximum points in these respective bays due to the need to avoid obstructions due to the building fit-out.

The response simulations were re-run using the FSD Active Limited Python code, this time including the predicted effects of the two AMDs at TP01 and TP02. The results are shown in Fig. 25.3.

The impact of the AMDs is clear in the bays in which they have been simulated. The responses have been reduced from values significantly exceeding the allowable limit of $RF = 4$ to values significantly below the allowable limit of $RF = 4$. It is also interesting to note that the beneficial effects of the AMDs are quite limited to the bays in which they are installed. This is a common feature that is due to the localization of modes of vibration that are being controlled by the AMDs.

Figure 25.4 shows the predicted uncontrolled and controlled frequency response functions (FRFs) at the two points at which the AMDs were assumed to be installed. The significant reduction in FRF amplitudes is clearly evidence from these FRF plots.

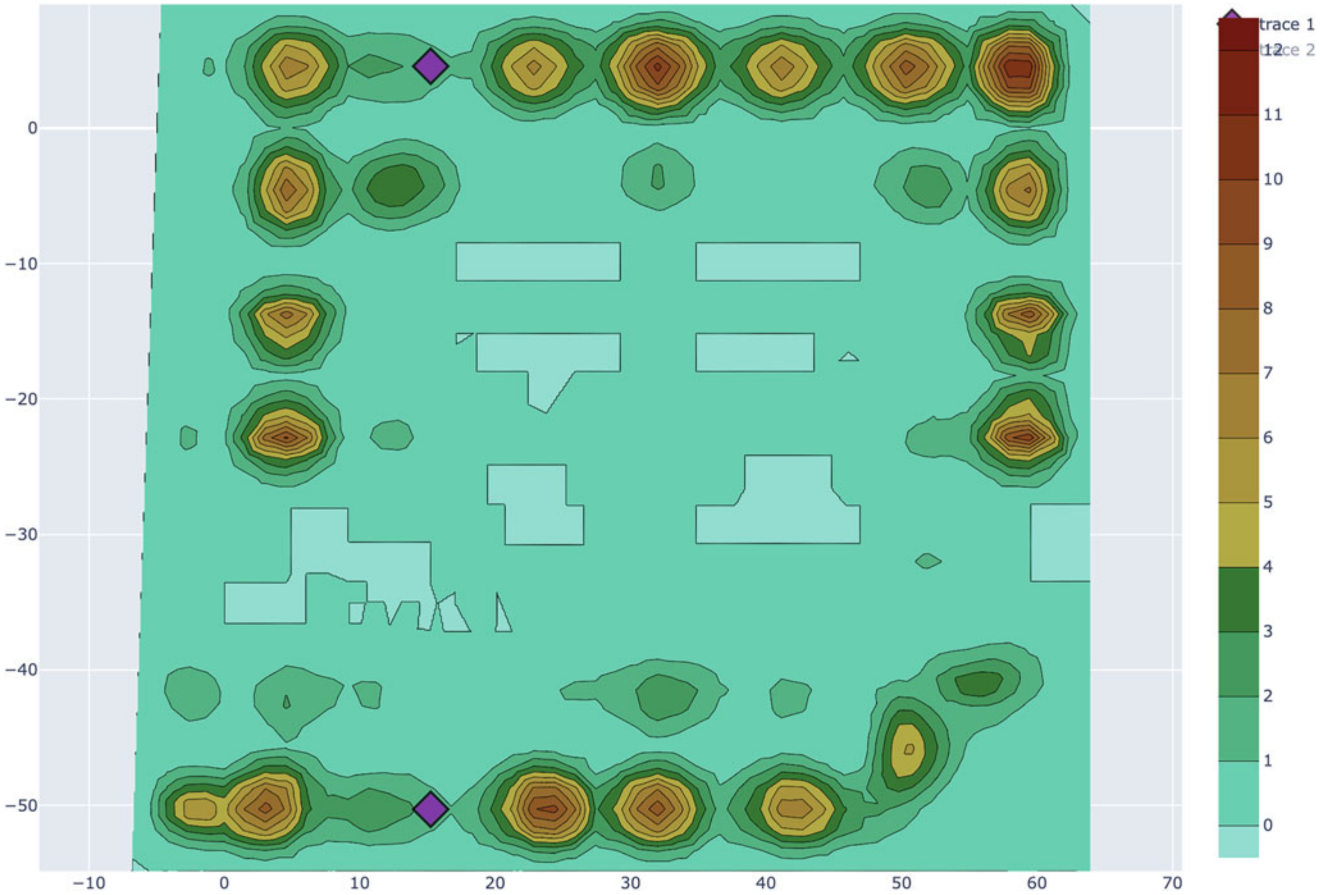

Fig. 25.3 Contour plot of predicted responses due to pedestrian excitation calculated using low frequency approach including AMDs

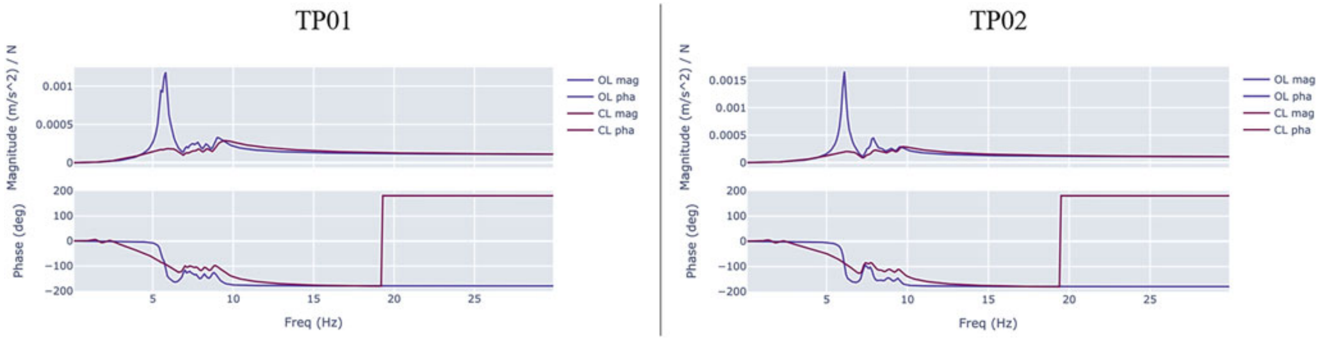

Fig. 25.4 Accelerance FRF plots without control (blue) and with control (purple)

25.4 Experimental Work

The experimental work was carried out in October 2022. Two CALM®FLOOR units were used in order to carry out both frequency response function measurements and to assess vibration responses under pedestrian excitation both with and without active vibration control.

First, FRF measurements were carried out by using one AMD unit as a shaker providing a broadband random excitation signal from 2 to 100 Hz. This force was measured using a PCB 333B50 accelerometer on the inertial mass, providing an indirect measurement of the force provided to the structure. The response of the floor structure was measured using a PCB 626B03 accelerometer mounted on the floor. Both signals were measured and processed using a Data Physics Quattro digital spectrum analyzer and laptop. An image of the AMDs and accelerometer on the floor at TP01 is shown in Fig. 25.5, with

Fig. 25.5 CALM®FLOOR AMD units and accelerometer used for FRF measurement at TP01

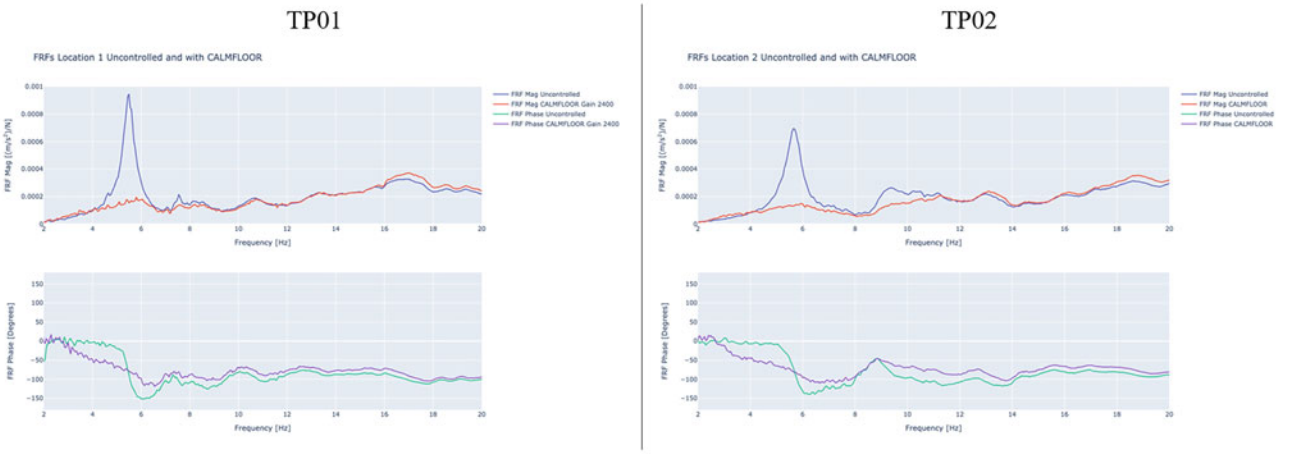

Fig. 25.6 Experimental FRFs without and with control from CALM®FLOOR AMD

a similar setup being used at TP02. The AMDs were mounted directly onto the top concrete surface of the composite slab via bespoke-designed feet with three points of contact and were simply held in place by gravity. A number of raised access flooring panels were removed to accommodate this.

Figure 25.6 shows the FRF results measured at TP01 and TP02. They closely resemble their simulated counterparts as shown in Fig. 25.4.

Pedestrian response measurements were carried out by having three pedestrians walk along walking paths adjacent to TP01 and TP02 at a pacing rate chosen to excite the dominant floor mode at each location with the third harmonic of the relevant ground reaction force. Each pedestrian walked along the walking path four times (forwards-return-forwards-return). After all three pedestrians completed their walking, the AMD was switched on and all three pedestrians repeated their nominally identical walking activity.

Acceleration response data were measured using the PCB 626B03 accelerometers and Data Physics Quattro spectrum analyzer and were subsequently processed using bespoke in-house developed Python code. The results from these measurements are shown in Figs. 25.7 and 25.8 for TP01 and TP02, respectively. The upper plot in each figure shows the W_b frequency weighted acceleration time history. The lower plot shows the 1s RMS trend which has been normalized by a baseline acceleration of 0.005 m/s^2 to give an RF trend. The generally accepted limit of RF = 4 for office buildings is indicated by the green horizontal line.

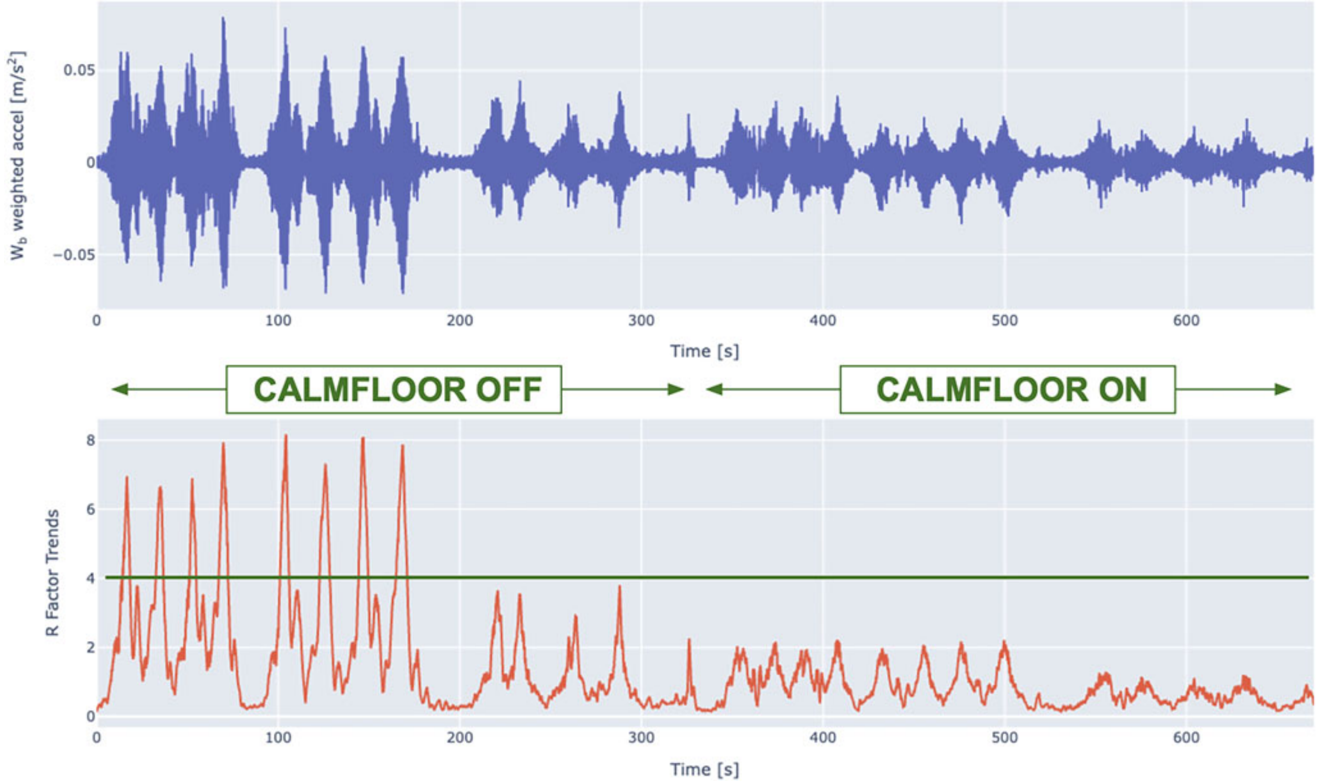

Fig. 25.7 Pedestrian response measurements at TP01 – walking at 110 steps per minute

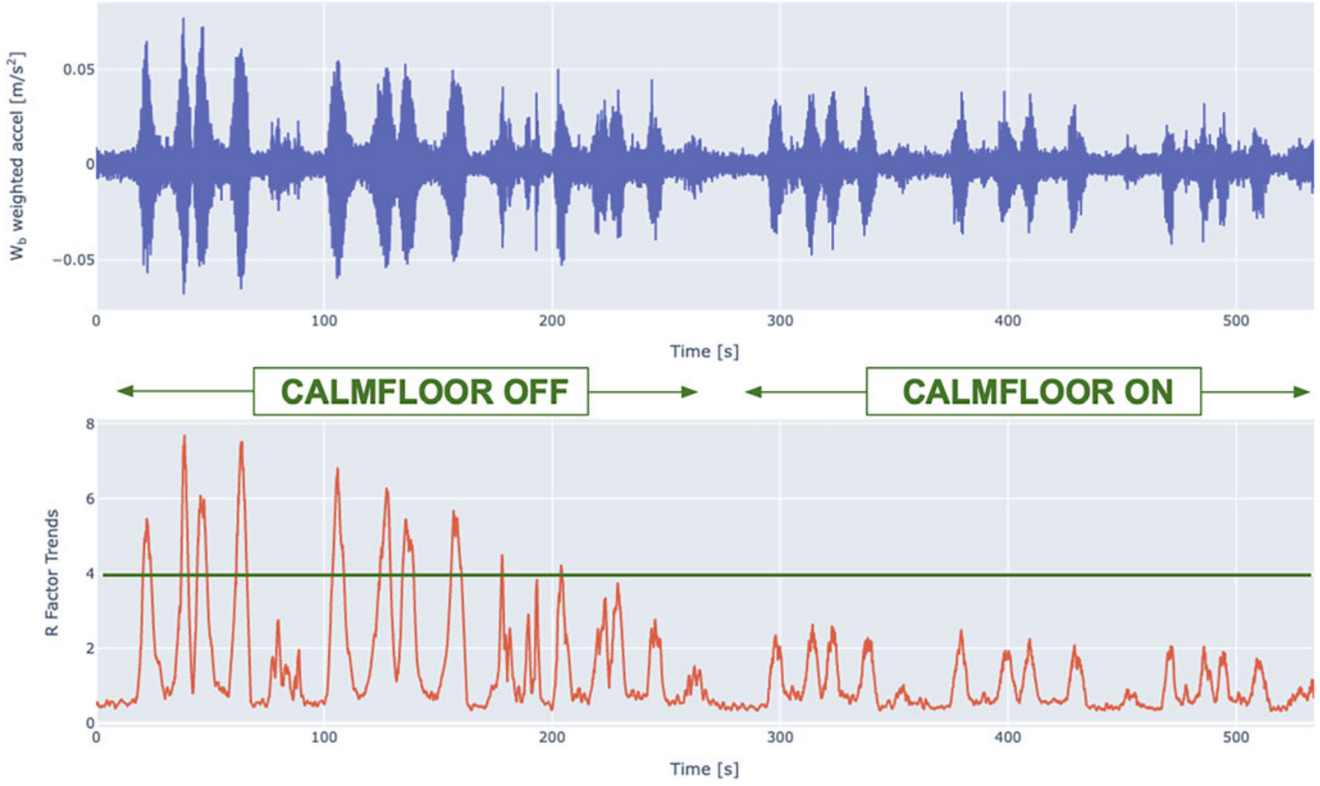

Fig. 25.8 Pedestrian response measurements at TP02 – walking at 112 steps per minute

It can be seen that the first two pedestrians consistently produced R factor responses at both locations in the region of RF = 7 to RF = 8 when the AMD was not in operation. The third pedestrian did not produce quite so high responses, typically in the region up to RF = 4. Such variability is quite common considering the natural variability of human excitation.

When the CALM®FLOOR units were switched on, the responses produced by all three pedestrians were significantly reduced, typically down to the region of RF = 2. Subjective assessment of the performance of the floor structure by observers who were sitting on the floor whilst the measurements were being made, was that the floor felt far improved when the AMDs were in operation and that there was noticeably less movement of computer screens on desks that were supported by the floor.

25.5 Conclusions

This chapter has presented analytical and experimental study of the effectiveness of AMD technology applied to a steel-concrete composite floor system in a multi-story office building.

CALM®FLOOR AMDs were installed at two locations in the building, corresponding with locations reported by the building users as being typical of relatively lively points on the structure.

The simulation studies showed excellent potential performance of the AMDs, with significant reductions in FRF amplitudes and response reductions from well over the allowable limit of RF = 4 to significantly below RF = 4. The reductions were localized to the bays in which the AMDs were installed.

The experimentally measured FRFs had very similar characteristics to those predicted from simulations and also demonstrated similar reductions in magnitude as those from analysis. Pedestrian response measurements also showed excellent reductions in magnitudes, with up to 75% reductions in responses from around RF = 8 to around RF = 2 being observed.

Deployment of AMDs throughout the building would clearly have the potential to significantly improve the performance of the whole of the environment, with very minimal disruption given the very small size of the AMDs compared with other more significant interventions such as tuned mass dampers or structural modifications.

References

1. Willford, M., Young, P.: A Design Guide for Footfall Induced Vibration of Structures – CCIP-016. The Concrete Centre, Surrey (2006)
2. BSI: BS6841:1987 Guide to Measurement and Evaluation of Human Exposure to Whole-Body Mechanical Vibration and Repeated Shock. British Standards Institution (BSI), London, UK (1987)

Chapter 26
Experimental Investigation of a Variable Inertia Rotational Mechanism

Anika T. Sarkar, Carter A. Manson, and Nicholas E. Wierschem

Abstract Recent advances in passive structural control systems have included devices that exploit nonlinear behavior. The explicit inclusion of nonlinearities allows these passive devices to be designed to have behavior and performance that varies with different load types and amplitudes. The variable inertial rotational mechanism (VIRM) is an example of a nonlinear passive control device and consists of a mechanism that converts linear motion into rotational motion and an attached flywheel that includes masses that can move radially inside the flywheel. The radial motion of the VIRM flywheel masses results in the flywheel moment of inertia continuously varying during the response of the device. Despite a potentially small physical mass, the VIRM can provide to a system large added mass effects that can vary greatly depending on the flywheel moment of inertia. The large and variable mass effects provided by the VIRM can significantly shift the natural frequency and reduce the response amplitude of an underlying structure. While the VIRM has been investigated numerically by a number of authors, the experimental study of these devices has been limited. Moreover, most of the studies have considered semi-active or active variable inertia flywheels. The investigation of passive VIRMs are rare. This study aims to address these gaps in knowledge and experimentally investigate the response modification and pseudo resonance frequency changes of an underlying structure produced by the VIRM considering different loading conditions. For this experimental investigation, a VIRM was designed and fabricated that utilizes a lead screw and a flywheel that contains masses connected to springs that can move radially in the flywheel. This VIRM was then attached to a single-degree-of-freedom structure and subjected to different excitation types using a shake table. With data from these experimental tests, the overall fundamental frequency and the response of the system was evaluated using the experimentally estimated system transfer functions. The results of this study show that the inclusion of the VIRM reduces the response amplitude and significantly shifts the pseudo resonance frequency of the underlying structure and that these shifts in pseudo resonance frequency are highly dependent on the loading amplitude.

Keywords Variable Inertia · Nonlinear · Shake Table Testing · Natural Frequency Shifts

26.1 Introduction

Inerters and inerter-based devices have been substantially studied during the last decade to overcome the limitations of conventional vibration mitigation strategies in civil engineering structures. The inerter is a linear two-terminal rotational inertial mechanism that generates a force proportional to the relative acceleration across its terminals. The inerter, like other rotational inertial mechanisms, converts translational motion into the rotational motion of a flywheel and, in the process of doing so, can create significant added mass effects.

Researchers have previously studied linear inerter-based devices that provide constant effective mass effects in structures. However, as the research advances, attention is paid to nonlinear rotational inertia mechanisms. The rotational inertia produced by these nonlinear devices can vary depending on the device's response. One example of a nonlinear device is the variable inertia rotational mechanism (VIRM), which has a moment of inertia that can change based on the rotational velocity of its flywheel.

In the VIRM, multiple symmetrically spaced masses are mounted inside the device's flywheel using springs and guides, allowing radial mass movement within the guides. The vibration of the structure drives the ball-screw mechanism connecting

---

A. T. Sarkar · C. A. Manson · N. E. Wierschem (✉)
Department of Civil and Environmental Engineering, Tickle College of Engineering, University of Tennessee, Knoxville, TN, USA
e-mail: nwiersch@utk.edu

H. Y. Noh et al. (eds.), *Dynamics of Civil Structures, Volume 2*, Conference Proceedings of the Society for Experimental Mechanics Series, https://doi.org/10.1007/978-3-031-36663-5_26

the VIRM, which increases the absolute rotational velocity of the flywheel. When the flywheel rotational velocity decreases, the masses move back toward their original position. Note that the flywheel rotational velocity is proportional to the relative velocity of the structure between the connection points of the VIRM.

Several researchers have recently investigated VIRMs to reduce the response amplitude of dynamic systems. In most studies, active and semi-active control mechanisms were used, and numerical simulations were primarily used for analysis [1–3]. The experimental investigation on passive VIRMs is also rare [4, 5]. Furthermore, limited research has been done to assess the effect of variable inertia on the natural frequency changes of the underlying structure.

This work experimentally explores the natural frequency changes of a base-excited single degree-of-freedom (SDOF) structure with a VIRM. The SDOF structure is also tested, where the VIRM is replaced with a fixed inertia rotational mechanism (FIRM) and no flywheel to compare frequency changes and responses. Sine sweep excitations with various intensities are applied to it to understand the effect of the dynamically changing inertia of the VIRM on the structure's natural frequency change and response reduction.

This chapter is structured as follows. The next section introduces the equations of motion (EOM) of the VIRM combined with a SDOF structure. The Experimental Setup section describes the designed test apparatus, instrumentation, and the loading considered. The Experimental Results section describes the test results, and the last section discusses the conclusions.

26.2 EOM of VIRM Attached to a SDOF System

In this study, a SDOF system attached to a VIRM is subjected to a ground motion $\left(\ddot{u}_{\mathrm{g}}\right)$, as presented in Fig. 26.1. The VIRM is placed between the rigid mass (m_{s}) and the base and is parallel to the spring with stiffness (k_{s}) and a damper with viscous damping coefficient (c_{s}). The masses (m_{sd}) inside the flywheel are constrained such that they can move radially in the flywheel when the absolute rotational velocity $\left(\dot{\theta}\right)$ of the flywheel increases. The radial motion causes a restoring force (F_{bsd}) in the nonlinear springs, and the viscous dampers (c_{sd}) dissipate energy in the system. For the FIRM case, the masses are fixed at the initial position, x_0 in the flywheel frame and the nonlinear springs, and the viscous dampers inside the flywheel are removed.

The equations of motion of the VIRM combined system with primary system displacement relative to the ground, u_s, and slider radial displacement, x, and the primary system with the FIRM are expressed in Eqs. (26.1) and (26.2), respectively,

$$\begin{aligned} &m_{\mathrm{s}}\ddot{u}_{\mathrm{s}} + J\alpha^2\left(\ddot{u}_{\mathrm{s}} - \ddot{u}_{\mathrm{g}}\right) + 2nm_{\mathrm{sd}}x\dot{x}\alpha^2\dot{u}_{\mathrm{s}} + nm_{\mathrm{sd}}x^2\alpha^2\left(\ddot{u}_{\mathrm{s}} - \ddot{u}_{\mathrm{g}}\right) + c_{\mathrm{s}}\dot{u}_{\mathrm{s}} + k_{\mathrm{s}}u_{\mathrm{s}} = -m_{\mathrm{s}}\ddot{u}_{\mathrm{g}} \\ &m_{\mathrm{sd}}\ddot{x} - m_{\mathrm{sd}}x\alpha^2\dot{u}_{\mathrm{s}}^2 + F_{\mathrm{bsd}}(x) + c_{\mathrm{sd}}\dot{x} = 0 \end{aligned} \tag{26.1}$$

$$m_{\mathrm{s}}\ddot{u}_{\mathrm{s}} + J\alpha^2\left(\ddot{u}_{\mathrm{s}} - \ddot{u}_{\mathrm{g}}\right) + nm_{\mathrm{sd}}{x_0}^2\alpha^2\left(\ddot{u}_{\mathrm{s}} - \ddot{u}_{\mathrm{g}}\right) + c_{\mathrm{s}}\dot{u} + k_{\mathrm{s}}u = -m_{\mathrm{s}}\ddot{u}_{\mathrm{g}} \tag{26.2}$$

where J is the static rotational inertia and n is the number of slider masses in the VIRM/FIRM.

As seen from Eq. (26.2), the EOM of the system with a FIRM is linear; thus, the dynamic properties of this system should be constant. In contrast, Eq. (26.1) shows a nonlinear EOM for the system with a VIRM. The nonlinear components include a coefficient on an acceleration term that grows with increased slider radial position, as well as a complicated nonlinear term combining slider velocity, slider position, and primary system velocity. The nonlinear components of the VIRM EOM should result in dynamic properties that vary with the amplitude of the system response. Previous numerical studies have shown this

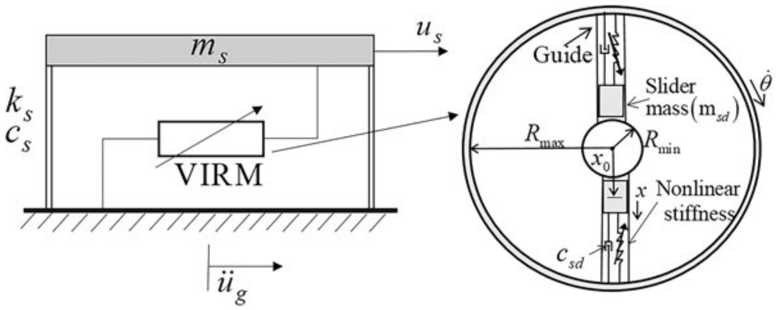

Fig. 26.1 Schematic diagram of a SDOF primary system with VIRM (left), VIRM flywheel with two masses at their initial location (right)

system capable of apparent softening behavior [6]. The next sections of this work will experimentally investigate potential softening and vibration mitigation that results from the VIRM.

26.3 Experimental Setup

A modified die set test apparatus with four springs is used to create a simplified SDOF environment. The reason behind using the die set is that die sets are precisely aligned and designed to primarily move along one axis, which helps to avoid any alignment issues arising from the oscillating system. The schematic configuration of the experimental setup is presented in Fig. 26.2. This figure shows that springs connect the top and bottom mass plates. To align the two mass plates precisely, guide pins with guide bushings are used. Moreover, two adapter plates connect the VIRM flywheel to the primary structure with a lead-screw mechanism. Although the motion of the die set is configured to be limited to the vertical direction, some horizontal and torsional movement can be present in the structure.

The primary mass, $m_s = 17.92$ kg, is an aluminum plate with dimensions of 18inch × 18inch × 1.25inch. The spring stiffness was selected such that the natural frequency of the structure without any rotational inertial components (lead screw or flywheel) is 5.3 Hz.

The modified die set was attached to the shake table, and eight PCB piezoelectric accelerometers were secured to both the die set and the shake table and were used to collect data with a sampling rate of 10,240 Hz. One accelerometer was placed on the shake table measuring the input ground acceleration, and one was on the base plate of the structure measuring the transferred excitation. The rest of the accelerometers were placed on the top mass plate to ensure measurements in the x, y, and z directions. The die set was vertically excited by the shake table using forward sine-sweep signals in acceleration control along a frequency range of 1–8 Hz for 90 seconds. Various percentages (10%, 20%, 30%, 40%, and 50%) of a baseline 0.1 g acceleration amplitude sweep were applied to evaluate potential nonlinear structural behavior at different levels of excitation.

These tests were repeated with the VIRM replaced with a FIRM and with the experimental setup where the flywheel was removed, and the lead screw remains connected to the die set, referred to as the no flywheel case. The decision to include the lead screw in the no flywheel case was made considering that much of the intrinsic damping in the setup comes from the passage of the lead screw through the lead screw nut. Thus, with the lead screw present in all cases, the differences resulting from each of the cases considered should primarily be due to the different mass effects provided by the devices. Note that in the no flywheel case, there will still be some added mass effects due to the rotational inertia of the lead screw, bearing, and shaft collars. Also, note that tests with the no flywheel case were not performed past 30% scaling of the loading due to the resulting large response amplitude in this case.

When the slider masses in the VIRM do not move in the flywheel, the rotational inertia provided by the VIRM is the same as the static rotational inertia of the FIRM. However, when the masses move inside the guide, the total flywheel moment of inertia consists of this static rotational inertia and a contribution from the changing radial position of the slider masses. Note that, the slider masses do not move beyond half the radius distance of the flywheel for the loads considered. In this study, inertance of the FIRM at initial position is 23 kg, and the inertance of the VIRM when the masses are at the halfway position along the radius of the flywheel is 40 kg.

In this study, one accelerometer measuring in the vertical direction is focused on in the analysis to present the influence of different excitation amplitudes on the overall natural frequency change and the structure's response. To investigate the

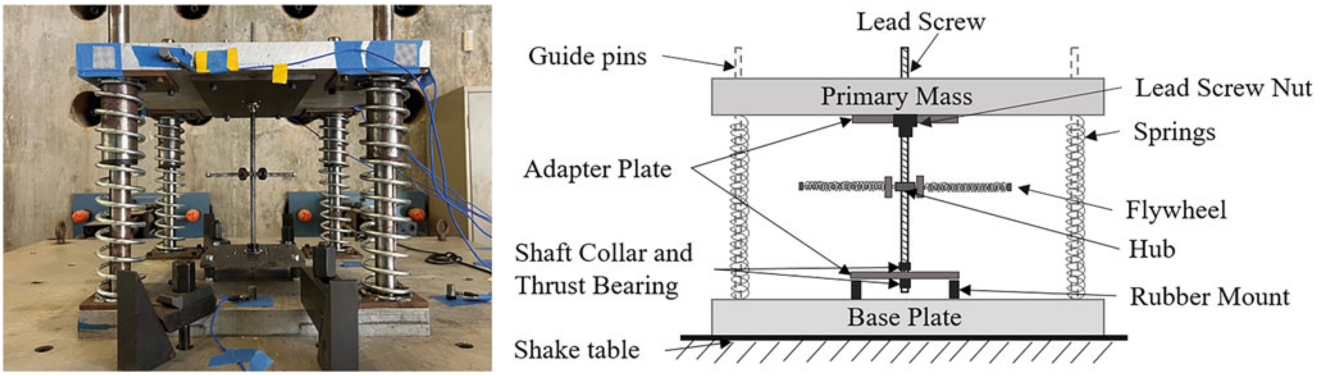

Fig. 26.2 Experimental test setup (left), schematic configuration of the structure with the VIRM (right)

response in the frequency domain, this accelerometer reading and the measured ground acceleration are utilized to produce estimated frequency response functions (FRFs). The estimated FRFs are produced using Welch's average periodogram method which depends on factors such as, signal duration, window, number of points [7]. Each test was done five times to allow for averaging, a Hanning window was applied to each test data set to reduce spectral leakage, 0% overlap ratio was used, and the same number of points as one test is utilized in this estimation.

26.4 Experimental Results

This section presents the experimental results for different amplitude swept sine loadings applied to the experimental setup described in the previous section. As discussed above, the results presented primarily consist of time histories of the vertical primary mass acceleration and FRFs showing the relationship between the applied vertical table acceleration and the vertical primary mass acceleration.

Figure 26.3 shows the vertical acceleration time history response of the primary structure for three different ground acceleration amplitudes. It can be observed that the acceleration response increases for higher excitation levels, and the peak response of the structure with no flywheel rises most rapidly as the excitation amplitude increases. The structure with no flywheel has the highest acceleration response for all excitation amplitudes compared to the structures with flywheels. The figure also shows that the structure with the FIRM has a lower response than the structure with no flywheel, but that the VIRM structure has the lowest acceleration response for all the excitation amplitudes considered.

The average root mean square (RMS) acceleration responses for the primary structure with no flywheel, FIRM, and VIRM are presented in Table 26.1. These average RMS values were computed by averaging the resulting RMS values of the absolute acceleration from all of the individual tests with the same device and loading properties. The RMS value is significant as it provides a measure corresponding to the overall amplitude of the acceleration responses. Table 26.1 shows that the average RMS acceleration for all the structural configurations increase as higher scaling of load is applied to it. As no tests were done above 30% scaling of the baseline loading for the no flywheel case, there are no numerical values reported for those cases. The primary structure with no flywheel has the highest average RMS acceleration response compared to the FIRM and VIRM cases for all the loading amplitudes considered. It is observed that at low load amplitude, the average RMS of the FIRM and VIRM are the same. For instance, at 10% and 20% load amplitude, the structure has the same average RMS acceleration of 0.08 g and 0.13 g with the FIRM and the VIRM, respectively. The similar response behavior of the FIRM and VIRM could be because at low load amplitudes, the masses in the VIRM stay close to the initial position. Hence, the VIRM behaves very similarly to the FIRM. As higher load amplitudes are applied to the structure, the average RMS acceleration is lower for the VIRM cases compared to the FIRM cases.

FRFs relating the absolute acceleration response and ground acceleration input corresponding to the structure with no flywheel and the structure with the VIRM and the FIRM are shown in Fig. 26.4. Although the tests were done for a sine sweep with frequency range between 1 and 8 Hz, it can be observed in this figure that there is noise at low and high

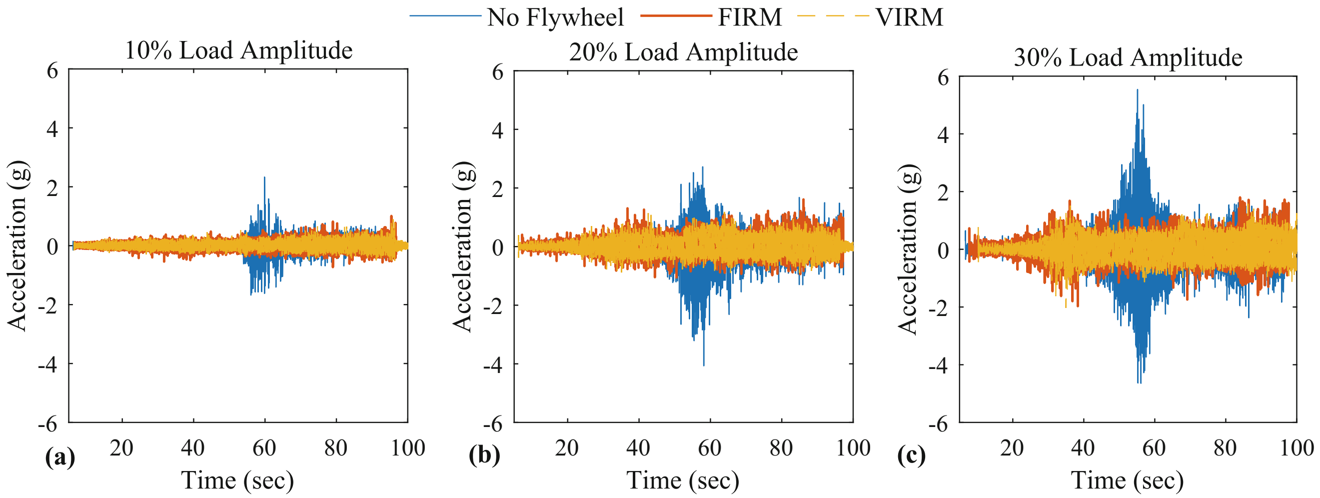

Fig. 26.3 Acceleration time history of the primary structure for sine-sweep excitations with three different amplitudes: (**a**) 10% (**b**) 20% (**c**) 30%

Table 26.1 Average RMS acceleration of the primary structure with no flywheel, VIRM and FIRM configurations at different loading amplitudes

		Average RMS acceleration (g)				
Load amplitude		10%	20%	30%	40%	50%
Primary structure configurations	No flywheel	0.11	0.27	0.39	–	–
	FIRM	0.08	0.13	0.18	0.21	0.24
	VIRM	0.08	0.13	0.17	0.19	0.23

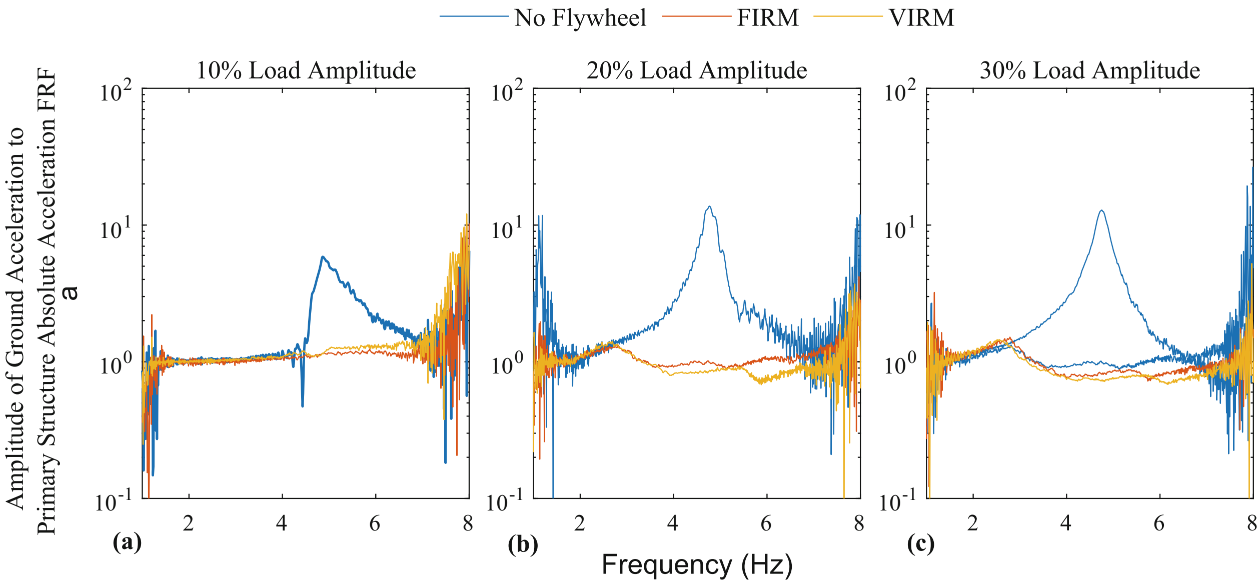

Fig. 26.4 FRFs of the primary structure at different ground acceleration amplitudes: (**a**) 10% (**b**) 20% (**c**) 30%

frequencies for all the load amplitudes, likely resulting from the windowing used, which impacts results at the beginning and end of the sweep more significantly. The pseudo resonance frequencies can be identified from this figure as the frequencies the peak values occur at, ignoring noise. This figure shows that the pseudo resonance frequency of the structure with no flywheel reduces when it is connected to a FIRM or VIRM flywheel and is the lowest when it is attached to the VIRM flywheel. For instance, at a 20% excitation amplitude, the pseudo resonance frequency of the structure with no flywheel, FIRM, or VIRM are 4.78 Hz, 2.81 Hz, and 2.69 Hz, respectively. Figure 26.4 also shows the frequency response behavior of the primary structure for different loading amplitudes. At 10% load amplitude, the structure with the VIRM or the FIRM has a very similar and low response amplitude across the frequency ranges. It is observed that the pseudo resonance frequency of the structure with no flywheel reduces with increasing excitation amplitude. The pseudo resonance frequency of the structure with no flywheel changes from 4.86 to 4.75 Hz given an increase in load scaling from 10% to 30%. This behavior is not anticipated for the structure with no flywheel but it could be because at high levels of loading, the lead screw connection in the flywheel can provide some nonlinearities to the structure. It is also observed that the pseudo resonance frequency of the VIRM structure reduces at higher levels of loading. For example, when the excitation amplitude increases from 20% to 30%, the pseudo resonance frequency with the VIRM reduces from 2.69 to 2.56 Hz.

The influence of the loading amplitude on the response modification and pseudo resonance frequency shifts is investigated with Fig. 26.5 and Table 26.2. Table 26.2 lists the peak FRF values at the pseudo resonance frequencies. This table shows that these peak values increase as higher load amplitude is applied for all the structure configurations. It also shows that the structure with no flywheel has the highest peak amplitude, as seen in Fig. 26.4. Moreover, there is no beneficial reduction in the peak structure response amplitude when the FIRM is replaced with a VIRM at low load amplitudes, but there are some benefits at higher load amplitudes.

Figure 26.5 shows FRFs relating the absolute acceleration response and ground acceleration input over a wider range of input amplitudes, 20–50%, and for the VIRM and FIRM only. Figure 26.5a shows that the FIRM's pseudo resonance frequencies are very similar for all the load conditions; for example, 2.81 Hz at 20% load amplitude and 2.76 Hz at 50% load amplitude. The slight difference in frequencies could be because of noise in the FRF estimate. Figure 26.5b shows that the pseudo resonance frequency reduces when the FIRM flywheel is replaced with a VIRM flywheel for all the loading amplitudes. The shift in natural frequency is because the slider mass movement in the VIRM flywheel increases the added

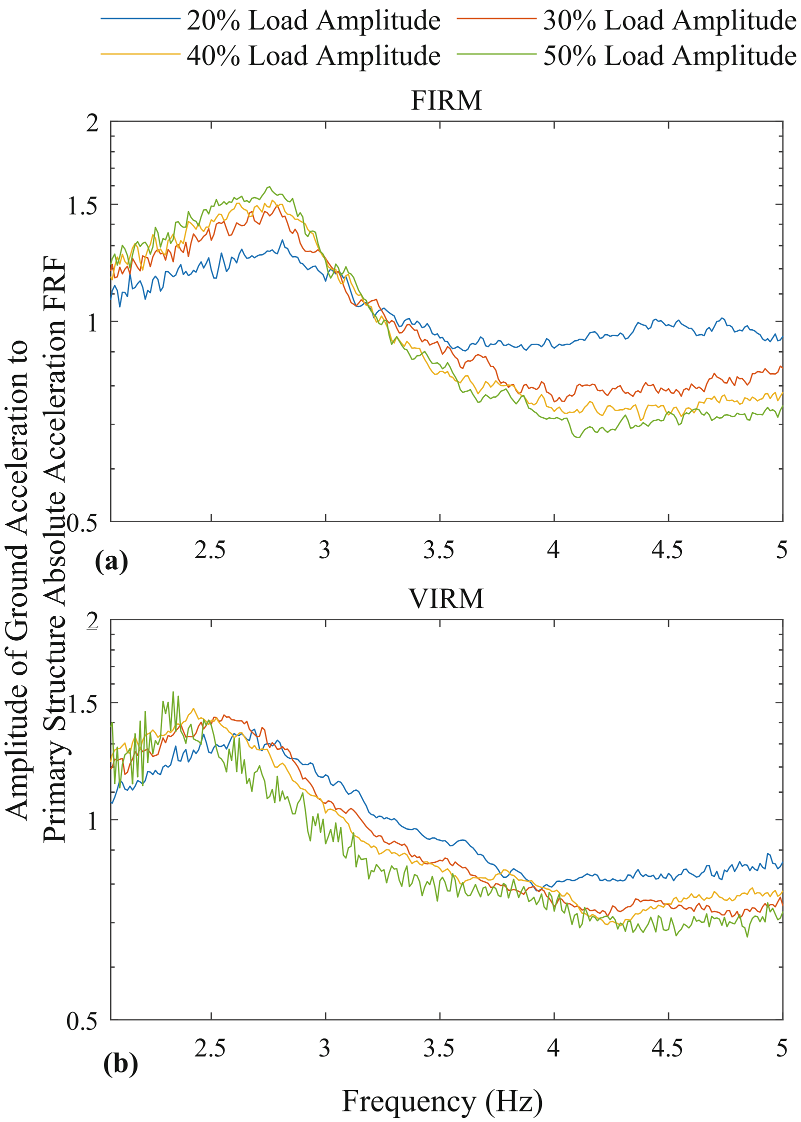

Fig. 26.5 FRFs of the primary structure with the VIRM and the FIRM for 20%, 30%, 40%, and 50% excitation amplitudes

Table 26.2 Peak FRF (ground acceleration to absolute acceleration) value at pseudo resonance frequency for primary structure with no flywheel, VIRM, and FIRM configurations at different loading amplitudes

		Peak FRF value at pseudo resonance frequency				
Load amplitude		10%	20%	30%	40%	50%
Primary structure configurations	No flywheel	5.81	13.77	12.87	–	–
	FIRM	1.15	1.33	1.50	1.52	1.60
	VIRM	1.23	1.37	1.44	1.47	1.56

effective mass in the structure. Hence, the additional effective mass reduces the natural frequency of the structure. This figure also shows that the peak FRF values increases and pseudo resonance frequency decreases as higher ground excitation is provided and large response results. For instance, the peak FRF amplitude increases from 1.37 to 1.56, and the pseudo resonance frequency reduces from 2.68 to 2.33 Hz for an increase in ground excitation amplitude from 20% to 50% in the structure with the VIRM. Note that this shift in pseudo resonance frequency with increased amplitude is much larger than seen for either the no flywheel or FIRM cases.

26.5 Conclusion

This chapter experimentally investigates the dynamic behavior of a VIRM in a SDOF structure. In this chapter, the structure is excited with a sine sweep ground motion. The results of this study show that the VIRM can notably reduce the pseudo-resonance frequency and response amplitude of the structure. The study also reveals that the variable rotational inertia can shift the pseudo resonance frequency with excitation amplitude. Overall, the chapter suggests that the VIRM can affect structure dynamics and response significantly, although further research regarding various excitations, such as seismic ground motion, is necessary.

Acknowledgements This research was sponsored by the National Science Foundation under Grant No. 1944513. The findings, opinions, recommendations, and conclusions in this chapter are those of the authors alone and do not necessarily reflect the views of others, including the sponsors.

References

1. Mahato, A.C., Ghoshal, S.K., Samantaray, A.K.: Influence of variable inertia flywheel and soft switching on a power hydraulic system. SN Appl. Sci. **1**(6), 605 (2019). https://doi.org/10.1007/s42452-019-0623-0
2. Dong, X., Xi, J., Chen, P., Li, W.: Magneto-rheological variable inertia flywheel. Smart Mater. Struct. **27**(11), 115015 (2018). https://doi.org/10.1088/1361-665X/aad42b
3. Kushwaha, P., Ghoshal, S.K., Dasgupta, K.: Dynamic analysis of a hydraulic motor drive with variable inertia flywheel. Proc. Inst. Mech. Eng. Pt. I: J. Syst. Contr. Eng. **234**(6), 734–747 (2020). https://doi.org/10.1177/0959651819875914
4. Xu, T., Liang, M., Li, C., Yang, S.: Design and analysis of a shock absorber with variable moment of inertia for passive vehicle suspensions. J. Sound Vib. **355**, 66–85 (2015). https://doi.org/10.1016/j.jsv.2015.05.035
5. Yang, S., Xu, T., Li, C., Liang, M., Baddour, N.: Design, modeling and testing of a two-terminal mass device with a variable inertia flywheel. J. Mech. Des. **138**(9), 095001 (2016). https://doi.org/10.1115/1.4034174
6. Wierschem, N.E.: Shift in natural frequencies of structures with a variable inertia rotational mechanism. Presented at the Engineering Mechanics Institute Conference 2022, Baltimore, MD, USA, May 02, 2022
7. MathWorks: Signal processing toolbox: user's guide (R2022a). https://www.mathworks.com/help/pdf_doc/signal/signal.pdf (2022). Accessed 15 Aug 2022

Chapter 27
Deep-Learning-Based Friction Modeling of Dry Interfaces for Structural Dampers

Daniel Coble, Liang Cao, Austin R. J. Downey, and James Ricles

Abstract Friction-based dampers have gained attention as a cost-effective way to provide structural control during natural hazards. However, the dry friction interfaces in these systems result in a highly nonlinear damping response during the reversal of damper travel, termed damper backlash. Moreover, the stick-slip phenomena intrinsic to the sliding response of dry friction interfaces make the accurate modeling of friction-based structural dampers challenging. Dynamic friction modeling for structural dampers currently relies on analytical models to approximate the damper's response at a current location given the damper's state and average out the complex system responses during travel reversal or stick-slip movement to obtain a model of the system's performance. In this chapter, we propose the use of a deep learning model to capture the temporal dynamics of the system that when combined with the LuGre friction model provides a physics-informed machine learning approach for inferring the damping force of a dry friction interface given the state of the model. Specifically, this chapter uses a long short-term memory model to infer the LuGre friction model's parameters. A methodology for parameter identification using truncated backpropagation through time is given, which allows for real-time updating. Model validation is performed using a 9 kip rotary friction damper designed for high damping performance and mechanical simplicity. The model is validated with data from real natural hazard events and used in a real-time hybrid simulation. The performance, reliability, and accuracy of the deep-learning-based friction model are discussed.

Keywords Friction modeling · Physics-informed machine learning · LuGre model · Structural control · Damper

27.1 Introduction

Damping systems such as viscous dampers and tuned mass dampers are commonly used to mitigate damage from earthquake and wind events [1]. Friction dampers have the potential to be implemented as cost-effective and mechanically reliable systems capable of producing large damping forces [2]. However, modeling the nonlinear dynamics of friction dampers is challenging. Such modeling is complicated by various nonlinear phenomena present in dry friction interfaces, such as hysteresis and the stick-slip phenomenon. Furthermore, due to the nature of their mechanical linkages, friction dampers exhibit a phenomenon termed backlash, where friction momentarily drops during reversal of travel.

Physics-based models describe simplified friction systems and have the ability to account for properties such as hysteresis and stick-slip phenomena [3]. However, there is concern that physics-based models cannot accurately represent the complexities of real systems. Physics models typically ignore the backlash effect or use state-based modeling schemes that can be difficult to implement and manage. Alternatively, data-driven models such as machine learning (ML) may capture system dynamics but lack the informed structure of a physics-based model. Of particular concern is: (1) the ability of the

---

D. Coble
Department of Mechanical Engineering, University of South Carolina, Columbia, SC, USA
e-mail: dncoble@email.sc.edu

L. Cao · J. Ricles
Department of Civil and Environmental Engineering, Lehigh University, Bethlehem, PA, USA
e-mail: lic418@lehigh.edu; jmr5@lehigh.edu

A. R. J. Downey (✉)
Department of Mechanical Engineering, University of South Carolina, Columbia, SC, USA

Department of Civil and Environmental Engineering, University of South Carolina, Columbia, SC, USA
e-mail: austindowney@sc.edu

H. Y. Noh et al. (eds.), *Dynamics of Civil Structures, Volume 2*, Conference Proceedings of the Society for Experimental Mechanics Series, https://doi.org/10.1007/978-3-031-36663-5_27

model to produce physically consistent results and (2) how models generalize to data dissimilar to the training set. In general, physics-informed machine learning uses ML techniques within the informed structure of a physics model, with the goal of more accurately representing physical systems while conforming to the two problems given above [4]. Relevant to this work, with parameter prediction, ML is used to produce intermediate parameter values that are used by the physics model.

In this chapter, a physics-informed deep learning approach is further developed to model nonlinear dynamics of the dry friction interface present in structural dampers [5]. The LuGre dry friction model [6] provides the structure for the physics-based modeling where the LuGre model's parameter that considers the rising rate of friction is augmented with a deep learning model trained on experimental time-series data to capture the backlash effect. Parameter estimation comes from a long short-term memory (LSTM) model, and a methodology for the indirect training of the LSTM model is presented. The characterization data come from a 9 kip rotary friction damper that displays the backlash effect [7]. The experimental dataset used in this chapter is made available through a public repository [8]. The contribution of this chapter is twofold: (1) a deep-learning-based friction modeling approach for dry interface modeling is presented and (2) the intermediate value calculation from the deep learning model is investigated to measurement of the estimated parameter before, during, and after the backlash region.

27.2 Background

The banded rotary friction device (BRFD), shown in Fig. 27.1, is a rotary friction damper in which the friction force is produced as an internal steel drum rotates against a static double wrap band. In a proposed implementation of the BRFD, linear displacement from interstory drift is transduced into angular displacement. During semi-active control, the electric actuators connected to either end of the band alter band tension to control the dominant damping force. Both ends of the band are connected to electric actuators. During semi-active control, the electric actuators alter band tension to alter the dominant damping force. Figure 27.2 shows the BRFD test setup at NHERI Lehigh Experimental Facility used to capture the experimental data used in this chapter where a hydraulic actuator produces the displacement profile. Characterization tests consisted of a sinusoidal displacement profile with a period varying between 1 and 20 seconds. The initial band tension was set to be constant, and the band actuators did not activate during the tests. Band tension is measured by load cells attached on either side of the band, and the damping force is measured by an internal load cell from the hydraulic actuator.

The BRFD benefits from a phenomenon known as the self-energizing, or positive servo effect. As the drum rotates, the grip pressure between the drum and band increases, consequently increasing the normal force on the friction interface. As the self-energizing effect is dependent on the direction of velocity, during reversal of travel, the effect depletes before being reactivated in the other direction. When the friction band is not energized in either direction, termed the backlash region, the

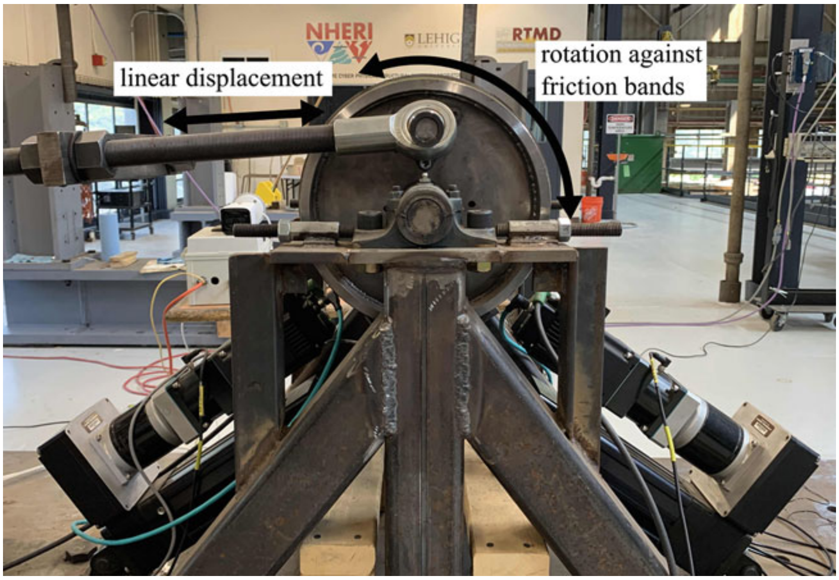

Fig. 27.1 The banded rotary friction device [7]

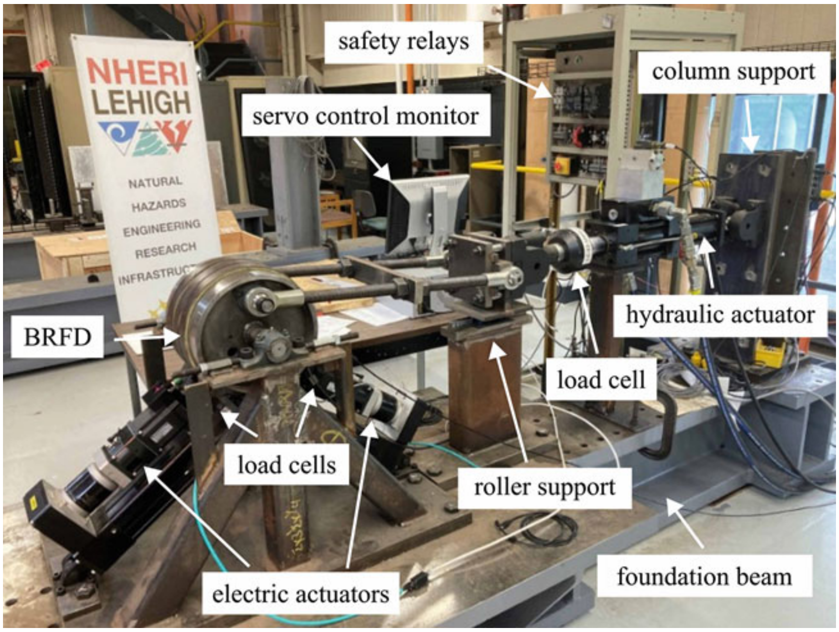

Fig. 27.2 BRFD test setup at NHERI Lehigh Experimental Facility [9] that was used to create the open-source experimental dataset [8] used in this chapter

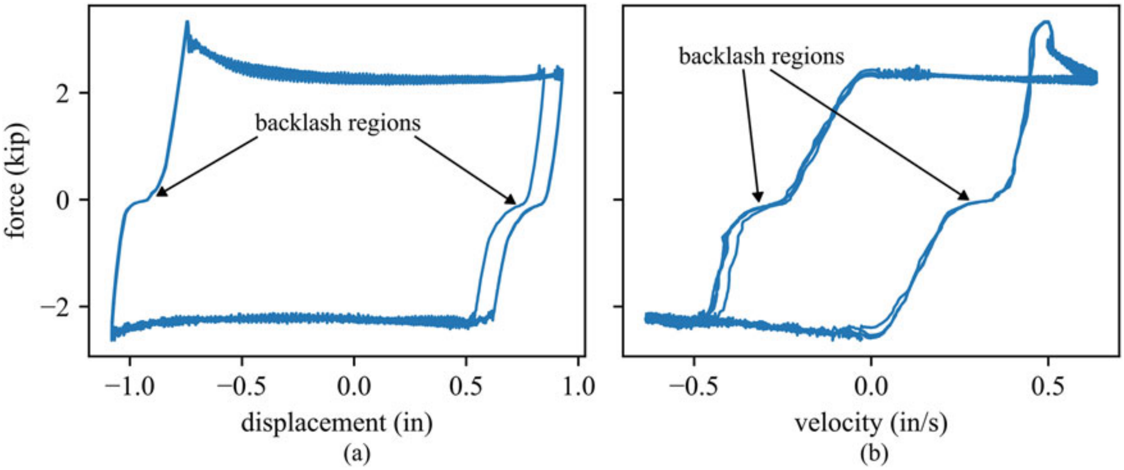

Fig. 27.3 Friction force produced by the BRFD plotted against: (**a**) displacement and (**b**) velocity with backlash regions labeled

force momentarily reduces to zero. The backlash effect can be seen in the S-shaped deflection in the hysteresis curve shown in Fig. 27.3b.

The LuGre dry friction model, shown in Eqs. 27.1–27.3, is a commonly used dry friction model inspired by representing energy dissipation as the deflection of bristles in contact between two surfaces in relative motion.

$$\dot{z} = v - \sigma_0 \frac{|v|}{g(v)} z \tag{27.1}$$

$$F = \sigma_0 z + \sigma_1 \dot{z} + \sigma_2 v \tag{27.2}$$

$$g(v) = F_{\mathrm{c}} + (F_{\mathrm{s}} - F_{\mathrm{c}})\, e^{|\frac{v}{v_S}|^2} \tag{27.3}$$

with the state parameter z and velocity input v. Equation 27.1 is generally unsolvable, but a solution can be found that is locally true (i.e., $v \approx$ const) that motivates this analysis:

$$z(t+\varepsilon) = \frac{g(v)v}{\sigma_0|v|} + \left(z(t) - \frac{g(v)v}{\sigma_0|v|}\right) e^{-\sigma_0 \frac{|v|}{g(v)} \varepsilon}. \tag{27.4}$$

Notably, σ_0 appears as the rate of change variable in the exponential decay function from $z(t)$ to the steady-state value $z_{ss} = \frac{g(v)v}{\sigma_0|v|}$. Yet σ_0 also appears in the expression for the steady-state value. The extreme values of z_{ss} are given when $g(v)$ is at its maximum and $v/|v| = \mathrm{sgn}(v)$ is either positive or negative. As z is always approaching z_{ss}, these values also serve as extreme values for z. This is called the boundedness property and is given as

$$|z| \leq \frac{F_\mathrm{s}}{\sigma_0}. \tag{27.5}$$

The backlash effect could be captured by augmenting the LuGre model to allow a time-dependent rate of change variable. However, in the form above, we see that σ_0 both controls the rate of change as well as the steady-state value z_{ss}. When σ_0 is constant, this is inconsequential since z is multiplied by σ_0 to produce the steady-state force $F_{ss} = g(v)\mathrm{sgn}(v) + \sigma_2 v$. Such a derivation does not apply to a time-dependent σ_0. In particular, there is potential for a “slewing” effect, whereby force will change dramatically even though z changes only minorly, as σ_0 drives changes in F. In the most extreme case, F may become discontinuous or violate the boundedness property. A solution to this is to modify the model by defining the state variable as $y = \sigma_0 z$. The model given in Eqs. 27.6–27.8 is equivalent to the standard LuGre model when σ_0 is constant but does not produce a slewing effect when σ_0 is variable.

$$\dot{y} = \sigma_0 \left(v - \frac{|v|}{g(v)} y\right) \tag{27.6}$$

$$F = y + \frac{\sigma_1}{\sigma_0}\dot{y} + \sigma_2 v \tag{27.7}$$

$$g(v) = F_\mathrm{c} + (F_\mathrm{s} - F_\mathrm{c})\, e^{|\frac{v}{v_S}|^2}, \tag{27.8}$$

and boundedness is represented as

$$|y| \leq F_\mathrm{s}. \tag{27.9}$$

Recurrent neural networks (RNNs) are a type of neural network designed to process time-sequence data. A generic RNN contains weight matrices for the current timestep input and a recurrent weight matrix, which connects to a state vector from the previous timestep. Such a connection allows RNNs to produce inference based on all previous timesteps. Long short-term memory (LSTM) is a type of RNN designed to solve the vanishing gradient problem. LSTMs have become the most common form of RNN and have shown success in areas such as speech recognition and machine translation. Equations 27.10–27.15 show the calculations of an LSTM for one timestep.

$$f_t = \sigma\left(W_f x_t + U_f h_{t-1} + b_f\right) \tag{27.10}$$

$$i_t = \sigma\left(W_i x_t + U_i h_{t-1} + b_i\right) \tag{27.11}$$

$$o_t = \sigma\left(W_o x_t + U_o h_{t-1} + b_o\right) \tag{27.12}$$

$$\tilde{c}_t = \tanh\left(W_c x_t + U_c h_{t-1} + b_c\right) \tag{27.13}$$

$$c_t = f_t \circ c_{t-1} + i_t \circ \tilde{c}_t \tag{27.14}$$

$$h_t = o_t \circ \tanh\left(c_t\right), \tag{27.15}$$

Fig. 27.4 Dataflow through the model in: (**a**) forward inference and (**b**) training through backpropagation

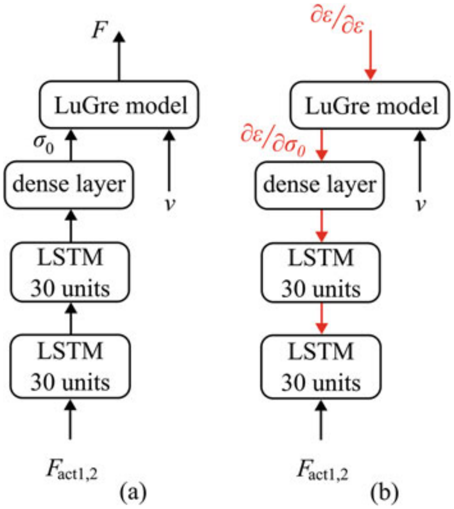

where σ is the sigmoid activation function. W and U are the current timestep and recurrent connection weight matrices, respectively.

In a direct training approach, the parameter in question would be measured along with the training inputs to train the physics-ML model. However, direct measurement of the dynamic parameters of the LuGre model, including σ_0, is impossible. Therefore, training the LSTM model prediction of σ_0 proceeded using an indirect approach. In the indirect method, the error gradient from the model prediction is backpropagated through the LuGre model to produce an error gradient for the prediction of σ_0. Backpropagation is then used to train the LSTM prediction. Figure 27.4 shows forward inference and backpropagation in the model. The error gradient with respect to σ_0 is an intermediate value to the error gradient with respect to the model weights. Multiple model configurations were tested with the best results given by the model shown in Fig. 27.4, containing two stacked LSTM cells with 30 units and a dense layer. Band tension is used as the input to a LSTM model.

27.3 Analysis

Figure 27.5a shows a force–velocity plot of a characterization test fitted to a LuGre model with a least-squares approach. The model does not capture the dynamics of the backlash region, and model's rising rate is roughly an average of those in the three distinct regions before, during, and after backlash region. Figure 27.5b shows the same test plotted with the physics-ML model. The model fits the distinct regions of reversal travel and produces a smaller error. Table 27.1 shows error in normalized root mean squared error (NRMSE) and signal-to-noise ratio (SNR) for the LuGre comparison models and the physics-ML model. Formulas for NRMSE and SNR are given in equations. For each dataset, a separate LuGre comparison model was fitted. In contrast, the same physics-ML model is used across all datasets. Overall NRMSE error was reduced 53% from the LuGre model to the physics-ML model.

$$\text{NRMSE} = \frac{\sqrt{\sum_{t=1}^{T}(y_t - \hat{y}_t)^2}}{T(y_{\max} - y_{\min})} \tag{27.16}$$

$$\text{SNR}_{\text{dB}} = 10 \times \log\left(\frac{\sum_{t=1}^{T} y_t^2}{\sum_{t=1}^{T}\left(y_t - \hat{y}_t\right)^2}\right). \tag{27.17}$$

Intermediate value calculation produces an indirect measurement of the estimated parameter. In the case of friction damping, this is useful as direct measurement of σ_0 is not possible. Figure 27.6 shows a time-series plot of the LSTM model's prediction of σ_0 during reversal of travel. The model produces three distinct values during the three phase of the backlash cycle. In the initial drop, the bands are de-energized, and the average σ_0 value is 23 kip/in. During the backlash region, σ_0 averages 3 kip/in. After the band is re-energized in the opposite direction, σ_0 prediction rises to 48 kip/in.

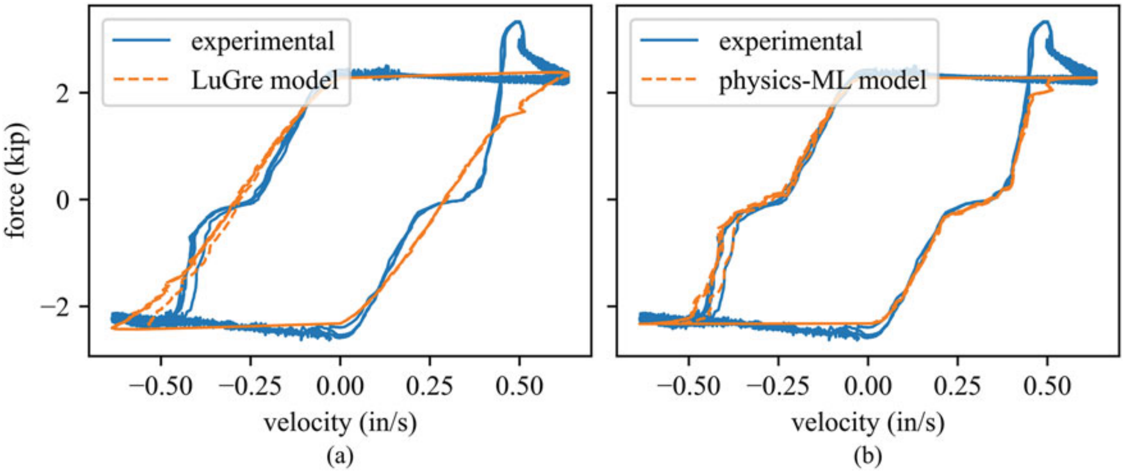

Fig. 27.5 Force–velocity hysteresis plots for the 0.1 Hz dataset, showing the predictions obtained from the: (**a**) LuGre model and (**b**) physics-ML model

Table 27.1 Error from LuGre and physics-ML models

	LuGre model		Physics-ML model	
Dataset	SNR (dB)	NRMSE	SNR (dB)	NRMSE
0.05 Hz	13.22	6.65%	19.26	3.32%
0.1 Hz	13.49	6.1%	19.88	2.92%
0.5 Hz	9.74	8.2%	19.44	2.69%
1.0 Hz	8.97	9.06%	17.91	3.24%
Overall	12.85	6.71%	19.39	3.16%

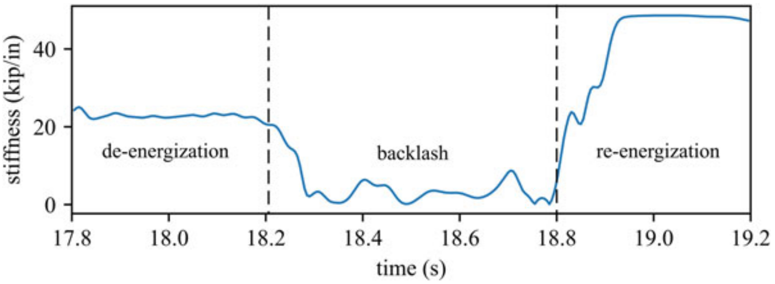

Fig. 27.6 Model prediction of σ_0 during a reversal of travel with the three regions annotated

27.4 Conclusion

The design of a model for dry friction systems was presented and applied to a 9 kip rotary friction damper. This new model augmented the LuGre friction model to accept a time-variable σ_0 parameter, and time-series estimation of the parameter was produced by an LSTM model. An indirect methodology for training the LSTM model was demonstrated. The resulting model fitted the data with an SNR of 19.39 dB and an NRMSE of 3.16%. Such results reduced error by 53% compared to LuGre models fitted using a least-squares method. Finally, the use of the deep learning model as a way of indirect measurement was investigated, and the ML model was shown to produce parameter predictions in three distinct regions during reversal of travel, matching the expected results of backlash behavior.

Acknowledgments The National Science Foundation provided support for this work through Grants 1850012, 1937535, and 2037771. The National Science Foundation's support is sincerely thanked. The authors' opinions, results, conclusions, and recommendations in this material are their own and do not necessarily reflect the views of the National Science Foundation.

References

1. Soong, T.-T., Spencer, B.: Supplemental energy dissipation: state-of-the-art and state-of-the-practice. Eng. Struct. **24**(3), 243–259 (2002)
2. Saaed, T.E., Nikolakopoulos, G., Jonasson, J.E., Hedlund, H.: A state-of-the-art review of structural control systems. J. Vibrat. Control **21**(5), 919–937 (2015)
3. Armstrong-Hélouvry, B., Dupont, P., De Wit, C.C.: A survey of models, analysis tools and compensation methods for the control of machines with friction. Automatica **30**(7), 1083–1138 (1994)
4. Willard, J., Jia, X., Xu, S., Steinbach, M., Kumar, V.: Integrating scientific knowledge with machine learning for engineering and environmental systems. ACM Comput. Surveys **55**, 1–37 (2022). Just Accepted
5. Ricles, J., Harvey, P., Villalobos Vega, E., Karras, J.: Research experiences for undergraduates (REU), NHERI. In: 2022: Deep Learning-Based Friction Modeling of Dry Interfaces for Structural Dampers. DesignSafe (2022)
6. Canudas-de-Wit, C., Olsson, H., Åström, K., Lischinsky, P.: A new model for control of systems with friction. IEEE Trans. Autom. Control **40**(3), 419–425 (1995)
7. Downey, A., Cao, L., Laflamme, S., Taylor, D., Ricles, J.: High capacity variable friction damper based on band brake technology. Eng. Struct. **113**, 287–298 (2016)
8. Coble, D., Cao, L., Ricles, J., Downey, A.: Dataset-Friction-Damper-with-Backlash. GitHub, San Francisco (2022)
9. Cao, L., Marullo, T., Al-Subaihawi, S., Kolay, C., Amer, A., Ricles, J., Sause, R., Kusko, C.S.: NHERI Lehigh experimental facility with large-scale multi-directional hybrid simulation testing capabilities. Front. Built Environ. **6**, 107 (2020)

Chapter 28
Development of Semi-active Cam-Lever Friction Device on a Small-Scale Structure Subjected to Earthquake Loads

Alejandro Palacio-Betancur and Mariantonieta Gutierrez Soto

Abstract Damping devices installed in building structures increase resilience against natural hazards such as earthquakes and high winds. Structural control devices are divided into passive, semi-active, active, and hybrid systems. Semi-active vibration control has received considerable attention because it combines the reliability of passive control systems with the versatility to adapt like active systems but with a smaller magnitude of power consumption. Among semi-active devices, variable-friction dampers are promising because they only require a variable clamping force to a surface to dissipate mechanical energy into heat. Factors that drive the adoption of new technology in structural engineering are driven by cost saving, ease of use, technology effectiveness, and reliability of response. Based on these design goals, this research focuses on the design and characterization of semi-active cam-lever friction damper devices. The proposed device applies a normal force to frictional surfaces through slipping bolts that are attached to a cam-double-lever mechanism. This configuration consists of a cam-lever that has a varying radius cam attached to a lever and a slider-crank mechanism that transforms the rotational movement of the first lever into a linear movement of an actuator. This provides a large mechanical advantage to easily adjust the position of the levers and change the tension of the slipping bolts. The feasibility of this device is studied with a small-scale prototype using additive manufacturing of components and an Arduino microcontroller to change the position of the levers. The device is installed in a single-DOF structure that is subjected to harmonic motions and earthquakes using a shake table. The results show that the mechanical advantage and the speed of response of the system are a function of the geometry of the components of the cam-levers. It is also shown that the slipping bolts can have a minimum pre-tension to make the device work as a passive device if the actuation system fails. This initial pilot study opens pathways in advanced mitigation strategies for smart structures.

Keywords Cam-lever · Semi-active · Control · Friction damper · Vibration mitigation · Earthquake

28.1 Introduction

The protection of civil infrastructure against natural hazards including earthquakes and strong winds led to the development of structural control systems to mitigate the effects of strong vibrations in real time. These are composed of several components such as sensors, data acquisition systems, communication systems, filters, controllers, devices, among others. However, the efficiency of the system is highly dependent on the capabilities of the device installed in the structure because it is the component in charge of modifying the rigidities, masses, or damping of the structure. The damping devices can be divided into three main types: passive, active, and semi-active [1]. Passive devices dissipate energy based on the response of the structure. Therefore, they do not require an external power source, but they are only efficient in a narrow frequency band of excitation because they have constant properties. Active devices use an external power source to apply forces to the structure according to the computer's decisions, but these forces can dissipate and add energy to the system that may increase the response of the structure in some cases [2]. On the other hand, semi-active devices provide the best of both vibration control solutions, they require a smaller magnitude of power compared to active devices, and they guarantee stability because

---

A. Palacio-Betancur (✉)
Department of Civil and Environmental Engineering, The Pennsylvania State University, University Park, PA, USA
e-mail: ajp7096@psu.edu

M. G. Soto
School of Engineering Design and Innovation, The Pennsylvania State University, University Park, PA, USA
e-mail: mvg5899@psu.edu

H. Y. Noh et al. (eds.), *Dynamics of Civil Structures, Volume 2*, Conference Proceedings of the Society
for Experimental Mechanics Series, https://doi.org/10.1007/978-3-031-36663-5_28

they do not add energy to the system. Moreover, semi-active devices can be subdivided into variable friction [3], variable orifices [4], variable fluid [5], and variable stiffness [6]. From these types of devices, friction is an attractive alternative because they have low deterioration and fatigue over time leading to low maintenance cost, and its components are easily obtainable leading to low construction costs. More specifically, variable-friction devices can dissipate energy, independent of velocity, by applying a normal force with an actuator to a surface, and dissipate mechanical energy into heat. Researchers have tried different actuation systems including pneumatic [7], hydraulic [8], electromagnetic [9], electro-mechanical [10], and piezoelectric [11].

However, the implementation of these variable-friction devices in real buildings is limited to issues of reliability or difficulties to produce large forces comparable to active devices. To address these issues, this research studies a novel variable-friction device that controls the normal force through a cam-lever mechanism that provides mechanical advantage to a linear actuator. The feasibility of this device is studied with a small-scale prototype using additive manufacturing of components, an Arduino microcontroller to change the position of the levers, and a shake table to subject the device to different motions. The following sections describe the device, the experimental setup, and the results showing the initial insights into the capabilities of this device.

28.2 Proposed Device

The proposed variable-friction device consists of a traditional slipping connection with a cam-lever mechanism that controls the normal force (N) applied to the connection through perpendicular slipping bolts as shown in Fig. 28.1. The cam-lever mechanism has a varying radius cam attached to a slider-crank mechanism that transforms the rotational movement of the first lever into a linear movement of the actuator. In addition, the cam is in contact with a stiffness regulator that has much lower stiffness than the slipping bolts to allow an easier rotation of the cam, and at the same time, a lower force requirement for the actuator (P). Therefore, the device will generate a damping force (F) according to the number of friction surfaces, the friction coefficient of the friction material, the stiffness of the regulator, the radius of the cam, the lengths of the levers, and the position of the actuator. In addition, the slipping bolts can have a pre-tension applied to them to provide a passive damping force when the actuation system is not working.

28.3 Experimental Setup

The small-scale prototype was built with a combination of additive manufacturing, wood plates, and steel components that guaranteed a working mechanism. The outer plates, middle plate, and end plates shown in Fig. 28.1b were cut out of plywood of $3/8$ in thickness. The slipping bolts, nuts, axles connecting the levers, and ball bearings that guarantee rotations in the mechanism are made out of steel. The cam, levers, and axle that supports the nuts are made out of Polylactic Acid (PLA) with 100% infill. The stiffness regulator is composed of four springs with 7.5 N/mm stiffness connected to the wood plate and a PLA plate. Also, this plate contains a roller that is in contact with the cam in a specific location that will generate the normal load (N) shown in Fig. 28.2b. The levers are moved by the micro-linear servo PQ12-R with 30:1 gearing from Actuonix with a maximum capacity of 18 N and maximum of stroke of 20 mm. The right side of the device was rigidly connected to

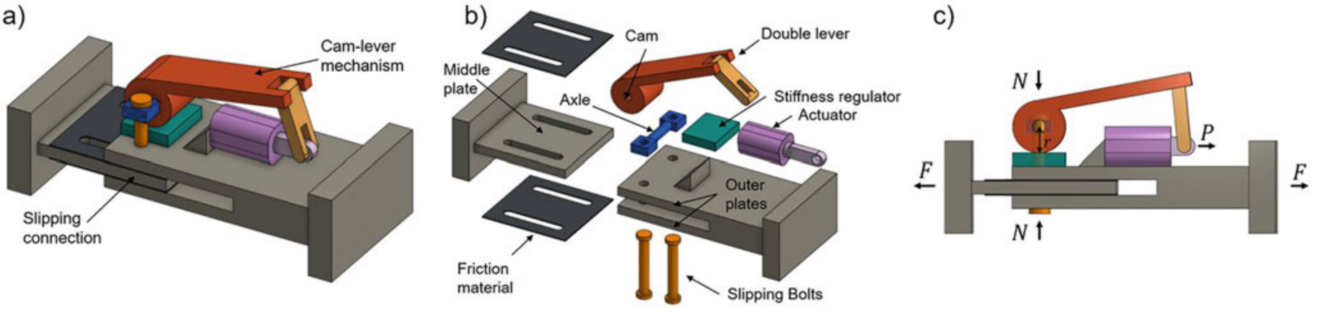

Fig. 28.1 Proposed semi-active friction device with cam-lever mechanism: (**a**) Device, (**b**) Components, (**c**) Force diagram

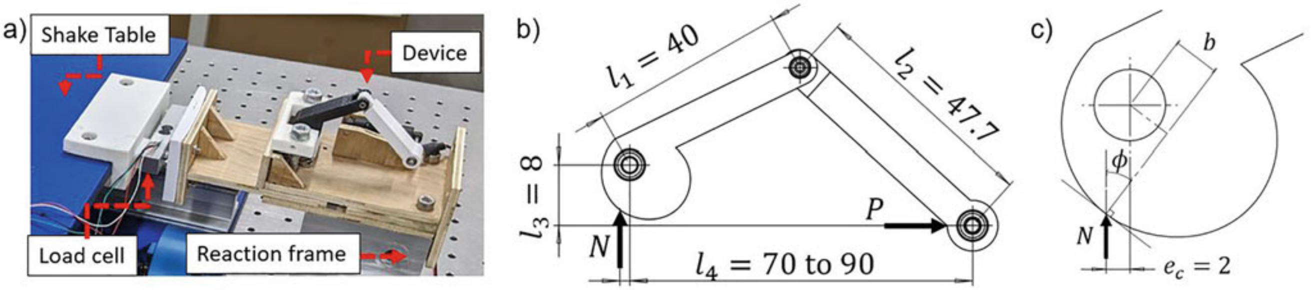

Fig. 28.2 Experimental setup: (**a**) Configuration, (**b**) Levers geometry, and (**c**) Cam geometry

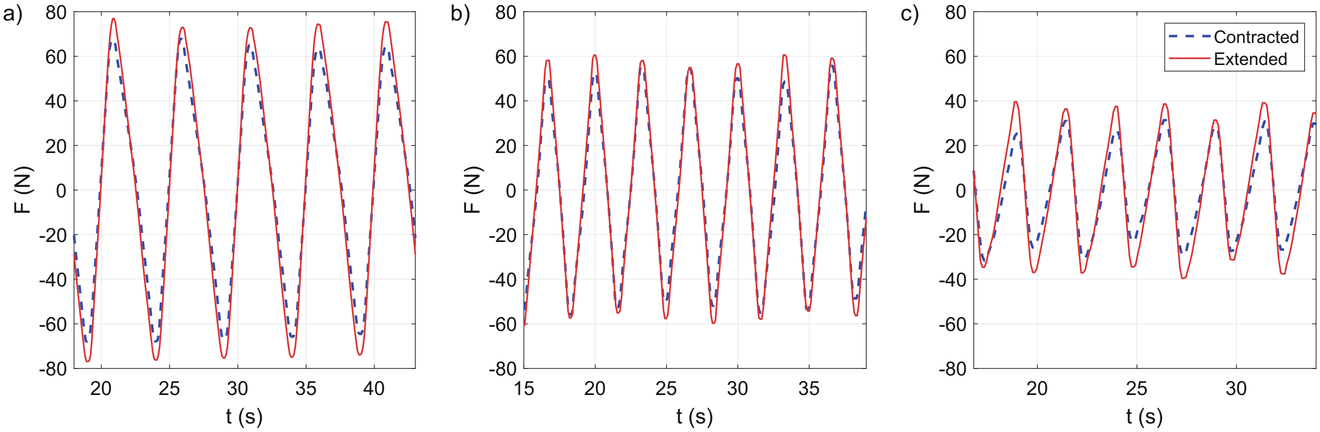

Fig. 28.3 Force response to harmonic excitation for two actuator positions: (**a**) 0.2 Hz, (**b**) 0.3 Hz, (**c**) 0.4 Hz

a reaction frame made out of aluminum as shown in Fig. 28.2a. The slipping connection is connected to a load cell, and the QUANSER Shake Table II that will subject the device to different motions. The actuator and load cell are connected to an Arduino to collect data and give the desired position commands to the actuator.

The geometrical properties of the cam-lever mechanism are given in Fig. 28.2b that can be modeled as a four-bar mechanism with l_3 as a rigid link, l_4 as a varying length link, and l_1, l_2 are links with constant length that will rotate as a function of the location of the actuator. In addition, the geometric properties of the cam are shown in Fig. 28.2c that shows how the normal force N can generate a torque with lever arm b around the axis of the cam according to the pressure angle ϕ. The pressure angle and lever arm are a function of the cam profile and the eccentricity e_c. This chapter considers three cam profiles: linear, harmonic, and cycloid. These profiles change from a minimum radius of 10 mm to a maximum radius of 12 mm in a total rotation of 25.9°.

28.4 Analysis

The feasibility of the proposed device is evaluated in three phases. The first one estimates the load capacity of the device under harmonic motions when the actuator is contracted or fully extended, the second one studies the response of the semi-active mechanism with a simple on–off controller when it is subjected to harmonic motions, and the third one evaluates the response of the system under earthquake motions. The maximum displacement for all motions is 10 mm, and Fig. 28.3 shows the measured forces when the device is subjected to sine waves with 0.2 Hz, 0.3 Hz, and 0.4 Hz. It is important to note that the force increases when the actuator is extended ($l_4 = 90$) for all frequencies, meaning that the normal force (N) is effectively increased when the cam rotates and compresses the springs.

The second phase of testing implements an on–off controller that fully extends the actuator when the displacement and velocity of motion have the same direction. These tests are necessary to evaluate the speed of response of the system and how different cam profiles generate different force profiles according to the variation of the pressure angle. Cam 1 shows the response of the linear profile, Cam 2 is the harmonic profile, and Cam 3 is the cycloid profile. The linear profile showed the maximum force response (Fig. 28.4a) because the other two cam profiles have higher pressure angles leading to larger lateral

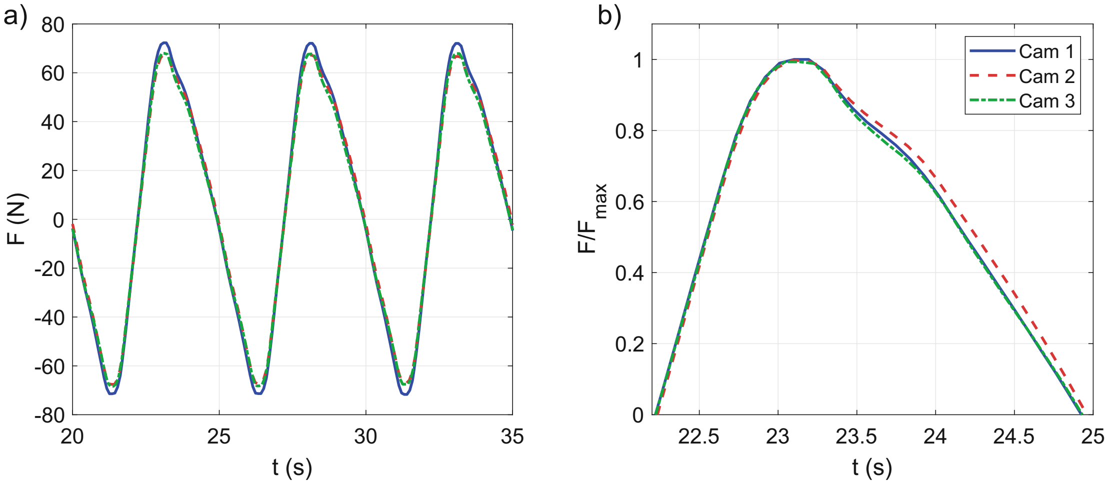

Fig. 28.4 Semi-active force response with different cam profiles: (**a**) Absolute force and (**b**) Normalized force

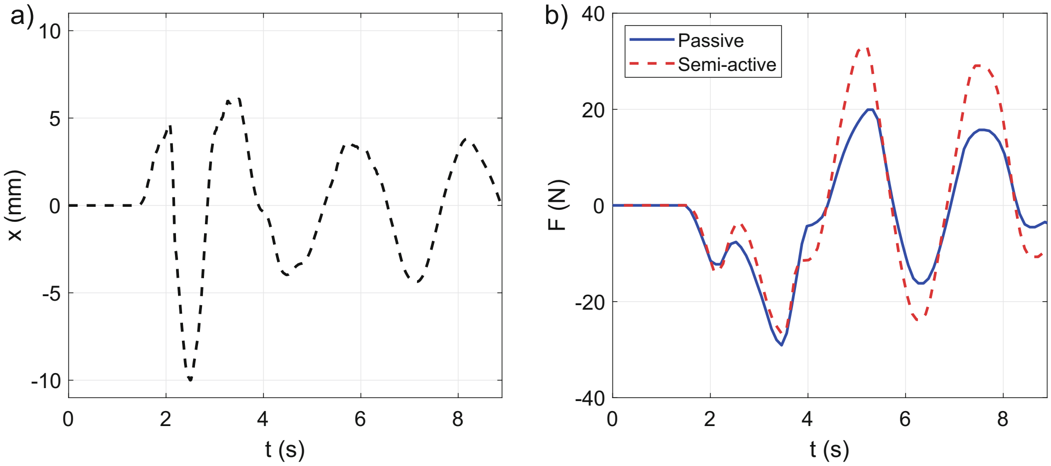

Fig. 28.5 Force response to earthquake simulation: (**a**) Predefined displacement, (**b**) Force response for passive and semi-active scenarios

loads on the spring and not the desired vertical load. On the other hand, Fig. 28.4b with normalized forces gives a better idea of how the response varies for each profile. The three profiles have a similar rise response when trying to increase load; however, Cam 3 has a faster decay that makes it a desired behavior because it can follow the controller commands faster. Therefore, this profile will be used for the third phase of testing.

For the last phase, a predefined displacement was generated from the response of a single-degree-of-freedom (DOF) structure with a natural frequency of 1 Hz and a damping ratio of 5% subjected to El Mendocino Earthquake. The test was performed when the device was on passive control, meaning that the actuator is contracted, and a semi-active control that uses the same on–off controller than the previous phase. Figure 28.5 shows the predefined displacement and how each control approach generates forces. The semi-active approach increases the forces considerable according to the control law, and it decays at the same rate as the passive approach as can be seen in the last two peaks of the response.

28.5 Conclusion

The protection of civil infrastructure against natural hazards requires technology that would enhance its performance. Advanced mitigation strategies using vibration control devices in structures can reduce these harmful effects. This research provides a pilot study on a novel semi-active cam-lever friction device. The results of this experimental study show the capability of this device to provide initial insights into its response during harmonic excitation and earthquake loading.

Future work includes the characterization of mechanical behavior numerically and the evaluation of the scalability of the proposed device to medium and large scales.

Acknowledgments The authors acknowledge Assistant Professor Jared Butler for theoretical advice about design of machinery, Assistant Research Professor Richard Auhl for advising and providing materials for the experimental setup, members of the DREAM Structures Lab Sumant Rokade and Aaron Rohlfing for help with additive manufacturing, and David Caballero-Russi for assistance during the experimental testing.

References

1. Housner, G., Bergman, L.A., Caughey, T.K., Chassiakos, A.G., Claus, R.O., Masri, S.F., Skelton, R.E., Soong, T.T., Spencer, B.F., Yao, J.T.P.: Structural control: past, present, and future. J. Eng. Mech. **123**(9), 897–971 (1997)
2. Zambrano, A., Betancur, A.P., Burbano, L., Niño, A.F., Giraldo, L.F., Soto, M.G., Giraldo, J., Cardenas, A.A.: You make me tremble: A first look at attacks against structural control systems. In: Proceedings of the 2021 ACM SIGSAC Conference on Computer and Communications Security, pp. 1320–1337 (2021)
3. Lu, L.Y., Lin, T.K., Jheng, R.J., Wu, H.H. : Theoretical and experimental investigation of position-controlled semi-active friction damper for seismic structures. J. Sound Vibrat. **412**, 184–206 (2018)
4. Yang, J.N., Bobrow, J., Jabbari, F., Leavitt, J., Cheng, C.P., Lin, P.Y.: Full-scale experimental verification of resettable semi-active stiffness dampers. Earthquake Eng. Struct. Dyn. **36**(9), 1255–1273 (2007)
5. Yuan, X., Tian, T., Ling, H., Qiu, T., He, H.: A review on structural development of magnetorheological fluid damper. Shock Vibrat. **2019** (2019)
6. Liu, Y., Matsuhisa, H., Utsuno, H.: Semi-active vibration isolation system with variable stiffness and damping control. J. Sound Vibrat. **313**(1–2), 16–28 (2008)
7. Mehmood, A., Laghrouche, S., El Bagdouri, M.: Modeling identification and simulation of pneumatic actuator for VGT system. Sensors Actuat. A Phys. **165**(2), 367–378 (2011)
8. Kannan, S., Uras, H.M., Aktan, H.M.: Active control of building seismic response by energy dissipation. Earthquake Eng. Struct. Dyn. **24**(5), 747–759 (1995)
9. Lorenz, M., Heimann, B., Härtel, V.: A novel engine mount with semi-active dry friction damping. Shock Vibrat. **13**(4–5), 559–571 (2006)
10. Narasimhan, S., Nagarajaiah, S.: Smart base isolated buildings with variable friction systems: H controller and SAIVF device. Earthquake Eng. Struct. Dyn. **35**(8), 921–942 (2006)
11. Xu, Y.L., Ng, C.L. : Seismic protection of a building complex using variable friction damper: experimental investigation. J. Eng. Mech. **134**(8), 637–649 (2008)

Chapter 29
Vibration Control Using Frictional Tuned Mass Dampers with Stick-Slip Motion

Mohsen Amjadian

Abstract Tuned mass dampers (TMDs) are proven to be effective in reducing both the acceleration and displacement responses of civil structures subjected to earthquake. The basic idea behind the use of a TMD in civil structures is to create an alternative path for the flow of mechanical energy in the dynamic system of primary structure to deviate the input seismic (or wind) energy from entering its key structural components such as beams and columns. This is achieved by storing and dissipating the input seismic energy in the TMD itself as it oscillates with the vibration of primary structure. The process of energy dissipation in the TMD can be carried out using solid friction by allowing the mass of TMD to slide over a surface attached to the primary structure rather than using viscous damping that is usually provided by viscous fluid dampers connecting the mass of TMD to the primary structure. The former method is relatively simpler to implement and it has a lower cost of installation, operation, and maintenance as well. A TMD that uses friction for energy dissipation is termed as frictional TMD (FTMD). Although the energy dissipation mechanism of FTMD is simple and cost-effective, it is susceptible to stick-slip motion, a highly nonlinear phenomenon occurring at low velocities when the dynamic state of moving mass abruptly shifts from the sliding phase to the sticking phase or vice versa. In particular, during the sticking phase when the mass of FTMD sticks to the friction surface, the FTMD can neither store nor dissipate the input seismic energy. The objective of this chapter is to study how stick-slip motion can affect the energy dissipation capability a FTMD and the seismic performance of primary structure. For this purpose, a 3DOF dynamic model is employed to model the interaction of FTMD with the primary structure (two-story base-isolated building) during the stick-slip motion. The friction force is described by a modified version of the Karnopp friction model in which a sticking velocity is defined to characterize the boundary between the sticking and sliding phases and perform a parametric nonlinear time-history analysis of 3DOF dynamic model. The numerical results show that for a given ground motion acceleration it is feasible to adjust both the mass of FTMD and the normal force in such a way that the intensity of ground motion remains above the breakaway level to avoid sticking, allowing the FTMD to slides continuously during the earthquake.

Keywords Vibration Control · Tuned Mass Damper · Friction · Energy Dissipation · Stick-Slip Motion

29.1 Introduction

A tuned mass damper (TMD) is a passive vibration control system consisting of a mass, a spring, and an energy dissipation component that can be installed on a civil structure in order to mitigate its vibration under an external excitation such as wind or earthquake [1]. The basic idea behind the use of a TMD is to create an alternative path of energy flow in the dynamical system of primary structure in order to deviate a large portion of the external energy from entering the dynamical system through an energy storing and dissipating process in the TMD while moving with the vibration of primary structure [2]. The role of mass and spring is to tune the frequency of TMD with the predominant frequency of primary structure to enable the TMD to resonate out of phase with the vibration of primary structure, and the role of damper is to dissipate the external energy. The classical TMDs use viscous fluid dampers for energy dissipation that connect the TMD to the primary structure. Friction is another form of energy dissipation that has recently been considered for energy dissipation in TMDs by allowing the mass of TMD to slide over a surface attached to the primary structure. TMDs that use friction for energy dissipation are termed as frictional TMDs (FTMDs), and they are expected to have a lower cost of installation, operation, and maintenance

---

M. Amjadian (✉)
Department of Civil Engineering, College of Engineering and Computer Science, The University of Texas Rio Grande Valley, Edinburg, TX, USA
e-mail: mohsen.amjadian@utrgv.edu

H. Y. Noh et al. (eds.), *Dynamics of Civil Structures, Volume 2*, Conference Proceedings of the Society
for Experimental Mechanics Series, https://doi.org/10.1007/978-3-031-36663-5_29

compared to the classical TMDs with viscous fluid dampers. In order for a TMD to be effective in reducing the displacement of a structure, a large mass ratio must be used, implying that a heavier TMD demands a higher damping to sustain its effectiveness. This is exactly the case in a FTMD because as the weight of TMD increases the normal force acting on the friction surface between the TMD and structure increases too, resulting in a higher damping due to the increase of friction.

FTMDs have been subject of many studies and experiments in the recent decades. In one of the first studies, Inaudi and Kelly (1995) studied a nonlinear in which two lateral friction dampers were used to dissipate energy. They showed that the efficacy of proposed FTMD is comparable to that of TMDs with linear viscous dampers for a wide range of excitation intensity [3]. Ricciardelli and Vickery (1999) studied the response of a linear SDOF system with linear stiffness and dry friction damping subjected to harmonic excitation. They proposed closed-form expressions for the proposed FTMD optimum parameters and the steady-state amplitudes of vibration. The authors showed that although FTMDs may be less effective for low values of the excitation, they tend to be more effective as the amplitude of the excitation is increased [4]. Gewei and Basu (2011) proposed an approximate analytical method for the design of an FTMD. It was found that the performance of FTMD can be equally competitive to a viscously damped TMD for certain parameters. It was concluded that the optimal friction coefficient for the FTMD is dependent on the intensity of excitation [5]. Pisal and Jangid (2016) investigated the effectiveness of FTMDs in suppressing the dynamic response of civil structures by studying a 2DOF dynamic model. They conducted a parametric study to investigate the effects of key parameters such as the mass ratio, the tuning frequency ratio, and the slip force on the performance of TMFD. It was founded that there is an optimum value of the slip force at which the response of primary structure decreases significantly, and this optimum value increases with the increase in the value of mass ratio. However, the range of variation of the slip force depends on the characteristics of earthquake [6].

Even though the results of literature review presented above show that FTMDs are promising passive damping devices, it is however possible for them to experience a stick-slip motion specifically when the weight of FTMD is increased to improve its energy dissipation capacity by increasing the normal force acting on the friction surface. This phenomenon is very important and can significantly downgrade the performance of a FTMD; but it has not been studied well in the literature. In particular, during the sticking phase when the mass of FTMD sticks to the friction surface, the effectiveness of FTMD is reduced dramatically as it can neither store nor dissipate the input seismic energy. The objective of this chapter is to study how the stick-slip motion can affect the energy dissipation capability of a FTMD and its impact on the seismic performance of primary structure overall. For this purpose, the FTMD is installed on the dynamic model of a 2DOF base-isolated building model (studied in the previous work of author [2]) to control the lateral deformation of base-isolation system during the stick-slip motion.

29.2 Mathematical Modeling of the Problem

Figure 29.1 shows a FTMD mounted on the top floor (i.e., superstructure floor) of a 2DOF base-isolated building model subjected to a horizontal ground motion with the acceleration $\ddot{x}_g$. This dynamic model has three degrees of freedom x_s, x_b, and $x_d = x_b + u_d$ representing the displacements of superstructure and base floors of the base-isolated building, and the displacement of FTMD relative to the ground, respectively, and u_d is the displacement of FTMD relative to the superstructure. Two configurations are considered to study the performance of FTMD in this study. In the first model, the mass of FTMD is allowed to slide over the surface of superstructure floor as shown in Fig. 29.1a. The normal force is constant and equal to the weight of FTMD as $N_{f0} = W_d$ in this model. In the second model shown in Fig. 29.1b, a different mechanism is used to generate a normal force equal to $N_f = \lambda_f N_{f0}$ where λ_f is the normal force factor and $0 < \lambda_f < \infty$. The normal force acts on the top surface of mass of the FTMD. In this configuration, the magnitude of normal force can be modified prior to earthquake.

The governing equation describing the motion of base-isolated building subjected to an earthquake with the horizontal acceleration $\ddot{x}_g$ is described by the following equation:

$$\mathbf{M}\ddot{\mathbf{U}} + \mathbf{C}\dot{\mathbf{U}} + \mathbf{K}\mathbf{U} + \boldsymbol{\Lambda}_f \mathrm{F}_f = -\mathbf{M}\boldsymbol{\iota}_g \ddot{x}_g \tag{29.1a}$$

where F_f is the friction force; $\mathbf{U} = \{x_b, x_s, x_d\}^T$ is the displacement vector; $\boldsymbol{\iota}_g = \{+1, +1, +1\}^T$ is the ground acceleration influence vector; $\boldsymbol{\Lambda}_f = \{0, -1, +1\}^T$ is the friction force influence vector; and $\mathbf{M}$, $\mathbf{C}$, and $\mathbf{K}$ are the mass, damping, and stiffness matrices which are defined as

$$\mathbf{M} = \begin{bmatrix} m_b & 0 & 0 \\ 0 & m_s & 0 \\ 0 & 0 & m_d \end{bmatrix}, \mathbf{C} = \begin{bmatrix} c_b + c_s & -c_s & 0 \\ -c_s & c_s + c_d & -c_d \\ 0 & -c_d & c_d \end{bmatrix}, \mathbf{K} = \begin{bmatrix} k_b + k_s & -k_s & 0 \\ -k_s & k_s + k_d & -k_d \\ 0 & -k_d & k_d \end{bmatrix} \tag{29.1b}$$

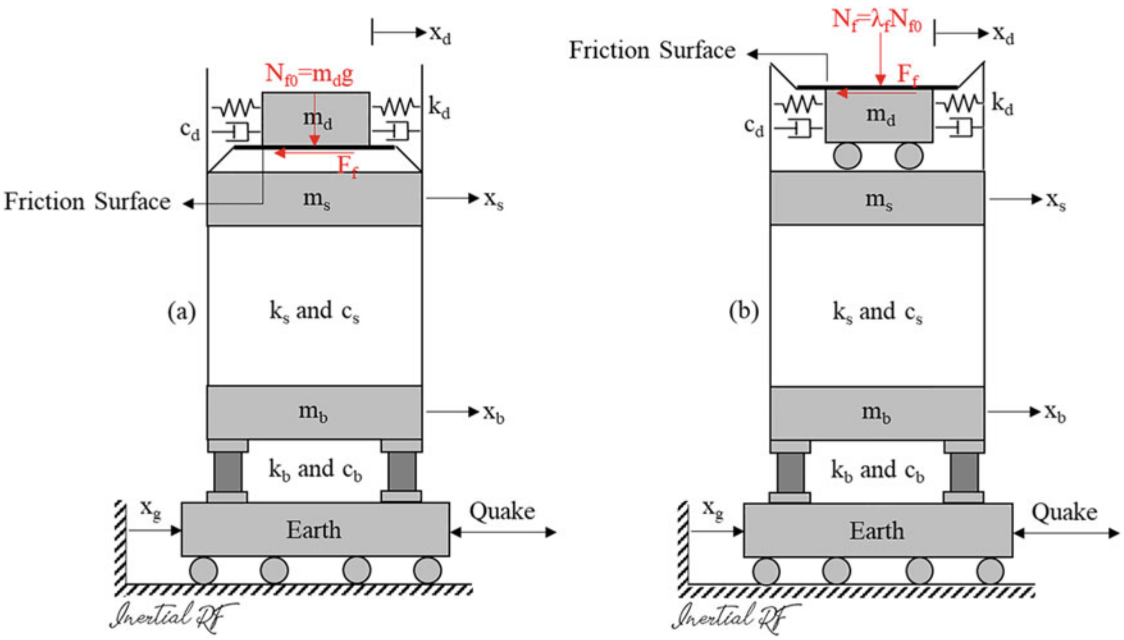

Fig. 29.1 A FTMD mounted on the top floor of a 2DOF base-isolated building subjected to horizontal ground motion with the (**a**) weight-dependent normal force and (**b**) weight-independent normal force

Table 29.1 Parameters of the 2DOF base-isolated model taken from [2]

Parameter	Value	Unit
m_s	29,485	Kg
ω_s	20.944	Rad/s
ξ_s	2	%
m_b	6800	Kg
ω_b	2.513	Rad/s
ξ_b	2	%

where m_b, m_s, and m_d are the mass of base floor, superstructure, and FTMD, respectively; c_b, c_s, and c_d are the damping coefficients of base floor, superstructure, and FTMD, respectively; and k_b, k_s, and k_d are the stiffness coefficients of base floor, superstructure, and FTMD, respectively. The damping and stiffness coefficients of the elastomeric rubber bearings and the superstructure can be written as

$$c_b = 2\xi_b\left(m_b + m_s\right)\omega_b,\ k_b = \left(m_b + m_s\right)\omega_b^2,\ c_s = 2\xi_s m_s\omega_s \text{ and } k_s = m_s\omega_s^2 \tag{29.1c}$$

where ξ_b and ω_b are the critical damping ratio and natural frequency of the elastomeric rubber bearings, and ξ_s and ω_s are the critical damping ratio and natural frequency of superstructure. Table 29.1 shows the values of these parameters as recommended by Ramallo et al. (2002) for a smart base isolation system [2, 7].

29.3 Friction Model with Stick-Slip Motion

The friction force F_f in Eq. (29.1c) is computed using the modified version of Karnopp Friction Model (KFM) described by [8–10],

$$F_f = \begin{cases} F_{fsl}\,\mathrm{sgn}\left(\dot{u}_d\right) \times \vartheta_{fs} & \left|\dot{u}_d\right| \ge v_{f0} \\ \mathfrak{R}_{fe} & \left|\dot{u}_d\right| < v_{f0}\ \left|\mathfrak{R}_{fe}\right| < F_{fst} \\ F_{fst}\,\mathrm{sgn}\left(\mathfrak{R}_{fe}\right) & \left|\dot{u}_d\right| < v_{f0}\ \left|\mathfrak{R}_{fe}\right| \ge F_{fst} \end{cases} \tag{29.2a}$$

Fig. 29.2 Force-velocity behavior of the modified version of the KFM

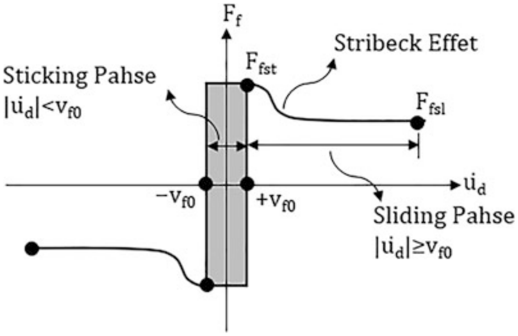

where $F_{\mathrm{fsl}} = \mu_{\mathrm{fsl}} N_{\mathrm{f}}$ and $F_{\mathrm{fst}} = \mu_{\mathrm{fst}} N_{\mathrm{f}}$ are the sliding and sticking friction forces, respectively, with μ_{fsl} and μ_{fst} ($\mu_{\mathrm{fst}} \geq \mu_{\mathrm{fsl}}$) being the kinetic and static friction coefficients, respectively; $\Re_{\mathrm{fe}}$ is the force that acts on the friction surface during the sticking phase; v_{f0} is the natural sticking velocity that defines the boundary between the sticking phase and sliding phase; and ϑ_{fs} is a dimensionless coefficient representing the Stribeck effect (See Fig. 29.2) and is given by [10]

$$\vartheta_{\mathrm{fs}} = 1 + \left(\frac{\mu_{\mathrm{fst}}}{\mu_{\mathrm{fsl}}} - 1\right) \mathrm{e}^{-\left|\frac{\dot{\mathrm{u}}_{\mathrm{d}} - \mathrm{sgn}(\dot{\mathrm{u}}_{\mathrm{d}}) v_{\mathrm{f0}}}{v_{\mathrm{fs}}}\right|^{\mathrm{s}}} \tag{29.2b}$$

where v_{fs} is the Stribeck velocity, and s is a constant. The force $\Re_{\mathrm{fe}}$ acts as a reaction to the external force that is applied to friction surface during the sticking phase (i.e., when $\ddot{\mathrm{u}}_{\mathrm{d}} = 0$) to satisfy the static equilibrium of system. This force is obtained using the following formula:

$$\Re_{\mathrm{fe}} = -\left(\mathbf{\Lambda}_{\mathrm{d}}^{\mathrm{T}} \mathbf{M}^{-1} \mathbf{\Lambda}_{\mathrm{f}}\right)^{-1} \mathbf{\Lambda}_{\mathrm{d}}^{\mathrm{T}} \left(\mathbf{M}^{-1} \mathbf{C} \dot{\mathbf{U}} + \mathbf{M}^{-1} \mathbf{K} \mathbf{U} + \boldsymbol{\iota}_{\mathrm{g}} \ddot{\mathrm{x}}_{\mathrm{g}}\right) \tag{29.3}$$

where $\mathbf{\Lambda}_{\mathrm{d}} = \mathbf{\Lambda}_{\mathrm{f}}$. Figure 29.2 shows the force-velocity behavior of the modified version of the KFM described above. In this study, it is assumed that $\mu_{\mathrm{fsl}} = 0.150$, $\mu_{\mathrm{fst}} = 0.175$, $s = 2$, $v_{\mathrm{fs}} = 0.01$ m/s, and $v_{\mathrm{f0}} = 0.0025 v_{\mathrm{fs}}$.

29.4 Energy Balance Equation

The equation of motion of FTMD in term of the displacement of FTMD with respect to the superstructure is

$$m_{\mathrm{d}} \ddot{\mathrm{u}}_{\mathrm{d}} + k_{\mathrm{d}} u_{\mathrm{d}} + F_{\mathrm{f}} = -m_{\mathrm{d}} \left(\ddot{\mathrm{x}}_{\mathrm{g}} + \ddot{\mathrm{x}}_{\mathrm{s}}\right) \tag{29.4a}$$

By taking integration from both the sides of equation in term of u_{d} and manipulating the resulted equation, we obtain the following equation for the balance of energy in the FTMD,

$$E_{\mathrm{dK}}(t) + E_{\mathrm{dS}}(t) + E_{\mathrm{dD}}(t) = E_{\mathrm{dI}}(t) \tag{29.4b}$$

where E_{dK}, E_{dS}, E_{dD}, and E_{dI} are the kinetic, stored, dissipated, and the relative input energy functions of the FTMD, respectively, which are defined as

$$E_{\mathrm{dK}}(t) = \frac{1}{2} m_{\mathrm{d}} \dot{\mathrm{u}}_{\mathrm{d}}^{2},\ E_{\mathrm{dS}}(t) = \frac{1}{2} k_{\mathrm{d}} u_{\mathrm{d}}^{2},\ E_{\mathrm{dD}}(t) = \int_{0}^{\mathrm{t}} F_{\mathrm{f}} \dot{\mathrm{u}}_{\mathrm{d}} \mathrm{d}\tau, \text{ and } E_{\mathrm{dI}}(t) = -\int_{0}^{\mathrm{t}} m_{\mathrm{d}} \left(\ddot{\mathrm{x}}_{\mathrm{g}} + \ddot{\mathrm{x}}_{\mathrm{s}}\right) \dot{\mathrm{u}}_{\mathrm{d}} \mathrm{d}\tau \tag{29.4c}$$

These energy functions are used to evaluate the performance of FTMD in both storing and dissipating the input seismic energy during the sliding and sticking phases.

29.5 Ground Motion Record

The time history analysis of 2DOF base-isolated building model is performed for a far-field ground motion acceleration record (1979 Imperial Valley earthquake) selected from PEER database as listed in Table 29.2 [11]. This record has been modified and scaled using the wavelet adjustment method to match the ASCE 7–10 Maximum Considered Earthquake (MCE) design response spectrum over the period range $T_n = 0.5$–5 s [12] that covers the period range $0.5T_D$ to $1.25T_M$ recommended by ASCE 7–10 where $T_D < T_b$ and $T_M < T_b$ are the effective periods of the base-isolated building at the design and maximum displacements, respectively, and $T_b = 2\pi/\omega_b = 2.5$ s. Figure 29.3a shows the response spectrum of the unscaled record. Figure 29.3b shows the design response spectrum, representing an earthquake with the return period of 2475 years in an area in California with site class = B, $\xi = 5\%$, and PGA = 0.876 g [2].

29.6 Results and Discussion

The key parameters of FTMD are: (1) the mass ratio, $\mu_d = m_d/(m_d + m_s)$, (2) the frequency ratio, $f_d = \omega_d/\omega_b$, and (3) the normal force ratio, $\lambda_f = N_f/N_{f0}$. The latter parameter characterizes the energy dissipation in FTMD due to friction by considering stick-slip motion. A preliminary time history analysis is performed to study the performance of FTMD in reducing the displacement of base floor by taking stick-slip motion into account for two different cases of friction: (i) $\lambda_f = 0.1$ and (ii) $\lambda_f = 3.0$ assuming that $\mu_d = 0.05$ and $f_d = 1.0$. It should be noted that case (i) and case (ii) represent low and high normal forces in the FTMD, respectively. Figure 29.4a, b compares the time history of displacement of base floor in case (i) to that in case (ii). It is seen that the FTMD has a better performance in case (i) compared to case (ii). The displacement of base floor in case (ii) is not only higher than the displacement of base floor in case (i) but also higher than that in the case without FTMD by an increase of 27%. Figures 29.4c, d show that this poor performance is due to stick-slip motion of the FTMD in this case compared to case (i) in which the FTMD experiences a smooth and continuous sliding over the frictional surface due to a small normal force decreasing the displacement of base floor by 48%. Figures 29.4e, f show the lack of ability of FTMD in both dissipating and storing the seismic input energy during the stick-slip motion compared to case (i) when the FTMD has a smooth and continuous sliding. It is also of interest to see how the increase of ground motion intensity can influence the performance of FTMD in limiting the displacement of base floor. Figure 29.5 shows the variations of maximum displacement of the base floor and maximum displacement of the FTMD with the PGA of the ground motion for the two cases (i) and (ii) by assuming that $\mu_d = \{0.025, 0.05, 0.075\}$, and $f_d = 1.0$. Figure 29.5a–c shows that by increasing PGA from 0.1 to 1.0 g the maximum displacement of base floor increases proportionally in case (i), and the maximum reduction is achieved for heavier FTMDs. However, this is not true for the FTMD in case (ii) due to the sticking of FTMD to the frictional surface at low PGAs below the breakaway level of sliding. The breakaway level depends on the mass of FTMD; it is seen that for $\mu_d = 0.025$, 0.05, and 0.075 it is equal to $\text{PGA}_{br} = 0.4$ g, 0.375 g, and 0.35 g, respectively.

Table 29.2 Ground motion acceleration record used for the time history analysis

RSN	Name	Year	Magnitude (M)	Station	Component	PGA (g)
0169	Imperial Valley	1979	6.5	Delta	DLT352	0.356

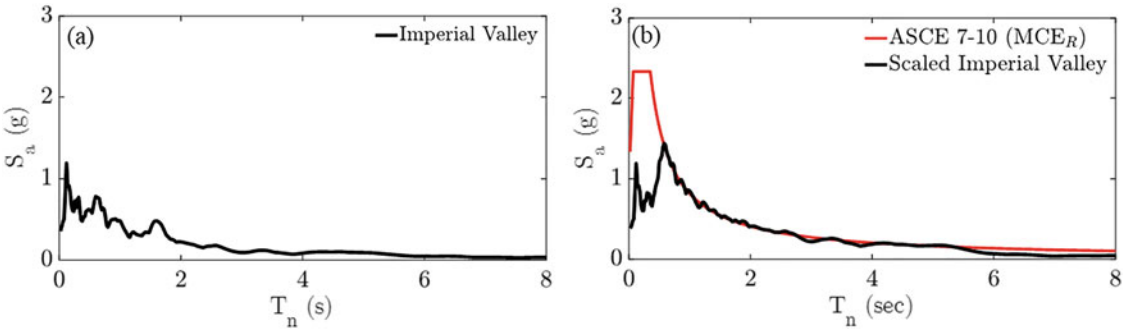

Fig. 29.3 Response spectrum of the ground motion record (**a**) unscaled record (**b**) scaled record matched to the ASCE7–10 MCER design response spectrum for $T_n = 0.5$ sec to $T_n = 5.0$ sec

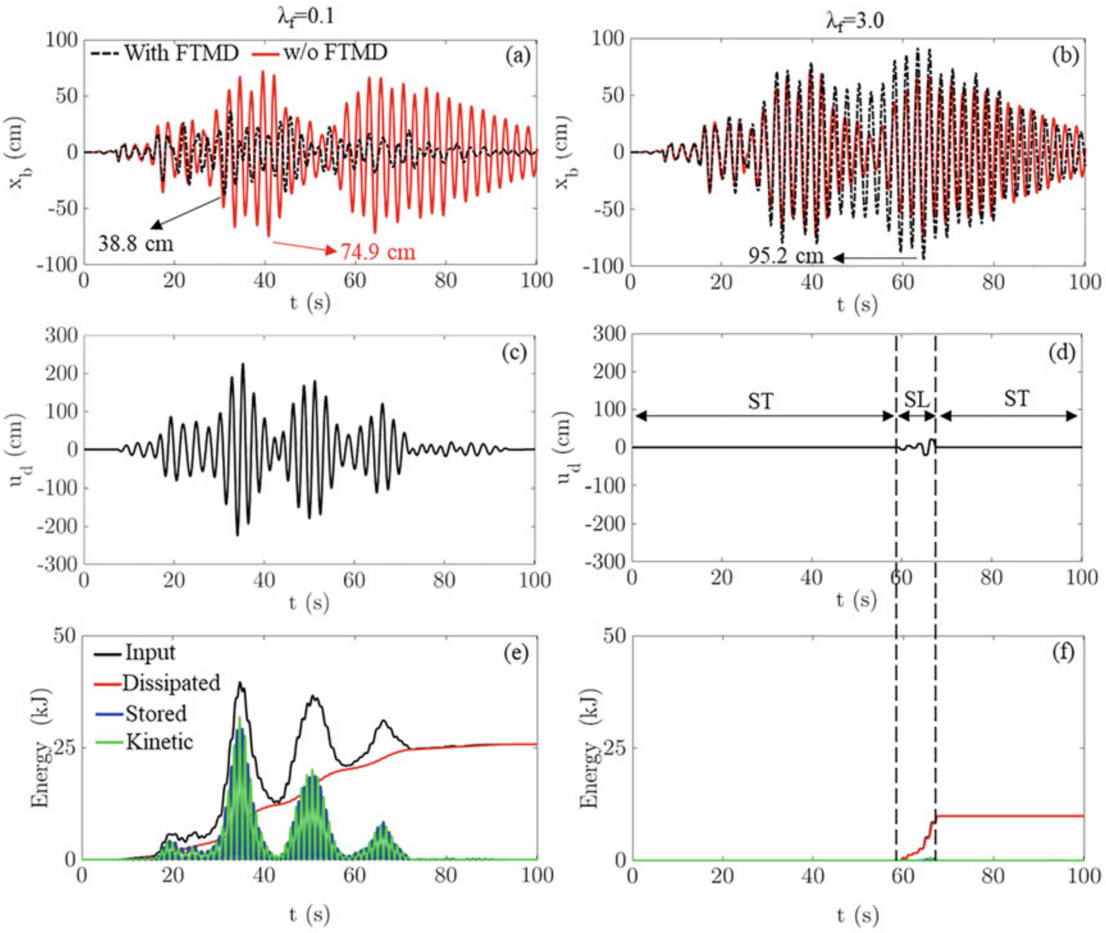

Fig. 29.4 Comparison between the time history response of system for $\lambda_f = 0.1$ and $\lambda_f = 3.0$: (**a**, **b**) displacement of the base floor with and without FTMD, (**c**, **d**) displacement of FTMD, and (**e**, **f**) input, dissipated, stored, and kinetic energy functions

Figure 29.6 shows the variations of maximum displacement of the base floor and the maximum displacement of FTMD with the normal force factor λ_t and the frequency ratio f_d for $\mu_d = \{0.025, 0.05, 0.075\}$ subjected to 1979 Imperial Valley earthquake. It is seen that the highest performance of FTMD is achieved for heavy FTMDs with $\lambda_f < 1$ and $f_d = 1.0$ implying that when the friction is very low and the FTMD is in resonant with the base isolation system as can be seen from Figs. 29.6a–c. However, as the value of λ_f and f_d increases, the performance of FTMD decreases drastically. This is due to the lack of ability of FTMD in dissipating and storing the seismic input energy during the stick-slip motion. The optimum values of parameters of FTMD are chosen to be $\mu_d = 0.075$ ($m_d = 2.72$ tons), $\lambda_f = 0.1$, and $f_d = 1.0$, resulting in 60% reduction in the displacement of base floor from $x_{bmax} = 0.749$ m to $x_{bmax} = 0.30$ m as shown on Fig. 29.6c. The corresponding value for the maximum displacement of FTMD is $u_{dmax} = 1.53$ m as shown in Fig. 29.6f.

29.7 Conclusion

This chapter studies the performance of a Frictional TMD (FTMD) in reducing the displacement of elastomeric bearings installed on a two-story base-isolated building subjected to earthquake by considering the effects of stick-slip motion on the energy dissipation capability of FTMD. The FTMD consists of a mass attached to the primary structure through a linear spring sliding while sliding relative to the primary structure through a frictional surface with the normal force $N_f = \lambda_f W_d$. It was found that allowing the mass of FTMD to slide over the primary structure when $\lambda_f \geq 1$ and it is in resonance with

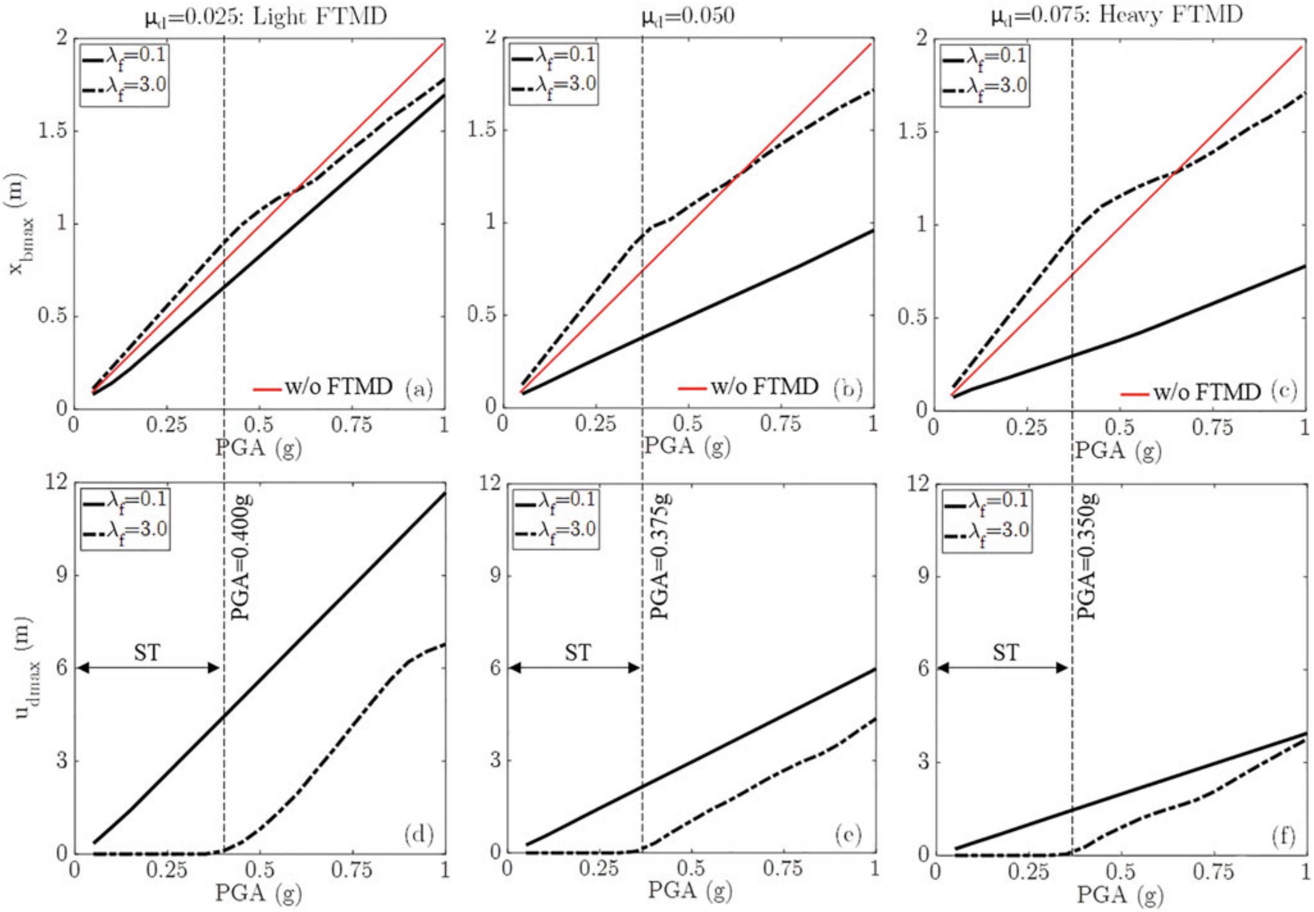

Fig. 29.5 Variation of the maximum displacements of (**a**–**c**) the base floor and (**d**–**f**) the FTMD with the PGA of ground motion acceleration for $\lambda_f = 0.1$ and 3.0, $f_d = 1.0$, and $\mu_d = 0.025$, 0.05, and 0.075

the frequency of isolation system ($f_d = \omega_d/\omega_b = 1.0$) is not an optimum design to control the displacement of base isolation system as the FTMD potentially sticks to the frictional surface when the ground motion intensity is below the breakaway friction level. The best performance is achieved when $\lambda_f < 1$ and the FTMD has a high mass ratio $\mu_d = m_d/(m_s + m_b)$. For a given ground motion acceleration record, it was concluded that $\lambda_f = 0.1$ and $\mu_d = 0.075$ are the optimum parameters of FTMD, resulting in the maximum reduction in the displacement of base floor up to 60%. The result of this study clearly shows the importance of considering the effects of stick-slip motion on the dynamic behavior of FTMDs, particularly in the cases when the static and sliding friction coefficients of frictional surface are high.

Acknowledgements The author would like to thank the University of Texas Rio Grande Valley for the travel grant through the Faculty Travel Support Program.

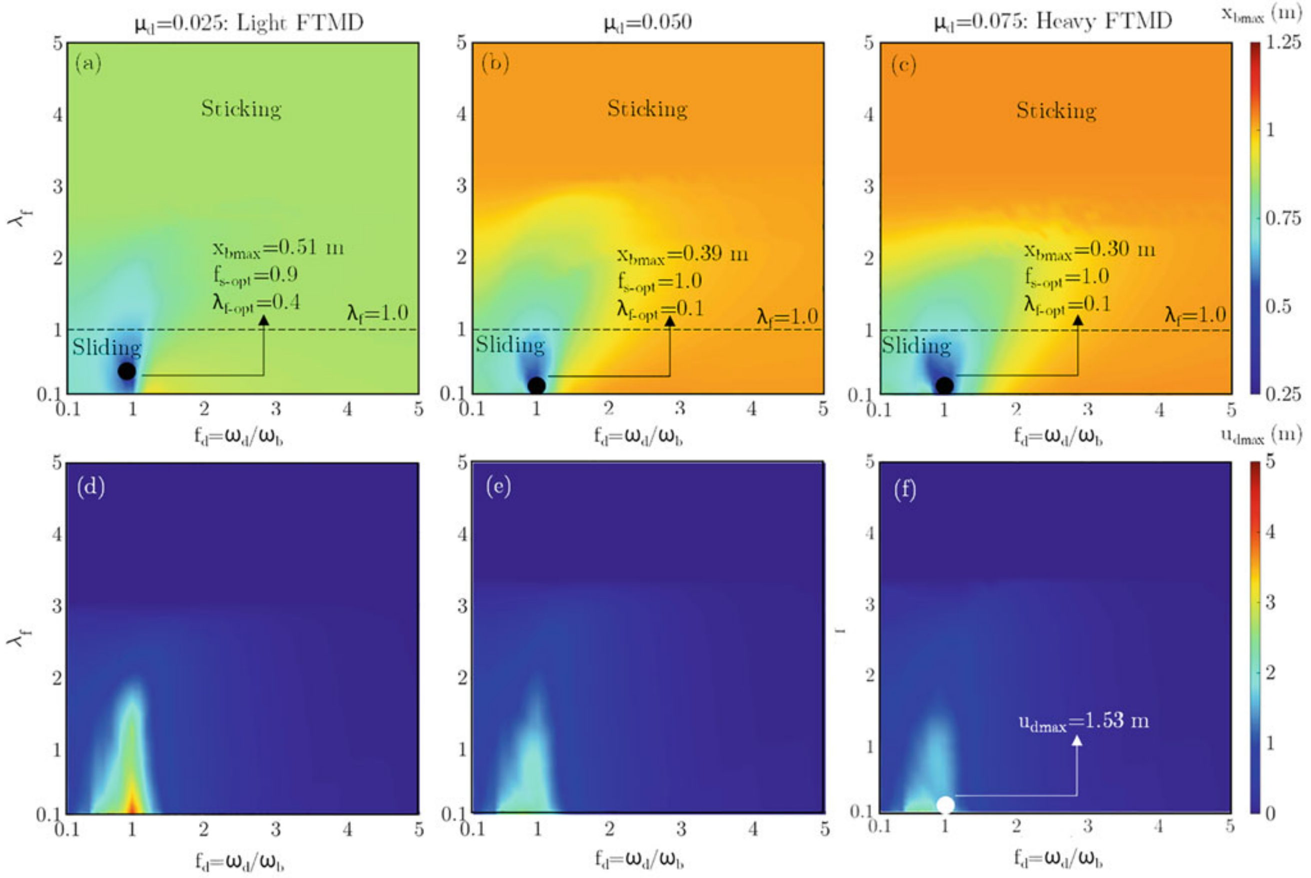

Fig. 29.6 Variation of the maximum displacements of (**a–c**) the base floor and (**d–f**) the FTMD with the normal force factor λ_f, the frequency ratio f_d, and the mass ratio μ_d under the 1979 Imperial Valley earthquake

References

1. Ormondroyd, J., Den Hartog, J.P.: The theory of the dynamic vibration absorber. Am. Soc. Mech. Eng. **50**, 9–22 (1928)
2. Amjadian, M.: A study on the use of an energy-regenerative tuned mass damper for vibration control and monitoring of base-isolated buildings. In: Active and Passive Smart Structures and Integrated Systems XVI, vol. 12043, pp. 252–261 (2022). https://doi.org/10.1117/12.2610866
3. Inaudi, J.A., Kelly, J.M.: Mass damper using friction-dissipating devices. J. Eng. Mech. **121**(1), 142–149 (1995). https://doi.org/10.1061/(ASCE)0733-9399(1995)121:1(142)
4. Ricciardelli, F., Vickery, B.J.: Tuned vibration absorbers with dry friction damping. Earthq. Eng. Struct. Dyn. **28**(7), 707–723 (1999). https://doi.org/10.1002/(SICI)1096-9845(199907)28:7<707::AID-EQE836>3.0.CO;2-C
5. Gewei, Z., Basu, B.: A study on friction-tuned mass damper: harmonic solution and statistical linearization. J. Vib. Control. **17**(5), 721–731 (2011). https://doi.org/10.1177/1077546309354967
6. Pisal, A.Y., Jangid, R.S.: Dynamic response of structure with tuned mass friction damper. Int. J. Adv. Struct. Eng. **8**(4), 363–377 (2016). https://doi.org/10.1007/s40091-016-0136-7
7. Ramallo, J.C., Johnson, E.A., Spencer, B.F.: ‘Smart’ base isolation systems. J. Eng. Mech. **128**(10), 1088–1099 (2002). https://doi.org/10.1061/(ASCE)0733-9399(2002)128:10(1088)
8. Olsson, H., Åström, K.J., Canudas De Wit, C., Gäfvert, M., Lischinsky, P.: Friction models and friction compensation. Eur. J. Control. **4**(3), 176–195 (1998). https://doi.org/10.1016/S0947-3580(98)70113-X
9. Karnopp, D.: Computer simulation of stick-slip friction in mechanical dynamic systems. J. Dyn. Syst. Meas. Control. **107**(1), 100 (1985). https://doi.org/10.1115/1.3140698
10. Amjadian, M., Agrawal, A.K.: Seismic response control of multi-story base-isolated buildings using a smart electromagnetic friction damper with smooth hysteretic behavior. Mech. Syst. Signal Process. **130**, 409–432 (2019). https://doi.org/10.1016/J.YMSSP.2019.05.018
11. PEER: PEER ground motion database. Shallow Crustal Earthq. Act. Tecton. Regimes NGA-West2 (2013) [Online]. Available: http://ngawest2.berkeley.edu/
12. Hancock, J., et al.: An improved method of matching response spectra of recorded earthquake ground motion using wavelets. J. Earthq. Eng. **10**(sup001), 67–89 (2006). https://doi.org/10.1080/13632460609350629

Chapter 30
A Simulink Model for the Dynamic Analysis of Floating Wind Turbines

Jiayao Meng, Ross A. McAdam, and Manolis N. Chatzis

Abstract The drive to maximize the wind-energy harnessing capabilities of modern societies is gradually leading toward the design of floating wind turbines (FWT). To guide such designs, accurate numerical models that predict the dynamic behavior of the systems are crucial to ensure their structural reliability. This chapter presents a new Simulink implementation of the FWT modeling with a focus on the wave-platform interaction. The hydrostatic and hydrodynamic forces applied to the floating platform are calculated using a numerical and an analytical approach. The numerical approach makes use of the open-source boundary element method (BEM) code, Nemoh. In the analytical approach, which is initially limited to a planar response of the FWT, a matched eigenfunction expansions method is examined to evaluate closed-form solutions of the velocity potential and the resulting force. This second approach offers deeper insights into the dynamic system and potentially higher computational efficiency compared to Nemoh. Both approaches are implemented as Simulink subsystems that are integrated with the remaining system in the time domain. The large variety of libraries in Simulink also enables the detailed modeling of other physics including aerodynamics, structural dynamics, and controls. The aerodynamic loads are applied at different cross-sections along the blade using the unsteady blade/element momentum method. While their flexibility can be accounted for, the blades and tower are modeled as rigid bodies in the present study, and the effect of the mooring lines is taken into account as a resulting stiffness matrix. The industry-standard ROSCO controller is also employed. Validation against the most popular tool OpenFAST is carried out on the 5-MW ITIBarge FWT, and the overall agreement demonstrates the capability of the developed Simulink model to perform accurate dynamic analysis for FWTs.

Keywords FWT · Modeling · Dynamics · Simulink · Offshore

30.1 Introduction

Offshore wind energy has the potential of meeting the total world's electricity demand and could contribute significantly to achieving the target of limiting global temperature rise to 1.5 °C by 2050 [1]. Around 80% of the offshore wind resource is in waters deeper than 60 m, where the deployment of bottom-fixed offshore wind turbines may not be economically viable. Floating wind turbines (FWTs), which are relatively insensitive to water depth, provide promising alternatives to harness substantial offshore wind resources in deep waters far from the shore. However, the contradictory objectives of structural safety under the harsh ocean environment and of competitive cost-of-energy to attract market investments bring about great difficulties in the FWT design. The reliable and cost-effective design of FWTs is one of the key drivers to unleash the offshore wind potential.

A reliable design of the FWT should ensure the structural integrity and serviceability under the combined effects of gravitational and inertial loads, aerodynamic loads, hydrodynamics loads, mooring loads, and ice loads (where applicable) [2]. The comparison to field measurements is the most direct means of validating a FWT's design concept, and it has been deployed in the "Hywind Demo" and "Hywind Scotland" projects [3, 4]. However, in parallel to such experimental data, numerical modeling of such structures needs to be further developed. In light of this, simulation tools that can perform

---

J. Meng (✉) · M. N. Chatzis
Department of Engineering Science, University of Oxford, Oxford, UK
e-mail: jiayao.meng@eng.ox.ac.uk; manolis.chatzis@eng.ox.ac.uk

R. A. McAdam
Ørsted Power (UK), London, UK
e-mail: rosmc@orsted.com

H. Y. Noh et al. (eds.), *Dynamics of Civil Structures, Volume 2*, Conference Proceedings of the Society
for Experimental Mechanics Series, https://doi.org/10.1007/978-3-031-36663-5_30

fully coupled aero-hydro-elastic dynamic analysis are highly demanded. Several popular simulation tools are available for the dynamic analysis of FWTs, e.g., OpenFAST [5], Bladed [6], and HAWC2 [7]. Code-to-code, as well as code-to-experiment, verifications have been investigated through a series of projects led by the NREL (the phase IV of OC3 [8], phase II of OC4 [9], phase II of OC5 [10], and phase I of OC6 [11]). Despite each of these codes providing a reasonable representation of various domains of the problem, each of them makes use of a different set of assumptions, and some of the aforementioned codes are not open-source. The advantage of a code developed entirely in MATLAB/Simulink has the potential of easily integrating the multi-physics toolboxes developed by the multiple different communities working on the problem of estimating the overall performance of FWTs.

In this chapter, the tower of the FWT is assumed to be fixed on a floating platform. The movement of this platform has a strong influence on the overall dynamic performance of the system. Therefore, the accurate description of the wave-body interaction problem is crucial for the coupled dynamic analysis of FWTs. The BEM codes, e.g., WAMIT [12], AQWA [13], Nemoh [14], are commonly used to calculate the hydrodynamic forces for the dynamic analysis of FWTs in popular tools (e.g., OpenFAST). BEM codes are of advantage when dealing with the floating platform of arbitrary geometries. As an alternative, the analytical approach employing the separation of variables and eigenfunction expansion matching methods can provide closed-form solutions to the wave-platform boundary value problem (BVP) [15]. It offers deeper insights into the dynamic system and potentially higher computational efficiency compared to the numerical method, which solves the BVP by discretizing the calculation region. Both methods are studied in the present work to provide hydrodynamic coefficients for the FWT modeling.

In this conference paper, the tower, hub, nacelle, and platform are modeled as single rigid bodies separately, the blade is modeled as a sequence of rigid bodies with distributed masses and inertias, and the mooring system is represented with a stiffness matrix in Simulink. The aerodynamic loads calculated by the unsteady dynamic blade element/momentum method [16] and the hydrodynamic loads determined by both numerical (Nemoh) and analytical methods are integrated into the Simulink model. The industry-standard ROSCO controller [17] is implemented in the model to regulate the power generation. The 5-MW ITIBarge FWT is taken as an example to validate the analytical wave-platform interaction modeling approach as well as the Simulink implementation of the FWT system. The hydrodynamic loads calculated from the analytical approach are shown in the example to compare well with those obtained from Nemoh. The dynamic responses of both Simulink–Nemoh and Simulink–Analytical models are also shown to be in good agreement with the OpenFAST–Nemoh model, which indicates the capability of the developed model in Simulink to accurately capture FWT dynamics.

30.2 Wave-Platform Interaction Modeling

Two right-handed Cartesian coordinate systems are defined to describe the 3D movements of a FWT platform as well as the wave kinematics in an open sea of finite depth H (as shown in Fig. 30.1). Let O be the intersection point of the tower centerline and the mean free wave surface when the FWT is in an equilibrium position. The coordinate system $OXYZ$ is earth-fixed with the plane OXY lying on the mean free surface, OX pointing downwind, and OZ pointing upward. The other coordinate system $O'X'Y'Z'$ is fixed on the platform and coincident with $OXYZ$ when there is no perturbation. The translational displacement from O to O' in the surge, sway, and heave degree of freedom (DoF) is denoted as ξ_1, ξ_2, ξ_3, respectively, and the rotation of roll, pitch, and yaw DoF as ξ_4, ξ_5, ξ_6, respectively, with the Euler angle sequence being Cartesian $X \rightarrow$ rotated Y following the ξ_4 transformation $\rightarrow$ rotated Z following the ξ_4 and ξ_5 transformations, as shown in Fig. 30.1.

30.2.1 *Equations of the Boundary Value Problem (BVP)*

Ideal fluid (homogeneous, inviscid, and incompressible) without rotational motion and surface tension is assumed here, in which case the flow can be completely described by a velocity potential $\Phi(x, y, z, t)$ satisfying Laplace's equation

$$\nabla^2 \Phi = 0, \tag{30.1}$$

where $\nabla^2 = \frac{\partial^2}{\partial x^2} + \frac{\partial^2}{\partial y^2} + \frac{\partial^2}{\partial z^2}$, throughout the whole domain Ω enclosed by the free surface S_F, body surface S_B, sea bottom S_D, and far-field boundary S_∞ (see Fig. 30.1). The fluid pressure $p(x, y, z, t)$ can be obtained from Bernoulli's equation

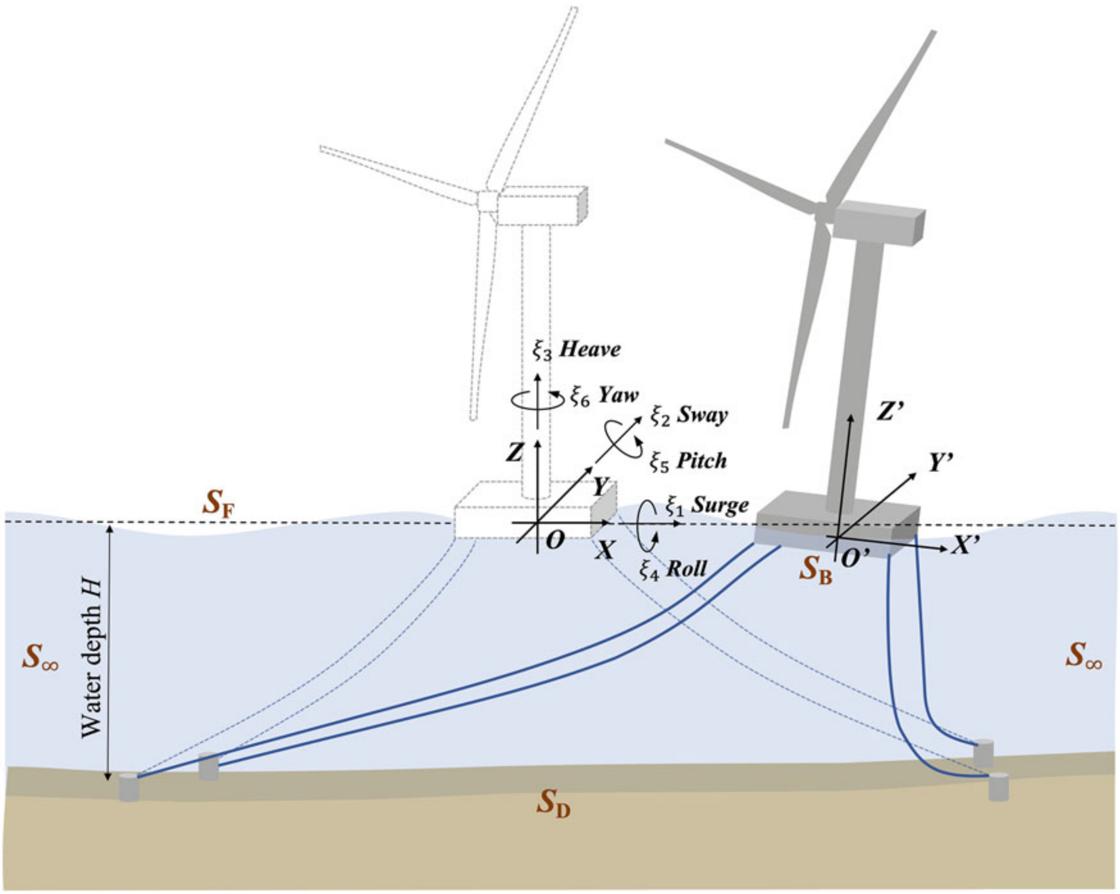

Fig. 30.1 Coordinate system of a floating wind turbine. Only 6 platform DoFs are shown here

$$p = -\rho \frac{\partial \Phi}{\partial t} - \frac{1}{2}\rho (\nabla \Phi)^2 - \rho g z, \tag{30.2}$$

where ρ is the fluid density and g the gravitational acceleration. By assuming small-wave amplitudes relative to the wavelength, and small displacements and rotations of the platform relative to the platform characteristic dimension, the BVP that Φ should satisfy can be linearized on the still water level ($\overline{S}_F$) and mean wetted body surface ($\overline{S}_B$). This simplification allows for the decomposition of Φ into an incident wave potential Φ_I, radiation potential Φ_R, and diffraction potential Φ_D. Φ_R handles the nonhomogeneous body surface boundary condition, Φ_I is an exogenous input to the fluid-body system, and Φ_D is used to cancel out the influence of Φ_I onto the body surface. The total velocity potential can be written as

$$\begin{aligned}\Phi(x, y, z, t) &= \Phi_R(x, y, z, t) + \Phi_I(x, y, z, t) + \Phi_D(x, y, z, t) \\ &= \Re\left\{\frac{1}{2\pi}\int_{-\infty}^{\infty}\left\{\overline{\mathbf{V}}(\omega)\cdot \boldsymbol{\phi}_R(x, y, z, \omega) + \overline{\eta}(\omega)\left[\phi_I(x, y, z, \omega) + \phi_D(x, y, z, \omega)\right]\right\} e^{i\omega t}\, d\omega\right\},\end{aligned} \tag{30.3}$$

where $\boldsymbol{\phi}_R$ is the radiation wave potential vector corresponding to different platform DoFs, which is, however, independent of the platform velocity; ϕ_I, ϕ_D are the incident and diffraction wave potential, respectively, and they are independent of the wave elevation; $\overline{\mathbf{V}}(\omega), \overline{\eta}(\omega)$ are Fourier transform of the body velocity $\mathbf{V}(t) = \dot{\boldsymbol{\xi}}(t)$ and wave amplitude at the origin $\eta(t)$, respectively. The governing equations of the linear BVP in frequency domain can then be derived and summarized as follows:

$$\begin{cases} \nabla^2 \phi = 0, & \mathbf{X} \in \Omega \\ \dfrac{\partial \phi}{\partial z} - \dfrac{\omega^2}{g}\phi = 0, & \mathbf{X} \in \overline{S}_F : z = 0 \\ \dfrac{\partial \boldsymbol{\phi}_R}{\partial \mathbf{n}} = \overline{\mathbf{n}}, \quad \dfrac{\partial(\phi_I + \phi_D)}{\partial \mathbf{n}} = 0, & \mathbf{X} \in \overline{S}_B \\ \dfrac{\partial \phi}{\partial z} = 0, & \mathbf{X} \in S_D : z = -H, \end{cases} \tag{30.4}$$

where $\mathbf{X} = [x \ y \ z]^\mathsf{T}$ is the field point, $\mathbf{n}$ the normal vector at body surface pointing out of fluid, and $\overline{\mathbf{n}} = [\mathbf{n}; \ \mathbf{r} \times \mathbf{n}]$, $\mathbf{r}$ is the position vector on the body surface. According to Airy's wave theory, the incident wave propagating along positive X direction takes the form

$$\phi_I(x, y, z, \omega) = \frac{ig}{\omega} \cdot \frac{\cosh[k(z+H)]}{\cosh(kH)} e^{ikx}, \tag{30.5}$$

where k is the wave number satisfying the dispersion relation

$$\omega^2 = gk \tanh(kH). \tag{30.6}$$

In addition, to guarantee the uniqueness of the solutions to Eq. 30.4, the radiation conditions at infinity [18] are introduced:

$$\lim_{x \to \pm\infty} \left(\frac{\partial \boldsymbol{\phi}_R}{\partial x} \mp ik\boldsymbol{\phi}_R \right) = 0, \quad \lim_{x \to \pm\infty} \left(\frac{\partial \phi_D}{\partial x} \mp ik\phi_D \right) = 0. \tag{30.7}$$

With the velocity potentials (Φ_I, Φ_R, and Φ_D), hydrodynamic pressure p can be obtained according to Bernoulli's equation (Eq. 30.2) with the high-order term $\frac{1}{2}\rho(\nabla\Phi)^2$ neglected, and the hydrodynamic forces acting on the body can be determined by integrating the pressure over the body surface $\overline{S}_B$. The total force/moment can be expressed as the sum of hydrostatic force/moment $\mathbf{F}_{HS}$, radiation force/moment $\mathbf{F}_R$, and wave excitation force/moment $\mathbf{F}_{Wt}$:

$$\begin{aligned} \mathbf{F}_{HS} &= -\rho g \iint_{\overline{S}_B} z\overline{\mathbf{n}}\, dS = \mathbf{F}_B - \mathbf{K}_{HS}\boldsymbol{\xi}(t), \\ \mathbf{F}_R &= -\rho \iint_{\overline{S}_B} \frac{\partial \Phi_R}{\partial t} \overline{\mathbf{n}}\, dS = -\frac{1}{2\pi} \int_{-\infty}^{\infty} \left[\boldsymbol{\lambda}(\omega) i\omega \overline{\mathbf{V}}(\omega) + \boldsymbol{\mu}(\omega)\overline{\mathbf{V}}(\omega) \right] e^{i\omega t}\, d\omega, \\ \mathbf{F}_{Wt} &= -\rho \iint_{\overline{S}_B} \frac{\partial}{\partial t}(\Phi_I + \Phi_D)\overline{\mathbf{n}}\, dS = \Re\left\{ \frac{1}{2\pi} \int_{-\infty}^{\infty} \overline{\eta}(\omega)\mathbf{F}_W(\omega) e^{i\omega t}\, d\omega \right\}, \end{aligned} \tag{30.8}$$

where $\mathbf{F}_B$ is static buoyance force that is balanced by gravitational force of the structure, $\mathbf{K}_{HS}$ the hydrostatic restoring stiffness, and $\boldsymbol{\lambda}$, $\boldsymbol{\mu}$, and $\mathbf{F}_W$ denote the frequency-dependent added mass, radiation damping, wave excitation force transfer function matrices, respectively,

$$\begin{aligned} \boldsymbol{\lambda}(\omega) &= \rho \iint_{\overline{S}_B} \overline{\mathbf{n}} \left[\boldsymbol{\phi}_R^{Re} \right]^\mathsf{T} dS, \\ \boldsymbol{\mu}(\omega) &= -\rho\omega \iint_{\overline{S}_B} \overline{\mathbf{n}} \left[\boldsymbol{\phi}_R^{Im} \right]^\mathsf{T} dS, \\ \mathbf{F}_W(\omega) &= -\rho i\omega \iint_{\overline{S}_B} (\phi_I + \phi_D)\, \overline{\mathbf{n}}\, dS. \end{aligned} \tag{30.9}$$

The equations of motion of the floating platform built upon the hydrodynamic coefficients (Eq. 30.9) are a set of linear equations:

$$\left\{ -\omega^2 \left[\mathbf{M} + \boldsymbol{\lambda}(\omega) \right] + i\omega\boldsymbol{\mu}(\omega) + \mathbf{K}_{HS} \right\} \overline{\boldsymbol{\xi}}(\omega) = \overline{\eta}(\omega)\mathbf{F}_W(\omega), \tag{30.10}$$

where **M** is the rigid-body mass of the platform. Despite the simplicity of the frequency-domain analysis approach, it cannot capture the nonlinear dynamic behavior and time transients of the system, which are crucial for the dynamic analysis of FWTs. In light of this, Cummins equation [19] is introduced, which converts the frequency-domain equations (Eq. 30.10) into a set of integro-differential equations with constant coefficients and convolution terms

$$[\mathbf{M} + \boldsymbol{\lambda}(\infty)]\,\ddot{\boldsymbol{\xi}}(t) + \int_0^t \mathbf{K}(t-\tau)\dot{\boldsymbol{\xi}}(\tau)d\tau + \mathbf{K}_{HS}\boldsymbol{\xi}(t) = \mathbf{F}_{Wt}, \tag{30.11}$$

where $\mathbf{K}(t)$ is the impulse response function representing the fluid-memory effect:

$$\mathbf{K}(t) = \frac{2}{\pi}\int_0^\infty \boldsymbol{\mu}(\omega)\cos(\omega t)d\omega. \tag{30.12}$$

30.2.2 Numerical Approach to Solving the BVP: BEM

The boundary element method, BEM, solution is based on Green's Theorem that transfers the computation region from the whole fluid domain to closed boundary surfaces. The free-surface Green function source potential $G(\mathbf{x}, \mathbf{y})$ ($\mathbf{x}$: source point, $\mathbf{y}$: field point) that is introduced to derive the boundary integral equation automatically satisfies Laplace's equation, free-surface, sea-bottom, and radiation boundary conditions (Eq. 30.4 except that on $\overline{S}_B$, and Eq. 30.7). As a result, the integration region reduces to only the body surface $\overline{S}_B$ and thus significantly increases the computational efficiency. The reduced boundary integral equations take the form of

$$\begin{aligned} 2\pi\phi_{Rj}(\mathbf{y}) + \iint_{\overline{S}_B} \phi_{Rj}(\mathbf{x})\frac{\partial G(\mathbf{x},\mathbf{y})}{\partial \mathbf{n}(\mathbf{x})}d\mathbf{x} &= \iint_{\overline{S}_B} \overline{n}_j(\mathbf{x})G(\mathbf{x},\mathbf{y})d\mathbf{x}, \\ 2\pi\phi_D(\mathbf{y}) + \iint_{\overline{S}_B} \phi_D(\mathbf{x})\frac{\partial G(\mathbf{x},\mathbf{y})}{\partial \mathbf{n}(\mathbf{x})}d\mathbf{x} &= -\iint_{\overline{S}_B} \frac{\partial \phi_I(\mathbf{x})}{\partial \mathbf{n}(\mathbf{x})}G(\mathbf{x},\mathbf{y})d\mathbf{x}, \end{aligned} \tag{30.13}$$

where j denotes the platform motion in the j-th Dof. The mean wetted surface $\overline{S}_B$ can be approximated by a set of quadrilateral or triangular plane panels $\overline{S}_B \approx \sum_{l=1}^N s_l$, where $l = 1, 2, \ldots, N$, N denotes the number of panels, and s_l denotes the surface of the l-th panel. The velocity potentials are assumed to be constant over each of the panels. In doing so, the boundary integral equations Eq. 30.13 can be discretized into a set of linear algebraic equations that enables a robust numerical solution method:

$$\begin{aligned} 2\pi\phi_{Rj}(\mathbf{y}_r) + \sum_{l=1,l\neq r}^{N} \phi_{Rj}(\mathbf{x}_l)D_{rl} &= \sum_{l=1,l\neq r}^{N} \overline{n}_j(\mathbf{x}_l)S_{rl}, \\ 2\pi\phi_D(\mathbf{y}_r) + \sum_{l=1,l\neq r}^{N} \phi_D(\mathbf{x}_l)D_{rl} &= -\sum_{l=1,l\neq r}^{N} \frac{\partial \phi_I(\mathbf{x}_l)}{\partial \mathbf{n}(\mathbf{x})}S_{rl}, \end{aligned} \tag{30.14}$$

where

$$D_{rl} = \iint_{s_l} \frac{\partial G(\mathbf{x},\mathbf{y}_r)}{\partial \mathbf{n}(\mathbf{x})}d\mathbf{x}, \quad S_{rl} = \iint_{s_l} G(\mathbf{x},\mathbf{y}_r)d\mathbf{x}. \tag{30.15}$$

With the solution of velocity potentials over all panels, the added mass, radiation damping, and wave excitation force coefficients can be calculated using the discretized version of Eq. 30.9.

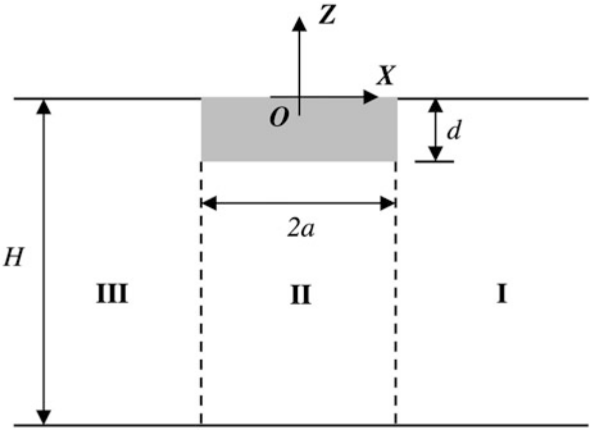

Fig. 30.2 Sketch of the 2D rectangular platform in the OXZ plane with infinite length in the Y-axis

30.2.3 Analytical Approach to Solving the BVP

The simple geometry of a 2D rectangular platform submergence area allows us to divide the fluid domain into 3 regions as depicted in Fig. 30.2. In doing so, a set of simplified BVPs with fewer inhomogeneous boundary conditions in each region are yielded, and the analytical solution to the problem can be sought. However, the conditions at the upper ($-d < z < 0$) and lower ($-H < z < -d$) parts of the same interface (e.g., $x = a$) are distinct. The exact analytical solution for this mixed boundary value problem only exists under very few cases [20]. The approximation approach of the weighted residuals method developed by Zheng et al. [15] is employed to obtain the analytical solution in this chapter.

The BVP of the radiation potential for pitch Dof in region II ($\phi_{R_{\rm II}}^{pitch}$) is presented to demonstrate the analytical method. $\phi_{R_{\rm II}}^{pitch}$ satisfies

$$\begin{cases} \dfrac{\partial^2\phi_{R_{\rm II}}^{pitch}}{\partial x^2} + \dfrac{\partial^2\phi_{R_{\rm II}}^{pitch}}{\partial z^2} = 0, & -H < z < -d,\ |x| < a \\ \dfrac{\partial\phi_{R_{\rm II}}^{pitch}}{\partial z} = -x & z = -d \\ \dfrac{\partial\phi_{R_{\rm II}}^{pitch}}{\partial z} = 0. & z = -H. \end{cases} \tag{30.16}$$

The general solution can be obtained by applying the method of separation of variables,

$$\phi_{R_{\rm II}}^{pitch} = -\frac{(z+H)^2x - x^3/3}{2(H-d)} + A_{20}x + B_{20} + \sum_{n=1}^{\infty}\left[A_{2n}e^{\beta_n(x+a)} + B_{2n}e^{-\beta_n(x-a)}\right]\cos\left[\beta_n(z+H)\right], \tag{30.17}$$

where A_{20}, B_{20}, A_{2n}, B_{2n} are constant coefficients and $\beta_n = \pm\frac{n\pi}{H-d}$. By similar means, the radiation wave potentials in regions I and III can be obtained and expressed as infinite series

$$\begin{aligned} \phi_{R_{\rm I}}^{pitch} &= A_{10}e^{ik(x-a)}\cosh\left[k(z+H)\right] + \sum_{n=1}^{\infty}A_{1n}e^{-\kappa_n(x-a)}\cos\left[\kappa_n(z+H)\right], \\ \phi_{R_{\rm III}}^{pitch} &= A_{30}e^{-ik(x+a)}\cosh\left[k(z+H)\right] + \sum_{n=1}^{\infty}A_{3n}e^{\kappa_n(x+a)}\cos\left[\kappa_n(z+H)\right], \end{aligned} \tag{30.18}$$

where A_{10}, B_{30}, A_{1n}, A_{3n} are constant coefficients, k the wave number determined by Eq. 30.6, and κ_n is the eigenvalues defined by

$$\omega^2 = -g\kappa_n\tan(\kappa_n H). \tag{30.19}$$

To determine the unknown coefficients of the orthogonal series in Eqs. 30.17 and 30.18, the continuity conditions of the pressure and normal velocity between two neighboring regions ($x = \pm a$) are imposed. Take the interface between regions I and II ($x = a$) as example, and continuity conditions for the radiated potentials in the pitch Dof can be expressed as

$$\begin{aligned} &\int_{-H}^{-d} \phi_{R_{\mathrm{I}}}^{pitch}\Big|_{x=a} \cos\left[\beta_n(z+H)\right] dz = \int_{-H}^{-d} \phi_{R_{\mathrm{II}}}^{pitch}\Big|_{x=a} \cos\left[\beta_n(z+H)\right] dz, \\ &\int_{-H}^{0} \frac{\partial \phi_{R_{\mathrm{I}}}^{pitch}}{\partial x}\bigg|_{x=a} \cos\left[\kappa_n(z+H)\right] dz = \int_{-d}^{0} z\cos\left[\kappa_n(z+H)\right] dz + \int_{-H}^{-d} \frac{\partial \phi_{R_{\mathrm{II}}}^{pitch}}{\partial x}\bigg|_{x=a} \cos\left[\kappa_n(z+H)\right] dz. \end{aligned} \tag{30.20}$$

Once all unknown coefficients are determined, the radiated and diffracted potentials can be obtained from Eqs. 30.17–30.18.

30.3 Aero-Hydro-Elastic-Control Modeling in Simulink

The FWT is a complex mechanical system including multiple components of blades, hub, nacelle, tower, floating platform, and moorings that are subjected to wind and wave loads, as well as components of generator and gearbox that operate under the regulation of the control system. MATLAB/Simulink provides a general multibody simulation package, Simscape/Multibody, which allows for the implementation of rigid and deformable body dynamics, the computation of aerodynamic and hydrodynamic loads and can be integrated with other Simulink modules for the application of control laws. Moreover, Simulink features visualization capability for 3D modeling and response. The topology of a generic FWT model in Simulink proposed in this chapter is illustrated in Fig. 30.3.

The world frame (inertia coordinate system) is defined on the still water surface. A 6-Dof joint is used to define the 3D movements of the floating platform with respect to the world frame. The hub, nacelle, and floating platform that have relatively small internal deformation can be modeled as rigid bodies with the lumped mass and inertia being defined at their centers of mass (CoM). The tower and blades deformabilities are not taken into account in the present work. They are therefore modeled as an assembly of rigid bodies with distributed mass and inertia properties. In the rotor-nacelle assembly

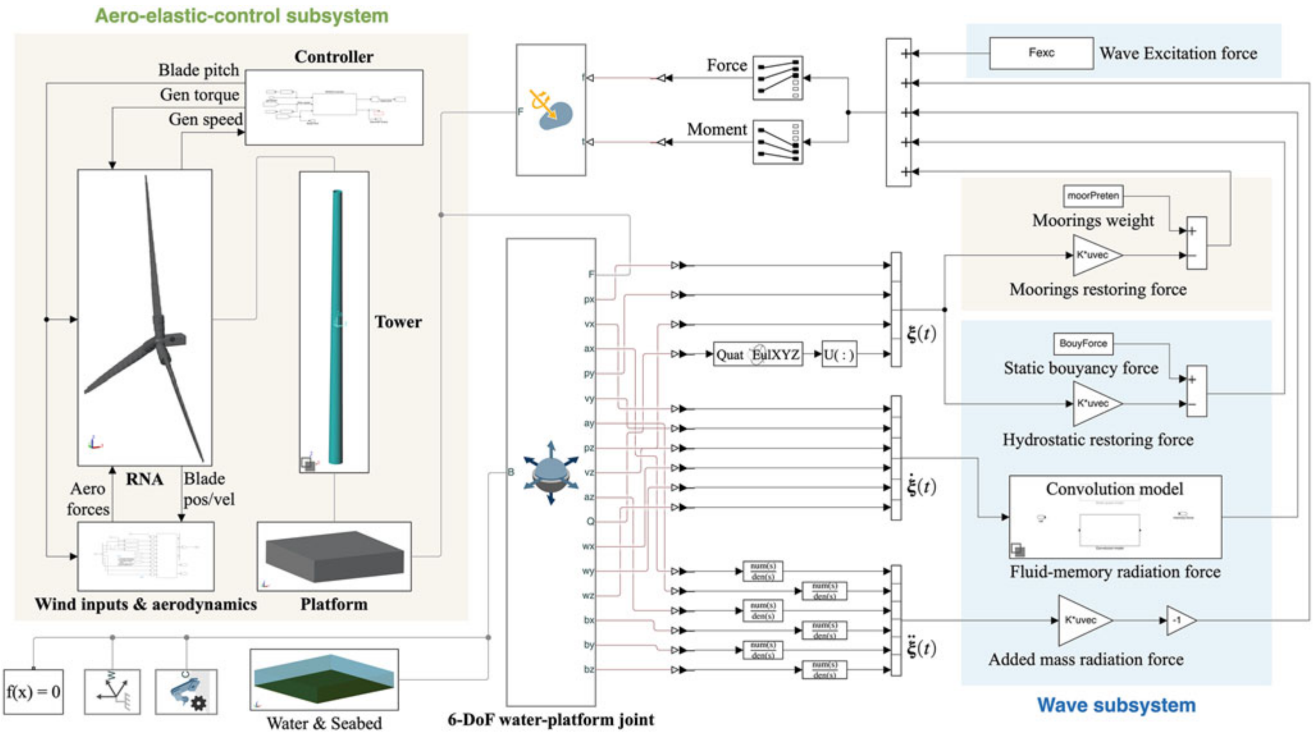

Fig. 30.3 Topology of a generic floating wind turbine developed in MATLAB/Simulink environment

(RNA), the low-speed shaft is at one end connected to the blades that are free to rotate under wind actions, and at the other end connected to the generator via a gearbox. The rotational speed of the generator is measured and fed into the controller that then outputs the blade pitch and generator torque commands to regulate the power generation following the ROSCO control strategy. A series of sensors are deployed along the blade to measure the instantaneous position and velocity at different blade cross-sections with respect to the world frame. The blade position signals are transferred to the wind inputs and aerodynamics subsystem to interpolate the inflow wind velocities felt on the blade sections from a grid of spatial wind field generated by TurbSim [21]. The inflow wind velocities, blade velocities as well as blade pitch angle are then passed to the aerodynamic computation function, which adopts the unsteady blade/element momentum method to evaluate the aerodynamic forces applied on each blade section.

The wave-body interaction effects can be determined by solving the linear BVP numerically or analytically. In order for the time-domain integration of the wave subsystem with the remaining FWT system, the direct results of the frequency-dependent hydrodynamic coefficients $\boldsymbol{\lambda}(\omega)$, $\boldsymbol{\mu}(\omega)$, $\boldsymbol{F}_W(\omega)$ obtained from both methods are converted into the infinite-frequency added mass $\boldsymbol{\lambda}(\infty)$, fluid-memory impulse response function $\mathbf{K}(t)$, and wave excitation force $\mathbf{F}_{Wt}(t)$ according to Cummins equation (Eq. 30.11). The infinite-frequency added mass is represented as a matrix as shown in Fig. 30.3, which is multiplied by the platform acceleration $\ddot{\boldsymbol{\xi}}(t)$ to get the added-mass radiation force. The fluid-memory impulse response function (Eq. 30.12) is imported in the convolution integral model coded in a Matlab function block as shown in Fig. 30.3, which receives the platform velocity $\dot{\boldsymbol{\xi}}(t)$ to calculate the fluid-memory radiation force. The integral is calculated up to a specified time horizon to enhance the computational efficiency. The hydrostatic and moorings restoring effects are both modeled with stiffness matrices, which are multiplied by the platform displacement $\boldsymbol{\xi}(t)$ to get the restoring forces. The wave excitation force is calculated by the inverse Fourier transform given the wave amplitude $\overline{\eta}(\omega)$ as presented in Eq. 30.8 and is imported as time-series data in the Simulink model. The aforementioned forces as well as the weight of moorings and displaced water by the platform are summed and applied to the 6-DoF water-platform joint as shown in Fig. 30.3. After building the full system and specifying wind and wave inputs, the time-domain dynamic analysis can be carried out by solving the equations of motion numerically using Simulink inbuilt ODE solvers.

30.4 Example and Discussions

An example of the 5-MW ITIBarge FWT [22] is taken to evaluate the Simulink modeling approach by comparing the results against those calculated from a popular FWT simulation code, OpenFAST (v3.2.1). The wave-platform interaction effect can be determined by either the open-source BEM code, Nemoh, or the analytical method. The analytical model is developed using the MATLAB/Symbolic Math Toolbox. The width of the ITIBarge cross-section is $2a = 40\,\mathrm{m}$, draft $d = 4\,\mathrm{m}$, and the water depth $H = 150\,\mathrm{m}$. The first 10 terms in the eigenfunctions of radiation and diffraction potentials at each region (e.g., 30.17, 30.18 for the radiation problem in pitch DoF) are taken to calculate the potential functions in the analytical method. In order to obtain the pseudo-2D results from the 3D BEM code Nemoh, the out-of-plane length (along Y-axis) of the platform is taken as 20 times its width (800 m in total). The analytical results are correspondingly multiplied by that length in Y-axis. The comparison between the analytical and Nemoh's results in terms of the impulse response function $\mathbf{K}(t)$ (Eq. 30.12) and wave excitation force $\mathbf{F}_W(\omega)$ (Eq. 30.9) is illustrated in Fig. 30.4a and b, respectively. It can be found that the results calculated from both methods agree well that indicates the accuracy of the analytical method. Nemoh suffers from numerically induced oscillations at certain frequencies, whereas the analytical method tends to give results that are less prone to numerically induced noise.

Only the 3 platform DoFs of surge, heave, and pitch are activated in both Simulink and OpenFAST models to investigate the planar dynamic response of the full FWT system. The ITIBarge platform is moored with 8 catenary mooring lines. Their weight and restoring stiffness are obtained from the quasi-static mooring analysis code, MAP++[23], and are imported in both Simulink and OpenFAST models. Cummins equation (Eq. 30.11) is adopted in OpenFAST to determine the hydrodynamic loads, with the time horizon of the convolution integral being set the same as that in the Simulink model (0∼40 s). The infinite-frequency added masses, fluid-memory impulse response functions, and wave excitation force transfer functions obtained from Nemoh and analytical methods are imported in the Simulink model, which are labeled as "Simulink–Nemoh" and "Simulink–Analytical," respectively. Nemoh's results are imported in OpenFAST, which is taken as the benchmark and labeled as "OpenFAST–Nemoh." In addition, the computation methods to evaluate the aerodynamics and controls in OpenFAST are set to be consistent with those employed in the Simulink model. In this case, the comparison between "Simulink–Nemoh" and "Simulink–Analytical" models demonstrates the effects of different hydrodynamic approaches on the system behavior, and the comparison between "OpenFAST–Nemoh" and "Simulink–Nemoh" models can be used to examine the implementation of FWT modeling in Simulink.

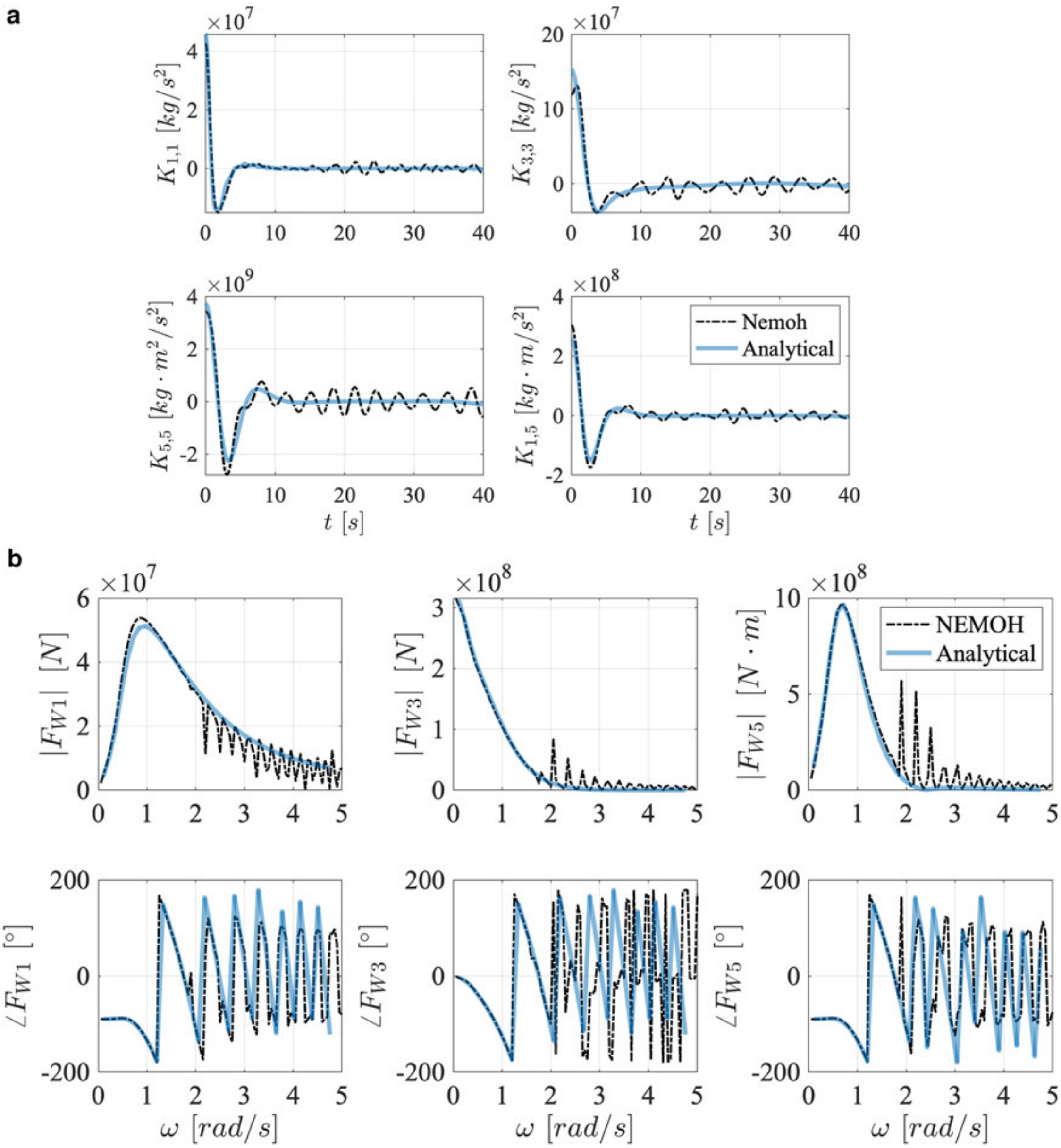

Fig. 30.4 Comparison of the impulse response functions $\mathbf{K}(t)$ and wave excitation force transfer function $\mathbf{F}_W(\omega)$ in surge–1, heave–3, and pitch–5 DoFs calculated from Nemoh and analytical methods. (**a**) Fluid-memory impulse response functions. (**b**) Wave excitation force transfer function

A steady wind field of 8 m/s, which is constant over time, is applied to both models. The JONSWAP wave spectrum [22] with the significant wave height of 2 m, the peak-spectral period of $10s$, wave direction along X-axis, and the frequency limit of 0–10 rad/s is set in OpenFAST to generate random wave amplitude time series (see Fig. 30.5). In light of the good agreement of the wave excitation transfer functions between the analytical and Nemoh results as shown in Fig. 30.4b, the wave excitation forces calculated from the wave series in OpenFAST are directly imported to the Simulink model. The time series of wave excitation force in pitch DoF is shown in Fig. 30.5. The platform pitch rotation of both the OpenFAST model and Simulink model is also depicted in Fig. 30.5, which shows well agreement among the three models. The operation conditions of the turbine for three models are compared in Fig. 30.6. The good match of rotor speed Ω_r, aerodynamic torque T_{aero}, and mechanical power generation P demonstrates the accurate implementation of the aerodynamic force and controller in Simulink compared to OpenFAST. The overall agreement in the three models verifies the ability of the developed Simulink model to predict the dynamic behavior of FWTs using either numerical or analytical hydrodynamic modeling approaches.

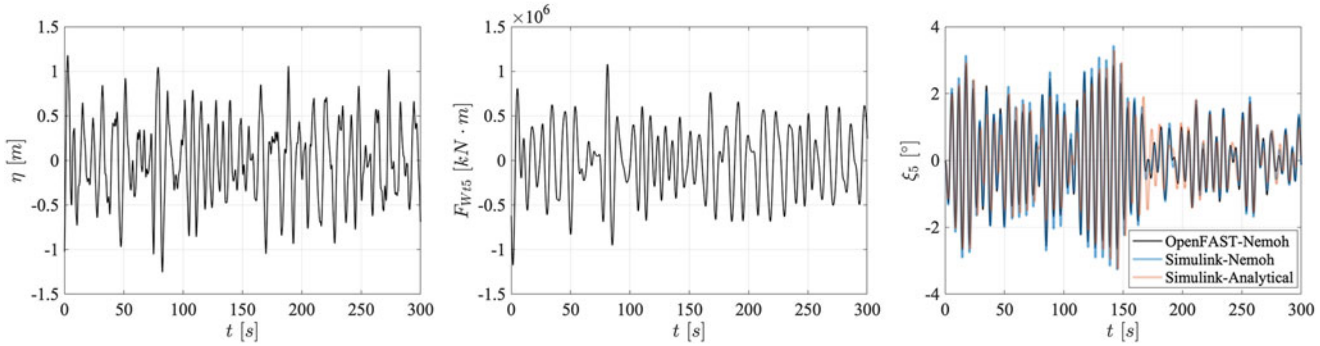

Fig. 30.5 Wave elevation η, wave excitation force in Pitch DoF F_{Wt5}, and platform pitch rotation ξ_5 for different models

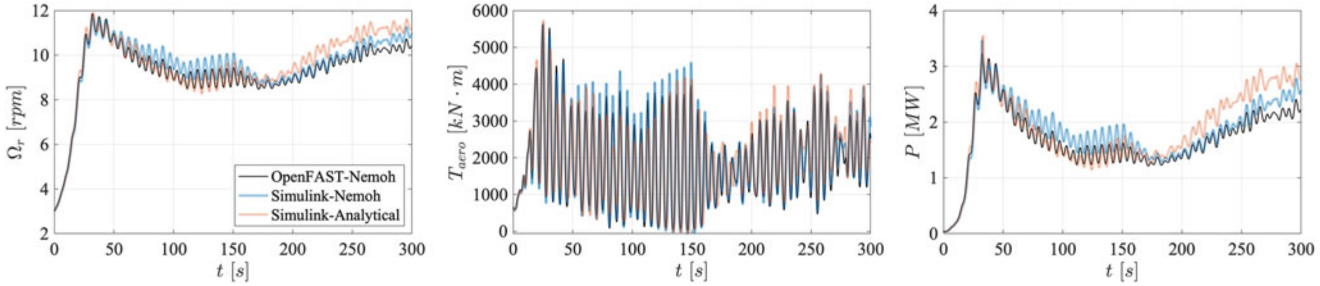

Fig. 30.6 Rotor speed Ω_r, aerodynamic torque T_{aero}, and mechanical power P obtained from different models

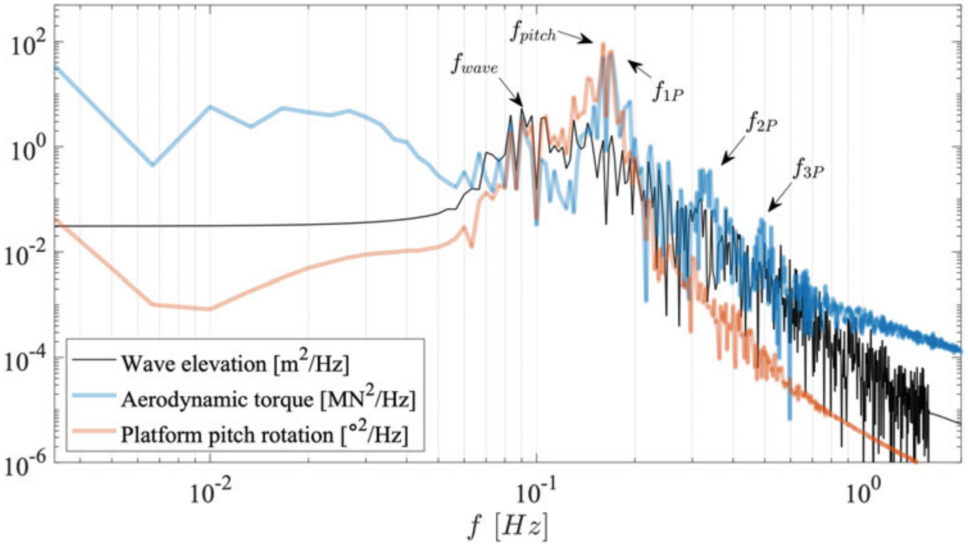

Fig. 30.7 Wave elevation, aerodynamic torque, and platform pitch rotation in the frequency domain

Figure 30.7 illustrates the wave elevation η, aerodynamic torque T_{aero}, and platform pitch rotation ξ_5 from the "Simulink–Analytical" model in the frequency domain. The predominant frequency of the wave excitation f_{wave}, natural frequency of the system in pitch DoF f_{pitch}, and the blade rotational speed and its multiples f_{1P}, f_{2P}, f_{3P} are also annotated. The platform movements modify the relative wind velocity felt by the blades and thus lead to peaks at f_{wave} and f_{pitch} in the aerodynamic torque, which also explains the occurrence of f_{1P}, f_{2P}, f_{3P} effects even under the steady wind excitation. However, due to the large inertia difference between the platform and the rotor, the platform motion is hardly affected by the loads from the rotor.

30.5 Conclusions

A new simulation framework for the dynamic modeling of FWTs is developed in this chapter. An analytical wave-platform interaction model is developed in the Symbolic Math Toolbox in MATLAB. The open-source BEM code, Nemoh, is taken as a benchmark evaluation of the analytical method. The hydrodynamic coefficients obtained from the analytical method agree well with those calculated from Nemoh and are free from the numerically induced noise. An implementation scheme involving the structural modeling, aerodynamics, and controls using Simscape/multibody and other extensive Simulink libraries is proposed in this chapter. The wave subsystem includes the additional hydro-related mass and stiffness matrices and fluid-memory convolution integrals calculated from either the analytical method or Nemoh and is integrated with the remaining FWT system. The Simulink model is validated against OpenFAST by examining the example of a 5 MW ITIBarge FWT with rigid blades and tower under steady wind and stochastic wave. In both Simulink and OpenFAST models, only the planar DoFs of surge, heave, and pitch are activated, and the out-of-plane length of the platform is taken sufficiently long to adapt to the implementation of the 2D analytical model. The Simulink model shows good agreement with OpenFAST in terms of the aerodynamic and hydrodynamic loads, controller behavior as well as platform response, which indicates Simulink model's capability to carry out robust dynamic analysis of FWTs. Future works will demonstrate the effects occurring from the flexibility of tower and blades.

References

1. IRENA, World energy transitions outlook 2022: 1.5 °C pathway (2022)
2. Wind Energy Generation Systems Part 3–2: Design Requirements for Floating Offshore Wind Turbines, IEC TS 61400-3-2:2019 (2019).
3. Skaare, B., Nielsen, F.G., Hanson, T.D., Yttervik, R., Havmøller, O., Rekdal, A.: Analysis of measurements and simulations from the Hywind demo floating wind turbine. Wind Energy **18**(6), 1105–1122 (2015)
4. Jacobsen, A., Godvik, M.: Influence of wakes and atmospheric stability on the floater responses of the Hywind Scotland wind turbines. Wind Energy **24**(2), 149–161 (2021)
5. OpenFAST Documentation, version v3.2.0. https://openfast.readthedocs.io/en/main/. Accessed 01 Oct 2022
6. Using Sesam and Bladed in one workflow, DNV GL (2020)
7. Hawc2 info. https://www.hawc2.dk/hawc2-info. Accessed 01 Oct 2022
8. Jonkman, J., Musial, W.: Offshore Code Comparison Collaboration (OC3) for IEA Wind Task 23 Offshore Wind Technology and Deployment, Technical Report, National Renewable Energy Lab. (NREL), Golden, CO (United States) (2010).
9. Robertson, A., Jonkman, J., Vorpahl, F., Popko, W., Qvist, J., Frøyd, L., Chen, X., Azcona, J., Uzunoglu, E., Guedes Soares, C., et al.: Offshore code comparison collaboration continuation within IEA wind task 30: Phase II results regarding a floating semisubmersible wind system. In: International Conference on Offshore Mechanics and Arctic Engineering, vol. 45547, p. V09BT09A012. American Society of Mechanical Engineers, New York (2014)
10. Robertson, A.N., Wendt, F., Jonkman, J.M., Popko, W., Dagher, H., Gueydon, S., Qvist, J., Vittori, F., Azcona, J., Uzunoglu, E., et al.: OC5 project phase II: validation of global loads of the DeepCwind floating semisubmersible wind turbine. Energy Procedia **137**, 38–57 (2017)
11. Wang, L., Robertson, A., Jonkman, J., Yu, Y.-H.: OC6 phase I: improvements to the OPENFAST predictions of nonlinear, low-frequency responses of a floating offshore wind turbine platform. Renewable Energy **187**, 282–301 (2022)
12. Wamit, Inc.: The state of the art in wave ineraction analysis. https://www.wamit.com/. Accessed 01 Oct 2022
13. ANSYS, AQWA Theory Manual (2015)
14. Nemoh: https://github.com/LHEEA/Nemoh. Accessed 01 Oct 2022
15. Zheng, Y., You, Y., Shen, Y.: On the radiation and diffraction of water waves by a rectangular buoy. Ocean Eng. **31**(8–9), 1063–1082 (2004)
16. Hansen, M.: Aerodynamics of Wind Turbines. Routledge, Milton Park (2015)
17. ROSCO documentation, version v2.6.0. https://rosco.readthedocs.io/en/latest/. Accessed 01 Oct 2022
18. Wehausen, J.V.: The motion of floating bodies. Ann. Rev. Fluid Mech. **3**(1), 237–268 (1971)
19. Cummins, W.E.: The impulse response function and ship motions. Schiffstechnik **9**, 101–109 (1962)
20. Duffy, D.G.: Mixed Boundary Value Problems. Chapman and Hall/CRC, Boca Raton (2008)
21. Turbsim, https://www.nrel.gov/wind/nwtc/turbsim.html. Accessed 01 Oct 2022
22. Jonkman, J.M.: Dynamics Modeling and Loads Analysis of an Offshore Floating Wind Turbine, University of Colorado at Boulder (2007)
23. Map++, https://www.nrel.gov/wind/nwtc/map-plus-plus.html. Accessed 01 Oct 2022

Chapter 31
Evaluating Rhythmic Jumping on Vibrating Platform Using Kinematic Data

Nimmy Mariam Abraham, Genevieve Williams, and Stana Živanović

Abstract Rhythmic jumping can be expected on grandstands during music and sports events and imparts dynamic load on to the structure. This often results in safety and serviceability concerns. Human interaction with vibrations is the key aspect that influences both human and structural response and therefore evaluating this interaction is important. To this end, this paper has compared four methods of analysing rhythmic jumping on vibrating structures using kinematic data. Vector coding method was found to be the most informative. The original vector coding procedure has been modified in this paper to propose a new strategy for classifying the coordination patterns between feet and platform motion. The method can be used to evaluate whether a jumper can achieve a target frequency and target timing of the jumping as well as to quantify the variability in jumping over time. In addition, the method enables quantification of duration of contact phase of a jumping cycle.

Keywords Rhythmic jumping · Vertical harmonic vibration · Kinematics · Vector coding · Coupling angle

31.1 Introduction

Rhythmic jumping occurs when a person alternates between contact and flight phases at a given frequency. It is one of the most common activities during music and sports events on grandstands. People jumping generate larger dynamic force than other human activities including walking, dancing, stamping, hand clapping, swaying, abrupt rising, standing and bobbing. A recent example of a partial collapse of the football stadium in the Netherlands, amid crowd celebrations in response to players jumping in celebration on the pitch [1], is an illustration of potential vulnerability of stands to human actions. In many cases, the frequency of rhythmic jumping or one of its integer multiples matches one of the natural frequencies of the structure, causing large vibration response, referred to as resonance. Besides frequency match, the severity of vibrations depends on human-structure interaction (HSI) and the liveliness (i.e. proneness to vibration) of the structure [2]. The HSI here refers to adaptation of the human kinematics (i.e. body motion) and the resulting ground reaction force (GRF) to the structural vibration and impact of this adaptation on structural behaviour. This paper investigates the adaptation of human kinematics while rhythmically jumping on a vibrating platform. Specifically, the coordination between feet and platform movement is analysed for four scenarios at which the human targeted landing on the platform at different platform positions in the vibrating cycle. This study identifies and compares different methods for analysing rhythmic jumping activity on vibrating platforms.

N. M. Abraham (✉) · S. Živanović
Faculty of Environment, Science and Economy, University of Exeter, Exeter, UK
e-mail: na484@exeter.ac.uk; S.Zivanovic@exeter.ac.uk

G. Williams
Faculty of Health and Life Sciences, University of Exeter, Exeter, UK
e-mail: G.K.R.Williams@exeter.ac.uk

H. Y. Noh et al. (eds.), *Dynamics of Civil Structures, Volume 2*, Conference Proceedings of the Society for Experimental Mechanics Series, https://doi.org/10.1007/978-3-031-36663-5_31

31.2 Test Details and Data

Tests were conducted at the VSimulators, i.e. the motion platform facility of the University of Exeter. The test set up includes VSimulators platform into which AMTI force plates are embedded and an OptiTrack motion capture system consisting of a system of cameras. Test subjects (TSs) were asked to jump rhythmically on the platform at specified target frequencies for conditions of vibrating and stationary platform. Platform vibrations were vertical and harmonic with specific vibration parameters (e.g. frequency of 2 Hz and amplitude of 2 m/s^2). To facilitate recording of body motion, the TSs were required to wear motion capture suits on which reflective markers were attached. Conventional full body marker set comprising of 39 markers was adopted. Additionally, four markers were placed at the four corners of the platform to enable recording of platform motion. Kinetic (i.e. GRF) and kinematic data (i.e. marker trajectories) were collected of which only the vertical displacement of the left toe marker and one of the platform markers are analysed here. The test series involved rhythmic jumping by 10 test subjects on vibrating and stationary surfaces. A TS photographed during one of the trials is shown in Fig. 31.1. The data from tests performed by TS4 are analysed here.

TS4 was 24 years old, male, 182 cm tall, had body mass of 65.8 kg and stated that he exercised about 6 hours per week and was not prone to motion sickness. The TS was asked to perform jumping on the vibrating surface at a metronome controlled jumping frequency of 2 Hz. The platform's vibration magnitude was 2 m/s^2, and vibration frequency was 2 Hz. The TS was instructed to land at specific time instances in vibration cycles of the platform. These were landing on the platform while at its (i) lowest position in the vibrating cycle (trough), (ii) reference position and on the way up (mid-up), (iii) highest position (peak) and (iv) reference position and on the way down (mid-down). The target timing instance was presented to the TS through a metronome beat. The timing of the beat for the four cases is visualised in Fig. 31.2. The duration of each trial was set based on the target jumping frequency to accommodate 40 cycles of jumping.

The raw displacement data were low pass filtered using a fourth order zero phase Butterworth filter with a cut off frequency of 10 Hz. The first 10 cycles of jumping in each test were excluded from the analysis so that only steady-state action of the TS is considered.

31.3 Analysing Rhythmic Jumping on Vibrating Platform

A cycle of rhythmic jumping consists of a flight phase that occurs between take-off and landing and a contact phase that occurs between landing and take-off. During the contact phase, load is exerted on the structure through feet contact with the platform. If vibration is present, the jumper's feet get driven by the platform until the take-off. This results in the adaptation of toe movement based on the target timings for landing on the platform. Hence, jumping on a vibrating platform differs from that on a stationary platform. Given that the toe displacement gets adapted based on the target timings for landing on the platform, an important question is whether a jumper can achieve a target set in terms of frequency and timing of the

Fig. 31.1 TS jumping on VSimulators platform

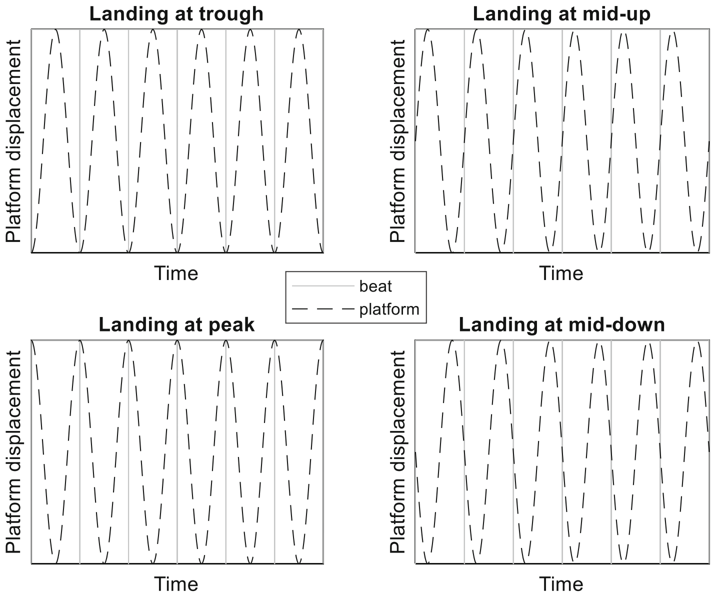

Fig. 31.2 Four cases of target timings for landing on the platform

jumping. Quantifying the variability in jumping over cycles and estimating the duration of contact phase where loading on the supporting structure happens are also significant. To address these intricacies, four methods of analysis are employed and compared. The first method is based on qualitative comparison of time histories. The second is discrete relative phase (DRP), which considers discrete variables to analyse every vibration and jumping cycle. The third method looks at the correlation between platform and toe motion via displacement-displacement plots. Finally, the fourth method uses the vector coding technique to present coupling angle between platform and toe displacements.

31.4 Qualitative Comparison of Time Histories

The most direct way to compare the kinematic data is to visualise the time histories of the signals of interest. Figure 31.3a shows the vertical displacement of toe marker and the position of platform while the TS jumps at 2 Hz on a stationary platform. The timing of metronome beats is indicated for reference. As it is cumbersome to extract information from this representation, the same data is plotted in Fig. 31.3b on a cycle-by-cycle basis. Landing, take-off, contact phase and flight phase are also indicated.

The cycle-by-cycle representation allows qualitative understanding of variability over cycles from the spread of the displacement profile across the cycles. The achievement of target frequency can be qualitatively assessed from the time of occurrence of a specific event, for example the peak displacement across the cycles. The achievement of target timing for landing on the platform can be visualised by comparing the shape of the displacement profiles of platform and toe. This is relevant for a vibrating platform, where a displacement profile exists. The flight and contact phases can also be observed from Fig. 31.3b. Figure 31.4 shows the time history of toe and platform displacements on a cycle-by-cycle basis for jumping under vibrations at four target timings. It can be seen that the TS landed approximately a quarter of cycle earlier than the beat at all four target timings. Variability in jumping across cycles can be assessed, and success in achieving target frequency and target timing can be evaluated from the plots in Fig. 31.4. The shape of the toe displacement profile during contact phase is distinct for each target landing timing while jumping on vibrating platform. The adaptation of toe motion in the contact phase can be visualised by comparing them with the displacement profile on stationary profile in Fig. 31.3b. Figure 31.4 indicates that the variability of contact phase across vibration cycles is low compared to that in flight phase in all the cases shown here. While this qualitative insight is useful, it neither quantifies the coordination between platform and jumping, nor its variability.

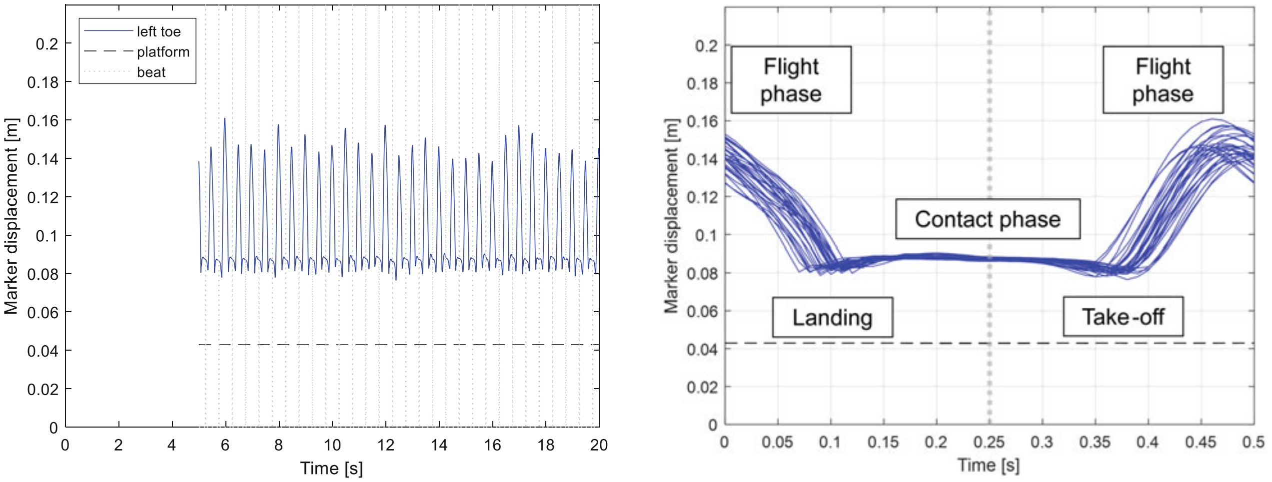

(a) *(b)*

Fig. 31.3 Toe displacement (blue continuous) and platform position (black dashed) for jumping on stationary platform (**a**) Time history (**b**) Time history on a cycle-by-cycle basis (grey dotted pointer indicates the timing of metronome beat)

31.5 Discrete Relative Phase (DRP)

DRP represents cycle-by-cycle time delay (latency) of an event in the motion of a segment with respect to the motion of another segment [3]. In the present context, the segments are platform and toe. The peak displacement of each cycle is used as the event to evaluate DRP as

$$\mathrm{DRP} = \frac{(t_2 - t_1)}{T} \times 360^\circ \tag{31.1}$$

where t_1 is time to peak platform displacement, t_2 is time to peak toe displacement and T is the period of the platform's vibration cycle. The variation of DRP between toe and platform displacements across cycles while jumping under vibrations at four target timings is shown in polar plots in Fig. 31.5. A DRP of 90° indicates landing at the trough position of the platform. DRP is 180° for landing at mid-up, 270° for landing at peak and 0° for landing at mid-down positions of platform. Note that the TS landed approximately a quarter of cycle earlier than the target in all four cases. An example of inconsistent landing timing can be seen in Fig. 31.5d. This method has the merit of quantification of target achievement over the qualitative results obtained from the previous qualitative comparison. However, the quantification is with respect to a discrete event during a vibration cycle, which therefore does not provide insight into the adaptation of toe motion during a vibration cycle. The information on flight and contact phases and coordination during a cycle except during the chosen event cannot therefore be obtained.

31.6 Qualitative Comparison of Displacement-Displacement Plots

This method involves plotting platform displacement against toe displacement and observing the correlation between them. This is similar to time history method, but the information on both the displacements are combined into a single plot rather than separate plots. The correlation between toe and platform displacements across cycles while jumping under vibrations at four target timings is shown in Fig. 31.6.

The plots provide qualitative information on target achievement and the phases in a cycle. The spread in the graph represents variability across cycles. A unique feature that contains information on platform-activity correlation is the slope of the graph. A positive slope indicates a positive correlation where both the platform and the toe move in the same direction, either up or down. A negative slope shows a negative correlation where the platform and the jumper move in the opposite directions. The contact phase is separated from the flight phase by a positively sloping region with low variability across cycles. In Fig. 31.6a, the correlation is positive throughout, with regions of two different slopes for contact and flight phases.

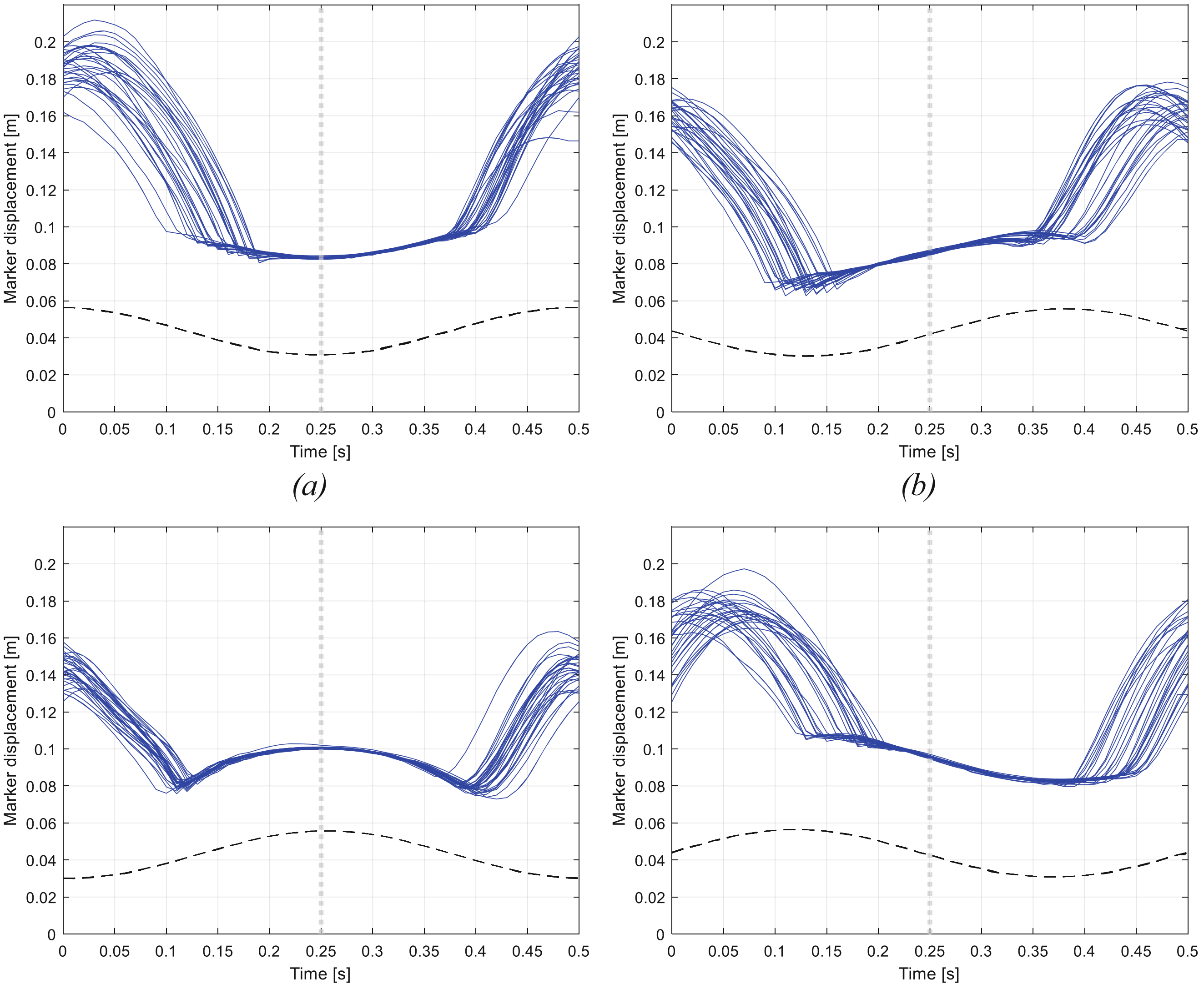

(a) *(b)* *(c)* *(d)*

Fig. 31.4 Toe (blue continuous) and platform (black dashed) displacements on a cycle-by-cycle basis for jumping on vibrating platform with target landing at (**a**) trough (**b**) mid-up (**c**) peak (**d**) mid-down positions of platform (grey dotted pointer indicates the timing of metronome beat)

In Fig. 31.6b, the correlation is positive during the contact phase, whereas the flight phase has regions of both positive and negative correlations. In Fig. 31.6c, the correlation is positive in the contact phase and negative in the flight phase. In Fig. 31.6d, the correlation is positive during the contact phase, whereas the flight phase has regions of both positive and negative correlations. Thus, the overall shape of the plots suggests the timings of landing on the platform. The change in correlation during a cycle observed in this representation cannot be captured using the previous methods. Nevertheless, this method provides only a qualitative approach in understanding the coordination between jumping and the platform's vibration.

31.7 Modified Vector Coding

Vector coding is another technique that can be employed to understand the dynamic interaction between platform and toe displacements while jumping on a vibrating platform. In this method, the relative motion between two segments is quantified by calculating the vector orientation between adjacent points, referred to as coupling angle [4–6]. Coupling angle (γ) between

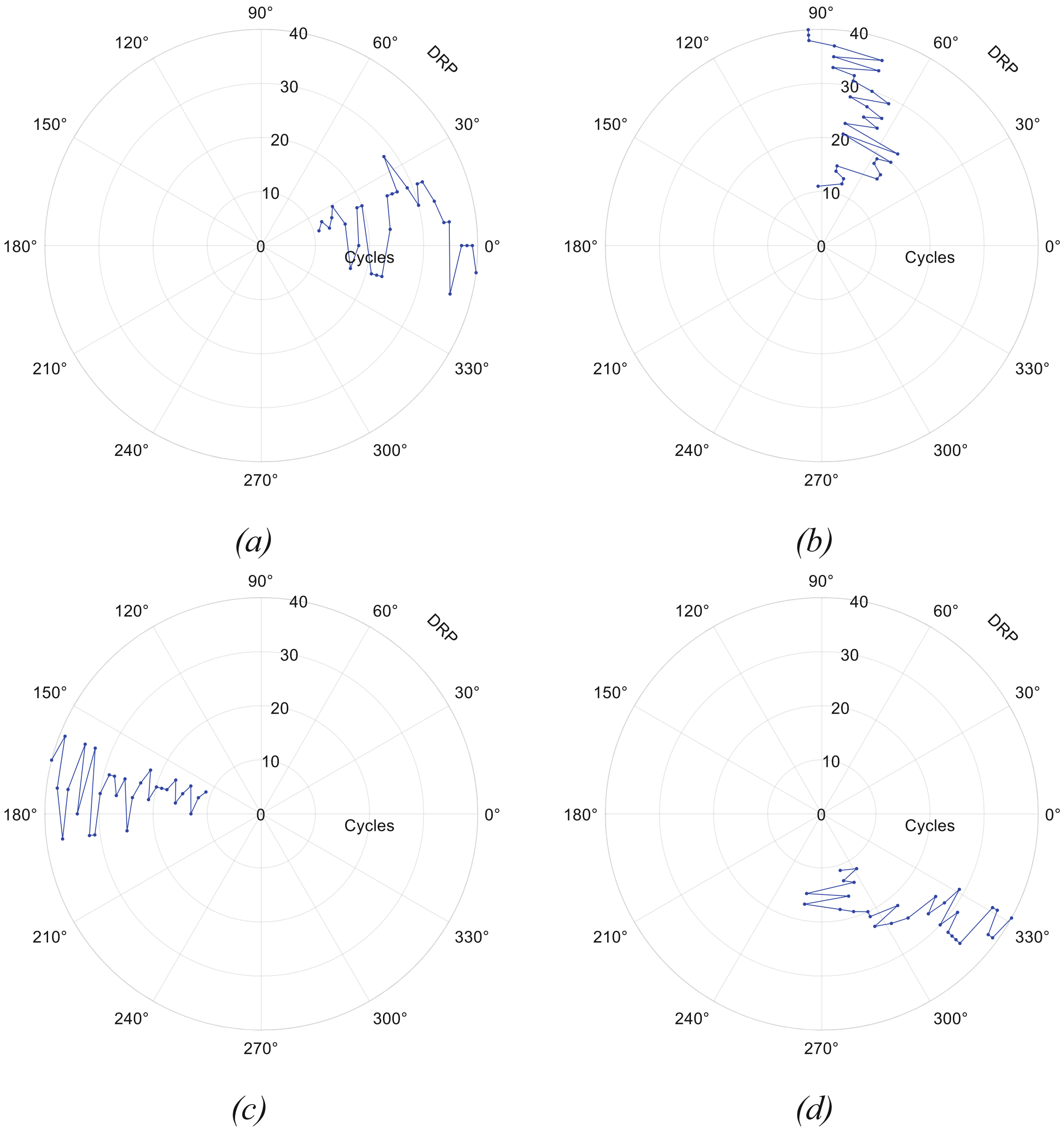

(a) *(b)*

(c) *(d)*

Fig. 31.5 DRP between toe and platform displacements for jumping on vibrating platform with target landing at (**a**) trough (**b**) mid-up (**c**) peak (**d**) mid-down positions of platform

y and x, representing platform displacement and body displacement in this case, respectively, is defined as

$$\gamma = \tan^{-1}\left(\frac{y_{i+1} - y_i}{x_{i+1} - x_i}\right) \tag{31.2}$$

where $i = 1, 2, 3\ldots$ are the instants where the displacements are recorded. Calculation of coupling angle is illustrated in Fig. 31.7. Coupling angle is represented by a value between 0° and 360°. As it is directional, circular statistics can be applied to calculate the mean and variability of multiple cycles of a task like rhythmic jumping. Classification of the coupling angle into distinct classes (bins) based on the pre-defined range in which the angles fall helps to understand movement coordination during jumping. The usually identified four coordination patterns are: in-phase (22.5°–67.5°, 202.5°–247.5°), anti-phase (112.5°–157.5°, 292.5°–337.5°), body-dominant phase (0°–22.5°, 157.5°–202.5°, 337.5°–360°) and platform-dominant phase (67.5°–112.5°, 247.5°–292.5°).

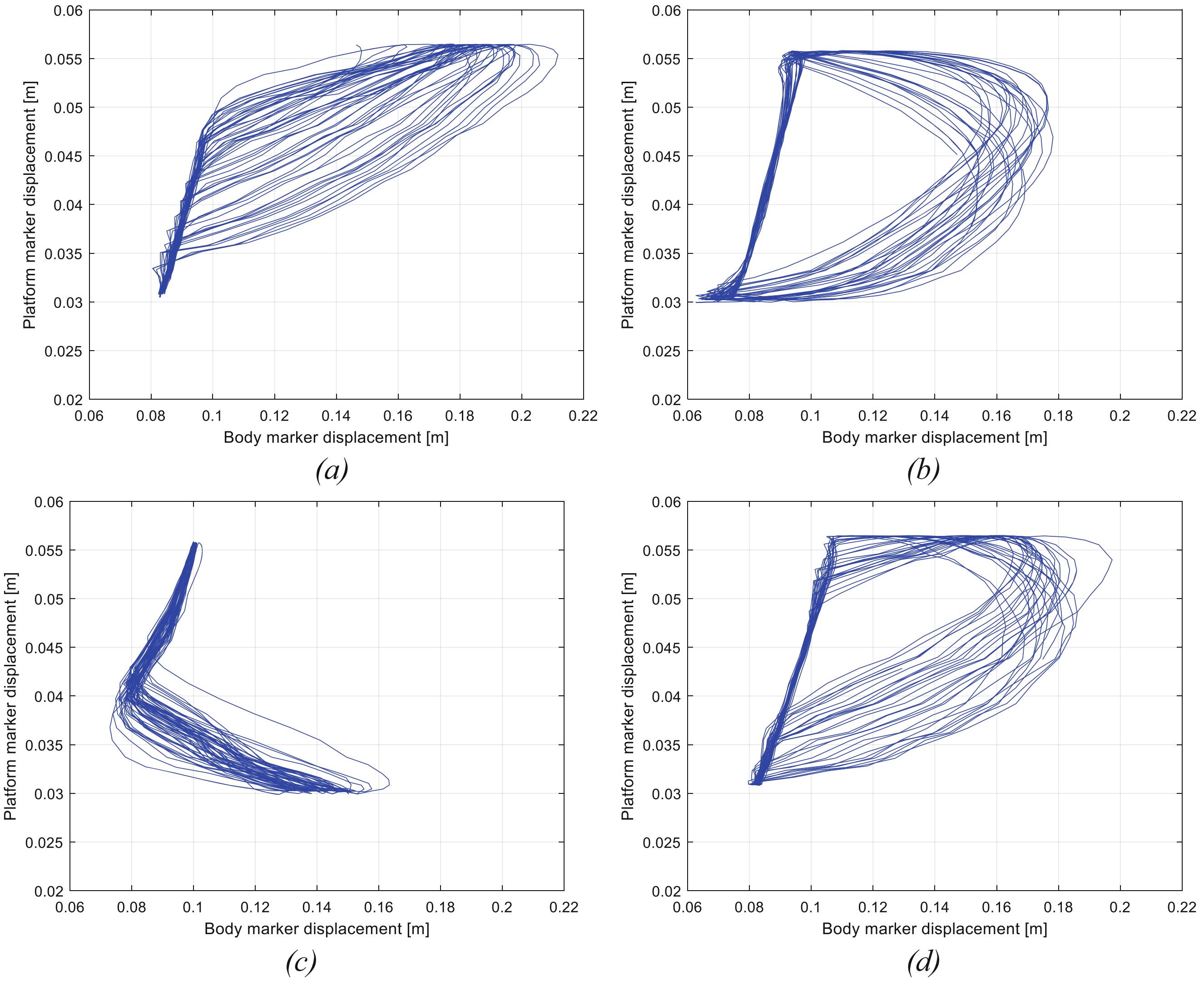

Fig. 31.6 Correlation between toe and platform displacements for jumping on vibrating platform with target landing at (**a**) trough (**b**) mid-up (**c**) peak (**d**) mid-down positions of platform

In this study, the bins are modified based on the ratio of maximum displacements of platform ($y_{\max}$) to that of toe ($x_{\max}$) for each trial. The new bins are flight in-phase and anti-phase (around 0° and 180°), contact in-phase (around 45° and 225°), platform dominance (around 90° and 270°) and anti-phase during transition between phases (around 135° and 315°). The bin edges (b_i) are calculated as shown in Fig. 31.8. This modification allows to negate dominancy of toe displacement over platform displacement and separates out the contact phase from the rest of the cycle. Thus, the ratio of contact phase duration to the time period of the cycle can be calculated from the ratio of population falling in the contact phase bin.

Figure 31.9 shows the polar plots of coupling angle and their respective bins while jumping under vibrations at four target timings for landing on the platform. In Fig. 31.9a, the toe displacement is always in phase with the platform displacement. The contact and flight phases are separated using the modified bins. In Fig. 31.9b and 31.10d, the contact phase is always in phase, whereas the flight phase has both in-phase and anti-phase regions. In Fig. 31.9c, the contact phase is always coordinated in phase in contrast to the anti-phase coordination of the flight phase. Thus, the adaptation of toe motion while jumping at four target landing instances is quantified through binning of coupling angles. The percentage duration of contact phase are 26.9, 27.8, 36.9 and 32.9 for target landing at trough, mid-up, peak and mid-down, respectively. This does not include the duration of landing and take-off. The contact duration is minimum when the target landing is at the trough and maximum when it is at the peak of the vibration cycle. Figure 31.10 shows the coefficient of variation (CoV) of coupling angle between toe and platform displacements across cycles at the four target timings for landing on the platform. CoV indicates the variability across cycles of jumping at instances along cycle. Variability is high during change in direction of

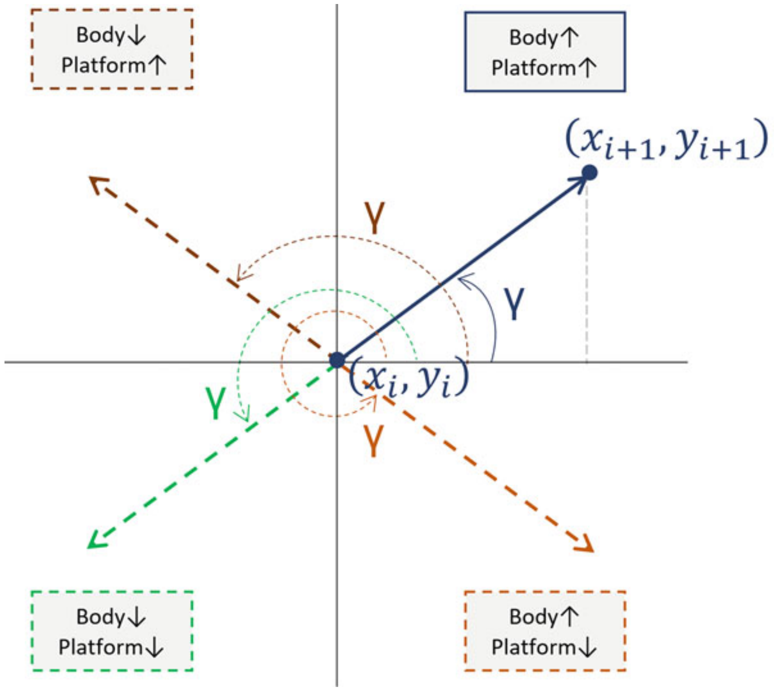

Fig. 31.7 Calculation of coupling angle for different coordination patterns

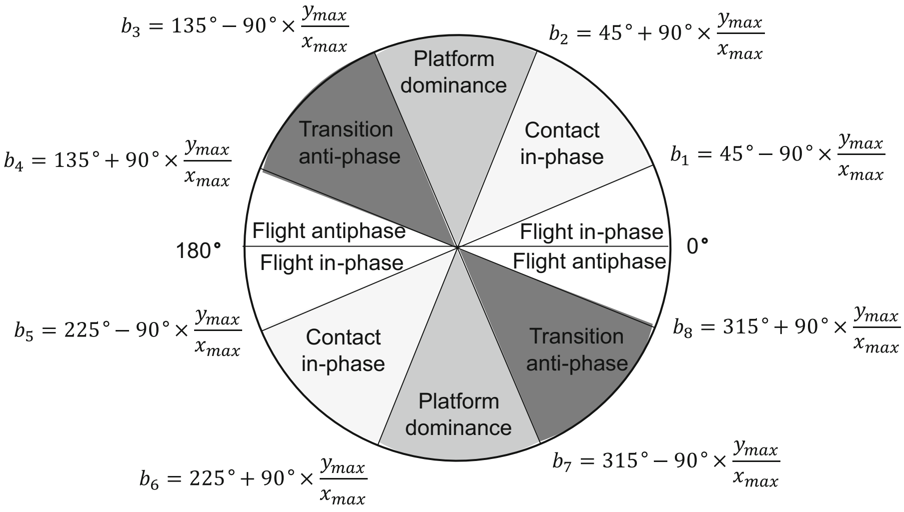

Fig. 31.8 Modified definition of coupling angle bins

toe motion, i.e., during landing, take-off and at peak displacement. At these instances, the coupling angle shifts across bins leading to higher variability at transitions. The variability is in general low during contact phase.

31.8 Comparison and Discussion

Some aspects of rhythmic jumping have been analysed using qualitative comparison of time histories, DRP, qualitative comparison of displacement-displacement plots and modified vector coding. The methods using time histories and displacement-displacement plots provide qualitative insight into events during a jumping cycle and across all cycles in a trial. The adaptation of toe displacement in the contact phase is observed and the variability across jump cycles is qualitatively assessed. Using DRP method, the latency of peak displacements between platform and toe was calculated,

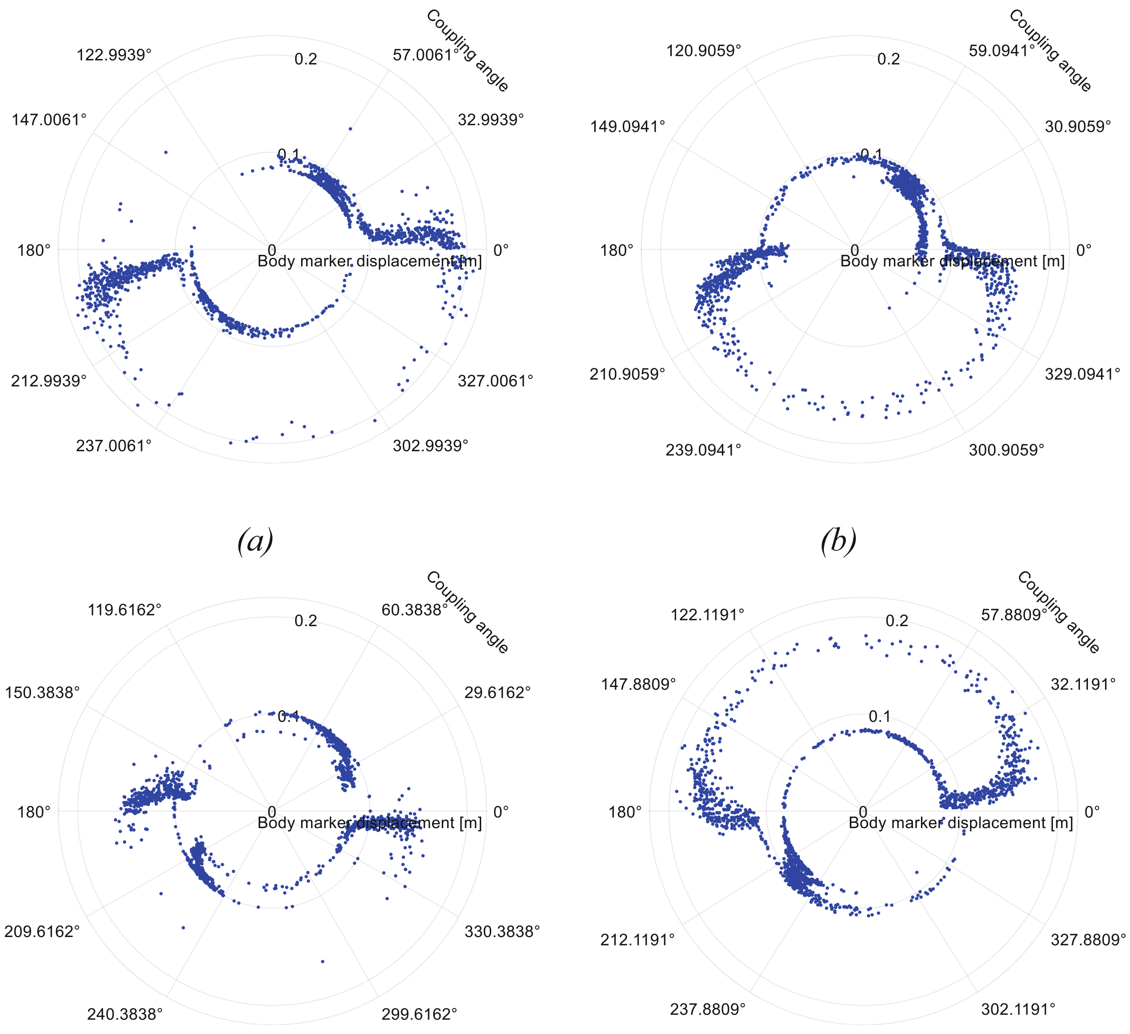

(a) *(b)*

(c) *(d)*

Fig. 31.9 Polar plots of coupling angle between toe and platform displacements (angular axis) against toe displacement (radial axis) for jumping on vibrating platform with target landing at (**a**) trough (**b**) mid-up (**c**) peak (**d**) mid-down positions of platform

which enabled assessment of target achievement. However, this method is based on one discrete point in a cycle only. Vector coding technique is employed to evaluate the coordination between platform and toe motion by calculating coupling angles throughout jumping cycles. A modified binning strategy for coupling angle is adopted to classify the instants during a jumping cycle into contact and flight phases. This allowed systematic verification of target achievement based on expected coordination patterns for a given target timings for landing on the platform. The CoV of coupling angles revealed the variability of toe displacement across cycles of jumping. Furthermore, the duration of contact phase is calculated as a percentage of total duration of the jumping cycle. Thus the modified vector coding technique proposed in this paper is a powerful method for analysing rhythmic jumping under vibrations. All the methods reviewed here are entirely based on kinematics, thus can be adopted for field tests by using one or few inertial measurement unit(s) placed at representative body landmarks. Finally, this study shows that toe displacement is an informative variable that can be used to extract knowledge on HSI during jumping. The reason is that the toes are in direct contact with the platform, thereby being the most influenced part of the body.

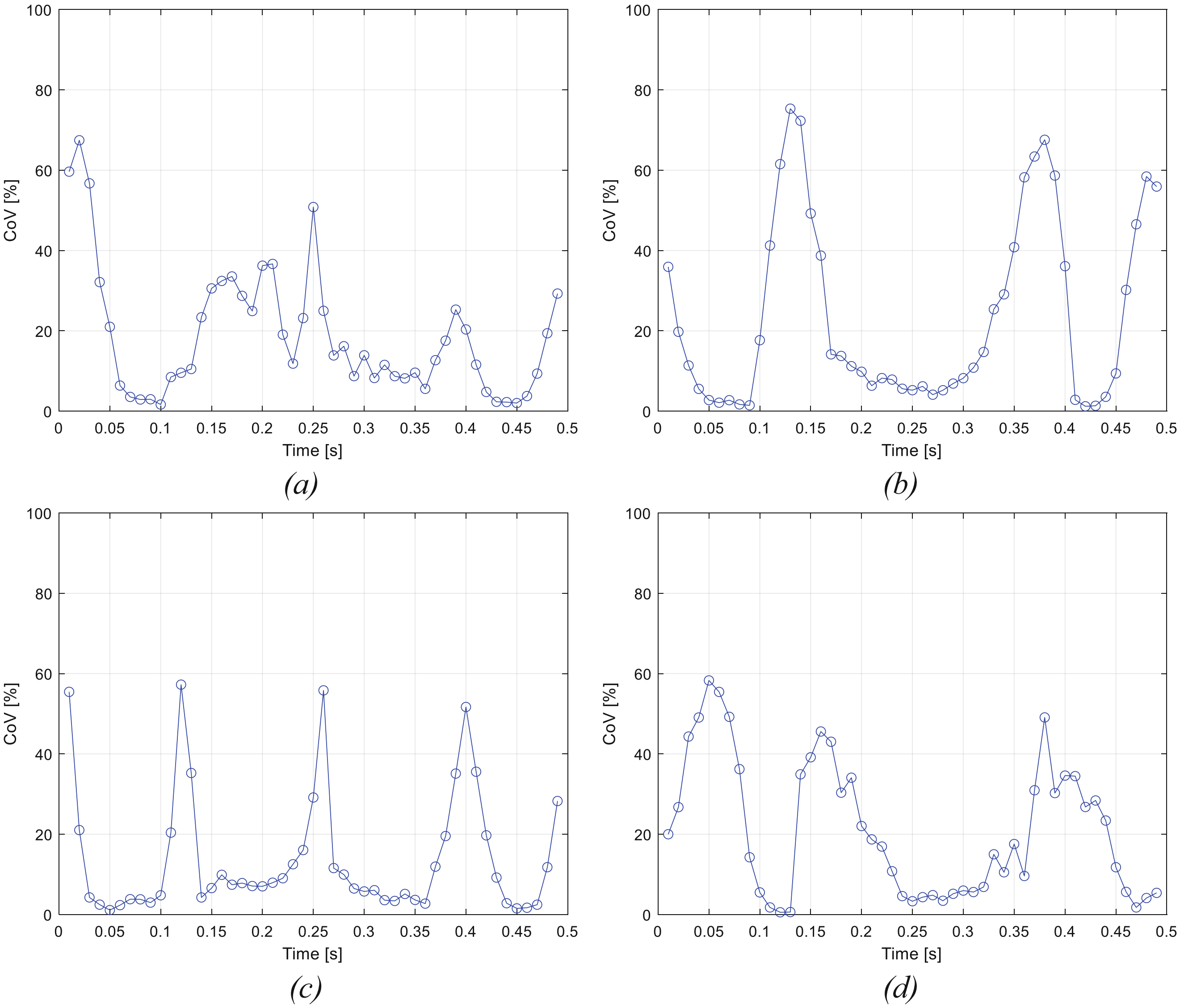

(a) (b) (c) (d)

Fig. 31.10 CoV of coupling angle between toe and platform displacements across cycles for jumping on vibrating platform with target landing at (**a**) trough (**b**) mid-up (**c**) peak (**d**) mid-down positions of platform

31.9 Conclusion

This study has identified and compared four methods for analysing rhythmic jumping activity on vibrating platforms with emphasis on target timings for landing on the platform. A modified vector coding technique has been proposed and demonstrated for a case where a TS jumped at 2 Hz on a platform, vibrating in the vertical direction following harmonic vibration with frequency of 2 Hz and amplitude of 2 m/s^2. This method provides insights into a jumper's coordination with platform and thus his adaptation under vibrations for target timings of landing at trough, mid-up, peak and mid-down positions of the platform. This is achieved by analysing the coordination patterns of coupling angle based on a novel binning strategy. The CoV of coupling angle indicates the variability in jumping across cycles of a trial. The contact phase of jumping cycle, where loading on the structure occurs, is quantified as a percentage of the duration of the jumping cycle. The duration of contact phase are 26.9, 27.8, 36.9 and 32.9% of vibration cycle for target landing at trough, mid-up, peak and mid-down, respectively. This indicates a shorter contact for target landing at the trough compared to longer contact in case of target landing at the peak of the vibration cycle. Vector coding is identified as the most powerful technique in comparison with other methods based on time history, DRP and displacement-displacement correlation. The future work will include evaluation of the consequence of adaptation of toe displacement in GRF.

Acknowledgements The first author gratefully acknowledges scholarship provided by the Faculty of Environment, Science and Economy (formerly the College of Engineering, Mathematics and Physical Sciences) at the University of Exeter. Sincere thanks go to Sigong Zhang and Bintian Lin for their support during the experimental program.

References

1. Then24 [online]. Nijmegen football stadium: part of the grandstand collapses among celebrating fans – no injuries. https://then24.com/2021/10/17/nijmegen-football-stadium-part-of-the-grandstand-collapses-among-celebrating-fans-no-injuries/, 17 October 2021
2. Živanović, S., Pavic, A., Reynolds, P.: Vibration serviceability of footbridges under human-induced excitation: a literature review. J. Sound Vib. **279**(1–2), 1–74 (2005)
3. Wheat, J.S., Glazier, P.S.: Measuring coordination and variability in coordination. In: Movement system variability, pp. 167–181 (2006)
4. Brazil, A., Needham, L., Exell, T., Wilson, C., Irwin, G.: A novel method for comparing vector coding profiles. ISBS Proc. Arch. **38**(1), 316 (2020)
5. Chang, R., Van Emmerik, R., Hamill, J.: Quantifying rearfoot–forefoot coordination in human walking. J. Biomech. **41**(14), 3101–3105 (2008)
6. Needham, R., Naemi, R., Chockalingam, N.: Quantifying lumbar–pelvis coordination during gait using a modified vector coding technique. J. Biomech. **47**(5), 1020–1026 (2014)

Chapter 32
vPERFORM: The Development of Footfall Loading Models for Human Walking on Vibrating Surfaces

Sigong Zhang, Stana Živanović, and Genevieve Williams

Abstract The design for structural vibration induced by human walking is currently based on loading models obtained on rigid surfaces. It is largely unknown how footstep forces would be modified due to human-structure interaction if the surfaces are vibrating. The 2-year project, vPERFORM, aims to identify vertical vibration conditions under which the human-structure interaction occurs and model the interaction to reflect experimental observations of human walking on a vibrating structure. Experiments were carried out in a state-of-the-art facility, VSimulators, to investigate the influence of vibration amplitude, frequency and exposure time on the interaction during normal walking on a treadmill placed on a vibrating platform. Fifteen test subjects were recruited, and ground reaction forces and kinematics data were recorded using force plates and motion capture systems, respectively. In addition, the metabolic cost was also measured to clarify the role of energy optimization in human walking in a vibrating environment. This paper presents details of the experimental program as well as selected preliminary results on ground reaction forces of human walking on the vibrating platform.

Keywords Vibration serviceability · Human induced vibration · Human-structure interaction · Ground reaction forces · DLFs

32.1 Introduction

An ever-increasing use of building materials with high strength-to-weight ratios has led to development of slender and lightweight structures with dazzling structural forms, especially in case of landmark public structures such as footbridges, walkways and corridors between buildings, at airports and shopping centres. Such a trend is fuelled by the urgent need to improve sustainability through minimising use of materials in construction. It follows that structures are more sensitive to human-generated dynamic loading than ever before, and their design is largely governed by vibration serviceability limit state. Assessment of structural vibration induced by human walking is currently based on loading models obtained on rigid surfaces. It is largely unknown how footstep forces would be modified due to human-structure interaction if the surfaces are vibrating.

Pedestrians start interacting with vibrating structures under certain and still largely unknown conditions, resulting in vibration-dependent dynamic force and unacceptably large errors in predictions of the actual vibration response [5]. Bachmann and Ammann [2] reported that vertical vibration displacement of more than 10 mm (corresponding to 1.6 m/s^2 at 2 Hz) can disturb one's natural steps on a rigid surface. Bocian et al. [3] applied a bipedal model to simulate pedestrians interacting with a vertically vibrating bridge, and the effect of the interaction was quantified in terms of the self-excited forces generated by the bridge motion. They found that pedestrians can effectively act as positive or negative dampers to the vibrating structures, depending on the ratio of vibrating frequency to walking step frequency. Dang and Živanović [4]

S. Zhang (✉)
School of Engineering, Newcastle University, Newcastle Upon Tyne, UK
e-mail: sigong.zhang@newcastle.ac.uk

S. Živanović
Faculty of Environment, Science and Economy, University of Exeter, Exeter, UK
e-mail: S.Zivanovic@exeter.ac.uk

G. Williams
Faculty of Health and Life Sciences, University of Exeter, Exeter, UK
e-mail: G.K.R.Williams@exeter.ac.uk

H. Y. Noh et al. (eds.), *Dynamics of Civil Structures, Volume 2*, Conference Proceedings of the Society
for Experimental Mechanics Series, https://doi.org/10.1007/978-3-031-36663-5_32

conducted tests to investigate human walking patterns on a footbridge deck simultaneously excited by a shaker and a walker (fundamental frequency $f_1 < 2.5$ Hz) with pre-excited vibration levels up to 1.2 m/s^2. Test results suggested that step-to-step variability increased along with the increase in the vibration levels, and deck vibration tended to reduce the human-induced force when step frequency was close to the vibrating frequency. Only three test subjects participated in the tests. Ahmadi et al. [1] recorded ground reaction forces (GRFs) and structural vibration responses for 18 participants walking on a higher-frequency footbridge ($f_1 = 6$ Hz). They confirmed that the vibrating bridge deck induced a statistically significant drop in the magnitude of the walking force harmonics in the vicinity of deck vibrating frequency. It should be noticed that both testing programmes were conducted on structures on which a two-way interaction between the structure and the walker had developed.

To further understand pedestrian interaction with vibrating support surfaces under a range of vibration conditions, a comprehensive test program in a cutting-edge platform, VSimulators, at the University of Exeter, UK was carried out within the vPERFORM project. Test participants, instrumented by reflective markers attached to body anatomical landmarks, were asked to walk on a treadmill placed on the platform. Both GRFs and markers trajectories were recorded using force plates and motion capture systems, respectively. In addition, the metabolic cost was also measured to clarify the role of energy optimization in human walking in a vibrating environment. Test details and selected results on ground reaction forces are presented herein.

32.2 Experimental Program

Fifteen participants performed tests and fourteen of them (7 male, 7 female, age 26.2 ± 5.2 years) completed all tasks. The test program contained three visits to the laboratory for each participant: pre-test visit and two visits for testing. Two sets of tests were performed during testing visits: metabolic measurement under multiple long continuous vibration and multiple short intermittent vibration tests.

During the first (pre-test) visit, the physical data (e.g. leg length) was measured and normal walking speeds (NWS) were measured in a 6-meter overground walking test. The overground NWS was then used as the input to the treadmill. This same speed was used in all tests by a participant. Participants were asked to walk on the treadmill for 10 min (habituation walking trial). Their preferred step frequency (denoted as f_0) was determined from the kinematic data as the average step frequency during the middle 4 minutes of walking in the habituation walking trial. The preferred step frequency was used to set the vibrating frequency of the platform.

The second visit consisted of two walking trials, each lasting 20 min, for each participant. For each trial, the participant continuously walked on treadmill (Fig. 32.1a) at their selected NWS for 20 minutes and their metabolic cost was measured

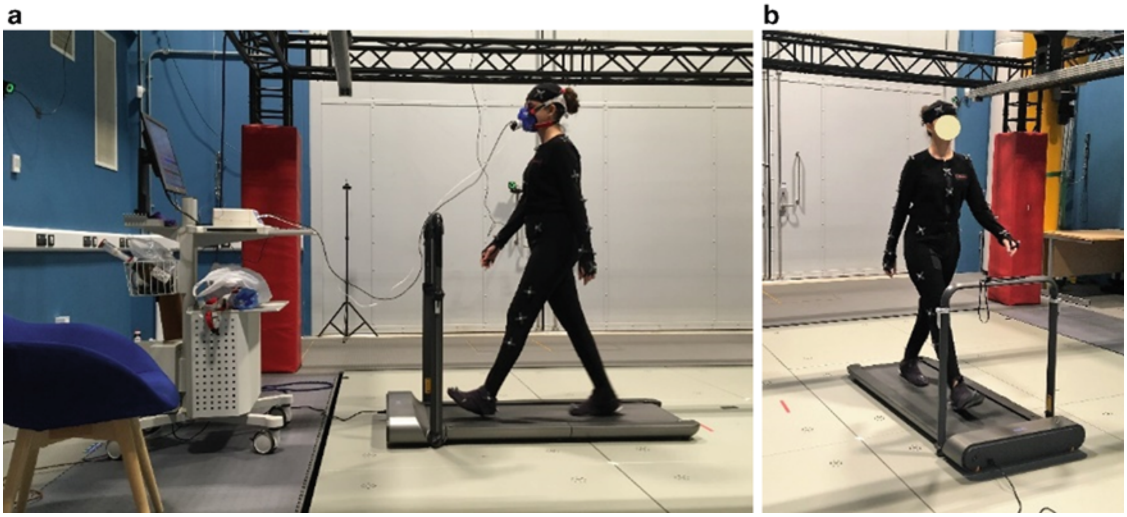

Fig. 32.1 Experimental setup (**a**) metabolic measurement under multiple long continuous vibration and (**b**) multiple short intermittent vibration tests

along with marker trajectories and GRFs. Initially, the platform was stationary (5 min warm-up session, no vibration) followed by three vibrating periods with different frequencies (5 min each). The platform frequencies were applied in the following order: $2f_0$, $1.1f_0$ and $0.9f_0$. For the first 20-min trial, the vibrating acceleration of the platform was 0.5 m/s^2. For the second 20-min trial, it was 2 m/s^2.

Each participant performed three walking trials in the third visit, each around 15 min in duration. The setup is illustrated in Fig. 32.1b. During each trial, the participant continuously walked on the treadmill. At the start of each trial, the platform was stationary for 4 min. This was followed by 11 vibration frequency conditions. The chosen platform vibrating frequency (f_v) to preferred step frequency (f_0) ratios were 0.8, 0.9, 0.95, 1, 1.05, 1.1, 1.5, 1.9, 2, 2.1 and 3. The 11 frequency-conditions were presented in random order. Each frequency condition lasted 45 s. The platform vibration was on during the first 5 s and last 25 s of the condition to simulate different exposure times, while the platform was stationary during the middle 15 s of the condition. This was followed by 15 s no platform vibration condition before proceeding to the next frequency ratio. The amplitude was the same for all vibrating conditions in one walking trial. The amplitude in the three trials was 0.5 m/s^2, 1 m/s^2 and 2 m/s^2, and it was applied in a random order.

32.3 Results

An analysis was performed on GRFs obtained from force plates within the platform. Step frequency and dynamic loading factors (DLFs) were studied. Preliminary results show that walking step frequency tended to match the platform vibrating frequency when they were close ($0.9f_0$ to $1.1f_0$ in current tests), and such trend was more notable for the larger vibration magnitudes. Outside this range, the platform vibration introduced additional force components (self-induced forces) at the vibrating frequency and its integer multiples. The key finding for DLFs is that all platform vibrations significantly increased the DLFs, which contrasts with the results in Dang and Živanović [4] and Ahmadi et al. [1] where reductions were detected for the harmonics close to the vibrating frequencies.

32.4 Discussion

The current project aims to address how vertical vibrations influence pedestrian's walking and resulting dynamic force by using a state-of-the-art motion simulator platform. Human walking behaviours and ground reaction forces on vibrating surfaces are being examined to reveal the influence of the platform-to-human component of the human-structure dynamic interaction. The current results show that the platform vibration leads to an increase in DLFs when compared with DLFs measured on the non-vibrating platform. This preliminary finding suggests that the form of pedestrian interaction with vibrating structure might change depending on the ability of the walker to alter structural vibration.

Note that in the test programme part conducted on VSimulators, one-way interaction was observed, i.e. how platform vibration influences the walker, while walker's actions did not have any influence on the platform vibration. The second test part of vPERFORM was carried out on a footbridge, which exhibits two-way human-structure interaction. Further results will combine these two test parts together.

Acknowledgements This project has received funding from the European Union's Horizon 2020 research and innovation programme under the Marie Skłodowska-Curie grant agreement No. 898216.

References

1. Ahmadi, E., Caprani, C., Živanović, S., Heidarpour, A.: Vertical ground reaction forces on rigid and vibrating surfaces for vibration serviceability assessment of structures. Eng. Struct. **172**, 723–738 (2018)
2. Bachmann, H., Ammann, W.: Vibrations in structures induced by man and machines. IABSE, Zurich (1987)
3. Bocian, M., Macdonald, J.H., Burn, J.F.: Biomechanically inspired modeling of pedestrian-induced vertical self-excited forces. J. Bridge Eng. **18**(12), 1336–1346 (2013)
4. Dang, H.V., Živanović, S.: Influence of low-frequency vertical vibration on walking locomotion. J. Struct. Eng. **142**(12), 04016120 (2016)
5. Živanović, S.: Benchmark footbridge for vibration serviceability assessment under vertical component of pedestrian load. J. Struct. Eng. **138**(10), 1193–1202 (2012)

Chapter 33
Evaluating and Modifying Existing Building Structures for Vibration-Sensitive Applications

Steven Lank and Hal Amick

Abstract Designing a vibration-sensitive facility, such as a laboratory building, as part of a tenant-improvement or renovation project can introduce significant challenges. Often in these projects, the existing building structure has not been designed to meet the vibration requirements of planned sensitive instruments or research, and therefore mitigation measures must be implemented to achieve the desired criteria. This paper will discuss structural dynamic evaluation, analysis, and design for vibration-sensitive facilities, with a focus on specific issues associated with tenant improvement and renovation projects. Via a series of case studies, various strategies for reducing vibration on an existing structure will be presented, including pre and post mitigation measurement results for each case. These case studies will help to illustrate conditions where certain approaches, including structural retrofits, the use of tuned mass dampers, the use of nonstructural elements, and other strategies, may or may not be effective or feasible.

Keywords Building vibration · Laboratories · Structural retrofit · Tuned mass damper

33.1 Introduction

When designing a vibration-sensitive facility, such as a laboratory or sensitive manufacturing facility, achieving the required criteria is challenging enough in a new construction project, requiring careful coordination between the architect, lab planners, structural, mechanical, and process engineers, and others. Designing vibration-sensitive spaces as part of a tenant-improvement or renovation project, where the building structure and equipment may not have been designed with the planned sensitive research or equipment in mind, can introduce additional challenges. In some cases, the existing vibration conditions in such projects are less than ideal because the facility was originally designed for office, retail, or some other less-sensitive application. Given the scarcity of land available for new development in desirable urban, transit-adjacent areas, the prevalence of developer-driven research parks, and the potential cost-savings from reusing existing facilities, these challenges are becoming a fact of life for many prospective sensitive facilities.

This paper will discuss structural dynamic evaluation, analysis, and design for vibration-sensitive facilities, with a focus on specific issues associated with tenant improvement and renovation projects. Various strategies for controlling vibration and improving the performance in existing facilities will be presented via a series of case studies.

33.2 Walker-Induced Vibration

There are many vibration sources that are of potential concern for a sensitive facility. This includes vibration generated by building mechanical, electrical, process, and other equipment, vibration due to turbulent flow through associated mechanical and process piping and ductwork, and vibration sources exterior to the building such as nearby roadways or trains. For

S. Lank (✉) · H. Amick
Brisbane, CA, USA
e-mail: steven.lank@colingordon.com; hal.amick@colingordon.com

H. Y. Noh et al. (eds.), *Dynamics of Civil Structures, Volume 2*, Conference Proceedings of the Society for Experimental Mechanics Series, https://doi.org/10.1007/978-3-031-36663-5_33

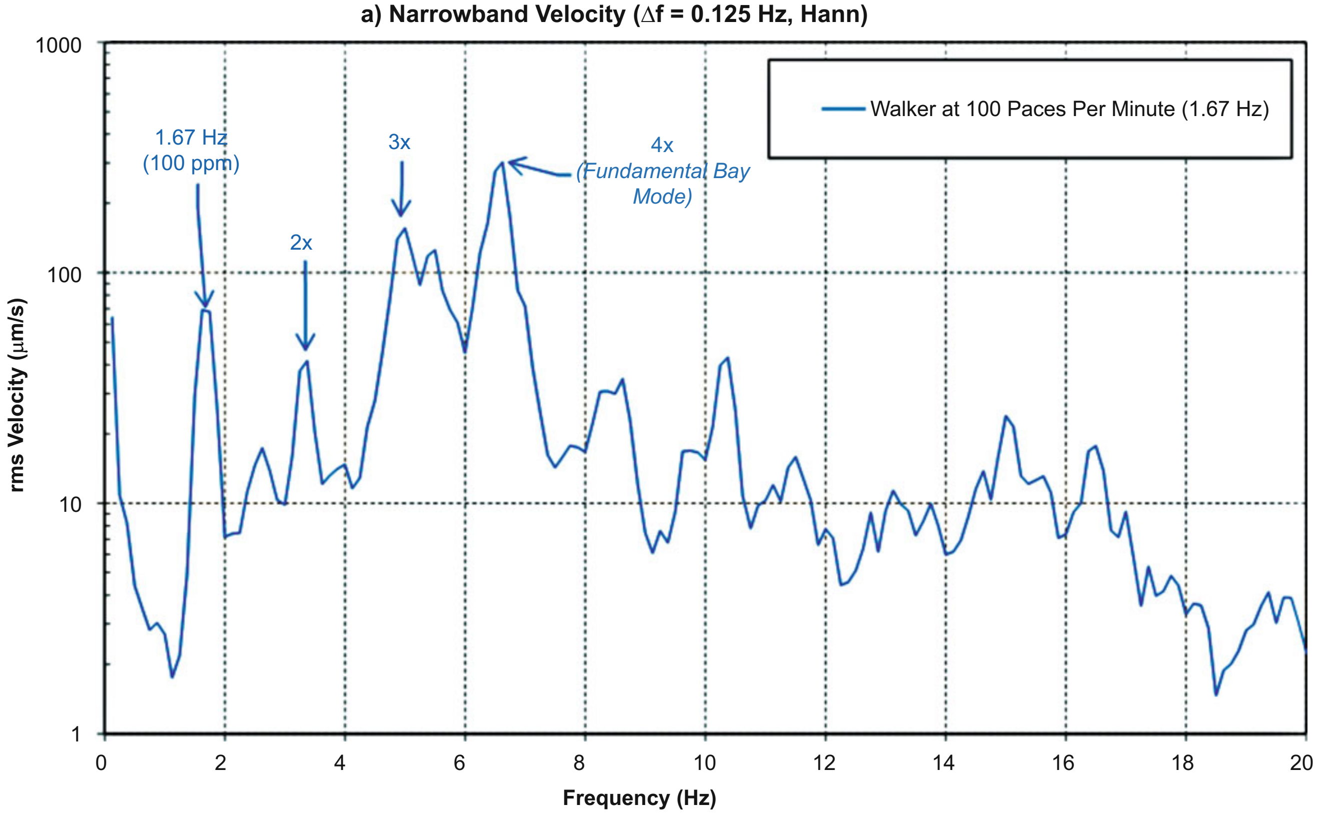

Fig. 33.1 FFT spectrum of a person walking at 100 paces/min (ppm) through a 14.3 × 10 m structural bay with a 6.6 Hz fundamental resonance frequency. Integer multiples of the walker pace rate, corresponding with peaks in the vibration spectrum, are indicated

the case studies presented in this study, however, the primary vibration source of concern is people walking on the floor. Walker-induced vibration is often the most significant concern for vibration-sensitive spaces located on suspended floors.[1]

Floor vibrations are generated when a person walks on the floor because the load due to the walker varies with time. It consists of an initial pulse as the heel strikes, then a plateau as the weight transitions to the front of the foot as the person moves forward, then a drop-off as the foot is lifted to take the next step. For vibration-sensitive facilities, floor vibrations due to walkers are typically evaluated in the frequency domain, in large part because most criteria for vibration-sensitive instruments, as well as the typical generic VC criteria intended to represent various classes of sensitive instruments [1], are defined as a function of frequency. Figure 33.1 shows an FFT velocity spectrum measured as a person walked repeatedly at 100 paces per minute (ppm) through a 14.3 m × 10 m structural bay. A characteristic of any repeated-impact spectrum is that it will exhibit response peaks at the impact rate and integer multiples thereof, as well as a major peak at the fundamental resonance frequency of the structure being impacted (in this case, the floor). In this case, we see a peak at the pace rate of 1.67 Hz and the ×2 through ×4 multiples. The ×4 multiple in this case approximately corresponds to this floor's fundamental resonance frequency of 6.7 Hz.

Importantly, the highest vibration amplitudes generated by a person walking on floors of the type discussed in this study tend to occur at the fundamental vertical resonance of the structural floor bay[2] where the walker and receiver are located. The typical deformed shape at the fundamental resonance of a conventionally framed, rectangular floor bay – extracted from a finite element model of a floor structure – is shown in Fig. 33.2. The highest amplitude response occurs at the least stiff

---

[1] Exceptions to this include very stiff suspended floors designed to very stringent vibration criteria (e.g. semiconductor fabrication cleanrooms and imaging suites), where continuous vibration generated by building equipment and piping often exceeds walker-induced amplitudes as well as slabs-on-grade, where the very high damping provided by the continuous subgrade below tends to mitigate significant vibration impacts from typical walkers. While many of the concepts discussed in this study are somewhat applicable to these floors, our focus will be on walker-induced vibration.

[2] The structural floor bay is defined as the portion of the structural floor that is bounded by the surrounding columns – typically four columns in the case of a rectangular or square bay.

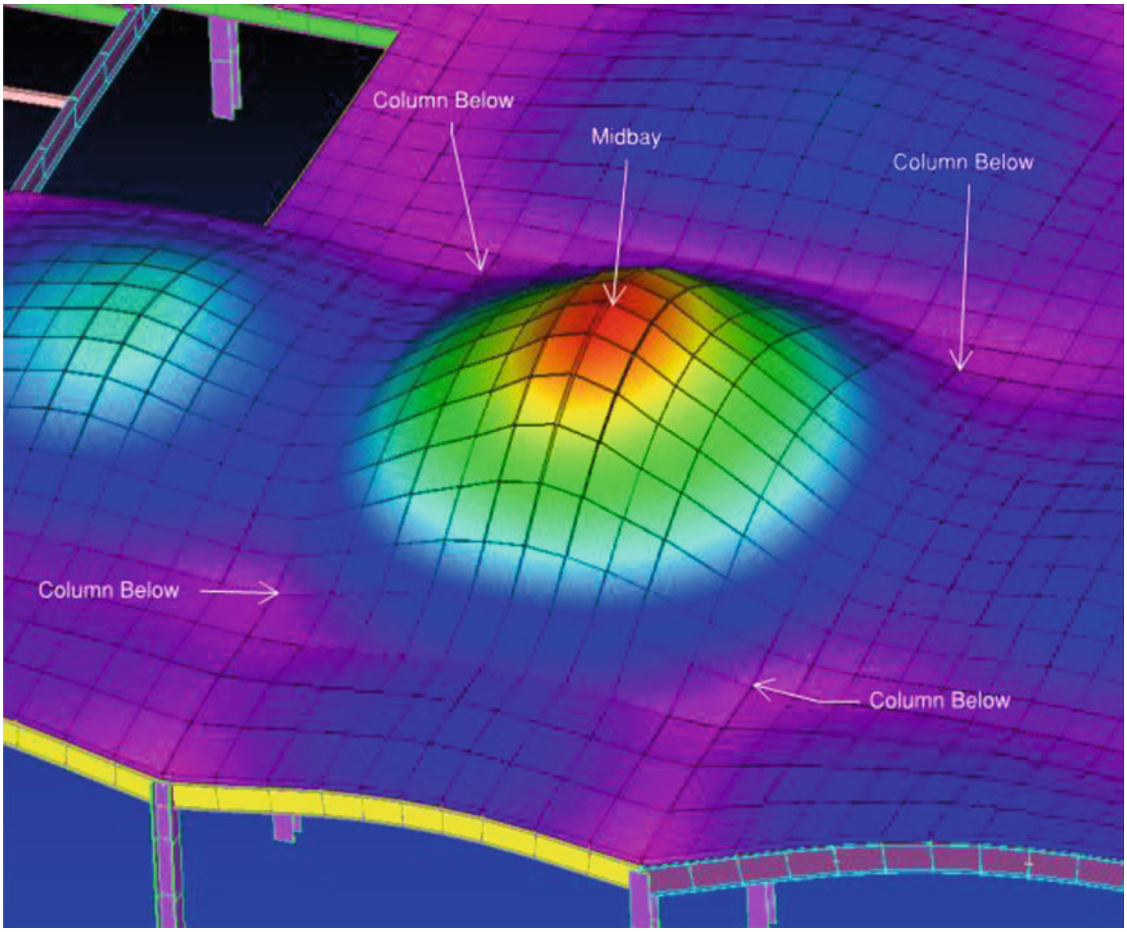

Fig. 33.2 Isometric view of finite element model of a typical structural floor, showing the deformed shape of a typical floor bay at its fundamental resonance frequency

portion of the bay – the point furthest from all the surrounding columns, or the "midbay." Lower resonance frequencies may be predicted via modeling that encompass more than one bay; however, field studies have shown that those modes generally are not excited by typical walkers [2]. Higher modes can be excited by walkers, however amplitudes at those frequencies tend to be significantly lower. Reducing the walker-induced vibration amplitudes occurring at the fundamental resonance frequency of the bay, particularly at the midbay, was therefore the primary focus of the case studies discussed below.[3]

33.3 Building Modification Case Studies

In this section, we will present case studies involving vibration-sensitive applications that were to be added to existing building structures originally designed with another application in mind. In each case, vibration measurements were conducted within the existing building prior to construction of the new facility and then repeated once the renovation or tenant improvement – including any structural retrofits or other modifications installed for vibration control purposes – was completed.

Vibration measurements will typically be presented as RMS velocity in one-third octave frequency bands – which is the format of the standard VC curves often used as design criteria for sensitive facilities [1]. In some cases, narrowband FFT vibration spectra and/or the measured dynamic stiffness spectra will be presented as well to further illustrate the change

---

[3] Prediction of footfall-induced vibration, which is an important step in the design of a new structure or modifications to an existing structure, is beyond the scope of this study.

in dynamic performance before and after the building modifications were completed. In most cases, results from a single structural bay may be shown for illustration purposes, however the sensitive areas and any mitigation measures installed typically extended over multiple bays supporting sensitive equipment.

33.3.1 Case 1 and 2: Fit-Out Only

In most cases, a tenant improvement or renovation project involving vibration-sensitive spaces begins with a measurement survey to document the existing conditions. In the case of a tenant improvement project, this often involves measurements conducted with the building in “core and shell” conditions, with only the bare building structure and envelope in place and minimal architectural, mechanical, furniture, or components – which we will define generally as “fit-out” – installed. This additional fit-out will tend to contribute additional damping to the structure, which can reduce the maximum amplitude generated by a typical walker. In some cases, full-height partitions above and below the floor can contribute some added stiffness to the floor structure in addition to damping, further reducing the vibration amplitudes. Therefore, it is typically expected that the walker-induced amplitudes measured at a given location in core and shell conditions will be at least somewhat lower when the fit-out of the building is complete.

This is exemplified in Case 1, a multistory tenant improvement of a core and shell building for biotechnology laboratories. The structural floor in this case was a composite 62 mm thick lightweight concrete slab over 76 mm metal deck supported on steel beams. Typical structural floor bays were framed with 10 m span W24×68 girders, supporting 6.9 m W16×31 beams spaced 3.4 m on center.

Figure 33.3 shows walker-induced vibration amplitudes measured in Case 1 facility at the same location with the same individual walker, walking location, and walker pace rate on two separate occasions under two conditions: core and shell conditions and at the conclusion of the tenant improvement work with all fit-out in place. Vibration amplitudes are shown from 1 to 160 Hz in one-third octave format but only up to 40 Hz in narrowband FFT format – the latter to better illustrate the dynamics at the lower frequencies of interest. The fit-out in this case consisted primarily of typical fixed lab benches and case work, as well as mechanical ductwork and ceilings suspended below the slab. The fundamental bay resonance has not changed significantly between the two tests – which is as expected given that no additional stiffening elements were added to the floor structure. The highest vibration amplitude, however, is reduced by more than 2 times (>6 dB), which is likely due in large part to the added damping provided by the fit-out. This is evident in the FFT spectrum on the right in Fig. 33.3, where the sharp (high-Q) peak at the fundamental resonance at around 7.25 Hz measured under core and shell conditions has broadened and decreased significantly in amplitude once fit-out was completed.

While the 6 dB reduction exhibited in Case 1 above is a significant improvement, some caution is advisable when evaluating the expected improvement that will be provided by fit-out alone. Many modern labs and sensitive manufacturing facilities include open layouts with minimal partitions, utilities, furniture, and no suspended ceilings. An example of such a facility is Case 2, which is an advanced medical technology manufacturing facility. Measurements were conducted in two bays on the same level with identical structural framing but differing fit-out. The structural floor in this case was again a composite system, with 76 mm thick normal weight concrete slab over 76 mm metal deck supported on steel beams. Typical

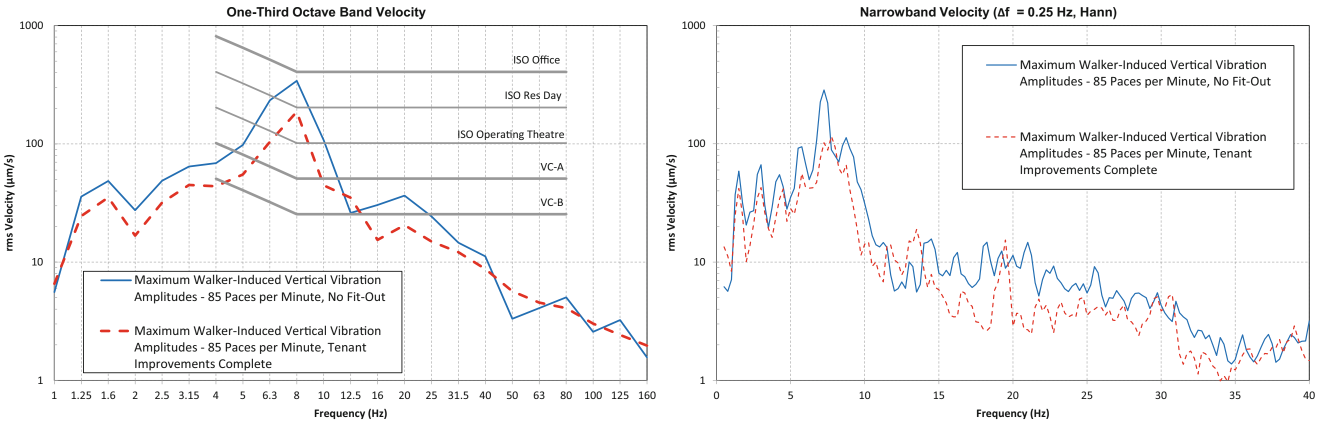

Fig. 33.3 Walker-induced vibration amplitudes in typical wet lab – before and after tenant improvement works

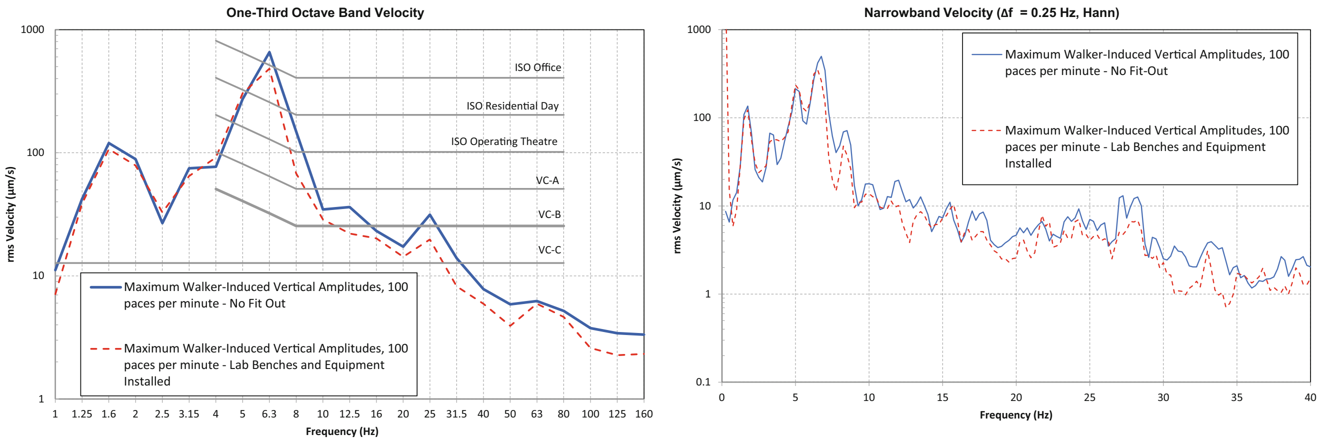

Fig. 33.4 Case 2 – Walker-induced vibration amplitudes in identical structural bays – with and without fit-out

structural floor bays were framed with W24×68 girders spanning 9.1 m, supporting 12.2 m W16×31 beams spaced 3.0 m on center. One bay was essentially a bare structure, with no partitions, furniture, utilities, or ceilings installed below. The other bay, as well as the bay directly below, was fully fit out for vibration-sensitive manufacturing processes. In this case, the fit-out consisted primarily of the installation of a number of portable lab benches and ductwork suspended below, with no other partitions, ceilings, or utilities installed.

The walker-induced vibration amplitudes in the two Case 2 bays are shown in Fig. 33.4. In this case, note that the difference in amplitudes with and without fit-out is small – with a reduction of only around 2 dB. Measurements of the damping at the fundamental resonance frequency in each bay showed 1.5% of critical damping in the fit-out bay compared to 1.0% in the bay without fit-out – a fairly minor increase of only 0.5% due to fit-out. The result is a relatively minor difference in maximum walker-induced vibration amplitudes between the two cases – with maximum amplitudes that are within typical expected measurement variability.

The impact of fit-out on vibration performance also needs to be considered when evaluating a building for a renovation project. In these cases, existing elements – particularly partitions on the slab under test as well as full-height partitions located directly below the slab – could significantly impact the measurements of the existing conditions. If these elements are to be removed as part of the renovation – as is often the case for more modern designs that are intended to provide a more open architectural layout – the vibration amplitudes after the renovation could be significantly higher than those measured prior to the start of work. In these cases, follow-up vibration measurements after the demolition phase of the renovation is complete can be advisable to provide a more accurate documentation of the anticipated performance.

33.3.2 Case 3 and 4: Conventional Structural Retrofits

In cases where vibration performance improvements due to fit-out alone are expected to be insufficient to meet project criteria, one common approach to further reduce vibration is to stiffen the floor structure. Walker-induced vibration amplitudes are generally inversely proportional to the stiffness and fundamental resonance frequency of the bay, and structural retrofits can be used to increase both.

Case 3 involved a portion of the 4th floor of a building that was being fit out as a vibration-sensitive vivarium space for biology research, requiring VC-A (50 μm/s RMS) performance. The existing floor structure supporting the vivarium space utilized a one-way joist slab, with an 83 mm lightweight concrete slab on a 76 mm steel deck, framed with W21×44 joist beams spanning 12.8 m and spaced of 2.4 m on center, supported by W24×55 girders spanning 7.9 m. Initial vibration measurements on this slab showed walker-induced amplitudes of up to around 2000 μm/s RMS, around 40× (32 dB) higher than the VC-A criterion. Structural retrofits were proposed to reduce the vibration amplitudes, including tube-steel (HSS) elements welded beneath the existing steel beams supporting the floor, as well as an additional 100 mm topping slab installed atop the existing slab. Photos of the topping slab and stiffening steel are shown in Fig. 33.5.

Figure 33.6 shows walker-induced vibration amplitudes measured as part of Case 3. Measured vibration amplitudes at a single location on the floor are shown for three separate conditions: core and shell, core and shell with structural retrofits installed, and with the final fit-out complete. The results show that the structural retrofits reduced the maximum walker-

Fig. 33.5 Case 3 – Photos of topping slab (left) and tube steel stiffeners from below (right, with fireproofing applied)

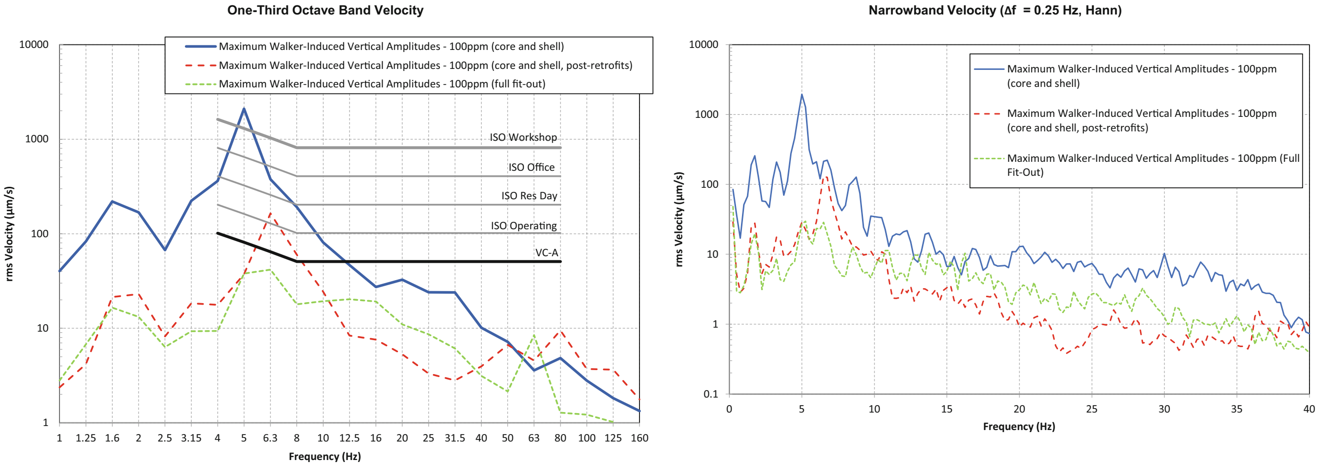

Fig. 33.6 Case 3 – Walker-induced vibration amplitudes at the same location 4th floor vivarium space at various stages of completion. Walker at 100 paces per minute through the middle of the structural bay in all cases

induced amplitudes by roughly 10 times (20 dB), significantly increasing the fundamental resonance frequency of the floor as well. Notably, the added stiffness from the retrofits reduces the amplitudes at nearly all frequencies, including at low frequencies around the walker pace rate. Walker-induced amplitudes are further reduced around the bay resonance once the partitions, ceilings, casework, and other fit-out are installed – with the final conditions meeting the VC-A criterion.

Case 4 involves the 2nd and 3rd floors of an existing core and shell building that were being fitted out to house vibration-sensitive optical tables to be used for advanced technology research and development. The instruments in this case, which included optical tables and high-magnification optical microscopes, required vibration criteria as stringent as VC-A (50 µm/s RMS). The existing structural floor in this case was a 64 mm normal weight concrete slab over 50 mm steel deck supported on steel beams. Typical bays were framed with 14.8 m span W24×62 beams spaced 3.0 m on center supported by 9.1 m span W24×76 girders. Walker-induced vibration amplitudes within the existing core and shell building exceeded 700 µm/s RMS, well above the VC-A criterion.

Structural retrofits were implemented to reduce the floor vibration amplitudes, including WT stiffeners welded beneath all existing beams and girders, and an additional 100 mm thick normal weight concrete topping slab was added. In this case, due in part to the relatively thin existing concrete slab, supplemental columns and a new girder were also required at the midspan of the existing beams to provide further stiffness. Example photos of the WT stiffeners welded to the underside of the existing beams, new columns, and new girders are shown in Fig. 33.7. Notable, the number of structural bays that could be retrofitted was limited by the total mass of added concrete that could be added to the building without required seismic retrofits.

Figure 33.8 compares the walker-induced vibration amplitudes measured at a single location in Case 4 in the base core and shell conditions, as well as after structural retrofits and fit-out were complete. The combination of stiffening the floor and the added damping from fit-out in this case reduced the maximum walker-induced amplitudes by more than 14× (23 dB).

Fig. 33.7 Case 4 – Stiffening steel and new columns and girders

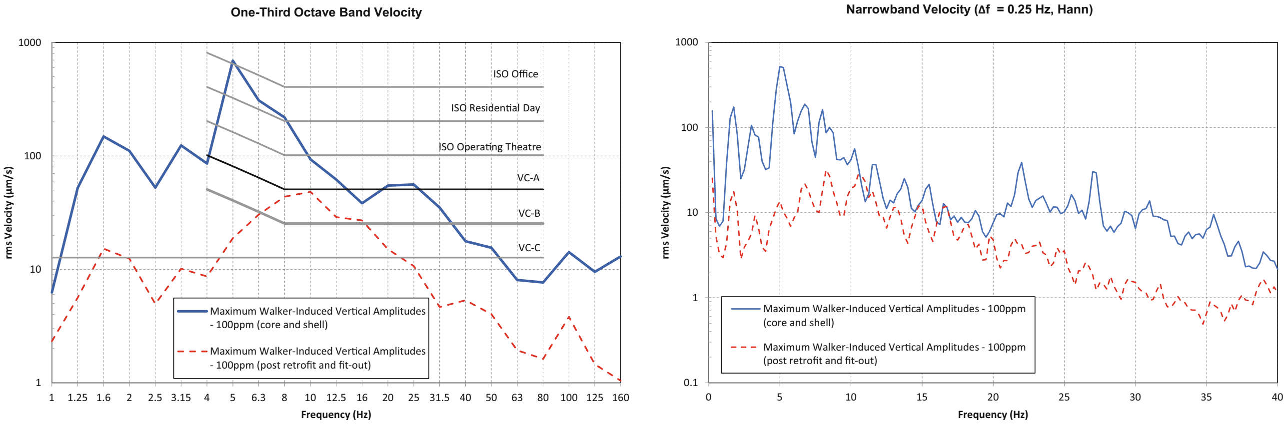

Fig. 33.8 Case 4 – Walker-induced vibration amplitudes in 2nd Floor optics lab before and after retrofits and fit-out

33.3.3 Case 5: High-Strength Topping Slab

In some cases, many of the conventional approaches for stiffening the floor slab discussed above are not an option due to project limitations. This occurred in Case 5, which involved a 200 mm thick concrete flat slab supporting subfab level of an existing semiconductor fab built in the 1990s, with typical structural bays that were 7.2 m × 7.2 m. Results from this Case have been summarized as part of prior presentations [3]. The floor, which was initially designed for gravity loads from equipment only, required upgrades to achieve the VC-B (25 µm/s RMS) vibration performance needed for new process equipment that would be installed as part of a facility upgrade. Existing floor bays contained service penetrations of various sizes, which impacted the existing vibration performance, however a uniform solution applicable across the over 400 individual structural bays involved was required. Structural retrofits including additional helper columns, added beams under the floor, and even additional diagonal braces or truss-like elements were considered and analyzed as potential solutions. However, these options were eventually rejected due to the very stringent space limitations associated with a manufacturing facility of this type.

Eventually, a retrofit was designed that involved the installation of a new concrete topping slab to help stiffen the existing structure. Due to space limitations, however, the maximum allowable depth of the new topping slab was only 50 mm. To achieve the required improvement in vibration performance using only this thin topping slab, an extremely high strength concrete with minimum compressive strength of 99.3 MPa was utilized. The Young's modulus of the concrete, which is critical to the stiffness of the bay and therefore vibration performance, was around 2× that of concrete used for the base building. Achieving this concrete strength required the use of a low water-to-cement ratio along with special high-strength aggregate, which is visible in the core sample from the topping slab shown in Fig. 33.9. An adequate bond between the

Fig. 33.9 Core sample of 50 mm concrete topping slab installed for Case 5 showing high-strength aggregate (brown)

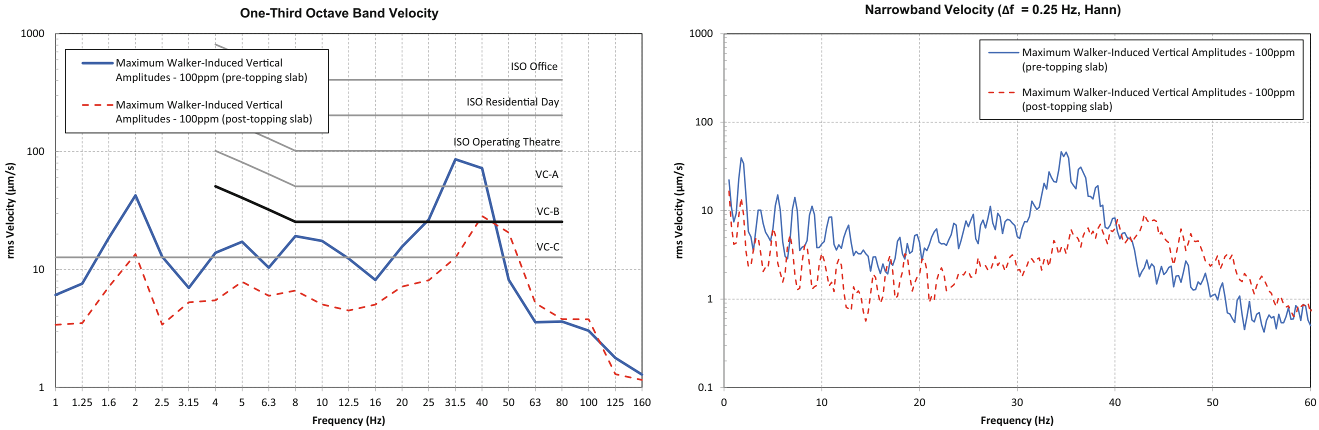

Fig. 33.10 Case 5 – Measured walker-induced amplitudes before and after installation of high-strength topping slab

existing slab and new topping slab, which is critical for shear transfer for low-amplitude vibration, was ensured by scoring the existing slab prior to pouring the new slab.

Vibration spectra due to a typical walker in an example location on the floor, measured before and after the installation of the topping slab, are shown in Fig. 33.10. The addition of the topping slab reduces the maximum vibration amplitudes by around a factor of 4 (12 dB), meeting the VC-B criterion. The plots show that the fundamental resonance frequency of the bay increases somewhat with the addition of the topping slab, likely due to the added stiffness. The results shown are typical of the bays that were retrofitted, though it's notable that walker-induced vibration amplitudes were reduced by a factor of up to 6× in selected bay, with amplitudes as low as 7 μm/s.

The peak in the frequency spectrum around the resonance frequency has a lower Q with the added topping slab, indicating that additional damping may have been introduced by the addition of the slab. The changes in dynamic performance are further illustrated by the dynamic stiffness measurement results at this location, shown in Fig. 33.11. Note that the dynamic stiffness at frequencies well below the fundamental resonance frequency, which can generally be assumed to approximate the static stiffness, increases by around 3 dB. However, the dynamic stiffness at its lowest point (at the fundamental resonance frequency of the bay) increases by around 8 dB. In addition to added damping, this difference could be due in part to the repetitive floor structure in the subfab – where adjacent bays having the same thickness and column spans contribute to the dynamic response, due to similar or identical resonance frequencies. The application of the topping slab, which would have added a slightly different amount of mass to each floor bay depending upon the sizes of the individual penetrations, could result in greater differences in resonance frequencies between adjacent bays, resulting in a lower amplitude response at resonance. Regardless, the results show that the retrofit was successful in achieving the project vibration criterion.

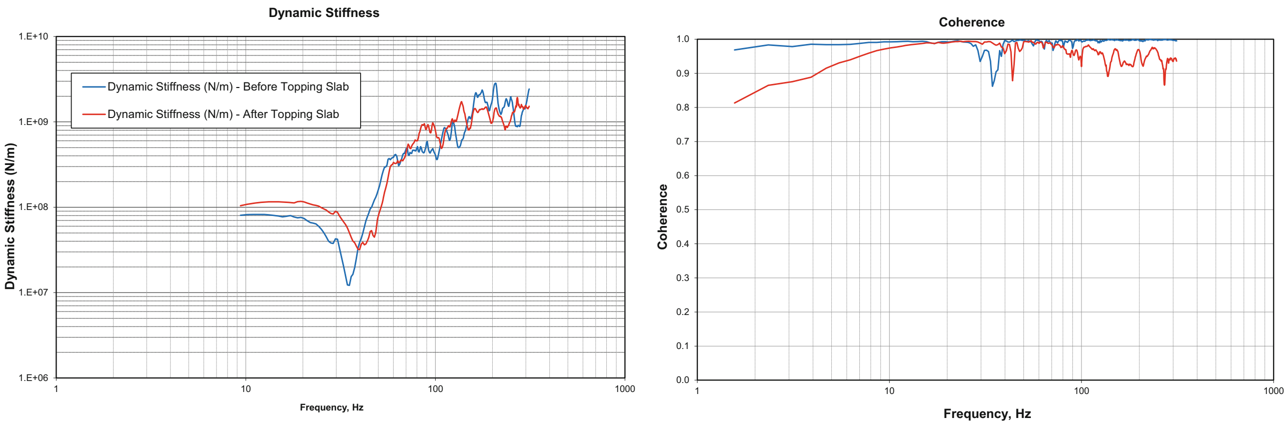

Fig. 33.11 Case 5 – Measured dynamic stiffness and mobility before and after installation of topping slab

33.3.4 Case 6: Structural Retrofits and Tuned Mass Damper Systems

Case 6 involved another tenant improvement project for a sensitive biotechnology lab facility. The building in this case had recently been constructed by a developer for use as a lab facility, however the vibration design of the floors was more appropriate for office occupancy. As part of the tenant improvement project, new lab spaces were to be constructed occupying six structural bays on the second level. Typical floor bays were framed with 14.3 m W24×55 beams spaced 3.4 m on center, supported on 10 m span W27×84 girders. The steel beams supported an 83 mm lightweight concrete slab on a 50 mm thick steel deck. Tissue culture research and sensitive instruments such as optical and confocal microscopes, flow cytometers, plate readers, and mass spectrometers were to be utilized in these labs, requiring the floor structure to provide VC-A (50 μm/s RMS) performance.

Once again there were significant limits on the structural retrofits that could be installed as part of the project to help improve the vibration performance. New columns could not be installed due to contaminated soil beneath the building – excavation for new column footings would have required decontamination procedures, introducing significant project delays. Additionally, the labs were located directly above the main entry lobby and conference center for the building – and therefore dropping additional columns into these spaces was not preferred architecturally. Additionally, no additional concrete topping slabs could be installed in this case. Additional concrete would add significant mass to the building, triggering potential seismic upgrade requirements for the entire building. Additional damping benefits from the fit-out were assumed to be minimal, due to the open lab layouts with minimal partitions above and below most bays.

Stiffening of the existing beams and girders was feasible, however, and a retrofit design was devised that involved the installation of new WT and tube steel (HSS) sections welded to the underside of the existing members. However, stiffening the beams alone was not sufficient to meet VC-A. Modeling of the structure indicated that any further stiffening of the beams and girders would have diminishing returns without also stiffening the concrete slab and/or reducing the floor spans via the installation of new columns. Since these were not viable options for the project, an alternative of a tuned mass damper (TMD) system was considered instead to help further reduce walker-induced vibration.

TMD systems used to control floor vibration consist of a large mass, typically on the order of 2 to 10% of the mass of the floor bay, which is attached to the floor via a set of springs and dampers at the approximate location of maximum deformation at the frequency of concern – typically the middle of the structural bay, though not always. The system is designed and adjusted so when the floor is excited, the mass oscillates on the spring and damper system at the designed frequency – which is typically tuned to the fundamental resonance frequency of the floor bay. The oscillation of the mass dampens the vibration of the floor at resonance. Importantly, a tuned mass damper will *only* reduce the vibration amplitudes at the frequency it is tuned to. While vibration at the fundamental bay resonance is typically the worst case in terms of walker vibration, vibration amplitudes measured on the existing floors in this case exceeded the criterion at other frequencies as well – with amplitudes as high as roughly 200 μm/s at lower frequencies, predominantly at the walker pace rate and the first few harmonics. A TMD would not be expected to reduce these amplitudes. The TMD will also have minimal impact on the frequency of the floor resonance, meaning that a TMD installation alone would still result in a floor with a relatively low frequency resonance that is easily excitable by walkers. For these reasons it was advisable to combine any TMD installation with structural retrofits that increase the bay stiffness at least somewhat, rather than try to rely on the TMD to provide all

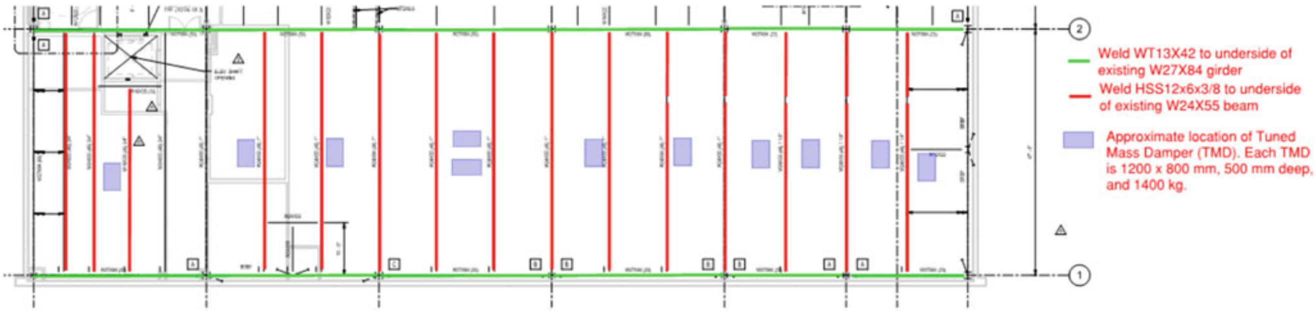

Fig. 33.12 Case 6 – Level 2 structural framing plan showing location of new WT and HSS members and TMDs

the necessary attenuation. The retrofit design including additional steel and added TMDs is shown as a markup of the base building structural drawings in Fig. 33.12 below.

There were several important considerations in implementing a floor vibration mitigation design involving TMDs, which are summarized below:

- The tuned mass damper must be adjusted to match the floor resonance with a high level of precision to be most effective. This tuning will generally be performed by the TMD manufacturer during installation, however the TMD must be designed to operate within a narrow range[4] of frequencies before shipment and installation. While the column spacing and framing designs for most bays were generally very consistent, the location of existing full height walls – as well as new full-height walls that would be installed as part of the tenant improvement – significantly altered the dynamics of each bay. Fundamental resonance frequencies for bays that were nearly identical structurally ranged from around 7 to 10.5 Hz. Predicting these resonance frequencies required very careful and detailed finite element modeling. These frequencies were then verified via measurements once the retrofits and most partitions were installed, with any adjustments communicated to the TMD vendor.
- In addition to impacting the fundamental resonance frequency, full-height partitions in the level below also impacted the fundamental mode shape within each bay. Figure 33.13 shows color contours illustrating the predicted deformed shape of one bay in the building (Bay 4, or the fourth bay from the left) which was to have a full-height partition below running north-south down the approximate middle of the structural bay. Note that the full-height partition serves to stiffen the middle of the bay, resulting in the highest deformation (the red area of the contours) occurring closer to the quarter bay – between the partition and the column line. Since the TMDs must be installed at the location of maximum deflection for the mode to which it is tuned for maximum benefit, this meant that the TMDs for this bay were shifted closer to the quarter bay rather than centered on the midbay as with other bays. Note that, as shown in Fig. 33.12, similar considerations were required for the second bay from the left.
- The TMD installation involves adding significant weight to the underside of the floor structure. Two dampers were required in each bay in this case, each weighing approximately 1400 kg. The project structural engineer was required to confirm that the existing structure could support the new load, as well as work with the TMD manufacturer on the required details for attaching the TMD to the structure.

Photos of selected TMDs as installed on the underside of the structure are shown in Fig. 33.14.

Walker-induced vibration amplitudes in a representative retrofitted bay are shown in Fig. 33.15 under three separate conditions: core and shell, core and shell plus steel retrofits and partitions installed, and final fit-out with TMDs installed and operating. The results show that the structural steel retrofits significantly reduce the walker-induced vibration amplitudes – by around 2× (6 dB). The introduction of the TMD reduces the amplitudes further, to the point that the VC-A criterion is met. The narrowband FFT spectra show that the effect of the TMD is most pronounced around the resonance frequency of the bay, as expected. Some reduction in the amplitudes at other frequencies is evident as well, which could be due to the added mass of the TMD and/or added damping from further fit-out installed between the post-retrofit measurements and post-TMD measurements. The results show that the combination of added steel, TMDs, and damping from fit out were sufficient to achieve the project criteria.

---

[4] The frequency range is generally dependent upon the specific design of the TMD and the amount of attenuation required.

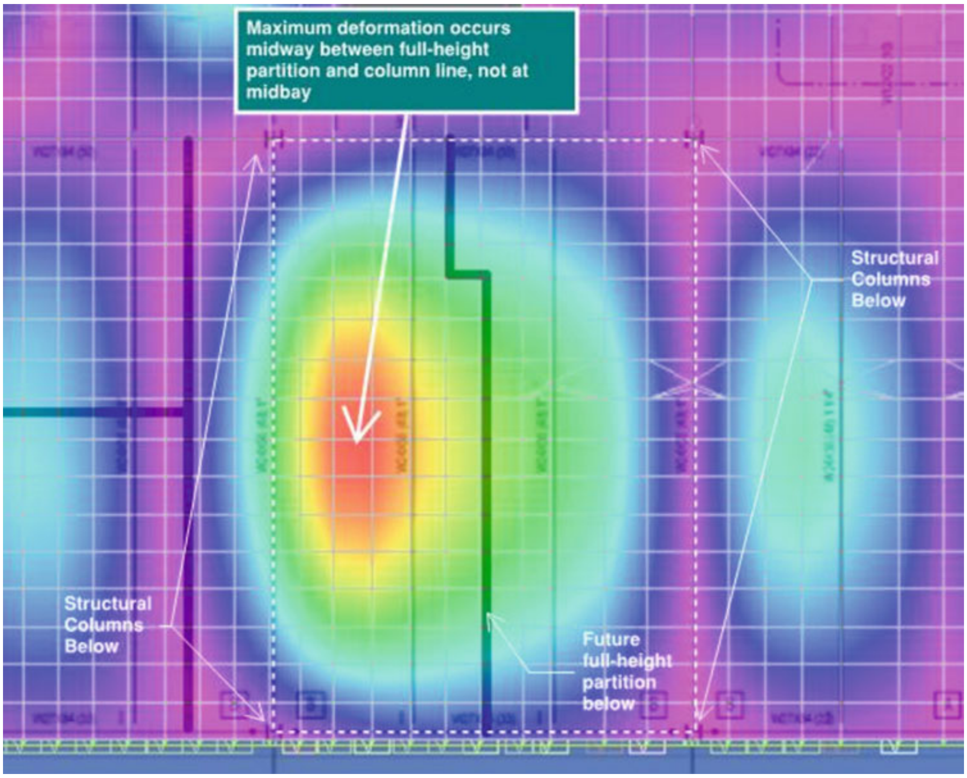

Fig. 33.13 Case 6 – Deformed shape of fourth bay from the left at 7.2 Hz. Structural bay indicated as white dashed line

Fig. 33.14 Case 6 – Tuned mass dampers mounted to the underside of the floor structure

33.4 Conclusion

The case studies presented here show that buildings designed for more conventional occupancies can be upgraded for use in vibration-sensitive applications via several different methods. There are many considerations required when evaluating an existing building, as well as assessing potential options for reducing floor vibration where necessary. The specific approach for reducing vibration amplitudes in an existing structure will generally be dependent upon the specific project details and limitations, however the examples shown here show that in many cases these limitations can be overcome while still achieving the project criteria.

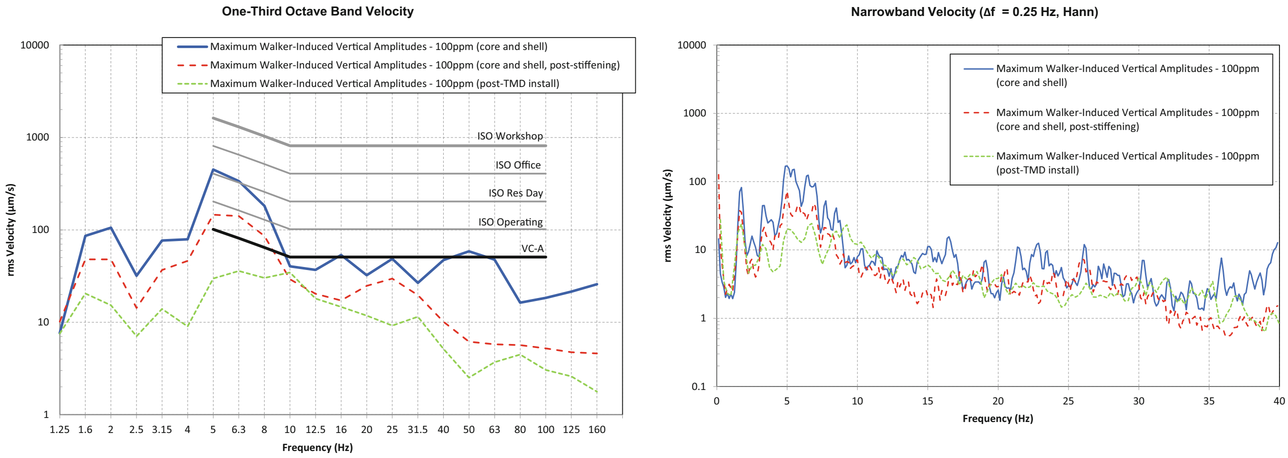

Fig. 33.15 Case 6 – Measured walker-induced vibration amplitudes in a representative bay throughout vibration mitigation installation

Acknowledgements Vibration data presented in this paper were collected by the authors as well as Michael Gendreau, Lee Gorny, Blong Xiong, Stephen Jaeger, and Ning Tang of Colin Gordon Associates.

References

1. Amick, H., Gendreau, M., Busch, T., Gordon, C.: Evolving criteria for research facilities: vibration. In: Proceedings of SPIE Conference 5933: Buildings for Nanoscale Research and Beyond, San Diego, CA, 31 Jul 2005 to 1 Aug 2005
2. Gendreau, M., Tang, N., Amick, H., Wu, C.: Mode selection for Footfall analysis of floors. In: Proceedings of IMAC XXVII Conference and Exposition on Structural Dynamics, Orlando FL, USA (9 to 12 February 2009)
3. Gendreau, M., Amick, H.: Improvement of footfall vibration of suspended concrete floors: two case studies, Invited Paper, presented at the 166th Meeting of the Acoustical Society of America, San Francisco, California, 2–6 December 2013

Chapter 34
Vibration Serviceability Evaluation of a Modular Steel Plate Floor Assembly

Onur Avci, Maria Mercado Celin, Matthew Eatherton, W. Samuel Easterling, Ben Schafer, Jerome F. Hajjar, and Ron Klemencic

Abstract Preliminary results of vibration serviceability evaluation of a new, modular steel floor framing system for commercial building structures are presented. The proposed system intends to increase the speed of construction by eliminating the placing of a concrete deck and thus reduce the time from conception to occupancy for steel building structures. The relatively lightweight floor system has been studied for vibration serviceability, and the results presented herein are a summary of the analytical research conducted before the experimental phase of the project. The analytical work presented in this study includes the vibration serviceability assessment per AISC Design Guide 11 (Vibrations of Steel-Framed Structural Systems Due to Human Activity) and computational simulations using finite element software.

Keywords Floor vibration serviceability · Steel-framed floor systems · Structural steel · Modular construction

34.1 Introduction

Structural vibrations on elevated building floors, footbridges, staircases, and stadia can cause occupancy discomfort. For building floors, vibration serviceability has become a limit state for steel-framed systems with the potential to govern structural design over the strength and deflection limit states [1].

The most economical solution is to avoid potential problems at the design stage, however predictions related to vibration serviceability continue to include multiple uncertainties and assumptions in the assessment procedures. The levels of human-induced dynamic excitations, effects of structural and nonstructural components (and their simulation in a computer model), and acceptability criterion for human comfort and sensitive equipment operation are only a few of the aspects that include uncertainties. Combinations of multiple assumptions for such uncertainties tend to decrease the accuracy of vibration serviceability predictions even with state-of-the-art design guides. In addition, slender architectural design trends, use of high-strength and lightweight systems, and relatively less inherent damping can make the vibration problem worse [2].

O. Avci (✉)
Department of Civil and Environmental Engineering, Engineering Sciences Building, West Virginia University, Morgantown, WV, USA
e-mail: onur.avci@mail.wvu.edu

M. M. Celin · M. Eatherton
Department of Civil and Environmental Engineering, Virginia Polytechnic Institute and State University, Blacksburg, VA, USA
e-mail: mariamercado@vt.edu; meather@vt.edu

W. S. Easterling
Iowa State University, Ames, IA, USA
e-mail: wse@iastate.edu

B. Schafer
Department of Civil and Systems Engineering, Johns Hopkins University, Baltimore, MD, USA
e-mail: schafer@jhu.edu

J. F. Hajjar
Department of Civil and Environmental Engineering, Northeastern University, Boston, MA, USA
e-mail: jf.hajjar@northeastern.edu

R. Klemencic
Magnusson Klemencic Associates, Seattle, WA, USA
e-mail: rklemencic@mka.com

H. Y. Noh et al. (eds.), *Dynamics of Civil Structures, Volume 2*, Conference Proceedings of the Society for Experimental Mechanics Series, https://doi.org/10.1007/978-3-031-36663-5_34

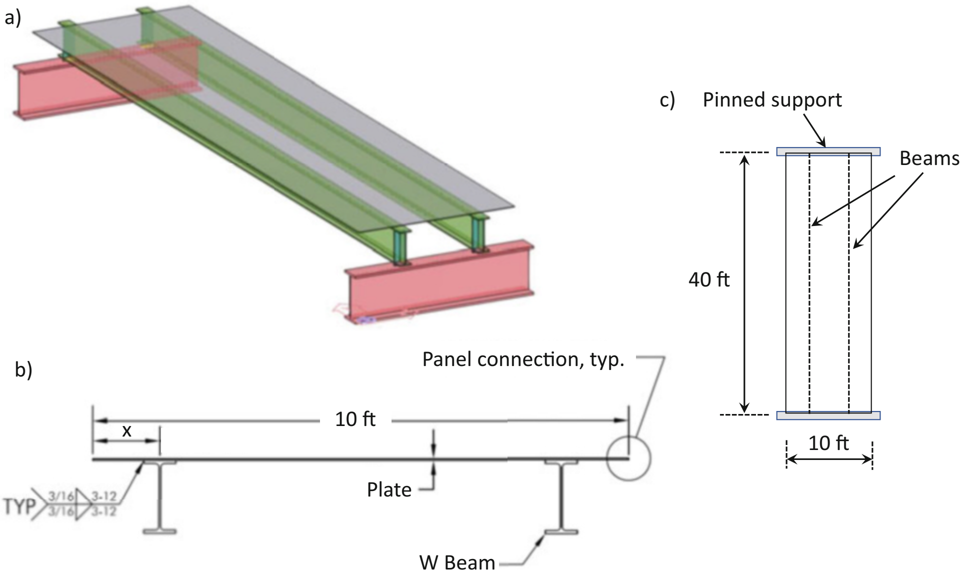

Fig. 34.1 Modular steel plate assembly – single module. (**a**) 3D view, (**b**) cross-sectional view, and c) plan view

In an ongoing research project, the authors have been focusing on a new modular steel floor framing system for commercial building structures. The goal of this new system is to eliminate the use of a concrete deck and increase the speed of construction. Because this type of floor system has never been used, the vibration serviceability assessment requires careful attention (in addition to comprehensive assessments on gravity strength, ductility, local buckling, diaphragm behavior, connection and fastening methods, detailing, fabrication, handling, geometric imperfections, erection, acoustics, fire protection, collapse assessment, etc.)

The vibration serviceability assessment procedures on the modular steel plate floor include analytical and experimental stages. The authors have been focusing on the analytical part of the assessment process to determine a range of configurations to be fabricated and experimentally tested in a controlled laboratory environment. For the first part of experimental testing, the configurations are envisioned to consist of a single 10 ft. wide module that is one bay in length (40 ft). The configurations will include combinations of various member sizes (plate thicknesses and beam cross-sections) and beam spacings for single module assemblies (10 ft. × 40 ft). After the evaluation of experiments on single module assemblies, full bay modules (30 ft. × 40 ft) will be fabricated and tested for the second part of experimental testing. Single bay and full bay modules are depicted in Figs. 34.1 and 34.2. It is important to note that there is a 250 lbs/ft. loading on the overhang of the 30 ft. × 40 ft. specimen (Fig. 34.2) to represent the load to simulate the weight of the exterior façade on one side of the specimen.

34.2 Vibration Serviceability Assessment Per AISC Design Guide 11 Procedures

The analytical studies performed on this modular steel system have been based on the vibration serviceability assessment criterion specified in AISC Design Guide 11 [3] (hereafter referred to as DG11), and computational simulations using finite element software.

DG11 contains the most widely used floor vibration evaluation method in North America (and most parts of the world). In this method, the critical bay is idealized as a single degree of freedom (SDOF) system with the fundamental frequency and effective mass of the floor bay. The walking-induced dynamic load is simply the product of the body weight of the walking person and a curve-fit of the dynamic coefficients per Rainer et al. [4], as stated in [5]. The evaluation criterion is shown in Eq. (34.1). The vibration serviceability evaluation of an elevated floor bay is considered to be "satisfactory" if the peak acceleration, a_p, does not exceed the tolerance limit, a_o, which is 0.5%g for low-frequency floors (f_n< 9 Hz) being used as offices, residences, and quiet occupant spaces.

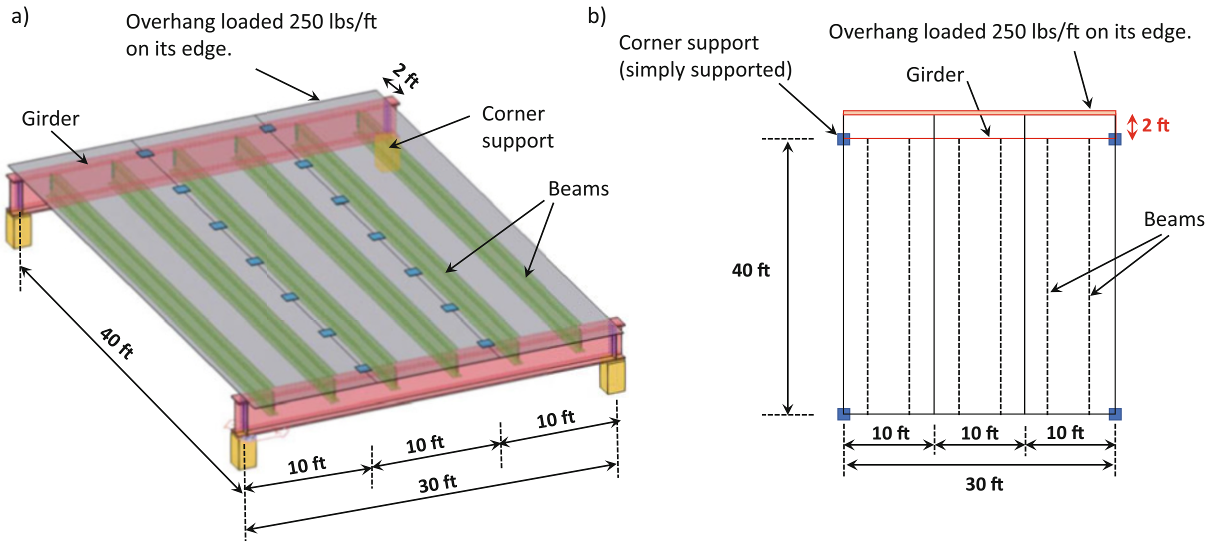

Fig. 34.2 Modular steel plate assembly – full bay specimen. (**a**) 3D view and (**b**) plan view

$$\frac{a_\mathrm{p}}{g} = \frac{P_\mathrm{o} e^{-0.35 f_n}}{\beta W} \le \frac{a_\mathrm{o}}{g} \tag{34.1}$$

where:

f_n = bay fundamental frequency, Hz
β = critical damping ratio
W = effective panel weight, lbs.

As described in [3, 5], P_o is a constant force (65 lbs. = 289.1 N) that is the product of 157 lbs. (698.4 N), part of the dynamic coefficient, and an adjustment factor, 0.5, that accounts for incomplete resonant build-up and the fact that the walker, affected occupant, or both are probably not at midbay of the floor being evaluated. The natural frequency of the bay is calculated using Eq. (34.2); yet, it is important to note that this equation underestimates the natural frequency of the bay according to Pabian et al. [6]. The authors prefer to denote f_n as $f_{n\mathrm{BG}}$ to highlight the fact that contributions from beam and girder modes are only considered for the bay frequency calculations.

$$f_{n\mathrm{BG}} = 0.18\sqrt{\frac{g}{\Delta_\mathrm{b} + \Delta_\mathrm{g}}} \tag{34.2}$$

In Eq. (34.2), Δ_b is the beam deflection while Δ_g is the girder deflection due to the weight supported at midspan, computed using the classical equation for a simply supported beam with uniform mass and flexural rigidity. Based on Eq. (34.2), the vibration response of the beam and girder are included in the natural frequency calculations while the slab component (plate in the design being evaluated) is not included. Similarly, In Eq. (34.1), the effective weight, W, is a weighted average of the effective weights from the beam bending mode and girder bending mode [5]. Again, the plate bending mode is not included in the calculations.

For the scope of analytical work presented in this paper, DG11 procedures have been used to evaluate each specimen for comparison with the acceptability criterion. There have been cases where Eq. (34.1) predicts accelerations very close to the limit (e.g., 0.5%g for quiet spaces). Considering that human perception of floor vibration is very subjective, such predictions neither indicate that the floor is unsatisfactory nor satisfactory. It is important to note that when the predicted acceleration is 0.5%g plus or minus 0.03%g, which is arbitrarily set, and when the bay did not have many complaints, the evaluation is counted as agreeing with observed acceptability. Note that a similar tolerance was used for similar prediction methods mentioned in [7, 8]. Yet, the tolerance levels are not the scope of the presented paper.

On another note, Eq. (34.2) can be written as

$$\frac{1}{{f_{n\mathrm{BG}}}^2} = \frac{1}{{f_b}^2} + \frac{1}{{f_g}^2} \tag{34.3}$$

which is known as Dunkerly's relationship.

As mentioned earlier, the effective weight of a floor system is a combination of the effective weights of the beam and girder panels. The effective weight of a panel can be written as:

$$W = wBL \tag{34.4}$$

where:

$W =$ effective panel weight, lbs.
$w =$ supported weight per unit area
$L =$ length of the panel
$B =$ effective width of the panel

The effective width of a beam (joist) panel is

$$B_\mathrm{j} = C_\mathrm{j}\left(D_\mathrm{s}/D_\mathrm{j}\right)^{1/4} L_\mathrm{j} \le \frac{2}{3}\ \text{(Building Floor Width)} \tag{34.5}$$

where B_j is the effective width of the beam panel, C_j is 2.0 for a typical bay without free edges and 1.0 for typical edge panels (with beams parallel to an interior edge, mezzanine condition), D_s is the slab element (steel plate in this configuration) transformed moment of inertia per unit width, D_j is the effective moment of inertia of the beam per unit of width, and L_j is the length of the beam.

The effective width of a girder panel is.

$$B_\mathrm{g} = C_\mathrm{g}\left(D_\mathrm{j}/D_\mathrm{g}\right)^{1/4} L_\mathrm{g} \le \frac{2}{3}\ \text{(Building Floor Length)} \tag{34.6}$$

where B_g is the effective width of the girder panel, C_g is 1.6 for girders supporting joists connected to the girder flange and 1.8 for girders supporting beams connected to the girder web, D_j is the same as previous, D_g is the effective moment of inertia of the girder per unit width, and L_g is the length of the girder.

When $B_\mathrm{j} > L_\mathrm{g}$, the mid-span girder deflection is reduced by $L_\mathrm{g} / B_\mathrm{j} \ge 0.5$, which is:

$$\Delta_\mathrm{g}{}' = \frac{L_\mathrm{g}}{B_\mathrm{j}} \Delta_\mathrm{g} \tag{34.7}$$

The effective weight for the combined mode is

$$W = \frac{\Delta_\mathrm{j}}{\Delta_\mathrm{j} + \Delta_\mathrm{g}} W_\mathrm{j} + \frac{\Delta_\mathrm{g}}{\Delta_\mathrm{j} + \Delta_\mathrm{g}} W_\mathrm{g} \tag{34.8}$$

The effective weight for the combined mode of vibration is a function of the relative stiffness of the beam or joist to the girder and the effective weight of the beam or joist panel and the girder panel, where.

$$W_\mathrm{j} = w_\mathrm{j} B_\mathrm{j} L_\mathrm{j}, \text{ the effective weight of the beam panel (also used as } W_\mathrm{b}) \tag{34.9}$$

$$W_\mathrm{g} = w_\mathrm{g} B_\mathrm{g} L_\mathrm{g}, \text{ the effective weight of the girder panel} \tag{34.10}$$

If beams, joists, or girders are continuous over their supports and an adjacent span is greater than 70% of the center span length, then the effective weight of that panel (W_j or W_g) can be increased 50% to account for continuity. Similarly, for open-web steel joist systems, when joist bottom chord extensions are installed and connected before concrete is placed, the effective weight of the joist mode can be increased by 30% [9]. Because the continuity effects are not predominantly realized when girders frame directly into columns, either shear or moment connected, this increase does not apply to such girders; yet, when the girder passes over a column top, the increase is applicable per DG11 [3].

It is important to note that the DG11 equations discussed so far were derived for traditional steel-framed floor systems with concrete decks. Considering the flexibility of the modular steel plate assembly presented herein, the plate frequency and its contribution to the overall dynamic response of the floor structure requires a closer look. The fact that the plate vibrations behavior is not included in the DG11 procedures is because the DG11 calculations were developed for standard steel-framed floor systems in which the slab element is a composite or noncomposite concrete slab spanning between beam members, which is considerably stiffer than the steel plate of the modular assembly being considered herein. The fact that the concrete slab is very stiff, it has a large fundamental frequency, which means it does not make a notable impact on the bay frequency and effective weight predictions. In the case of flexible slab elements such as the steel plate being discussed here, the effect of the plate will need to be reflected in Eq. (34.2).

Based on this, Eqs. (34.2), (34.3), and (34.8) are modified to reflect the effect of plate contribution to the overall vibration response of the assembly in Eqs. (34.11)–(34.13), respectively:

$$f_{n\mathrm{PBG}} = 0.18\sqrt{\frac{g}{\Delta_{\mathrm{p}} + \Delta_{\mathrm{b}} + \Delta_{\mathrm{g}}}} \tag{34.11}$$

$$\frac{1}{{f_{n\mathrm{PBG}}}^2} = \frac{1}{{f_{\mathrm{p}}}^2} + \frac{1}{{f_{\mathrm{b}}}^2} + \frac{1}{{f_{\mathrm{g}}}^2} \tag{34.12}$$

$$W = \frac{\Delta_{\mathrm{p}}}{\Delta_{\mathrm{p}} + \Delta_{\mathrm{j}} + \Delta_{\mathrm{g}}} W_{\mathrm{p}} + \frac{\Delta_{\mathrm{j}}}{\Delta_{\mathrm{p}} + \Delta_{\mathrm{j}} + \Delta_{\mathrm{g}}} W_{\mathrm{j}} + \frac{\Delta_{\mathrm{g}}}{\Delta_{\mathrm{p}} + \Delta_{\mathrm{j}} + \Delta_{\mathrm{g}}} W_{\mathrm{g}} \tag{34.13}$$

where:

Δ_{p} is the plate deflection due to the weight supported at midspan, and f_{p} is the plate panel frequency.

For the analytical work of the modular steel plate assemblies, the authors focused on six specimens with various beam and girder cross-sections, plate thicknesses, beam spacings, damping ratios, live loads, and superimposed dead loads. Full bay specimen properties, the results for the vibration serviceability evaluations per DG11, and preliminary finite element model analysis results are summarized in Table 34.1.

It is important to highlight that the total damping ratios listed in Table 34.1 include various components. The possible contributing sources to the overall damping ratio are from the structural system, ceiling and ductwork, office fit-out, and architectural raised access floor.

In Table 34.1, the frequency and acceleration predictions are shown for both cases (including and excluding steel plate contribution to the overall dynamic response of the floor system). $f_{n\mathrm{PBG}}$ indicates the frequency that is calculated by considering the plate, beam, and girder frequency contributions. $f_{n\mathrm{BG}}$ indicates the frequency that is calculated by considering beam and girder frequency contributions only.

It is observed that when the contributions from the plate frequency are not included in the calculations, the bay frequency is consistently higher than the case it is included ($\mathrm{fn}_{1\mathrm{BG}} = 8.70$ Hz vs. $\mathrm{fn}_{1\mathrm{PBG}} = 6.48$ Hz for Specimen 1, $\mathrm{fn}_{1\mathrm{BG}} = 8.50$ Hz vs. $\mathrm{fn}_{1\mathrm{PBG}} = 8.36$ Hz for Specimen 2, etc.)

On another note, when the contributions from the plate frequency are not included in the calculations, the predicted accelerations per DG11 (ap/g per $\mathrm{fn}_{1\mathrm{BG}}$) are very close to satisfying the 0.5%g limitation set by DG11. When the contributions from the plate frequency are included in the calculations, the predicted accelerations per DG11 (ap/g per $\mathrm{fn}_{1\mathrm{PBG}}$) are observed to be above the 0.5%g limitation set by DG11. Yet, it is important to note that when angle stiffeners (L6×4×5/16 @ 4 ft. OC) are used between the beam centerlines (Specimen 2), the ap/g value per $\mathrm{fn}_{1\mathrm{PBG}}$ (0.54%) is relatively closer to the ap/g value per $\mathrm{fn}_{1\mathrm{BG}}$ (0.51%) which are both in the vicinity of 0.50% limitation set by DG11 for offices, residences, and quiet areas.

The $\mathrm{fn}_{1\mathrm{PBG}}$ predictions are consistently lower than the $\mathrm{fn}_{1\mathrm{BG}}$ predictions, which indicates the fact that the flexibility of the plate is lowering the bay frequency. As such, when $\mathrm{fn}_{1\mathrm{PBG}}$ values are used in DG11 acceleration predictions, the results are much higher than the 0.50% limitation (e.g., 1.44 for Specimen 1; 0.99 for Specimen 3; 0.79 for Specimen 4; 1.68 for Specimen 5; and 3.03 for Specimen 6).

The authors developed finite element models for the six specimens listed in Table 34.1. The FE model natural frequency predictions for the first bending modes ($\mathrm{fn}_{1\mathrm{FE}}$) are observed to be less than the DG11 predictions (e.g., $\mathrm{fn}_{1\mathrm{BG}} = 8.70$ Hz, $\mathrm{fn}_{1\mathrm{PBG}} = 6.48$ Hz, and $\mathrm{fn}_{1\mathrm{FE}} = 5.60$ Hz for Specimen 1), except the Specimen 6 where the $\mathrm{fn}_{1\mathrm{FE}}$ value is between DG11 predictions of $\mathrm{fn}_{1\mathrm{PBG}}$ and $\mathrm{fn}_{1\mathrm{BG}}$ ($\mathrm{fn}_{1\mathrm{BG}} = 8.36$ Hz, $\mathrm{fn}_{1\mathrm{PBG}} = 4.22$ Hz, and $\mathrm{fn}_{1\mathrm{FE}} = 5.67$ Hz). FE model predictions for the

Table 34.1 Summary of vibrations serviceability evaluation per DG11 and finite element model analysis

Specimen code	SM-68-3/8	SM-68-3/8-St	SM-94-1/2	SM-68-1/2	SM-94-3/8	SM-94-1/2
Specimen number	1	2	3	4	5	6
Plan dimensions	30 ft × 40 ft	30 ft × 40 ft	30 ft × 40 ft	30 ft × 40 ft	30 ft × 40 ft	30 ft × 40 ft
Beam sections	W24×68	W24×68	W24×94	W24×68	W24×94	W24×94
Beam spacing (ft) (CL distance)	5.0	7.5	5.0	5.0	5.0	7.5
Stiffener b/w beams	NA	L6×4×5/16 @4ft	NA	NA	NA	NA
Girder sections	W33×263	W33×263	W33×263	W33×130	W33×263	W33×263
Plate thickness (in.)	3/8	3/8	1/2	1/2	3/8	1/2
Weight (psf) (w/1 girder in 30′ × 40′ bay)	35.5	37.4	45.8	37.3	40.7	45.8
Pick weight for 10′ × 40′ panel (lbs)	11565	12338	15687	13607	13645	15687
Pick weight for 10′ × 40′ panel (tons)	5.78	6.17	7.84	6.80	6.82	7.84
Total damping ratio (%)	5.0	5.0	3.8	6.0	3.7	3.5
SDL (psf)	12	12	19	5	12	12
LL (psf)	0	0	8	8	0	8
Plate Panel fn (Hz)	9.70	45.60	11.40	13.50	9.74	4.88
Beam Panel fn (Hz)	10.10	9.87	9.62	9.76	11.10	10.20
Girder Panel fn (Hz)	17.01	16.69	14.04	11.11	16.25	14.71
fn$_{1\text{PBG}}$ (Hz) (Plate + Beam + Girder)	6.48	8.36	6.51	6.44	6.68	4.22
fn$_{1\text{BG}}$ (Hz) (Beam + Girder)	8.70	8.50	7.93	7.33	9.19	8.36
ap/g (%) per fn$_{1\text{PBG}}$	*1.44*	*0.54*	*0.99*	*0.79*	*1.68*	*3.03*
ap/g (%) per fn$_{1\text{BG}}$	0.50	0.51	0.49	0.50	0.50	0.51
DG11 ap/g (%) limit for fn < 9 Hz	0.50	0.50	0.50	0.50	0.50	0.50
fn$_{1\text{FE}}$ (Hz) (Bending Mode 1)	5.60	6.82	5.49	5.09	5.89	5.67
fn$_{2\text{FE}}$ (Hz) (Bending Mode 2)	6.87	11.27	7.14	6.91	7.26	7.51
fn$_{3\text{FE}}$ (Hz) (Bending Mode 3)	9.49	19.88	10.09	9.45	9.66	10.97
fn$_{4\text{FE}}$ (Hz) (Bending Mode 4)	15.16	25.40	18.74	20.81	15.00	16.26
ap/g (%) FE-BM1 (DG11 Chap.7)	*0.685*	0.223	0.366	0.302	*0.776*	0.435

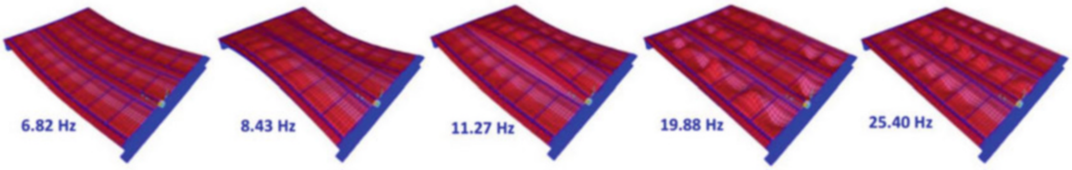

Fig. 34.3 Full bay FE model predictions for mode shapes for Specimen 2

first four bending mode frequencies are shown in Table 34.1. Exemplary FE model mode shapes for Specimen 2 are shown in Fig. 34.3.

Based on the DG11 Chapter 7 procedures (Finite Element Analysis Methods), acceleration predictions at midbay of full bay specimens are calculated per Eq. (34.14):

$$a_{\text{p}} = \text{FRF}_{\max}\alpha Q\rho \tag{34.14}$$

where:

FRF$_{\max}$ = maximum FRF magnitude at frequencies below 9 Hz.

Q = bodyweight = 168 lbs.

α = dynamic coefficient = $0.09e^{-0.075 f_n}$.

ρ = resonant build-up factor

For the first bending modes, ap/g values per fn$_{1\text{FE}}$ results exceed the 0.5%g limitation set by DG11 for Specimen 1 (0.685) and Specimen 5 (0.776). Corresponding ap/g values per fn$_{1\text{FE}}$ results for the remaining specimens are lower than the DG11 limitation; Specimen 2 (0.223), Specimen 3 (0.366), etc. One important observation made from the FE model acceleration predictions per DG11 Chapter 7 is that specimens with 1/2 in. plate thickness resulted in better acceleration responses than the specimens with 3/8 in. plate thickness. The acceleration response for the bending modes higher than the first mode will be studied as future work, using the special requirements for frequencies above 9 Hz (high-frequency floors) per DG11.

34.3 Future Work

For the first part of experimental testing, six single module assemblies (10 ft. × 40 ft) listed in Table 34.1 will be fabricated and dynamically tested in a laboratory environment. Experimental modal testing will be performed using an electrodynamic shaker and accelerometers. The shaker excitations will be applied at various locations on the specimen surfaces, and acceleration data will be collected at all critical locations. Modal frequencies and acceleration levels will be identified. Experimental results will be compared to the analytical results shown in Table 34.1. Tests will be conducted with and without architectural raised access floor (RAF) to understand their effect on the damping ratios of the modular floor system. After the evaluation of experiments on single module assemblies, full bay modules (30 ft. × 40 ft) will be fabricated, and experimental modal testing will be repeated for the second part of experimental testing.

As a continuation of the analytical studies presented in this paper, the dynamic response of the specimens to higher modes will be studied. DG11 procedures for high-frequency floors (HFF) will be followed for modes with frequencies higher than 9 Hz.

Acknowledgments This work was supported by the Charles Pankow Foundation, the MKA Foundation, the American Institute of Steel Construction, NUCOR Corporation, and Schuff Steel. Any opinions, findings and conclusions, or recommendations expressed in this material are those of the authors and do not necessarily reflect the views of the sponsors.

References

1. Murray, T.M.: Design to prevent floor vibrations. Eng. J. **12** (1975)
2. Barrett, A., Avci, O., Setareh, M., Murray, T.M.: Observations from vibration testing of in-situ structures. In: Proc., Struct. Congr. Expo. ASCE Struct. Congr., ASCE Reston, Va. (2006), pp. 1–10
3. Murray, T.M., Allen, D.E., Ungar, E.E., Davis, D.B.: Vibrations of Steel-Framed Structural Systems Due to Human Activity: Second Edition. American Institute of Steel Construction (2016)
4. Rainer, J.H., Pernica, G., Allen, D.E.: Dynamic loading and response of footbridges. Can. J. Civ. Eng. **15**, 66–71 (1988). https://doi.org/10.1139/l88-007
5. Allen, D.E., Murray, T.M.: Design criterion for vibrations due to walking. Eng. J. **30**, 117–129 (1993)
6. Pabian, S., Thomas, A., Davis, B., Murray, T.M.: Investigation of Floor Vibration Evaluation Criteria Using an Extensive Database of Floors (2013). https://doi.org/10.1061/9780784412848.216
7. Royvaran, M., Avci, O., Davis, B.: Analysis of floor vibration evaluation methods using a large database of floors framed with W-shaped members subjected to walking excitation. J. Constr. Steel Res. (2019)
8. Royvaran, M., Avci, O., Davis, B.: An overview on floor vibration serviceability evaluation methods with a large database of recorded floor data. In: Conf. Proc. Soc. Exp. Mech. Ser., 2021. https://doi.org/10.1007/978-3-030-47634-2_10
9. Avci, O.: Modal parameter variations due to joist bottom chord extension installations on laboratory footbridges. J. Perform. Constr. Facil. **29** (2015). https://doi.org/10.1061/(ASCE)CF.1943-5509.0000635